# Thermochromic solar absorber coatings with elevated transition temperature

## Anna KRAMMER

To my parents.

# Abstract

Due to their simple design and operation, solar thermal collectors for domestic hot water generation and space heating are one of the most common solar energy harvesting systems in use today. During cold periods, all the absorbed energy is useful. During hot periods, however, when solar radiation is abundant and demand is low, stagnation occurs. Storage is limited and excess heat cannot be diverted. The heat transfer fluid evaporates and the temperature of the solar absorber can exceed 200°C even in central European latitudes. Glycols in the heat transfer fluid degrade, and the frame, thermal insulation and selective absorber coating deteriorate and become less efficient.

A new generation of solar collectors is envisaged that can absorb and repel heat in a controlled manner by changing their optical properties in the infrared spectral region. Thermochromic $VO_2$ based absorber coatings change their optical properties according to temperature. Through the perfectly reversible thermochromic transition, at a critical temperature $T_C = 68$°C, the thermal emittance of the absorber changes markedly, from $\approx 0.05$ below $T_C$ to $\approx 0.35 - 0.4$ above $T_C$. In this thesis, increased transition temperatures, beneficial for solar absorber applications, are achieved by Ge doping of $VO_2$ films. For 5.9 at.% Ge doping, a $T_c \approx 96$°C is observed. Ge doping also leads to the increase of thermal emittance modulation $\Delta\varepsilon$, especially due to increased thermal emittance in the high-temperature state. Moreover, crystalline switching films are sputtered at substrate temperature as low as $\approx 310$°C.

Advanced thermochromic concepts involving Fabry-Pérot inspired multilayers with greatly enhanced thermal emittance modulation, absorbers with light-trapping black spinel nanoneedles or plasmonic W nanoparticles obtained by means of nanoimprint lithography are investigated.

For the main selective solar absorber application, the thermochromic function is successfully integrated into the multilayered coating design. First, absorbers based on $VO_2$ or $VO_2$:Ge and nanocrystalline Cu-CoMnO$_x$ black spinel layers are proposed. However, a large thermal emittance modulation of $\Delta\varepsilon > 0.3$, is accompanied by an unwelcome increase of the solar absorptance with increasing temperature. Simulations indicate that a relatively high n and k material inserted between the substrate and the thermochromic layer can revert the change in solar absorptance. The concept is adapted to industrial absorber designs and improved absorbers, based on Al//TiAlSiN//$VO_2$:Ge//$SiO_2$, with decreasing $\alpha_{sol}$ and increasing $\varepsilon_{th}$ over the thermochromic phase transition are reported for the first time.

The positive emittance and negative absorptance modulation of the absorbers limit the collector stagnation temperature by nearly 20°C, to a maximum $T_{stagnation} \approx 159$°C. This leads to a shorter duration of stagnation conditions and an overall reduction of thermal charges on the system. Glycol degradation is hindered, leading to important reductions in maintenance costs. At $T_{stagnation} \approx 150$°C and at 3 bar pressure typically present in such systems, evaporation of the heat transfer fluid in the collector loops is avoided.

Accelerated aging tests in dry and humid conditions reveal the environmental stability of the thermochromic absorber coatings and a minimum service lifetime of 25 years is guaranteed for multilayers with antireflective and oxidation barrier coatings.

# Keywords

Thin films, magnetron sputtering, thermochromics, vanadium dioxide, Ge doping, elevated transition temperature, solar absorber coating, lowered stagnation temperature, thermal emittance modulation, nanostructured absorber.

# Résumé

Les capteurs solaires thermiques pour la production d'eau chaude sanitaire et le chauffage des locaux sont l'un des systèmes de récupération d'énergie solaire les plus utilisés aujourd'hui. Pendant les périodes froides, toute l'énergie absorbée est utile. Pendant les périodes chaudes, cependant, lorsque le rayonnement solaire est abondant et la demande faible, une stagnation se produit. Le fluide caloporteur s'évapore et la température de l'absorbeur solaire peut dépasser 200°C même sous les latitudes centrales européennes. Les glycols contenus dans le fluide caloporteur se dégradent et le cadre, l'isolation thermique et le revêtement de l'absorbeur sélectif se détériorent.

Une nouvelle génération de capteurs solaires qui peut absorber et repousser la chaleur de manière contrôlée est envisagée. Les revêtements absorbants à base de $VO_2$ thermochrome changent leurs propriétés optiques en fonction de la température. Grâce à la transition thermochrome parfaitement réversible, à une température critique $T_C = 68°C$, l'émissivité thermique $\varepsilon_{th}$ de l'absorbeur change considérablement, passant de $\varepsilon_{th} \approx 0.05$ en dessous de $T_C$ à $\varepsilon_{th} \approx 0.35-0.4$ au-dessus de $T_C$. Une augmentation de la température de transition, avantageuse dans le cas des capteurs solaires, est obtenue par dopage avec du Ge. Avec 5.9 %at de Ge, une $T_C \approx 96°C$ est observée. Le dopage avec Ge conduit également à l'augmentation de la modulation de l'émissivité thermique $\Delta\varepsilon$. De plus, les films cristallins et thermochromes sont obtenus par pulvérisation cathodique avec une température de substrat relativement basse ($\approx 310°C$).

De nouveaux concepts thermochromes impliquant des multicouches inspirées d'interféromètre de type Fabry-Pérot, des absorbeurs avec des spinelles nanoaiguilles ou des nanoparticules plasmoniques de W obtenues par nano-impression, sont étudiés.

La fonction thermochrome est intégrée avec succès dans la conception du revêtement multicouche des absorbeurs solaires sélectifs. Tout d'abord, des absorbeurs basés sur $VO_2$ et $VO_2$:Ge et $CuCoMnO_x$ sont proposés. Cependant, la grande modulation de l'émittance thermique de $\Delta\varepsilon > 0.3$ observée, s'accompagne d'une augmentation indésirable de $\alpha_{sol}$. Les simulations indiquent qu'un matériau avec des indices optiques n et k relativement élevé, inséré entre le substrat et la couche thermochrome peut inverser l'augmentation de $\alpha_{sol}$. Le concept est adapté aux absorbeurs industriels TiAlSiN. Des absorbeurs, basés sur Al//TiAlSiN//$VO_2$:Ge//$SiO_2$, présentant une diminution de $\alpha_{sol}$ et une augmentation de $\varepsilon_{th}$ au cours de la transition de phase thermochrome, sont rapportés pour la première fois.

La modulation positive de $\varepsilon_{th}$ et celle négative de $\alpha_{sol}$ des absorbeurs multicouches réduisent la température de stagnation du collecteur de près de 20°C, la limitant à 159°C. Cela conduit à une durée plus courte des conditions de stagnation et à la réduction globale des charges thermiques sur le système. La dégradation du glycol est réduite, conduisant à des diminutions importantes des coûts de maintenance. À $T_{stagnation} \approx$ 150°C et à une pression de 3 bars typiquement présente dans de tels systèmes, l'évaporation du fluide caloporteur dans les boucles du collecteur est évitée.

Des tests de vieillissement accéléré dans des conditions sèches et humides révèlent la résistance aux conditions extérieures des revêtements absorbants thermochromes et une durée de vie de plus de 25 ans est attendue pour les multicouches avec des revêtements antireflet et anti-oxydation.

# Mots clés

Couches minces, pulvérisation cathodique, thermochromie, dioxyde de vanadium, dopage Ge, température de transition élevée, revêtement absorbant solaire, température de stagnation abaissée, modulation de l'émittance thermique, absorbeur nanostructuré.

# Contents

# Nomenclature

## Units

| | |
|---|---|
| ° | Degree of arc |
| °C | Celsius degree |
| A | Ampere |
| at.% | Atom percent |
| bar | Bar |
| C | Coulomb |
| eV | Electron volt |
| F | Farad |
| h | Hour |
| Hz | Hertz |
| J | Joule |
| K | Kelvin |
| kg | Kilogram |
| l | Litre |
| m | Meter |
| min | Minute |
| Pa | Pascal |
| rad | Radian |
| s | Second |
| S | Siemens |
| sccm | Standard cubic centimeters per minute |
| V | Volt |
| W | Watt |
| Ω | Ohm |

## Constants

| | | | |
|---|---|---|---|
| $c_0$ | speed of light | 299 792 458 | m/s |
| e | elementary charge | $1.6021 \cdot 10^{-19}$ | C |
| h | Planck constant | $4.13566733 \cdot 10^{-15}$ | eV·s |
| $\hbar$ | reduced Planck constant | $6.582119514 \cdot 10^{-16}$ | eV·s |
| $k_B$ | Boltzmann constant | $8.61733326 \cdot 10^{-5}$ | eV·K$^{-1}$ |
| $\pi$ | pi | 3.141 592 653 589 793 | - |
| $\sigma$ | Stefan-Boltzmann constant | $5.670\ 374\ 419... \times 10^{-8}$ | W·m$^{-2}$·K$^{-4}$ |

# Variables

| | | |
|---|---|---|
| $\alpha_{sol}$ | solar absorptance | [-] |
| $\alpha\lambda$ | spectral absorptance | [-] |
| $\varepsilon_{th}$ | thermal emittance | [-] |
| $\varepsilon\lambda$ | spectal emittance | [-] |
| $\tau\lambda$ | spectral transmittance | [-] |
| $\tau$ | transmittance | [-] |
| $\rho\lambda$ | spectral reflectance | [-] |
| $\rho$ | reflectance | [-] |
| $\lambda$ | wavelength | [m] |
| $T$ | temperature | [K] |
| $S$ | selectivity | [-] |
| $G\lambda$ | solar spectral irradiance | $[W{\cdot}m^{-2}{\cdot}m^{-1}]$ |
| $G_{sol}$ | solar irradiation | $[W{\cdot}m^{-2}]$ |
| $E_b$ | spectral irradiance of a blackbody | $[W{\cdot}m^{-2}{\cdot}m^{-1}]$ |
| $\alpha_{coeff}$ | absorption coefficient | $[m^{-1}]$ |
| $\rho_{DC}$ | electrical resistivity | $[\Omega{\cdot}m]$ |
| $\Psi$ | relative ellipsometric amplitude change | [-] |
| $\Delta$ | relative ellipsometric phase difference | [-] |
| $r_p, r_s$ | complex reflection coefficients for p-/s-polarized light | [-] |
| $|r_p|, |r_s|$ | amplitude diminution for p-/s-polarized light | [-] |
| $\delta_P, \delta_S$ | phase changes for p-/s- components | [-] |
| $N$ | complex refractive index | [-] |
| $\varepsilon$ | complex dielectric permittivity | $[F{\cdot}m^{-1}]$ |
| $n$ | real refractive index | [-] |
| $k$ | extinction coefficient | [-] |
| $R$ | electrical resistance | $[\Omega]$ |
| $\Theta$ | angle of incidence | [°] |
| $K$ | shape factor | [-] |
| $I_t$ | tunnelling current | [A] |
| $\Phi$ | work function | [eV] |
| $\psi_n$ | Schrödinger wave function | [-] |
| $U$ | potential energy | [eV] |
| $E_B$, B.E. | binding energy | [eV] |
| $E_{kin}$, K.E. | kinetic energy | [eV] |
| $E_F$ | Fermi energy, Fermi level | [eV] |
| $h_{rad}$ | radiative heat transfer coefficient | $[W{\cdot}m^{-2}{\cdot}K^{-1}]$ |
| $h_{conv}$ | convective heat transfer coefficient | $[W{\cdot}m^{-2}{\cdot}K^{-1}]$ |
| $C_p$ | specific heat capacity | $[J{\cdot}kg^{-1}{\cdot}K^{-1}]$ |
| $q_{gen}$ | generated heat | $[W{\cdot}m^{-2}]$ |
| $q_{in}, q_{out}$ | inlet, outlet heat flux | $[W{\cdot}m^{-2}]$ |
| $\eta_p, \eta_s$ | tilted optical admittance for p- and s-components | [-] |
| $k$ | thermal conductivity | $[W{\cdot}m^{-1}{\cdot}K^{-1}]$ |
| $\eta$ | efficiency | [-] |
| $E$ | electric field strength | $[V{\cdot}m^{-1}]$ |
| $H$ | magnetic field strength | $[A{\cdot}m^{-1}]$ |
| $\eta$ | optical admittance in free space | [S] |
| $\nu$ | frequency | [Hz] |

# Chemical elements

| | |
|---|---|
| Ag | Silver |
| Al | Aluminum |
| Ar | Argon |
| Au | Gold |
| Ba | Barium |
| Bi | Bismuth |
| Ca | Calcium |
| Co | Cobalt |
| Cr | Chromium |
| Cu | Copper |
| F | Fluorine |
| Fe | Iron |
| Ga | Gallium |
| Ge | Germanium |
| H | Hydrogen |
| He | Helium |
| La | Lanthanum |
| Mg | Magnesium |
| Mn | Manganese |
| Mo | Molybdenum |
| N | Nitrogen |
| Nb | Niobium |
| Nd | Neodymium |
| Ni | Nickel |
| O | Oxygen |
| Pr | Praseodymium |
| Re | Rhenium |
| Si | Silicon |
| Sm | Samarium |
| Sr | Strontium |
| Ta | Tantalum |
| Ti | Titanium |
| V | Vanadium |
| W | Tungsten |
| Zn | Zinc |

# Acronyms and abbreviations

| | |
|---|---|
| AC | Alternating Current |
| AFM | Atomic Force Microscopy |
| AM1.5G | Reference Solar Spectral Irradiance at Air Mass 1.5 (ASTM G-173-03) |
| BSE | Backscattered Electron |
| CAE | Constant Analyzer Energy |

| | |
|---|---|
| c-DMFT | Cluster-Dynamical Mean-Field Theory |
| CHA | Concentric Hemispherical Analyser |
| CIME | Center for Electron Microscopy |
| cos | cosine of an angle |
| CRR | Constant Retardation Ratio |
| CSP | Concentrated Solar Power |
| DC | Direct Current |
| DCMS | Direct Current Magnetron Sputtering |
| DFT | Density Functional Theory |
| DHW | Domestic Hot Water System |
| DMFT | Dynamical Mean-Field Theory |
| DOS | Density Of States |
| e.g. | *exempli gratia* in Latin, "for example" |
| EDX | Energy Dispersive X-ray Analysis |
| $E_g$, $E_G$ | Band Gap |
| EPFL | École Polytechnique Fédérale de Lausanne |
| ESCA | Electron Spectroscopy for Chemical Analysis |
| FFT | Fast Fourier Transform |
| FTIR | Fourier-Transform InfraRed spectroscopy |
| FWHM | Full-Width at Half-Maximum |
| GGA | Generalized Gradient Approximation |
| GIXRD | Grazing Incidence X-ray Diffraction |
| HiPIMS | High-Power Impulse Magnetron Sputtering |
| IBA | Ion Beam Analysis |
| ICDD | International Center Diffracion Data |
| ICP-OES | Inductively Coupled Plasma Optical Emission Spectrometry |
| IEA-SHC | International Energy Agency. Solar Heating and Cooling Programme |
| IR | Thermal infrared range of the electromagnetic spectrum (0.8 - 50 μm) |
| ISO | International Organization for Standardization |
| $LCoH_{sol}$ | Levelized Cost of Solar Heat |
| LDA | Local Density Approximation |
| LESO-PB | Solar Energy and Building Physics Laboratory |
| LSMO | $La_{1-x}Sr_xMnO_3$ |
| MBE | Molecular Beam Epitaxy |
| MCT | Mercury-Cadmium-Telluried |
| MF | Medium Frequency |
| MIR | Middle infrared range of the electromagnetic spectrum (2.5 - 20 μm) |
| MIT | Metal-to-Insulator Transition |
| MOCVD | Metal Organic Chemical Vapour Deposition |
| MS | Magnetron Sputtering |
| NIL | Nanoimprint Lithography |
| NIR | Near infrared range of the electromagnetic spectrum (780-2500 nm) |
| NIST | National Institute of Standards and Technology |
| NN | Nanoneedle |
| NP | Nanoparticle |

p-DC          Bipolar-pulsed Direct Current
p-DCMS        Bipolar-pulsed Direct Current Magnetron Sputtering
PDF           Powder Diffraction File
PE            Pass Energy
PID           Proportional Integral Derivative
PLD           Pulsed Laser Deposition
$p(O_2)$      Oxygen partial pressure
RBS           Rutherford Backscattering Spectrometry
RF            Radio-Frequency
SE            Secondary Electron
SEA           Spectroscopic Ellipsometry Analyzer software
SEM           Scanning Electron Microscopy
SFOE          Swiss Federale Office of Energy
sin           sine of an angle
SolCoSi       Solar Collector Simulator
STM           Scanning Tunneling Microscopy
STS           Scanning Tunneling Spectroscopy
$T_{amb}$     Ambient temperature
tan           tangent of an angle
$T_c$         Transition temperature during cooling
$T_C$         Critical transition temperature
TC            Thermochromic Collector
$T_h$         Transition temperature during heating
$T_{in}$      Inlet fluid temperature
$T_{MIT}$     Metal-to-Insulator Transition temperature
$T_{stagnation}$  Collector tagnation temperature
$T_t$         Transition temperature
UED           Ultrafast Electron Diffraction
UPS           Ultraviolet Photoelectron Spectroscopy
UV            Ultraviolet
VB            Valence Band Edge
VIS           Visible range of the electromagnetic spectrum (380-780 nm)
VTIP          Vanadium oxytriisopropoxide
WD            Working Distance (SEM)
XPS           X-ray Photoelectron Spectroscopy
XRD           X-ray Diffraction

# Chapter 1    Introduction

This thesis aims at developing new solar absorber coatings with temperature dependent optical response, suitable for the prevention of overheating in solar thermal installations. The switchable multi-layered absorber is based on thermochromic vanadium dioxide thin film and is deposited by a physical vapor deposition method, magnetron sputtering. A particular Metal-to-Insulator Transition (MIT) of the vanadium dioxide and the consequent changes in its optical properties occurring at 68° C makes this oxide promising for standard flat-plate solar thermal collectors and the subject of the present thesis.

The research has been carried out in the framework of a long-term mandate from the Swiss Federal Office of Energy, in the Solar Energy and Building Physics Laboratory of the École Polytechnique Fédérale de Lausanne.

## 1.1    Context

As governments around the world grapple with the unequivocal evidence for climate change, ambitious policies targeting the energy transition to renewables and the consequent reduction in greenhouse gases (GHG) are implemented worldwide. At the heart of Swiss climate policy is the CO2 Act which stipulates a reduction of GHG by at least 20% from their 1990 levels, by 2020 and another 50-80% reduction by 2050 [FOEN, 2019]. The greater use of renewables is also spurred by the binding Federal Energy Act, with renewable energy targets formulated in the Energy Strategy 2050.

At present, about a third of the $CO_2$ emissions and approximately 50% of Switzerland's primary energy demand are attributable to buildings with 30% used for heating, air-conditioning and hot water, 14% for electricity and around 6% for construction and maintenance [SFOE, 2019]. Therefore, for the targets of the Swiss climate strategy to be met, buildings should be at the forefront of renewable transition and energy efficiency.

In the Swiss residential sector in particular, by far the largest energy consumption is attributed to space heating, with over two-thirds of the energy share (67.5%), followed by domestic hot water (13.7%). Although these are typically the applications that solar thermal technologies are well suited for, only about 10% of the heat is produced from renewables, and specifically solar thermal provided only 0.4 % of the space heating and 4.7 % of the water heating energy needs of Swiss households in 2017 [Kemmler, 2018].

While their growth has slowed down since 2014 mostly due to policy support in favour of solar photovoltaic (PV) panels, globally, solar thermal systems still rank in the top three renewable sources driving the energy transition with a cumulative solar thermal capacity of 480 $GW_{th}$ reached in 2018 (Figure 1.1). Also in 2018, strong growth rates reported in 10 out of the 20 largest solar thermal markets worldwide point to a turnaround in the solar thermal sector, a trend that is expected to continue [IEA-SHC, 2019].
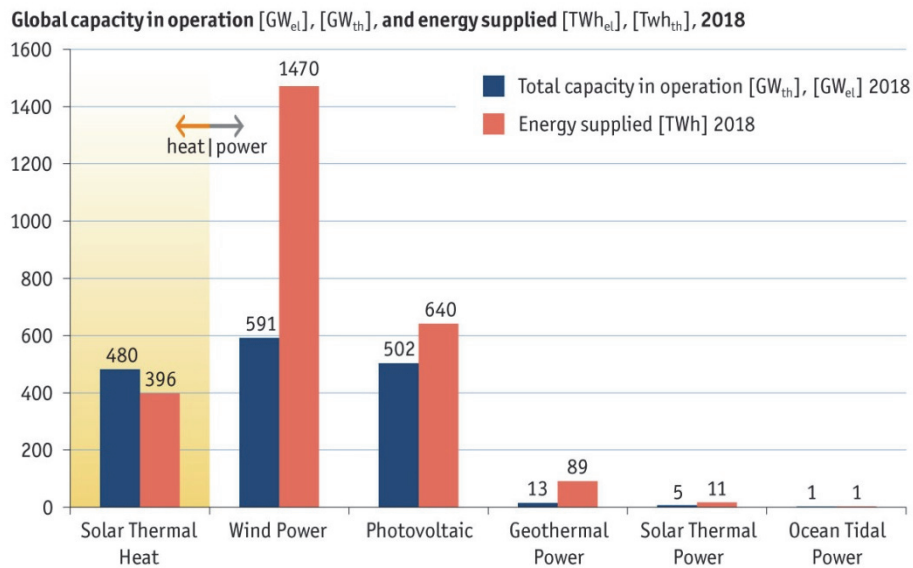
Figure 1.1. Global capacity in operation and annual energy yields of the main renewable technologies in 2018. Source: Solar Heat Worldwide 2019 [IEA-SHC, 2019].

Most widespread solar thermal systems, representing more than 90% of worldwide annual installations, are the small-scale systems for domestic hot water (DHW) and to some extent solar-combi systems for water and space heating in single or multi-family houses, hotels or public buildings. Recently, due to their favorable economics, large-scale solar thermal plants connected to district heating systems (Figure 1.2) have been expanding, with Denmark leading by far in number of installed systems. Another sector where solar thermal is rapidly gaining ground is in low-temperature industrial applications, such as foods and beverages, textiles, agriculture or chemicals.



Figure 1.2. A 14.1 $MW_{th}$ district heating plant with 20,125 $m^2$ installed collector area in Jelling Varmeværk, Denmark. Source: [Savosolar Oyj, 2019].

## 1.2     State of the art of solar thermal collectors

### 1.2.1  Solar thermal technologies

A solar thermal collector is a heat exchanger, which collects and/or concentrates the incoming solar radiation onto an absorber surface, transforms it into heat and conveys it to a heat transfer fluid (air, water or oil) that flows through the collector. Generally solar thermal collectors are divided in two main categories: stationary, non-concentrating and tracking, concentrating collectors. The former includes:

- flat plate collectors,

- evacuated tube collectors,

while the most prevalent of the latter category are:

- linear Fresnel collectors and

- parabolic trough collectors.

Point focus collectors such as parabolic dish or heliostat field collectors for very high temperature solar thermal power applications are not considered here. For an exhaustive review on various types of solar thermal collectors the reader is referred to [Kalogirou, 2004; Suman, 2015]. The collector types listed herein differ in their operating temperature ranges, making them suitable for different applications (Figure 1.3).
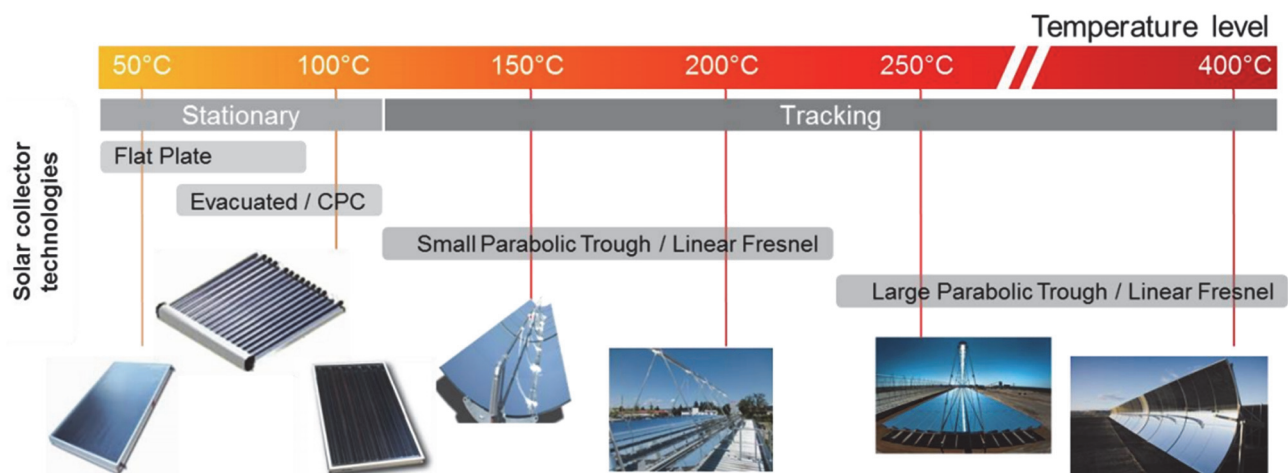


Figure 1.3. Stationary and tracking solar collector technologies with their corresponding operating temperature ranges. Source: IEA SHC Task 49 [IEA-SHC, 2016].

The overwhelming majority of installed solar thermal collectors are non-concentrating collectors with a fixed orientation and inclination, mostly employed for domestic hot water generation. A typical solar thermal water heating system (Figure 1.4) consists of:

- the collector absorbing the solar radiation;
- a storage tank with a heat exchanger in closed-loop systems;
- a back-up heater for when the solar radiation is insufficient;
- an expansion vessel or a drainback tank for when the heat transfer is limited or interrupted;
- the pipework with the pumps and valves, and
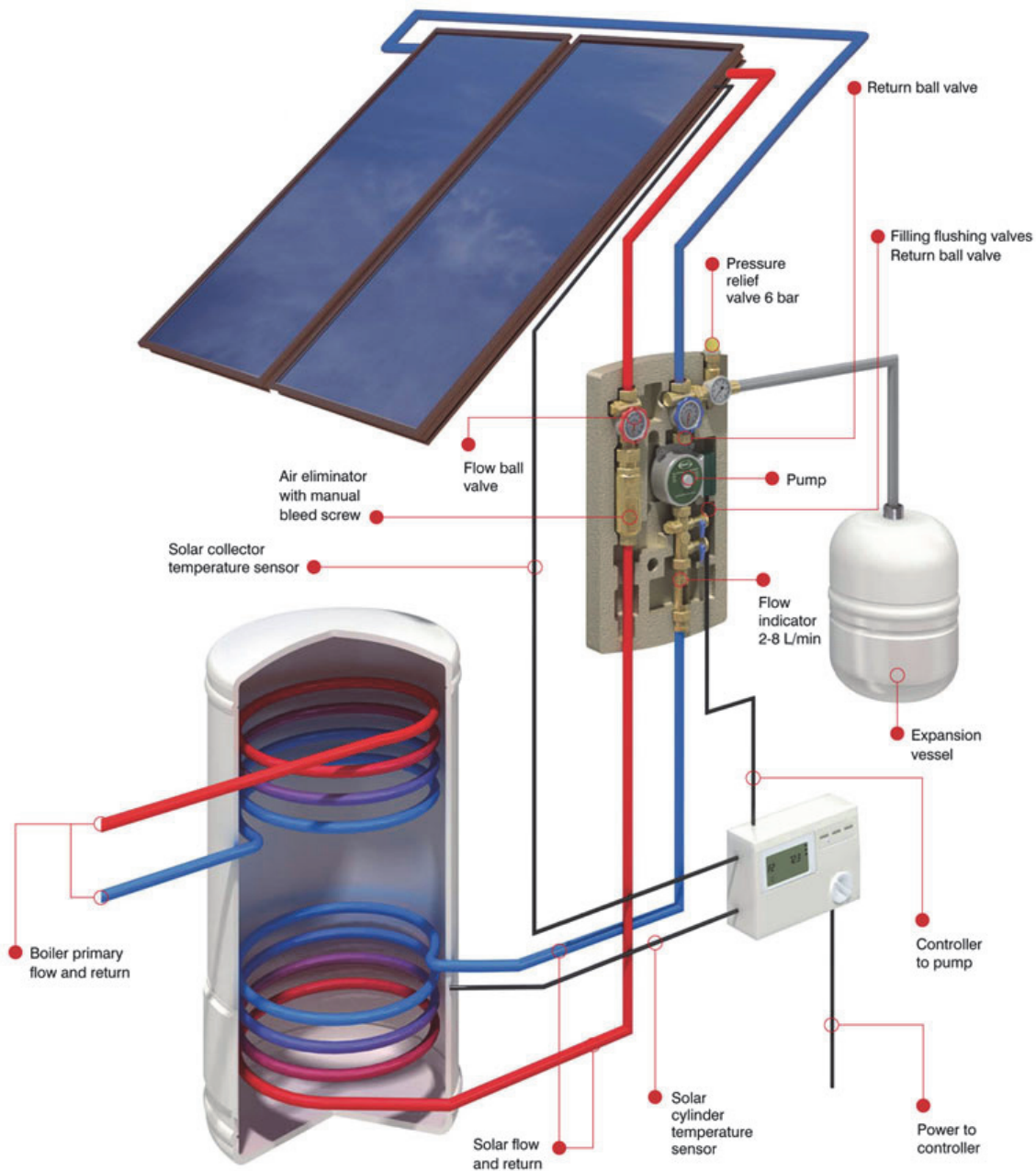
- a monitoring system.



Figure 1.4. Typical solar water heating system. Source: [Grant, 2019]

Closed-loop systems are standard in regions where temperatures drop below freezing. As the heat transfer fluid circulating through the collector must be a non-freezing liquid, usually a water-glycol mixture, the heat is transferred to the sanitary water supply via a heat exchanger.

As for the employed collector, in Europe flat plate collectors dominate with more than 80% share of the total installed capacity, therefore it is the one described in detail here. A flat plate collector is a rectangular aluminum frame with a transparent glass cover which houses the absorber, the pipes bonded to the absorber plate and the insulation (Figure 1.5). The glass is usually a low iron glazing with high transmittance and minimized reflectance. The piping where the heat transfer fluid is circulating is comprised of meander/serpentine or harp shaped copper risers and header.
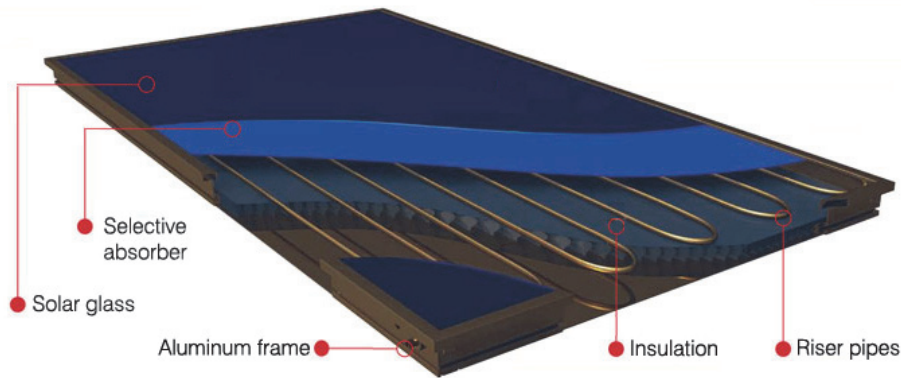
Figure 1.5. Main elements of a flat plate solar collector. Source: [Grant, 2019]

The heat conduction occurs within a rather narrow area along the welding seam between the copper pipes and absorber plate. Generally, high quality solar collectors reach efficiencies of above 70%, but new multi-channel absorber profiles (Figure 1.6), with increased heat transfer area between the absorbing surface and the heat transfer fluid, can lead to a further 4 to 10 percentage points increase in thermal conversion efficiency [VTT, 2017].
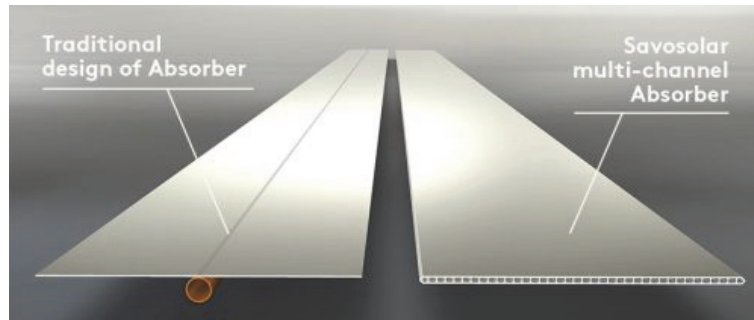


Figure 1.6. Traditional absorber design versus an extruded aluminum multi-channel absorber with increased heat transfer area. Source: [Savosolar Oyj, 2019].

Collector efficiencies depend on the absorption of a high fraction of the incident solar radiation and the successful limitation of the thermal losses due to conduction, convection and radiation. Detailed evaluation of collector performance and efficiency, taking into account conduction, convection and collector geometry, is given elsewhere [Duffie and Beckman, 1980]. For a simplified approach, the collector efficiency η can be expressed as a function of the optical properties of the absorber and the transparent glass cover:

$$\eta = \tau_{\text{glass}}\alpha_{\text{sol}} - \varepsilon_{\text{th}}\sigma\Delta T^4/G_{\text{sol}}, \hspace{3cm} \text{Equation 1.1}$$

where $\tau_{\text{glass}}$ [-] is the transmittance of the glass cover, $\alpha_{\text{sol}}$ [-] is the solar absorptance of the absorber, $\varepsilon_{\text{th}}$ [-] is the thermal emittance of the absorber, $\sigma$ [W·m$^{-2}$·K$^{-4}$] is the Stefan-Boltzmann constant, $\Delta T$ [K] is the effective temperature difference for radiative exchange and $G_{\text{sol}}$ [W·m$^{-2}$] is the incident solar radiation (or solar irradiation) [Hutchins, 2003]. It is then apparent that the efficiency is greatly dependent on the temperature, decreasing exponentially with increasing temperatures, and on the optical properties of the absorber.

## 1.2.2 Solar selective absorbers

The absorber is the key element of any solar collector responsible for the efficient conversion and control of the solar and thermal radiation. The absorber should have a high absorptance $\alpha_{sol}$ over the solar spectrum (0.3 – 2.5 µm), while also warranting a low thermal emittance $\varepsilon_{th}$, to reduce the radiative losses over the thermal infrared spectrum (2.5 – 25 µm). This behavior is called spectral selectivity and it can be achieved by depositing a short-wavelength absorbing, but infrared transmitting thin film coating on top of an infrared-reflective metal sheet - usually aluminum or copper due to their good thermal conductivity. The absorber surface is then black to the incoming solar radiation, but it is a mirror in the infrared spectral region of a blackbody of the same temperature as the absorber. Hence, the behavior of an ideal absorber is described by a step-function, changing reflectance from 0, over the solar spectrum, to 100 at the 2.5 µm limit. The spectral reflectance curve of an ideal selective absorber, along with the reference standard solar spectrum at the Earth's surface (AM 1.5G) and the normalized intensity distribution of a blackbody at 100°C are displayed in Figure 1.7.
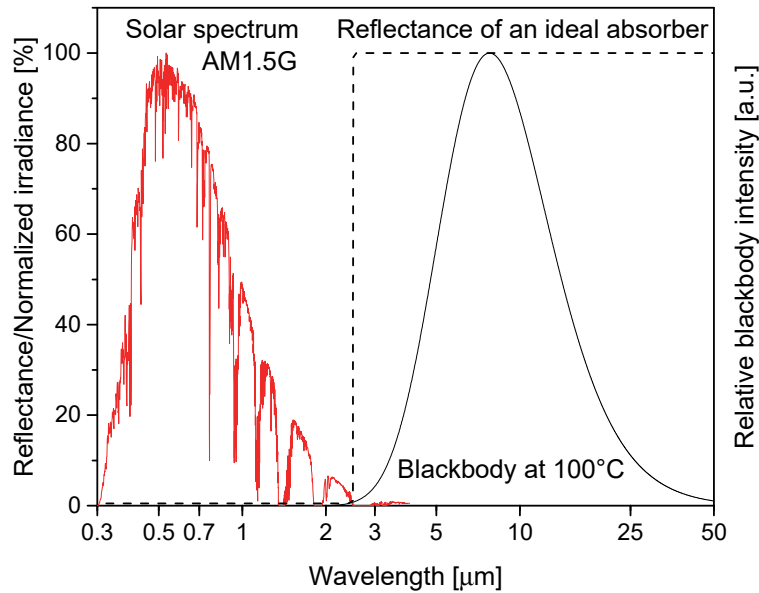


Figure 1.7. Spectral reflectance of an ideal selective absorber, the normalized standard solar radiation at the Earth's surface (AM 1.5G) and the normalized radiation distribution of a blackbody at 100°C.

The solar absorptance $\alpha_{sol}$ is the ratio between the absorbed and the incident radiation and is defined as:

$$\alpha_{sol} = \frac{\int_{\lambda_1}^{\lambda_2} \alpha_\lambda G(\lambda) d\lambda}{\int_{\lambda_1}^{\lambda_2} G(\lambda) d\lambda} \text{ [-]},$$

Equation 1.2

where $G_\lambda$ is the incident solar irradiance, $\alpha_\lambda$ is the spectral absorptance of the material and $\lambda_1$ and $\lambda_2$ are the lower and the higher wavelength limits of the spectral distribution. According to the international standard for solar absorbers (ISO 22975-3), the solar absorptance is determined between $\lambda_1$ = 0.30 µm and $\lambda_2$ = 2.5 µm spectral range. The spectral absorptance values, $\alpha_\lambda$ are calculated from the measured hemispherical spectral reflectance, $\rho_\lambda$ according to:

$$\alpha_\lambda = 1 - \rho_\lambda.$$

Equation 1.3

For opaque materials the spectral emittance, $\varepsilon_\lambda$ can be expressed in terms of spectral absorptance, $\alpha_\lambda$ using Kirchhoff's law:

$$\alpha_\lambda = \varepsilon_\lambda. \qquad\qquad \text{Equation 1.4}$$

The thermal emittance of the absorber, $\varepsilon_{th}$ is determined by weighting the spectral emittance with the Planck spectral distribution, $E_b(\lambda)$ of a blackbody at the operating absolute temperature T = 373 K.

$$\varepsilon_{th} = \frac{\int_{\lambda_1'}^{\lambda_2'} \varepsilon_\lambda E_b(\lambda) d\lambda}{\int_{\lambda_1'}^{\lambda_2'} E_b(\lambda) d\lambda} \ [\text{-}]. \qquad\qquad \text{Equation 1.5}$$

According to the standard, the relevant range is $\lambda_1' = 2.5$ µm to $\lambda_2' = 50$ µm. Generally, spectral emittance data are only available up to lower wavelengths, e.g. 20 µm, and the assumption of constant $\varepsilon_\lambda$ between the highest measured wavelength and 50 µm is accepted.

The blackbody emission at a temperature T is given by Planck's law:

$$E_b(\lambda) = \frac{8\pi hc^2}{\lambda^5} \left( \frac{1}{e^{hc/k_B \lambda T} - 1} \right) \left[ \frac{W}{m^2 \cdot m} \right], \qquad\qquad \text{Equation 1.6}$$

where h is the Planck constant, c is the speed of light and $k_B$ is the Boltzmann constant. The wavelength where the emission spectrum has a maximum, $\lambda_{max}$ is given by Wien's law:

$$\lambda_{max} T = 2897.8 \ [\text{µm} \cdot \text{K}]. \qquad\qquad \text{Equation 1.7}$$

The solar spectrum reaches its maximum around 0.55 µm and the blackbody emittance of an absorber, at the normal operating temperature of around 100°C, peaks at 7.8 µm. Therefore, the solar absorptance and thermal emittance of selective solar absorber at these specific wavelengths is of particular interest.

Finally, we define the absorber selectivity, S as the ratio of solar absorptance, $\alpha_{sol}$ and thermal emittance, $\varepsilon_{th}$:

$$S = \frac{\alpha_{sol}}{\varepsilon_{th}}. \qquad\qquad \text{Equation 1.8}$$

Modern selective solar absorbers readily achieve $\alpha_{sol} > 0.95$ and $\varepsilon_{th} < 0.1$ or even $\varepsilon_{th} < 0.05$ and typical selectivity values vary between 12 and 20.

Today, highly selective solar absorber coatings are commonly deposited by sputtering and are usually metal-dielectric composites or metal-nitrides/oxynitrides (e.g. $Ni:SiO_2$, $TiNO_x$, TiAlSiN etc.) thin film stacks with graded refracting index – increasing towards the metal substate. For a comprehensive review on various solar selective coatings with reported deposition methods and $\alpha_{sol}$, $\varepsilon_{th}$ and S values, the reader is directed to [Feng, 2014; Suman, 2015; Ibrahim, 2018].

## 1.2.3  Stagnation and overheating

Highly selective absorber coatings, albeit ensuring high collector efficiencies, also lead to elevated stagnation temperatures in the collector. Stagnation occurs when the flow of the heat transfer fluid in the collector is interrupted, while still being exposed to strong solar irradiation. Such situations can occur due to power failures, pump failure, servicing or simply due to a lack of hot water demand e.g. during holiday times. If no more heat is drawn from the collector but solar radiation is further absorbed, the collector heats up until the conductive, convective and radiative heat losses equal the absorbed solar radiation and thermal equilibrium is achieved. The stagnation temperature is then the highest temperature reached by the collector. It is dependent on the environmental conditions, with higher insolation leading to higher

stagnation temperatures. Commonly, flat-plate solar collectors reach stagnation temperatures of 180° - 200° C. In this temperature range, overheating of the collector occurs.

Overheating is one of the major lasting problems of traditional solar collectors with highly selective absorbers. Even in central European latitudes, when the solar radiation is abundant and the heat demand is low, overheating of the collector occurs several times per year. Without measures for stagnation handling and overheating prevention, the system can reach temperatures of 200° C or higher. At such temperatures, the collector loop components such as sealing, insulation and even the absorber itself can be critically damaged. Additionally, the evaporation of the heat transfer fluid might occur, generating stresses in the collector. The dependence of the evaporation temperature of propylene glycol – water mixtures on the system pressure is displayed in Figure 1.8.a [IEA SHC Task 49, 2015] Depending on the type of solar thermal system, large expansion vessels and pressure controlled safety valves are designed to absorb or release the excess of generated vapor. The former complicates the design, the latter leads to the loss of the heat transfer fluid, thus additional maintenance: both increase the costs. Finally, there is the issue of thermal cracking and decomposition of glycols. Glycols are commonly added to water to prevent the freezing of the the heat transfer medium. Increasing the glycol concentrations lowers the freezing temperature (Figure 1.8.b). However, glycols being organic compounds are sensitive to elevated temperatures. Sustained exposure at temperatures above 140° C induces a premature aging of the heat transfer fluid that is indicated by a darkening of the fluid. Between 140° - 160°C, thermal cracking and decomposition of most glycols starts. Even solid residue formation might occur, posing the risk of blocking the pipes. For the long-term, reliable and low-maintenance operation of solar thermal systems, the stagnation temperature and the stagnation loads of the collector should be limited.
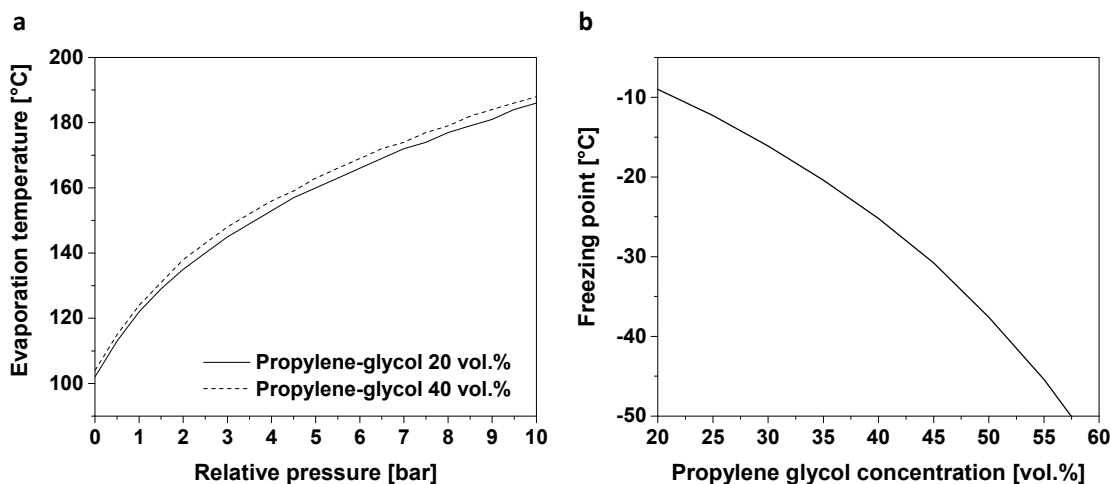


Figure 1.8. Frost protection as function of the propylene glycol concentration in the heat transfer fluid. Data from Tyfocor® Technical Information sheet. Pressure dependence of the evaporation temperatures of propylene glycol – water mixtures of different concentrations. Data from [IEA SHC Task 49, 2015].

Maintenance costs in particular, significantly increase the overall cost of delivered solar heat and, therefore, hinder the cost-efficiency and attractiveness of solar thermal installations. The International Energy Agency (IEA) Solar Heating & Cooling Programme (SHC) Task 54 investigated the maintenance costs specifically due to overheating. Maintentance costs were determined for a reference standard domestic hot water system (DHW) with flat plate collector, a "general" optimized system where typical stagnation loads and vaporization of the heat transfer fluid are avoided and for a "heat pipe" system with temperature limitation and additional advantages considered such as less heat transfer fluid and easier replacement.

It was found that by limiting the stagnation temperature and avoiding the evaporation of the heat transfer fluid, the overall maintenance costs can be halved (from 77 €/year calculated for the reference system to 39 €/year for a general system with temperature limitation and to even less for heat pipe collector). Maintaining the heat transfer fluid is by far the most relevant cost driver followed by the investment costs of the expansion vessels. The share of the Levelized Cost of Solar Heat (LCoH$_{sol,fin}$) attributed to maintenance is also roughly halved (Figure 1.9).
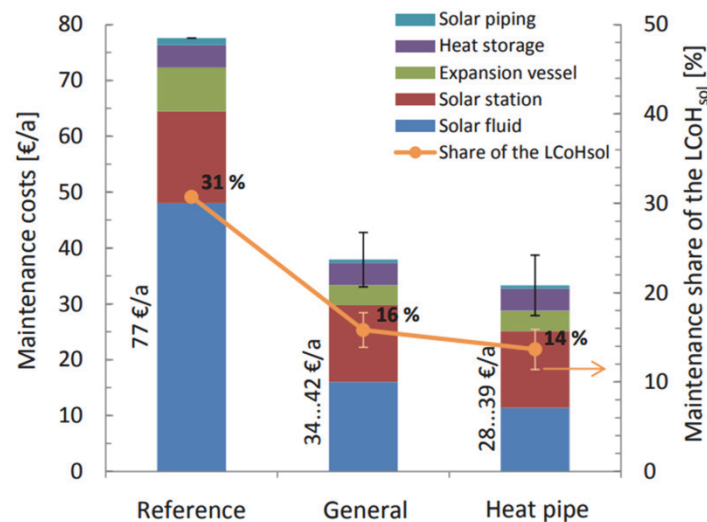
Figure 1.9. Annual maintenance costs of a reference system versus two alternative, optimized systems: a general system, where the vaporization of the heat transfer fluid is avoided, and a heat pipe system, with temperature limitation (through the decoupling of the absorber plate and the solar circuit fluid) and less solar fluid needed. The corresponding share of the Levelized Cost of Heat (LCoH$_{sol,fin}$) is also shown. Source: [IEA SHC Task 54, 2018].

## 1.2.4 Overheating prevention

As stagnation conditions are common, stagnation handling measures are widespread. Conventional small-scale solar thermal systems for domestic applications are often equipped with relatively large and costly expansion vessels, able to absorb the expansion of the heat transfer fluid and the volume of evaporated fluid. Furthermore, when defined critical pressure levels are reached, safety valves are actuated in order to release the vaporized solar fluid. This leads to a partial emptying of the system and, thus, increases maintenance costs. Nonetheless, these measures are only adopted to cope with the heated and vaporized heat transfer medium. Overheating of the collector is not prevented.

To effectively prevent overheating, the efficiency of solar collectors should decrease once a maximum allowed temperature is reached (Figure 1.10). The maximum allowed temperature is usually limited to a temperature below the evaporation temperature of the heat transfer fluid, at the pressure present in the system. For a safe and durable operation, ideally, this upper temperature limit should be set at ~95°C, just below the evaporation temperature of water and safely below the evaporation temperature of glycol-water mixtures. Then, the lifetime of the solar fluid can be significantly extended and by avoiding the consequent pressure loads the mechanical stresses in the collector are avoided.
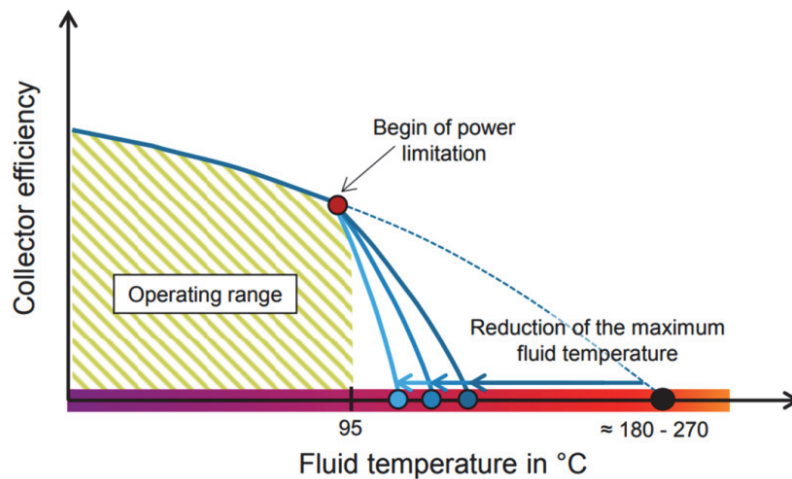
Figure 1.10. Characteristic efficiency curves of a standard collector and collectors with overheating prevention. By curbing the collector efficiency via active cooling technologies/increase of thermal losses/decrease of heat transfer rate, high collector temperatures and consequent pressure loads in the collector loop can be avoided. Source: [IEA SHC Task 54, 2018].

For overheating prevention, several approaches based on additional cooling systems or collector draining strategies are pursued. Usually these methods increase the costs and design complexity as they require complex hydraulic systems and control technologies. In the case of active cooling systems such as water-water plate heat exchanger or fan-driven water-to-air heat exchanger, the high demand of resources (cooling water, electricity) constitutes further disadvantages [IEA SHC Task 49, 2015]. In a drain-back collector system, the heat transfer fluid is drained from the collector at a pre-defined temperature or whenever the pump is stopped. Then, evaporation and ageing of the fluid is avoided, but the collector itself is still exposed to high temperatures.

Approaches for overheating prevention directly in the collector are also available:

- Solar thermal collectors with heat pipes designed to limit the temperature loads by exploiting the dry-out limit.
- High performance collectors with dual closed loop heat pipe system.
- Use of thermochromic absorber coatings with temperature dependent optical properties.

Heat pipe collectors

The efficient use of heat pipes for temperature limitation in flat-plate collectors has been demonstrated on prototype collectors [Jack, 2014; Schiebler, 2018]. By placing heat pipes in between, a thermal decoupling of the absorber plate and solar circuit fluid is achieved (Figure 1.11.a). In such an aluminum heat pipe prototype collector, the maximal measured stagnation temperature at the manifold was 140°C, whereas the absorber plate reached typical stagnation temperatures. [Jack, 2014]

Solar irradiation leads to the evaporation of the heat transfer fluid which then reverts to its liquid state inside the condenser, where the absorbed heat is transferred to the domestic hot water circuit and it flows back to the evaporator area of the heat pipe. Above a certain temperature the condensation is interrupted, the heat transfer by two-phase flow (liquid-saturated vapour) inside the heat pipe is surpressed and the so called "dry-out" begins. After further heating, all the remaining liquid evaporates and the heat transfer to the condenser is interrupted (Figure 1.11.b).
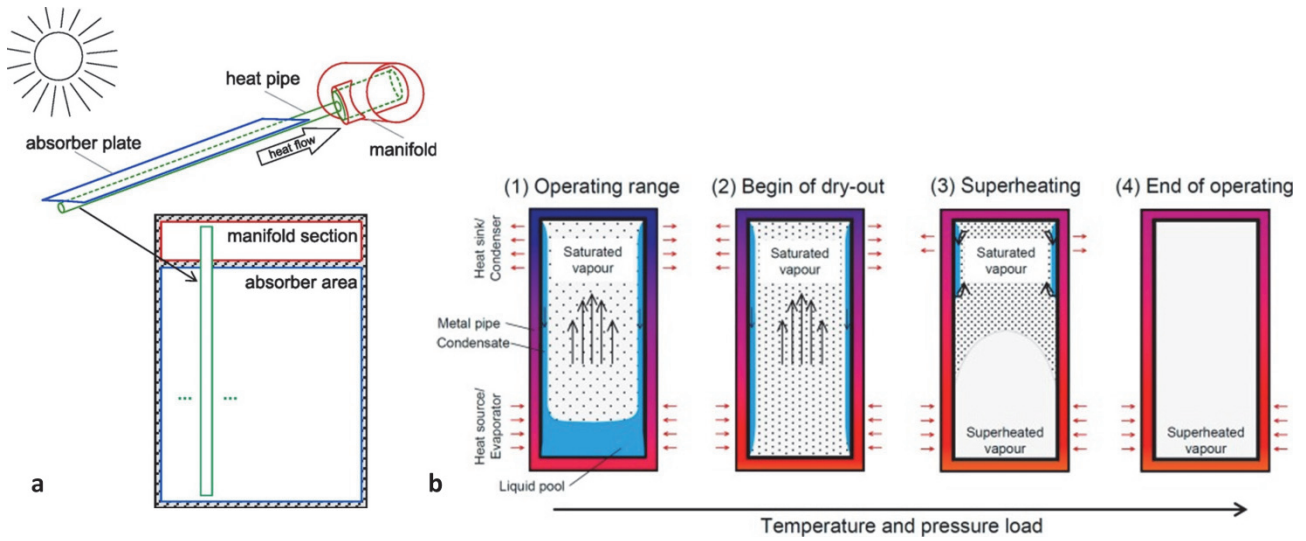
Figure 1.11.  a) Schematic drawing of a flat plate heat pipe solar collector. b) Operating stages of collector heat pipes: (1) transfer by two-phase flow, (2) dry-out limit, (3) superheating of the vapour, (4) end of operating. [Schiebler, 2018]

Based on the same principle of self-regulating heat pipes, dry-connected inside the collector heat exchanger, vacuum tube collectors with temperature dependent shutdown are commercialized by Viessmann (Vitosol 200-TM, Vitosol 300-TM) [Viessmann, 2019].

Collector with transparent honeycomb insulation and overheating protection

Dual loop heat pipe systems constitute another state-of-the-art solution for overheating prevention. A highly efficient collector is achieved by using a transparent honeycomb polymer insulation, which reduces considerably the convection related thermal losses. Additionally, it also provides resistance to infrared back-radiation from the absorber surface. (Figure 1.12.a)
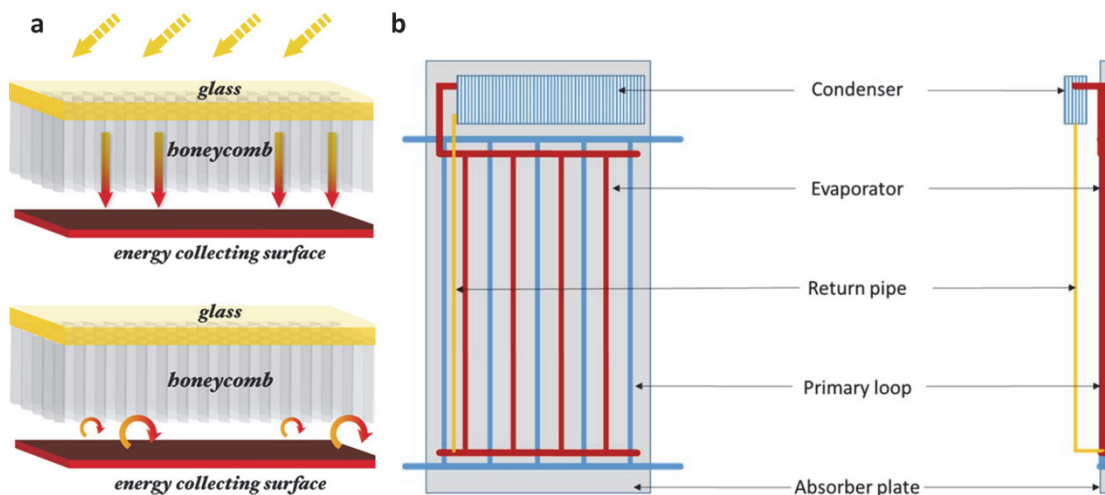


Figure 1.12. a) Schematic of the collector cross-section with the transparent honeycomb insulation. Solar irradiation passes through the transparent glass cover and insulation, heating the absorber, while convection losses are suppressed by the thick insulation layer. Source: [TIGI, 2018]. b) Schematic of the dual loop heat pipe system. Overheating prevention kicks in when the temperature of the absorber reaches the evaporation temperature of the liquid in the secondary loop (evaporator). The evaporator is connected to a condenser through which the heat is dissipated to the surrounding. Source: [IEA SHC Task 49, 2015]

However, the high collector performance can lead to internal temperatures of above 250°C. To limit the collector temperature, a secondary heat-pipe circuit, independent of the primary heat transfer loop is proposed (Figure 1.12.b). As soon as the temperature of the absorber reaches the evaporation temperature of the fluid in the secondary loop (the evaporator), a large amount of the thermal energy is transferred from the absorber to the secondary heat transfer fluid in the form of latent heat necessary for the evaporation. Through a closed loop pipe, the evaporator is connected to a condenser situated outside the collector case which dissipates the heat to the environment. In this manner, a fast transition between thermal isolation and thermal coupling between collector interior and external environment is achieved.

Thermochromic absorbers

Thermochromic thin films offer one of the more elegant and simple solutions to overheating. The temperature dependent optical response makes thermochromic thin films a promising candidate for novel smart selective absorber applications. Thermochromic absorbers can be engineered to undergo a dramatic increase in thermal emittance once a critical temperature is reached, thus decreasing the absorber temperature by dissipating heat to the environment. Some of the earliest works proposing thermochromic absorber coatings for overheating protection of solar collector systems are [Huot, 2008; Paone, 2009; Paone, 2013]. Recently, the efficiency and reliability of such thermochromic solar thermal systems has been demonstrated at the collector scale [Mercs, 2016]. In that work, a thermochromic multilayered absorber coating based on a mixture of vanadium and aluminum oxides $VO_2//V_nO_{2n\pm1}//Al_2O_3//SiO_2$ is proposed. The coating undergoes a reversible change in thermal emittance, changing from 0.06 to 0.42 at a critical temperature around 70°C (Figure 1.13). Due to the increase in infrared emittance (Figure 1.13.b and c), a large part of the heat is emitted and the stagnation temperature is reduced by more than 35°C. The maximum temperature in the thermochromic collector was determined at 154° C compared with the 190° C stagnation temperature of the standard collector.
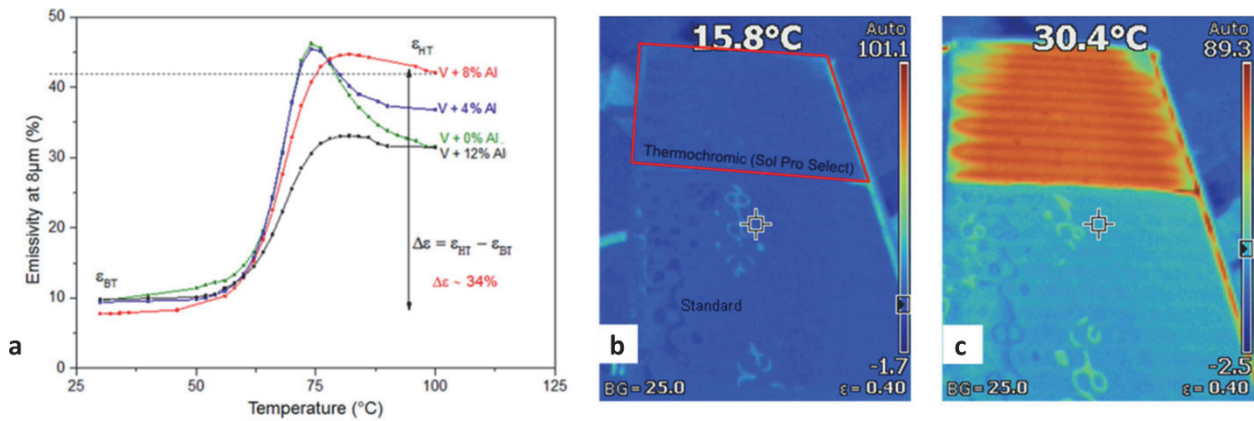


Figure 1.13. a) Evolution of the infrared emittance at 8μm of $VO_2//V_nO_{2n+1}//Al_2O_3//SiO_2$ coatings with Al content from 0 to 12 at.%. Infrared pictures of a standard and a thermochromic absorber welded on the same piping. b) T=13°C and c) T=83°C. Images reproduced from [Mercs, 2016]

For its second-generation thermochromic collectors, Viessmann claims an even larger Δε and stagnation temperatures not exceeding 150° C are reported (Figure 1.14). At such temperatures and at an operating pressure of 3 bar present in the collector, evaporation of the heat transfer fluid is avoided. Limitations on the installed collector area are lifted and an extended lifetime guaranteed.
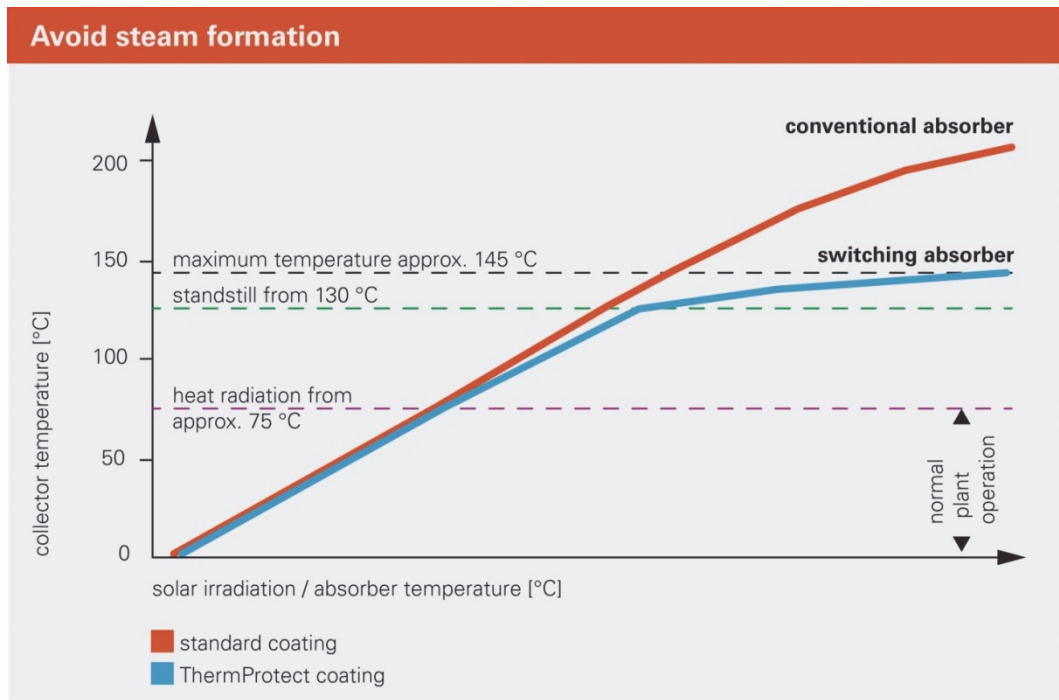
Figure 1.14. Evolution of the stagnation temperature with the exposure time, for a standard thermal solar collector and for a collector equipped with the second generation Viessmann thermochromic absorber (Vitosol 100-FM, Vitosol 200-FM). Reproduced from [SunWindEnergy, 2017]

# 1.3   Objectives

The first and so far only thermochromic absorber based solar thermal collectors are commercialized by Viessmann Werke GmbH & Co., proving the feasibility of thermochromic absorbers at the collector scale. However, the proposed vanadium and aluminum oxide based absorber decreases its thermal efficiency already at 70-75°C – close to the 68°C transition of the pure $VO_2$ films.

For this idea to be efficiently implemented in practice, an elevated phase transition temperature of vanadium dioxide based switchable layer is desired (95°C < $T_{transition}$ < 100°C). Then, a premature decrease in selectivity could be avoided. **Therefore, one of the main objectives of this work is to determine a dopant that can successfully increase the phase transition temperature of $VO_2$ thin films.** Cr, Si and Ge doped films are thoroughly investigated through a wide range of structural, morphological, optical, electrical and electronic characterization techniques. Doped films are deposited by co-sputtering and from alloy targets alike.

Naturally, attempting to change the properties of the material, a sound **understanding of the employed physical processes** is required; the influence of the deposition methods (traditional magnetron sputtering versus high power impulse magnetron sputtering), deposition parameters (e.g. substrate temperature, oxygen partial pressure) and the importance of the substrate choice are discussed.

Once high-quality switching films are obtained, their integration into the multilayered solar absorber coatings is targeted. For **a successful integration of thermochromic films and efficient absorber performance**, simulations based on the optical indeces of the constituting layers are essential. Multiple absorber designs are proposed and evaluated. Over the thermochromic phase transition, a switch from low to high thermal emittance is imperative, furthermore, a change from high to low solar absorptance is desired. Accelerated aging tests of the absorber coatings are carried out.

Furthermore, this thesis also aims at **exploring some other advanced concepts based on thermochromic thin films**.  The potential of an enhanced thermochromic switch in Fabry-Pérot type multilayers, ultra-black nanoneedle absorbers with dynamic emittance and the effects of nanoimprinting on thermochromic films are investigated.

Achieving the above listed objectives, would have ramifications reaching besides the solar thermal field, with $VO_2$ films switching at elevated temperatures being sought after in micro- and nanodevice applications or enhanced emittance modulation that could be tailored to well-defined wavelength ranges for various cooling applications.

## 1.4   Outline

This work explores the topic of thermochromic vanadium dioxide and, particularly, its potential application as novel solar selective absorber coatings. The structure of the thesis has been laid out as follows:

- Chapter 1. gives a short introduction to solar thermal collectors in the current economic and environmental context. It touches on the state of the art of thermal solar collectors, the challenges faced and the corresponding current solutions and limitations. The objectives of the thesis are formulated and the content outline is stated.

- Chapter 2. aims to briefly summarize the theoretical considerations behind thermochromism and the fundamentals of the much discussed and disputed metal-to-insulator transition in $VO_2$. Doping adds another layer of complexity to deciphering the driving mechanisms behind the phase transition. The main approaches are presented.

- In Chapter 3. the experimental techniques employed throughout this work are described. The thin film deposition methods, with particular focus on magnetron sputtering, numerous thin film characterization techniques and thin film simulation methods are detailed.

- Chapter 4. addresses the experimental particularities between the different deposition techniques or the influence of substrate choice. Main experimental parameters are given in this chapter, touching on the importance of substrate temperature or carefully controlled oxygen partial pressure.

- Chapter 5. describes the effect of doping – particularly Ge doping - on $VO_2$ thin films. The sputtered films are analyzed in detail. The implications of doping on the thermochromic properties (temperature dependent electrical resistivity), thermal emittance (FTIR) and electronic properties (UV and X-ray photoelectron spectroscopy) are assessed. Furthermore, scanning tunneling microscopy and spectroscopy (STM/STS) experiments are also carried out in the attempt to determine the local electronic band gaps and offer insights into the doping homogeneity at the grain level.

- Chapter 6. discusses the efficient integration of the thermochromic thin film into the multilayered solar absorber coating. Multilayered thin film designs are proposed and evaluated both by means of simulation (based on the n and k optical constants of constituting layers) and experimentally. Coatings exhibiting not only a modulation in thermal emittance but also in solar absorptance are investigated.

- In Chapter 7. advanced thermochromic concepts are explored. Such concepts include: Fabry-Pérot interferometer inspired multilayered coatings where the switching modulation of thin $VO_2$ films is significantly enhanced; combination of black oxide nanoneedles with thermochromic films for solar absorbers with ultra-high absorptance and dynamic emittance; imprinting of metal nanostructures on thermochromic thin films.

- Chapter 8. concludes this thesis highlighting the main findings and the implications of these achievements to the field of solar absorbers and beyond.

# Chapter 2     The physics of thermochromic VO$_2$

The underlying physics of strongly correlated materials represents one of the central themes of contemporary condensed matter physics and has implications spanning beyond fundamental science. Metal-to-insulator transitions in correlated materials are ofttimes accompanied by a symmetry lowering structural phase transition. The intrinsic coupling of the seemingly concurrent transitions, obscures the basic understanding of the governing mechanisms.

Since the discovery of its first-order metal-to-insulator transition (MIT) in 1959 [Morin, 1959], vanadium dioxide became one of the most emblematic correlated electron materials. This chapter attempts a brief introduction into the intriguing physics of VO$_2$ and the main theories regarding the origin and mechanism of the transition.

## 2.1    Strongly correlated materials

In strongly correlated electron systems there is a complex interplay between multiple, at times competing degrees of freedom, resulting in unusual electronic behavior. Emergent physical properties are strongly influenced by electron-electron interactions, which might be of Coulomb repulsion in nature, or can involve spin, orbital and lattice coupling as well.

Typically, strongly correlated electron materials are transition metal oxides, where electron-electron interactions come from spatially expansive d or f orbitals that form relatively narrow energy bands, with electrons at the limit of localization. A prototype strongly-correlated material, vanadium dioxide is a transition-metal oxide with narrow d electron bands. Small changes in external parameters giving rise to radical changes in physical properties is characteristic for correlated electron systems and VO$_2$ exhibits such extreme sensitivity to small changes in temperature, pressure or doping.

### 2.1.1   From band theory to the Mott-Hubbard model

In classical band theory, a non-interacting, free-electron model of the electronic structure of solids is considered. Electrons are free to move in the crystal lattice and any interaction between them is neglected. Most materials are accurately described by this nearly-free-electron picture, where the electron-electron interactions are negligible with respect to their kinetic energy. However, the nearly-free-electron picture fails to adequately describe several transition metal oxides.

While in conventional semiconductors the significant overlap of s- and p- hybridized orbitals gives rise to large valence and conduction bands, the spatially localized and directional 3d orbitals of transitional metal oxides have smaller orbital overlap and yield narrow conduction bands. In these partially occupied, narrow conduction bands the kinetic energy of electrons becomes comparable with the electrostatic repulsion

forces (Coulomb repulsion) between individual electrons. Electrons are localized by the electron-electron interactions and do not contribute to the conduction.

Mott insulators refer to a class of materials, which should be conductive according to classical band theory, but experimentally behave as insulators. The atypical behavior is attributed to a correlation induced transition from a metallic to an insulating phase.

The Hubbard model is the simplest model used to describe Mott insulators and able to predict the Mott transition. It considers the electrons localized at discrete sites and the conduction is attributed to the electrons hopping between the orbitals of neighboring atoms. The model relies on two terms: a kinetic term concerning the hopping of electrons between sites (that is a function of the interatomic spacing between neighboring atoms), t and a potential term consisting of an on-site repulsion, U. When the repulsive Coulomb potential becomes dominant over the hopping integral (U > t), it can break the lattice periodicity and split the band. An energy gap opens up and conduction is prevented.

The phase transition in $VO_2$ is a result of the interplay between atomic structure, charge, spin and orbital dynamics. The interdependence between crystal structure and electronic degrees of freedom, sets vanadium dioxide in a critical regime, where a single pure crystal undergoes a metal-to-insulator transition at $T_C$ = 341 K. Through the first-order transition between the low and high temperature phases, $VO_2$ suffers changes in the electronic band structure and its crystal structure too.

## 2.2    $VO_2$ background

Several vanadium oxides exhibit a metal-to-insulator transition at a critical phase transition temperature. Among them, it is vanadium dioxide amassing the overwhelming share of interest, due to its near room temperature MIT transition at 341 K [Morin, 1959]. However, the MIT properties of $VO_2$ are highly sensitive to process conditions such as oxygen partial pressure, substrate temperature or deposition method. This is due to the particularly complex V-O phase diagram with numerous, intermediate vanadium oxide phases (Figure 2.1). If the oxygen partial pressure deviates even slightly from the ideal ratio, incorporated point defects organize in a long-range order [Hirotsu, 1982] and lead to the formation of homologous series of phases:

- Magnéli phases: oxygen deficient $V_nO_{2n-1}$ series with $3 \leq n \leq 9$, [Schwingenschlögl, 2004] and

- Wadsley phases: oxygen rich $V_nO_{2n+1}$ phases with n = 2, 3, 6 [Katzke, 2003].

Most Magnéli phases exhibit an MIT transition at a certain temperature. Wadsley phases, on the other hand, exhibit no MIT transition with the exception of $V_6O_{13}$. A direct dependence between the transition temperature of different vanadium oxide phases and the vanadium/oxygen ratio cannot be established.

The metal-to-insulator transition of $VO_2$ is accompanied by a congruent change in crystal symmetry, from the high temperature, high symmmetry rutile phase to the low-temperature, low-symmetry monoclininc phase. By decreasing/increasing the temperature, a reversible electrical resistivity modulation of four to five orders of magnitude is measured in $VO_2$ single crystals. Besides temperature, the MIT can also be triggered by high electric fields [Stefanovich, 2000; Gopalakrishnan, 2009] or pressures (above 10 GPa) [Peruc-

chi, 2009; Bai, 2015]. It is an ultrafast transition, taking place on the subpicosecond to few nanosecond timescale, when optically or electrically triggered [Cavalleri, 2001; Leroy, 2012; Appavoo, 2014].
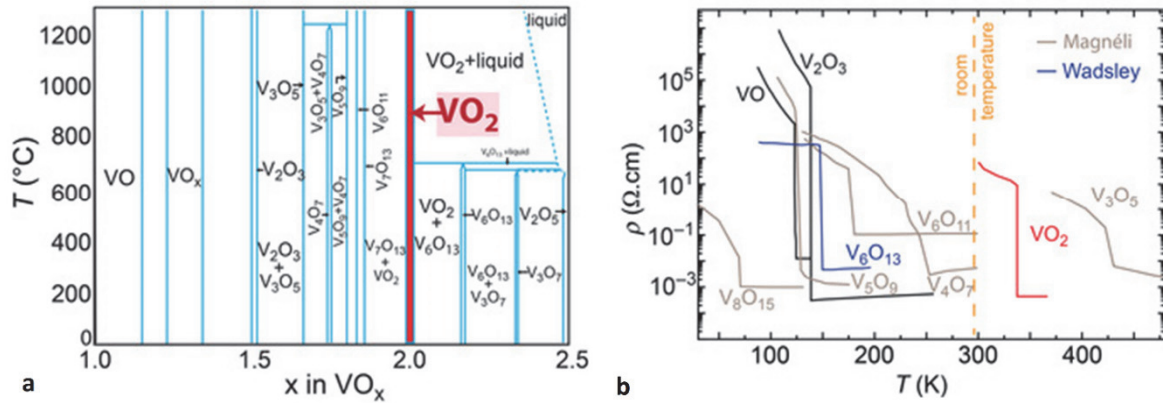


Figure 2.1. a) Phase diagram of the $VO_x$ system ($1 \leq x \leq 2.5$). b) Temperature dependent resistivity curves of various vanadium oxide phases, comprising several belonging to the Magnéli and Wadsley series. Several oxides exhibit an MIT with a large modulation of resistivity (e.g. $V_2O_3$ with an eight order of magnitude transition), but generally occurring at temperatures much below room temperature. $VO_2$ exhibits the largest transition near room temperature. Reproduced from [Brahlek, 2017].

However, single crystals cannot withstand the structural distorsions associated with the transition and break during thermal cycling. Thin films on the other hand resist to stresses during a large number of cycles (more than $10^8$ cycles without failure reported for sol-gel deposited $VO_2$ films [Guzman, 1996]) and are, therefore, preferred for practical applications.

Despite the highly challenging growth of the targeted, single phase and defect-free vanadium dioxide films, significant advances have been achieved and, today, there is an abundance of growth methods allowing for the deposition of good quality, switching $VO_2$ thin films. [Brahlek, 2017] reported a comprehensive run-down of the main deposition methods with the corresponding $VO_2$ resistivity modulation across the MIT for given film thicknesses. The comparison is graphically summed up in Figure 2.2.
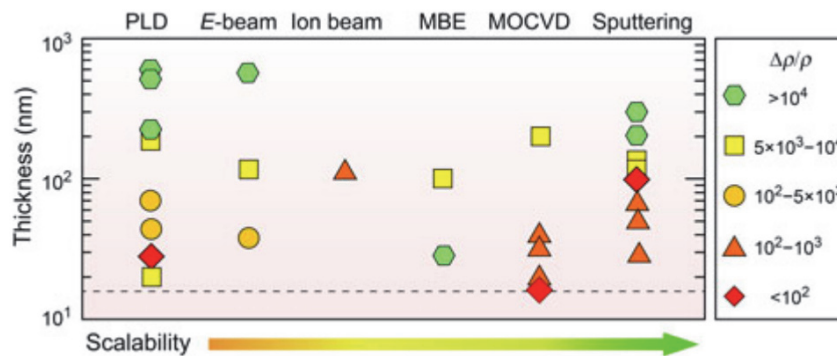


Figure 2.2. The resistivity modulation of $VO_2$ films across the MIT (marked by different symbols) plotted for the various deposition methods and film thicknesses. The deposition methods are arranged according to their scalability, starting from pulsed laser deposition (PLD), through electron beam, ion beam, molecular beam epitaxy (MBE), metal organic chemical vapour deposition (MOCVD) to sputtering. The dashed line marks the thickness limit at which the $VO_2$ film on sapphire substrate is completely relaxed. Reproduced from [Brahlek, 2017].

As a general trend, the resistivity modulation is improving with film thickness and for thicknesses above 100 nm, an MIT ratio of above four orders of magnitude are achieved across the compared deposition methods. On the other hand, the resistivity modulaton deteriorates with decreasing film thickness. However, there are some exceptions where remarkable MIT ratios have been observed in very thin $VO_2$ films. One such example is the PLD method by which high-quality $VO_2$ films of only ≈20 nm thickness, exhibiting a resistivity modulation of almost four orders of magnitude have been achieved [Jeong, 2013]. Another example concerns a combinatorial approach for the $VO_2$ growth based on a V-effucion cell (thermal source) and a metal organic gas (vanadium oxytriisopropoxide, VTIP) injector. By supplying the oxygen in a pre-bonded form (the oxygen containing VTIP precursor), a film of only 30 nm thickness with a four orders of magnitude change in resistivity has been uniformly deposited on the wafer-scale [Zhang, 2015].

Brahlek et al. chose only fully relaxed films grown on sapphire substrates for their comparison (thickness limit for $VO_2$ film relaxation marked by the dashed line in Figure 2.2) as strain can also affect the resistivity modulation across the MIT.

$VO_2$ films can be grown epitaxially on a range of substrates (e.g. $Al_2O_3$ or $TiO_2$). The crystal orientation of the substrate governs the orientation of the growing film, which, depending on the film thickness, can be pseudomorphically strained or strain-relaxed. An example of the temperature dependent electrical resistivity curve of a strained, 10 nm thin- and a strain-relaxed, 70 nm thin $VO_2$ film grown on (001) $TiO_2$ substrates by pulsed layer depositon are shown in Figure 2.3. Similarly, the resistivity curves of $VO_2$ films of different thicknesses, grown on a wide range of $Al_2O_3$ or $TiO_2$ cuts are also displayed. A remarkable reduction of the phase transition temperature to below 300 K is observed in strained $VO_2$ films deposited on (001) $TiO_2$ substrates.
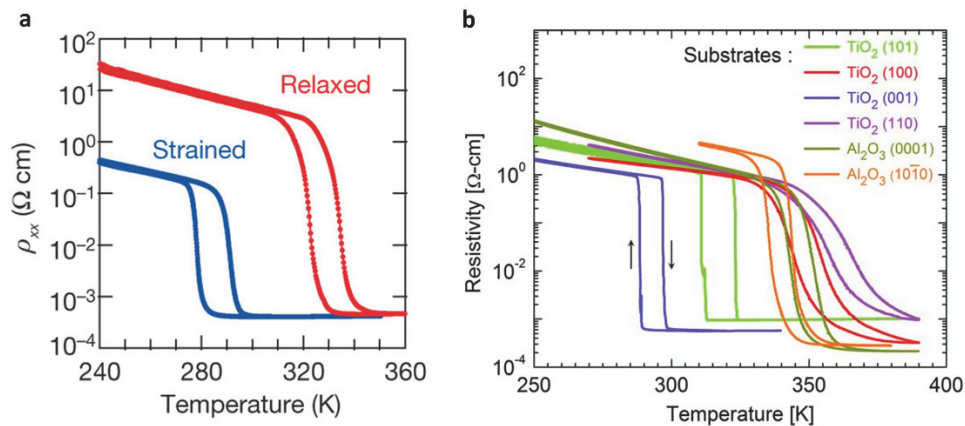


Figure 2.3. a) Resistivity curves of strained (10 nm) and relaxed (70 nm) $VO_2$ films grown on (001) $TiO_2$ substrates [Nakano, 2012]. b) Resistivity curves of $VO_2$ films of different thicknesses, grown on various orientations of $TiO_2$ and $Al_2O_3$ single-crystal substrates by pulsed laser deposition [Jeong, 2013].

Small deviatons from the stoichiometric $VO_2$ composition can also critically influence the film properties, including the phase transition temperature. Oxygen-deficient films are generally more conductive in the insulating phase than their stoichiometric counterparts. Moreover, lowered transition temperatures, $T_c$ in slightly oxygen deficient films [Brückner, 1975] and increased $T_c$ in slightly oxygen enriched films [Kimizuka, 1974] have been reported early on. Several more recent studies confirm these observations [Fan, 2013; Kim, 2014] and even a surpression of the phase transition temperature by 238 K to $T_c$ = 103 K [Zhang, 2011] or $T_c$ < 5 K [Jeong, 2013] has been reported for $VO_2$ nanobeams or electrolyte-gated thin films. Hence, oxygen vacancies stabilize the metallic, rutile phase even down to cryogenic temperatures, while, in a complementary manner, oxygen rich growth conditions favour the insulating, monoclinic $VO_2$ phase.

The reversible MIT is characterized by a thermal hysteresis. The hysteresis width has been reported to depend on the surface morphology of $VO_2$ films and to be controllable by $O_2$ flow rate, temperature and annealing time [Zhang, 2014]. Generally, smaller average grain sizes lead to a larger hysteresis width, while larger grains lead to a narrower hysteresis. Doping of $VO_2$ thin films has been consistently reported as reducing the hysteresis width [Chen, 2014; Krammer, 2017a].

Finally, concerning the environmental stability of $VO_2$, coatings face oxidation problems accompanied by a decrease in the MIT modulation amplitude. The use of a protective layer is suggested in order to limit or avoid film degradation in hot and damp conditions [Chang, 2019]. Nonetheless, $VO_2$ thin films have successfully passed a test series including thermal shock and vibration resistance, preliminary radiation tests for their use as smart radiatior devices in space applications. Peeling tests confirmed a strong adhesion of $VO_2$ coatings to aluminum substrates [Haddad, 2009] and it is an important finding from the perspective of $VO_2$ thermochromic absorber coatings.

## 2.3   Crystal and electronic structure of $VO_2$

The first-order phase transition in $VO_2$ is accompanied by a symmetry lowering structural distortion. Atoms rearrange between the high symmetry, tetragonal rutile (R) structure (space group $P4_2/mnm$ with lattice constants a = b ≈ 4.55 Å and c ≈ 2.88 Å) adopted in the high temperature, metallic state and a monoclinic (M1) crystal structure (space group $P2_1/c$ with a ≈ 5.75 Å, b ≈ 4.52 Å, c ≈ 5.38 Å and β = 122.6°) in the low temperature, insulating phase (Figure 2.4.a).

The rutile is characterized by regularly spaced vanadium atoms, with V-V distances ≈ 2.86 - 2.88 Å (very slight divergence in published values). Each vanadium atom is surrounded by six oxygen atoms, forming corner- and edge-sharing $[VO_6]$ octahedra chains along the c axis (Figure 2.4.b). The monoclinic lattice is the result of the distortion and doubling of the tetragonal, rutile unit cell volume ($a_M = 2c_R$). The characteristic feature of the monoclinic M1 phase is the dimerization of the V atoms, with V-V pairs of alternate shorter (2.65 Å) and longer (3.12 Å) distances along the monoclinic a axis. The V dimers adopt a a zig-zag pattern as they are slightly tilted with respect to the rutile c-axis.
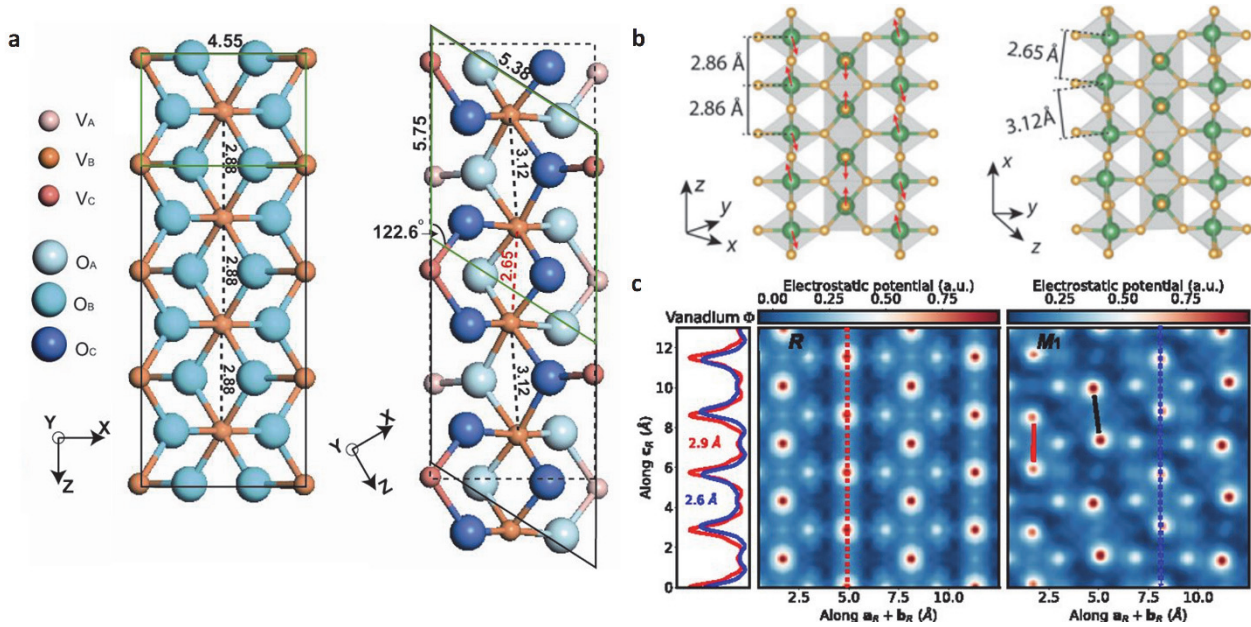
Figure 2.4. a) Schematic representation of the rutile, R (left) and the monoclinic, M1 (right) lattice structures of $VO_2$. Adapted from [Nag, 2011]. b) Along the c axis of the tetragonal structure, octahedral $VO_6$ units form chains by edge-sharing, while neighboring octahedral chains are interlinked by corner-sharing. In the monoclinic structure, zig-zag octahedra strings emerge. Adapted from [Brahlek, 2017]. c) Reconstruction of the real-space electrostatic potential, $\Phi(x)$ from ultrafast electron diffraction patterns. V-V dimerization and tilting are absent in the rutile, but present in the mono-clinic M1 phase (the solid black line illustrates an in-plane tilt, the red line an out-of-plane tilt). The dashed red and blue line cuts show the unpaired/paired V-V distances of 2.9 Å and 2.6 Å, respectively. The values are in excellent agreement with published values. The real space view is reconstructed vertically along the rutile $c_R$ axis and horizontal cut is along the $a_R$ + $b_R$ direction. Adapted from [Otto, 2019].

Recently, ultrafast electron diffraction (UED) is used to reconstruct the real-space structure of the mono-clinic and rutile phases [Otto, 2019]. The photoinduced changes to the electrostatic crystal potential, $\Phi(x)$, determined from the measured UED intensities and plotted along the rutile $c_R$ axis (vertically) and along $a_R$ + $b_R$ (horizontally) are shown in Figure 2.4.c. The determined V-V bond lengths of 2.6 Å and 2.9 Å for paired and unpaired V atoms are in excellent agreement with the expected values. In the rutile $VO_2$ equally spaced V atoms, while in the monoclinic phase the dimerization and tilting of the V pairs is apparent. In the displayed view, adjacent V chains are rotated by 90° with the V-V dimers tilting in or normal to the plane.

John B. Goodenough proposed one of the earliest descriptions of the electronic structure of $VO_2$, based on crystal field and molecular orbital theory [Goodenough, 1971]. In his description, in rutile $VO_2$, the octahedral crystal field splits the V 3d orbitals into higher lying, double degenerate $e_g^\sigma$ and lower lying, triple degenerate $t_{2g}$ symmetry states (Figure 2.5). The tetragonal component of the crystal field further splits the $t_{2g}$ states into a $d_\pi$ doublet and a $d_\parallel$ orbital. The $d_\pi$ orbitals point toward the faces of the octahedron, while the $d_\parallel$ orbital is directed along the rutile c-axis, towards the V atoms in the neighbouring unit cells. The strong bonding of V-V atoms along this direction is at the origin of the metal behavior of the rutile phase.

Cooling below the critical transition temperature, the symmetry is lowered through the monoclinic distortion characterized by the dimerization of V chains and tilting of the V-V pairs. The structural distortions lead to:

- the splitting of the $d_\parallel$ into bonding and antibonding states, and

- the upshift of the anti-bonding $d_\pi$ states above the Fermi energy, $E_F$, as the tilting of the pairs increases the overlap of these states with O 2p states.

These band reorganizations lead to the opening of a Peierls-like band gap in the insulating M1 phase, when a single d electron occupying the $d_\parallel$ bonding state is considered. Goodenough has also suggested that the critical transition temperature, $T_C$ is not controlled by thermal excitations of electrons into the antibonding bands, but rather by the entropy of the lattice vibrational modes.
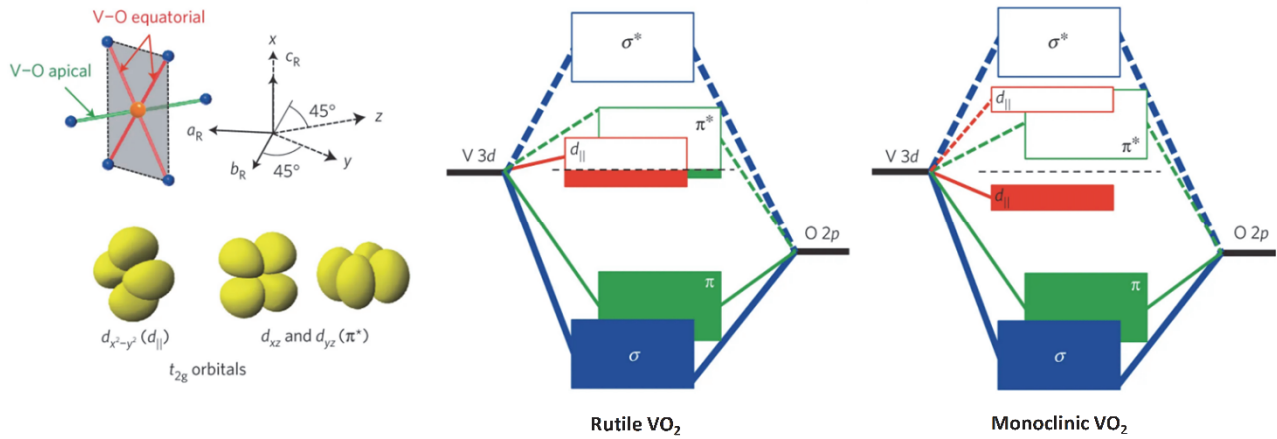


Figure 2.5. Schematic of the [VO6] octahedron and of the VO2 band structure in the metallic (rutile) and insulating (monoclinic) state. The illustrated, different equatorial and apical V-O distances are associated with the orthorhombic distortion that further splits the $t_{2g}$ orbitals into a $d_\parallel$ orbital and doubly degenerate $d_\pi$ states. The $d_\pi$ orbitals hybridize with O 2p orbitals, forming low energy, bonding and high energy, anti-bonding states. The $d_\parallel$ orbitals, parallel to the $c_R$ axis, are relatively non-bonding with respect to O 2p. In the metallic state, $d_\parallel$ and anti-bonding $d_\pi$ orbitals form the density of states at the Fermi level, while in the insulating state, the dimerization of V atoms leads to a splitting of the $d_\parallel$ orbital. Additionally, an antiferroelectric displacement leads to the upshift of the anti-bonding $d_\pi$ states. Adapted from [Aetukuri, 2013].

## 2.4 Phase transition controversy: Peierls versus Mott

Since its discovery more than half century ago and despite extensive research, the origin and primary mechanism behind the MIT has eluded scientists, making it the topic of heated controversy. There are in principle two approaches: the Peierls approach, where the MIT is attributed to electron-lattice interaction, and the Mott approach, where the transition is a result of electron-electron interaction. In the first approach, the transition is structurally driven and atomic rearrangements (lattice distortion and V-V dimerization) are solely responsible for the insulating nature of the low temperature phase. In the second, Mott-Hubbard approach, electron-electron correlations are dominant and the transition is charge driven.

In Goodenough's description the MIT is attributed to the zig-zag distortion and dimerization of V chains, therefore, is interpreted in terms of strong electron-phonon interactions belonging to the Peierls model. Subsequent density functional theory (DFT) simulations, based on single electron bands, seem to support the Peierls approach.

Wentzcovitch et al. performed electronic structure calculations based on density functional theory within local density approximation (DFT - LDA) and succesfully determined the M1 monoclinic structure to have

the lowest energy, with structural parameters in reasonable agreement with experiment. They denoted VO$_2$ as a band insulator (Peierls insulator), however, the bandgap of the monoclinic M1 phase remained unaccounted for - the top of the d$_\parallel$ band overlaps slightly with the bottom of the d$_\pi$ band [Wentzcovitch, 1994]. Cavalleri et al. used femtosecond laser excitation to initiate the transition and establish a time domain hierarchy [Cavalleri, 2004]. Results suggest that the disappearance of the band gap is due to optical phonons that cause the structural phase change. Authors conclude that the atomic rearrangement of the high temperature rutile lattice is essential for the occurance of the metallic VO$_2$. X-ray and neutron scattering experiments have also revealed the importance of lattice vibrations and, there too, anharmonic phonons, rather than electronic contributions, have been reported to drive the VO$_2$ phase transition [Budai, 2014].

While the Peierls phase transition can qualitatively explain a band gap opening induced by a strong dimerization of V atoms, electron-phonon coupling alone appears insufficient to accurately and quantitatively describe the MIT mechanism. Inconsistencies between theory and the rather large, experimental band gap of 0.6 – 0.7 eV, the magnetic properties of VO$_2$ ground states and the existence of intermediate insulating phases arise.

Soon after Goodenough's interpretation, Mott and Zylbersztejn proposed that electronic correlations are primarily responsible for the band gap opening [Zylbersztejn, 1975]. They argue that lattice distortion alone is insufficient and a significant Hubbard energy U is necessary to drive the MIT. Many others have followed, claiming the crucial role of electron correlations in the phase transition [Sommers, 1978; Rice, 1994].

In early experimental work, Pouget et al. showed that uniaxial stresses or Cr doping, even in trace amounts, lead to a second monoclinic, M2 and a triclinic, T insulating phases [Pouget, 1976]. Later, Eyert also reports on the intermediate M2 and T phases, in his comprehensive work on the metal-insulator transition of VO$_2$ [Eyert, 2002]. In contrast to the M1 phase, where all vanadium atoms dimerize and tilt along the c$_R$ axis, in the monoclinic M2 phase only half the V atoms pair, with no tilt in the dimerized chains, while the other half forms tilted chains of equally spaced atoms. The triclinic phase is an intermediate phase between the M2 and M1 phases, with the V atoms paired and tilted to different degrees. The V atoms positions for the metallic rutile and three insulating phases of VO$_2$ are shown in Figure 2.6.a.
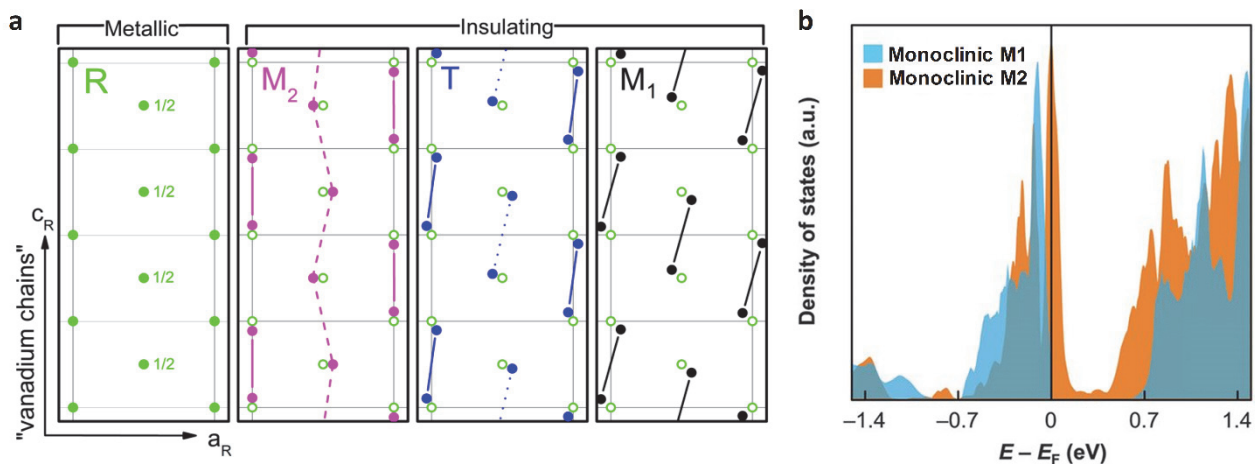


Figure 2.6. a) Vanadium atom positions in the metallic (rutile R) and three insulating phases (monoclinic M1, M2 and triclinic T). For each insulating phase, the displacement with respect to the rutile positions (open green circles) are illustrated. Reproduced from [Huffman, 2017]. b) Calculated density of states (DFT + U) for the monoclinic insulating M1 and intermediate, metal-like M2 phases. Adapted from [Lee, 2018].

The fact that the M2 is also insulating, in spite of the undimerized V chains, is a strong indicator that the physics of $VO_2$ is similar to that of Mott-Hubbard insulators [Rice, 1994]. Infrared microspectroscopy and spectroscopic microellipsometry on strained $VO_2$ crystals show that the first-order structural phase transition between the M2 and T phases, whose optical interband features are remarkably similar to those observed in monoclinic M1, does not impact the band gap and electronic structure. Due to this insensitivity of the band gap to the lattice distortion, authors claim that the insulating phases of $VO_2$ are Mott-Hubard insulators, ruling out the Peierls component and stating the Mott-Hubbard type Coulomb correlations as the driving contributor to the band gap opening [Huffman, 2017].

Data from infrared spectroscopy, ellipsometry and reflectance nano-imaging experiments suggest a Mott transition in metallic $VO_2$, as the standard quasi-particle charge conduction is found untenable, with the Ioffe-Regel-Mott limit of metallic transport breaking down due to strong electron correlations observed in rutile $VO_2$ [Qazilbash, 2006; Qazilbash, 2007].

Ultrafast electron diffraction combined with infrared transmissivity allow to monitor the structural and charge density reorganizations of $VO_2$. Through photoexcitation of the monoclinic phase, an intermediate monoclinic-like phase with the characteristic periodic lattice distortion, but metal-like mid-infrared optical porperties has been observed [Morrison, 2014].

In another recent study, an isostructural, electronically driven MIT is demonstrated in epitaxial $VO_2$ films [Lee, 2018]. Through an artificial bilayer of only 8 nm thick epitaxial $VO_2$ and slightly oxygen deficient $VO_{2-\delta}$ single layer deposited on (001) $TiO_2$ substrates, the MIT transition in the $VO_2$ layer occured at lower temperature than the strutural transition. This non-equilibrium monoclinic metallic phase does not occur in the abscence of the oxygen-deficient layer, as interface interactions suppress the electron correlations in the otherwise correlated insulator, without changing the crystal structure.

Another indication of unconventional, strongly correlated electron physics in $VO_2$ comes from the drastic, one order of magnitude breakdown of the Wiedemann-Franz law at high temperatures [Lee, 2017]. Typically, in conductive solids, the Wiedemann-Franz law requires that the electrical conductivity and the electronic contribution to the thermal conductivity are proportional to each other. The anomalously low electronic thermal conductivity in metallic $VO_2$ suggests a strong electron correlation where heat and charge diffuse independently.

From a computational approach, traditional band theory based DFT calculations, both within the local density approximation (LDA) or generalized gradient approximation (GGA), fail to predict a band gap for the insulating phases of $VO_2$ [Wentzcovitch, 1994; Eyert, 2002]. When the electronic correlations are accounted for via a Hubbard energy, U (DFT + U), the opening of a band gap in the monoclinic phases is predicted [Kim, 2013; Budai, 2014]. Moreover, corrections with hybrid functionals provide a more accurate description of the electron exchange and their ability to predict a bandgap opening within DFT indicate that the Hubbard interaction might not be essential for the MIT [Eyert, 2011]. Nonetheless, even with these considerations, DFT methods fail to determine the correct band gap and magnetic ground state in the monoclinic phase.

Dynamical mean-field theory (DMFT) simplifies the spatial dependence of the electron-electron correlation, while fully accounts for their dynamics making it a widely applicable approximation for the description of strongly correlated systems. By means of cluster-DMFT (c-DMFT), the electronic structure of both the metallic, rutile and insulating, monoclinic M1 $VO_2$ phases, as well as the previously elusive finite band gap could be successfully reproduced [Biermann, 2005]. Measured X-ray photoemission spectra agree well with the simulated c-DMFT spectra (Figure 2.7).
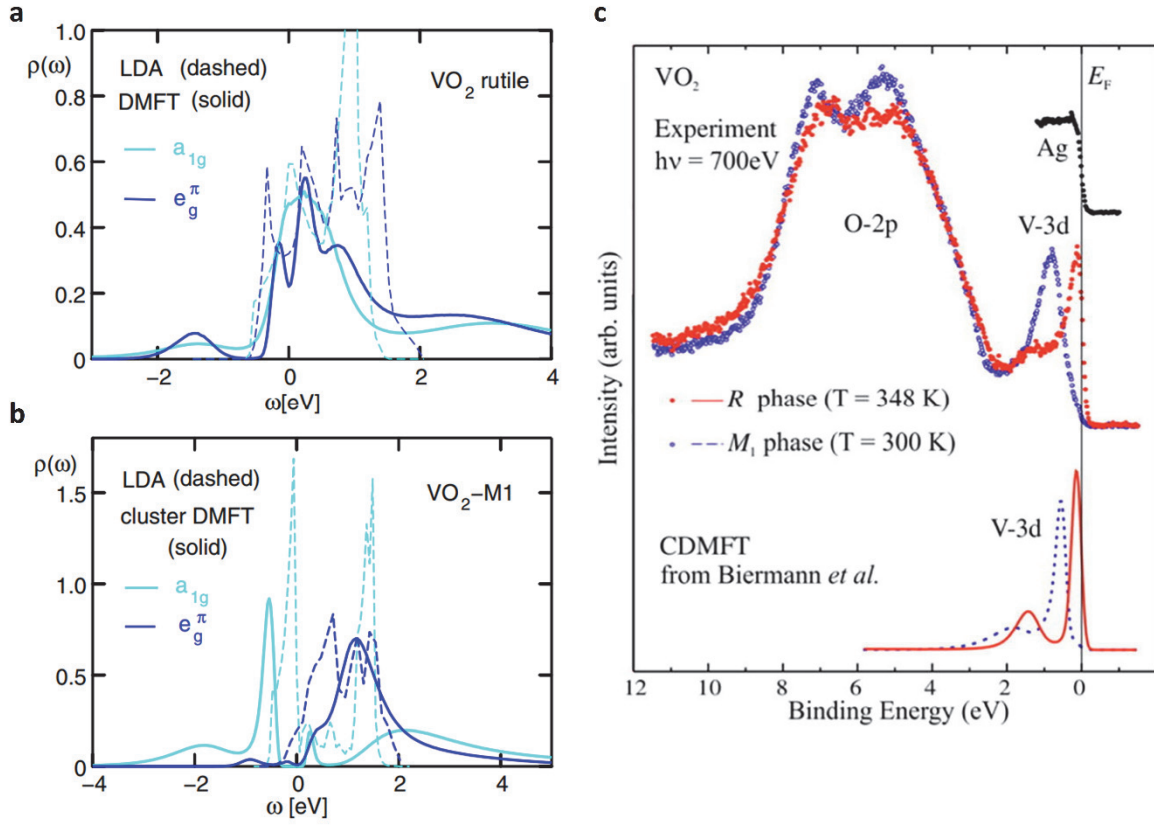


Figure 2.7. (a-b) Spectral functions of the rutile and monoclinic M1 phases calculated within the DMFT approximation (solid lines) in comparison to the LDA density of states (dashed lines). Reproduced from [Biermann, 2005]. c) Experimental X-ray photoemission spectra and corresponding theoretical results from c-DMFT calculations of the rutile and monoclinic $VO_2$ phases. Reproduced from [Liu, 2018].

These recent theoretical advances tend to bridge the gap bewteen purely Mott- or Peierls-like transitions. Instead, the joint effect of electron correlation and electron-phonon interaction is stressed and a cooperative Peierls-Mott transition is proposed, termed: "correlation assisted Peierls transition" [Biermann, 2005; Kim, 2013] or "Peierls assisted orbital selective Mott transition" [Weber, 2012].

For further details on the physics and applications of strongly correlated vanadium dioxide systems, the reader is directed to recent review articles [Brahlek, 2017; Liu, 2018].

## 2.5    Effects of doping

While the definite origin and sequence of the phase transition has been the subject of debate, by no means did it prevent extensive experimental studies on the modulation of the MIT characterisics from being carried out. Due to its remarkable change in electrical and optical properties close to room temperature, $VO_2$ is of paramount interest for practical applications e.g. ultrafast optical [Wang, 2005], steep-slope electronic switches [Vitale, 2017], tunable capacitors [Vitale, 2016], microbolometers [Émond, 2015], thermochromic smart windows [Granqvist, 1990; Zhao, 2014], smart radiators in solar thermal [Paone, 2014] or space [Benkahoul, 2011] applications, etc.

For the bulk of these applications, operating temperatures other than the 341 K of pure $VO_2$ are desired. Among the multiple methods employed to modulate the MIT (stress regulation, charge injection, film stoichiometry, film morphology), extrinsic doping and alloying have been one of the most popular.

The discovery of an MIT in $VO_2$ in 1959 has sparked considerable interest and, by the beginning of 1970s, a wide variety of dopants have been studied. It must be noted that early studies were mainly concerned by doped $VO_2$ single crystals, while thin films might yield different outcomes. Since then, data reported in literature concerning doping of both single crystals and thin films have been collected and compared for a wide range of elements. The values of change in phase transition temperature per at.% dopant, dT/dx also depend on preparation method and quality of $VO_2$. Moreover, changes in $T_C$ are limited. The sharpness of the MIT diminishes steadily with doping, up to a maximum dopant concentration beyond which the MIT is lost. Nonetheless, the typical dT/dx values of commonly studied dopants are summarized in Figure 2.8.
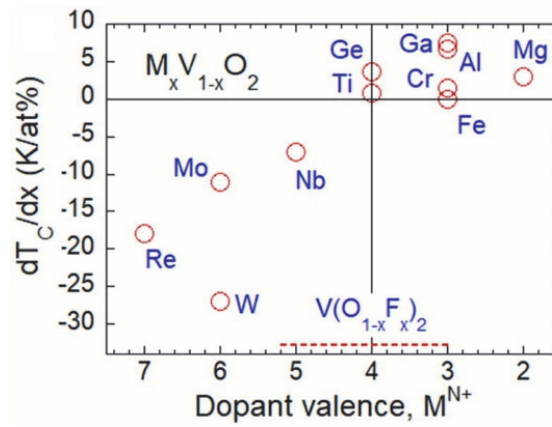


Figure 2.8. Change in the MIT phase transition temperature per at.% dopant as a function of dopant valence. The real valence states of dopants have not been experimentally confirmed as many are multi-valent. Reproduced from [Liu, 2018].

It is generally accepted that high-valence dopants with larger ionic radii than $V^{4+}$ (e.g. $W^{6+}$, $Mo^{6+}$, $Nb^5$) lower, while low valence metal ions with lower ionic radii (e.g. $Al^{3+}$, $Ga^{3+}$, $Cr^{3+}$, $Fe^{3+}$) increase the phase transition temperature. Donor-like substitutional dopants (with higher valence than the 4+ of V atoms), are thought to to screen the electron-electron interaction in the insulating state by the additional free electrons, hence lowering the $T_C$, while acceptor-like dopants (of valence lower than 4+) are believed to weaken the electrostatic screening and, therefore, increase the $T_C$. However, the structural effects induced by the size mismatch between $V^{4+}$ and dopant ion cannot be neglected. The mechanism through which dopants affect the MIT are even less established than the mechanism of the MIT itself. Whether the primary reason

for MIT modulation is the valence or the size of the ion is unclear, as it comes back to the same fundamental question of whether the origin of the MIT in pure $VO_2$ is electronic or structural in nature.

Interpetation of vacancies or interstitial defects poses similar challenges. For example, the presence of oxygen vacancies promotes the formation of $V^{3+}$ ions in order to maintain charge neutrality. In turn, $V^{3+}$ having a larger ionic radius than $V^{4+}$ (78 pm versus 72 pm) induces strain in the structure [Jaffari, 2017].

From Figure 2.8 it appears that dopants lowering the $T_C$ are much more efficient than those increasing the $T_C$ and that tungsten, W is the most efficient among them. Typically, W reduces the transition temperature by 23 – 27°C/at.%, depending on the deposition method, however, a reduction as high as 49-55°C/at.% W [Paone, 2015a] has been reported.

A charge-transfer mechanism is thought to take place by replacing $V^{4+}$ ions with $W^{6+}$.The transition temperature is lowered either as a result of larger ionic radius of tungsten over vanadium, or due to the insertion of extra electrons into the vanadium d band. It is suggested that W ions break up the homopolar $V^{4+}$-$V^{4+}$ bonds, forming $V^{3+}$-$W^{6+}$ and $V^{3+}$-$V^{4+}$ pairs for charge compensation [Tang, 1985]. The loss of homopolar $V^{4+}$-$V^{4+}$ bonding, electron doping and detwisting of the monoclinic lattice by $W^{6+}$ is thought to destabilize the insulating phase and to lower the transition temperature [Wu, 2014].

For room temperature applications, tungsten doping is well-established. However, dopants shifting the MIT towards higher temperatures proved less efficient. Although it is Ga showing the largest increase of temperature per at.%, the highest transition temperatures for doped $VO_2$ have been reported for $V_{0.8}Cr_{0.2}O_2$ films with $T_C \approx 100°C$ [Miyazaki, 2014] and for $V_{0.94}Ge_{0.06}O_2$ films with $T_C \approx 96°C$ [Krammer, 2017a].

As Ge doping of $VO_2$ films constitutes the main part of the present thesis, the results of recent electronic structure calculations of $VO_2$-$GeO_2$ alloys [Lu, 2019] are briefly summarized. Lu et al. have used density functional-theory within the generalized gradient approximation including an onsite repulsive potential (DFT GGA+U) to calculate the electronic structure of pure and alloyed $VO_2$. The method gives the correct ground states in the rutile and monoclinic phases, but yields slightly larger band gap for the M1 phase than experimentally determined (1.1 eV versus 0.7 eV). However, due to the large unit cells needed to treat dilute alloys, the more accurate methods (e.g. DMFT), able to reproduce all features of the electronic structure with the correct band gaps, are too computationally expensive.

Authors find that the opening of the band gap is mainly due to an antiferromagnetic ordering with a strong spin coupling along the V chains, thus favouring the Mott description. In their view, the rutile phase is non-magnetic (antiferromagnetic rutile would have a gap) and the monoclinic phase is antiferromagnetic (non-magnetic monoclinic phase is gapless). In $VO_2$-$GeO_2$ alloys, the monoclinic deformation disappears with Ge doping and the structure reverts to rutile as $GeO_2$ has a rutile phase. However, due to the spin ordering – present also in the absence of structural V-V pairing – a band gap of 0.78 eV is determined for the antiferromagnetic, low-temperature state (Figure 2.9). This is lower than the 1.1 eV calculated for pure $VO_2$ and it is mainly due a weaker spin pairing as a result of the larger V separation (some of the V atoms being substituted by Ge).

Total energy calculations with non-magnetic and antiferromagnetic spin ordering result in an increased energy difference between the metallic and insulating phases of $VO_2$-$GeO_2$ alloys compared to pure $VO_2$. This energy difference increase is equivalent to an increase of $T_C$ and is consistent with the experimental observations on Ge doped $VO_2$ thin films as described in Chapter 5.
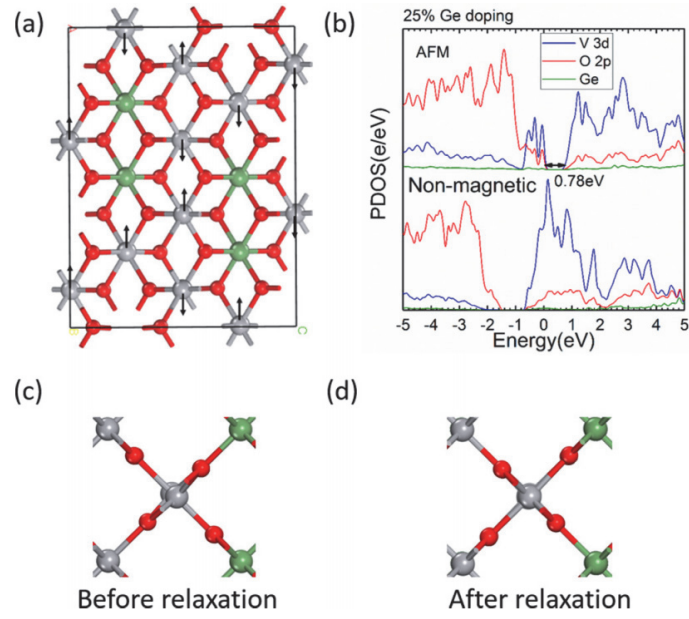
Figure 2.9. a) Unit cell structure and spin order in $VO_2$-$GeO_2$ alloy. Ge atoms (green spheres) substitute a quarter of the V atoms (grey spheres). b) Partial density of states calculated for the low-temperature, antiferromagnetic and high-temperature, non-magnetic phases of the $VO_2$-$GeO_2$ alloy. (c-d) Structure reverting to rutile after relaxation in $VO_2$-$GeO_2$ alloys. Reproduced from [Lu, 2019].

# Chapter 3    Experimental methods and numerical analysis

This chapter describes the adopted thin film deposition methods and the wide array of characterization techniques employed for the investigation of optical, electrical, structural, morphological and electronic film properties. The response of multilayered thin film coatings is simulated based on the transfer matrix formalism, while the thermal performance of the envisaged thermochromic flat-plate collectors is also predicted based on a numerical simulation model.

## 3.1    Thin film deposition

### 3.1.1 Magnetron sputtering

Sputtering is a physical vapour deposition technique and one of the main thin film coating methods. Today, most, if not all, remaining European solar absorber manufacturers produce their coatings by means of sputtering. It is a reliable deposition method offering good control of the film composition and thickness.

Sputtering is a plasma based vacuum process, where a source material, called target, is eroded by incoming high energy particles. This is achieved by applying a negative charge to the source material (cathode), resulting in the acceleration of free electrons away from the target. Then, these electrons collide with the inert, process gas atoms present in the vacuum chamber, usually Ar, ionizing them to $Ar^+$ and generating more free electrons in the process, thus, sustaining the plasma. The positively charged ions are accelerated toward the cathode. Upon the impact, atoms or atom clusters of the source material are ejected, or sputtered, and are deposited as a thin film on a substrate (anode) placed in their way. Meanwhile, the recombination of free electrons with the ions results in the release of photons, which give the plasma its characteristic glow.

However, in the classical sputtering process, deposition rate is slow and the substrate (anode) can be damaged by the flux of impinging free electrons. In magnetron sputtering, magnets are placed behind the cathode in order to confine the electrons in the magnetic field above the target surface. The electrons travel along the magnetic field lines leading to an enhanced probability of an ionising electron-atom collision. A denser, localized plasma results in significantly increased sputter rates.

To deposit oxide films from metallic targets, oxygen is introduced in the chamber. The ionized non-inert gas can react chemically with the sputtered atoms of metals or semimetals. The process is then called reactive magnetron sputtering. However, in a background of reactive oxygen gas, the target surface might oxidize as well, leading to lower conductivities (charging) and lower sputter yields. The oxide growing faster than the target being ablated can result in target poisoning. For poisoned targets, subsequent arcing renders the process unstable and generates damages in the films and targets alike. Pulsed-DC sputtering can suppress the positive charge build-up on the targets by alternating the applied potential. Applying a negative voltage

pulse of a few hundred volts for a time $\tau_{on}$, sputtering of the source material takes place. Then a reverse, positive low voltage is applied for a time $\tau_{rev}$, in order to remove any charge built-up on the target surface. $\tau_{on}$ should be short enough to avoid arcing and $\tau_{rev}$ should be long enough to remove the accumulated positive charges. The duration of a cycle, $\tau_{cycle} = \tau_{on} + \tau_{rev}$, determines the pulsing frequency and a duty cycle is defined as the fraction of a cycle in which the signal is active:

$$\text{Duty cycle} = \frac{\tau_{on}}{\tau_{cycle}}$$

<div align="right">Equation 3.1.</div>

By pulsing the DC voltage at typical frequencies in the range of $10 - 250$ kHz with duty cycles in the range of $50 - 90\%$, arcing during dielectric film depositions is successfully avoided, while still maintaining higher deposition rates compared to RF sputtering. Figure 3.1 shows the evolution of arcing rate with the pulsing frequency and duration of voltage reversal. In this work, the pulsing frequency is set to 250 kHz with a reverse time, $\tau_{rev}$ of 496 ns leading to a duty cycle of 87.6%. Pure $VO_2$ films and doped $VO_2$ films sputtered from alloy targets have been deposited by pulsed-DC magnetron sputtering.
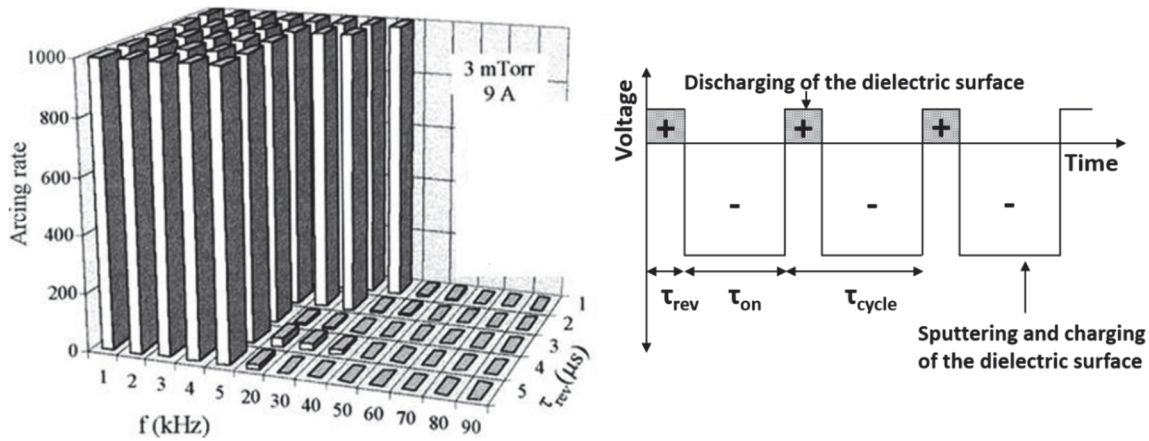


Figure 3.1. Arcing rate as function of pulse frequency and duration of voltage reversal for the reactive deposition of alumina in an $Ar/O_2$ mixture and profile of the applied voltage with time. Adapted from [Belkind, 1998].

RF sputtering, delivering AC power typically at 13.56 MHz, is suitable for the deposition of highly insulating and/or brittle materials. In this work, when the doped $VO_2$ films are deposited by co-sputtering of V and various dopant elements (e.g. Ge, Si or Cr), the magnetron of the dopant is run by an RF power supply as it provides a rather low deposition rate. Additionally, several magnets are removed from the magnetron in order to further limit the sputtering rate of the dopant targets.

In our experimental setup, shown in Figure 3.2, a confocal sputter-up configuration is adopted, having five different magnetron sources arranged in a circular way and tilted towards a common focal point where the substrate holder is placed. This allows for exceptional film uniformity and easy deposition of multilayered coatings or alloys by co-sputtering of different source materials without the need of substrate repositioning.
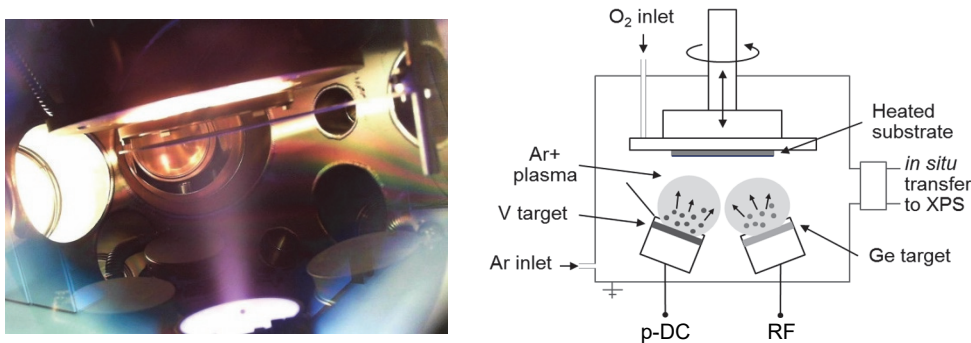
Figure 3.2. Photograph of the confocal chamber interior with a plasma discharge and heated substrate rotating above the magnetrons (left); schematic representation of the sputtering process and sputter chamber (right).

The sputtering process takes place in high vacuum conditions. The base bressure of the chamber is below $5 \cdot 10^{-8}$ mbar. Mass flow controllers regulate the flow of high purity process Ar gas (99.999%) and reactive $O_2$ gas (99.995%) in the chamber. However, for the deposition of pure and doped thermochromic $VO_2$ films, the oxygen partial pressure during the process must be precisely controlled. Care must be taken to avoid the formation of the oxygen poor $V_2O_3$ or the oxygen rich, thermodynamically stable, $V_2O_5$ phase. To that end, a Proportional Integral Derivative (PID) feedback control is employed, which regulates the oxygen flow based on the pressure readings of a Zirox XS22 lambda-probe oxygen sensor. This way the oxygen partial pressure is strictly kept in a narrow, predefined range.

Only crystalline $VO_2$ films exhibit a metal-to-insulator phase transition. For the crystalline structure to form, the substrates must be heated during the deposition. Samples are generally heated to 600°C nominal temperature at a rate of 30°C/min. The temperature is measured by a stationary thermocouple situated behind the rotating substrate holder, hence, the sample temperature differs from the nominal temperature. The temperature calibration curve is determined by measuring the sample temperature as a function of the set temperature (Figure 3.3). This is done with the help of a second thermocouple that is fixed to the surface of the sample holder during the heating ramp. It is found that the commonly set deposition temperature of 600°C corresponds to an actual sample temperature of 465°C. This calibration does not account for the additional sample heating resulting from the flux of incoming particles during the sputtering process.
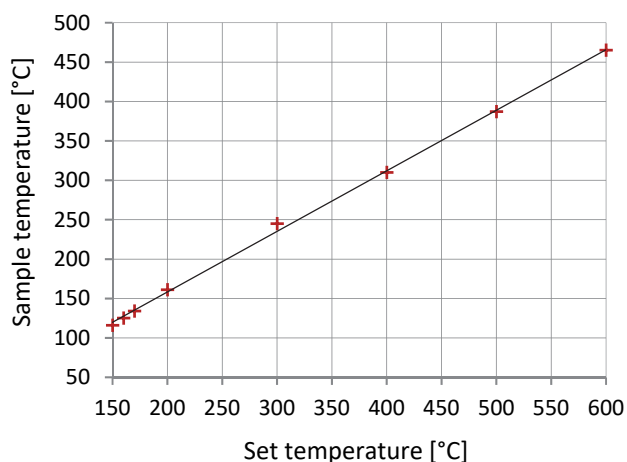


Figure 3.3. Temperature calibration for the sample holder.

For uniform substrate heating and film thickness, the substrates are rotated at 20 rpp, during the depositon. At the end of the sputtering process, samples are annealed during the controlled cooling stage, with a cooling rate of 30°C/min. This in-situ annealing step is essential for the formation of crystalline $VO_2$ structure, which is inhibited when samples are cooled freely to room temperature. A rapid cooling leads to amorphous vanadium oxide films.

Throughout this work, thin films are sputtered from 2" high purity metal, semimetal and oxide targets:

- V (Testbourne 99.95%)
- V-Ge 95-5 at.% (Testbourne 99.99%)
- Ge (Testbourne 99.999%)
- Si (AJA 99.999%)
- Cr (Testbourne 99.95%)
- CuCoMn (Testbourne 99.9%)
- W (Kurt J. Lesker 99.95%)
- Ti (Testbourne 99.99%)
- Ta (Testbourne 99.99%)
- Nb (Testbourne 99.99%)
- $La_{0.7}Sr_{0.3}MnO_3$ (Testbourne 99.9%).

Pieces of <100> Si wafers, of few centimeters in size, are the most common substrate types used in this work. Multilayered absorber coatings are deposited on reflecting Al substrates (50 mm x 50 mm x 0.5 mm Al sheets from Goodfellow or 50 mm x 50 mm SavoSolar multichannel Al). Furthermore, to study the influence of substrates on the thermochromic behaviour of thin films, fused silica, single crystal c-cut $Al_2O_3$ and GaN substrates are investigated.

The exact process parameters of each sputtered film are summarized in the beginning of the corresponding result section.

A view of the laboratory thin film deposition facility, where the experiments of this study have been carried out is shown in Figure 3.4. The particularity of the system constists of the interconnection of a vaccum deposition chamber with scanning tunneling microscopy/spectroscopy and UV and X-ray photoelectron spectroscopy characterization platforms. The vacuum connected setup, permits the analysis of film morphology, elemental composition and the electronic properties of pristine sample surfaces.
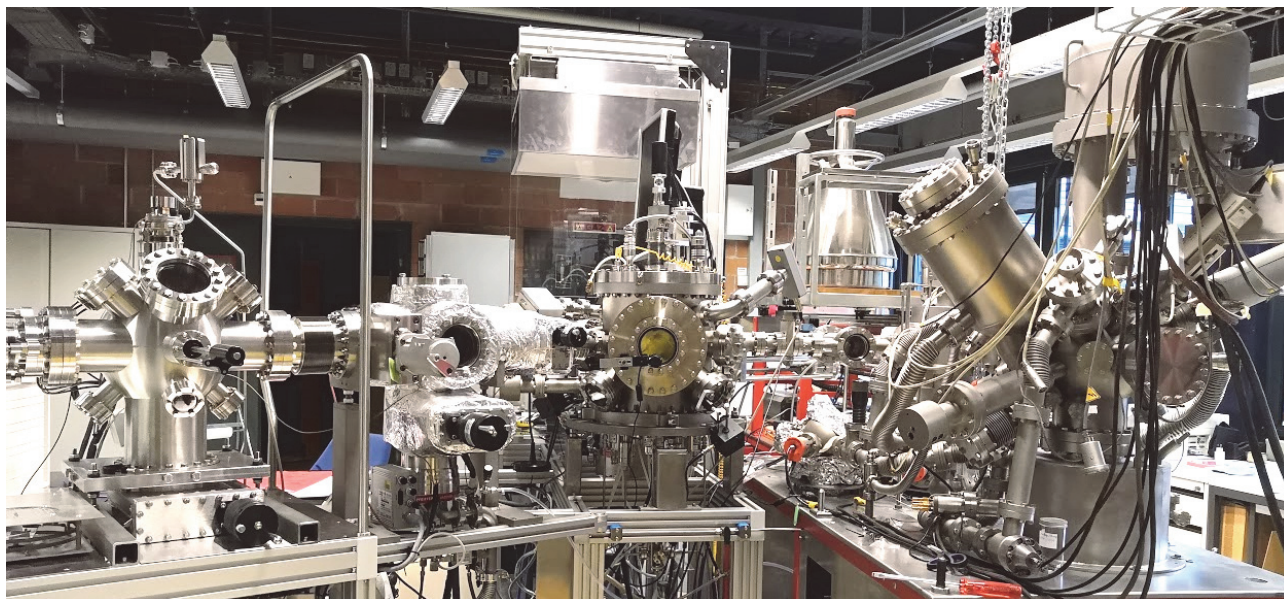
Figure 3.4. Thin film sputtering and characterization facility at LESO-PB. The high vacuum deposition chamber (center) is connected in-line with a scanning tunnelling microscope (left) and a UV and X-ray photoelectron spectrometer (right).

## 3.1.2  High power impulse magnetron sputtering (HiPIMS)

HiPIMS is a relatively recent advance in sputtering technology, that quickly become popular among researchers in the coating industry after Kouznetsov's seminal work on a "novel pulsed magnetron sputter technique utilizing very high power densities" published in 1999 [Kouznetsov, 1999]. Its popularity is due to the higher film quality of deposited films, which are denser and harder than for conventional magnetron sputtering, and to the convenience of upgrading existing magnetron sputtering systems to HiPIMS just by changing the power supply.

HiPIMS boosts the advantages of conventional magnetron sputtering by applying short, high amplitude voltage pulses to the cathode, generating a very dense plasma with a large fraction of ionized sputter atoms. Ionized sputter atoms are a particularity of HiPIMS systems as in magnetron sputtering it is the process and reactive gas atoms that are ionized. Besides sustaining the discharge, the charged film-forming particles, ensure a plasma-assisted thin film growth affecting the film microstructure. The discharge voltage is pulsed such that the peak current and power densities are about two orders of magnitude higher than for typical DC sputtering. To avoid overheating of the target and to keep the average operating power at manageable levels, the high-voltage pulses should be delivered in low duty cycles (<10%). The high amplitude discharge is typically operated with pulse lengths ranging from a few tens up to several hundreds of microseconds and pulse frequencies of tens to thousands of Hz. Typical HiPIMS plasma parameters compared with a DC magnetron sputtering plasma are given in Table 3.1.

Table 3.1. Typical plasma parameters for HiPIMS and DC magnetron sputtering (DCMS) [Valentene-Feliciano, 2013].

| Parameter | HiPIMS | DCMS |
|---|---|---|
| Peak Power Density [W·cm$^{-2}$] | 1000 | 1 |
| Current Density [A·cm$^{-2}$] | 1 – 1000 | 0.01 – 0.1 |
| Discharge Voltage [V] | 500 – 1000 | 500 |
| Process pressure [Torr] | $10^{-3} - 10^{-2}$ | $10^{-3} - 10^{-2}$ |
| Electron Density [m$^{-3}$] | $10^{18} - 10^{19}$ | $10^{16}$ |
| Electron Temperature [eV] | 1 – 5 | 1 – 7 |
| Degree of ionization [%] | 30 – 100 | < 5 |
| Ion energy [eV] | 20 | 5 |

The current and voltage curves of a HiPIMS discharge over a vanadium target (Figure 3.5) show that at peak power, the discharge is not an arc since the cathode voltage when the current peaks, is around 550 V, that is a typical magnetron value.
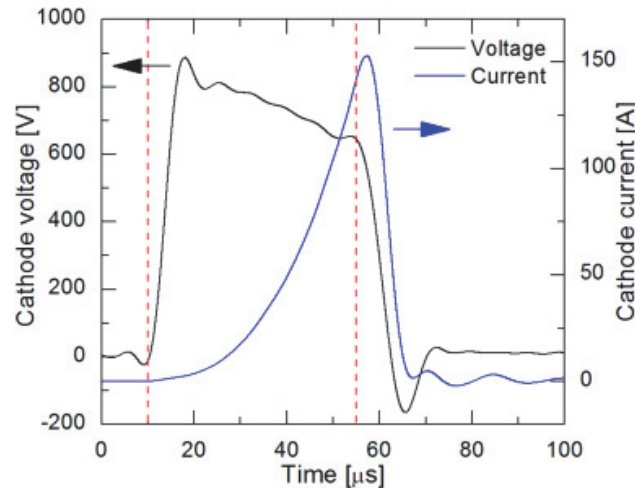


Figure 3.5. Current and voltage curves for a HiPIMS discharge over a vanadium target for a pulse length of 45 μs and peak cathode voltage of 900V in a reactive oxygen atmosphere. Dashed red lines correspond to the beginning and the end of the applied pulse. Reproduced with permission from [Loquai, 2016].

Owing to a significant fraction of the ionized sputter atoms returning to the target, the film deposition rates achieved by HiPIMS are significantly lower compared to conventional magnetron sputtering, being approximately half for an identical power input. This is one of the main drawbacks of HiPIMS.

Nonetheless, the high ionization levels and the high kinetic energy of the sputtered materials achieved in HiPIMS make this method promising for low-temperature deposition of crystalline films. In fact, there are several recent studies showing that good quality thermochromic VO$_2$ thin films have been successfully deposited at substrate temperatures of around 300°C and even on polymeric (Kapton) substrates [Vlcek, 2017; Portier, 2014; Loquai, 2016]. In the framework of this thesis, HiPIMS is briefly investigated as an alternative to conventional magnetron sputtering with the aim of lowering the substrate temperature.

## 3.2  Thin film characterization

## 3.2.1  Visible and near-infrared spectrophotometry

Spectrophotometry is the measurement of the relative intensity of reflected or transmitted light by a material, in this case a thin film, at a given wavelength. The measurement setup is composed of a light source, an integrating sphere and a spectrometer. In this work, the light source is an incandescent lamp that emits an isotropic radiation with a blackbody-like spectral distribution. With the use of an integrating sphere (LOT, RT-060-SF) the total and/or diffuse component of the thin film spectral reflectance, $\rho_\lambda$ and transmittance, $\tau_\lambda$ are determined. For the detection, an Oriel MultiSpec 125TM 1/8m spectrometer and an Instaspec IITM Silicon Photodiode Array Detector are used in the visible range ($0.36 - 0.8$ µm). In the near-infrared range ($0.8 - 2.5$ µm), a monochromator (Optronic Laboratories, OL 750-MPS) associated with a NIR-sensitive PbS detector (Optronic Laboratories, OL 730) are employed.

The determined spectra are relative to the spectrum of a white reference standard of known reflectance. The absolute error of the measurement is of ±2 percentage points.

With this set-up, the total spectral reflectance of thin films over the $0.36 - 2.5$ µm range is measured. For opaque materials, such as solar absorber coatings, the spectral transmittance, $\tau_\lambda$ is zero and the spectral absorptance, $\alpha_\lambda$ is directly determined from the spectral reflectance, $\rho_\lambda$ according to:

$$\rho_\lambda + \tau_\lambda + \alpha_\lambda = \rho_\lambda + \alpha_\lambda = 1. \qquad \text{Equation 3.2}$$

Then, the corresponding total solar absorptance, $\alpha_{sol}$, for the same $0.36 - 2.5$ µm spectral range is calculated with the AM 1.5G solar spectrum.

For sufficiently absorbing films, where multiple reflections can be neglected, the absorption coefficient, $\alpha_{coeff}$ can be approximated from the spectral reflectance and transmittance values according to:

$$\alpha_{coeff} = -\frac{1}{d}\ln\frac{\tau_\lambda}{1-\rho_\lambda} \ [cm^{-1}] \ \text{[Demichelis, 1987]} \qquad \text{Equation 3.3}$$

Plotting $(\alpha_{coeff}h\nu)^{1/r}$ vs. $h\nu$, where $h\nu$ is the photon energy, expressed in eV, and the value of the exponent $r$ depends on the nature of the electronic transition in the examined material:

- $r = 1/2$ for direct allowed
- $r = 3/2$ for direct forbidden
- $r = 2$ for indirect allowed
- $r = 3$ for indirect forbidden,

one obtains the Tauc plot from where the optical bandgap of the thin film material is determined.

## 3.2.2  Fourier Transform Infrared Spectrophotometry

The spectral reflectance in the mid-infrared range ($2.5 - 16.7$ µm) is measured with a Bio-Rad FTS-175C Fourier transform infrared spectrometer equipped with a 3" golden integrating sphere and a high-performance nitrogen-cooled Mercury-Cadmium-Telluried (MCT) detector.

At the core of the FTIR spectrometry is an interferometer which produces a signal in which every data point has information about every infrared frequency that comes from the source (high temperature SiC ceramic). Encoding all frequency information in one interferogram is achieved by using a beamsplitter that divides the incoming infrared beam into two beams, one striking a fix mirror and the other a moving mirror. The reflected beams recombine, but because of the different optical path travelled the beams generate an interfence pattern or interferogram. The beam is then directed to the sample, where some energy is absorbed and some is reflected. The reflected beam reaches the detector and the corresponding interferogram signal is processed into a frequency spectrum using a fast Fourier transform (FFT) algorithm. The final sample spectrum is relative to the reference spectrum measured for a gold standard. Schematic of the FTIR analysis process is shown in Figure 3.6.
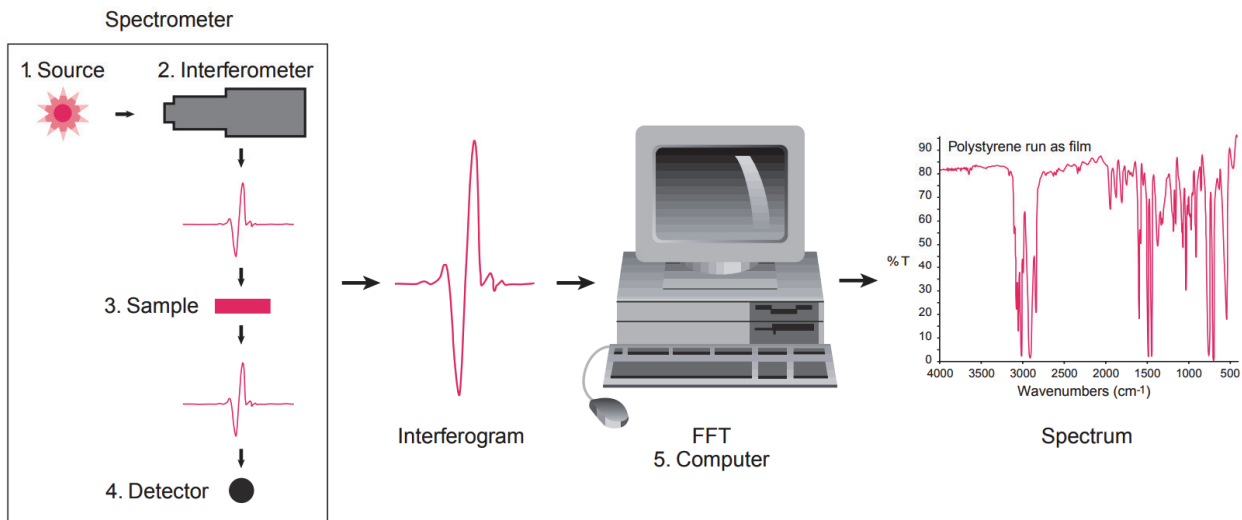


Figure 3.6. Schematic representation of the FTIR sample analysis process. Source: Thermo Nicolet Corporation.

For opaque materials, the spectral emittance $\varepsilon_\lambda$ is directly expressed from the spectral reflectance applying Kirchhoff's law:

$$\varepsilon_\lambda = \alpha_\lambda = 1 - \rho_\lambda.$$

Equation 3.4

The thermal emittance of the absorber, $\varepsilon_{th}$ is determined by weighting the spectral emittance, measured over the 2.5 – 14 µm spectral range, with the black body radiation of a body at T = 373° K (where a collector temperature of 100° C is considered for normal operating conditions).

In order to have a precise control of the sample temperature during FTIR spectrometry measurements, a customized, portable heating stage is built (Figure 3.7). It is designed in such way that the back-heated sample is placed very close to the integrating sphere opening, but without any direct contact with the surface of the sphere's enclosure. This is important, as the coating oxidizes after exposure to high temperatures. The thermocouple used to monitor the sample temperature is fixed inside the copper heating block. Due to the high thermal conductivity of Cu, the temperature inside the Cu block is considered to be the same as that of the sample fixed on it (samples are usually few hundred nanometers of thermochromic films deposited on 0.5mm conducting Al substrates).
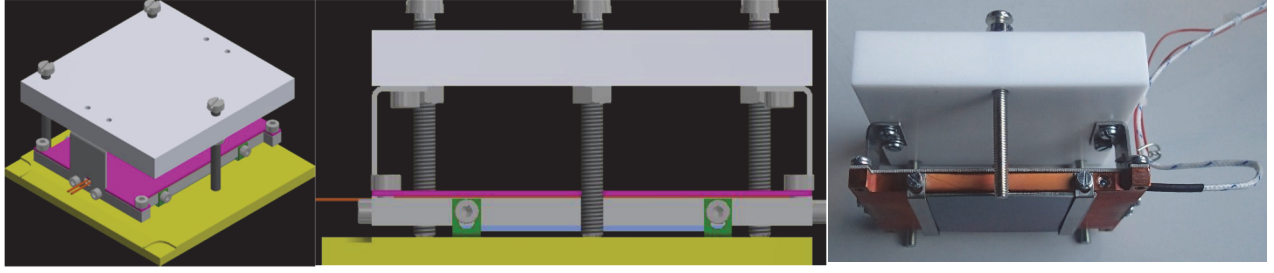
Figure 3.7. Schematic and photograph of the designed heating stage.

## 3.2.3 Ellipsometry

Ellispometry is an optical analysis technique used to determine the optical constants, n and k and the thickness of thin films. These values are not directly measured, instead the changes in the polarization of incident light reflected from a sample are recorded. The incident light is linearly polarized with both p- and s-components. The reflected light is elliptically polarized and it is described by a relative amplitude change, Ψ and a relative phase difference, Δ between p and s components (Figure 3.8). Measured quantities, Ψ and Δ, are related with the complex reflection coefficients, $r_p$ and $r_s$ corresponding to the s- and p- polarized light by the fundamental equation of ellipsometry:

$$\rho = \frac{r_p}{r_s} = \tan(\Psi)e^{i\Delta}$$

Equation 3.5

with

$$\tan(\Psi) = \frac{|r_p|}{|r_s|}$$

Equation 3.6

and

$$\Delta = \delta_P - \delta_S$$

Equation 3.7

where $|r_p|$ and $|r_s|$ are the amplitude diminution and $\delta_P$ and $\delta_S$ are the phase changes for the p- and s-components of the reflected light.
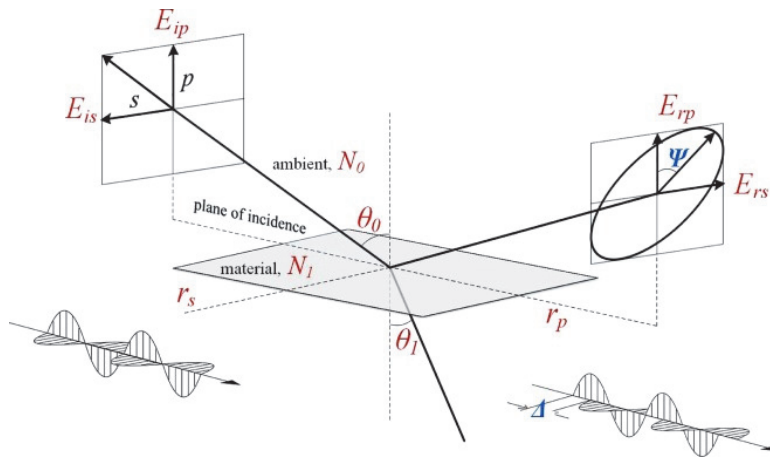


Figure 3.8. Principle of ellipsometric measurement. [Dorywalski, 2016]

The reflection coefficients $r_p$ and $r_s$ are related with the complex refractive index N = n - ik and with the complex delectric permittivity ε = $N^2$ by the Fresnel equations:

$$r_p = \frac{N_1 \cos\theta_0 - N_0 \cos\theta_1}{N_1 \cos\theta_0 + N_0 \cos\theta_1} = |r_p|e^{i\delta_p}$$

Equation 3.8

$$r_s = \frac{N_0 \cos\theta_0 - N_1 \cos\theta_1}{N_0 \cos\theta_0 + N_1 \cos\theta_1} = |r_s|e^{i\delta_s}$$

Equation 3.9

where $N_0$ and $N_1$ are the complex refractive indices of the ambient air and the measured material, respectively, $\theta_0$ is the angle of incidence and $\theta_1$ the angle of refraction. Then, the pseudodielectric permittivity is determined directly from the measured ellipsometric parameters, Ψ and Δ, with the following expression:

$$\langle\varepsilon\rangle = \sin^2\theta_0 \left[1 + \tan^2\theta_0 \left(\frac{1-\rho}{1+\rho}\right)^2\right]$$

Equation 3.10

The measured data is interpreted by means of nonlinear regression methods. An optical model of the sample is constructed and, based on the Fresnel equations, the theoretical values of Ψ and Δ are calculated for each wavelength and angle of incidence, $\theta_0$. Then, the experimental and theoretical data are fitted and the mean square error is minimized.

For non-absorbing films, the Cauchy dispersion law is commonly used to fit the shape of the optical constant, n versus wavelength, λ:

$$n(\lambda) = A + \frac{B}{\lambda^2} + \frac{C}{\lambda^4}$$

Equation 3.11

where the coefficients A, B and C are determined by fitting the equation to measured refractive indices at known wavelengths.

In this work, a Semilab SE-2000 visible ellipsometer is used to determine the optical constants and thicknesses of transparent $SiO_2$, $TiO_2$, $Ta_2O_5$ and NbO thin films. Sample roughness should be much lower than the wavelength of the light as rough surfaces result in light depolarization. Hence, for the ellipsometric measurements, the films are sputtered onto single crystal Si wafers. The samples are measured at four different incidence angles: 60°, 65°, 70° and 75°. The data analysis is performed with Winelli and SEA softwares. For the regression, initial film thicknesses are approximated from quartz balance measurements.

## 3.2.4  Four-point probe resistivity measurements

The electrical resistivity of conductive, uniform thin films is commonly measured by the four-probe point method in the Van der Pauw configuration. The contacts are placed at the corners of the generally square samples. A DC current is applied on contacts 1 and 2, while the voltage is measured from contacts 3 and 4 (Figure 3.9).
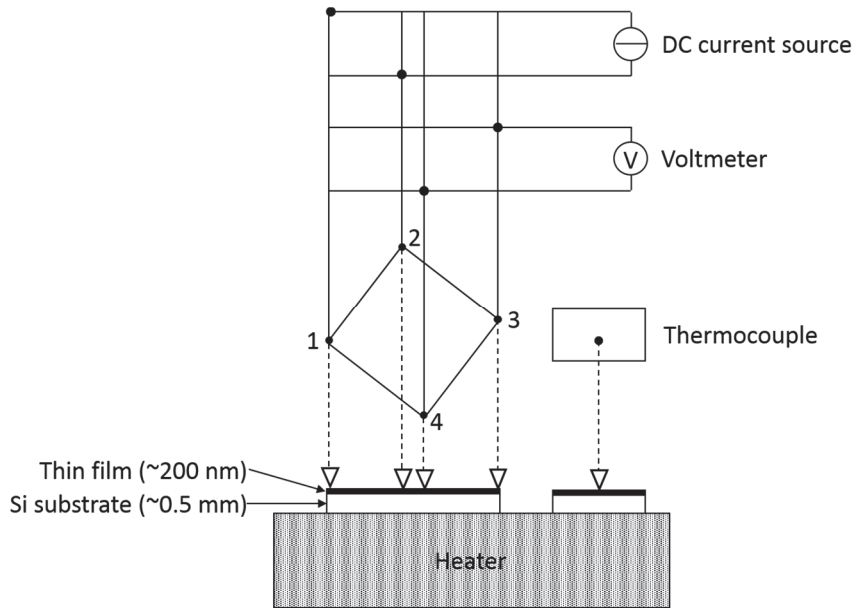
Figure 3.9. Setup for the electrical resistivity measurement. Adapted from [Springer, 2004].

The resistivity can be determined with the following relation:

$$\rho_{DC} = \frac{\pi \cdot t}{2 \ln 2} \cdot (R_{12} + R_{23}) \cdot f\left(\frac{R_{12}}{R_{23}}\right)$$

Equation 3.12

where t is the film thickness, f is the geometrical correction factor and $R_{12}$ and $R_{23}$ are the resistances between the points indicated by the indeces. For nearly square shaped samples $R_{12}$ and $R_{23}$ are considered to be equal and f is close to unity.

The resistivity of materials depends on the temperature. Increasing the temperature, the resistivity of metals increases, due to lattice vibrations and phonon scattering, while the resistivity of semiconductors decreases. In the particular case of $VO_2$, which exhibits a semiconductor-to-metal transition when thermally activated, a discontinuous change in resistivity of several orders of magnitude occurs. Therefore, measuring the temperature dependent film resistivity, is the most convenient and straightforward way to detect if the deposited sample is undergoing a thermochromic transition or not. The temperature, cycled between room temperature and 100°C, is measured by a thermochouple in direct contact with the sample surface. ρ vs. temperature curves are acquired both during heating and cooling of the samples as thermchromic properties exhibit hysteresis.

## 3.2.5  X-ray diffraction

X-ray diffraction (XRD) is a non-destructive analytical technique used for phase identification of crystalline materials. Incoming X-rays are scattered by the atomic crystal planes. When the path difference between successive scattering planes is an integer multiple of the X-ray wavelength, the interference is constructive and a diffraction peak is produced. The sample is in Bragg condition (Figure 3.10). Expression of the Bragg law is:

$$n\lambda = 2d\sin\theta$$

Equation 3.13

where n is an integer, λ is the wavelength of the incident X-rays, θ is the angle of incidence and d is the interplanar spacing of the crystal.
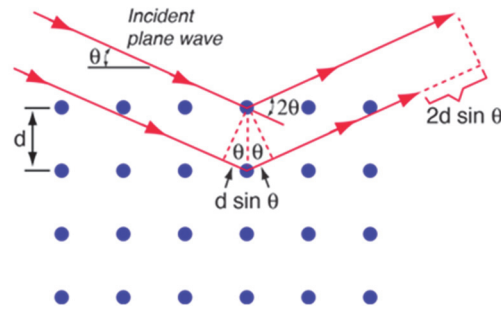
Figure 3.10. Illustration of Bragg diffraction and constructive interference of reflected X-rays. Source: [science-wise.info, 2019].

By varying the angle θ, the Bragg condition is satisfied by different d spacings in polycrystalline materials. The intensity of the diffraction peaks plotted against the angle at which they are measured, give the diffraction pattern that is characteristic for each compound. The crystalline phases are identified by matching the measured XRD spectrum against a database of recorded phases such as the Powder Diffraction File (PDF) of the International Center Diffracion Data (ICDD).

The width of the diffraction peak carries information about the sample crystallite sizes and can be determined from the Scherrer equation:

$$\tau = \frac{K\lambda}{\beta cos\theta}$$

Equation 3.14

where :

- τ is the mean size of the crystallites ;

- K is a shape factor, with a typical value of 0.9 for isotropic particles;

- λ is the wavelength of the X-ray radiation, λ = 1.54056 Å for the Cu Kα1 radiation;

- β is the full width at half maximum (FWHM) of the diffraction peak (the instrumental line broadening should be substracted);

- Θ is the Bragg angle.

The Scherrer equation gives the lower bound of the crystallite size and its applicability is limited to nano-scale crystallites (or coherently scattering domains). However, strain or crystal lattice imperfections (e.g. dislocations, twinning) can also contribute to the diffraction peak broadening. The Williamson-Hall method, Rietveld refinement or Double-Voigt approach are more sophisticated size-strain analysis methods.

The θ/2θ Bragg – Brentano diffraction geometry is the conventional scanning configuration, but it is not surface sensitive with a weak signal coming from the film and an intense signal from the substrate. Grazing Incidence X-ray Diffraction (GIXRD) has been developed to overcome this limitation in thin film phase analysis (Figure 3.11). In GIXRD, the incidence angle is fixed at a small angle (typically between 1 and 4°), thus the path length of X-rays through the film is increased, maximizing the signal from the thin layer and minimizing the substrate contribution. Due to the fixed angle of incidence, the analysis depth during the measurement is constant, while the moving detector arm also detects grains with crystal planes that are tilted with respect to the sample surface. By contrast, in conventional diffraction geometry, the analysis depth

varies during the symmetrical θ/2θ sweep (the incident X-ray source and the detector are both moved) and only grains oriented parallel to the surface are detected.
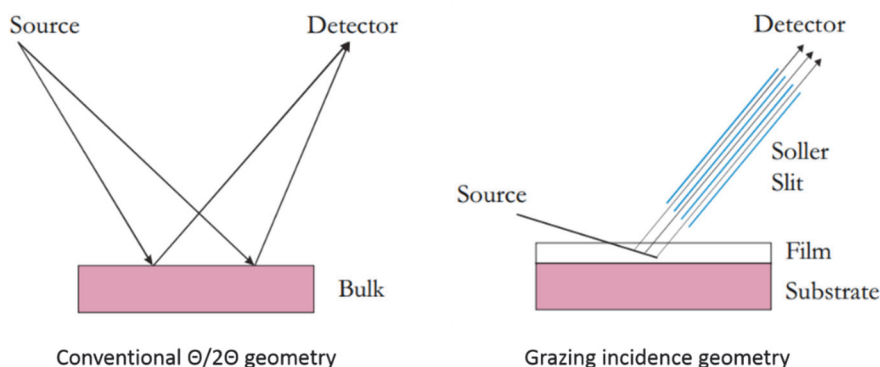


Figure 3.11. Schematic of the conventional θ/2θ Bragg-Brentano geometry for bulk analysis and GIXRD thin film geometry with longer beam path length in the film. Source: [H&M Analytical, 2015]

In this work, crystallinity and phase composition of the deposited films are determined at room temperature by grazing incidence X-ray diffraction (GIXRD, Empyrean system equipped with PIXcel-1D detector, monochromatic Cu Kα radiation, grazing incidence GI angle 4°).

## 3.2.6 Rutherford Backscattering Spectrometry

Rutherford Backscattering Spectrometry (RBS) is a quantitative Ion Beam Analysis (IBA) method for analysis of the surface layers of a solid material. A high-energy (MeV) $He^{2+}$ ion beam irradiates a sample and the energy distribution and yield of the backscattered $He^{2+}$ ions for a given angle is measured (Figure 3.12). The known backscattering cross sections for each element, enable a quantitative analysis of the elemental composition vs. depth, which is given by the measurement of the areal density (atoms/cm$^2$) and can be converted into nm when the layer density is known. The method can detect all elements except hydrogen but is best suited for heavy elements in a light matrix. Assuming that the density of the layer is known standard measurements have usually an absolute accuracy of ≈5% in depth and concentration, although the relative accuracy for a series of samples can be much smaller.

In this work, RBS is used for precise Ge quantification in the $Ge_xV_{(1-x)}O_{2+y}$ thin films and film thickness determination. The measurements are carried out at Ionlab Arc of the HES-SO University of Applied Sciences and Arts, Western Switzerland, under the supervision of Prof. Harry Withlow. The data is collected using a 1.7 MV tandetron accelerator with a 2 MeV $He^{2+}$ ion beam. The incident angle of the ion beam is 0°, normal to the sample surface, while backscattered particles are detected at 150° scattering angle. Data analysis is performed using the Ion Beam Analysis DataFurnace code [Barradas, 1997].
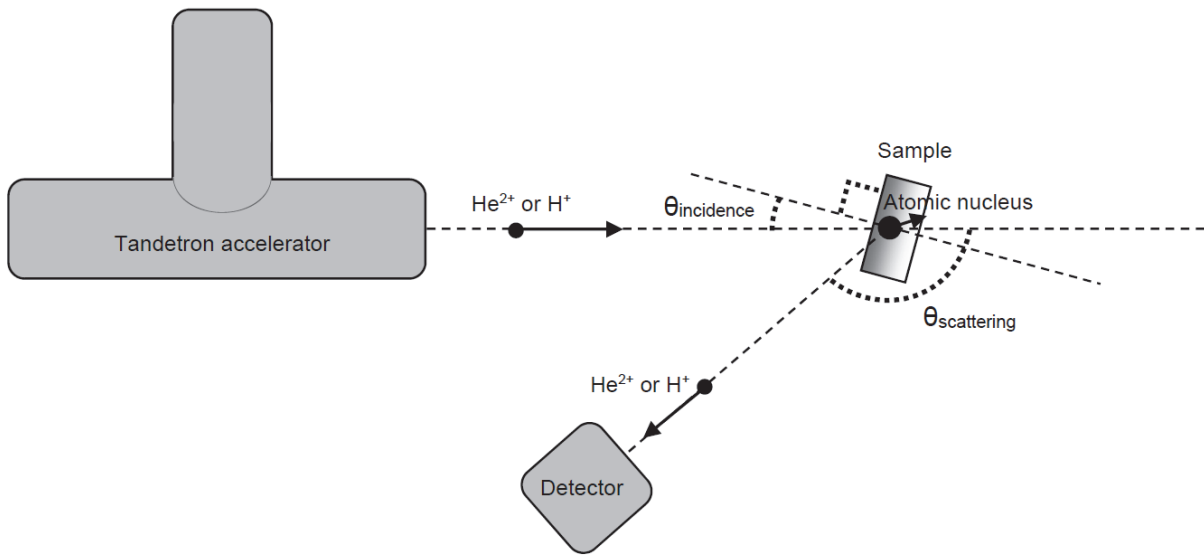
Figure 3.12. Experimental configuration of the RBS analysis. A 1.7MV Tandetron accelerator irradiates the sample with MeV $He^{2+}$ or $H^+$ ions. Part of the $He^{2+}$ ions backscattered by atomic nuclei inside of the target enter into a detector measuring their kinetic energy.

## 3.2.7 Scanning Tunneling Microscopy

Scanning tunneling microscopy (STM) is the first scanning probe microscope that allows real-space imaging of conductor or semiconductor surfaces with atomic resolution [Binnig, 1983]. When a conductive tip is brought within very small distance (≈10 Å) from a sample substrate, and a bias voltage is applied between the two, electrons begin to tunnel from one to another, depending on the sign of the applied bias.

Electron tunneling is based on quantum mechanics and on the wavelike behavior of electrons governed by the Schrödinger equation:

$$E\psi_n(z) = -\frac{\hbar^2}{2m}\frac{\partial^2\psi_n(z)}{\partial z^2} + U(z)\psi_n(z)$$

Equation 3.15

The wavefunction of electrons in a potential well, spreads into the barrier and tunnels to the other side of the potential barrier (Figure 3.13). From the continuity equations of the wavefunction and its derivatives at the boundaries, the probability of electrons tunneling through the barrier is found:

$$P = \frac{|\psi(z)|^2}{|\psi(0)|^2} = e^{-2kz}$$

Equation 3.16

where
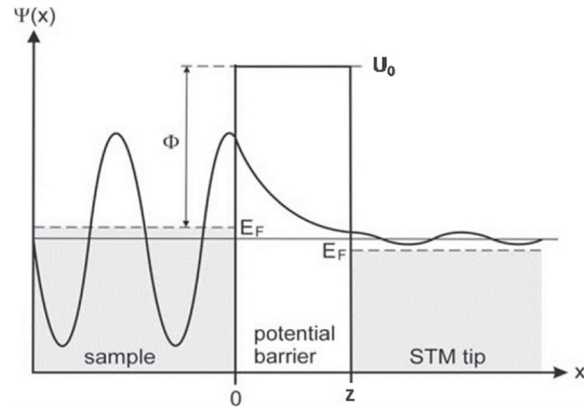
$$k = \frac{\sqrt{2m(U(z) - E)}}{\hbar}$$

Equation 3.17

Figure 3.13. Quantum tunnelling effect. The exponential damping of a wave function within a potential barrier of height Φ, which in the case of STM is the effective local work function – the minimum energy required to remove one electron from the sample and bring it to the vacuum level. [Trixler, 2013]

The tunneling current, $I_t$ is then proportional to the tunneling probability, and is an exponential function of the distance, z:

$$I_t \sim e^{-2kz} \hspace{4cm} \text{Equation 3.18}$$

This rapid, exponential decay of the tunneling current with the separation d, of about one order of magnitude change in $I_t$ for a ≈1 Å change in the sample-tip separation, gives STM the remarkable sub-angstrom sensitivity in the z direction.

Topographic images can be collected in constant-height or constant-current mode (Figure 3.14).
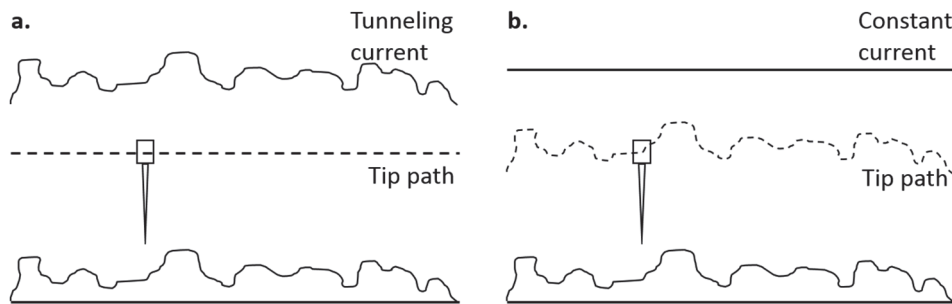


Figure 3.14.Comparison of constant-height (a) and constant-current (b) mode for STM.

In constant-height mode, the tunneling current varies depending on the topography and local electronic surface states. It is the faster scanning mode, but it is suitable for only relatively smooth surfaces. In constant-current mode, the piezo of the Z-axis scanner is actuated to adjust the tip-sample distance so that the tunneling current is kept constant. In this mode, irregular surfaces can be measured with high precision but the measurement is more time consuming.

In the I/V spectroscopy mode (Scanning Tunneling Spectroscopy, STS), the local electronic properties of the analysed surfaces are probed. Having the tip over a feature of interest and sweeping the bias voltage while measuring the tunneling current, the characteristic I-V curves and corresponding electronic structure information are obtained locally.

In this work, a SPECS SPM Arhus 150 scanning tunneling microscope is used to investigate the surface topography, particle size and roughness of pristine samples that are transferred under vacuum between the

deposition and the STM analysis chamber. Furthermore, in the particular case of pure and Ge doped $VO_2$ samples, the I-V characteristics and band gaps are determined locally by STS. In doped samples this also gives information about the doping homogeneity.

## 3.2.8  Atomic Force Microscopy

In atomic force microscopy (AFM), high-resolution topographical images of sample surfaces are obtained based on the interactions between a tip and a sample surface. Unlike STM, AFM allows the measurement of non-conductive samples. The main components of a typical AFM are: a flexible cantilever with a small tip at the free end, a laser and a position sensitive photodiode detector, and a piezoelectric scanner for precise displacement of the sample in the x, y, z direction .

When the tip approaches very closely the sample surface (range of interatomic distances), the attractive or repulsive forces manifest between the tip and the sample surface, causing a positive or negative bending of the cantilever. The deflection of the cantilever is monitored as the tip travels across the surface, hence a topographical image is obtained. The cantilever displacement is measured by focusing a laser beam on the back of the cantilever and recording the back-reflected beam with a position sensitive photodiode.

Measurements are done in contact, tapping or non-contact mode. In contact mode, the tip experiences repulsive van der Waals forces. Moving the tip closer or further away from the sample, the cantilever deflection is kept constant during scanning, and from the scanner height information the topographical image of the surface is obtained. In tapping mode, the cantilever oscillates close to its resonance frequency, "tapping" the surface. During scanning, the tip is adjusted to maintain the oscillation amplitude constant and it is this adjustment used to form the topography image. In non-contact mode, the tip oscillates above the sample during scanning. Changes in the oscillation amplitude indicate changes in the attractive van der Waals forces between sample and tip and surface topography is determined.

In this work, surface topography and particle sizes are determined by atomic force microscopy (AFM Multimode, Nanoscope IIIa; Bruker) in contact mode.

## 3.2.9  Scanning electron microscopy

In scanning electron microscopy (SEM), electrons, instead of light are used to obtain high resolution images of the studied samples. Samples are scanned by a beam of high energy electrons, which leads to the emission of backscattered electrons, secondary electrons, characteristic X-rays and Auger electrons from the sample surface and near-surface material. Backscattered electrons are high energy electrons resulting from elastic interactions between the incident beam and the sample, while secondary electrons are lower in energy and result from inelastic scattering. SEM reveals the surface morphology (Secondary Electron Imaging) and provides image contrast as a function of elemental composition (Backscattered Electron Imaging). Moreover, the chemical composition of the examined samples can be determined by Energy Dispersive X-ray Analysis (EDX), as the energy of emitted X-rays is characteristic to the atomic structure of the constituting elements.

SEM analysis are carried out at the Interdisciplinary Center for Electron Microscopy (CIME) of the École Polytechnique Fédérale de Lausanne on a Zeiss Gemini 300 SEM microscope.

## 3.2.10　　X-ray and UV photoelectron spectroscopy

X-ray Photoelectron Spectroscopy (XPS), also known as Electron Spectroscopy for Chemical Analysis (ESCA) and ultraviolet photoelectron spectroscopy (UPS) are surface sensitive, spectoscopic techniques based on the photoelectric effect.

XPS gives valuable information on both the electronic structure and chemical composition of the analysed material. The sample is irradiated with monoenergetic X-rays and emission of photoelectrons occurs. The measurement must be performed in ultra-high vacuum to prevent any surface contamination, as only photoelectrons from the outermost layers will be ejected (0 - 10 nm depth) and will reach the detector. The kinetic energy of the photoelectrons is measured with a concentric hemispherical analyser (CHA), which uses electrostatic fields that allow only electrons of a minimum required energy (the pass energy) to reach the multichannel plate detector. The energy-sensitive detector simultaneously measures the kinetic energy and number of electrons that escape from the surface of the analyzed material. The resulting scan is a spectrum of peaks at various kinetic energies. Knowing the kinetic energy, the binding energy can be calculated following a simple energy conversion relation:

$$E_B = h\nu - E_{kin} - \Phi_{spec}$$

Equation 3.19

where $E_B$ is the binding energy, $E_{kin}$ the kinetic energy, $h\nu$ the photon energy and $\Phi_{spec}$ is the work function (Figure 3.15). Each element has its characteristic atomic binding energies, therefore its own set of XPS peaks. Hence, XPS is used to identify elemental composition. Sample stoichiometry is determined by integrating the core level peaks of each element, after substracting a Shirley background, and using known atomic sensitivity factors [Scofield, 1976]. For compounds, the absolute error is in the order of 10%, however, the relative error between measurements is significantly lower.
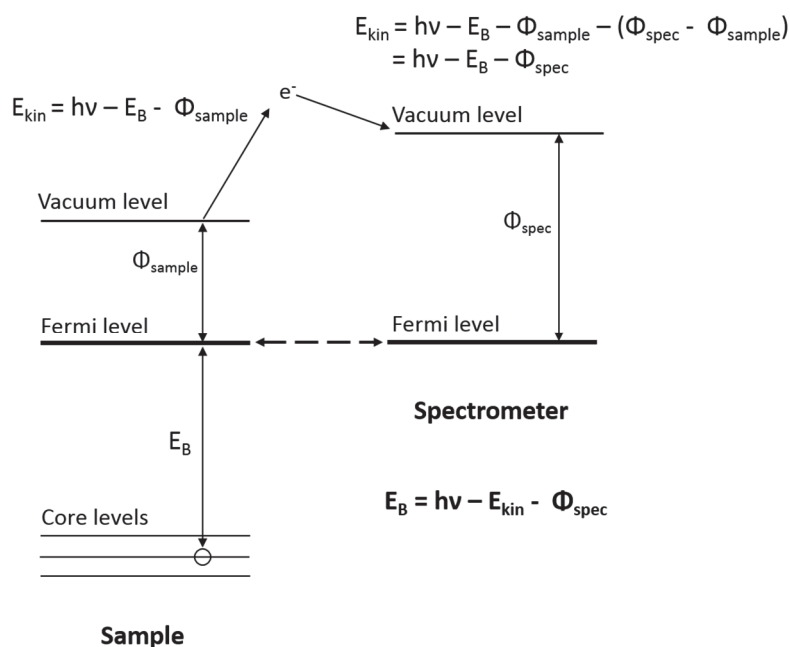


Figure 3.15. XPS energy conversion.

Almost all elements with the exception of very light elements such as H and He can be detected with XPS. The peak shape and shifts in peak position give information on the chemical environment of the elements e.g. oxidation state.

UPS is very similar to XPS the only difference being the radiation source. In XPS soft X-rays with photon energy >1000 eV are used, which lead to ionization and emission of core (inner shell) electrons. By contrast, UPS uses UV radiation of low photon energy in the range of 10 - 45 eV. Photons interact with the valence levels of the solid giving information on the valence band structure of the studied material (e.g. valence band maximum, VBM or the work function, Φ)(Figure 3.16).
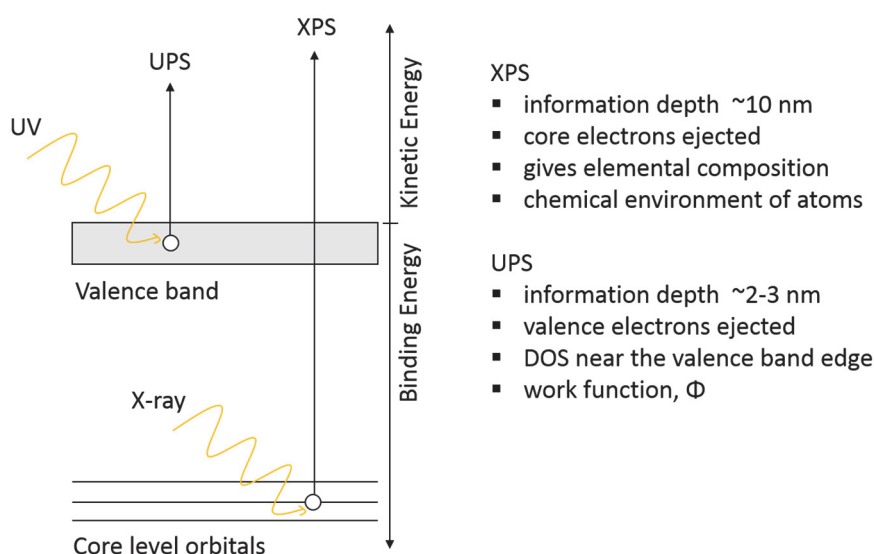


Figure 3.16. Comparison of XPS and UPS surface electron spectroscopies.

The X-ray and UV photoelectron spectroscopy analysis is performed on a SPECS Leybold EA11 MCD electron spectrometer and the base pressure in the measurement chamber, even without liquid nitrogen cooling, is in the range of $5 \cdot 10^{-10}$ mbar. The spectrometer is equipped with an X-ray source for the XPS (Mg Kα at hv = 1253.6 eV) and a He discharge lamp for the UPS measurement (He I at hv = 21.22 eV, He II at hv = 40.82 eV). The XPS survey spectra are taken at a pass energy of 50.4 eV, while the core level spectra are measured at 29.9 eV. The electron energy is calibrated with respect to the reference Au 4f7/2 core-level signal at 83.8 eV binding energy.

Due to the high surface sensitivity of photoelectron spectroscopy, in-situ characterization of the sputtered thin films is recommended. The samples are transferred under vacuum between the deposition chamber and the photoelectron spectrometer, therefore, the clean, as-deposited sample surfaces are analysed with no sputter-cleaning needed.

## 3.3 Numerical analysis

The optical response of the proposed multilayered thin film coatings is calculated based on the transfer-matrix method described herein. The calculated and/or measured solar absorptance and thermal emittance values of the absorber coatings, are used to predict the thermal performance of the proposed thermochromic flat plate collectors. The principles of the numerical simulation model are described.

### 3.3.1 Matrix formalism for multilayered coatings

The reflectance, ρ and transmittance, τ of a multilayer can be calculated from the Fresnel equations and are based on a matrix formulation of the continuity conditions for the electric and magnetic field components derived from the Maxwell equations.

In the following, the principles and basic equations describing the interaction of electromagnetic radiation with multiple interfaces are briefly summarized according to [Macleod, 2010; Mack, 2008].

The spectral behavior of any material is described by a fundamental quantity known as the complex refractive index, N:

$$N = n + ik \qquad \text{Equation 3.20}$$

where n is the real refraction index and k is the extinction coefficient. The former is defined as the ratio of the velocity of light in free space, $c_0$ to the velocity of light in the material, $v$:

$$n = \frac{c_0}{v} \qquad \text{Equation 3.21}$$

while the latter is a measure of the amplitude reduction of the electromagnetic wave during its propagation through the considered medium and it is related to the absorption coefficient, α$_{coeff}$ by:

$$\alpha_{coeff} = \frac{4\pi k}{\lambda} \qquad \text{Equation 3.22}$$

An incident, linearly polarized electromagnetic radiation reflects and refracts at the interface between two different media. The relationship between the incident and refracted angle is given by Snell's law:

$$N_0 \sin \theta_0 = N_1 \sin \theta_1 \qquad \text{Equation 3.23}$$

where $\theta$ stands for the angle of incidence/refraction and the indeces 0 and 1 represent the incident and exit media with respect to the boundary.

To simplify the oblique incidence calculations, the electromagnetic wave is split into two linearly polarized components, one with the electric vector aligned parallel to the plane of incidence, called p-polarized and another perpendicular to the plane of incidence, known as s-polarized. The tilted optical admittance, $\eta$ for p- and s-components are then introduced:

$$\eta_p = \frac{n - ik}{\cos \theta} \qquad \text{Equation 3.24}$$

and

$$\eta_s = (n - ik)\cos\theta \qquad\qquad \text{Equation 3.25}$$

Denoting $\eta_p$ or $\eta_s$ by $\eta$ for either polarization, the amplitude reflection and transmission coefficients, r and t, are determined according to:

$$r = \frac{\eta_0 - \eta_1}{\eta_0 + \eta_1} \qquad\qquad \text{Equation 3.26}$$

$$t = \frac{2\eta_0}{\eta_0 + \eta_1} \qquad\qquad \text{Equation 3.27}$$

For absorbing materials, the reflectance, ρ defined as the ratio of the reflected to the incident irradiance and the transmittance, τ defined as the ratio of the transmitted to the incident irradiance are expressed as:

$$\rho = \left(\frac{\eta_0 - \eta_1}{\eta_0 + \eta_1}\right)\left(\frac{\eta_0 - \eta_1}{\eta_0 + \eta_1}\right)^* \qquad\qquad \text{Equation 3.28}$$

and

$$\tau = \frac{4\eta_0 Re(\eta_1)}{(\eta_0 + \eta_1)(\eta_0 + \eta_1)^*} \qquad\qquad \text{Equation 3.29}$$

where * denotes the complex conjugate. The expressions are also valid for absorption-free media where k = 0 and, in which case, the equations are greatly simplified.

This analysis can be extended to find the reflectance of an assembly of thin films. Multiple interfaces lead to multiple reflections and transmissions and the multilayer properties are determined by a summation of all these reflected and transmitted waves which interfere constructively or destructively. As waves travel through thin layers of thickness d, the phase factor is multiplied by exp(iδ) for positive-going waves travelling in the direction of incidence, and by exp(-iδ) for waves travelling in the opposite direction, where:

$$\delta = \frac{2\pi N d \cos\theta}{\lambda} \qquad\qquad \text{Equation 3.30}$$

with $\delta$ the phase thickness and $d$ the physical film thickness.

Satisfying the continuity conditions for the tangential electric and magnetic field components at each interface, results in the characteristic matrix for each layer:

$$\begin{bmatrix} E_a \\ H_a \end{bmatrix} = \begin{bmatrix} \cos\delta & \dfrac{i\sin\delta}{\eta_1} \\ i\eta_1\sin\delta & \cos\delta \end{bmatrix} \begin{bmatrix} E_b \\ H_b \end{bmatrix} \qquad\qquad \text{Equation 3.31}$$

where the indices a and b denote the interfaces in the direction of the wave propagation, d is the thickness of the layer between the two interfaces and E is the electric field component and H is the magnetic field component at the respective interfaces.

By extension, for an assembly of n layers, the characteristic matrix is the product of the individual layer matrices, taken in the correct order:

$$\begin{bmatrix} E_a \\ H_a \end{bmatrix} = \left\{ \prod_{r=1}^{n} \begin{bmatrix} \cos \delta_r & \dfrac{i \sin \delta_r}{\eta_r} \\ i\eta_r \sin \delta_r & \cos \delta_r \end{bmatrix} \right\} \begin{bmatrix} E_m \\ H_m \end{bmatrix}$$

Equation 3.32

with $E_m$ and $H_m$ the electric and magnetic field components in the emerging medium, m. $E_m$ and $H_m$ are connected by the optical admittance:

$$\eta_m = \frac{H_m}{E_m}$$

Equation 3.33

Therefore, the characteristic matrix can be written as:

$$\begin{bmatrix} B \\ C \end{bmatrix} = \begin{bmatrix} E_a/E_m \\ H_a/E_m \end{bmatrix} = \left\{ \prod_{r=1}^{n} \begin{bmatrix} \cos \delta_r & \dfrac{i \sin \delta_r}{\eta_r} \\ i\eta_r \sin \delta_r & \cos \delta_r \end{bmatrix} \right\} \begin{bmatrix} 1 \\ \eta_m \end{bmatrix}$$

Equation 3.34

The amplitude reflection coefficient, r and the reflectance, ρ become:

$$r = \frac{\eta_0 - \dfrac{C}{B}}{\eta_0 + \dfrac{C}{B}}$$

Equation 3.35

and

$$\rho = \left( \frac{\eta_0 - \dfrac{C}{B}}{\eta_0 + \dfrac{C}{B}} \right) \left( \frac{\eta_0 - \dfrac{C}{B}}{\eta_0 + \dfrac{C}{B}} \right)^{*}$$

Equation 3.36

Finally, the transmittance, τ is:

$$\tau = \frac{Re(\eta_m)(1 - \rho)}{Re(BC)^{*}}$$

Equation 3.37

and the absorptance, α is:

$$\alpha = 1 - \rho - \tau = (1 - \rho)\left( 1 - \frac{Re(\eta_m)}{Re(BC)^{*}} \right)$$

Equation 3.38

With the above equations, the spectral behavior of multilayered systems can be calculated based on the optical constants and thicknesses of the constituting layers. As calculations are tedious, optical simulation programs are employed. In this work, the optical response of the proposed multilayered absorber coatings is simulated with TfCalc thin film design software.

## 3.3.2  Simulation of the thermal performance of flat plate solar collectors

A numerical simulation model, Solar Collector Simulator (SolCoSi) is employed to evaluate the thermal performance of the envisaged thermochromic flat plate collectors based on the measured solar absorptance, $\alpha_{sol}$ and thermal emittance, $\varepsilon_{th}$ values. The validated model [Perez-Espinosa, 2018], proposes a control volume discretization of the flat plate collector in both the axial direction – along the multilayer stack and in the longitudinal direction – along the flow direction of the heat transfer fluid (Figure 3.17).

The model assumes steady state conditions, conductive heat transfer in solids, convective heat transfer in fluids and temperature-dependent thermophysical properties. The main components of the considered collector are: a bottom insulation, the air gap between the insulation and absorber, the absorber plate, the air gap between the absorber plate and the cover and one (or more) transparent cover.

The model is based on the energy balance equation:

$$\rho C_p \delta \frac{dT}{dt} = q_{in} - q_{out} + q_{gen}$$

Equation 3.39

where $\rho$ is the density, $C_p$ is the specific heat, $\delta$ is the layer thickness, $dT/dt$ is the variation of the temperature with time and it is zero for steady state conditions, $q_{in}$ and $q_{out}$ represent the inlet and outlet heat flux per unit and $q_{gen}$ is the generated heat per unit in the considered control volume.

The temperature of each node is obtained from the energy equation applied to each control volume:

$$(Z_{i,j} + Z_{i-1,j} + Zs_{i,j} + Zs_{i,j-1})T_{i,j} = Z_{i,j}T_{i+1,j} + Z_{i-1,j}T_{i-1,j} + \\ Zs_{i,j-1}T_{i,j-1} + Zs_{i,j}T_{i,j+1} + q_{gen\ i,j}$$

Equation 3.40

with $Z_{i,j}$ denoting the thermal heat transfer coefficients in the axial direction and $Zs_{i,j}$ the conductive thermal resistances of solids in the longitudinal direction measured in W/m²K. $T_{i,j}$ is the temperature of the considered node and $q_{gen\ i,j}$ is the generated heat in W/m². The thermal resistance is given by

$$Zs_{i,j} = \frac{k_{i,j}}{\delta_{i,j}}$$

Equation 3.41

for solids with $k_{i,j}$ the thermal conductivity and $\delta_{i,j}$ the distance between nodes, and by

$$Z_{i,j} = h_{rad\ i,j} + h_{conv\ i,j}$$

Equation 3.42

for fluids with $h_{rad\ i,j}$ and $h_{conv\ i,j}$ the radiative and convective heat transfer coefficients.

The generated heat depends on the solar irradiance and the optical properties of the cover and absorber plate (transmittance, reflectance and absorptance). For detailed description of the model the reader is referred to [Perez-Espinosa, 2018].
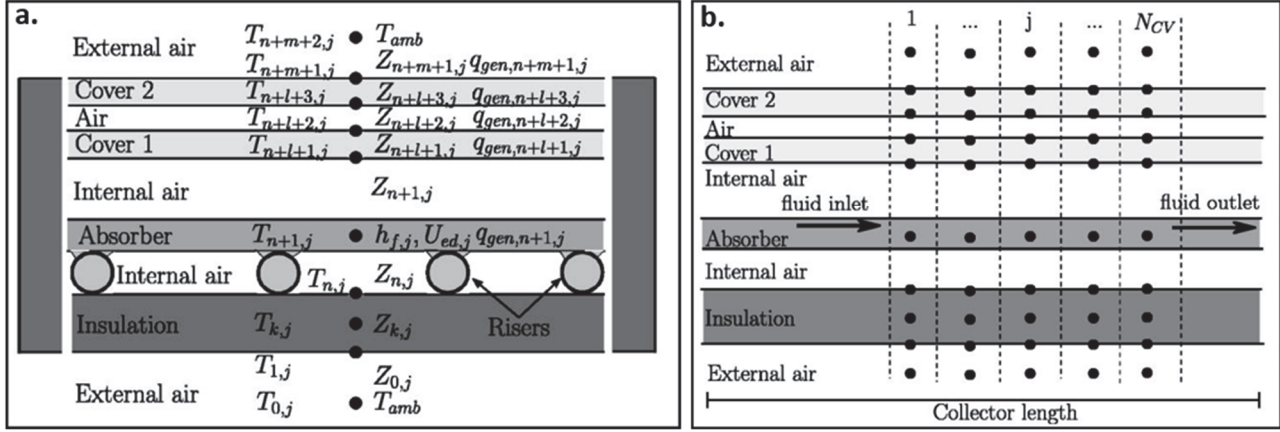


Figure 3.17. a. Axial discretization with the defined nodes and coefficients. b. Longitudinal volume discretization along the fluid flow direction. Reproduced from [Perez-Espinosa, 2018].

The efficiency of the thermal collector is expressed as a function of incident solar radiation, G, the fluid mass flow rate, m, the temperature difference between the inlet and outlet temperature and the absorber (or aperture) area, A according to:

$$\eta = mC_p(T_{out} - T_{in})/(GA)$$
<div align="right">Equation 3.43</div>

The efficiency of a solar thermal collector is not static as it changes with the operational conditions. Therefore, the collector efficiencies are determined for a series of inlet fluid temperatures, $T_{in}$, ambient temperatures, $T_{amb}$ and incident solar radiation, G. Then, the thermal efficiency is modelled as a quadratic performance curve according to:

$$\eta = \eta_0 + \frac{\eta_1 \Delta T}{G} + \frac{\eta_2 \Delta T^2}{G}$$
<div align="right">Equation 3.44</div>

$\eta_0$, $\eta_1$, $\eta_2$ are the curve coefficients where $\eta_0$ is the maximum collector efficiency and $\eta_1$, $\eta_2$ are parameters describing the thermal losses and $\Delta T = T_{in} - T_{amb}$.

The collector stagnation temperature is determined from the outlet fluid temperature for nearly zero mass flow conditions.

The complete list of parameters used for the simulation of the thermochromic collector performance is given in the Annex of this document.

# Chapter 4      Thermochromic VO$_2$ thin films

This chapter focuses on the deposition of pure VO$_2$ based thermochromic thin films. First, films sputtered onto Si substrates are studied and the minimum film thickness for achieving switching behavior is identified. Then, film behavior on several other substrates is reported. Furthermore, the effects of deposition parameters such as oxygen partial pressure and substrate temperature are investigated. Thin films deposited by high power impulse magnetron sputtering and traditional magnetron sputtering are compared, with focus on the influence of substrate choice. Finally, a perovskite-type oxide, La$_{0.7}$Sr$_{0.3}$MnO$_3$ is explored as alternative thermochromic material.

## 4.1      Magnetron sputtered VO$_2$ thin films

### 4.1.1   VO$_2$ sputtered on Si substrates

In this work, Si wafer pieces are the most often employed substrates due to convenience (e.g. easy handling and cutting), high temperature resistance (unlike soda-lime glass substrates where Na diffuses into the deposited thermochromic films and impacts the thermochromic film properties) and their relatively low cost. On Si substrates, high quality VO$_2$ thin films commonly reach higher than two orders of magnitude drop in the electrical resistivity over the thermochromic transition. Such an example is shown in Figure 4.1 for which the deposition parameters are listed in Table 4.1.
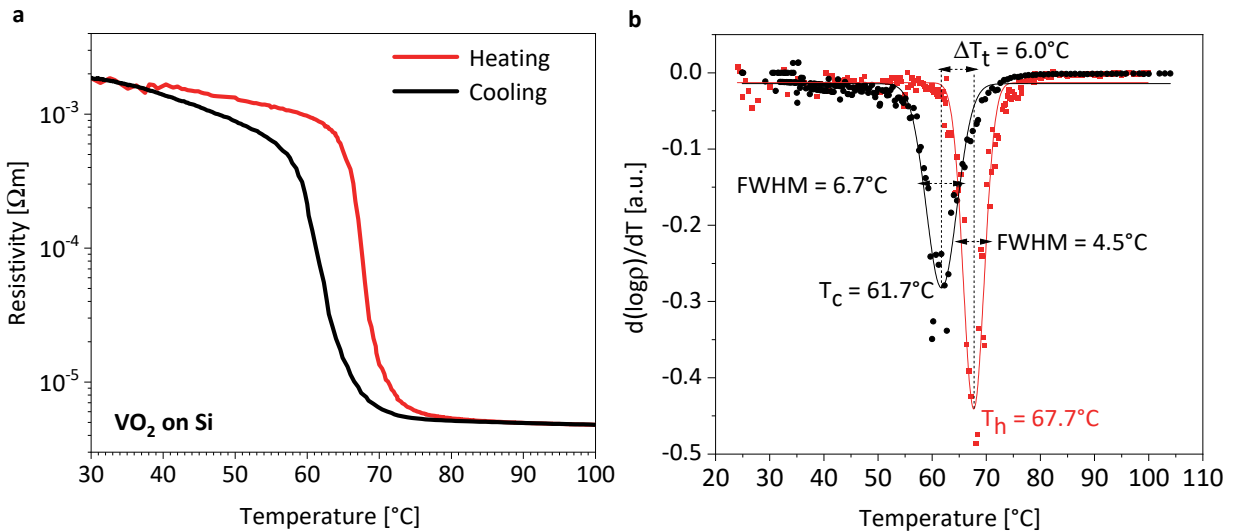


Figure 4.1. a) Temperature dependent electrical resistivity curves of a VO$_2$ thin film sputtered on Si. b) The corresponding d(log $\rho$)/dT vs T fitted curves whose minima denote the transition temperatures upon heating, T$_h$ and cooling, T$_c$. The difference between T$_h$ - T$_c$ gives the hysteresis width $\Delta$T$_t$, while the FWHM indicates the sharpness of the metal-to-insulator transition.

The thermochromic film properties are determined by plotting the first derivative of the logarithm of resistivity versus the temperature. The data is then fitted with Gaussian function whose minimum is taken as the thermochromic transition temperature and the full width at half maximum (FWHM) gives the sharpness of the transition. These values are determined for both the heating and the cooling cycle. The difference between the transition temperature during heating, $T_h$ and cooling, $T_c$ yields the hysteresis width, $\Delta T_t$.

Table 4.1. Process parameters used for the deposition of the VO$_2$ film displayed in Figure 4.1.

| Base pressure [mbar] | $< 5\cdot10^{-7}$ |
|---|---|
| Working pressure [mbar] | $8.22 \pm 0.02\cdot10^{-3}$ |
| O$_2$:Ar [sccm] | 1:10.9 to 1:11.1 |
| Substrate temperature [°C] | 465 |
| Film thickness [nm] | ≈240 nm |
| Applied power [W] | V: 150 (DC) |

For the pure VO$_2$ film displayed in Figure 4.1, the transition temperature during heating, $T_h$ is determined at 67.7°C and corresponds to the values reported in literature. The hysteresis width is ≈6°C and it is usual for polycrystalline thermochromic thin films.

Thermochromic samples might exhibit some heterogeneity in the electrical resistivity. The O$_2$ flow might be unevenly distributed in the chamber resulting in small quantities of vanadium oxides, other than VO$_2$, being scattered across the sample and inducing stresses in the film. An example of the temperature dependent electrical resistivity curves measured during heating in two different spots of the same VO$_2$ sample, one in the center and another closer to the edge, are shown in Figure 4.2. The difference in the transition temperature is substantial amounting to 4°C. Moreover, in the low temperature semiconducting state, the absolute resistivity values also differ, with the higher transition temperature corresponding to the spot with the higher resistivity values. Above the thermochromic transition, the resistivity values converge as the sample conductivity is given by the percolated metallic VO$_2$ domains. Higher transition temperatures and resistivity values are generally associated with slightly oxygen rich, non-stoichiometric VO$_2$ films.
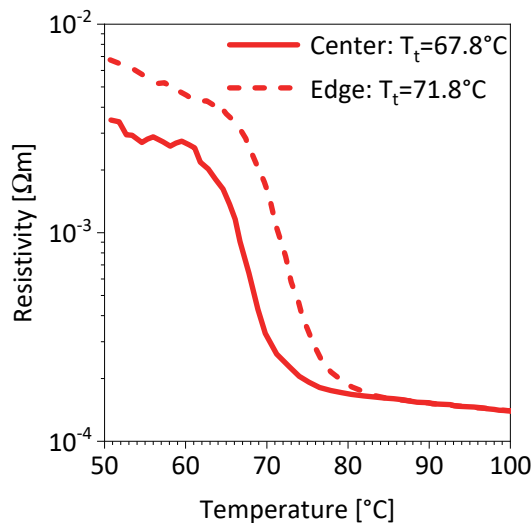


Figure 4.2. Electrical resistivity curves measured in two different spots on the same sample: one in the center and another close to the edge. Both curves are measured during heating.

## 4.1.2 VO₂ sputtered on other substrates

It has been observed that the thermochromic properties of even relatively thick VO$_2$ films of several hundred nanometers are strongly dependent on the substrate type. For the investigation of optical reflectance in the mid-infrared spectral range, an IR opaque, metal interlayer has been deposited between the Si substrate and the thermochromic VO$_2$ film. The material of choice is tungsten, due to its high thermal stability. Metal thin films of Al or Ag, although optically superior (e.g. lower thermal emittance), lack stability when heated to 600°C nominal substrate temperature during the VO$_2$ deposition.

However, thermochromic VO$_2$ films deposited directly on W covered Si substrates, exhibit cracks and appear to delaminate (Figure 4.3). Such flaking or peeling of the films could be the result of a poor adhesion between the VO$_2$ film and the W substrate due to lattice mismatch. A thin SiO$_2$ buffer layer is deposited on the W in order to mitigate the incompatibility between the substrate and film lattice.
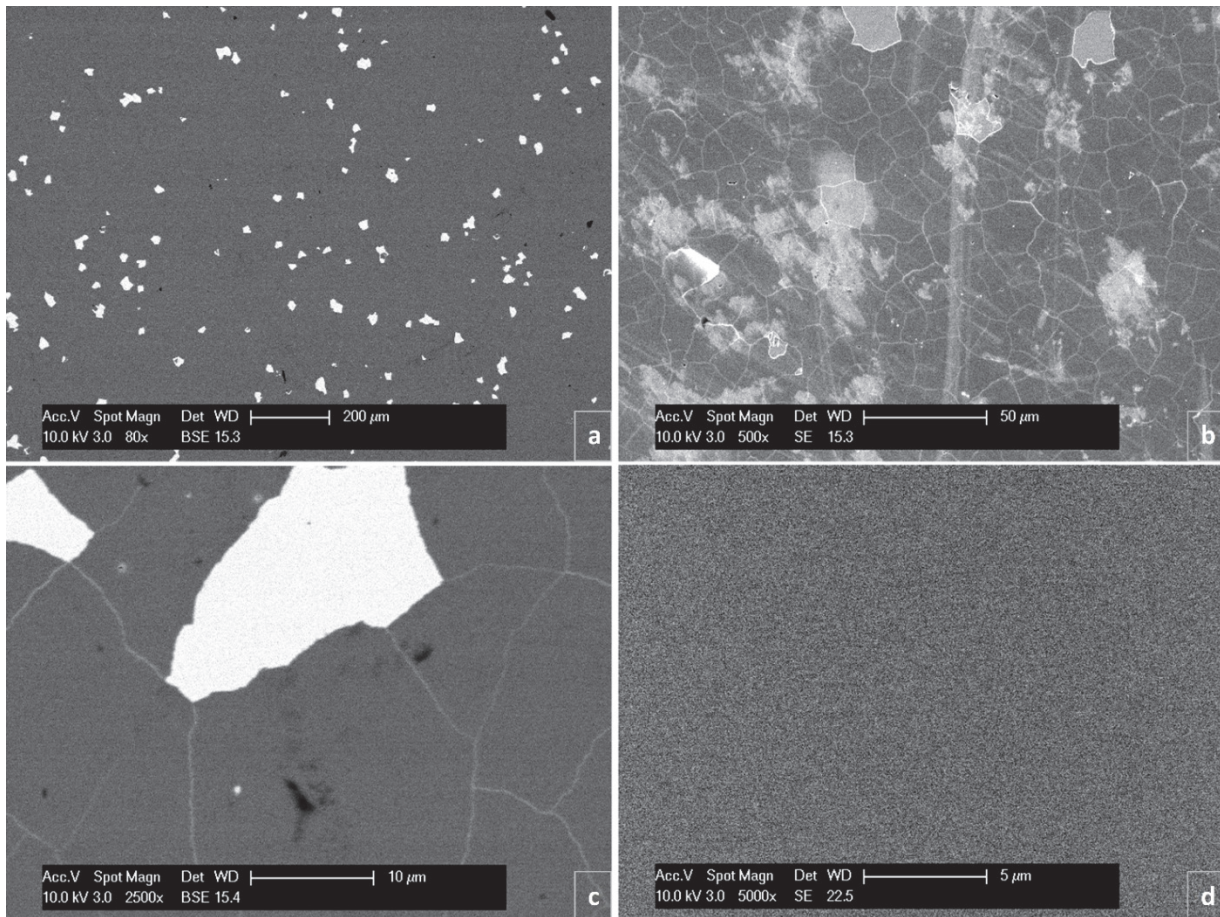


Figure 4.3. SEM images of VO$_2$ films deposited directly on W (a, b and c) and on W with an SiO$_2$ barrier layer (d). In the backscattered electron (BSE) imaging mode (a and c), the contrast results from the different atomic number (Z) of the sample material and the bright spots indicate the tungsten substrate. In secondary electron (SE) mode, the contrast is a result of the change in topography and it indicates the cracks in the film deposited directly on W (b), while no delamination is observed for the sample with the SiO$_2$ buffer layer (d).

The number of backscattered electrons reaching the detector is proportional to the atomic number of the species investigated. Hence, in the backscattered electron imaging mode, the bright spots visible on the sample (Figure 4.3.a and c) correspond to the W substrate where the film has delaminated from the substrate. For the VO$_2$ film directly sputtered on the W layer, the cracks are easily observed in the secondary

imaging mode as well (Figure 4.3.b). However, delamination and cracking are avoided for the sample with an SiO$_2$ buffer layer between film and W substrate (Figure 4.3.d). Despite the larger magnification in the case of the latter, the inspected surface is sufficient to observ any cracking would they occur.

The cracking could be a consequence of induced tensile stresses in the VO$_2$ film. Extrinsic tensile stresses have been shown to develop in VO$_2$ films during the cooling of the sample from the process to the room temperature as a result of the mismatch in thermal expansion coefficient between substrate and film [Case, 1984]. According to [Kucharczyk, 1979] the thermal expansion coefficient of VO$_2$ drops from $13.35 \cdot 10^{-6}$ K$^{-1}$ above T$_t$, to $5.71 \cdot 10^{-6}$ K$^{-1}$ below T$_t$, while that of tungsten varies from 4.32 to $4.5 \cdot 10^{-6}$ K$^{-1}$ between room temperature and 500°C [ITIA, 2019; Lahav, 1990; Knibbs, 1969].

The SiO$_2$ buffer layer seems to overcome the problem of film peeling. Moreover, during the sample depositions, thermochromic VO$_2$ has been sputtered onto a control Si//SiO$_2$ buffer substrate as well and the obtained thermochromic film exhibits a higher than three order of magnitude modulation of electrical resistivity (Figure 4.4). This is larger than values typically measured for films deposited directly on Si wafer, without SiO$_2$ buffer layer, and hint to the important influence of substrate choice on the thermochromic film properties. Additional depositions on GaN and Al$_2$O$_3$ show even larger modulations of above 4 and 4.5 orders of magnitude, respectively (Figure 4.4).
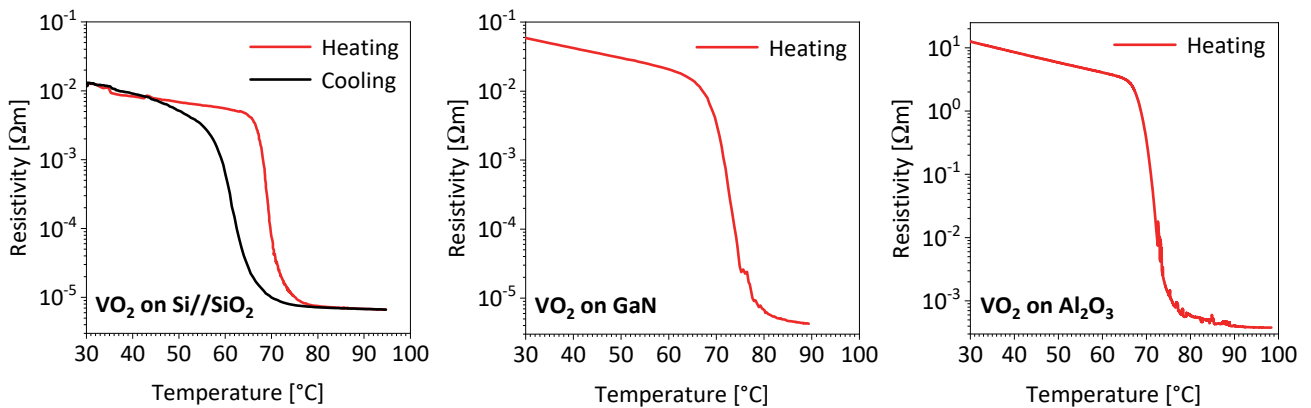


Figure 4.4. Temperature dependent electrical resistivity curves of VO$_2$ films sputtered on Si//SiO$_2$, GaN and Al$_2$O$_3$ substrates.

The enhanced crystallinity of thermochromic films grown on GaN and sapphire substrates might originate from the similar atomic arrangements of the rutile VO$_2$ lattice along the [010] direction and hexagonal GaN and Al$_2$O$_3$ lattices along the [0001] direction (Figure 4.5). The V-V distance along the c-axis of rutile is 2.88 Å and it is rather close to the 2.75 Å of the O-O distance in c-plane Al$_2$O$_3$ and to the 3.19 Å of Ga-Ga distance in the GaN c-plane.
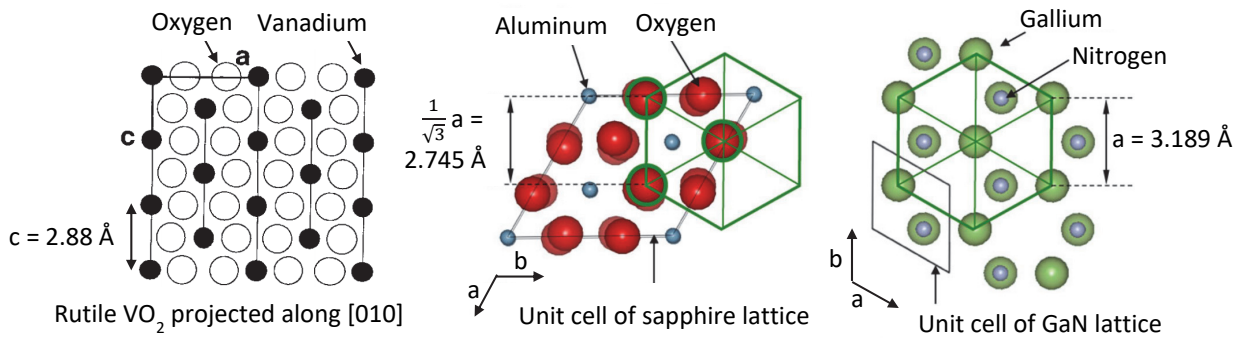
Figure 4.5. Rutile $VO_2$ projected along the [010] direction [Leroux, 1998] and the atomic arrangements of the sapphire and GaN c-plane. [Inaba, 2014]

At the critical temperature, $VO_2$ single crystals exhibit a change of five orders of magnitude in electrical resisitivity [Ladd, 1969]. High quality, epitaxial films with a showing a four orders magnitude transition have been reported on both sapphire [Jin, 1997; Kim, 1994; Zhang, 1994; Fan, 2013] and GaN substrates [Zhou, 2012]. Meanwhile, good quality films grown on Si substrate undergo a 2-3 orders of magnitude change in resistivity. These magnitudes agree well with the resistivity modulations determined in this work.

Finally, the substrate type and orientation seem to have a conclusive effect on film crystallinity and thermochromic behavior. The occurrence of local epitaxy is suspected for substrates with crystalline structure similar to that of rutile $VO_2$. Moreover, suitable substrates/seed layers enable the deposition of crystalline, switching thermochromic thin films even at reduced substrate temperatures [Loquai, 2016].

## 4.1.3 Minimum thickness for crystalline VO₂ films

For thicker $VO_2$ films, of several hundred nanometers, the film behavior gets closer to that of bulk $VO_2$, however, for rather thin films in the order of 30 nm or below, it is difficult to obtain strong switching contrast and the substrate choice becomes even more critical. Sapphire and GaN could enhance the thermochromic properties of $VO_2$ layers and might be promising substrates or seed layers for applications where such thin films are desired.

For the multilayered absorber designs, thin thermochromic films with thicknesses ranging from 20 nm to 100 nm and exhibiting a good switching behavior are of interest. In this work, the successful deposition of 30 nm thick $VO_2$ film on Si//SiO$_2$ substrates, undergoing a three order drop in resistivity over the semiconductor-to-metal transition, is reported (Figure 4.6).

Nonetheless, the deposition of very thin films with a large switching contrast remains challenging, especially on less suited substrate types. A precise control of the process parameters (substrate temperature and oxygen partial pressure) is essential. For efficient multilayered coatings, based on thin films in the order of 30 nm, the layer under the thermochromic $VO_2$ should, ideally, have compatible lattice parameters.
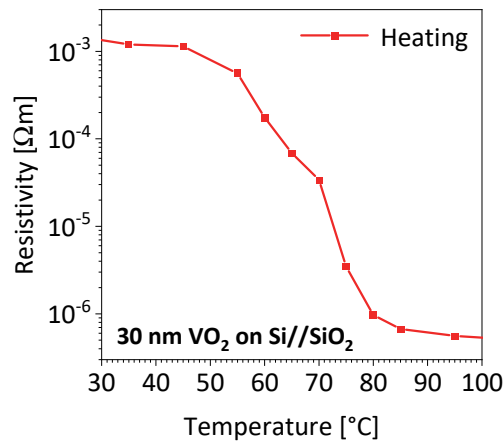
Figure 4.6. Temperature dependent electrical resistivity of a 30 nm thin $VO_2$ film deposited on Si//SiO$_2$ substrate.

## 4.1.4 Effect of the substrate temperature on film crystallization

In order to obtain switching thermochromic samples, the deposited films must be crystalline. Hence, another critical process parameter is the deposition temperature. Substrate temperatures have to be high enough to ensure a fast diffusion of atoms and facilitate atomic rearrangements into the $VO_2$ crystalline structure. At room temperature or when the temperature is not sufficiently high, film crystallization is hindered resulting in amorphous vanadium oxide films. The discontinuous film structure, with only short range order between the vanadium atoms leads to increased film resistivities and no thermochromic phase transition.

Two films sputtered at substrate temperatures of 465°C and 310°C (nominal temperatures of 600°C and 400°C, respectively) are compared (Figure 4.7). The film thickness (≈180 nm) and process parameters (e.g. oxygen partial pressure) are kept constant between the depositions. It is observed that a higher substrate temperature leads to a larger thermochromic modulation in the deposited films. At 465°C, a typical, slightly larger than 2.5 orders of magnitude modulation is obtained for thermochromic films deposited on Si substrate. At 310°C substrate temperature, the modulation magnitude is approximately halved and the sharpness of the transition is also reduced. Nonetheless, a more than one order of magnitude change in resistivity for a film sputtered at a substrate temperature as low as 310°C, is rather remarkable. It is lower than the 400 – 500°C commonly reported in literature for conventional sputtering or post-annealing of thermochromic $VO_2$ films. However, similar substrate temperatures have been reported for high impulse magnetron sputtered $VO_2$ films [Loquai, 2017; Fortier, 2014].

For the majority of samples discussed in this work, a substrate temperature of 465°C (nominal temperature 600°C) has been set. Exceptions to this are only the samples deposited on the XPS compatible Cu holder for which the temperature calibration curve, therefore, the exact sample temperature have not been determined.
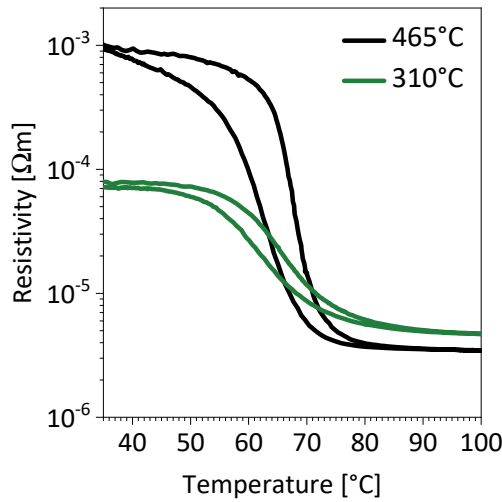
Figure 4.7. Electrical resistivity curves of films of identical thickness (≈180), sputtered at different substrate temperatures, while keeping all other process parameters constant.

## 4.1.5  Influence of $O_2$ partial pressure on thermochromism

The direct dependence of thermochromic properties on the $O_2$ partial pressure, $p(O_2)$ stems from the complex V-O phase diagram. Directly bordered by slightly sub- and supra-stoichiometric, $V_7O_{13}$ and $V_6O_{13}$, respectively, and in the close vicinity of numerous other stable vanadium oxides such as: $V_2O_3$, $V_3O_5$, $V_2O_5$, deposition of phase pure or even predominantly $VO_2$ containing films is challenging. Setting a well-defined oxygen mass flow rate is not sufficient as the amount of reactive oxygen in the plasma might differ between depositions (depending on the type of coatings deposited previously and the resulting state of the chamber walls, e.g. oxidized or metallic coatings). Instead, it is the oxygen partial pressure, $p(O_2)$ that is fixed during the sputtering process and it is adjusted from deposition to deposition in order to account for drifts in the chamber and target erosion. Maintaining the $p(O_2)$ within the narrow process range is achieved by a Proportional Integral Derivative (PID) feedback control, which regulates the flow of oxygen based on the readings of an oxygen sensor. Set PID values are inversely proportional to the oxygen partial pressure: a high PID means a low $p(O_2)$ and vice-versa.

Decreasing the PID values (increasing the oxygen partial pressure) in large steps, leads first to metallic films, then thermochromic and finally semiconducting ones (Figure 4.8.a). Adjusting the PID values just marginally around the thermochromic process window, films with different switching behaviour are obtained. The largest thermochromic modulation is obtained for optimum $p(O_2)$ and even slightly below or above the optimal value, the thermochromic modulation is significantly hindered (Figure 4.8.b).

Moreover, switching vanadium oxide films sputtered at slightly lower/higher $p(O_2)$, show decreased/increased absolute electrical resistivities compared to the optimized thermochromic film. Results also indicate that, generally, more conductive films tend to exhibit lower transition temperatures, while those with rather high resistivities show a higher transition temperature than the optimized thermochromic films. These observations are in accordance with literature, where an increase of the $VO_2$ transition temperature at higher $O_2$ partial pressures has been reported [Jiang, 2014].
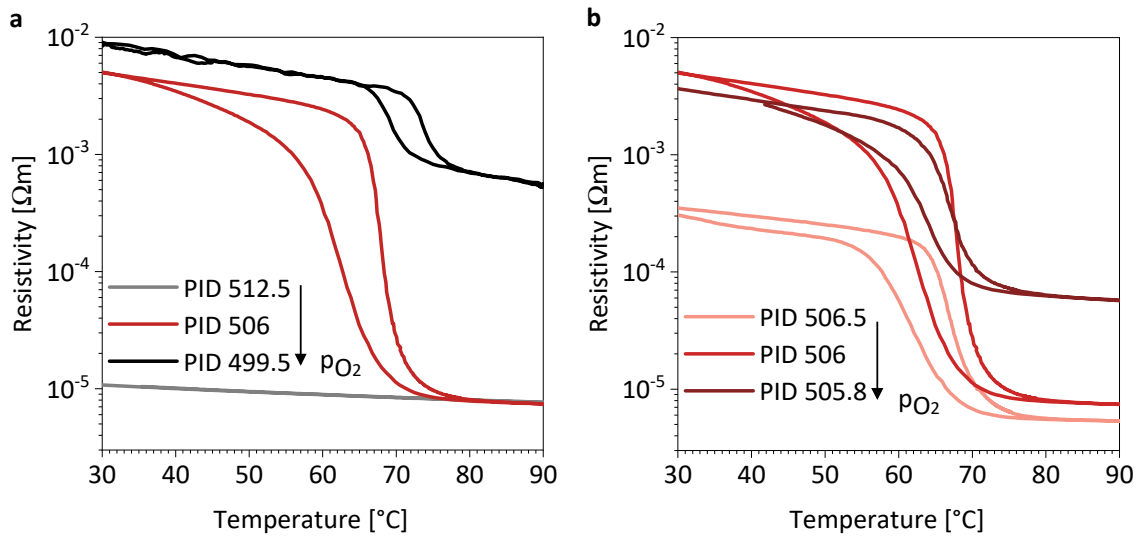
Figure 4.8. Effect of the $O_2$ partial pressure on the sputtering of thermochromic vanadium oxide thin films on Si substrates at 465°C. a) Large variations in $p(O_2)$ result in sweeping from metallic to thermochromic to semiconducting behaviour. b) Smaller changes in the $p(O_2)$ lead to differences in the thermochromic switching magnitude and in the corresponding film resistivities. Lower $p(O_2)$ lead to reduced absolute resisitivities, and vice-versa, with higher $p(O_2)$ leading to increased film resistivities. Only a narrow $p(O_2)$ range leads to an optimized thermochromic transition.

## 4.2    HiPIMS deposition of $VO_2$ thin films

HiPIMS (High Power Impulse Magnetron Sputtering) is a relatively recent development in sputtering technology. HiPIMS deposited thin films have been shown to exhibit several advantages over classical magnetron sputtered films such as a better substrate adhesion, very high density and lower surface roughness.

Previous studies on high impulse magnetron sputtered vanadium oxide thin films show that dense, stoichiometric $VO_2$ thermochromic films could be deposited at substrate temperatures of around 300°C - 350°C [Loquai, 2017; Fortier, 2014]. Furthermore, the addition of a $TiO_2$ seed layer enabled the deposition of switching films even at temperatures as low as 275°C [Loquai, 2016].

Besides, the significantly lower substrate temperatures than in conventional sputtering, HiPIMS deposited films show enhanced stability in highly oxidizing or humid environments. Due to the high film density and larger average grain size, HiPIMS films retain their thermochromic behavior for at least three times longer than conventional magnetron sputtered films, hence, in many cases providing sufficient film durability even without an additional diffusion barrier [Loquai, 2017].

In this work, HiPIMS is primarily employed to investigate whether high-quality, crystalline thermochromic films can be deposited at lower temperatures than with conventional magnetron sputtering (MS). Hence, a first sample series is deposited on Si at 465°C, 390°C and 310°C substrate temperatures (600°C, 500°C and 400°C nominal temperatures, respectively) and at constant oxygen flow. Because an adequate crystalline substrate might also improve the film crystallinity and thermochromic properties, a second series of samples is deposited on two different substrate types (Si and $Al_2O_3$), by both conventional and high power impulse magnetron sputtering. The depositions are carried out at substrate temperatures of 465°C and 310°C (nominal temperatures of 600°C and 400°C) and under constant oxygen partial pressure (PID control). The deposition matrix is sown in Table 4.2, while the process parameters for the first and second sample series

are summarized in Table 4.3. Profilometry measurement reveal a lower deposition rate for HiPIMS than for p-DCMS (pulsed-DC magnetron sputtering). For comparable film thicknesses the deposition times for the second set of experiments are adjusted accordingly. The similar thickness of the resulting films is confirmed by SEM cross section imaging.

Table 4.2. Deposition matrix for the second sample series.

| | MS | | HiPIMS | |
|---|---|---|---|---|
| | 310°C | 465°C | 310°C | 465°C |
| Si | ✓ | ✓ | ✓ | ✓ |
| $Al_2O_3$ | ✓ | ✓ | ✓ | ✓ |

Table 4.3. Process parameters used for the two set of experiments.

| Set of experiment | No. 1 | No. 2 | |
|---|---|---|---|
| Sputtering mode | HiPIMS | HiPIMS | p-DCMS |
| Applied power [W] | 150 | 150 | 150 |
| Pulse frequency [kHz] | 1 | 1 | 250 |
| Pulse length [µs] | 100 | 100 | 3.5 |
| Base pressure [mbar] | $< 5 \cdot 10^{-8}$ | $< 5 \cdot 10^{-8}$ | $< 5 \cdot 10^{-8}$ |
| Working pressure [mbar] | $8.2 \pm 0.3 \cdot 10^{-3}$ | $6.7 \pm 0.1 \cdot 10^{-3}$ | $7.1 \pm 0.2 \cdot 10^{-3}$ |
| $O_2$:Ar [sccm] | 1:9.8 | 1:9.8 to 1:10.6 | 1:7.9 to 1:8.5 |
| Substrate temperature [°C] (nominal temperature [°C]) | 465 (600) 390 (500) 310 (400) | 465 (600) 310 (400) | 465 (600) 310 (400) |
| Deposition time [min] | 60 | 100 | 60 |
| Film thickness [nm] | ≈110 | ≈180 | ≈180 |

## 4.2.1 HiPIMS deposited VO$_2$ thin films: dependence on substrate temperature

Thermochromic films deposited at substrate temperatures of 465°C, 390°C and 310°C are compared. A thermochromic switch is identified for all samples. However, the transition magnitude is steadily decreasing with the substrate temperature, shrinking from almost two orders of magnitude resistivity drop at 465°C to about one order of magnitude at 390°C and, finally, to a reduction of only $1 \cdot 10^{-5}$ Ωm at 310°C substrate temperature, that is barely observable in the logarithmic plot (Figure 4.9). In this first approach, it appears that HiPIMS does not bring a compelling advantage over conventional magnetron sputtering regarding the low temperature deposition of VO$_2$ layers. The film crystallinity is significantly limited by the reduction of substrate temperature, while thermochromic modulations of similar, or even larger, magnitude have been observed for films deposited at comparable substrate temperatures by conventional sputtering. Nonetheless, the one order of magnitude switch obtained at ≈390°C is comparable to the thermochromic behaviour of HiPIMS deposited VO$_2$ films reported in literature.
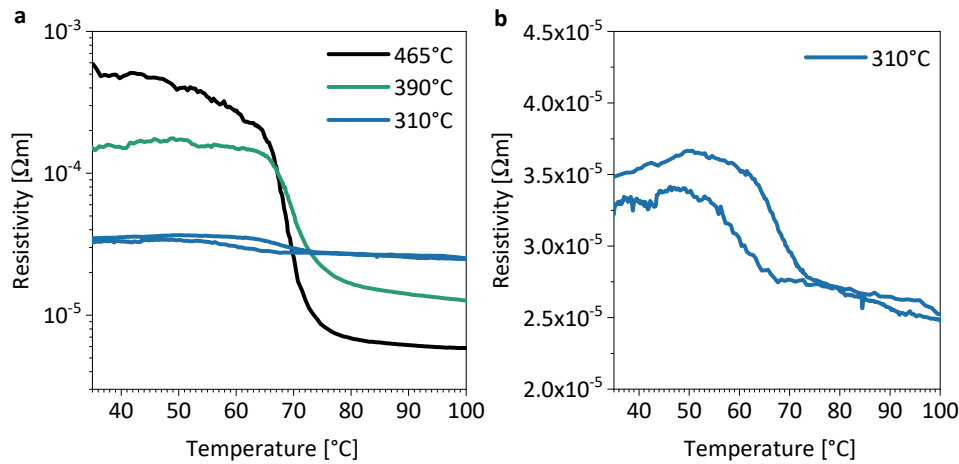
Figure 4.9. Temperature dependent electrical resistivity of the HiPIMS deposited VO$_2$ films at different substrate temperatures plotted in logarithmic scale (a) and in linear scale for the sample deposited at 310°C (b).

## 4.2.2 HiPIMS versus Magnetron Sputtering: influence of substrate and substrate temperature

At 465°C substrate temperature (Figure 4.10.a), VO$_2$ films deposited onto Si substrates by HiPIMS and conventional MS are comparable regarding the transition magnitude with slightly more and slightly less than three orders resistivity drop exhibited by the HiPIMS and MS deposited films, respectively. What is different, however, are the absolute values of electrical resistivity, with the HiPIMS film having more than two order of magnitude larger resistivities than the MS film. The HiPIMS film appears to be more oxygen rich, despite the lower O$_2$ content in the process gas mixture than during the magnetron sputtering ($\approx$10% O$_2$ for HiPIMS versus $\approx$12% O$_2$ for the MS deposition). This suggest that during the applied high power pulse, ionized species are more readily oxidized than in MS. Finally, the HiPIMS film exhibits a wider hysteresis and a steeper transition than the conventional magnetron sputtered film suggesting different film morphologies.

Also at 465°C, HiPIMS deposited VO$_2$ on sapphire shows a nearly doubled modulation magnitude compared to an identical film on Si, confirming once again the importance of the substrate choice. The remarkable transition of five orders of magnitude suggests a high crystalline film quality, with – likely – less defects in the dense HiPIMS films than in conventional MS films.
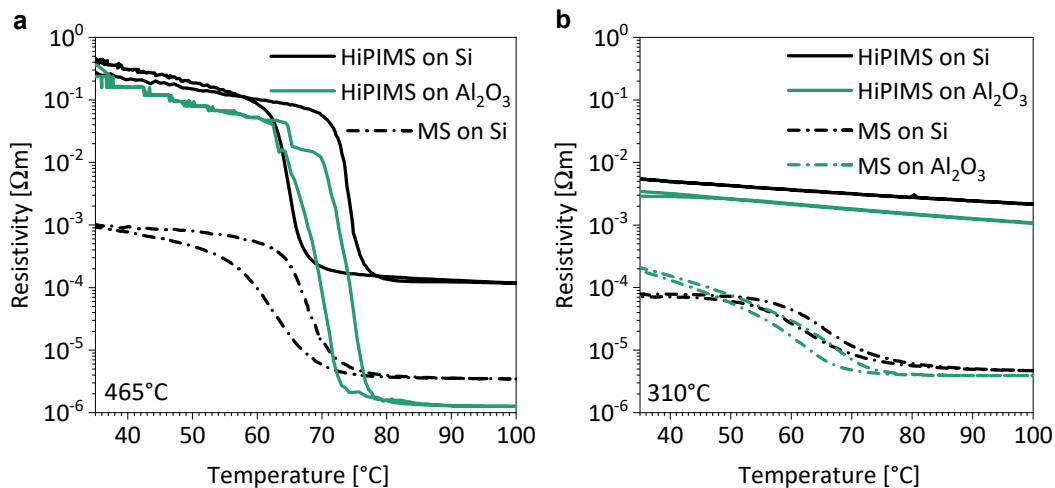


Figure 4.10. Comparison of HiPIMS and MS deposited films on Si and sapphire substrates at 465°C (a) and 310°C (b).

At 310°C substrate temperature, the HiPIMS films cease to exhibit a drop in electrical resistivity regardless of the substrate type. However, the conventional sputtered films undergo a transition of above one order of magnitude on Si and sapphire substrates alike. As expected, the transition is slightly larger on the sapphire substrate.

The results indicate better thermochromic performance for HiPIMS-deposited films at 465°C, but poorer performance at 310°C compared to conventional magnetron sputtering. This might be the result of two competing mechanisms:

- Amorphization by high energy ion impact,

- Crystallization by surface and bulk diffusion.

At 465°C substrate temperature, the diffusion of arriving atoms might be sufficiently fast to achieve crystalline order in the films. Furthermore, the impinging high energy atoms and ions might densify the film resulting in more compact, defect-free films. However, the arriving high energy species might also introduce disorder in the film and, at lower process temperatures, the amorphization by these high energy particles might dominate over the crystallization by the slowed-down atom diffusion.

The HiPIMS and p-DCMS deposited film morphology on the two different substrate types is depicted by SEM imaging (Figure 4.11). The SEM images on Si are of high-quality, but blurry on $Al_2O_3$ due to charging. Nonetheless, it is apparent that HiPIMS deposition leads to considerably larger grain sizes than conventional sputtering on both substrate types. This is counter-intuitive as a large grain boundary density is expected to result in higher film resistivities, but the contrary has been observed with higher absolute resistances measured for the HiPIMS deposited films at both process temperatures and on both substrate types. This indicates that the oxygen content in the films might have a bigger influence on the electrical behavior than the morphology. For more conductive HiPIMS films and similar to those deposited by MS, the oxygen partial pressure during HiPIMS might need to be further limited, as the high fraction of ionized species are easily oxidized already at lower oxygen partial pressures than in MS.

Concerning the substrate type, grains on Si are larger than on sapphire, regardless of the deposition method and appear to be highly oriented with visible crystal facets.
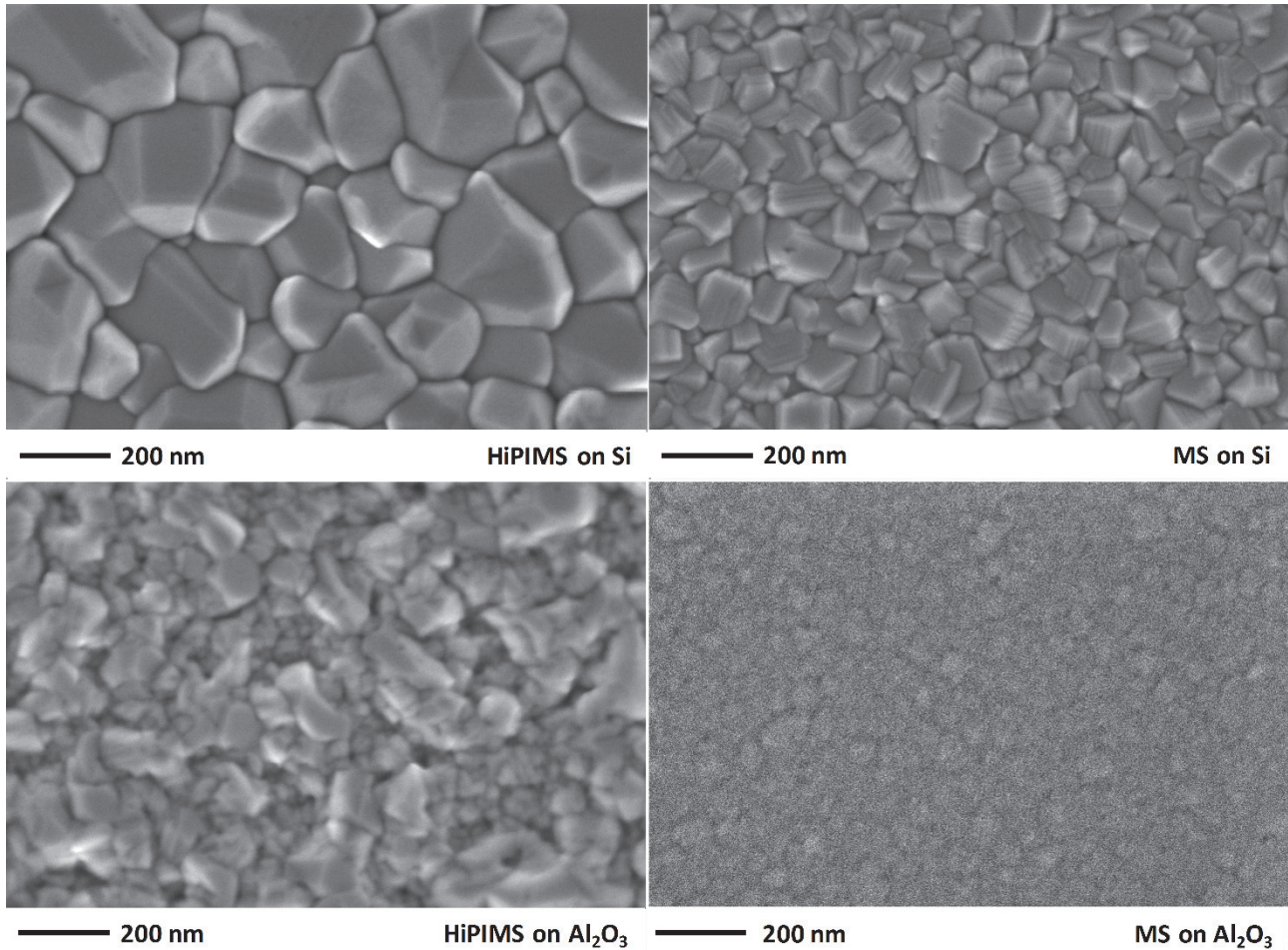
Figure 4.11. HiPIMS versus p-DCMS film morphology on Si and sapphire substrates observed by SEM. Films deposited at 465°C substrate temperature (600°C nominal temperature).

We conclude this section with the following observations:

- crystallization is influenced by three factors: ordering by surface and bulk diffusion which is related to the substrate temperature; film amorphization and densification that is linked to the fraction of ionized species and impinging particle energies;

- compare to magnetron sputtering, HiPIMS allows for a better film quality at high substrate temperatures, but brings no advantage at lower substrate temperatures where amorphization by impinging high-energy particles likely prevails over the temperature controlled surface and bulk diffusion;

- according to this reasoning, thermal evaporation might be a promising alternative for low temperature deposition of thermochromic $VO_2$ films;

- HiPIMS still offers several superior film properties (e.g. denser, more defect-free films) and could be of interest for microelectronic or other applications with specific requirements on film morphology;

- for large scale, solar thermal applications suitable seed layers might be employed to promote thermochromic film growth at lower substrate temperatures.

# 4.3 Alternative perovskite-type thermochromic thin films

Besides vanadium dioxide, perovskite-type oxides constitute another class of materials with potential in emissivity changing applications. Manganite perovskites of $A_{1-x}B_xMnO_3$ formula, where A is a trivalent cation of the rare-earth lanthanide series (e.g. La, Bi, Pr, Nd, Sm) and B is a divalent alkaline cation (e.g. Ca, Sr, Ba) are widely studied for their unique range of combined thermal, electrical and magnetic properties. Most notably, they triggered great interest due their colossal magnetoresistance effect (CMR), that is a large change in resistance as a result of an applied magnetic field [Jin, 1994; Mahendiran, 1996; Rao, 1998]. However, among these manganite perovskites, several have been reported to exhibit a temperature modulated optical switch in the IR making them promising for passive thermal regulation.

Thermochromic $Sm_{1-x}Ca_xMnO_3$ [Laffez, 2006; Ammar, 2009; Boileau, 2012], $La_{0.7}Ca_{0.3-x}Sr_xMnO_3$ [Fan, 2013], $La_{1-x}Ca_xMnO_3$ [Tachikawa, 2003; Shen, 2009] and $La_{1-x}Sr_xMnO_3$ [Shimakawa, 2002; Tang, 2008; Wu, 2010] have been studied, but in most cases the optical changes occur below the thermochromic transition temperature of $VO_2$. However, the $La_{0.7}Sr_{0.3}MnO_3$ composition exhibits a substantial infrared modulation even at higher temperatures. At 5 μm (2000 cm$^{-1}$) wavelength, the reflectance of a 150 nm thick $La_{0.7}Sr_{0.3}MnO_3$ film deposited on a Si substrate changes by nearly 25% between room temperature and 160°C (Figure 4.12), with a step decrease in reflectance occurring above 140°C [Soltani, 2006]. $La_{0.7}Sr_{0.3}MnO_3$ films are, therefore, of particular interest for the envisaged solar absorber application.
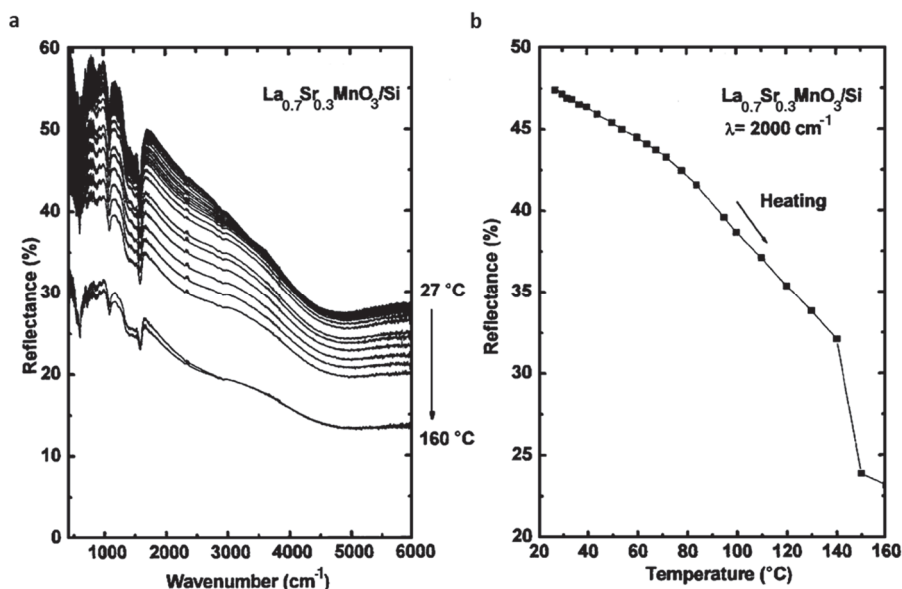


Figure 4.12. a) FTIR reflectance curves of a $La_{0.7}Sr_{0.3}MnO_3$//Si sample measured in the 400 – 6000 cm$^{-1}$ spectral range when heating from 27°C to 160°C. b) Temperature dependent sample reflectance at 2000 cm$^{-1}$ (5 μm) wavelength. Reproduced from [Soltani, 2006].

## 4.3.1 Deposition of $La_{1-x}Sr_xMnO_3$ thin films

In this work, $La_{1-x}Sr_xMnO_3$ (LSMO) films are sputtered from a $La_{0.7}Sr_{0.3}MnO_3$ target onto Si and Al substrates. The target composition has been confirmed at $La_{0.68}Sr_{0.32}MnO_3$ by inductively coupled plasma optical emission spectrometry (ICP-OES). Two sets of samples are sputtered:

- in a first approach, films are sputtered at room temperature and then subjected to post-annealing treatment;
- in a second approach, films are sputtered for in-line UPS and XPS analysis. During sputtering, the substrate is heated to 465°C (600°C nominal temperature, the maximum reachable in the sputter chamber).

The detailed deposition parameters, for both sample sets, are listed in Table 4.4.

Table 4.4. Process parameters of $La_{1-x}Sr_xMnO_3$ (LSMO) sputtered films by p-DCMS.

|  | 1st sample set | 2nd sample set |
|---|---|---|
| Base pressure [mbar] | < 5·10^{-8} | < 5·10^{-8} |
| Working pressure [mbar] | 5.77 ± 0.05·10^{-3} | 5.96 ± 0.02·10^{-3} |
| O_2:Ar [sccm] | - | -<br>1:4 |
| Deposition temperature [°C] | Room temperature | 465°C |
| Post-annealing [°C] | -<br>350<br>700 | - |
| Film thickness [nm] | ≈150 | ≈70 |
| Applied power [W] | 30 | 50 |
| Frequency [kHz] | 250 | 250 |

## 4.3.2 Characterization of $La_{1-x}Sr_xMnO_3$ thin films

The XRD spectra of 150nm thick LSMO films deposited on Si at room temperature and subjected to a 2 hour post-annealing treatment in dry air atmosphere, at 350°C and 700°C, respectively, are shown in Figure 4.13.a. Diffraction peaks are present only for the sample annealed at 700°C suggesting that the crystalline structure is formed only at temperatures higher than 350°C. This is in accordance with the practices reported in literature where, generally, process temperatures of above 500°C are employed [Soltani, 2006; Bhosle, 2007].

The film annealed at 700°C is polycrystalline, with preferential orientation in the (110) direction. All peaks can be indexed to the LSMO phase with pseudo-cubic structure according to [Liu, 2006]. The ideal perovskite structure is cubic, but due to the size of the cations and the Jahn-Teller effect, the LSMO structure is strained. $La_{1-x}Sr_xMnO_3$ films with x=0.3 the crystal structure is pseudo-cubic with a lattice parameter of a = 3.889 Å. The typical $La_{1-x}Sr_xMnO_3$ perovskite unit cell is shown in Figure 4.13.b. As all $La_{1-x}Sr_xMnO_3$ (x ≥ 0) have XRD peaks in similar positions, conclusions on film composition (Sr content) cannot be drawn.
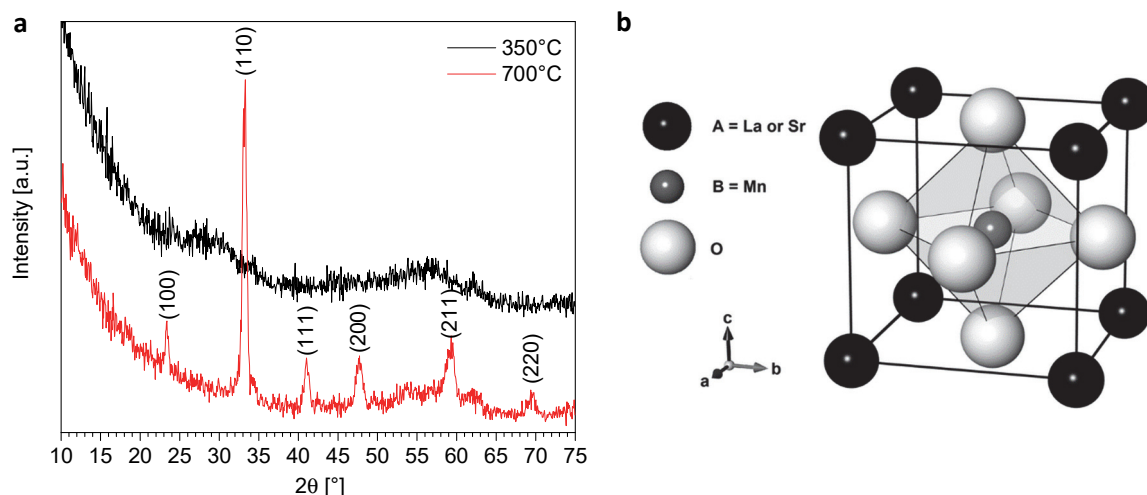
Figure 4.13. a) XRD spectra of two LSMO films annealed at 350°C and 700°C during two hours. Only the sample annealed at 700°C exhibits crystalline diffraction peaks that are indexed to the pseudocubic LSMO structure [Liu, 2006]. b) Cubic $La_{1-x}Sr_xMnO_3$ perovskite structure [Yunphuttha, 2016].

The second set of LSMO samples, sputtered at 465°C, in 100% Ar and 80% Ar – 20% $O_2$ atmoshpere, is characterised by in-line UPS and XPS. From the UPS He I spectra (Figure 4.14), a valence band maximum (VB) of ≈1.62 ± 0.02 eV and ≈1.3 ± 0.02 eV are determined for the samples deposited without and with additional $O_2$ in the plasma, respectively. According to [Lee, 2015a], LSMO is a p-type semiconductor, but with a Fermi level that is close to the middle of the band gap (merely 0.02 eV shifted), approximating the VB as half band gap is reasonable. Therefore, a band gap of $E_g \approx 3.2 \pm 0.05$ eV is found for the film sputtered in 100% Ar and an $E_g \approx 2.6 \pm 0.05$ eV is determined for the film deposited with 20% $O_2$ in the process gas. This is considerably higher than the 0.63 eV reported in [Lee, 2015a] for $La_{0.7}Sr_{0.3}MnO_3$ films sputtered on Pt(111)//Ti//SiO$_2$//Si(100) substrates. However, the band gap of thin $La_{0.7}Sr_{0.3}MnO_3$ has been shown to depend strongly on the type of substrate as a result of induced strains, varying greatly from 0.9 ± 0.2 eV on (001) LaAlO$_3$ to 2.1 eV ± 0.2 eV on (001) SrTiO$_3$ [Jalili, 2011]. Recently, a band gap of 2.64 eV, determined by XPS and XAS (X-ray absorption spectroscopy) analysis, has been reported for $La_{0.67}Sr_{0.33}MnO_3$ films deposited on (001) SrTiO$_3$ [Cheng, 2019]. That is matching the value determined in this work for the film sputtered with 20% $O_2$ in the Ar gas.

Furthermore, the work functions of $\Phi_m = 4.5 \pm 0.02$ eV and $\Phi_m = 4.9 \pm 0.02$ eV are determined for the LSMO film without and with additional $O_2$. Lee *et al*. report a similar work function of 4.8 eV for $La_{0.7}Sr_{0.3}MnO_3$ films [Lee, 2015a].
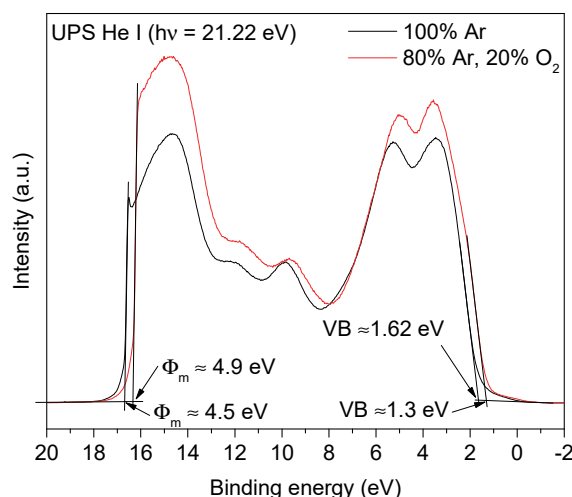
Figure 4.14. In-line UPS He I spectra of the LSMO thin films with the determined valence band edge, VB and work function of the material, $\Phi_m$.

The high-resolution La 3d, Sr 3d, Mn 2p and O 1s XPS core-level spectra (shown in Annex 1) reveal peak shapes and peak positions that are very similar to those reported by [Soltani, 2006] for $La_{0.7}Sr_{0.3}MnO_3$ films. One difference is the much weaker shoulder at 531 eV binding energy in the O 1s spectra, than reported in literature. As this peak is generally attributed to surface oxygen species such as chemisorbed oxygen or hydroxyls, the much weaker shoulder is expected for the in-situ transferred sample. Among the two samples analyzed, the transfer between deposition and measurement chamber of the one sputtered in pure Ar atmosphere has been slower, therefore, it exhibits a larger shoulder at 531 eV.

The chemical composition of the sample surface is determined from the La 3d, Sr 3d, Mn 2p and O 1s core level peak integration, after substracting a Shirley background and by taking into account the specific sensitivity factors of the elements. The results are summarized in Table 4.5. The quantification suggest an important strontium segregation at the surface, with much higher Sr to Mn ratios than expected for $La_{0.7}Sr_{0.3}MnO_3$ films, however, that is in perfect agreement with previous XPS observations and reported values (e.g. Sr:Mn = 0.89) [Bertacco, 2002; Soltani, 2006].

Table 4.5. XPS quantification of the LSMO surface composition [at.%] and the calculated cationic ratios.

|  | O [at.%] | La [at.%] | Sr [at.%] | Mn [at.%] | La:Mn | Sr:Mn |
|---|---|---|---|---|---|---|
| LSMO [100% Ar] | 60.2 | 17.2 | 10.4 | 12.2 | 1.41 | 0.85 |
| LSMO [80% Ar,20% O₂] | 62.2 | 16.0 | 10.9 | 10.9 | 1.47 | 1 |

The FTIR reflectance curves of the deposited LSMO samples are measured in the 2.5 – 14 µm spectral range, for temperatures from 50°C up to 180°C. The dependence of the reflectance on the temperature is illustrated by plotting the spectral reflectance at 8 µm wavelength against the temperature. The deposited $La_{1-x}Sr_xMnO_3$ thin films exhibit thermochromism as the reflectance is changing with temperature.

The $La_{1-x}Sr_xMnO_3$//Si samples sputtered at room temperature, exhibit very similar reflectance curves with a steady decrease of about 15% in reflectance with temperature, regardless whether the sample has been post-annealed or not. The only difference consists in the absolute reflectance values, the sample annealed at 700°C showing reflectance around 10% higher (Figure 4.15).
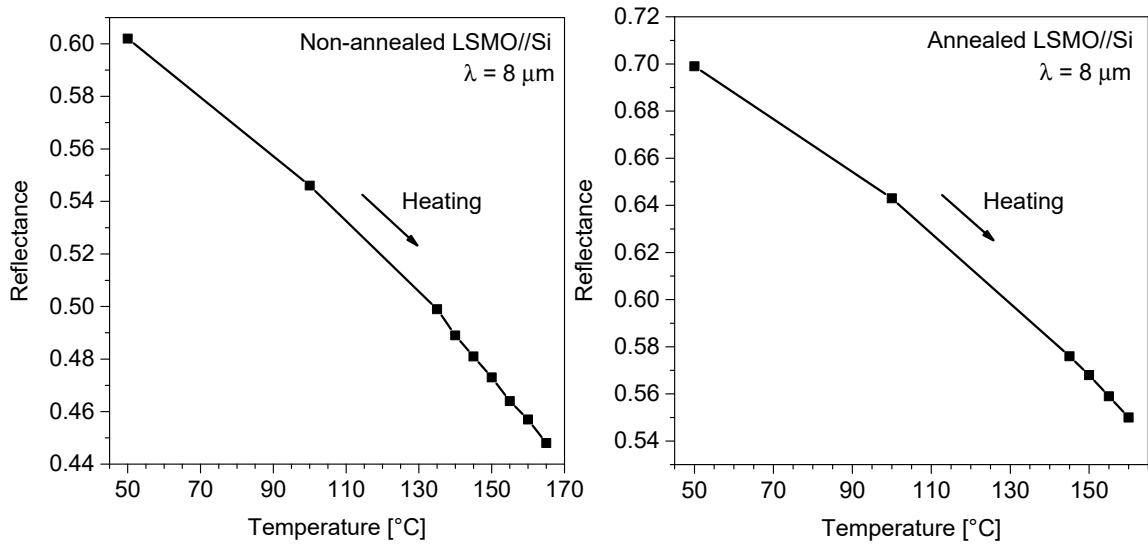
Figure 4.15. Temperature dependent reflectance curves of La$_{1-x}$Sr$_x$MnO$_3$ thin films sputtered on Si substrates at room temperature, then measured as deposited (left) and post-annealed at 700°C for 2 hours (right). Reflectance values are determined at 8 μm wavelength.
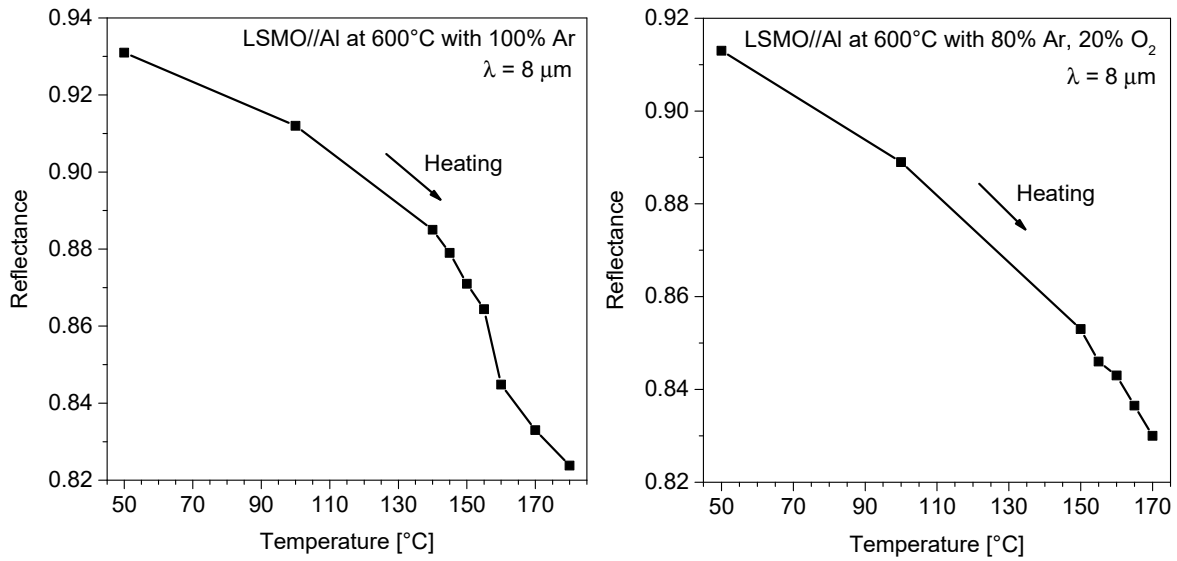


Figure 4.16. Temperature dependent reflectance curves of La$_{1-x}$Sr$_x$MnO$_3$ thin films sputtered on Al substrates at 465°C (600°C nominal), in pure Ar (left) and in mixed Ar-O$_2$ atmosphere (right). Reflectance values are determined at 8 μm wavelength.

The subsequent set of La$_{1-x}$Sr$_x$MnO$_3$ films sputtered on Al at 465°C substrate temperature, in pure and in 20% oxygen containing Ar plasma are also measured (Figure 4.16). In the presence of O$_2$, the reflectance changes in a steady fashion and amounts to a total decrease of ≈8% over the measured temperature range. However, the film sputtered in 100% Ar atmosphere, exhibits a small, but sudden drop in reflectance of about 2% above 150°C. This proves, that in principal, high temperature thermochromic switch in perovskite type La$_{1-x}$Sr$_x$MnO$_3$ films can be achieved. Nonetheless, at this stage the switching modulation is rather limited and further optimization of the deposition/post-deposition temperature and process gas mixture is required. As for VO$_2$ thin films, the substrate likely plays a critical role in film crystallization and has the potential to significantly improve the thermochromic switching modulation.

# Chapter 5     Doping of VO$_2$

Through doping with different elements, the optical and electrical properties of vanadium dioxide can be tuned and, most importantly, its transition temperature can be tailored to suit various applications. As the origin of the metal-to-insulator (MIT) transition in VO$_2$ is still an open subject despite extensive research and decade-long debates on the topic, so is the mechanism through which different dopants inflict their effects on the phase transition. Nonetheless, it is generally believed that donor-like dopants with large ionic radii (e.g. $W^{6+}$, $Mo^{6+}$, $Ta^{5+}$, $Nb^{5+}$) decrease the transition temperature $T_{MIT}$, while acceptor-like elements of low oxidation state and smaller ionic radii (e.g. $Al^{3+}$, $Cr^{3+}$, $Fe^{3+}$) increase $T_{MIT}$ (Figure 2.8). Tungsten has been considered the most efficient among dopants, enabling a reduction of $T_{MIT}$, with a nearly linear rate, of 49-55°C/at.% W dopant [Paone, 2015]. Therefore, for room temperature applications such as smart windows, tungsten doping is well-established. However, shifting the MIT towards higher temperatures has been less studied and the identified dopants proved less efficient.

Introduction of smart thermochromic VO$_2$ based solar thermal collectors and recent developments at microelectronic device level emphasize the importance of a reliable, inexpensive and efficient doping that enables a precise control over a wide range of elevated $T_{MIT}$ in vanadium dioxide thin films. Studies on dopants shown to increase the transition temperature were mainly published for single crystal or powder VO$_2$. Contrary to expectations, $Al^{3+}$ doping decreased the transition temperature and induced progressive amorphization of the VO$_2$ films [Paone, 2015; Chen, 2009; Gentle, 2008]. $Fe^{3+}$ was also reported to decrease the transition temperature in thin films [Phillips, 1987].

This chapter discusses the experimental observations of sputtered Cr, Si and Ge doped vanadium dioxide films. Co-sputtering allows for flexibility in adjusting the dopant concentration of the films by changing the applied power on the dopant target. Unlike the V target run by a pulsed-DC power supply, the dopant targets are powered by a radio frequency (RF) AC unit. To limit the doping, magnets are removed from the dopant magnetron, thus reducing the magnetic field and subsequently the plasma density. For successful dopants and dopant concentrations, the corresponding alloy targets are ordered, which then simplify the deposition process by eliminating the need for a second plasma.

## 5.1    Chromium (Cr) and Silicon (Si) doping

In the VO$_2$ lattice, V (IV) is thought to be 6-coordinate type with an ionic radius of 72 pm. In the octahedral coordination, Cr (IV) has an ionic radius of 69 pm, slightly lower than that of V (IV), which is expected to favor the increase of the transition temperature of the VO$_2$ crystal structure. Furthermore, Cr ions with oxidation states ranging from 2+ to 6+ can all take an octahedral coordination, in which cases also a charge imbalance could be induced. Therefore, Cr is deemed to be an interesting dopant choice. By contrast, Si (IV) doping uphelds the charge conservation and the effect coming from the size of the ionic radius is isolated. Si (IV) is significantly smaller than V (IV) with an ionic radius 54 pm in the octahedral coordination and an even lower 40 pm in the preferred tetrahedral coordination. Out of these considerents, both Cr and Si are investigated as dopant elements. The ionic radii cited here are Shannon ionic radii [Shannon, 1976].

## 5.1.1  Cr doping

Chromium doped thermochromic films have been deposited on <100> Si substrates by means of co-sputtering from metal V and Cr targets. When the applied power to the dopant target ranges from 0 to 60 W, the samples exhibit transition temperatures that do not appear to vary linearly with the doping (see Figure 5.1 and Table 5.1). Moreover, with the exception of one sample with 20W applied to the Cr target, all samples switch in a narrow temperature range, common for polycrystalline $VO_2$ thin films. This suggests that the doping level might be too low or that Cr has difficulties entering the $VO_2$ lattice. At higher applied powers, at least some of the sputtered Cr might enter the lattice and, for the two samples with the highest expected dopant concentration, an increase of the transition temperature with doping level is noticed. For the samples with 70 and 100W applied on the Cr target, transition temperatures of 71.4°C, respectively 74.5°C have been determined.
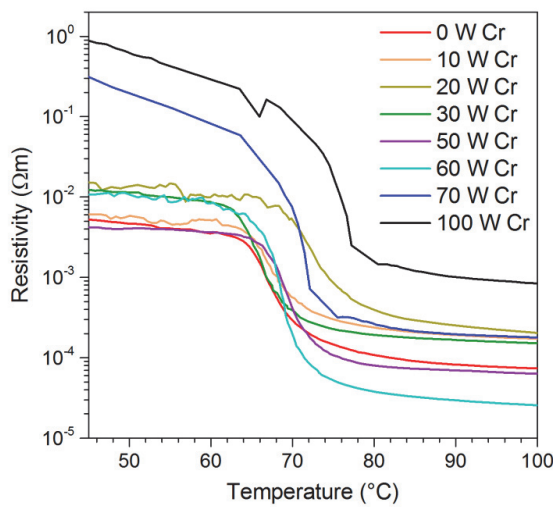


Figure 5.1. Electrical resistivity curves of pure and Cr doped $VO_2$ thin films measured during heating. The concentration of Cr in the films is changed by increasing the applied power on the dopant target.

Table 5.1. Pure and Cr doped samples with the corresponding phase transition temperatures measured.

| Sample [x]W on Cr target | $T_C$ [°C] |
|---|---|
| 0 | 67.7 ± 0.5 |
| 10 | 66.9 ± 0.5 |
| 20 | 72.4 ± 0.5 |
| 30 | 66.0 ± 0.5 |
| 50 | 69.6 ± 0.5 |
| 60 | 68.6 ± 0.5 |
| 70 | 71.4 ± 0.5 |
| 100 | 74.5 ± 0.5 |

Interestingly, although by doping usually the magnitude of the transition decreases, in the case of Cr doping, the switching magnitude is comparable to that of the reference sample (in some cases being even larger). Looking at the three samples with the largest expected Cr concentration (60, 70 and 100 W applied), a similar switching magnitude is recorded, however, the absolute resistivity values and transition temperatures are increased with doping. This suggests that the stronger the doping, the more semiconducting the films behave. A possible way to counter the increase in resistivity could be by reducing the oygen partial pressure during deposition with increasing doping.

While the above observations seem to indicate that, in principle, Cr is successful in increasing the transition temperature, for any practical purposes the increase in temperature is insufficient and only achieved at relatively high levels of doping. Also, out of practical considerations, the heavy flake formation in the deposition chamber should be noted. On one hand, this together with the varying electrical resistivity values determined on different parts of the same sample might suggest a possible segregation of the Cr or chromium oxide in the films.

On the other hand, SEM images of Cr doped $VO_2$ films and the corresponding EDX results do not support this hypothesis as the films appear to be rather uniform, with well defined crystalline grains ranging from ≈100 nm to ≈200 nm in size, and exhibit a homogeneous EDX elemental map for V, Cr and O alike (Figure 5.2). Furthermore, the measured XRD spectra of three doped samples with different Cr content show only diffraction peaks attributed to $VO_2$ (Figure 5.3.a). The data also shows that the diffraction peaks shift with the doping, higher the doping level larger is the shift. The peaks shift towards higher angles as expected for dopants with smaller ionic radius than that of the vanadium ion. Notably, even at high doping levels, no peaks associated with Cr or $Cr_xO_y$ are distinguishable. These observations support the case for Cr substitutional doping in the $VO_2$ crystal lattice.
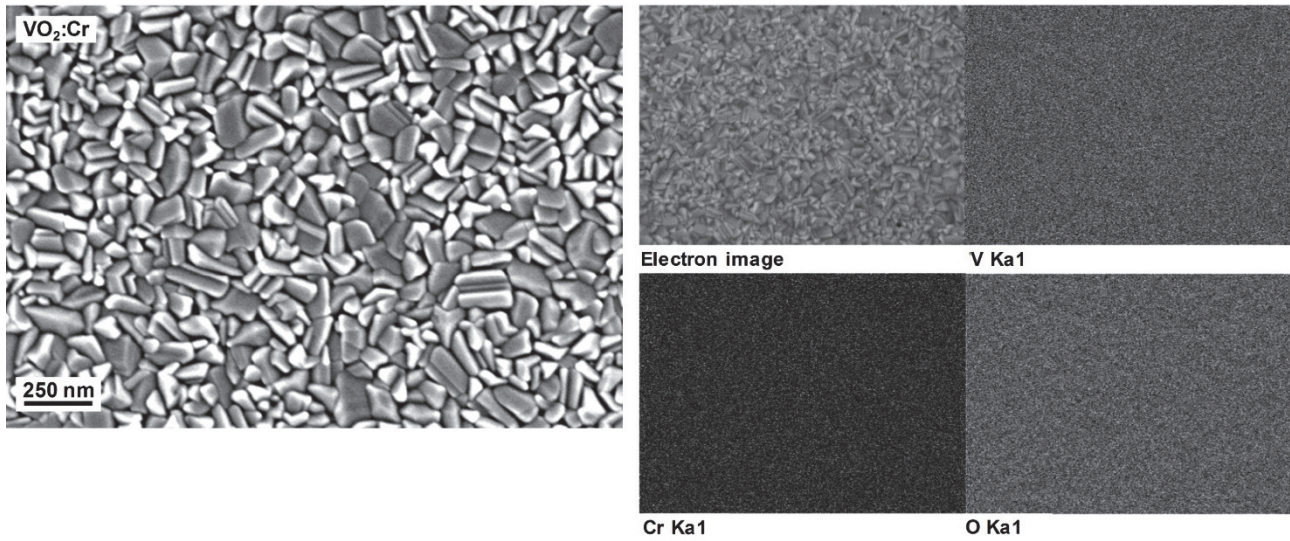


Figure 5.2. Plane view SEM image of a Cr doped $VO_2$ thin film (50 W applied to the Cr target) and EDX elemental mapping of V, Cr and O. The polycrystalline film appears to be homogeneous – no segregation observed.
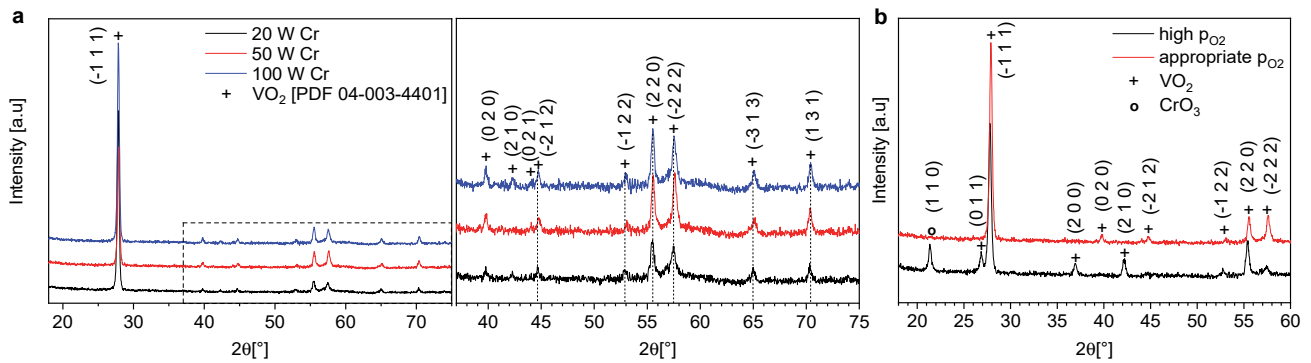


Figure 5.3. a) Grazing-incidence XRD spectra of three Cr doped $VO_2$ films. The power applied on the Cr target is 20, 50 and 100 W, respectively. All diffraction peaks are attributed to $VO_2$. b) XRD spectra of two samples sputtered with 50 W applied on the Cr target, but at different oxygen partial pressures, $p(O_2)$. The sample deposited at high $p(O_2)$ shows a different preferred grain orientation and $CrO_3$ segregation compared with the sample deposited at lower $p(O_2)$.

Nonetheless, if the deposition parameters are not carefully controlled, at too high oxygen partial pressure, segregation of chromium oxide might indeed occur. This is exemplified by two crystalline thin films, both deposited by applying 50 W to the Cr target, the only variable being the oxygen partial pressure during deposition (Figure 5.3.b). The XRD spectral comparison shows, that while both exhibit the diffraction peaks typical for $VO_2$, the preferred grain orientation varies. Finally, the additional peak at 21.3° present in the

sample deposited at higher oxygen partial pressures, is associated with the (1 1 0) peak of $CrO_3$, that is the strongest peak for crystalline $CrO_3$.

Outcomes

- Under controlled oxygen partial pressures, homogeneous Cr doped $VO_2$ films are deposited. No segregation is observed.

- $T_{MIT}$ does not appear to depend linearly on the doping concentration.

- A maximum $T_{MIT}$ of ≈74.5°C has been reached by Cr doping.

## 5.1.2 Si doping

*This section borrows part of its text and images from: Krammer, A., Bouvard, O., Schüler, A. Study of Si doped $VO_2$ thin films for solar thermal applications. Energy Procedia 122, 745-750, 2017. Available from: https://doi.org/10.1016/j.egypro.2017.07.390*

With Si doping, besides the precise determination of the thermochromic properties, the focus lies on understanding the changes induced at the electronic structure level. To that end, the samples are characterized by in-situ X-ray (XPS) and ultraviolet (UPS) photoelectron spectroscopy.

Film growth

Five samples, S1 to S5, of pure and Si doped vanadium dioxide films are deposited by reactive magnetron co-sputtering on <100> Si substrates. The composition of the films is varied by adjusting the RF power on the Si target between 0 and 25W. Higher the applied power, higher is the expected dopant concentration of the sample. The exact film deposition parameters are summarized in Table 5.2, while the individual samples with their corresponding applied power on the Si target is listed in Table 5.3.

Table 5.2. Process parameters used for the deposition of Si doped $VO_2$ films.

| Base pressure [mbar] | $< 3\cdot10^{-7}$ |
|---|---|
| Working pressure [mbar] | $6\pm0.2\cdot10^{-3}$ |
| $O_2$ partial pressure [mbar] | $6\pm0.2\cdot10^{-4}$ |
| Substrate temperature [°C] | 465 |
| Film thickness [nm] | ≈320 |
| Applied power [W] | V: 150 (DC) Si: 0 - 25 (RF) |

Table 5.3. List of deposited samples and corresponding applied power on the Si target.

| Sample | S1 | S2 | S3 | S4 | S5 |
|---|---|---|---|---|---|
| Power applied on the Si target [W] | 0 | 8 | 15 | 20 | 25 |

Four-point probe resistivity

The influence of Si doping on the thermochromic film properties is determined by measuring and plotting the electrical resistivity of the films between room temperature and 95°C (Figure 5.4). To precisely determine the phase transition temperature and hysteresis parameters, the derivatives of the resistivity variation with temperature, log ρ(T) vs. T are plotted for both heating and cooling directions. The curves are fitted with Gaussian functions whose minima are defined as the transition temperature for the heating, $T_h$ and cooling, $T_c$ cycle. The difference between $T_h$ and $T_c$ gives the hysteresis width, $\Delta T_t$, while the full width at half maximum of the derivative curve, FWHM, indicates the steepness of the transition. Smaller FWHM value means a steeper slope change, a sharper transition.

The pure VO$_2$ film switches at 67.8°C during heating. The transition temperature, the hysteresis width and the absolute resistivity values increase gradually with doping, up to a certain point, when film amorphization is induced and the switching character of the films is lost. The highest transition temperature achieved is ≈72.3°C and, in general, Si doping appears to enhance the semiconducting behavior of the films.
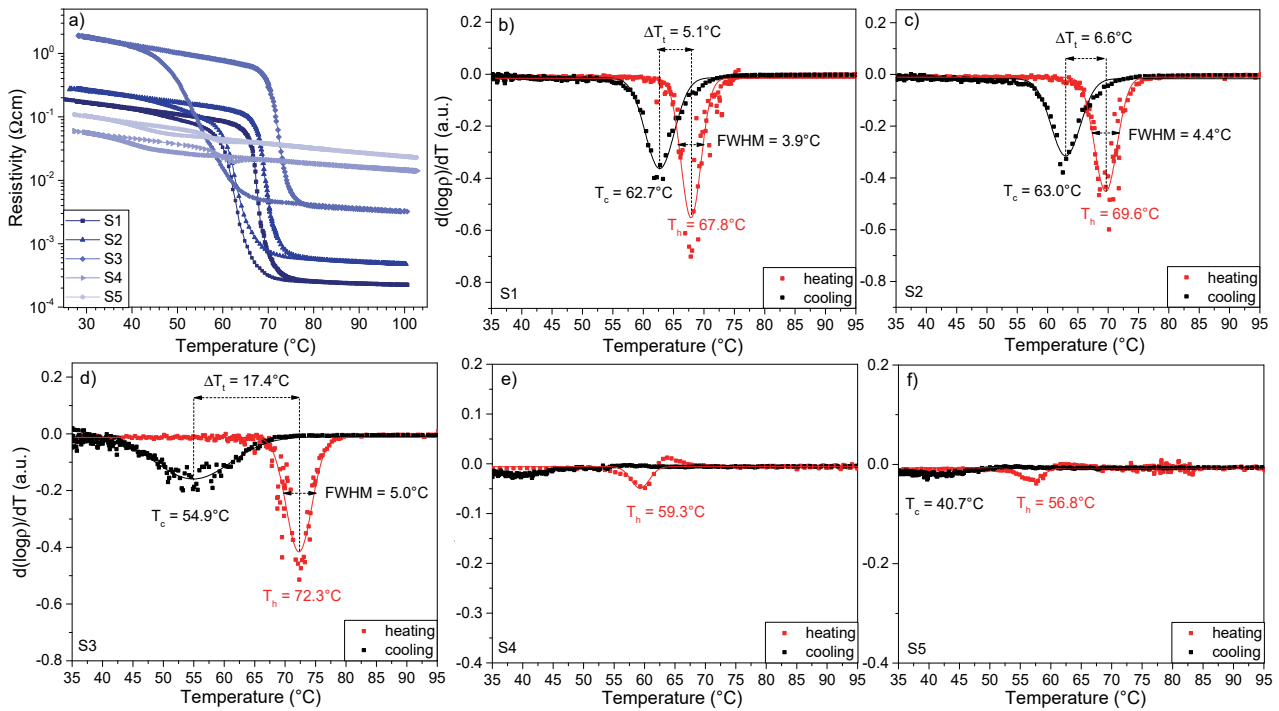


Figure 5.4. a) Temperature dependent resistivity curves of pure and Si doped VO$_2$ films. The d(logρ)/dT vs T plots for pure VO$_2$ (b) and V$_{(1-x)}$Si$_x$O$_2$ films with 8W (c), 15W(d), 20W (e), 25W( f) power applied on the Si target. Symbols denote measured data points, fitted with Gaussian functions. The minima indicate the transition temperature during heating, $T_h$ and cooling, $T_c$. The difference between the two is the hysteresis width, $\Delta T_t$. The FWHM gives the sharpness of the transition.

The three switching samples are characterized by photoelectron spectroscopy.

X-ray photoelectron spectroscopy

Elemental quantification is based on the O 1s, V $2p_{3/2}$ and Si 2p core-level peak integration, using Scofield sensitivity factors combined with calibration with pure $VO_2$ sample. A Shirley background is adopted. As expected, for the pure $VO_2$ sample no Si peaks are identified. For the two Si doped, switching samples, the quantification yields 1.2 and 1.5 at.% Si content, respectively. The ratio between the at.% of V and O is 1:2 for the pure sample and 1:2.05 for the two doped samples.

In Figure 5.5 the O 1s and V 2p core level spectra of the $VO_2$, $V_{0.988}Si_{0.012}O_2$ and $V_{0.985}Si_{0.015}O_2$ samples are shown. The spin-orbit splitting leads to the two-peak vanadium structure, $2p_{1/2}$ and $2p_{3/2}$. The core lines appear to shift to higher binding energies with Si doping. Broad V $2p_{3/2}$ lines are observed. This is consistent with literature where reported FWHM values of the $2p_{3/2}$ peaks range widely from 1.95 to 3.2 eV and have been explained by various multiplet configurations in the photoemission final states, resulting from core-hole - 3d electrons interaction [Demeter, 2000; Sawatzky, 1979]. Besides broadening, this core-hole – 3d electron coupling also results in satellite structures falling in the high-binding energy side of the O 1s peak and leading to the asymmetry around ≈531eV [Zimmermann, 1998].
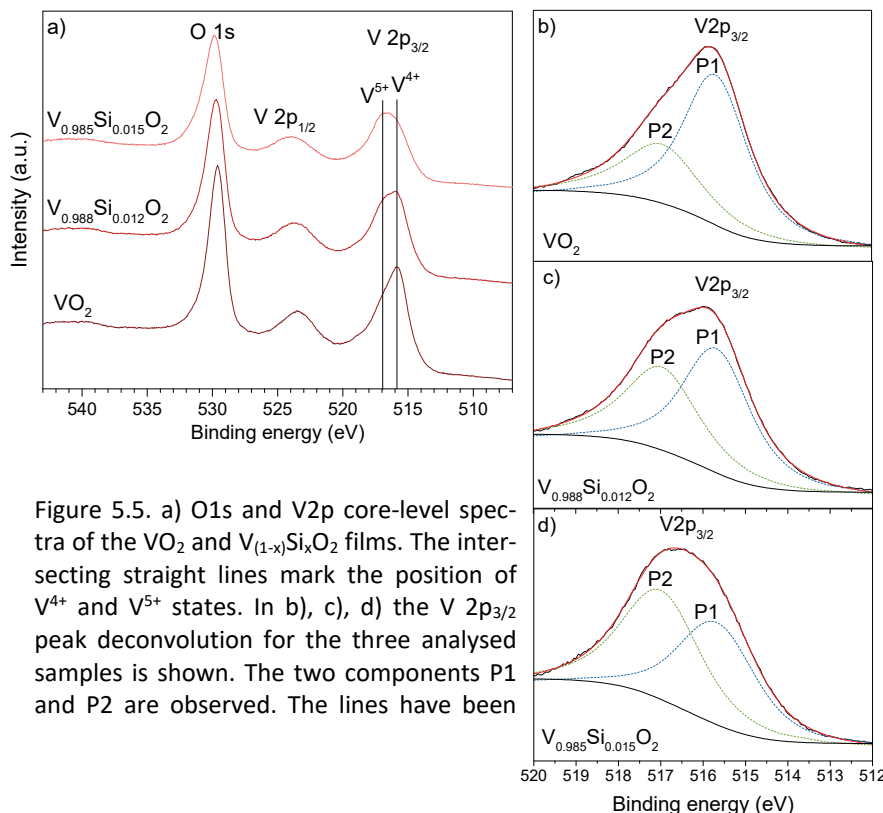


Figure 5.5. a) O1s and V2p core-level spectra of the $VO_2$ and $V_{(1-x)}Si_xO_2$ films. The intersecting straight lines mark the position of $V^{4+}$ and $V^{5+}$ states. In b), c), d) the V $2p_{3/2}$ peak deconvolution for the three analysed samples is shown. The two components P1 and P2 are observed. The lines have been

The V $2p_{3/2}$ peak deconvolution results in two components, P1 and P2, fitted with mixed Lorentzian-Gaussian curves. Peaking at ≈515.7 and ≈517 eV respectively, the two components coincide with the reported binding energies of the $V^{4+}$ and $V^{5+}$ $2p_{3/2}$ core lines. Indeed, component P1 is attributed to the $V^{4+}$ states as both its peak position and FWHM of ≈1.9 – 2.2 eV closely match those reported for V $2p_{3/2}$ core lines of highly pure $VO_2$ samples. As $VO_2$ surfaces readily over-oxidize into $V_2O_5$, it is also likely that a fair amount of $V^{5+}$ oxide is present. However, for P2 to be attributed solely to the $V^{5+}$ contribution, it is striking that rather small amounts of Si induce such stark changes in the P1:P2 ratio, especially when the V:O ratio

is basically unchanged (1:2). Furthermore, at 2.2 – 2.3 eV, the FWHM of the P2 component is broader than those reported for $V^{5+}$.

2p spectra of first row transition metals are challenging to interpret due to peak asymmetries, complex multiplet splitting, shake-up and plasmon loss structures and uncertain, overlapping binding energies. [Biesinger, 2010] In Ti-Al-N films, complex Ti 2p line shapes have been reported [Schüler, 2001a]. The authors interpret this in terms of a well screened main doublet and a poorly screened satellite doublet, which becomes dominant as the screening ability of conduction electrons is decreasing with Al content. Fine structured $2p_{3/2}$ core lines were also reported for NiO and Cu based materials and have been explained based on non-local screening effects. This means that an electron could be taken from a far oxygen atom and transferred to the photoionized site. [Hüfner, 2003] Therefore, it is possible that various satellite structures might be present in the higher binding energy side of the V $2p_{3/2}$ peaks as well. A small Si doping appears to significantly strengthen the P2 component which could be an indication of some non-local screening effects.

UV photoelectron spectroscopy

After the deposition, the three samples: $VO_2$, $V_{0.988}Si_{0.012}O_2$ and $V_{0.985}Si_{0.015}O_2$ are immediately transferred to the photoelectron spectrometer while still in the hot state. UPS He I spectra are measured continuously during sample cooling in order to observe the metal-to-insulator transition and its effects on the density of states at the Fermi level. Once the valence band edge does not shift and the sample reached its low temperature state, UPS He II spectra are measured too.

Figure 5.6 shows the He I and II spectra of the pure, 1.2 at.% and 1.5 at.% Si doped $VO_2$ films. For better legibility, a zoomed view of the Fermi level during the cooling process is displayed for each sample. A decrease of the density of states at the Fermi level, associated with V 3d states, is observed with Si doping. For the pure $VO_2$ film, the opening of a band gap during cooling marks the in-situ metal-insulator transition. For the sample with 1.2 at.% Si, only a vague Fermi edge is detectable while changes in the density of states with cooling are moderate. The sample with ≈1.5 at.% Si exhibits no noticeable changes to the valence band edge during cooling. Therefore, although in magnitude the resistivity modulation of the 1.5 at.% Si containing sample is similar to that of the pure and lighter doped $VO_2$ film, from an electronic point of view, it undergoes a semiconductor-to-semiconductor transition.

In both the He I and II spectra, broad shoulder-like features centred around 4.8 and 7 eV binding energies are identified. According to [Shin, 1990], these two bands at 4.8 and 7 eV are related to non-bonding O 2pπ and bonding O 2pσ orbitals with V d band. The intensity of the feature at 7 eV binding energy, indicated in the figure with the solid black line labelled "A", is changing with Si doping. This suggests that Si reduces the strong V 3d – O 2pσ band hybridization.
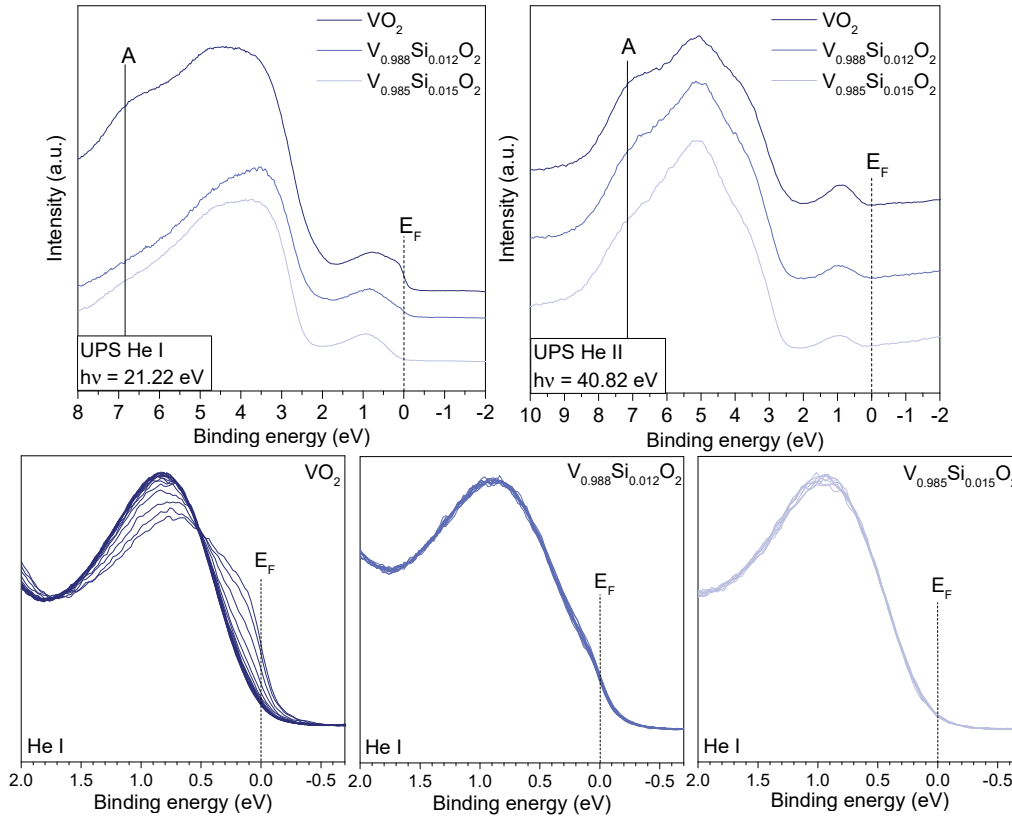
Figure 5.6. He I (measured at T > $T_{MIT}$) and He II (measured at T < $T_{MIT}$) valence band spectra of $VO_2$ and $V_{(1-x)}Si_xO_2$ films (top). A zoomed in view of the He I spectra near the Fermi level is given for all three samples (bottom). Only for the pure film is a shift in the DOS at the Fermi level observed – from a clear Fermi edge at T > $T_{MIT}$ to a band gap opening up at T < $T_{MIT}$. Dashed lines mark the Fermi energy level, solid lines indicate bonding O 2pσ orbitals with the V d band.

Outcomes

- Si raises the insulator-to-metal transition temperature, but, as in the case of Cr doping, the change is rather limited with a maximum increase of ≈4.5°C reached.

- Film amorphization is induced early by doping and, already above 1.5 at.% Si, the transition is lost.

- Like with Cr, the resistivity values continue to increase with doping over the measured temperature range.

- Through doping, the metallic character of the films in the hot state is hindered in favour of a semi-conducting behaviour. From the UPS spectra it is shown that the density of states at the Fermi level decreases with doping and at 1.5 at% Si a band gap has opened up.

- The decrease in intensity near the Fermi level with doping, could potentially translate in higher thermal emittance values, thus in better heat dissipation to the surroundings above the transition temperature

- V $2p_{3/2}$ XPS peak deconvolution shows that fitted components peak at 515.7 eV and 517 eV binding energy. The former is associated with $V^{4+}$ states, while for the origin of the latter $V^{5+}$ states, shake up and non-local screening satellites are considered. As doping levels increase, the second component becomes more important on the expense of the four-fold oxidized V atoms.

# 5.2    Germanium (Ge) doping

*This section borrows part of its text and images from: Krammer A., Magrez A., Vitale W. A., Mocny P., Jeanneret P., Guibert E., Whitlow H. J., Ionescu A. M., Schüler A. Elevated transition temperature in Ge doped VO$_2$ thin films. Journal of Applied Phyics 122, 045304, 2017.*

A quick literature study reveals that Ge, much like Cr or Al doping, is generally considered and cited as a dopant that raises the transition temperature of VO$_2$. Meanwhile, Cr or Al doping has been shown to have either very limited effect in increasing the temperature and/or induce film amorphization. To all intents and purposes, both Cr and Al doping proved unsuitable for the envisaged solar absorber application.

A deeper look at sources claiming the effect of Ge doping reveal that it originates from a 1968 patent by Futaki et al. [Futaki, 1968], which reported elevated transition temperatures in Ge doped VO$_2$ crystals. From there on, Ge was much referred to as a dopant which increases the MIT temperature and it was widely assumed that this effect would be applicable to thin films too. Therefore, this section sets out with the aim to study the effect of Ge doping on vanadium dioxide thin films.

In a first sample series the effect of Ge doping is investigated; the crystalline structure of the films is inferred from X-ray diffraction; film topography is studied by SEM; film composition is determined from EDX measurements. A second series of doped films is then deposited to confirm the effect of Ge doping and to optimize the doping concentration in the thermochromic films. Furthermore, complementary characterizations such as RBS – for precise elemental composition and AFM topography measurements are carried out.

## 5.2.1  Preliminary investigations

Ge doped VO$_2$ films co-sputtered by applying 10, 20 and 30 W power on the Ge target are compared. The measured transition temperatures for the heating and cooling cycle, whose average yields the metal-to-insulator phase transition temperature, and the hysteresis widths are listed in table Table 5.4.

Ge doped samples exhibit an increase in transition temperature, T$_{MIT}$ compared to the reference VO$_2$ sample. The T$_{MIT}$ is increasing continuously with the doping. On the other hand, the discontinous change in electrical resistivity is progressively reduced by increasing the level of doping, as is the hysteresis which completely disappears for the most heavily doped sample (Figure 5.7.a). Crossing a threshold of dopant concentration in the VO$_2$ lattice, the transition and the thermochromic character of the film is lost.

Table 5.4. Determined transition temperatures for samples with different applied power on the Ge dopant target.

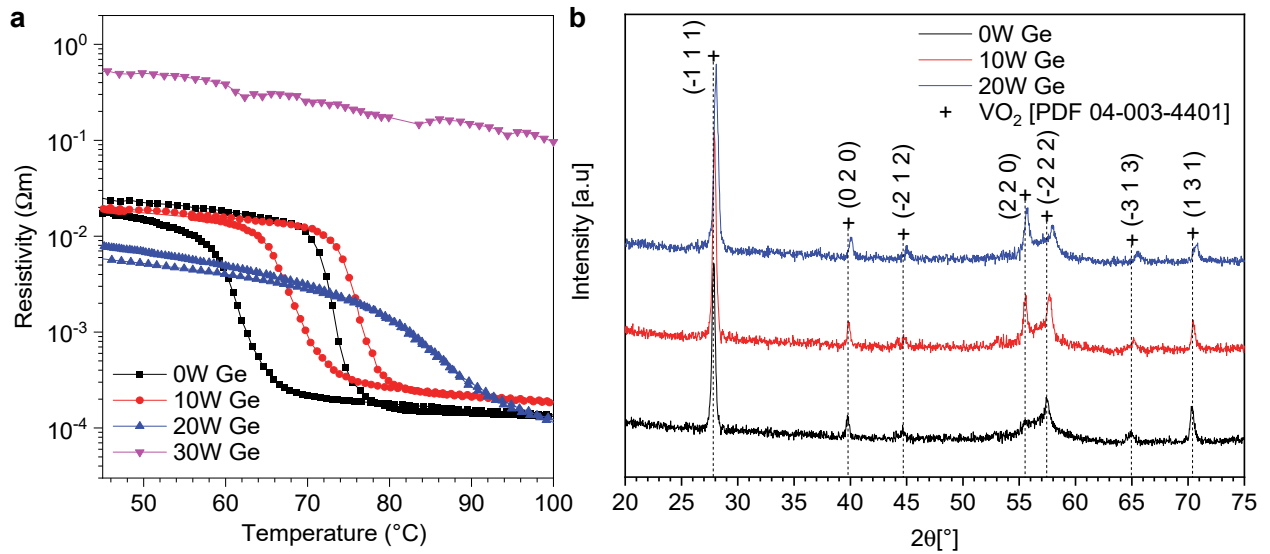| Power applied on the Ge target [W] | T$_h$ [°C] | T$_c$ [°C] | T$_{MIT}$ [°C] | ΔT$_t$ [°C] |
|---|---|---|---|---|
| 0 | 71.5 | 59.7 | 65.6 | 11.8 |
| 10 | 74.3 | 65.8 | 70.1 | 8.5 |
| 20 | 85.5 | 85.5 | 85.5 | 0 |
| 30 | - | - | - | - |

Figure 5.7. a) Temperature dependent resistivity curves of VO₂:Ge films of different Ge content. b) Grazing-incidence XRD spectra of VO₂ and VO₂:Ge films of different composition. All diffraction peaks are attributed to VO₂, but in the doped films the peaks are shifted towards higher angles.

The three switching films have been measured by X-ray diffraction and the spectra show well-crystallized films (Figure 5.7.b). Only VO₂ diffraction peaks are identified. In the doped samples the peak positions are shifted to higher angles. These shifts are the result of strain effects induced by planar stresses inside the film. Peaks shift to lower angles for compressive stresses and to higher angles for tensile stresses.

Ge (IV) has an ionic radius of 67 pm in the octahedral coordination and 53 pm in the tetrahedral coordination, both smaller than the ionic radius of vanadium atoms that they substitute. This generates tensile stresses in the film, causing peaks to shift to higher angles, which is in accordance with our results. Higher is the level of doping, stronger the peak shift.

From the plane sectional SEM images of the lightly doped sample with 10 W applied on the Ge target, grains showing advanced growth in the plane perpendicular to the substrate plane are observed (Figure 5.8). These parallelly oriented grains make up patterns in the film and the pattern formation is enhanced by Ge doping. In the sample with 20 W applied on the Ge, these patterns dominate the surface morphology and they are unformly spread over the film. In the patterns, the grains appear more elongated, acicular in comparison with the standard spherical or rounded grains typical for pure VO₂ films.

From the cross sectional SEM images, similar film thicknesses of ≈200 nm for the lightly doped sample and ≈220 nm for the sample with the higher dopant concentration are identified.

Information on the chemical composition of the doped films is obtained from complementary EDX measurements (Figure 5.9). Because of the patterning it is interesting to see whether the Ge concentration changes in the different regions. EDX spectra are taken locally on both lightly and strongly doped samples in the regions with rounded grains and acicular shaped grains. The Ge content in the sample with 10 W power applied on the dopant is determined at 0.35 at.% (close to the EDX detection limit), while for the sample with 20 W applied on the Ge, the concentration is ≈2.9 – 3 at.% Ge independently on the measured region type, patterned or not. This suggests that the films are homogeneous and there is no Ge segregation or phase separation in the films.
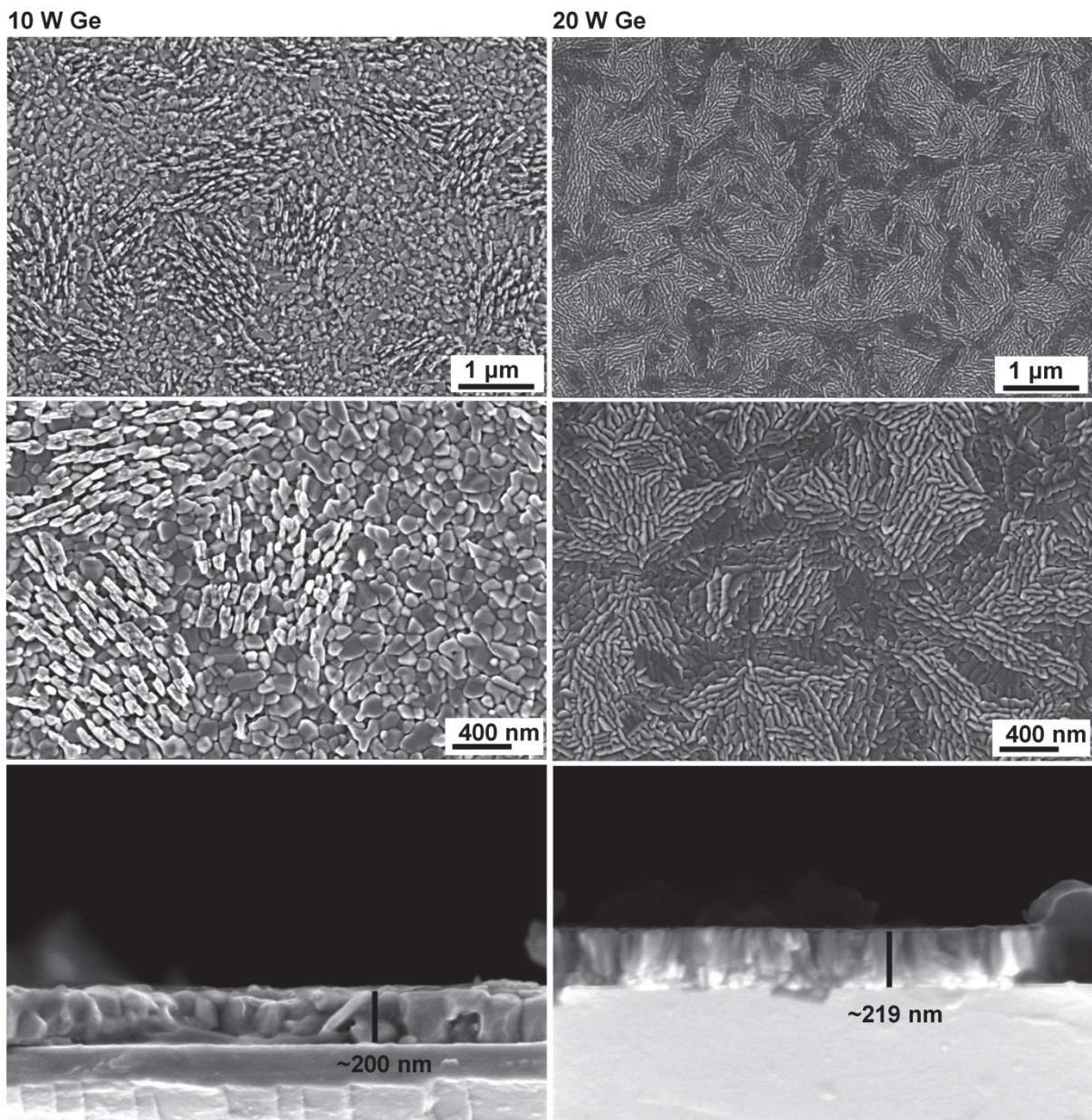
**10 W Ge**

**20 W Ge**



Figure 5.8. Plane view and cross sectional SEM images of the VO$_2$:Ge films  with 10 and 20 W applied on the dopant target. The acicular grain formation is more pronounced in the sample with the higher Ge content.
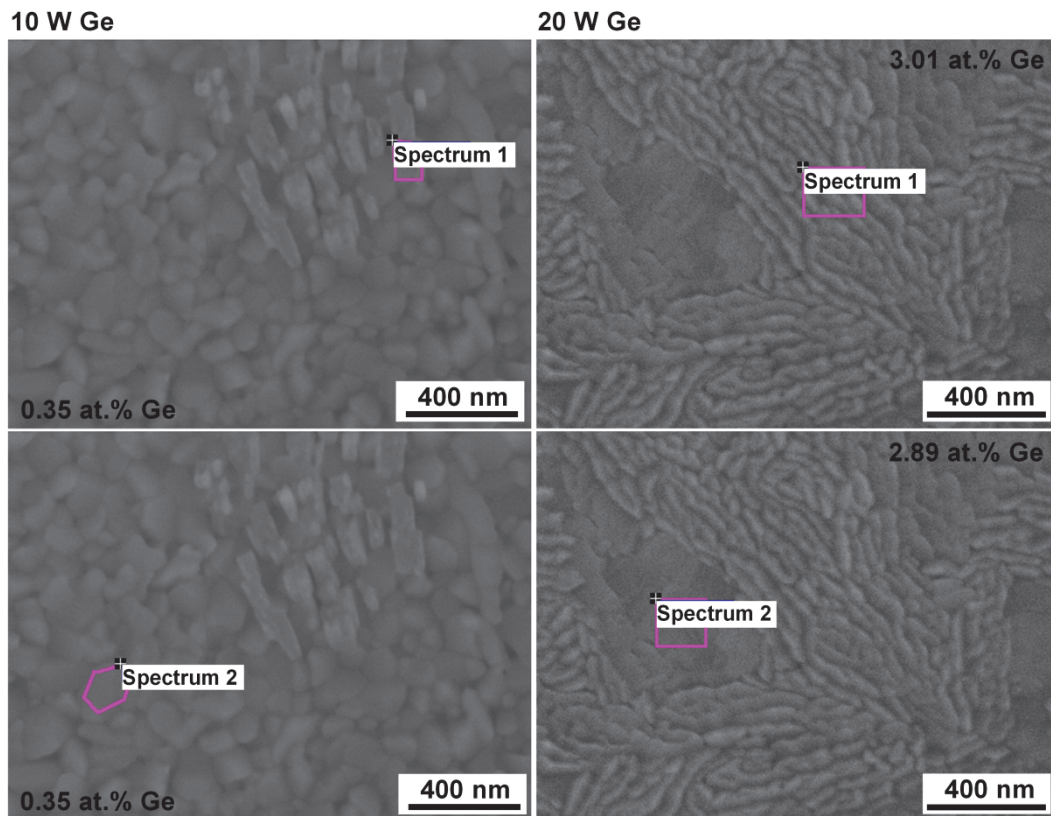
Figure 5.9. Electron images of the VO$_2$:Ge samples with the spots of the EDX measurements and the corresponding Ge concentrations determined from the EDX spectra.

Outcomes

- Deposited Ge doped VO$_2$ films are homogeneous and no segregation is observed.

- T$_{MIT}$ appears to depend directly on the doping concentration.

- A T$_{MIT}$ of ≈85.5°C has been reached with a Ge doping of ≈3 at.%.

## 5.2.2 Confirmation and optimization of Ge doping

A second sample series is deposited in order to confirm the effect of Ge alloying into $VO_2$. Furthermore, reaching a transition temperature of above 95°C is attempted for the envisaged solar thermal collector application.

Film growth

Vanadium dioxide based thin films, with different Ge content, are deposited by reactive magnetron sputtering in high-vacuum conditions. The 480 - 580 nm thick films are co-sputtered from V and Ge targets onto <100> Si substrates. The RF power applied on the Ge source is varied between 0 and 20 W. All the other deposition parameters are kept constant (Table 5.5).

Table 5.5. Process parameters used for the deposition of pure and Ge doped $VO_2$ films.

| Base pressure [mbar] | $< 5 \cdot 10^{-8}$ |
|---|---|
| Working pressure [mbar] | $7.7 \pm 0.2 \cdot 10^{-3}$ |
| $O_2$ partial pressure [mbar] | $4.1 \pm 0.2 \cdot 10^{-4}$ |
| Nominal temperature [°C] | 640 |
| Film thickness [nm] | 480 – 580 |
| Applied power [W] | V: 150 (DC) Ge: 0 - 20 (RF) |

Rutherford Backscattering Spectrometry

Precise Ge quantification in the $V_{(1-x)}Ge_xO_{2+y}$ thin films and determination of film thicknesses is achieved by Rutherford Backscattering Spectrometry (RBS). The simulated spectrum, based on a $V_{(1-x)}Ge_xO_{2+y}$ (monolayer)//Si (substrate) model, fits well the experimental RBS data. The energy spectra of the backscattered ions are displayed in Figure 5.10, where the yield of backscattered He ions is plotted against the channel number (backscattering energy). The Ge contribution is seen at high backscattering energies (high channel number) and is partly superposed on the V signal. At lower energies, the oxygen component is superposed on the Si substrate signal. The determined Ge content for each sample is given in Table 5.6. As expected, by increasing the applied power on the Ge target, the Ge concentration of the deposited films is gradually increasing.

Table 5.6. The Ge at.% as determined by RBS measurement.

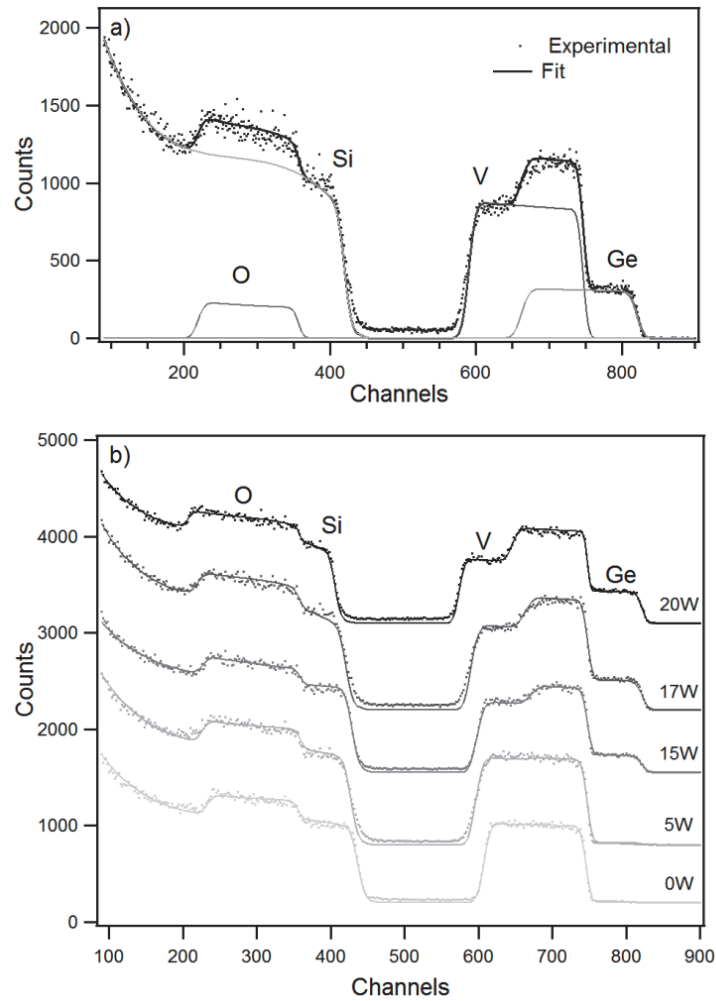| Power applied to the Ge target [W] | 0 | 5 | 15 | 17 | 20 |
|---|---|---|---|---|---|
| Ge content [at.%] | 0.1±0.1 | 0.5±0.1 | 4.3±0.2 | 5.9±0.3 | 8.6±0.4 |

Figure 5.10. a) Experimental data (points) and simulated RBS spectra (solid line) of the $V_{0.941}Ge_{0.059}O_{2+y}$ film. The result of the simulation agrees well with the experimental RBS spectrum. (b) Comparison of pure and increasingly doped $VO_2$ films by varying the applied power on the Ge target. The width of the V and O signals is related to the film thickness, while the peak height gives indication on the concentration of backscattered ions.

Four-point probe resistivity

The thermochromic properties of the films are studied from room temperature up to 120°C by determining their temperature dependent electrical resistivity (Figure 5.11). The electrical resistivity curves are plotted for all samples but the $V_{0.914}Ge_{0.086}O_{2+y}$, for which the measured resistivity is too high and does not allow for a reliable reading. The measured curves reveal the strong influence of Ge on the switching characteristics.

The MIT is characterized by (i) the phase transition temperature, $T_{MIT}$ defined as the average value of the transition temperature in heating and cooling cycles:

$$T_{MIT} = \tfrac{1}{2}\,(T_h + T_c) \qquad\qquad \text{Equation 5.1}$$

(ii) the hysteresis width $\Delta T_t$ and (iii) the full width at half maximum (FWHM) of the derivative curve, which indicates the steepness of the transition. The detailed values for the thermochromic phase transition parameters are summarized in Table 5.7.

Table 5.7. Detailed switching parameters determined for the differently doped vanadium dioxide films.

| Ge content [at.%] | $T_h$ [°C] | $T_c$ [°C] | $T_{MIT}$ [°C] | $\Delta T_t$ [°C] | FWHM [°C] |
|---|---|---|---|---|---|
| 0.1 | 70.0 | 62.5 | 66.3 | 7.5 | 5.7 |
| 0.5 | 73.6 | 65.6 | 69.6 | 8 | 7.8 |
| 4.3 | 78.1 | 73.5 | 75.8 | 4.6 | 14.0 |
| 5.9 | 96.6 | 90.6 | 93.6 | 6 | 30.1 |
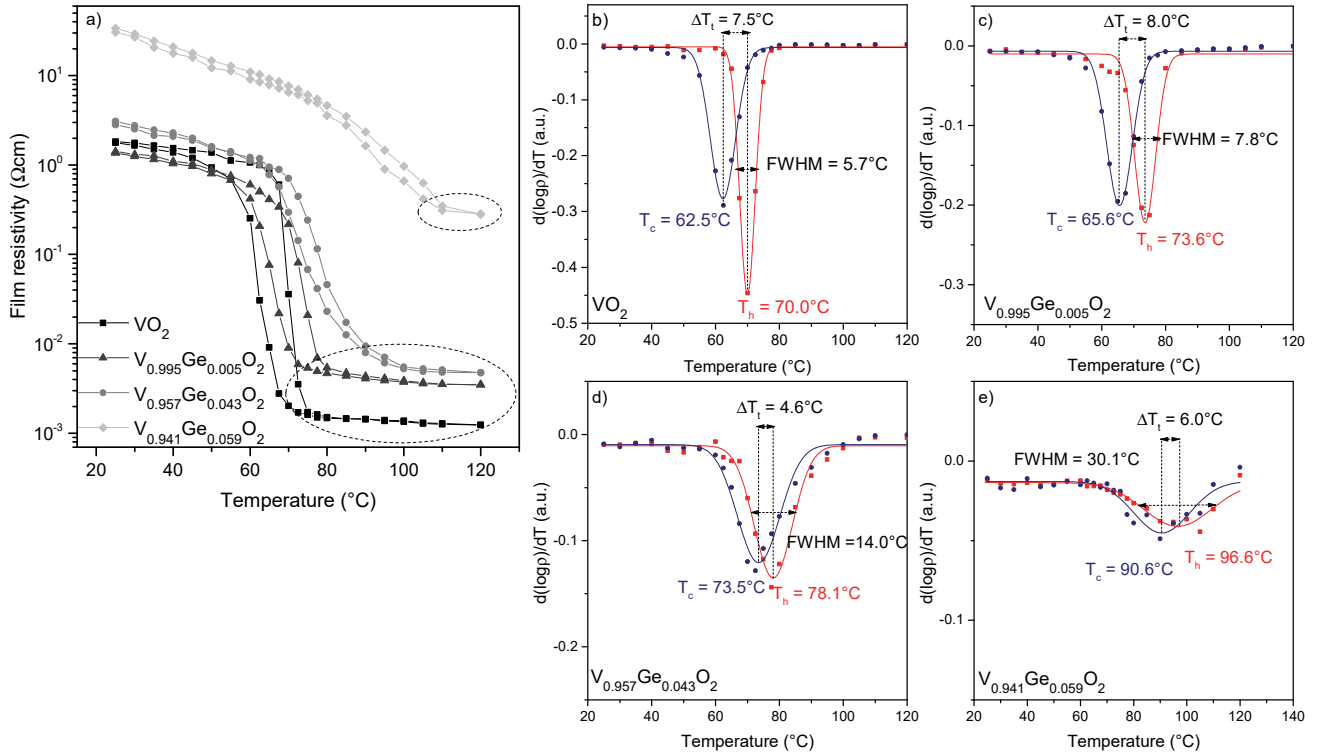


Figure 5.11. a) Temperature dependent electrical resistivities of $VO_2$ and $V_{(1-x)}Ge_xO_{2+y}$ films on Si (100) substrates. The transition temperature is progressively increasing with the Ge content. (b-e) The d(log ρ)/dT vs T curves are plotted for all samples. Measured data points (symbols) are fitted with Gaussian functions (lines) whose minima denote the transition temperatures upon heating, $T_h$ and cooling, $T_c$. The difference between $T_h$ - $T_c$ gives the hysteresis width $\Delta T_t$, while the FWHM determines the sharpness of the metal-to-insulator transition.

Again, the transition temperature is gradually shifted to higher values upon doping and it increases swiftly at higher Ge concentrations confirming the effect of Ge doping on the $VO_2$ phase transition. The shift towards increased $T_{MIT}$ suggests a stabilization of the low temperature, monoclinic phase. A notable increase in the transition temperature occurs only at rather high Ge concentrations e.g. ≈6 at.%. This is in accordance with previous studies where transition temperatures were observed to change significantly only for relatively large impurity concentrations exceeding 1 at.% [Goodenough, 1971; MacChesney, 1969].

Film resistivities increase as well, mainly in the high temperature phase. This in turn leads to lowered amplitude modulation of the MIT. The transition magnitude is slowly lowered from about three orders, for the pure $VO_2$ sample, to just slightly more than one order of magnitude for the sample with 5.9 at.% Ge. However, it is possible that this effect is due to non-stoichiometric oxygen in doped $V_{1-x}Ge_xO_{2+y}$ type films, induced by perturbations associated with the presence of a second plasma in the deposition chamber. A fine-tuning of the oxygen partial pressure might limit the decrease in transition magnitude.

Finally, the FWHM is steadily increasing with Ge addition. Hence, the transition becomes less abrupt, extending over a wide range of temperatures. The hysteresis width is generally narrowed with Ge addition, the opposite of what has been previously observed for Si doping.

X-ray diffraction

Crystallinity and phase composition of the deposited films are determined at room temperature by grazing incidence X-ray diffraction. The samples are polycrystalline and exhibit the typical diffraction peaks of the M1 $VO_2$ phase (space group P121/c1, a = 0.5742(4), b=0.4521(3), c=0.5373(4) nm, α = 90, β = 122.60(5), γ= 90°).

Furthermore, no characteristic peaks of other vanadium oxide phases have been observed, indicating single phase $VO_2$ films. Exception from the above was the $V_{0.914}Ge_{0.086}O_{2+y}$ film with no diffraction peaks distinguishable.

For clarity, only the XRD patterns of the least and most doped samples are displayed, that of pure $VO_2$ and of the samples with ≈5.9 at.% and 8.6 at.% Ge (Figure 5.12). The absence of certain peaks in the pure sample ([200], [210]) suggests a textured film with preferential orientation of the crystallites. For the film with 5.9 at.% Ge, the [200], [210] peaks are present as well. However, the intensity of the [-1 1 1] peak is much larger than that of the others peaks, indicating preferential orientation in the (-1 1 1) direction.
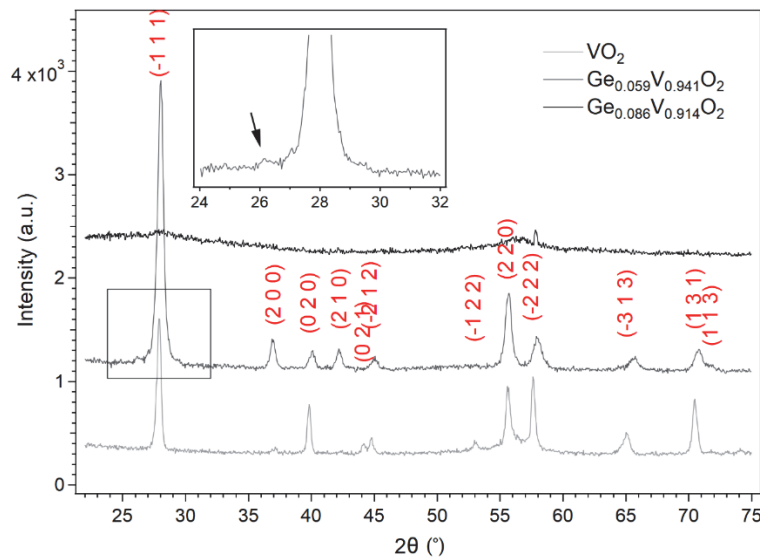


Figure 5.12. XRD spectra of $VO_2$, $V_{0.941}Ge_{0.059}O_{2+y}$ and $V_{0.914}Ge_{0.086}O_{2+y}$ films on Si (100) substrate. All diffraction lines were assigned to the $VO_2$ monoclinic phase according to PDF 04-003-4401.

At 5.9 at.% Ge content, the film shows a small feature at ≈26.2° (see inset Figure 5.12). This has been attributed to the (011) peak of $GeO_2$. Preliminary X-ray photoelectron spectra (XPS) of Ge doped vanadium oxide films with similar Ge concentrations, show broad 3d Ge core level peaks between 31.2 and 32.1 eV binding energies. In this range, contributions from $Ge^{2+}$, $Ge^{3+}$ and $Ge^{4+}$ peak components have been reported [Molle, 2006]. These observations suggest that Ge might be partly oxidized in the reactive environment during the deposition process.

Here too, the diffraction peaks shift towards higher angles, indicating smaller distances between the crystal planes. Moreover, the broadening of the peaks, compared to the pure sample, is attributed to the decrease of average grain size in the polycrystalline film with doping.

The crystallite size can be determined from the peak width (FWHM) through the Scherrer equation. The peak widths are corrected with respect to the reference Si peak (the Si wafer has been measured with the same optics and under the same conditions as the deposited films). The wavelength of the Cu Kα1 radiation is $\lambda = 1.54056$ Å, the shape factor K is 0.9 for isotropic particles. In these conditions, the crystallite size is found to be $\approx 26$ nm in the pure $VO_2$ sample and $\approx 10.6$ nm in the film with 5.9 at.% Ge. The sample with the highest Ge content, 8.6 at.%, appears to have undergone an amorphization of the film as diffraction peaks vanished. This is consistent with the absence of the MIT during the electrical resistivity measurements discussed in the previous section.

Atomic Force Microscopy

The evolution of film morphology and particle size with doping has been observed from contact mode AFM images. In Figure 5.13, the topographic (left) and lateral (right) AFM images of the three samples are shown.

The pure sample shows particles of variable sizes, ranging between 80 and 120 nm. At 5.9 at.% Ge content, the particles are smaller, $\approx 40$-70 nm in size, and show a slightly more uniform size distribution. At 8.6 at.% Ge concentration, the sample exhibits a smooth and uniform surface, characteristic of homogeneous, amorphous films. This general trend is in agreement with the resistivity and XRD measurements. However, the particle sizes observed with AFM considerably differ from the crystallite sizes determined from XRD peak widths. The Scherrer equation gives an approximation of the individual crystallite sizes, while the particles observed in AFM might contain several crystallites.

The decrease of the average grain size with Ge addition is expected as doping leads to disorder in the $VO_2$ crystal lattice. Therefore, Ge might introduce nucleation centers. High density of nucleation centers leads to increased nucleation velocities which, in turn, results in smaller grain sizes.

As reported in [Brassard, 2005], larger density of grain boundaries and associated defects, could lower the resistivity of the semiconducting state, while limiting the conductivity of the metallic state through grain boundary scattering of electrons. Thus, grain refinement results in less abrupt transitions. This trend has been observed from the electrical resistivity plots.
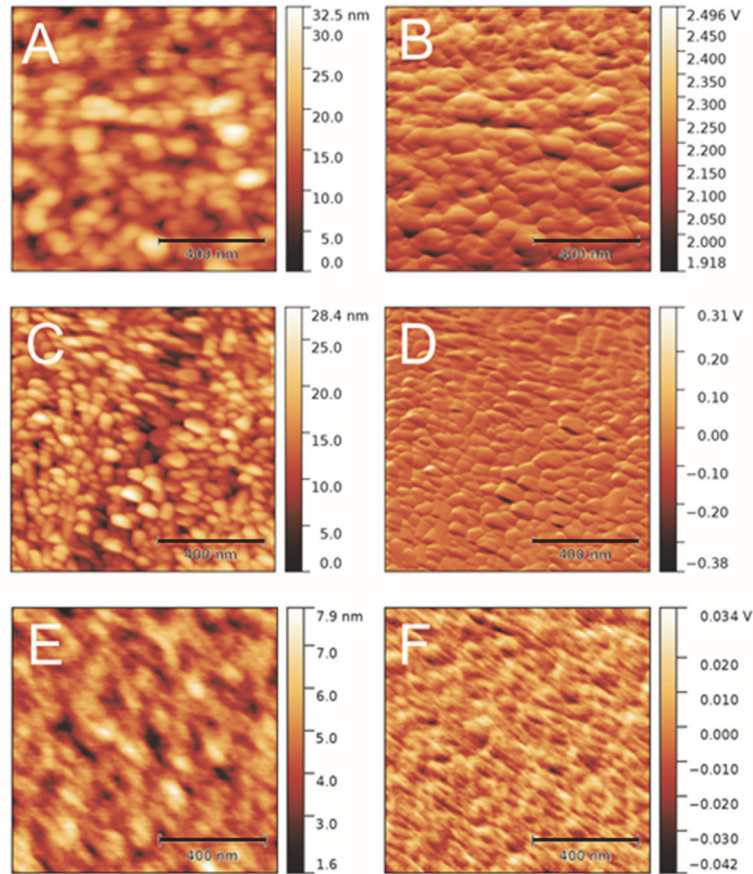
Figure 5.13. Topographic (left) and lateral (right) contact mode AFM images of pure (A,B), $V_{0.941}Ge_{0.059}O_{2+y}$ (C,D) and $V_{0.914}Ge_{0.086}O_{2+y}$ (E,F) films. The scale bar corresponds to 400 nm.

Furthermore, even above the transition temperature, the samples exhibit a semiconducting behavior with the resistivity showing a negative temperature coefficient (indicated by dashed ellipses in Figure 5.11). Small amount of other $VO_x$ phases, which do not undergo MIT, might be present, e.g. at grain boundaries, and influence the overall resistivity of the films above $T_{MIT}$. The more pure is the $VO_2$ film, larger is the transition amplitude. Inversely, when more non-stoichiometric $VO_x$ is present in the film, the resistivity drop is lowered due to the enhanced semiconducting behavior above $T_{MIT}$. It could be speculated then that Ge doping facilitates the formation of non-stoichiometric phases in the film. As already mentioned, an optimization of the oxygen partial pressure during deposition might counter the loss in transition magnitude.

Additionally to the decrease in transition amplitude, the sharpness of the transition is significantly reduced upon doping – larger FWHM. As suggested in [Ruzmetov, 2007], a possible explanation for such smeared out transitions, spreading over temperature ranges as high as ≈30°C may be that crystallites exhibit different MIT temperatures. The transition in the polycrystalline film occurs over the distribution of transition temperatures of the different crystallites. Such variation in the transition temperature of individual crystallites might come from the different levels of doping, if the doping is not homogeneous, or might be strain induced. Lattice disorder, defects and grain boundary density, in the doped films, are expected to be superior to those in pure $VO_2$. $V_{(1-x)}Ge_xO_{2+y}$ lattices are then strained due to the stresses coming from these grain boundaries and other defects.

$VO_2$ bulk single crystals exhibit very narrow hysteresis width of ≈0.5 - 1° C. [Ladd, 1969] High quality epitaxial $VO_2$ films show rather comparable widths of ≈1.5 - 2° C. [Jin, 1997; Hood, 1991] However, polycrystalline

VO$_2$ films might have considerably broader hysteresis loops, ranging from a few degree widths to more than 30°C in some cases [Zhang, 2014; Ruzmetov, 2007]. In polycrystalline films, numerous factors have been reported to affect the hysteresis such as grain size, crystallinity, nucleation defects, orientation of grain boundaries, grain shape etc. In general, the hysteresis widths of our doped polycrystalline VO$_2$ films are smaller than that of the pure film.

In [Lopez, 2002], a nucleation theory is proposed where the phase transition is nucleated on defects. According to this study, an increased number of nucleation seeds can potentially trigger the phase transition and lead to narrower hysteresis loops.

Ge might enhance the heterogeneous nucleation of VO$_2$ particles similarly to Ti in VO$_2$ [Du, 2011]. The larger density of grain boundaries and lattice disorder could be accountable for a higher effective defect concentration in doped samples. The increase in defect-induced nucleation site density in doped samples, might lead to a lowering of the free energy decrease for the MIT and a smaller $\Delta T$ – narrower hysteresis – can trigger the transition. Indeed, a narrowing of the hysteresis width in doped thermochromic samples is observed experimentally [Paone, 2015].

The role of lattice distortion and charge doping effects on the phase transition in doped vanadium dioxide systems is unclear. In [Wu, 2015] and references therein, an overview of the proposed mechanisms for the widely studied W$^{6+}$ doping is presented. Several studies attribute the reduction of T$_{MIT}$ to the increase of electron density, some claim that the effect of W$^{6+}$ on neighboring cells is only structural, while others have shown that both electronic contribution and local structure perturbations are responsible for the reduced T$_{MIT}$. The authors of the cited study [Wu, 2015] agree with the latter and conclude their comparative analysis on Ti and W doped VO$_2$ suggesting that charge doping is the more effective in regulating the transition temperature in VO$_2$, although the local structure perturbations induced by dopants have an inevitable influence on it. [MacChesney, 1969] also points out that, regardless of the origin of the transition, changes in the band structure are sensitive to changes in the lattice and speculate that the changes induced by dopants are the result of the interplay of size and charge. Small cations e.g. Al$^{3+}$, Ga$^{3+}$, Ge$^{4+}$ with empty d orbitals are more stable in lower anion coordination and seem to stabilize the low temperature phase. Additionally, when charge compensation is accomplished through the creation of V$^{5+}$ ions – smaller than V$^{4+}$, with empty d orbitals and unstable in an oxygen octahedron – a lower anion coordination is favored again [Goodenough, 1971].

The significant change in transition temperature reached through Ge doping – as in the case of W doping – is presumably the result of both lattice distortion and electronic effects.

Outcomes

- Pure VO$_2$ and V$_{(1-x)}$Ge$_x$O$_{2+y}$ films have been deposited.

- A direct correlation between the MIT characteristics, most notably the transition temperature and doping concentration has been established.

- A T$_{MIT}$ of ≈96°C has been reached with 5.9 at.% Ge. To the best of our knowledge, this is the highest transition temperature reported for doped VO$_2$ based thin films.

# 5.3 UPS and XPS study of Ge doped VO$_2$ films

*This section borrows part of its text and images from: Krammer A., Gremaud A., Bouvard O., Sanjines R., Schüler A. In situ photoelectron spectroscopic characterization of reactively sputtered, doped vanadium oxide thin films. Surface and Interface Analysis 48(7), 440-444, 2016.*

The electronic band structure of pure and Ge doped VO$_x$ and VO$_2$ samples are studied by in-situ UPS and XPS. Due to a different substrate holder used for the transfer to the photoelectron spectrometer, the reached sample surface temperature is lower than that for the standard holder and results in a first, non-switching sample series. In a second run, the nominal temperature is adjusted to 640°C in order to obtain switching thermochromic samples. The temperature calibration curve for the UPS/XPS-compatible holder has not been determined, therefore, in this section the nominal temperatures are given instead of the substrate temperatures.

## 5.3.1 VO$_x$ and VO$_x$:Ge deposited at 490°C

Film growth

Vanadium oxide based thin films, with different Ge content, are deposited on <100> Si substrates by reactive magnetron co-sputtering in high-vacuum conditions. The deposition parameters are listed in Table 5.8.

Table 5.8. Process parameters used for the deposition of VO$_x$ and VO$_x$:Ge films for UPS and XPS measurements.

| | |
|---|---|
| Base pressure [mbar] | < 5·10$^{-8}$ |
| Working pressure [mbar] | 2.6±0.1·10$^{-3}$ |
| O$_2$ partial pressure [mbar] | 1.9±0.1·10$^{-4}$ |
| Nominal temperature [°C] | 490 |
| Film thickness [nm] | ≈300 |
| Applied power [W] | V: 150 (DC) Ge: 0 - 50 (RF) |

UV photoelectron spectroscopy

The UPS He I spectra of the pure VO$_x$ film exhibits a Fermi edge and features at 0.72 eV, 4.3 eV and 7 eV binding energy. At room temperature, VO$_2$ is semiconducting, however, a Fermi edge could be expected for slightly oxygen-deficient, conducting VO$_{2-x}$ films. For the VO$_X$:Ge sample with 10 W Ge the Fermi edge disappears and the valence band edge is at 0.41 eV binding energy. The valence band shows more features than the other two samples, with structures at 1.3 eV, 3.6 eV, 5.4 eV and again 7 eV. The strongly doped film has its valence band edge at 0.6 eV and features around 1.5 eV, 4.25 eV and 7 eV binding energies (Figure 5.14.a).

According to [Romanyuk, 2007] the band at 4.3 eV binding energy could be assigned to non-bonding oxygen band, O 2pπ, while the one centered at 7 eV binding energy is associated to bonding O 2pσ orbitals with vanadium d band. An additional feature around 5.4 eV binding energy is present for the slightly doped sample. Romanyuk et al. also observed a third feature for V$_2$O$_{5-x}$ films with a relatively high V$^{5+}$ content, obtained during a two-step oxidation process from V$^0$ to V$^{4+}$ and V$^{4+}$ to V$^{5+}$. After the first oxidation step,

where vanadium 4+ states are dominant, the He I spectrum shape and feature position match those of the pure $VO_x$ sample from our study.
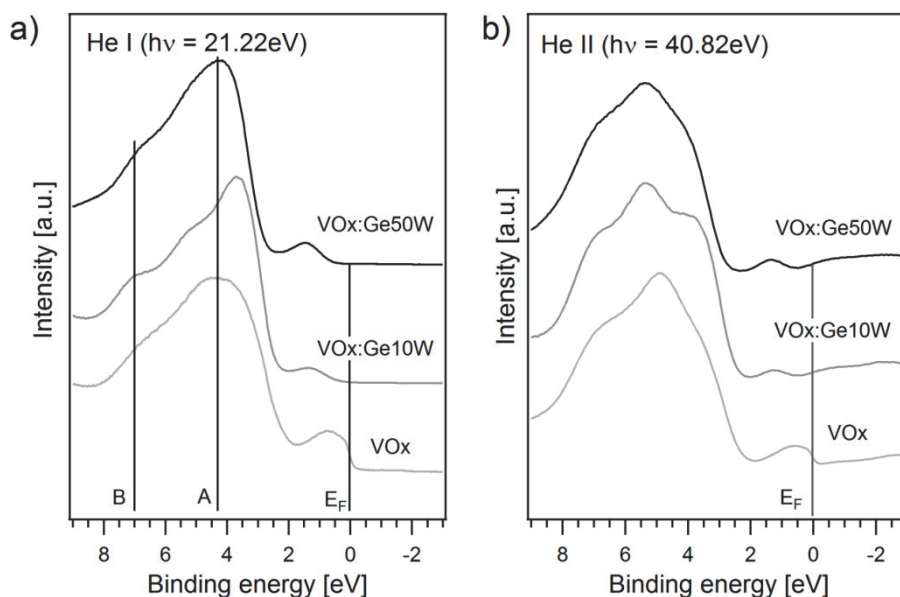


Figure 5.14. He I and He II valence band spectra of $VO_x$ and $VO_x$:Ge films. The intersecting straight lines mark the position of the Fermi edge as well as that of nonbonding (A) and bonding (B) oxygen 2p orbitals with vanadium d band [Romanyuk,2007]

The He II spectra show some similar features with the UPS He I (Figure 5.14.b). A Fermi edge is present for the $VO_x$ film and it disappears for both, slightly and strongly, doped ones. There are features present at 0.55 eV, 3.3 eV, 4.9 eV and 7 eV for the $VO_x$ film, at 1.25 eV, 3.8 eV, 5.35 eV and 7 eV for $VO_x$:Ge10W film and at 1.35 eV, 3.9 eV, 5.4 eV and 6.9 eV binding energies for the $VO_x$:Ge50W film.

Again, an additional feature appears for the slightly doped film at 3.8 eV binding energy. This is in accordance with the He II spectra of $V_2O_5$ which also exhibits three bands centered around 3.8 eV, 5.4 eV and 7 eV [Shin, 1990]. Shin et al. also published He II spectra for $VO_2$ and it is matched by the valence band spectrum of the pure $VO_x$ film. The He II spectrum of the strongly doped film also shows features associated with $V_2O_5$, such as the shoulder around 3.9 eV binding energy. It is less pronounced than in the case of the slightly doped film, however it still suggests the presence of vanadium atoms in both 4+ and 5+ oxidation states.

Therefore, the results point toward a chemical environment with predominantly four-fold oxidized V atoms in the $VO_x$ film and the dominant presence of $V^{5+}$ in the doped samples. In particular, the slightly doped vanadium oxide film with the more and better defined features seems to be more oxidized than the other two films.

The decrease in the density of states at the Fermi level and the shift in the states close to the valence band edge, associated predominantly with V 3d states, lead to the opening of a band gap and indicate that Ge doping, much like Si doping previously, increases the insulating character of the films.

X-ray photoelectron spectroscopy

The XPS survey spectrum of the pure $VO_x$ film shows only V and O Auger ($V_{LMM}$, $V_{LMV}$, $O_{KLL}$) and photoemission (O 1s, O 2s, V 2s, V 2p, V 3s, V 3p) peaks (Figure 5.15). For the weakly doped sample, the peaks associ-

ated with Ge (Ge 3p, Ge 3d) are hardly distinguishable, but are well-defined in the strongly doped sample. No C contamination of the samples is recorded.
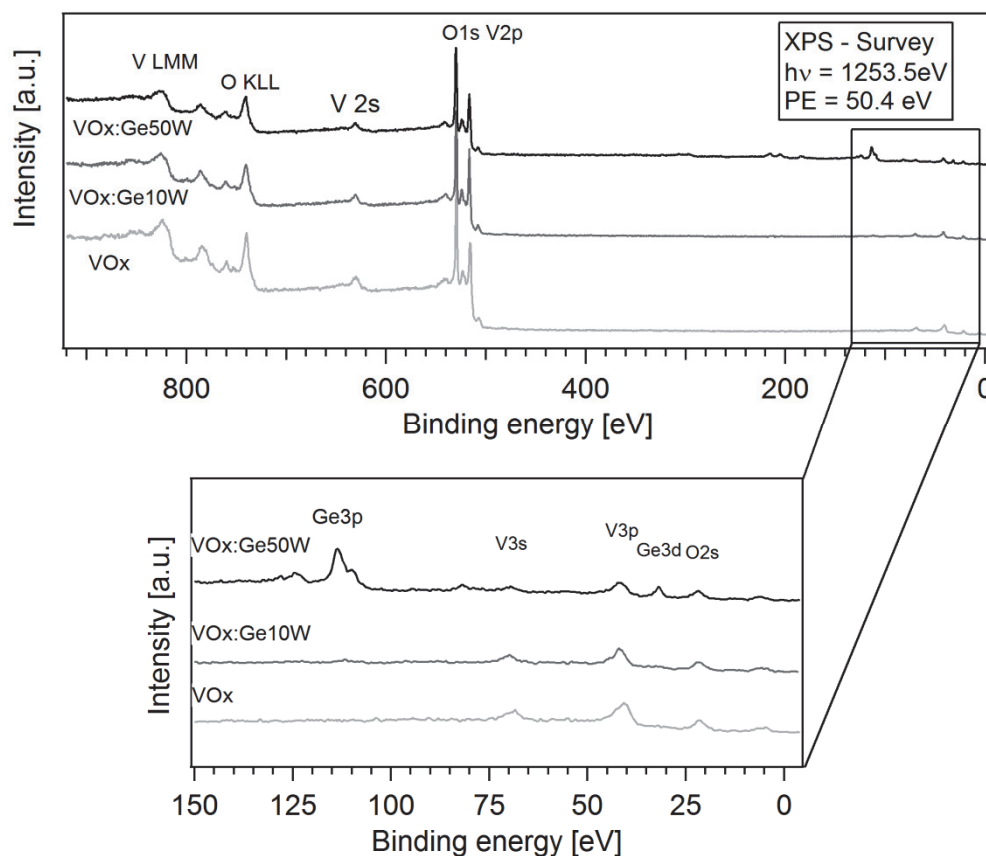


Figure 5.15. XPS survey spectra of $VO_x$ and $VO_x$:Ge films. Only peaks associated to V, O and Ge atoms are present. For all samples, C signal was below the detection limit.

The line shapes of the core-level spectra of O 1s, V 3p and Ge 3d peaks are shown in Figure 5.16. For all core-level spectra, background substraction and satellite correction is performed.

The O1s peak is at binding energy 529.46 eV for the pure oxide, 529.83 eV for the slightly doped film and 530.07 eV for the strongly doped one. For the pure $VO_x$ film, the O 1s peak is slightly asymmetric, while for the doped samples it becomes symmetrical. An asymmetry towards higher binding energies can be an indication of core-hole screening by conduction electrons with binding energy close to the Fermi level. An asymmetric peak suggests a manifold of states around the Fermi level. This idea is supported by the UPS He I and He II valence band spectra shown in Figure 5.14, where a Fermi edge is present for the pure $VO_x$ film.

Meanwhile, the quantification shows that the $VO_x$ film is slightly under-stoichiometric with regards to the composition of $VO_2$. Hence, the asymmetric peak could also be attributed to the oxygen deficient $VO_x$ and the presence of different vanadium oxidation states alike.

The V 3p peak is positioned at binding energy 40.1 eV for the $VO_x$ film, 41.8 eV for the $VO_x$:Ge10W film and 41.9 eV for the $VO_x$:Ge50W film. The V 3p peaks of the doped samples exhibit a shoulder around 40 eV binding energy, corresponding to the V 3p peak position of the pure, metallic sample. This suggests the presence of a multiphase material in the doped films.

For the lightly doped sample, a rather small and smeared out Ge 3d core-line shape is observable at around 31.1 eV binding energy, while for the strongly doped film a well-defined, symmetric peak is observed at 31.9 eV. According to [Zatsepin, 2015; Prabhakaran, 1993], a binding energy of 31.8 eV is attributed to GeO (II) type species. Therefore, the oxidation state of the Ge atoms in the $VO_x$:Ge50W film is thought to be predominantly 2+.The small and broad core-line structure in the weakly doped sample might indicate the presence of Ge atoms in multiple oxidation states. It could be possible then, that in the lightly doped film with a Ge content of only 0.3 at%, the Ge atoms enter the structure as dopant and adopt different oxidation states in different local chemical environments. However, in the strongly doped sample with a Ge content of 4.4 at%, the structure might not accommodate for all the Ge and it could segregate as GeO.
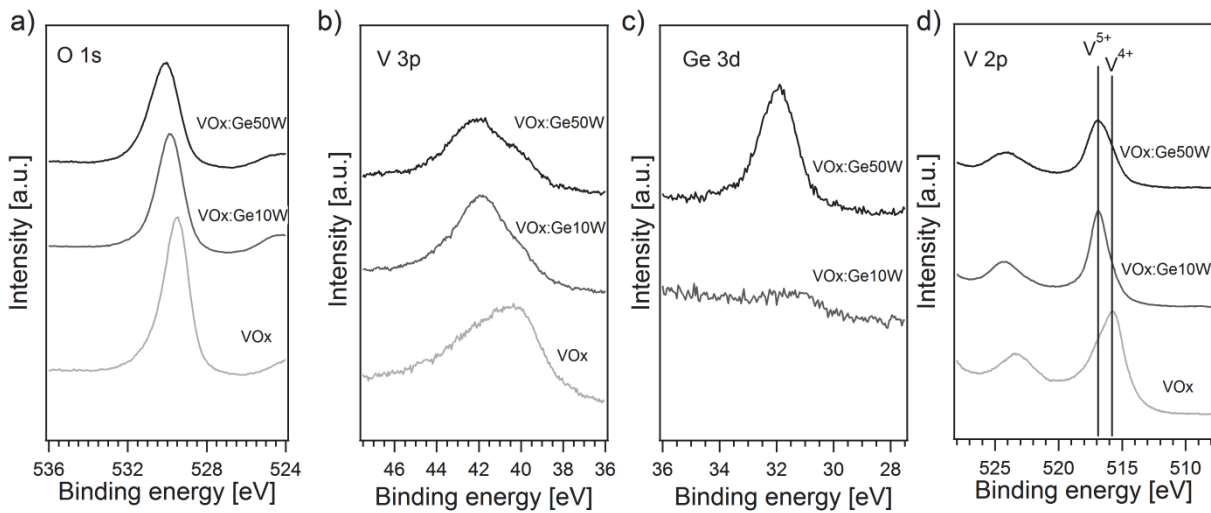


Figure 5.16. From left to right: O 1s, V 3p, Ge 3d and V 2p core-level spectra of $VO_x$ and $VO_x$:Ge films (Mg Kα excitation, hv = 1253.5eV, PE =29.925eV). The intersecting straight lines in the V 2p spectrum mark the position of $V^{4+}$ and $V^{5+}$ oxidation states

The film composition is evaluated from the O 1s, V 3p and Ge 3d core-level peak integration using Scofield sensitivity factors in combination with calibration obtained with a pure $VO_2$ sample.

Table 5.9. XPS elemental quantification of pure and Ge doped $VO_x$ films.

| Sample | V [at.%] | O [at.%] | Ge [at.%] |
|---|---|---|---|
| $VO_x$ | 34.1 | 65.9 | - |
| $VO_x$:Ge (10 W) | 31.8 | 67.9 | 0.3 |
| $VO_x$:Ge (50 W) | 25.5 | 70.1 | 4.4 |

In the V 2p core-level spectra, the solid black lines mark the reference position of V 2p$_{3/2}$ peak at 515.8 eV for $V^{4+}$ and at 516.9 eV binding energy for the $V^{5+}$ oxidation states [Romanyuk, 2007]. The V 2p$_{3/2}$ peak of the pure $VO_x$ film coincides with the position of $V^{4+}$, suggesting that V in 4+ oxidation states are dominant. However, the peak is rather broad, and contributions from $V^{5+}$ or other oxidation states might be also present. In the Ge doped films $V^{5+}$ states are dominant and the contribution of $V^{4+}$ states is less pronounced. Albeit vanadium atoms in a 4+ oxidation state would suggest the presence of a $VO_2$ film, such a film, if crystalline, should be semiconducting at room temperature and instead it exhibits a Fermi edge. One explanation for weak or lack of thermochromic behavior might be the formation of amorphous vanadium dioxide due to insufficient heating. Moreover, due to the slightly substoichiometric nature of the $VO_x$ film and de-

fects that may result in shifts to higher and lower oxidation states, a distribution of $V^{3+}$, $V^{4+}$ and $V^{5+}$ could be suspected, with the average composition suggesting a $V^{4+}$ oxidation state.

The relative positions of the O 1s, V 3p, Ge 3d and V 2p peaks for the three samples illustrate the difficulty of identifying the compounds based only on peak position. Additionally, the separation between tetravalent and pentavalent vanadium oxides is ≈1.1 eV, which makes unambiguous determination of mixed oxidation states difficult by peak position alone, especially when the compared samples exhibit different electronic behavior (metallic/insulating).

Consequently, the Wagner plot of the $L_3M_{23}V$ Auger transition and V $2p_{3/2}$ photoemission for the deposited $VO_x$, $VO_x$:Ge10W, $VO_x$:Ge50W and reference V, $VO_2$ and $V_2O_5$ compounds, is shown in Figure 5.17. The diagonal lines indicate the values of the Auger parameter, which is the sum of the Auger kinetic energy and the binding energy. The Auger parameter is particularly valuable because it is independent of charging and calibration concerns, hence small shifts could indicate a change in chemistry and be useful in determining oxidation states.

However, due to the consistency of the Auger parameter in vanadium compounds across various oxidation states, little is gained in the identification of the unknown $VO_x$ films. The precision in photoemission peak position is very high because the peak is sharp with high peak intensity, but the Auger peak is broad, allowing for less precise peak identification and larger error bars in the vertical direction, finally leading to difficulties in inferring much additional information from the Wagner plot.
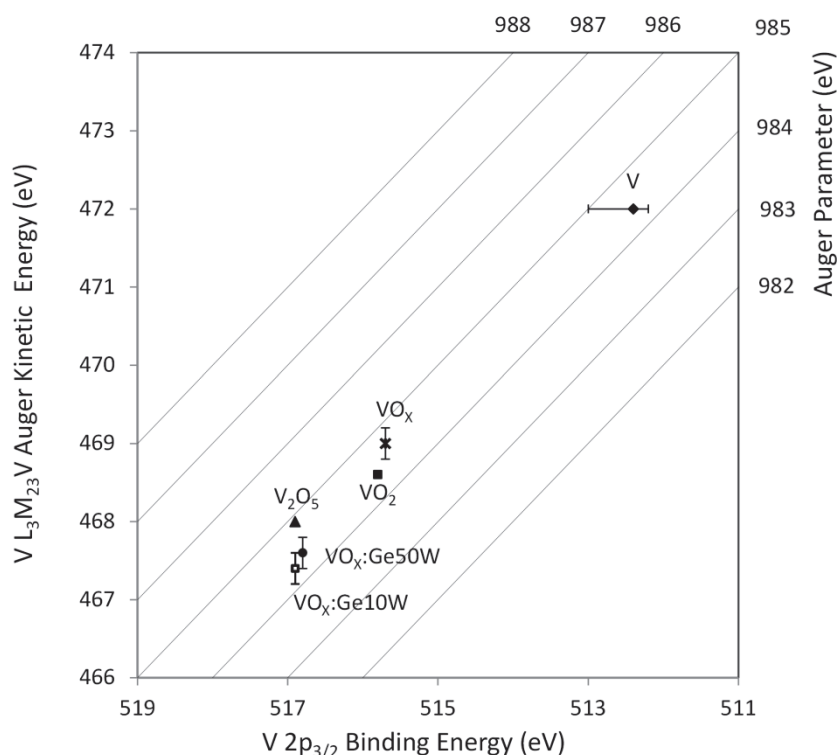


Figure 5.17. Wagner plot of the V $2p_{3/2}$ photoemission binding energy and V $L_3M_{23}V$ Auger electron kinetic energy for selected V compounds. Values for the V, $V_2O_5$ and $VO_2$ reference compounds have been retrieved from the NIST Standard Reference Database and Romanyuk et al. The plotted V reference value is the median value of the binding energies available in the database (the corresponding horizontal line indicates the range of available data). For the measured samples, vertical error bars show the uncertainty in Auger peak identification.

Outcomes

- The asymmetric O 1s core-level peak of the $VO_x$ sample can be correlated with the presence of a Fermi edge in the He I and He II valence band spectra.

- The elemental quantification yields a slight oxygen substoichiometry in the $VO_x$ film and over-stoichiometry in the $VO_x$:Ge films.

- The evolution of valence band spectra, from pure $VO_x$ exhibiting a Fermi edge to doped $VO_x$:Ge without a Fermi edge, indicates that Ge doping increases the insulating character of the films.

- In the pure film $V^{4+}$ states, while in the doped samples $V^{5+}$ states are predominant.

- Finally, insufficient film crystallinity or oxygen stoichiometry might be accountable for the non-switching behavior of the studied films.

## 5.3.2  $VO_2$ and $VO_2$:Ge deposited at 640°C

The nominal deposition temperature is increased progressively until sufficient film crystallization is achieved. Switching, crystalline films are deposited at 640°C. After the high-temperature deposition, samples are immediately transferred to the photoelectron spectrometer. During cooling, UPS spectra are taken at two-minute intervals. In this manner the transition from high temperature, metallic phase into the low temperature, semiconducting phase is observed in-situ (Figure 5.18).
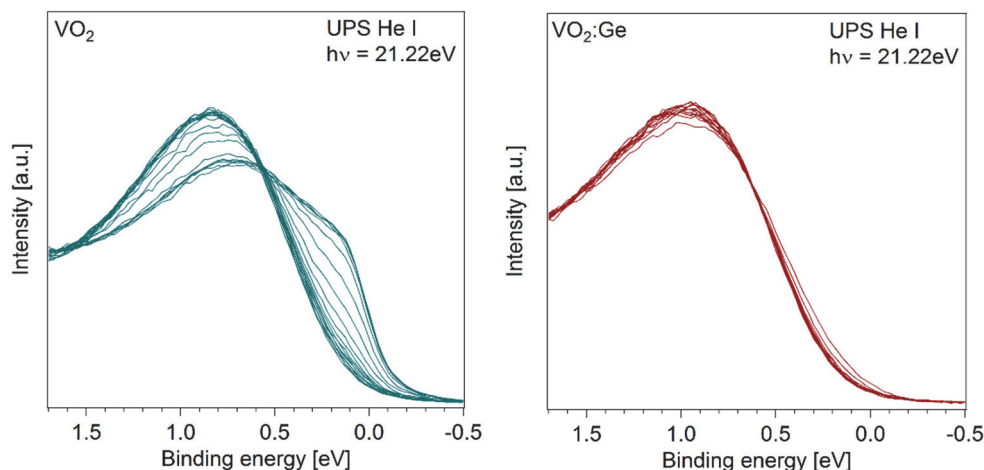


Figure 5.18. He I UPS spectra of pure and Ge doped switching $VO_2$ films showing the change in the density of states near the Fermi level during cooling.

In the $VO_2$ film, the Fermi edge – present in the hot state – vanishes during cooling. The density of states near the Fermi level shift and a band gap opens up, marking the metal-to-insulator transition. The $VO_2$:Ge film, even in the high temperature state exhibits no Fermi edge. Nonetheless, here too the density of states near the Fermi level shift toward higher binding energies during the cooling suggesting that the insulating character of the film is strengthened.

 The UPS spectra of the two samples can be correlated with the results of the electrical resistivity measurements (Figure 5.19). The $VO_2$ sample, which shows a clear Fermi edge in the hot state and a gap opening

near the Fermi level in the cold state, exhibits a sudden drop in resistivity of more than two orders of magnitude with very low resistivity values in the hot, metallic state. Meanwhile, the doped sample which exhibits only slight changes in the density of states at the valence band edge and lacks a Fermi edge even in the hot state, displays a rather smeared out transition of smaller magnitude than the pure sample. Moreover, the resistivity values in the hot state are considerably higher than in the case of pure $VO_2$. This could explain the absence of a true metallic character of the film.
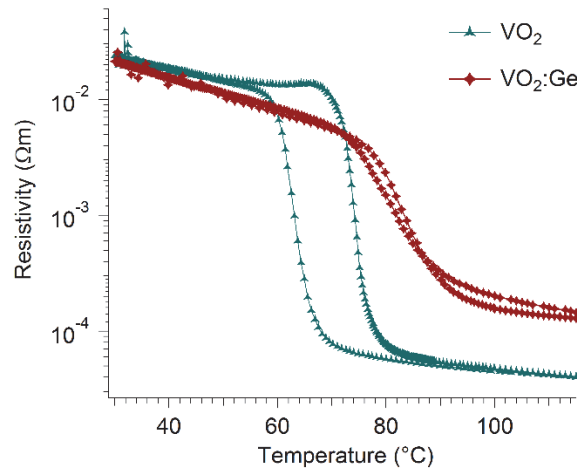


Figure 5.19. Temperature dependent electrical resistivity curves of the two samples studied by UPS.

Other than the already discussed differences concerning the Fermi edge, the He I and He II valence band spectra of the two films are very much alike, exhibiting the same type of band structure and features at the same positions (Figure 5.20). As before, the features marked with A and B in the He I spectra are attributed to non-bonding and bonding oxygen 2p orbitals with the vanadium d band. The He I spectra are measured at temperatures above the critical transition temperature, while the He II spectra are measured after the samples are cooled down, therefore, for the latter no Fermi edge is expected for either of the films.
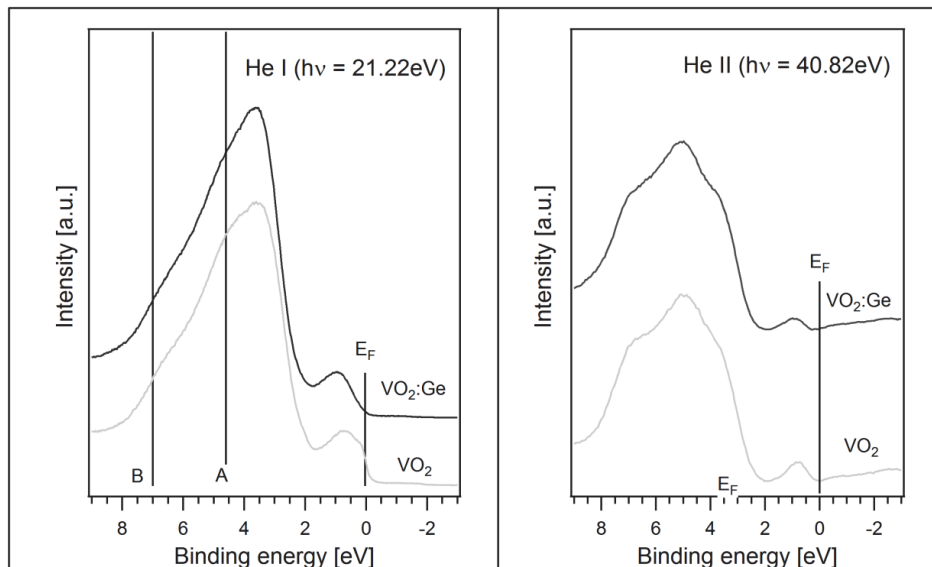


Figure 5.20. He I and He II valence band spectra of $VO_2$ and $VO_2$:Ge films. The intersecting straight lines mark the position of the Fermi edge as well as that of nonbonding (A) and bonding (B) oxygen 2p orbitals with vanadium d band.

The survey scans show only V and O peaks for the pure sample and additional Ge peaks for the doped sample (Figure 5.21). On the pristine sample surface no C contamination is detected.
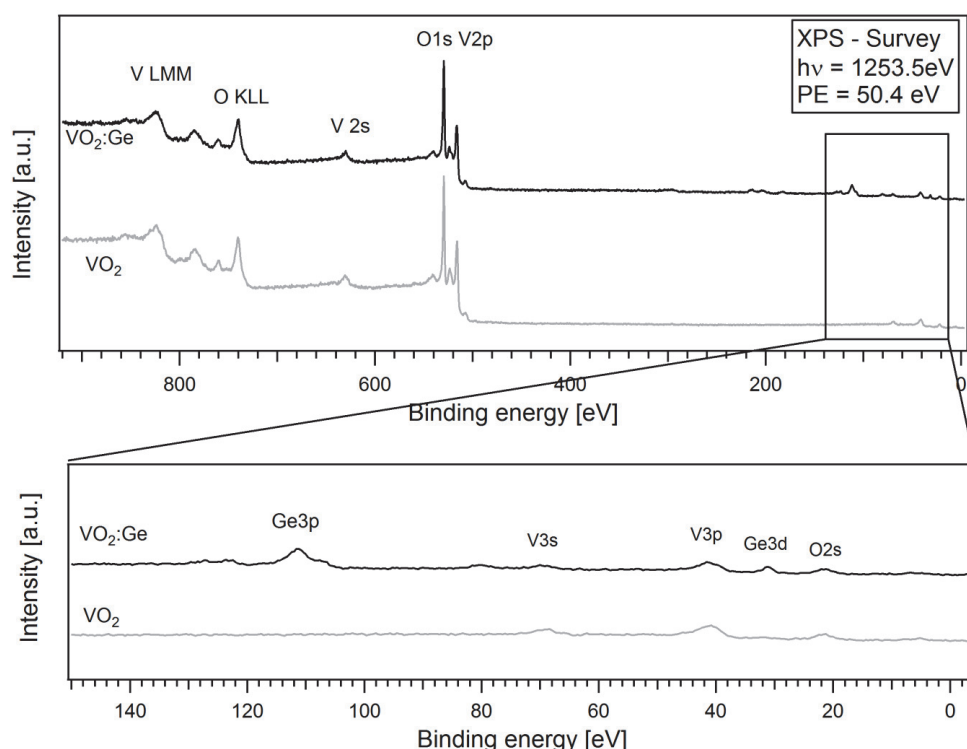


Figure 5.21. XPS survey spectra of $VO_2$ and $VO_2$:Ge films. Only peaks associated to V, O and Ge atoms are present. C was below the detection limit.

From the O 1s, V 3p and Ge 3d core peak integration (Figure 5.22), the chemical composition of the films is determined (Table 5.10). The pure $VO_2$ film is not stoichiometric. Although the transfer is done as soon as possible from the deposition chamber ($\approx 10^{-6}$ mbar) to the analysis chamber ($\approx 10^{-9}$ mbar), at $10^{-6}$ mbar only 1s is enough to form a monolayer of reactive impurity gas. Therefore, the surface might be slightly oxidized leading to a higher oxygen concentration than expected for stoichiometric, switching $VO_2$.

Table 5.10. XPS elemental quantification of pure and Ge doped $VO_2$ films.

| Sample | V [at.%] | O [at.%] | Ge [at.%] |
|--------|----------|----------|-----------|
| $VO_2$ | 31.1 | 68.9 | - |
| $VO_2$:Ge | 25.7 | 69.7 | 4.6 |

The samples are already in the low temperature, semiconducting state when measured by XPS. Therefore, the O 1s peak is symmetric for both films. The V 3p peaks are rather broad, with a shoulder around 42 eV which becomes more pronounced in the $VO_2$:Ge film suggesting a multicomponent structure. The Ge 3d peak of the doped sample is well-defined and symmetric.
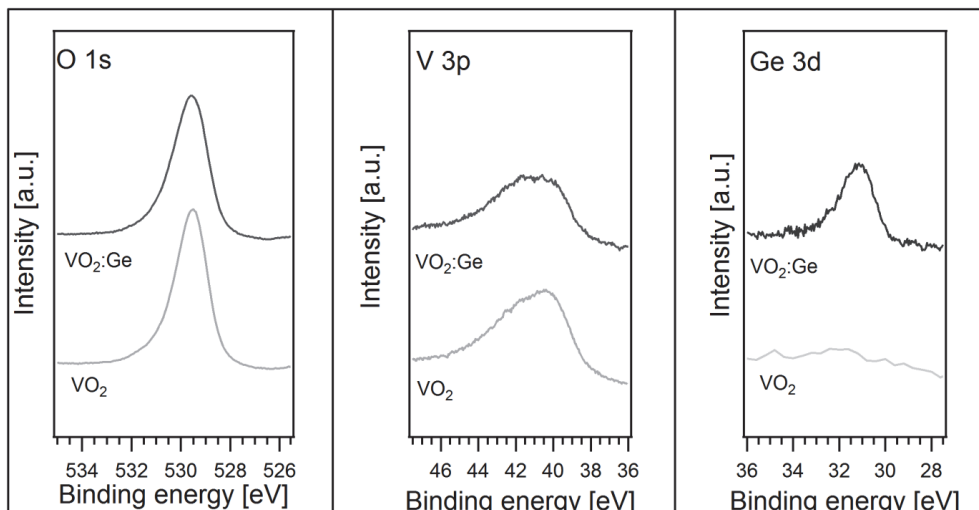
Figure 5.22. O 1s, V 3p and Ge 3d core level spectra of $VO_2$ and $VO_2$:Ge films (Mg Kα excitation, hν = 1253.5eV, PE =29.925eV).

Finally, the V 2p core level spectra are studied (Figure 5.23). Like for the V 3p, here too a shoulder is present in the pure $VO_2$ film and becomes larger in the Ge doped one suggesting the presence of a doublet. Considering the same reference as before [Romanyuk, 2007], it is assumed that in the Ge doped film the $V^{5+}$ states prevail on the expense of the $V^{4+}$ states which dominate in the pure film. Despite the oxygen partial pressure being lower during the deposition of the doped sample, the film seems to be more oxidized. Once again, this suggests that Ge doping enhances the semiconducting character of the thermochromic films.
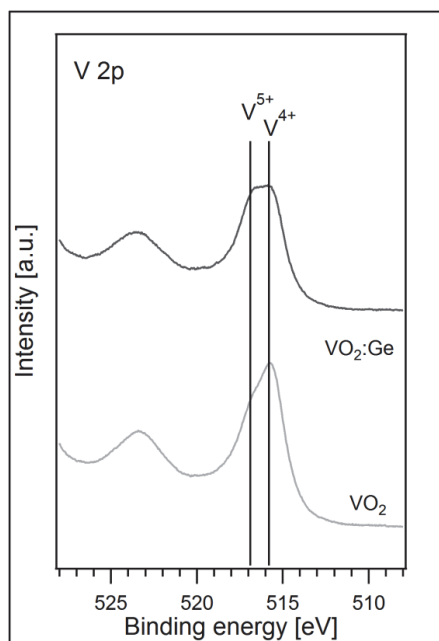


Figure 5.23. V 2p core-level spectra of the $VO_2$ and $VO_2$:Ge films (Mg Kα excitation, hν = 1253.5eV, PE =29.925eV). The intersecting straight lines mark the position of $V^{4+}$ and $V^{5+}$ oxidation states.

# 5.4    Effect of Ge doping on the thermal emittance

*This section borrows part of its text and images from: Krammer A., Demière F.T., Schüler A. Infrared optical properties of doped and pure thermochromic coatings for solar thermal absorbers. Proceedings of Solar World Congress 2017, 1-7, 2017. https://doi.org/10.18086/swc.2017.17.04*

The successful increase of the transition temperature of pure $VO_2$ thin films, from 68°C to ≈96°C, by Ge doping is significant and compares favourably with the − so far - only commercially available thermochromic solar absorber that is based on Al doped (4 − 12 at.%) $VO_2$ films with a $T_C$ of around 70 − 75°C. However, for efficient absorber coatings, the infrared spectral behavior of the thermochromic films is of chief importance. In this section, the spectral emittance of pure and Ge doped $VO_2$ films are measured and compared. The angular dependence of the thermal emittance is also discussed.

Film growth

Pure and Ge doped $VO_2$ films are deposited on 0.5 mm thick, 50 mm x 50 mm sized Al sheets (Goodfellow) for the Fourier transform infrared (FTIR) spectrometry and thermal imaging, and on Si wafer for the angular dependence determination. The used process parameters are summarized in Table 5.11.

Table 5.11. Process parameters of deposited $VO_2$ and $VO_2$:Ge for the study of thermal emittance.

| Base pressure [mbar] | < 5·10^{-8} |
|---|---|
| Working pressure [mbar] | 7.1±0.1·10^{-3} |
| $O_2$ partial pressure [mbar] | 5.3±0.2·10^{-4} |
| Substrate temperature [°C] | 465 |
| Film thickness [nm] | ≈210 - 215 |
| Applied power [W] | V: 150 (DC) |
| | Ge: 0, 8 , 12 (RF) |

Spectral emittance of $VO_2$

The total reflectance spectra of a $VO_2$ coated aluminium sheet is determined by FTIR spectrometry in the mid-infrared spectral range (2 - 15μm). The measurement is done both below and above the transition temperature, $T_C$ of vanadium dioxide. For opaque samples, the spectral emittance can be determined directly from the measured reflectance spectra.

The spectral emittance of the thermochromic film differs considerably between the room and high temperature states (Figure 5.24). Above 100°C collector temperature, the operating temperature should be limited to avoid thermal stresses on the system. As the spectral emittance of a blackbody at 100°C peaks at around 8 μm wavelength, the emittance modulation in this spectral region is of special interest. At 8 μm, the emittance changes markedly from 0.07 below $T_C$ to 0.32 above $T_C$.
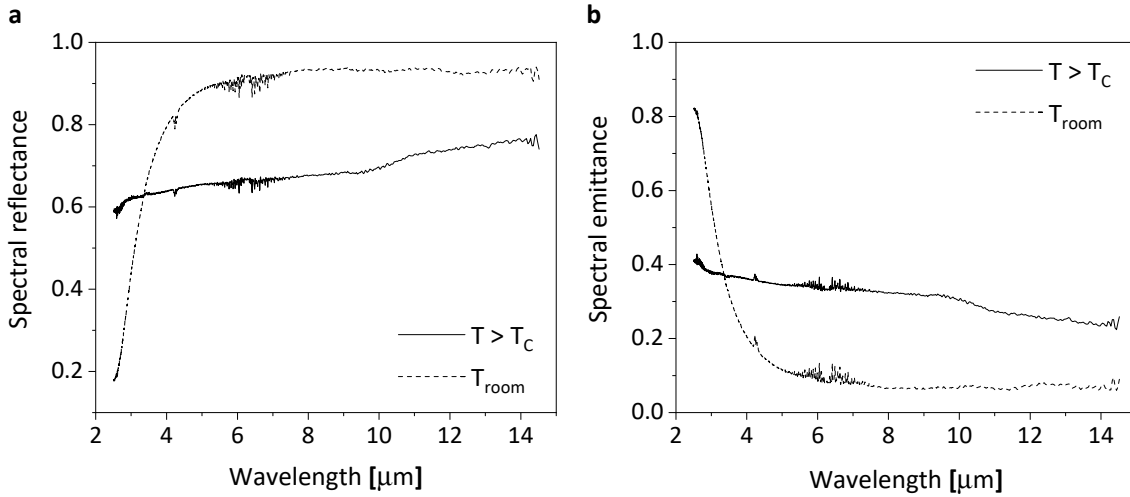
Figure 5.24. Spectral reflectance (a) and corresponding spectral emittance (b) of an Al substrate coated with ≈210 nm VO$_2$ film, measured both below and above the thermochromic transition temperature, T$_C$.

Angular dependence of the thermal emittance

The angular dependence of the emittance of a thermochromic VO$_2$ film deposited on Si wafer, above its critical transition temperature, is determined (Figure 5.25.a). Since the coating is supposed to show metallic properties, the emittance versus angle for a rough oxidized aluminum plate is measured for comparison. The measurements are performed at 100°C for the VO$_2$ and aluminium samples.

The metallic VO$_2$ film follows the same trend of directional emissivity as the Al plate, whose values are similar to those given in tables. They are roughly constant from normal angles to about 60 degrees from the normal. At angles higher than 60 degrees the thermal emittance rises and reaches a maximum at grazing angles. The thermal emittance is expected to drop to 0 when parallel to the surface, but this measurement could not be made precisely with the experimental setup. This behavior of the spectral directional emissivity of an opaque, isotropic medium is well described by the Fresnel equations [Teodorescu, 2007]:

$$\varepsilon_\lambda' = 1 - \frac{1}{2}\left(\frac{(n_\lambda\beta - \cos\theta)^2 + (n_\lambda^2 + k_\lambda^2)\alpha - n_\lambda^2\beta^2}{(n_\lambda\beta + \cos\theta)^2 + (n_\lambda^2 + k_\lambda^2)\alpha - n_\lambda^2\beta^2}\right.$$
$$\left. + \frac{(n_\lambda\gamma - \alpha/\cos\theta)^2 + (n_\lambda^2 + k_\lambda^2)\alpha - n_\lambda^2\gamma^2}{(n_\lambda\gamma + \alpha/\cos\theta)^2 + (n_\lambda^2 + k_\lambda^2)\alpha - n_\lambda^2\gamma^2}\right)$$

Equation 5.2

with:

$$\alpha^2 = \left(1 + \frac{\sin^2\theta}{n_\lambda^2 + k_\lambda^2}\right)^2 - \frac{4n_\lambda^2}{n_\lambda^2 + k_\lambda^2}\left(\frac{\sin^2\theta}{n_\lambda^2 + k_\lambda^2}\right),$$

Equation 5.3

$$\beta^2 = \frac{n_\lambda^2 + k_\lambda^2}{2n_\lambda^2}\left(\frac{n_\lambda^2 - k_\lambda^2}{n_\lambda^2 + k_\lambda^2} - \frac{\sin^2\theta}{n_\lambda^2 + k_\lambda^2} + \alpha\right),$$

Equation 5.4

$$\gamma = \frac{n_\lambda^2 - k_\lambda^2}{n_\lambda^2 + k_\lambda^2}\beta + \frac{2n_\lambda k_\lambda}{n_\lambda^2 + k_\lambda^2}\left(\frac{n_\lambda^2 + k_\lambda^2}{n_\lambda^2}\alpha - \beta^2\right)^{1/2}.$$

Equation 5.5

where $\varepsilon'_\lambda$ is the spectral emissivity at a wavelength λ, θ is the polar angle and $n_\lambda$ and $k_\lambda$ are the optical constants.

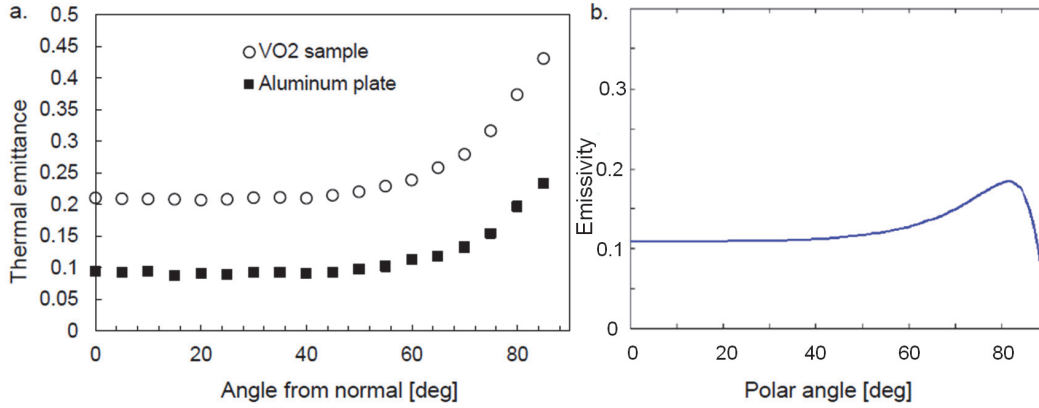Typical result for a metal with n = 1.5 and k = 7 is illustrated in Figure 5.25.b.



Figure 5.25. a) Angular dependence of the thermal emittance of $VO_2$ and Al plate. b) Typical directional emissivity of a metal according to Fresnel's relation with n=1.5 and k=7 [Teodorescu, 2007].

The emittance being higher at greater angles is beneficial as most thermal emittance measurements are done at normal angles. Therefore, the thermochromic coating will be more efficient at dissipating heat via radiation than what normal measurements would predict.

Spectral emittance of Ge doped $VO_2$

The spectral emittance of two Ge doped thermochromic coatings, deposited on Al, is measured (Figure 5.26). Like previously, the Ge content in the doped samples has been varied by applying 8 and 12 W power on the Ge target during deposition. This is calculated to correspond to 1.1 and 2.6 at.% Ge in the samples.

At room temperature, the pure and doped films show similar spectral behavior, however, at 100°C the emittance of the Ge doped sample is superior to that of the pure film. At 8 μm, the emittance of the $VO_2$:Ge sample, with 12W applied on the Ge target, changes from 0.06 to 0.41. That is roughly a 10% increase in spectral emittance modulation at 8 μm compared to the pure $VO_2$ film. If weighed over the mid-infrared spectral range (2.5 – 14 μm), the total thermal emittance of the two films is determined to be identical at room temperature, $\varepsilon_{VO2} = \varepsilon_{VO2:Ge} = 0.08$ and $\Delta\varepsilon_{VO2} = 0.23$ (0.08 at room temperature and 0.31 at 100°C) for the $VO_2$ film and $\Delta\varepsilon_{VO2:Ge} = 0.3$ (0.08 at room temperature and 0.38 at 100°C) for the $VO_2$:Ge film.
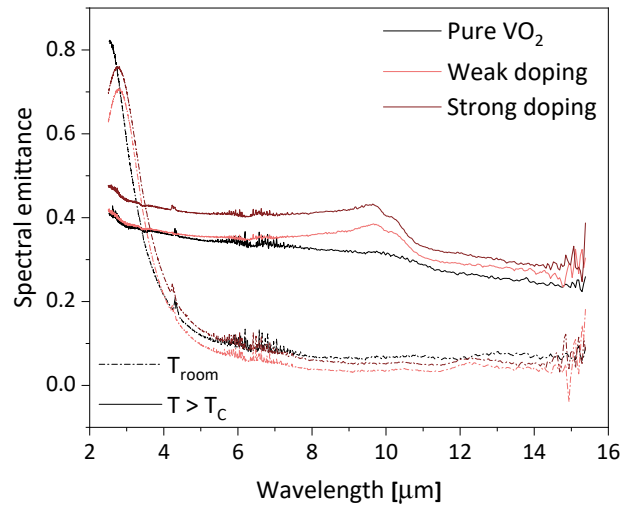
Figure 5.26. Spectral emittance change between the low (dashed line) and high temperature state (solid line) of three samples with different com-position: pure $VO_2$, weakly doped and strongly doped coatings.

This emittance change is intuitively depicted by infrared thermography (Figure 5.27). At room temperature the films are transparent to IR radiation and only the reflecting substrate is visible in the thermal image. When heated, the films switch into their high emittance state and are distinguishable on the Al substrate. Moreover, the higher thermal emittance of the $VO_2$:Ge over the pure $VO_2$ film can also be qualitatively concluded from the thermal image (the temperature scale is arbitrary as a constant $\varepsilon = 0.9$ has been set for the camera). Thus, Ge doping not only increases the transition temperature of the thermochromic transition, but it also improves the radiative cooling behavior of the solar collector in its switched, high temperature state.
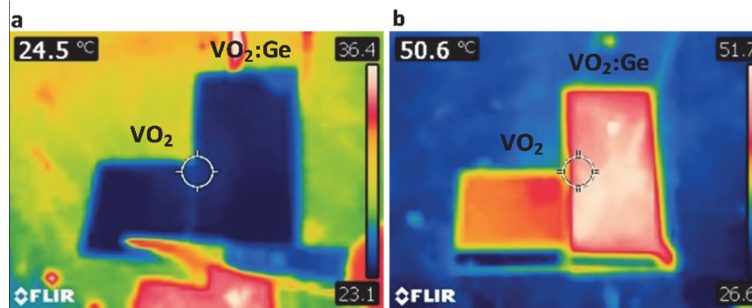


Figure 5.27. Thermal images of pure and Ge doped $VO_2$ coatings on Al substrates measured in the low (a) and high emittance state (b).

Using a simple model collector consisting of a glass cover, an air gap and a switchable absorber in thermal contact with the water pipes [Baldi, 2008] calculated the stagnation temperature map plotted as a function of solar absorptance and thermal emittance. Based this work and with the assumption that the switch only impacts the absorber emittance, while the solar absorptance remains relatively unchanged, the stagnation temperature is estimated to be lowered from ≈195°C to ≈150°C using pure $VO_2$ based absorbers and from ≈185°C to ≈140°C for Ge doped $VO_2$ based absorbers.

Outcomes

- At 8 μm, the emittance of a ≈210 nm VO$_2$ coating on Al substrate changes significantly from 0.07 to 0.32.

- In the high temperature, high emittance state, the thermal emittance of VO$_2$ increases with increasing the angle from normal incidence. This suggests that standard, normal emittance measurements underestimate the total emittance of the coatings.

- Finally, besides raising the phase transition temperature, Ge doping has the additional advantage of increasing the emittance of the thermochromic coating above T$_C$. In the high temperature state, a ≈10% increase in spectral emittance at 8 μm and 7% increase in total emittance modulation for the VO$_2$:Ge with ≈2.6 at.% Ge is recorded. Enhanced absorber emittance then leads to lower stagnation temperatures.

# 5.5 Ge doped VO$_2$ films sputtered from V-Ge alloy target

Co-sputtering at an industrial scale is challenging and sputtering from alloyed targets is proposed instead. A V-Ge alloy target with 5 at.% Ge is chosen to test the feasibility of depositing doped films directly from mixed targets (e.g. stable process in spite of the different sputter yields, conservation of the target composition in the deposited film). Plotting the Ge concentration versus the measured switching temperature determined for the co-sputtered VO$_2$:Ge films, for a V-Ge alloy target with 5 at.% Ge a ≈83°C transition temperature is expected (Figure 5.28).
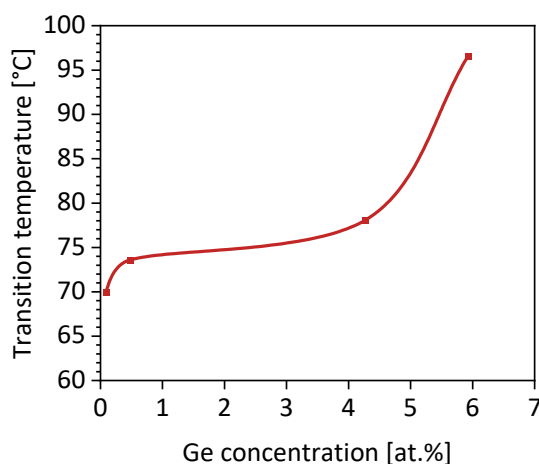


Figure 5.28. Ge concentration of the VO$_2$ film vs measured transition temperature.

Four-point probe resistivity

After slight adjustments of the process parameters such as the working and oxygen partial pressures, sputtering from V-Ge alloy target proved successful. Switching films have been sputtered and the temperature dependent resistivity curves of several of these samples are plotted in Figure 5.29.
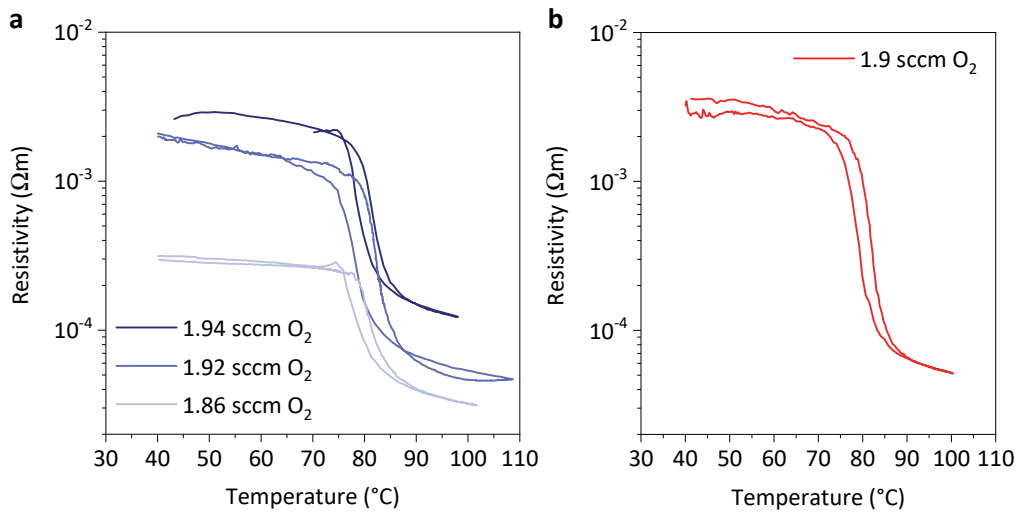
Figure 5.29. Temperature dependent electrical resistivity of VO$_2$:Ge films on Si (100) substrates deposited at different oxygen flows.

The magnitude of the thermochromic transition and the absolute resistivity values are strongly dependent on the oxygen partial pressure; even the transition temperature is slightly impacted by the O$_2$ flow. Higher is the set oxygen flow during the sputtering process, higher is the electrical resistivity of the deposited films and the corresponding transition temperatures, and vice versa (Figure 5.29.a).

The phase transition temperature is determined at ≈82°C, close to the expected transition temperature for a film with 5 at.% Ge content, and it represents a 15°C increase compared to the 68°C of pure VO$_2$ films. The transition temperature is rather constant, contained between 81-82°C for all studied O$_2$ flows.

Pure films generally exhibit three or more orders of magnitude increase in conductivity, but for doped samples significantly smaller modulations are common. The measured doped films undergo an approximately one order of magnitude transition, having measured the highest resistivity modulation of 1.6 order of magnitude for a film deposited with 1.9 sccm oxygen flow, at an O$_2$/Ar ratio of 1:9.1 (Figure 5.29.b). A 1.6 order of magnitude transition in a sample switching at 82°C is remarkable.

The relatively straightforward deposition of high-quality switching VO$_2$:Ge films from alloy targets instead of co-sputtering, makes the former the preferred process and strengthens the case for industrial upscaling of Ge doped VO$_2$ based selective solar absorber coatings.

Spectral emittance of Ge doped VO$_2$ sputtered from V-Ge alloy target

The spectral emittance of a ≈150 nm alloy-sputtered VO$_2$:Ge film is measured. The emittance modulation at 8 µm is Δε (8 µm) = 0.3, changing from ≈0.02 in the room temperature state to ≈0.31 at 100°C (Figure 5.30.a). This is larger than the emittance modulation of the thicker ≈210 nm VO$_2$ film. In order to compare the spectral emittance of the VO$_2$:Ge films sputtered from alloy target with that of pure VO$_2$ and a VO$_2$:Ge film deposited in the co-sputtering process, the corresponding measured spectra have been also plotted in Figure 5.30.b. As the compared film thicknesses are not exactly the same, only qualitative observations shall be made.

In the low temperature state, the three samples show the same behaviour, only varying in the absolute values as the emittance is thickness dependent. As expected, the thinnest $VO_2$:Ge film sputtered from the alloy target, shows the lowest emittance. However, in the high temperature state, the co-sputtered $VO_2$:Ge film exhibits rather constant and high spectral emittance until ≈10 μm where it suddenly decreases (a step-decrease), whereas for the $VO_2$:Ge sputtered from alloy target and pure $VO_2$ films the spectral emittance is decreasing gradually over the measured range. It is likely that the film sputtered from the alloy target is more homogeneous than the co-sputtered one, therefore, showing a similar behaviour to pure $VO_2$ films, whereas the co-sputtered $VO_2$:Ge could exhibit some phase mixture leading to the higher emittance (and feature between 8 – 11 μm). Indeed, in the XRD spectra of some of the previously co-sputtered $VO_2$:Ge films, a peak corresponding to GeO has been identified.
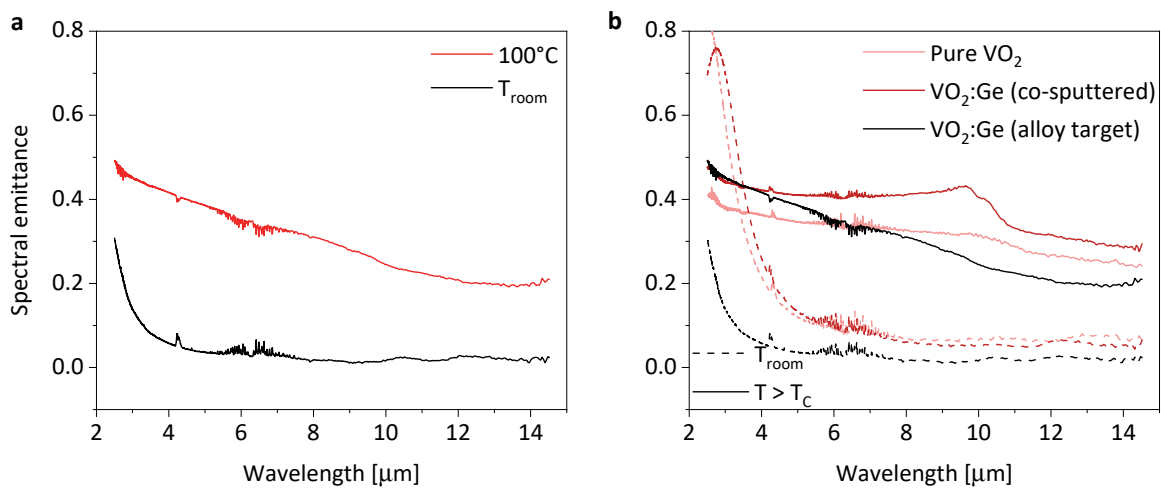


Figure 5.30. a) Spectral emittance change between the low (dashed line) and high temperature state (solid line) of a ≈150 nm thick $VO_2$:Ge film deposited from an alloy target; b) Comparison with ≈210 nm thick pure $VO_2$ and $VO_2$:Ge deposited by co-sputtering.

Morphology and doping homogeneity of $VO_2$:Ge films

The surface topography of the films has been investigated by STM. The observed grains vary in shape and size, ranging from ≈20 to 60 nm. Examples are shown in Figure 5.31. The grain sizes are smaller than those determined in pure $VO_2$ films deposited in similar conditions, however, it is comparable to the grain sizes in $VO_2$:Ge films deposited by co-sputtering. Smaller grains are expected in doped samples as dopants can significantly increase the density of defect induced nucleation sites, enhancing the heterogeneous nucleation of $VO_2$ particles.

Rounded (or spherical) and elongated (or acicular) grains are observed. The former are typical for pure vanadium dioxide films. However, the latter are particular and have been previously observed in Ge doped films obtained by co-sputtering (see Figure 5.8). Therefore, it is likely that Ge encourages the formation of such granular structures and it is tempting to assume that compositional differences might occur between the different grain types.

In order to check the sample homogeneity, the I-V curves are recorded locally, on individual neighboring grains, in a voltage interval from -1 to 1 V by single-point STS. If the Ge segregates in the regions with more

ordered, acicular grains, or even if the Ge concentration in neighboring grains slightly varies, the measured I-V characteristics should be different as STS is very sensitive to changes in the surface density of states.
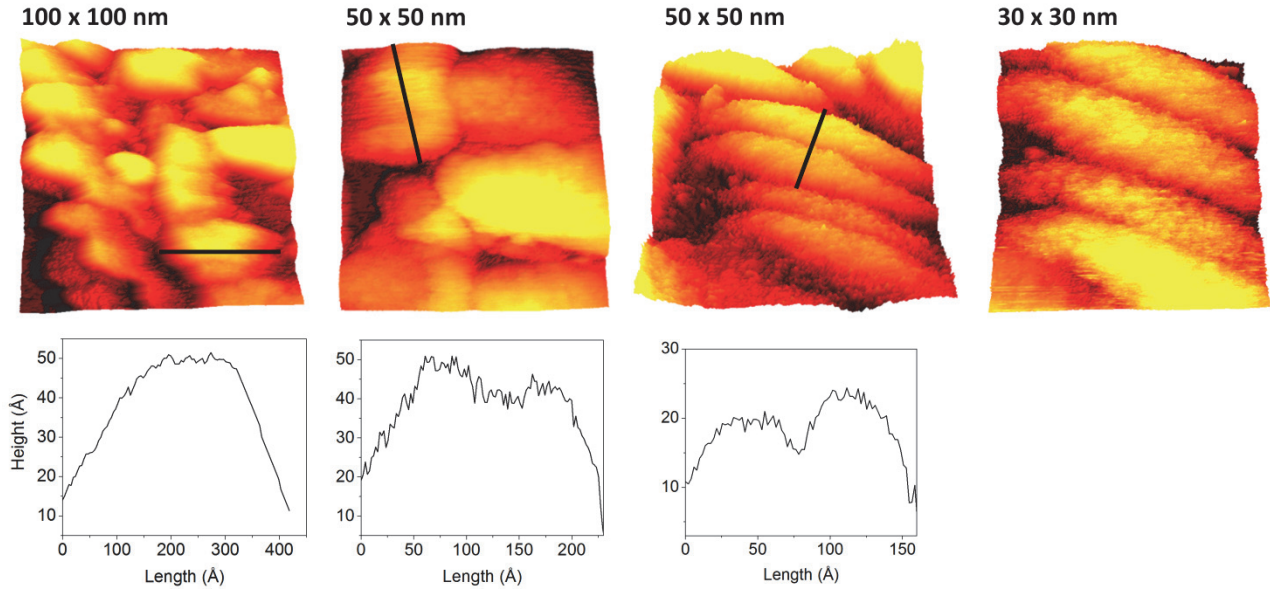


Figure 5.31. Different topographies and grain sizes of the Ge doped $VO_2$ thin films. The height profile of the grains gives an indication on the surface roughness.

The characteristic I-V curves of both spherical and acicular grains are measured (Figure 5.32). Plotting the derivative of the current versus the voltage, the local band gap is determined from the flat section of the curve. In noisy datasets, the band gaps might be prone to erroneous reading. From all measured single-point STS spectra, the determined band gap is ≈0.5 eV. This suggests a homogeneous sample and disproves the occurance of phase separation, Ge segregation or preferential doping in $VO_2$:Ge films sputtered from alloy target.

Calculated and measured band gaps for the insulating $VO_2$ phases have been reported in the range of 0.5 – 0.6 eV [Lee, 2015b; Tran, 2017; Verleur, 1968; Qazilbash, 2007; Shin, 1990]. STM and STS studies on $VO_2$ consistently report band gaps of 0.5 eV at room temperature [Yin, 2011; Chang, 2007]. This is in perfect agreement with our measurements of Ge doped $VO_2$.

The indirect optical band gap of the material is determined from the Tauc plot (Figure 5.33). Plotting ($\alpha$ hv)$^{1/2}$ vs. hv, where $\alpha$ is the absorption coefficient and hv the photon energy, the band gaps are determined from the extrapolation and intersection of the linear part of the curve. For pure $VO_2$ film (deposited on sapphire substrate) a band gap, $E_g$ = 0.61 ± 0.03 eV has been found. For the Ge doped case (film deposited on Si wafer), a very similar, only slightly smaller, bandgap of 0.59 ± 0.03 eV is found.

Density functional theory studies of $GeO_2$ – $VO_2$ alloys suggest a decrease of the $VO_2$ bandgap [Lu,2019], which seems to be confirmed by the optical measurements. Nonetheless, the difference being rather small and as graphical methods are not indubitably accurate, conclusions on the effect of Ge doping on the optical band gap of $VO_2$ should be cautious.
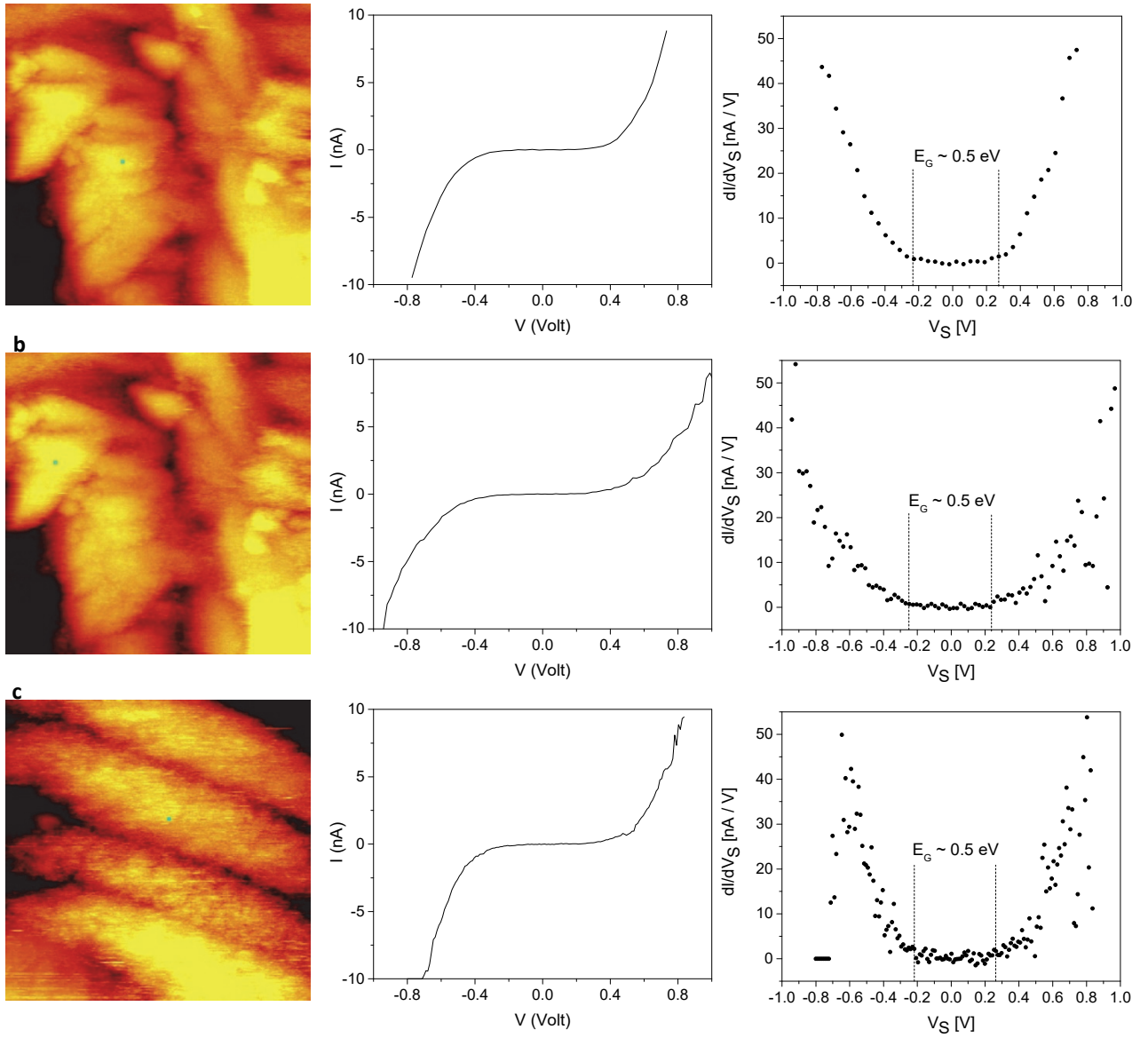
Figure 5.32. STM topography image of the VO₂:Ge thin film surface for a 100 x 100 nm rounded grain section (a-b) and a 30 x 30 nm acicular grain section (c); the characteristic I-V curves measured by single-point STS (marked by spots on the topographic images); the first derivative of the current, I vs. the voltage, V with the determined band gap, ≈0.5 eV for all grain types.
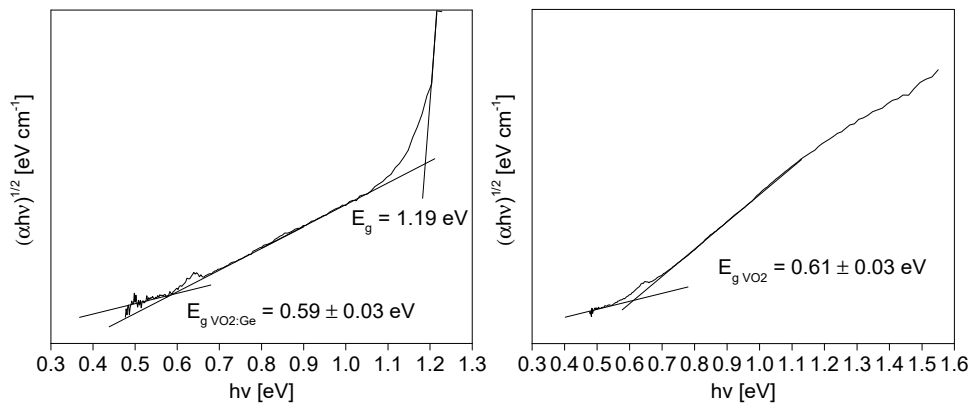


Figure 5.33. Tauc plot and the optical bandgap determined for pure and Ge doped VO₂ thin films. The absorption edge at 1.19 eV corresponds to the bandgap of Si (substrate).

<u>Outcomes</u>

An important step towards the industrial upscaling of Ge doped $VO_2$ thermochromic films for smart solar absorber coatings is achieved, as switching $VO_2$:Ge thin films have been deposited from V-Ge alloy target.

- Sputtering from a V-Ge alloy target is run in a stable mode; the process parameters are successfully adjusted.

- A first alloy target composition with 5 at.% Ge, leads to thermochromic films switching above 80°C – a ≈15°C increase compared to the pure $VO_2$ films.

- The deposited films are homogeneous; a band gap of ≈0.5 eV is determined throughout the sample.

- Other target compositions leading to transition temperatures of above 90°C shall be investigated.

# Chapter 6    Thermochromic absorber coating

In this chapter, first the shortcomings of single layer $VO_2$ or $VO_2$:Ge thermochromic absorbers are discussed. Then a multilayered thermochromic solar absorber design with a spinel $CuCoMnO_x$ is proposed and two absorber types – based on pure and Ge doped $VO_2$ – are sputtered and characterized. From the determined solar absorptance $\alpha_{sol}$ and thermal emittance $\varepsilon_{th}$ the thermochromic collector performance is simulated and the expected stagnation temperatures $T_{stagnation}$ predicted.

Improved absorber designs, with increasing $\varepsilon$ and decreasing $\alpha_{sol}$ over the thermochromic transition are proposed. Several examples of multilayered coating designs are proposed and their performance is evaluated by thin film simulations. Selected designs are deposited and measured. Finally, the durability of the thermochromic absorbers is assessed through accelerated aging tests.

## 6.1    Thermochromic selective absorber coatings based on single layer $VO_2$

$VO_2$ exhibits some spectral selectivity and the simplest absorber design would be a single $VO_2$ layer deposited on an Al substrate. The thermal emittance modulation of thermochromic $VO_2$ films has been shown to be thickness dependent [Guinneton, 2004]. The thicker is the film, larger is the resulting modulation of thermal emittance, with the switching amplitude seemingly stabilizing above thicknesses in the order of 200 nm (Figure 6.1).
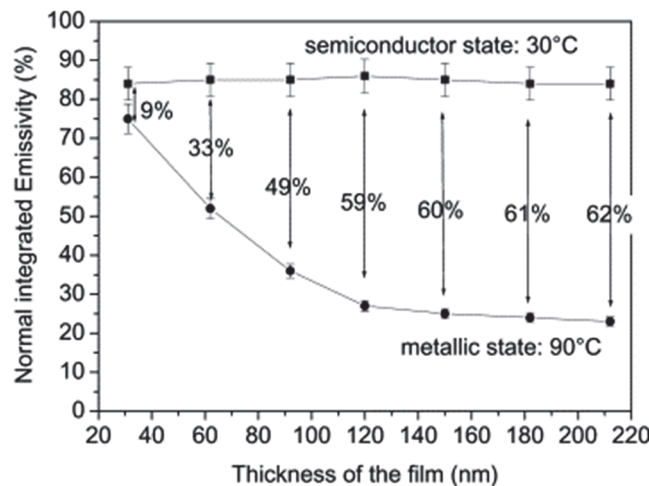


Figure 6.1. Influence of the film thickness on the modulation of normal integrated emittance (8 – 12 µm) for a single $VO_2$ layer deposited on amorphous Si substrate. Reproduced from [Guinneton, 2004].

A ≈270 nm thick $VO_2$ is deposited on an industrial multichannel Al substrate and the spectral emittance is measured both at room temperature and at 100°C over the 2.5 – 14 µm range. A remarkable emittance modulation of 0.5, from 0.135 to 0.635, is achieved at 8 µm wavelength (Figure 6.2). In terms of total thermal emittance, integrated over the entire measured specrum, the modulation is about 0.34, changing from 0.19 to 0.53 between the cold and hot state. For another sample of similar thickness, but with slightly dif-

ferent working and oxygen partial pressures, the $\Delta\varepsilon$ could be improved to 0.4 achieving a much more suitable thermal emittance of 0.07 in the low temperature state and an $\varepsilon$ of 0.47 at 100°C (Figure 6.3.a).
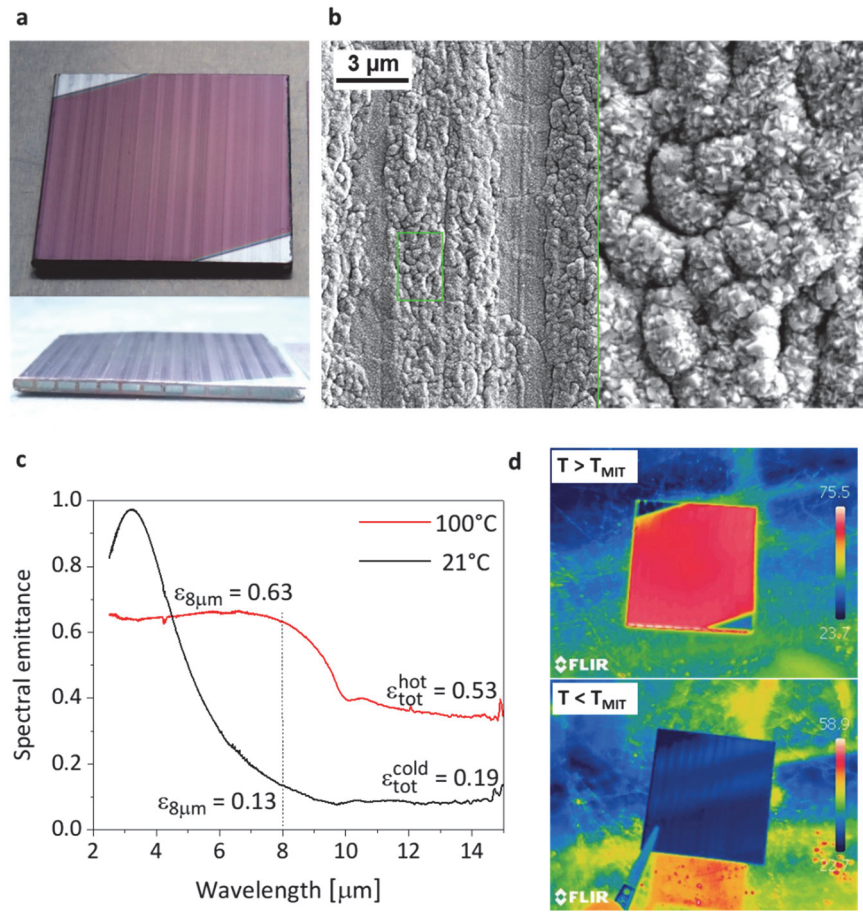


Figure 6.2. a) Photo of the deposited $VO_2$ film on the multichannel Al absorber. b) SEM image of the coating shows a rough surface with cauliflower-like structures, advantageous for increased absorptances. c) Measured spectral emittance in the mid-IR range and the determined total thermal emittances and spectral emissivities at 8 µm for both low and high temperature states. d) Thermographic images of the coating below and above the $T_{MIT}$.

However, the limitation of the single layer thermochromic absorber coating, as it is also hinted by the visible color of the absorber shown in Figure 6.2.a, is the rather poor solar absorptance. The simulated reflectance spectra of such a 270 nm thick $VO_2$ film on multichannel Al substrate is shown in Figure 6.3.b and a solar absorptance of $\alpha_{sol} = 0.71$ is determined. Although, this value is significantly improved by the addition of an antireflective $SiO_2$ top-layer, the predicted $\alpha_{sol} = 0.86$ is still below the solar absorptance values of commercially competitive absorbers. Therefore, in the following section, the focus is turned towards multi-layered solar absorber coatings.
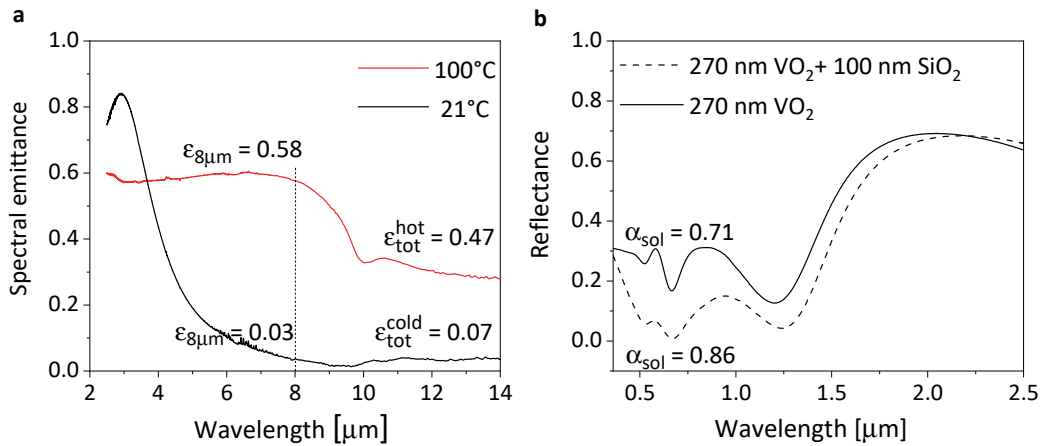
Figure 6.3. a) Measured spectral emittance of a 270 nm VO$_2$ single layer on Al multichannel absorber with improved thermal emittance modulation, $\Delta\varepsilon$ = 0.4. b) Simulated reflectance spectra of an identical 270 nm VO$_2$ single coating on Al multichannel absorber and a 270 nm VO$_2$ with a 100 nm anti-reflective SiO$_2$ top-coating with the corresponding solar absorptance values.

## 6.2    Thermochromic selective absorber coatings based on VO$_2$:Ge and spinel CuCoMnO$_x$

A multilayered absorber coating based on an aluminum substrate, pure or Ge doped vanadium dioxide thermochromic layer, a CuCoMnO$_x$ spinel film and an amorphous SiO$_{2-x}$ antireflective top-coating is proposed. The CuCoMnO$_x$ black selective spinel oxide is promising for its high temperature oxidation and corrosion resistance.

Complex spinel oxides exhibit an intrinsic spectral selectivity showing a weak absorption in the infrared spectral range, as few vibrational bands exist at 1000 cm$^{-1}$, and a strong electronic absorption in the visible spectral range (inter-band transitions) [Kaluža, 2001]. Most references on CuCoMnO$_x$ spinels for solar energy conversion report on the dip-coating deposition method and promising solar absorptance and thermal emittance values are achieved: $\alpha_{sol}$ = 0.855, $\varepsilon_{th}$ = 0.045 for a sample with three dipping/annealing cycles [Kaluža, 2001] or very similar values obtained after only a single dipping/annealing cycle with an SiO$_x$ protective over-coating [Vince, 2003]. More recent CuMnO$_x$ based work reports on improved $\alpha_{sol}$ = 0.94 and $\varepsilon_{th}$ = 0.06 after optimization and deposition of SiO$_2$ antireflective coating [Bayón, 2008a]. For an Al-CuMnO$_x$//FeMnCuO$_x$//SiO$_2$ multilayer, an even higher solar absorptance of 0.957 and thermal emittance of only 0.038 at 100 °C are reported [Farchado, 2018]. Additionally, a high thermal stability and corrosion resistance of sol-gel deposited CuCoMnO$_x$ has been demonstrated on two-meter long stainless steel tubes for concentrated solar power (CSP) applications [Joly, 2013]. In the present work, CuCoMnO$_x$ spinel films are deposited by means of magnetron sputtering – currently one of the most common industrial deposition method of black selective absorbers.

Deposition of thin films

All the oxide thin films discussed – $VO_2$, $VO_2$:Ge, $CuCoMnO_x$ and $SiO_{2-x}$ – are deposited by reactive magnetron sputtering (co-sputtering in the case of Ge doped samples) in high vacuum conditions (base pressure below $5 \cdot 10^{-8}$ mbar) . The oxide films are sputtered from 2" high purity metal and semimetal targets: vanadium (99.95%), germanium (99.999%), copper-cobalt-manganese (99.9%) and silicon (99.999%). The multi-layered thin film stacks have been deposited on Al sheets (Goodfellow, 50 mm x 50 mm, 0.5 mm thick). For the various characterizations of individual oxide thin films, <100> Si wafers are used as substrate.

For the oxygen partial pressure sensitive $VO_2$ film deposition the Proportional Integral Derivative (PID) feedback control is used to regulate the oxygen flow. The spinel $CuCoMnO_x$ and $SiO_{2-x}$, being less sensitive to fluctuations in oxygen, setting the oxygen flow is sufficient to obtain the desired oxide films. For uniform film thicknesses, the samples are rotated during deposition. The process parameters for all the different deposited oxides are summarized in Table 6.1.

Table 6.1. Deposition parameters of the various oxide thin films.

| | $VO_2$ | $VO_2$:Ge | | $CuCoMnO_x$ | $SiO_{2-x}$ |
|---|---|---|---|---|---|
| Base pressure [mbar] | $< 5 \cdot 10^{-8}$ | | | | |
| Working pressure [mbar] | $7.2 \pm 0.1 \cdot 10^{-3}$ | $7.1 \cdot 10^{-3}$ | | $4.1 \cdot 10^{-3}$ | $7 \cdot 10^{-3}$ |
| $O_2$ to Ar ratio | 1:11.8 to 1:12.3 | 1:12.3 to 1:13 | | 1:3.2 | 1:21 |
| Applied power [W] | | V | Ge | | |
| | 150 (DC) | 150 (DC) | 12 (RF) | 75 (MF) | 100 (RF) |
| Frequency [KHz] | - | - | | 250 | 13560 |
| Thickness [nm] | ≈ 210 | ≈ 215 | | 20 | 40 |
| Temperature [°C] | 465 | 465 | | 465 | - |

Thermochromic $VO_2$ and $VO_2$:Ge thin films

The first layer of the absorber is the thermochromic $VO_2$ or $VO_2$:Ge. In order to precisely determine the phase transition temperature and hysteresis in the films, the temperature dependent electrical resistivities are plotted for both the pure and Ge doped $VO_2$ (Figure 6.4).

As expected, in the Ge doped sample an increase in the phase transition temperature is observed, $T_h$ = 72.6°C, up from the ≈66°C in the pure sample. The increase is accompanied by a significant decrease in the phase transition amplitude.

The SEM images of the sputtered films shown in Figure 6.5, reveal a rather dense crystalline structure with an average grain diameter between 100 - 150 nm and a film thickness of ≈210 nm for the pure and ≈215 nm for the Ge doped $VO_2$ film.

The spectral emittance curves of these films have been discussed previously (Section 5.4). It is recalled that at 8 µm, the spectral emittance of pure $VO_2$ changes from 0.07 at room temperature to 0.32 at 100°C and for the $VO_2$:Ge from 0.06 to 0.41. The total thermal emittance modulation of the two films over the mid-infrared spectral range (2.5 – 14 µm) is $\Delta\varepsilon_{VO2}$ = 0.23 and $\Delta\varepsilon_{VO2:Ge}$ = 0.3.
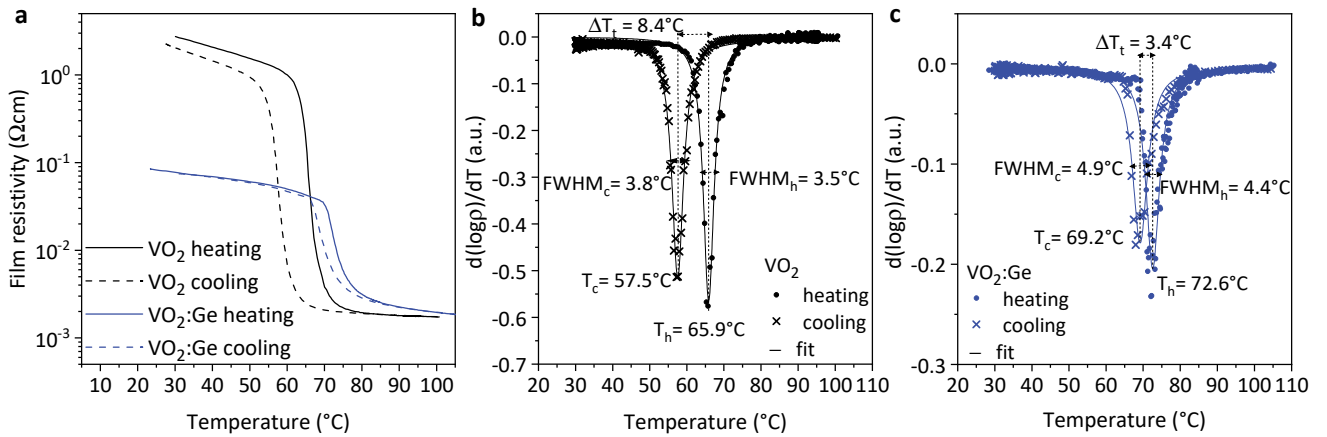
Figure 6.4. (a) Temperature dependent electrical resistivities of $VO_2$ and Ge doped $VO_2$ films on Si (100) substrates (b-c). The d(log ρ)/dT vs T curves of the pure and Ge doped samples. Measured data points (symbols) are fitted and the determined minima denote the transition temperatures upon heating, $T_h$ and cooling, $T_c$. The difference between $T_h$ - $T_c$ gives the hysteresis width $\Delta T_t$, while the FWHM determines the sharpness of the metal-to-insulator transition.
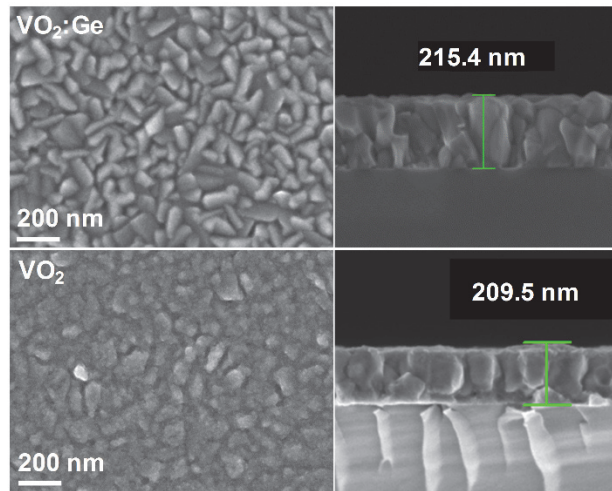


Figure 6.5. Plane and cross-sectional scanning electron microscopy (SEM) images showing the morphology and thickness of the pure and Ge doped thermochromic thin films.

## CuCoMnO_x spinel absorber

The Solar Energy and Building Physics Laboratory disposes with considerable experience in the sol-gel deposition of black selective spinel oxide coatings on 2 m long tube collectors. In this work, $CuCoMnO_x$ spinel films are deposited by magnetron sputtering. Therefore, the process parameters must be accurately determined and the obtained films are thoroughly investigated by structural, morphological, optical and electronical characterizations.

First, the XRD patterns of two, ≈100 nm thin, $CuCoMnO_x$ films sputtered at substrate heater temperature of 240°C and 465°C are shown in Figure 6.6. For the film deposited at 240°C, only one broad peak is present between 41° − 45°. Many Co-Mn and Cu-Mn oxides exhibit peaks in this range and the exact crystalline phase cannot be identified. The temperature might be insufficient for the formation of the spinel crystal structure. However, the film deposited at 465°C, exhibits rather broad diffraction peaks – an indication of nanocrystalline film. The peaks at 2θ of 36.4°, 44.2°, 54.8° and 58.5° can be assigned to diffraction lines

produced by the (311), (400), (422) and (511) planes of CuCoMnO$_x$. The peaks can be indexed to the spinel structure in space group Pnma according to JCPDS 47-0324 [He, 2015; Yang, 1991]. The peak at 2θ of 38.9° is assigned to CuO. Other authors have previously reported the formation of CuO crystallites for Cu-Co mixed spinels. When the calcination is done above 400°C, the obtained CuCoMnO$_x$ or Cu-Co spinels are not structurally pure, rather the predominantly spinel structure is accompanied by trace amount of tenorite CuO [Yang, 1991; Li, 1990]. The size of the grains is estimated via the Scherrer equation from the full width at half maximum (FWHM) of the (400) and (511) peaks and it is found to be around 9 nm.
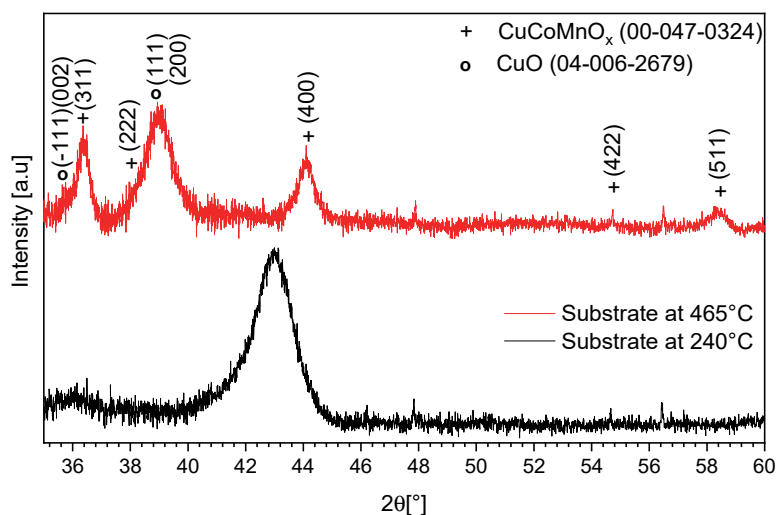


Figure 6.6. X-ray diffraction spectra of the CuCoMnO$_x$ films measured at 240°C and 465°C. At 240°C, there is only one broad peak and many Cu-Mn and Mn-Co oxides exhibit peaks in the 41°-45° range. At 465°C, only two phases are identified: spinel CuCoMnO$_x$ and tenorite CuO.

The morphology of CuCoMnO$_x$ films deposited on Si wafers has been investigated by both SEM and STM (Figure 6.7). The plane sectional SEM image reveals a porous structure with agglomerates of 30 to 70 nm in size. This is larger than the grain sizes estimated from the XRD peak broadening and suggests that the observed agglomerates are likely made up by smaller crystalline grains. The in-line STM has a superior resolution and is capable of visualizing just few nanometer large crystallites. Indeed, the STM image and 3D representation show several agglomerates made up of multiple, well-defined nanocrystallites. Typical crystallite sizes ranging from 5 to 10 nm are determined. Thus, the crystallite sizes closely match those determined by XRD. In a study on Ni$_x$-, Zn$_x$-, Cu$_x$- Co$_{2-x}$MnO$_4$ spinels, rather similar morphologies with nanocrystalline porous films have been reported [Le, 2016].
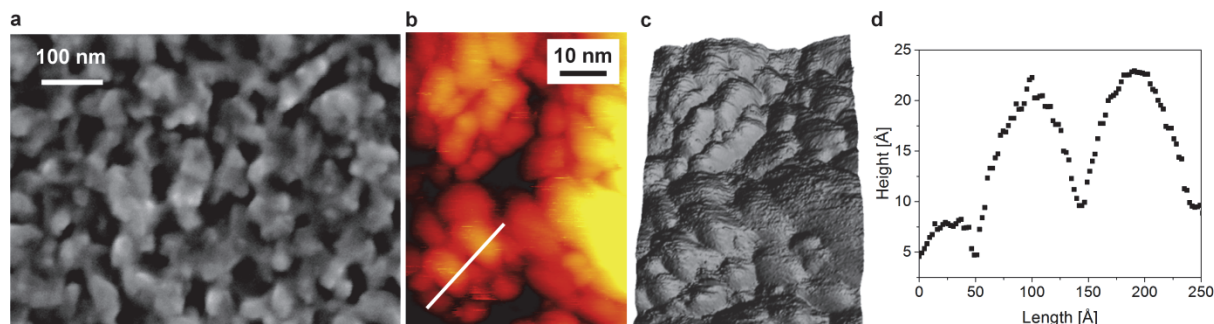


Figure 6.7. a) SEM image of ≈100 nm thin CuCoMnO$_x$ spinel film on Si substrate. b, c) STM image and the corresponding 3D representation of CuCoMnO$_x$ nanocrystallites which make up the larger grains observed with SEM. d) The height vs length profile of the linescan shown in (b) depicting grains of sizes ranging between 5 and 10 nm.

A rough film surface is in general favorable for reaching high absoptance values. The reflectance curve of a 100 nm thin CuCoMnO$_x$ deposited on reflecting Al substrate is measured (Figure 6.8). The film is absorbing over the solar spectrum and its reflectance increases around 2 – 2.5 µm to values above 90% exhibiting good selective behavior. The calculated solar absorptance and thermal emittance are α$_{sol}$ = 0.74 and ε$_{th}$ = 0.02 (selectivity, S = α/ε = 37). To be noted that these values correspond to a single 100 nm thin CuCoMnO$_x$ layer with no SiO$_{2-x}$ top coating.
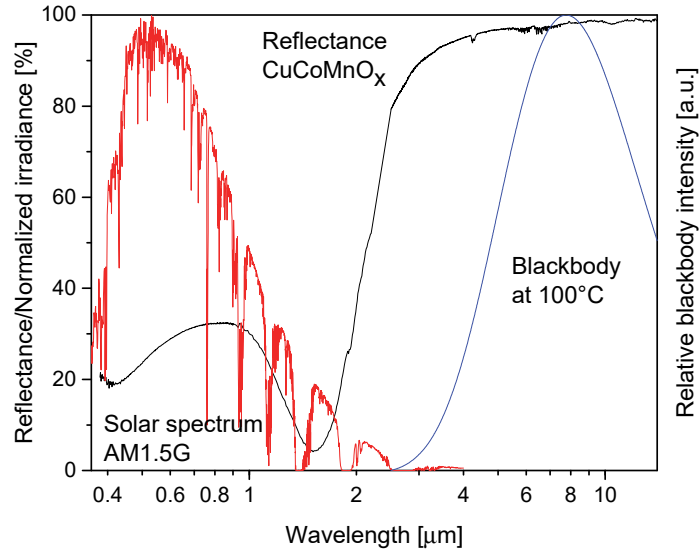


Figure 6.8. Spectral reflectance of a 100 nm thin CuCoMnO$_x$ film deposited on an Al substrate, the normalized standard solar radiation at the Earth's surface (AM 1.5G) and the normalized blackbody radiation at 100°C.

By UPS, the density of electronically filled states is measured. Due to the in-line transfer, sample contamination is avoided, no Ar etching of the surface is required and the as-deposited sample can be measured. The He I and He II UPS spectra are displayed in Figure 6.9. From these, the valence band edge and the cut-off energy of the secondary electrons can be directly determined. The work function of the material, Φ$_m$ is then given by

$$\Phi_m = h\nu - (E_{cutoff} - E_F)$$ 
<div align="right">Equation 6.1</div>

where hv is the incident photon energy, E$_F$ is the Fermi edge and E$_{cutoff}$ is the onset of the secondary electron cutoff. The valence band edge, VB is determined at 0.38 eV in both He I and II spectra, while the work function is found to be 5 eV. The optical band gap of the material is determined by plotting the Tauc relation for both direct and indirect allowed transitions and band gaps of 0.56 eV and 0.45 eV, respectively, are found. Both values suggest that the material is n-type semiconductor. This is in good agreement with the findings reported in [Huang, 2015], where authors similarly determine a valence band edge at 0.67 eV and an optical band gap of 0.69 eV in a Mn-Co-Ni-O spinel film, concluding the n-type character of the film. There, the determined work function is 3.96 eV.

In the He I spectrum four features labelled A, B, C and D are visible at ≈5.2 eV, 3.8 eV, 3.05 eV and 1.2 eV. In the He II spectrum the features are more pronounced and occur at very similar positions – although only three out of the four: at 5.2 eV labelled A*, C* at 3.05 eV and D* at 1.2 eV. The feature appearing at ≈3.8 eV in the He I spectrum is not present in the He II spectrum. The strongest peak around 3 eV is attributed to

the Cu 3d states [Kukuruznyak, 2006; Wang, 2016]. The peak at the low energy side of the spectrum, around 1.2 eV, was also observed in a series of Co-Mn oxide compositions [Broemme, 1990]. Others associated it with Co 3d bands in $Co_3O_4$ [Langell, 1999]. The weaker peak at ≈5.2 eV is arising due to the mixing of the metal 3d levels with O 2p states, while the additional peak found in the He I spectrum at 3.8 eV, could be a 3d-derived feature resulting from Co 3d orbitals with $e_g$ character.
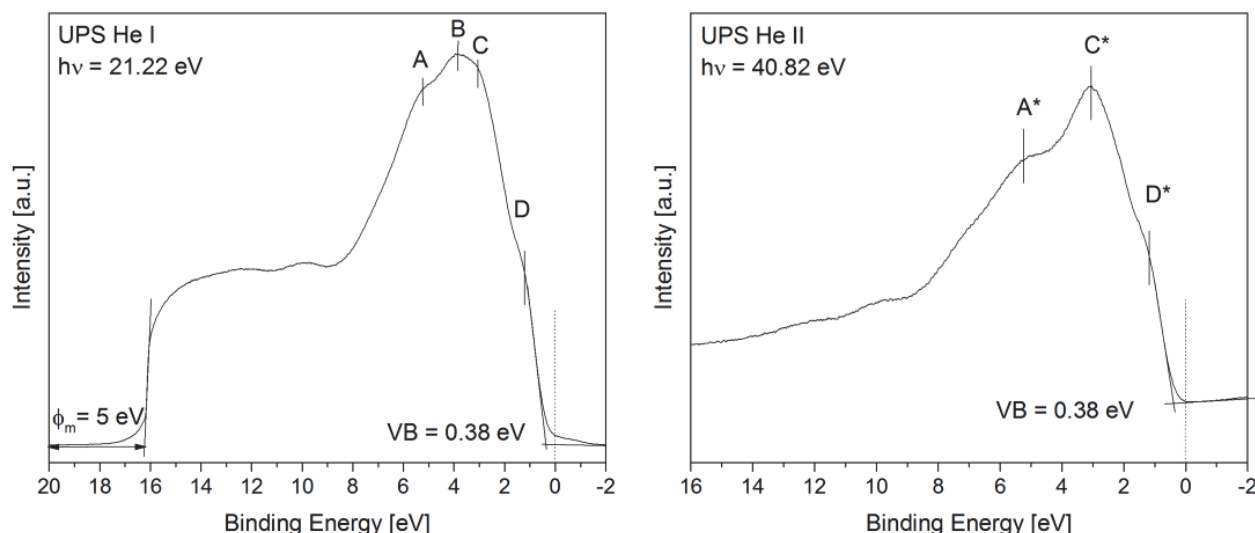


Figure 6.9. In-line UPS He I and He II spectra of the $CuCoMnO_x$ spinel film. The valence band edge, VB and work function of the material, $\Phi_m$ have been determined at 0.38 eV and 5 eV, respectively. Features labelled A, B, C, D in He I and A*, B*, D* in He II spectra are associated to metal 3d levels mixing with O 2p states, Cu 3d states and Co 3d states, respectively.

The measured Cu 2p spectrum (Figure 6.10.a) is typical for CuO as reported in the reference work of Biesinger et al. [Biesinger, 2010]. The Cu 2p shows significantly split spin-orbit components, with the separation between the Cu $2p_{1/2}$ at 952.4 eV and the Cu $2p_{3/2}$ at 932.5 eV binding energies being 19.9 eV. This agrees well with the split of 19.8 eV reported for pure CuO [Hussain, 1989]. The strong shake-up satellite between 938 eV and 945 eV is also an indication of an open $3d^9$ shell and dominant Cu(II) species, while the Cu LMM Auger emission line measured at 917.9 eV (not shown here), closely fits the reference position of 917.88 eV reported for CuO (compiled from the NIST database [Wagner, 2012] based on a survey of 12 literature sources). A small shoulder at ≈2 eV below the energy of the main Cu $2p_{3/2}$ peak could be attributed to the presence of small amount of $Cu^+$ species. The formation of $Cu^+$ species in Cu-Mn spinel oxides annealed at temperatures above 450°C has been reported [Bayón, 2008b], where a solid state redox reaction occurs and Cu(II) is partially reduced to Cu(I) due to the oxidation of some Mn(III) to Mn(IV). Similarly, $Cu^+$ species have been observed in $CuCoMnO_x$ spinels as well. [Geng, 2011]

The Co 2p spectrum (Figure 6.10.b) consists of two main lines: $2p_{3/2}$ at 779.8 eV and $2p_{1/2}$ at 795.1 eV with a spin-orbit splitting of 15.3 eV and two broad satellites at ≈786 and 803 eV binding energy. As very similar doublet separation and binding energies have been reported for both CoO and $Co_3O_4$ (Co $2p_{3/2}$ NIST database average of 780.45 eV for CoO and 779.88 eV for $Co_3O_4$), the position of satellite peaks should be considered for determining the Co oxidation states. In [Wei, 2008; Zhu, 2009], authors discuss that the energy gap between the Co $2p_{3/2}$ main peak and satellite peak is highly dependent on the oxidation states: an energy gap of ≈6 eV is related to $Co^{2+}$, while for an energy gap of ≈9 − 10 eV, a 3+ valence is assigned to the Co atom. In the measured spectrum, a broad satellite between 785 and 792 eV is present, and although the individual satellite peaks at ≈6 and ≈10 eV separation are not well-distinguishable, it is likely that both Co(II)

and Co(III) are present. Studies on $Co_3O_4$ [Oku, 1976] or $MnCo_2O_4$ [Li, 2013] spinel compounds, report on very similar Co 2p spectral shape and binding energies to those measured here, while the peaks are best fitted considering two spin-orbit doublets characteristic of $Co^{2+}$ and $Co^{3+}$ and two pairs of shake-up satellites. Another relevant study on $(Co,Mn)_3O_4$ spinel nanowires [Cheng, 2013] prepared at 500°C concludes the presence of both $Co^{2+}$ and $Co^{3+}$ in the sample, showing the Co $2p_{3/2}$ and Co $2p_{1/2}$ at 779.7 eV and 795.0 eV and the corresponding satellite peaks at 786.2 and 803 eV which match closely the binding energies determined in this work. Finally, when comparing with the Co oxide references from [Biesinger, 2011] the measured spectrum is close to that of CoO, with the notable difference of the broader satellite peak – characteristic of $Co_3O_4$. Biesinger reports 780 eV binding energy for reference CoO and 779.6 eV for $Co_3O_4$, while in the present work it is determined at 779.8 eV. Based on the wide Co 2p core lines, their binding energies, the spin-orbit splitting values, the shape and the separation of the satellite peaks, it is concluded that both Co (II) and Co (III) species are present in the spinel film.

The core level data of manganese with its multiple oxidation states (0, I, II, III, IV, VI, VIII) and multiplet splitting with overlapping binding energies are challenging to interpret. The Mn $2p_{3/2}$ main peak is found at 641.7 eV and the $2p_{1/2}$ at 653.1 eV with a spin-orbit splitting of 11.4 eV (Figure 6.10.c). This compares well to the peak structures, the binding and splitting energies reported for $(Co,Mn)_3O_4$ [Cheng, 2013], $CoMn_2O_4$ spinel [Li, 2013] or $MnCo_2O_4$ [Zhu, 2009]. Published spectra of standard pure MnO showed characteristic shake up satellite above 645 eV binding energy [Biesinger, 2011; Oku, 1975]. The lack of any shake up satellite in the measured spectrum suggests the absence of Mn(II). Moreover, the previously reported 640.3 [Biesinger, 2011] or 640.6 eV [Oku, 1975] binding energy of Mn(II) is rather low compared to the one determined here. $Mn^{2+}$ species could be further oxidized to $Mn^{3+}$ and $Mn^{4+}$ during the high temperature deposition and the consequent annealing process. In their study on Cu-Mn-O spinel thin films, Bayon et al. report on the lack of $Mn^{2+}$ in the films even when starting from Mn(II) precursors and also propose that a further oxidation to $Mn^{3+}$ and $Mn^{4+}$ occurs in the solution or during the annealing process [Bayón, 2008b]. Indeed, authors found that in all cases the broad Mn $2p_{3/2}$ peak could be fitted considering only two components: $Mn^{3+}$ and $Mn^{4+}$ and observed an increase in the amount of $Mn^{4+}$ with increasing annealing time and temperature. As the lowest percentage of $Mn^{4+}$ was determined for the pure $MnO_x$ sample – all other samples containing Cu – it was inferred that a $Cu^{2+} + Mn^{3+} \rightarrow Cu^+ + Mn^{4+}$ reaction must be occurring during the annealing process. Therefore, in the presence of Cu, some of the $Mn^{3+}$ could be partially oxidized to $Mn^{4+}$ and $Cu^+$ is formed. In the present work, the $Mn^{4+}$ has been assigned a reference binding energy of 642.5 eV, while a binding energy of 641.7 eV is associated with the $Mn^{3+}$ based on NIST database averages and pure reference samples discussed in [Biesinger, 2011]. These reference positions are indicated in Figure 6.10.c by vertical straight lines. The comparison of the measured spectrum with literature suggests the existence of manganese in both 3+ and 4+ oxidation states, while the presence of a small shoulder on the Cu $2p_{3/2}$ peak, attributed to $Cu^+$ species, fits the interpretation proposed by Bayon et al. [Bayón, 2008b]

Finally, the O 1s core level spectrum is composed of a main peak at 529.5 eV, assigned to the oxygen in the spinel lattice, and a shoulder around 531.5 eV attributed to surface oxygen species such as chemisorbed oxygen or oxygen ions in low coordination (Figure 6.10.d). This is in accordance with what has been reported previously for Cu-Co-Mn-Si oxide spinels [Joly, 2015], in various spinel cobaltites (Cu-, Mn- and Ni-cobaltites) [Zhu, 2009], in Cu-Co mixed spinel oxides [Li, 1990; Tavares, 1998] and in $MnO_2$ and spinel $Mn_2O_3$ [Oku, 1975].
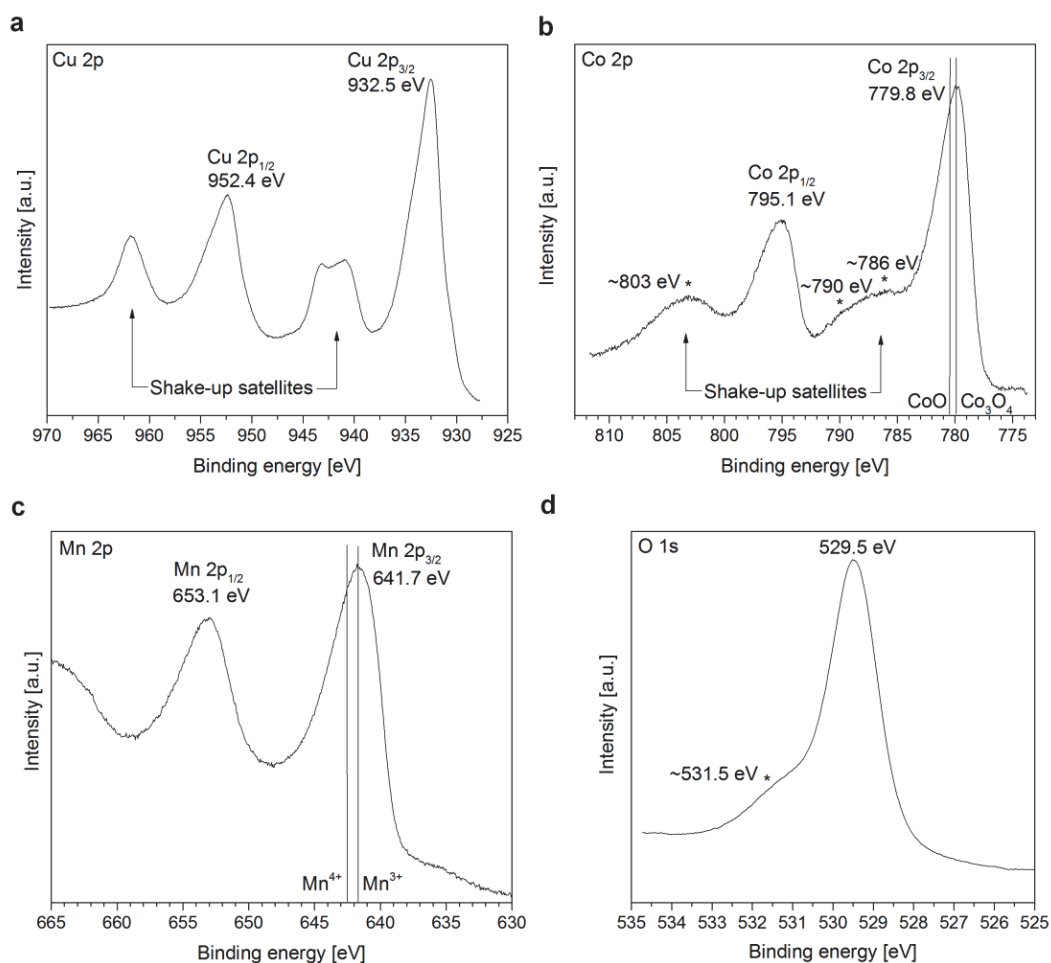
Figure 6.10. In-line XPS core level spectra of Cu 2p (a), Co 2p (b), Mn 2p (c) and O 1s (d) (measured with Mg Kα X-ray source with hν = 1253.6 eV, at a pass energy of 29.925 eV). Asterisks denote the positions of the satellite peaks, while vertical straight lines indicate the reference positions from literature.

Core-level spectroscopy provides also quantitative information on the chemical composition of studied samples. The concentration of different elements is determined by integration over the Cu 2p, Co 2p, Mn 2p and O 1s core-level signals after subtracting a Shirley background (Table 6.2). The resulting stoichiome-try corresponds to $CuCoMnO_4$ spinel and CuO, in a 1:1 oxide ratio, indicating a CuO rich surface. While the presence of CuO is in accordance with the outcome of the XRD measurements, where tenorite CuO has been identified in the $CuCoMnO_4$ spinel film, the bulk and surface stoichiometry are likely different with spinel dominating the bulk phase and considerable enrichment in CuO occurring at the surface as a result of Cu diffusion.

Table 6.2. XPS quantification of the $CuCoMnO_x$ film.

| Element | Orbit | Atom [%] |
|---------|-------|----------|
| Cu      | 2p    | 26.0     |
| Co      | 2p    | 12.9     |
| Mn      | 2p    | 9.6      |
| O       | 1s    | 51.5     |

The main findings of the UPS and XPS analysis are summerized herein:

- A work function of 5 eV and a valence band maximum at 0.38 eV are determined. From the valence band maximum and the calculated optical band gaps, the n-type semiconductor nature of the film is inferred.

- The Cu 2p, Co 2p, Mn 2p and O 1s core level spectra are in agreement with data reported in literature and formation of the spinel structure is confirmed.

- Transition metals such as Cu, Co, Mn can adopt multiple oxidation states. In the presence of Cu, partial oxidation of Mn might occur according to the redox reaction: Cu(II) + Mn(III) → Cu(I) + Mn(IV). On the other hand, Mn(IV) can oxidize Co(II) to Co(III). In the deposited $CuCoMnO_4$ spinel film Cu in the Cu(I) and Cu(II) states, Mn in the Mn(III) and Mn(IV) states and Co as Co(II) and Co(III) are identified.

- The quantification yields that both spinel $CuCoMnO_4$ and CuO are present at the surface, suggesting a Cu rich surface (Cu diffusion).

Multilayered absorber coating

Based on the previously discussed individual thin films, a multilayered absorber design, with suitable film thicknesses, is proposed according to Figure 6.11.a. Two absorbers consisting of an IR reflective Al substrate, a ≈210 nm thermochromic layer, a ≈20 nm $CuCoMnO_x$ spinel type absorber and a ≈40 nm $SiO_{2-x}$ anti-reflective and oxidation barrier top-layer are deposited. The first absorber, A1 is based on pure $VO_2$, the second absorber, A2 is based on Ge doped $VO_2$.
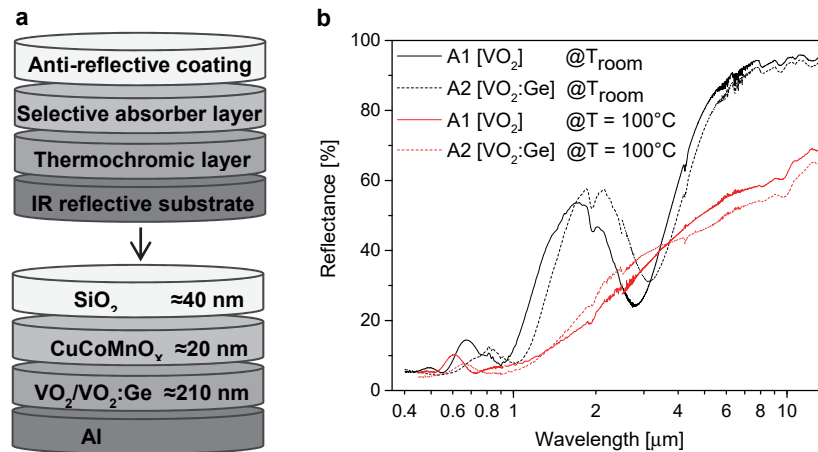


Figure 6.11. (a) Schematic drawing of the solar absorber multilayered coating and proposed film thicknesses. (b) Reflectance curves of the absorbers A1 ($VO_2$ based) and A2 ($VO_2$:Ge based), measured in the 0.4 – 14 µm spectral range both below, at $T_{room}$, and above the thermochromic transition temperature, at T = 100°C.

According to simulations, the multilayered absorber A1 is expected to yield $\alpha_{sol}$ = 0.77, $\varepsilon_{th}$ = 0.07 in the low temperature state and $\alpha_{sol}$ = 0.87 and $\varepsilon_{th}$ = 0.21 in the high temperature state. The optical response of the envisaged thin film stack is predicted based on the optical constants n and k of the individual layers, either

directly determined from ellipsometry measurements (in the case of $SiO_{2-x}$) or adopted from literature (from [Paone, 2015b] for $VO_2$ in both the cold and hot state, from [Joly, 2015] for $CuCoMnO_x$) and Semilab SEA database (for Al substrate).

The experimentally measured reflectance curves for absorbers A1 and A2, both at room temperature and at 100°C are shown in Figure 6.11.b. The corresponding solar absorptance and thermal emittance values are summarized in Table 6.3. The final absorber coating retains an excellent thermal emittance modulation over the thermochromic transition. The difference in thermal emittance, $\Delta\varepsilon$ of 0.31 and 0.33 are determined for absorber A1 and A2, respectively. Although the changes over the thermochromic transition occur mainly in the near- and mid-infrared spectral region, some difference in the optical response in the visible spectral range is also recorded. A 0.05 and 0.07 increase in solar absorptance is measured for absorber A2 and A1 which is detrimental for an efficient overheating limitation.

Table 6.3. Experimentally determined solar absorptance and thermal emittance values of the deposited multilayered absorber coatings.

| Absorber type | $\alpha_{sol}$ at $T_{room}$ | $\alpha_{sol}$ at T = 100°C | $\varepsilon_{th}$ at $T_{room}$ | $\varepsilon_{th}$ at T = 100°C | $\Delta\varepsilon$ |
|---|---|---|---|---|---|
| A1 [$VO_2$] | 0.84 | 0.91 | 0.09 | 0.4 | 0.31 |
| A2 [$VO_2$:Ge] | 0.87 | 0.92 | 0.11 | 0.44 | 0.33 |

The experimentally measured $\alpha_{sol}$ and $\varepsilon_{th}$ for the pure $VO_2$ based absorber indicate a better absorber performance than what is predicted by simulation. In terms of $\alpha_{sol}$, at both room temperature and 100°C, the achieved values are higher than predicted by 0.07 and 0.04, respectively. Both simulation and measurement corroborate an increase of $\alpha_{sol}$ over the thermochromic transition.

In terms of $\varepsilon_{th}$, simulated and measured values are rather consistent at room temperature with 0.07 versus 0.09. The films being highly transparent to the infrared radiation, it is the total coating thickness and, mostly, the IR reflective substrate that govern the multilayer response. However, in the high temperature state, the values diverge significantly from 0.21 to 0.40. This considerable difference might arise from traces of other vanadium oxides such as $V_2O_3$ or $V_2O_5$ present in the film, which could significantly increase the emittance in the high temperature state. For solar thermal applications, where at high operating temperatures a high $\varepsilon_{th}$ is desired, these results are favorable. Variation between simulated and measured spectral behavior is expected as the optical constants are not directly determined, but adopted from literature on $VO_2$ films deposited at slightly different process parameters.

With the experimentally determined solar absorptance and thermal emittance values of the novel thermochromic absorbers, it is possible to predict the thermal performance of a prospective thermochromic collector and to compare it with that of a standard flat plate collector. This is achieved using a free and validated numerical simulation model (SolCoSi) [Pérez-Espinosa, 2018]. The simulation is based on a nodal model which combines the multilayer method of Cadafalch with a discretization also in the longitudinal direction [García-Valladares, 2009; Cadafalch, 2009]. For the simulation, the parameters of a standard flat plate collector, with a single glass cover and aluminum absorber are used. To simulate the performance of a thermochromic solar collector, only the absorptance and the emittance of the standard selective absorber coating ($\alpha_{sol}$ = 0.95; $\varepsilon_{th}$ = 0.05) are exchanged with those of absorber A1 and A2. The collector efficiency is determined based on the inlet fluid temperature, $T_{in}$ and collector aperture area. The complete list of used collector parameters and test conditions is given in Annex 2.

As expected, the efficiency of the standard collector is constantly decreasing with increasing fluid temperature (Figure 6.12). The thermochromic collectors exhibit a similar trend, with a small drop in efficiency at the phase transition temperature where the absorber emittance suddenly increases – at 66°C for the collector based on A1 absorber and ≈73°C for the collector with the A2 absorber.

The predicted stagnation temperature for the standard flat plate collector is 177°C. In comparison, both thermochromic collectors are expected to have stagnation temperatures of 152°C (Table 6.4). The 25°C reduction in stagnation temperature is mostly due to the remarkable thermal emittance modulation, $\Delta\varepsilon$ = 0.31 for absorber A1 and $\Delta\varepsilon$ = 0.33 for absorber A2, and it happens in spite of the increasing solar absorptance over the thermochromic transition. Another contributing factor, is the slightly lower $\alpha_{sol}$ of the thermochromic absorber in the high temperature state compared to that of a standard absorber. At normal operating temperatures, the $\alpha_{sol}$ of the thermochromic absorber is even more modest and considerably limits the collector performance. At low temperatures, higher $\alpha_{sol}$ is desired.

Nonetheless, the important reduction of 25°C, shortens significantly the duration of stagnation conditions. Glycol degradation is also hindered, bringing about important reductions in maintenance costs. Moreover, at stagnation temperatures only 2°C lower, around 150°C and at 2 – 2.5 bar overpressure typically present in such systems, evaporation of the heat transfer fluid in the collector loops could be entirely avoided.
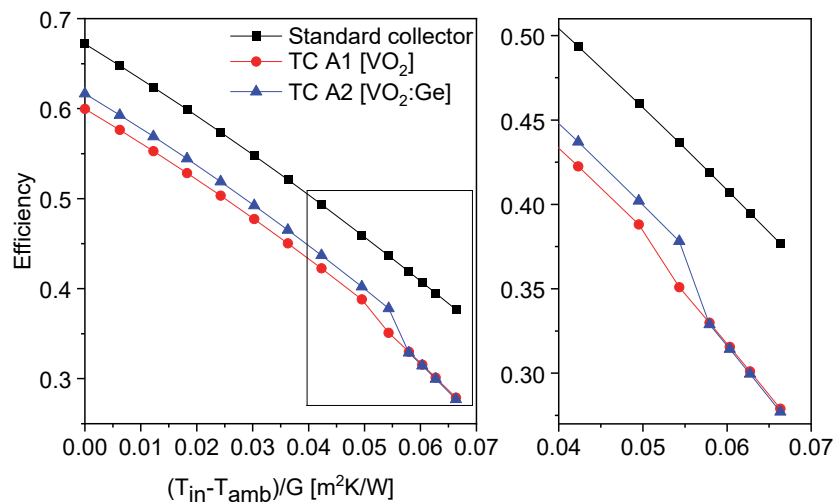


Figure 6.12. Simulated efficiency curves of the three flat plate collectors considered: standard collector, thermochromic collector based on A1 type absorber (with $VO_2$) and thermochromic collector based on A2 type absorber (with $VO_2$:Ge). The collector efficiency is plotted against the ratio between the temperature difference of the inlet fluid temperature, $T_{in}$ and ambient temperature, $T_{amb}$ and the incident solar radiation, G.

Table 6.4. Simulated collector stagnation temperatures for the different absorber types considered.

| Absorber type | Standard selective | Thermochromic A1 [$VO_2$] | Thermochromic A2 [$VO_2$:Ge] |
|---|---|---|---|
| $T_{stagnation}$ [°C] | 177 | 152 | 152 |

Summary

Solar absorber coatings combining thermochromic Ge doped $VO_2$ with high oxidation resistant $CuCoMnO_x$ spinel absorber have been deposited by magnetron sputtering.

The deposited spinel is porous of nanocrystalline nature with grains ranging from 5 to 10 nm in size (XRD, STM) that form agglomerates of ≈30 - 70 nm (SEM). In-line UPS and XPS spectra of $CuCoMnO_x$ spinel are reported here for the first time. XPS and XRD results are congruent and indicate the successful formation of the spinel phase. However, the presence of CuO has also been corroborated by both characterization methods. Therefore, instead of phase pure $CuCoMnO_x$ spinel, a spinel-CuO phase mixture is observed, but bulk and surface stoichiometry seem to differ significantly. XPS quantification suggests an important CuO surface enrichment with the same order of magnitude of Cu atoms bonded in the $CuCoMnO_4$ and CuO structures, while in the bulk the spinel is dominating (only small CuO peaks in the XRD spectrum).

For pure spinel films the substrate temperature during deposition should be adjusted. High temperatures are necessary to form crystalline spinel thin films and we show that at 240°C substrate temperature the spinel structure is not yet formed. However, literature indicates that phase separation and CuO formation occurs above 400°C. Therefore, for single phase $CuCoMnO_x$ spinel films, the process window between 240°C and 400°C substrate temperatures might be of interest.

The measured reflectance curves of the pure and Ge doped $VO_2$ based absorbers are rather similar. The doped $VO_2$ based absorber, A2 outperforms the emittance values reached by absorber A1 by 0.04 in the high temperature state and 0.02 in total emittance modulation. However, these comparable values suggest, that in the case of limited Ge doping as in the present study, the n and k optical constants of $VO_2$:Ge are fairly close to those of pure $VO_2$. Hence, it is adequate to use the latter for the simulation of $VO_2$:Ge based multilayer coatings. It is interesting to see if this holds true also for heavily doped samples as required for reaching high switching temperatures of above 95°C.

For the $VO_2$:Ge based thermochromic absorber, the measured solar absorptance and thermal emittance values of 0.87 and 0.11 in the cold state and 0.92 and 0.44 in the hot state are very encouraging. The deposited thermochromic absorbers exhibit a switch in both α and ε, however, from the perspective of overheating prevention, the switch in α occurs in the wrong direction as it is increasing with the temperature. This is mainly due to the presence of a reflectance peak around 1.8 and 2 μm wavelength in the room temperature spectra of the pure and Ge doped based absorbers, respectively, and its disappearance when measured at 100°C. Efforts should be made to reduce this peak and it might be resolved by novel multi-layered designs.

The strong emittance modulation, Δε of up to 0.33, leads to prospective thermochromic collector stagnation temperatures of 152°C. That is 25°C lower than for a standard collector and it is sufficient to largely limit the glycol degradation and the evaporation of the heat transfer fluid in the collector system.

The proposed film thicknesses for the multilayered absorber are realistic in range and are reasonable for industrial adoptation. Furthermore, as all involved layers are oxide based, a very high stability of the solar absorber coating in air is expected. However, aging test are needed to confirm the high durability potential of thermochromic and spinel oxide based selective absorbers.

# 6.3    Improved thermochromic absorber designs

Visible color change of $VO_2$ and $VO_2$:Ge thin films on certain Al substrates already hinted towards a switching solar absorptance, which was ignored in a first approximation as the optical changes of vanadium dioxides are known to be the strongest in the near- and mid-infrared spectral range. However, the solar absorptance modulation turns out to be rather significant and, unfavourably for the envisaged solar absorber application, it increases with temperature by 0.07 for a ≈210 nm $VO_2$ based absorber measured at 100°C.

Despite the strong emittance modulation of the thermochromic absorbers discussed, the simultaneous increase in solar absorptance over the thermochromic transition renders the overall decrease in collector efficiency underwhelming.

Would the solar absorptance stay constant, a much more important cutback in efficiency would be expected. Let us assume two solar absorbers, A3 and A4, with a constant solar absorptance of 0.84 and 0.95, respectively, and undergoing the same thermal emittance modulation as measured for absorber A1 (Table 6.5). The corresponding collector efficiency curves and stagnation temperatures are determined (see Figure 6.13 and Table 6.6). Throughout this chapter, absorber A1, the first thermochromic $VO_2$ based absorber deposited, will be used for comparison with the new and improved absorber designs proposed.

In normal operating conditions, absorbers A1 and A3 yield identical collector efficiencies that are lower than that of a standard collector, due to the somewhat poorer αsol and εth of 0.84 and 0.09. Above the phase transition, the efficiency of collector A3 is decreasing more decidedly as the emittance modulation occurs in the absence of an increase in solar absorptance. The lowest stagnation temperature of 147°C is predicted and at this temperature the evaporation of the heat transfer medium and glycol degradation is suppressed.

Assuming higher αsol values of 0.95, as customary in standard absorbers, the simulated efficiencies at normal operating temperatures are more adequate and considerably outperform the efficiency of collector A1. With a constant αsol, a favourable Tstagnation of 155°C, more than 20°C lower than that of a standard collector, would result based solely on the thermal emittance modulation.

Table 6.5. Measured solar absorptance and thermal emittance of the multilayered absorber coating A1 [$VO_2$] and assumed values for two absorbers, A3 and A4, of constant $\alpha_{sol}$.

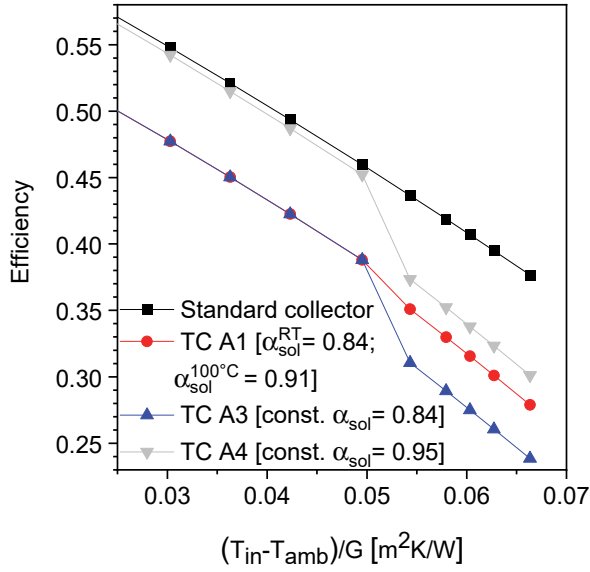|  | $\alpha_{sol}$ | | $\varepsilon_{th}$ | | Δα | Δε | ΔTot |
|---|---|---|---|---|---|---|---|
|  | $T_{room}$ | T = 100°C | $T_{room}$ | T = 100°C |  |  |  |
| Measured A1 | 0.84 | 0.91 | 0.09 | 0.40 | -0.07 | 0.31 | 0.24 |
| Scenario A3 | 0.84 | 0.84 | 0.09 | 0.40 | 0 | 0.31 | 0.31 |
| Scenario A4 | 0.95 | 0.95 | 0.09 | 0.40 | 0 | 0.31 | 0.31 |

Figure 6.13. Efficiency curves of a standard flat plate collector and thermochromic collectors based on absorber A1 (measured), A3 and A4 (assumed).

Table 6.6. Calculated stagnation temperatures for flat plate collectors with different absorbers: standard selective, thermochromic A1 (measured) and thermochromic A3 and A4 (assumed scenarios).

| Absorber type | $T_{stagnation}$ [°C] |
|---|---|
| Standard selective | 177 |
| Thermochromic A1 (measured) | 152 |
| Thermochromic A3 (assumed) | 147 |
| Thermochromic A4 (assumed) | 155 |

However, for best performance in normal operating conditions and enhanced overheating protection, a switch from high to low $\alpha_{sol}$ accompanying the large thermal emittance modulation is desired. In the following, new multilayered designs with improved absorptance in the low temperature state and lower absorptance in the high temperature state are proposed.

Optimization of the multilayered thin film stack is performed with the aim of minimizing the reflection peak around 1.8 µm in the low temperature state and maximizing the near-IR reflectance in the high temperature state. Both the black $CuCoMnO_x$ spinel oxide and the $VO_2$ are not sufficiently absorbing in the near-IR spectral range. The integration of a layer with higher n and k constants between the high index metal substrate and thermochromic oxide layer is proposed. Metal nitride films are commonly used in the solar absorber industry and exhibit appropriate optical constants for the envisaged graded refracting index absorbers. In a first proof of concept, thermochromic absorber designs based on $Ti_{1-x}Al_xN$ layers, where x = 0.14 and 0.38, as described in [Schüler, 2001b] are simulated.

Three examples of multilayered coating designs are shown in Figure 6.14 and the spectral reflectance of coating no.1 is displayed, for both room and high temperature states, in Figure 6.15. The NIR reflectance peak is present in both states, however, at low temperatures it is found at higher wavelengths, above 2 µm, whereas at high temperatures it shifts to lower wavelengths peaking around 1.2 µm. This shift of the reflectance peak leads to a decrease of $\alpha_{sol}$ in the order of 3 – 5% for all proposed designs, while thermal emittances are expected to increase by 16 – 18 %. The total modulation over the thermochromic transition is above 21% for all proposed coatings (Table 6.7). These are the first reported multilayered thermochromic coating designs with simultaneously decreasing $\alpha_{sol}$ and increasing $\varepsilon_{th.}$
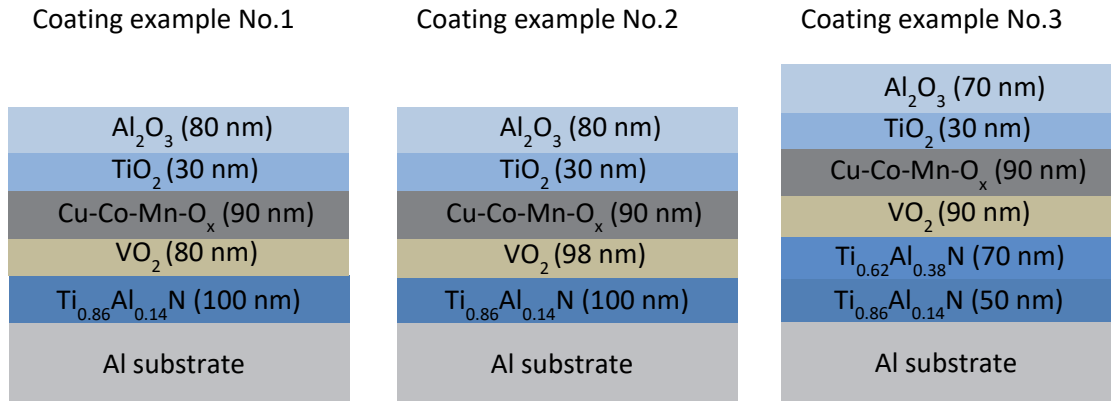
Coating example No.1

| Al$_2$O$_3$ (80 nm) |
| TiO$_2$ (30 nm) |
| Cu-Co-Mn-O$_x$ (90 nm) |
| VO$_2$ (80 nm) |
| Ti$_{0.86}$Al$_{0.14}$N (100 nm) |
| Al substrate |

Coating example No.2

| Al$_2$O$_3$ (80 nm) |
| TiO$_2$ (30 nm) |
| Cu-Co-Mn-O$_x$ (90 nm) |
| VO$_2$ (98 nm) |
| Ti$_{0.86}$Al$_{0.14}$N (100 nm) |
| Al substrate |

Coating example No.3

| Al$_2$O$_3$ (70 nm) |
| TiO$_2$ (30 nm) |
| Cu-Co-Mn-O$_x$ (90 nm) |
| VO$_2$ (90 nm) |
| Ti$_{0.62}$Al$_{0.38}$N (70 nm) |
| Ti$_{0.86}$Al$_{0.14}$N (50 nm) |
| Al substrate |

Figure 6.14. Examples of multilayered thermochromic absorber designs with negative $\alpha_{sol}$ modulation over the thermocrhomic phase transition.

Table 6.7. Simulated solar absorptance, $\alpha_{sol}$ and thermal emittance, $\varepsilon_{th}$ values of the proposed multi-layered coating designs.

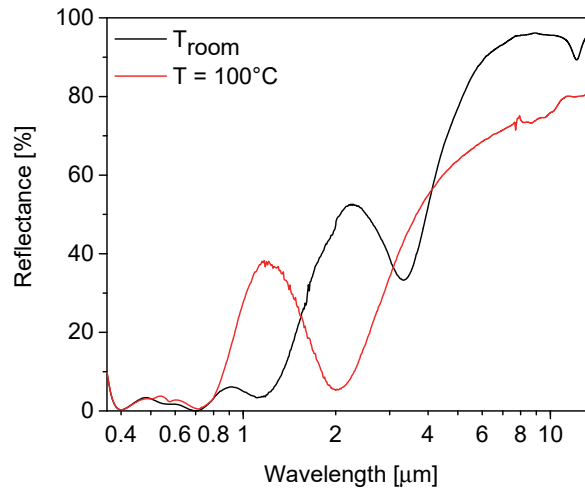| Coating example | $\alpha_{cold}$ [%] | $\alpha_{hot}$ [%] | $\varepsilon_{cold}$ [%] | $\varepsilon_{hot}$ [%] | $\Delta\alpha$ [%] | $\Delta\varepsilon$ [%] | $\Delta$Tot [%] |
|---|---|---|---|---|---|---|---|
| No.1 | 93.7 | 89.6 | 9.0 | 26.6 | 4.1 | 17.6 | 21.7 |
| No.2 | 93.9 | 89.0 | 10.6 | 27.0 | 4.9 | 16.4 | 21.3 |
| No.3 | 92.2 | 89.2 | 10.9 | 28.3 | 3.0 | 17.4 | 21.4 |



Figure 6.15. Simulated reflectance spectra for the proposed multi-layered coating design no.1, both below and above the thermochromic transition.

In the framework of a collaboration with a solar absorber manufacturer, the integration of thermochromic layers into the commercial solar absorber coating is targeted. The industrial absorber is based on a TiAlSiN selective layer, that is similar to the TiAlN films proposed previously, and it typically consists of a multi-channel Al substrate//80 nm TiAlSiN//30 nmTiAlSiON//100 nm SiO$_2$.

The optical constants of the TiAlSiN, TiAlSiON and SiO$_2$ layers, in the 250 – 2500 nm range, have been published elsewhere [Rebouta, 2012]. For the same spectral range, the optical constants n and k and film thicknesses of pure and Ge doped VO$_2$ layers have been determined (Figure 6.16) by fitting of the reflectance and transmittance spectra in the SCOUT software [Theiss,2012]. Details about the assumed models and their adaptation can be found in literature [Theiss,2012; Rebouta, 2012]. As expected, the extinction

coefficients of the doped film are somewhat lower than for the pure VO$_2$ film. Nonetheless, the results confirm that for limited Ge content, as is the case for 5 at.% Ge in the VO$_2$ film, pure and alloyed films have comparable optical constants allowing for rather adequate multilayer simulations of VO$_2$:Ge containing coatings even when only optical data of pure VO$_2$ films are available.
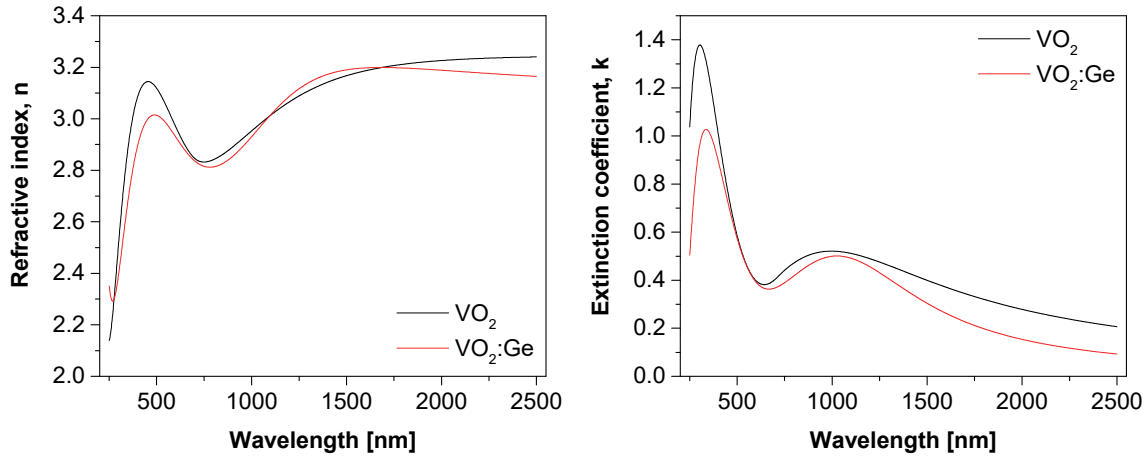


Figure 6.16. Refractive index, n and extinction coefficient, k determined in the 250 – 2500 nm spectral range for pure and Ge doped VO$_2$ layers at room temperature.

Simulations based on these optical constants reveal that VO$_2$ or VO$_2$:Ge can efficiently replace the TiAlSiON, while no adjustments to the first deposited metal nitride layer are necessary. Thinner the thermochromic layer, higher is the expected $\alpha_{sol}$. On the other hand, sputtered thermochromic films need a minimum thickness of ≈30 nm to exhibit switching behavior, with thicker films showing more important emittance modulation. It is found that a 50 nm VO$_2$ or VO$_2$:Ge ensures a satisfactory emittance increase of $\Delta\varepsilon_{th} > 0.2$, while keeping the $\alpha_{sol}$ above 0.93.

Hence, an absorber A5, based on an Al substrate//80 nm TiAlSiN//50 nm VO$_2$//100 nm SiO$_2$, is proposed (Figure 6.17). The spectral reflectance of the absorber at room temperature shows no peak in the near-infrared and exhibits an absorption edge above 2 μm. At 100°C, the absorption edge shifts to lower wavelengths by roughly 1 μm, leading to lower $\alpha_{sol}$ values than in the low temperature state.

The corresponding optical properties, summarized in Table 6.8, are used to predict the performance of the new thermochromic collector (Figure 6.18). The determined $T_{stagnation}$ of 156°C, is more than 20°C lower than the stagnation temperature of standard collectors, while very similar efficiencies are achieved in normal operating conditions, e.g. $\eta_{max\_standard}$ = 0.67 and $\eta_{max\_thermochromicA5}$ = 0.66. In contrast, the first thermochromic VO$_2$ based absorber, A1 yielded considerably lower maximum collector efficiencies, $\eta_{max}$ of only 0.6 (Table 6.9).

Table 6.8. Simulated solar absorptance, $\alpha_{sol}$ and thermal emittance, $\varepsilon_{th}$ values of the proposed absorber coating, A5.

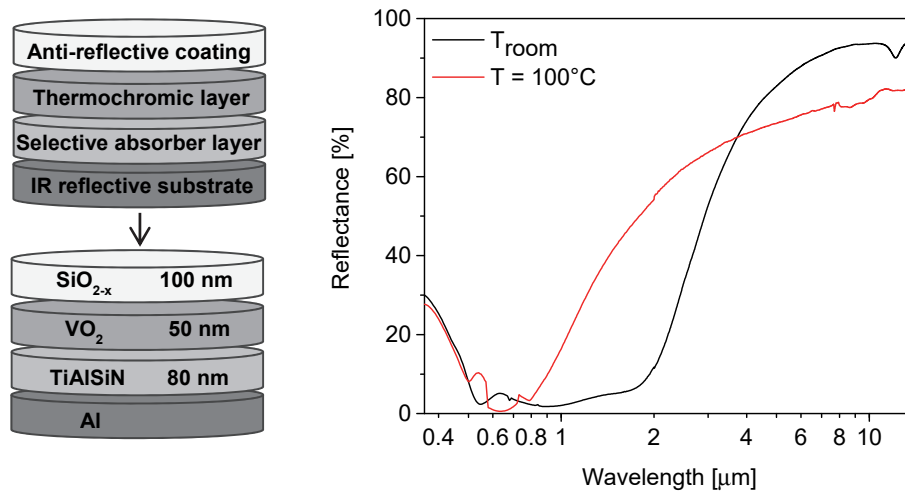| Coating | $\alpha_{cold}$ [%] | $\alpha_{hot}$ [%] | $\varepsilon_{cold}$ [%] | $\varepsilon_{hot}$ [%] | $\Delta\alpha$ [%] | $\Delta\varepsilon$ [%] | $\Delta$Tot [%] |
|---|---|---|---|---|---|---|---|
| Absorber A5 | 93.4 | 84.8 | 9.4 | 21.6 | 8.6 | 12.2 | 20.8 |

Figure 6.17. Schematic of the multilayered solar absorber coating, A5 with proposed film thicknesses and the corresponding reflectance curves below and above the thermochromic transition temperature, at $T_{room}$ and at T = 100°C.



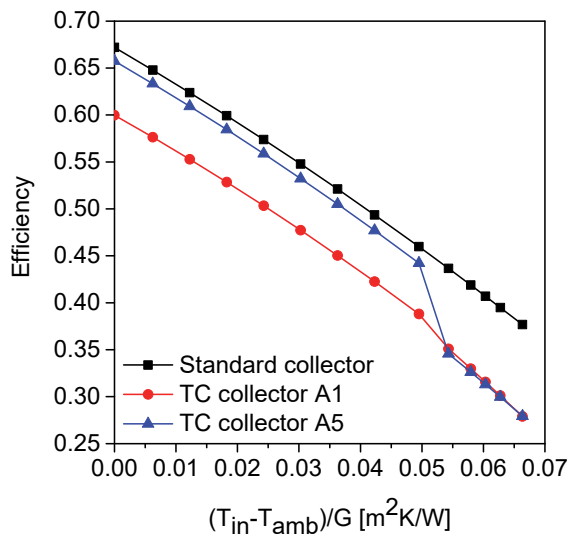Table 6.9. Predicted collector stagnation temperatures and maximum efficiencies for the three absorber types: standard selective, thermochromic A1 and A5.

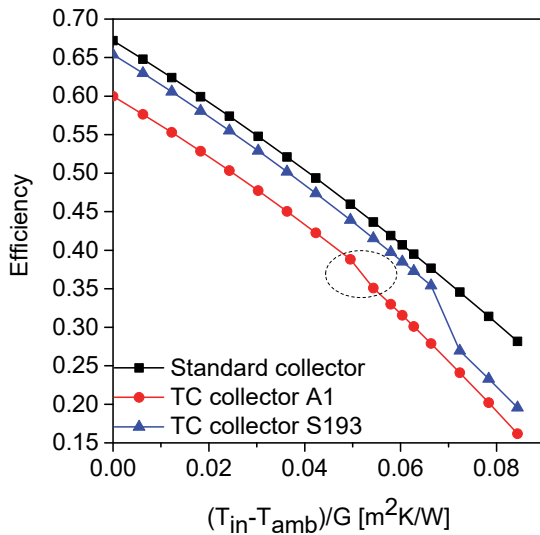| Absorber type | $T_{stagnation}$ [°C] | $\eta_{max}$ |
|---|---|---|
| Standard selective | 177 | 0.67 |
| Thermochromic A1 | 152 | 0.60 |
| Thermochromic A5 | 156 | 0.66 |

Figure 6.18. Thermal efficiency curves simulated for a standard collector, a thermochromic collector based on absorber A1 (increasing $\varepsilon_{th}$ and $\alpha_{sol}$) and A5 (increasing $\varepsilon_{th}$, but decreasing $\alpha_{sol}$).

Based on the very promising simulated results, the deposition of the proposed design is attempted. The first sputtered layer of TiAlSiN is measured to be only 68 nm thick instead of 80 nm, therefore, the simulation is adjusted for the new thickness. The newly determined optical constants are listed in Table 6.10 . The differences are small with only slightly lower αsol and εth reached, due to the thinner TiAlSiN layer.

Then, a Al//68nm TiAlSiN//50nm VO$_2$:Ge//100 nm SiO$_2$ multilayer is sputtered. Additionally, coatings with ≈60 nm, ≈65 nm and ≈130 nm VO$_2$:Ge are also sputtered. Measured $\alpha_{sol}$ and $\varepsilon_{th}$ are given in Table 6.11.

The first thermochromic multilayered absorber with increasing thermal emittance and decreasing solar absorptance, predicted by thin film simulations, has been successfully demonstrated experimentally. For thin, ≈50 – 60 nm VO$_2$:Ge films the switch in $\alpha_{sol}$ occurs in the right direction: from high to low over the thermochromic phase transition. However, for thicker 65 - 130 nm VO$_2$:Ge films, this trend is reversed and

the solar absorptance, $\alpha_{sol}$ increases with the temperature. Therefore, a precise control of the thicknesses is required.

Table 6.10. Determined $\alpha_{sol}$ and $\varepsilon_{th}$ of the simulated coating designs after adjusting the TiAlSiN thickness to the experimentally measured value.

| Coating [Simulated] | $\alpha_{cold}$ [%] | $\alpha_{hot}$ [%] | $\varepsilon_{cold}$ [%] | $\varepsilon_{hot}$ [%] | $\Delta\alpha$ [%] | $\Delta\varepsilon$ [%] | $\Delta$Tot [%] |
|---|---|---|---|---|---|---|---|
| Al//68nm TiAlSiN//50nm VO$_2$//100nm SiO$_2$ | 92.6 | 84.9 | 7.9 | 20.0 | 7.7 | 12.1 | 19.8 |

Table 6.11. Experimentally measured $\alpha_{sol}$ and $\varepsilon_{th}$ of the deposited multilayered absorber coatings.

| Sample [Deposited] | $\alpha_{cold}$ [%] | $\alpha_{hot}$ [%] | $\varepsilon_{cold}$ [%] | $\varepsilon_{hot}$ [%] | $\Delta\alpha$ [%] | $\Delta\varepsilon$ [%] | $\Delta$Tot [%] |
|---|---|---|---|---|---|---|---|
| S19 ($\approx$130 nm VO$_2$:Ge) | 89.5 | 91.7 | 11.6 | 34.9 | -2.2 | 23.3 | 21.1 |
| S192 ($\approx$65 nm VO$_2$:Ge) | 91.2 | 91.6 | 9.5 | 28.6 | -0.4 | 19.1 | 18.7 |
| S10 ($\approx$60 nm VO$_2$:Ge) | 91.5 | 91.3 | 11 | 23 | 0.2 | 12 | 12.2 |
| S193 ($\approx$50 nm VO$_2$:Ge) | 92.6 | 90.5 | 8.5 | 25.1 | 2.1 | 16.6 | 18.7 |



Table 6.12. Predicted collector stagnation temperatures and maximum efficiencies for the three absorber types: standard selective, thermochromic A1 and S193.

| Absorber type | $T_{stagnation}$ [°C] | $\eta_{max}$ |
|---|---|---|
| Standard selective | 177 | 0.67 |
| Thermochromic A1 | 152 | 0.60 |
| Thermochromic S193 | 159 | 0.65 |

Figure 6.19. Thermal efficiency curves simulated for a standard collector, a thermochromic collector based on absorber A1 (increasing $\varepsilon_{th}$ and $\alpha_{sol}$) and S193 (increasing $\varepsilon_{th}$, but decreasing $\alpha_{sol}$).

The n and k of VO$_2$:Ge are available only between 0.36 – 2.5 µm and only for the room temperature state. Therefore, in the case of $\alpha_{cold}$, identical measured and simulated values are compelling ($\alpha_{cold\_simulated}$ = $\alpha_{cold\_measured}$ = 92.6%). For $\alpha_{hot}$, $\varepsilon_{cold}$ and $\varepsilon_{hot}$, the simulation is based on the optical constants of pure VO$_2$ films, therefore, larger deviations between predicted and measured values are expected. Because Ge doping mainly improves the radiative properties of the film in the high temperature state, the largest differences between simulated and measured values are observed for $\varepsilon_{hot}$. For the sample with $\approx$60 nm VO$_2$:Ge, the thermal emittance modulation is surprisingly low, and the $\varepsilon_{cold}$ is rather high suggesting a likely impure VO$_2$:Ge phase. As expected the thermal emittance modulation is increasing with thermochromic layer thickness, but on the expense of inferior solar absorptance values at normal operating temperatures.

Based on the measured optical properties of absorber S193, with 50 nm $VO_2$:Ge, the predicted collector stagnation temperature is 159°C and maximum collector efficiency, $\eta_{max}$ = 0.65 (Table 6.12). This compares favourably to collectors with standard selective absorbers ($T_{stagnation}$ = 177°C, $\eta_{max}$ = 0.67) and it is closely matching the simulated collector performance for the very similar absorber A5 (Al//80nm TiAlSiN//50nm $VO_2$:Ge//100 nm $SiO_2$).

The sudden efficiency drop is expected at 81°C which is the phase transition temperature of the $VO_2$:Ge films with 5 at.% Ge. This is a big step forward from the performance of a collector with absorber A1, the first deposited thermochromic absorber coating. It is recalled that absorber A1 yielded a $\alpha_{cold}$ = 0.84, $\alpha_{hot}$ = 0.91, $\varepsilon_{cold}$ =0.09 and $\varepsilon_{cold}$ = 0.4 with a total modulation of $\Delta Tot$ = 0.24. This is still larger than the $\Delta Tot$ < 0.19 determined for absorber S193. Yet, the latter outperforms the former per a large margin (see Figure 6.19). This is due to the so-called performance criteria (PC) of a solar absorber coating being expressed by $\alpha_{sol}$ - $0.5\varepsilon_{th}$ according to ISO 22975-3. The expression reflects that the absorber performance is primarily dependent on the solar absorptance, weighing twice as much as the thermal emittance.

Summary

Multilayered absorber coatings with increasing $\varepsilon_{th}$ and decreasing $\alpha_{sol}$ when heated above the thermochromic transition temperature have been simulated.

The improved designs are based on the inclusion of a metal nitride layer (e.g. $Ti_{1-x}Al_xN$) between the Al substrate and the thermochromic thin film. The first experimental $\varepsilon_{th}$-increasing and $\alpha_{sol}$-decreasing thermochromic absorber has been successfully demonstrated on an Al//68nm TiAlSiN//50nm $VO_2$:Ge//100 nm $SiO_2$ multilayer.

The improved thermochromic absorber could reduce the stagnation temperature of a thermal collector system to 159°C (compared to the 177°C simulated for the standard one), while keeping a high maximum collector efficiency.

# 6.4   Aging of thermochromic absorbers

The aging properties and environmental stability of the improved thermochromic absorbers have been evaluated. Samples S19, S10 and S193 are selected to undergo accelerated aging tests according to the ISO 22975-3:2014 standard. Samples S19 and S10 are tested in the original sample size. S193 is cut in four identical, smaller pieces and, therefore, a smaller sample with two newly exposed cross-sections is selected for aging.

The samples are tested under the following conditions:

S19: aging for 600h at 300°C in dry air (measured before and after aging);

S10: aging for 600h at 40°C and 100% relative humidity (measured before and after aging);

S193: aging for 600h at 278°C in dry air (measured at each aging step: 0 h, 18 h, 36 h, 75 h, 150 h, 300 h and 600 h).

The detailed results of the accelerated aging tests are displayed for each sample in the corresponding table.

Table 6.13. Accelerated aging test in dry air during 600 h at 300°C.

| Sample | $\alpha_{cold}$ [%] | $\alpha_{hot}$ [%] | $\varepsilon_{cold}$ [%] | $\varepsilon_{hot}$ [%] | $\Delta\alpha$ [%] | $\Delta\varepsilon$ [%] | PC |
|---|---|---|---|---|---|---|---|
| S19 at t = 0 h | 89.5 | 91.7 | 11.6 | 34.9 | -2.2 | 23.3 | |
| S19 at t = 600 h | 91.5 | 96.6 | 11.8 | 35.3 | -5.1 | 23.5 | -1.9 |

Table 6.14. Accelerated aging test at 100% relative humidity and at 40°C during 600 h.

| Sample | $\alpha_{cold}$ [%] | $\alpha_{hot}$ [%] | $\varepsilon_{cold}$ [%] | $\varepsilon_{hot}$ [%] | $\Delta\alpha$ [%] | $\Delta\varepsilon$ [%] | PC |
|---|---|---|---|---|---|---|---|
| S10 at t = 0 h | 91.5 | 91.3 | 11 | 23 | 0.2 | 12 | |
| S10 at t = 600 h | 88.1 | 89.2 | 13.7 | 33 | -1.1 | 19.3 | 4.8 |

Table 6.15. Accelerated aging test in dry air during 600 h at 278°C.

| Sample | $\alpha_{cold}$ [%] | $\alpha_{hot}$ [%] | $\varepsilon_{cold}$ [%] | $\varepsilon_{hot}$ [%] | $\Delta\alpha$ [%] | $\Delta\varepsilon$ [%] | PC |
|---|---|---|---|---|---|---|---|
| S193 at t = 0 h | 93.2 | 91 | 8.1 | 23.9 | 2.2 | 15.8 | |
| S193 at t = 18 h | 93.4 | 91.4 | 9.4 | 24.2 | 2 | 14.8 | 0.45 |
| S193 at t = 36 h | 93.2 | 92.2 | 8.4 | 21.6 | 1 | 13.2 | 0.15 |
| S193 at t = 75 h | 93.8 | 93.3 | 8.9 | 21.6 | 0.5 | 12.7 | -0.2 |
| S193 at t = 150 h | 93.8 | 93.9 | 8.2 | 18.6 | -0.1 | 10.4 | -0.55 |
| S193 at t = 300 h | 94.7 | 94.9 | 9.2 | 18.0 | -0.2 | 8.8 | -0.95 |
| S193 at t = 600 h | 95.3 | 95.9 | 9.2 | 16.9 | -0.6 | 7.7 | -1.55 |

Full-sized samples S19 and S10 have shown no degradation of the thermochromic switch with aging. On the contrary, the thermal emittance of the sample aged in humid conditions (S10), while did slightly increase at room temperature (< 3% increase), it also improved by a remarkable 10% in the high temperature state resulting in an even larger modulation of the thermal emittance. The solar absorptance decreased only by ≈3% during the accelerated aging. The sample aged in dry air (S19), showed an improvement in solar absorptance at normal operating conditions by 2%, while maintaining the same thermal emittance.

The smaller sample cut from S193 and aged in dry air, exhibits a remarkable stability in the optical properties measured at room temperature, with the beneficial, increase in solar absorptance also present. Note that the optical properties of the smaller, cut S193 sample have been remeasured and, therefore, the initial values are slightly different from the those reported for the larger sample at t= 0 h (Table 6.11). Nonetheless, the values are similar and within the measurement error.

Concerning the thermochromic modulation, the sample exhibits a steady decrease at each aging step. In the high temperature state, the solar absorptance increases, while the thermal emittance decreases gradually. Hence, the overall thermochromic modulation is significantly limited. Deterioration of vanadium dioxide based thermochromic films in air, due to exposed surfaces and interfaces has been already reported in literature [Chang, 2019].

After cutting, sample S193 has two exposed cross-sections through which the $VO_2$ film is readily oxidized to the thermodynamically stable $V_2O_5$. On the other hand, samples S19 and S10 covered by the undamaged antireflective and oxidation barrier top coating, show no signs of degradation of the thermochromic prop-

erties. These findings confirm the importance of exposed VO$_2$ surfaces, but also prove that, AR coatings – if not damaged – are sufficient to adequately protect the thermochromic layer from oxidation.

Finally, full-sized samples have successfully passed the accelerated aging tests in dry and humid conditions alike. The requirements of a minimum service life of 25 years have been met according to the ISO 22975-3:2014 standard: performance criteria, PC < 5%.

# Chapter 7    Advanced thermochromic concepts

The previous chapters detailed the deposition of pure and Ge doped VO₂ thermochromic thin films and discussed their integration into multilayered solar absorber coatings. Here, several novel, advanced thermochromic concepts are proposed, based on the developed thermochromic thin films.

The concept of Fabry-Pérot interferometers is adapted to multilayered thermochromic thin film designs and leads to a much enhanced thermal emittance modulation between the phases below and above the critical phase transition temperature. Other novel approaches concern the nanostructuring of thermochromic solar absorber coatings. In particular, spinel oxide nanoneedle deposition and nanoimprint lithography on thermochromic VO₂ based underlayers have been investigated. Nanostructuring improves the solar absorptance significantly, while the temperature dependent thermal emittance is successfully maintained.

## 7.1    Enhanced emittance switch in Fabry-Pérot inspired multilayers

A Fabry-Pérot interferometer consists of two parallel mirrors separated by a spacer of a given thickness d. In multilayered thin film coatings, the spacer is usually a dielectric layer. The light entering the Fabry-Pérot cavity is reflected multiple times between the mirror surfaces before exiting the structure (Figure 7.1). The reflected beams interfere and only the ones that interfere constructively are transmitted. The wavelength of the radiation passing through the Fabry-Pérot filter depends on the refractive index and thickness of the spacer. Due to this wavelength selectivity, reflection interference filters can be designed to exhibit enhanced optical reflection or transmission over the desired wavelengths or spectral bands.
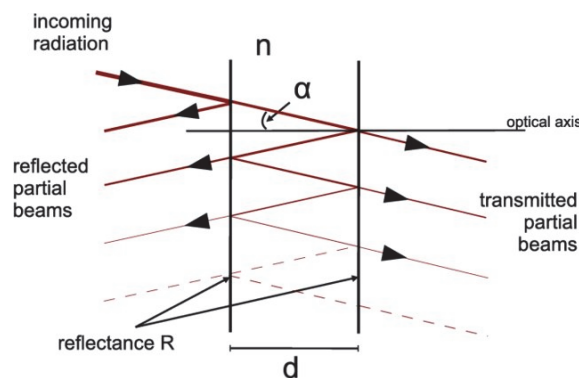


Figure 7.1. Fabry-Pérot interferometer with the two highly reflecting plates separated by a distance d constituting a resonating cavity where the multiple beam interference occurs. Reproduced with permission from [Kuhn, 2014].

Here, the Fabry-Pérot concept is adapted to thermochromic layers, which behave as dielectrics below and become metallic above the critical transition temperature. The aim is to maximize the thermal modulation of the thermochromic multilayered coatings, especially in the mid-infrared $7 - 10\ \mu m$ spectral range.

In literature, a similar concept has been discussed, where an emittance range of 0.49 was obtained across the semiconductor-to-metal transition for a VO$_2$ (≈30 nm)//SiO$_2$ (850 nm) stack deposited on Au substrate [Hendaoui, 2013]. Sun et al. report on further enhancement of the emittance modulation in a 80 nm Al//1200 nm SiO$_2$ spacer//50 nm VO$_2$ based structure with patterned thermochromic layer. This is due to plasmonic resonances in the thermochromic meta-surface [Sun, 2018]. Nonetheless, the thick SiO$_2$ spacer layer used in both approaches leads to a large absorption band around 8-10 µm, region of high importance in radiative applications.

Our optical simulations suggest that the mid-infrared absorption can be avoided by using TiO$_2$ as dielectric spacer layer. A multilayered interference coating based on an Al substrate//650 nm TiO$_2$ spacer//30 nm VO$_2$//650 nm TiO$_2$ spacer is proposed according to Figure 7.2.a.

A surprisingly large emittance modulation is observed around 8 µm wavelength. The total thermal emittance, calculated over the 2.5 – 10 µm range, changes remarkably from $\varepsilon_{th}$ = 0.18 below the transition temperature, to a quasi-blackbody behaviour with $\varepsilon_{th}$ = 0.97 above $T_C$. The magnitude of the emittance modulation is striking for such a thin thermochromic layer. In comparison, the same thickness of VO$_2$ on Al, without the spacer layer (Figure 7.2.b), switches negligibly from 0.01 to 0.02 in thermal emittance.

The thermal emittance values are estimated from the simulated reflectance values at normal incidence. The optical constants of the dielectric spacer – sputtered TiO$_2$ thin film – are determined by ellipsomety.
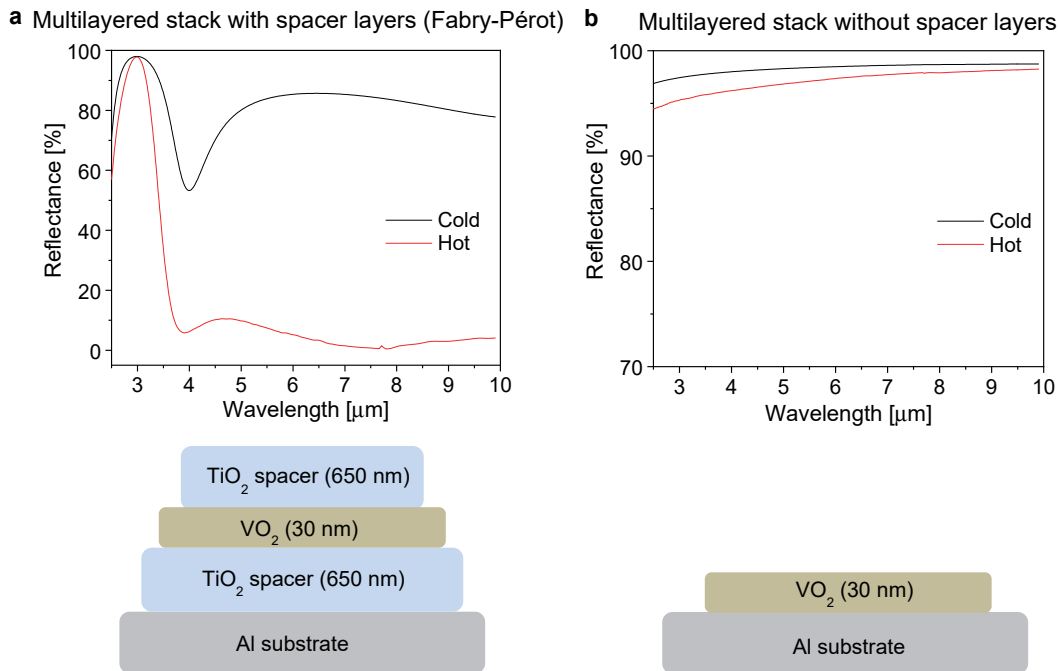


Figure 7.2. Schematic and simulated reflectance spectra of the a Fabry-Pérot inspired thermochromic multilayer design (a) and the reflectance spectra of a thermochromic layer of identical thickness, but without dielectric spacers (b).

The experimental validation of Fabry-Pérot inspired multilayers, with enhanced thermal emittance modulation, is attempted. However, the sputter rate of TiO$_2$ is rather low with 1.6 nm/min. The ensuing long deposition process could not be run in a stable mode. Subsequent arcing altered the optical properties of the deposited titanium oxide layer.

While the total thermal emittance of the multilayer increases from 0.44 to 0.73, the magnitude of the modulation is lower than expected and the overall spectral shape differs significantly from the simulated one (Figure 7.3).
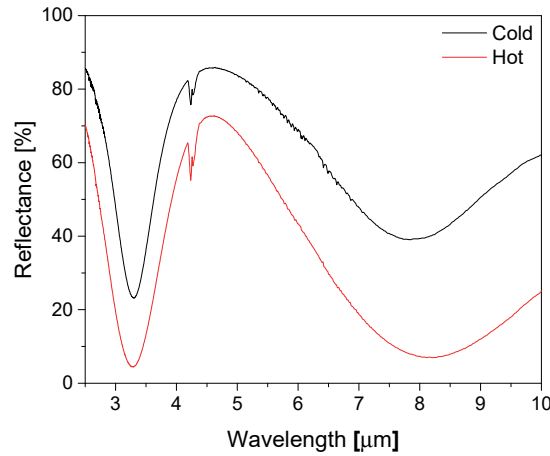


Figure 7.3. Measured reflectance spectra of the Al substrate//650 nm $TiO_2$//30 nm $VO_2$//650 nm $TiO_2$ structure.

As an alternative to $TiO_2$, $Ta_2O_5$ spacer layer has been proposed. The simulations have been adjusted to the new oxide type and the spectral measurements validate the applicability of the Fabry-Pérot concept to thermochromic multilayers. For an Al substrate//808 nm $Ta_2O_5$//30 nm $VO_2$//808 nm $Ta_2O_5$ interference coating, an excellent emittance modulation of ≈0.5 is recorded around the region of interest of 8 µm (Figure 7.4). About the same magnitude of total emittance modulation over the 2.5 – 10 µm spectral range is maintained, increasing from 0.34 to 0.84. Generally, the emittance modulation of a thermochromic layer is proportional to its thickness. Our simulations predict a $\Delta\varepsilon_{th}$ of only 0.01 for a 30 nm thin $VO_2$ deposited on an Al substrate. In the Fabry-Pérot inspired multilayer deposited here, the thermal modulation of a 30 nm thin thermochromic layer is 50-fold enhanced by inserting a dielectric spacer between the metallic, Al substrate and the thin thermochromic layer.
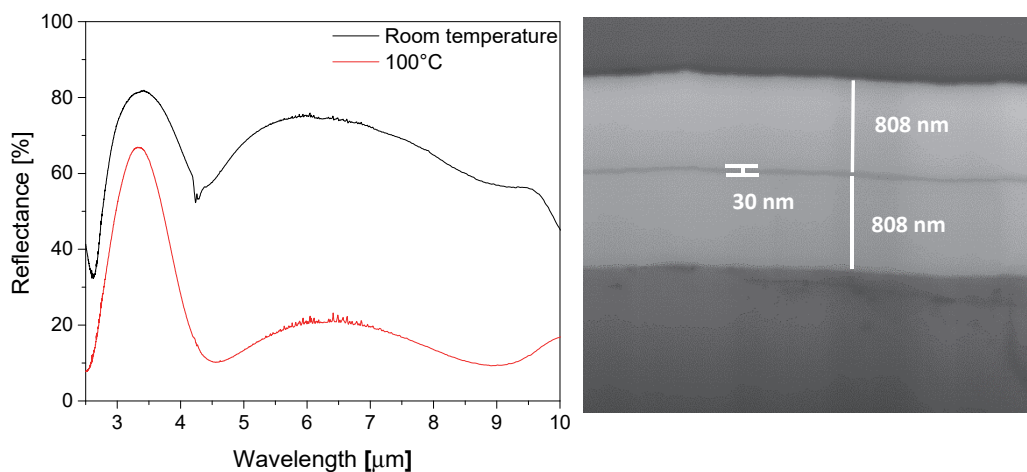


Figure 7.4. Reflectance of the Al substrate//808 nm $Ta_2O_5$//30 nm $VO_2$//808 nm $Ta_2O_5$ multilayer measured at room temperature and at 100°C (left). SEM image of the multilayer cross section with the determined layer thicknesses (right).

Thermochromic technologies have already impacted the building sector with the advance of vanadium dioxide based smart windows. An enhanced thermal switching could be promising for radiative cooling

applications and heat island mitigation in future cities (e.g. for thermal regulation of roofs or building enve-lopes).

## 7.2    Spinel oxide nanoneedles

Nanostructured absorbers with ultra-high solar absorptance, $\alpha_{sol}$ of over 0.99 have been reported recently [Rubin, 2019]. The impressive $\alpha_{sol}$ values are achieved through the growth of $Co_3O_4$ and $CuCo_2O_4$ nanon-eedles with a high aspect ratio, exhibiting an extreme light trapping effect. These refractory spinel oxide nanoneedles are suitable for high-temperature solar thermal applications.

A collaboration with the authors of this study, Dr. Elizabeth Rubin, Ka Man Chung and Prof. Renkun Chen from the Thermal Energy Materials and Physics (TEMP) Laboratory at the University of California San Diego, was set up. The motivation is to combine the ultra-high solar absorptance of the nanoneedles with the temperature dependent thermal emittance response of thermochromic films. Hence, a multilayer consist-ing of a metallic, reflecting substrate, a $VO_2$:Ge thermochromic film and the highly absorbing, black spinel $Co_3O_4$ nanoneedles is imagined.

The spinel nanoneedles are synthetized through a hydrothermal process described in detail in [Rubin, 2019] and briefly summarized here. $CoCl_2 \cdot 6H_2O$ and urea are dissolved in deionized water and placed in an auto-clave at 90°C along with the substrate. Then, cobalt-hydroxide-carbonate $[Co_x(OH)_y(CO_3)_z]$ nucleates on the substrate. As the nuclei grow, $CO_3^{2-}$ from the urea, drives the anisotropic growth of nanoneedles. Finally, in order to decompose the $[Co_x(OH)_y(CO_3)_z]$ to $Co_3O_4$, the sample is annealed at 300°C for 4 h. The schematic of the involved process steps is shown in Figure 7.5.
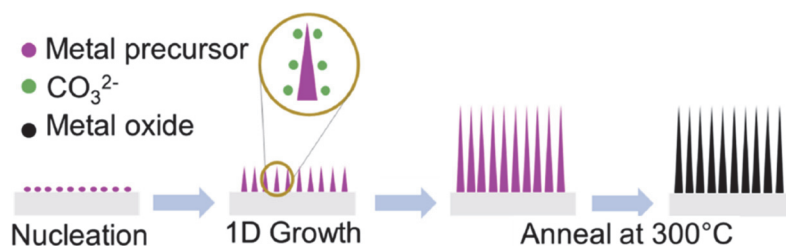


Figure 7.5. Schematic of the steps involved in the hydrothermal growth of spinel $Co_3O_4$ nanoneedles. Adapted from [Rubin, 2019].

The choice of substrate is limited by the high, ≈450°C deposition temperature of the first, thermochromic layer and by the highly alkaline environment necessary for growing the nanoneedles. In the published work, the black spinel nanoneedles were grown on Haynes 230 substrates, but it limits the spectral selectivity of the absorber due to its rather high thermal emittance of around 0.55. In this work, $VO_2$:Ge films were typi-cally grown on Al absorber sheets. However, a high pH environment of ≈13-14 pH can dissolve the Al sub-strate. Hence, a Si wafer with a 10 nm Ti and 50 nm Pt layer is selected as substrate, due to the low thermal emittance and high chemical stability of Pt. Pt is also thought to be stable at high temepratures. The Ti in-terlayer serves only to facilitate the adhesion between the Si and Pt.

A 280 nm thick $VO_2$:Ge film has been deposited on the selected Pt substrate. Visually, the sample appears hazed. SEM reveals two type of grains: the typical, ≈100 nm sharp edged grains and more rounded, over-grown grains, large enough to interfere with visible light leading to the hazed appearance (Figure 7.6.a).
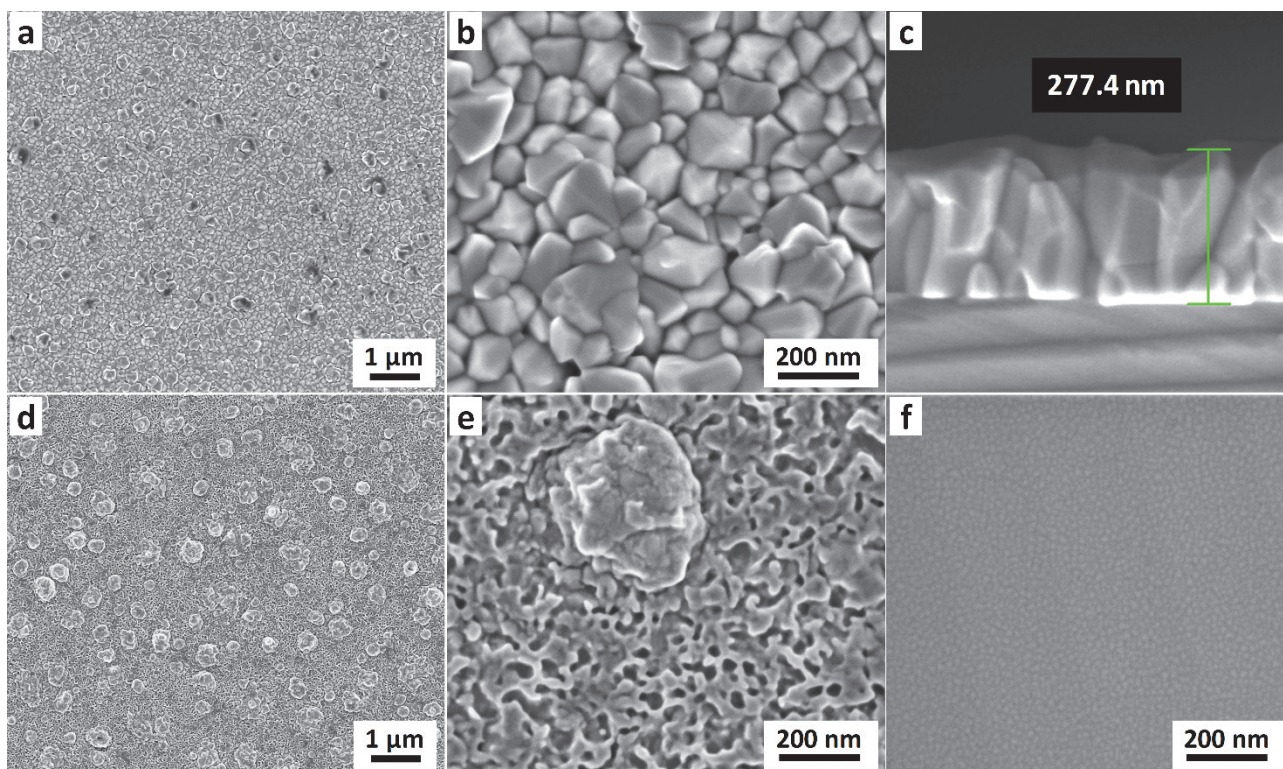
Figure 7.6. a-b) Plane view SEM image of sputtered $VO_2$:Ge surface at different magnifications. c) Cross-section of the $VO_2$:Ge film. d-e) Surface of the Pt substrate after being exposed to temperatures of 450°C. f) Surface of the as-received Pt surface.

This is growth type is unusual for thermochromic $VO_2$ films and it is suspected that it is the Pt substrate which undergoes changes during the heating step. As-received Pt coated Si substrates (Figure 7.6.f) are compared with ones exposed to the 450°C deposition temperature (Figure 7.6.d-e). Indeed, while the Pt coating on the as received substrate exhibits a completely smooth and flat surface, the substrate heated at 450°C shows plenty of large structures. It appears to have melted, de-wet the Si substrate and agglomerate resulting in a porous, rough surface when cooled.

This substrate roughening increases considerably the emittance of the substrate. Indeed, infrared spectral measurements confirm that the thermal emittance of the Pt substrate exposed to high temperatures increases to 0.2 compared with the 0.05 of the as-received substrates. For future experiments, other high-reflectivity substrate, stable at high deposition temperatures should be selected. Nonetheless, the growth of nanoneedles on the existing substrates has been carried out by our collaborators and the samples have been sent back for optical measurements.

Before the growth of $Co_3O_4$ nanoneedles, the measured solar absorptance of the thermochromic sample is ≈0.82, both below and above $T_C$. The temperature dependent IR modulation is confirmed, with the thermal emittance increasing from 0.26 at room temperature to 0.39 above the phase transition temperature. The rather high emittance of the thermochromic sample in the low temperature, IR transparent state is mainly due to the high emittance ($\varepsilon_{th}$ = 0.2) of the rough Pt substrate that has agglomerated during the exposure to high deposition temperatures (Figure 7.7).
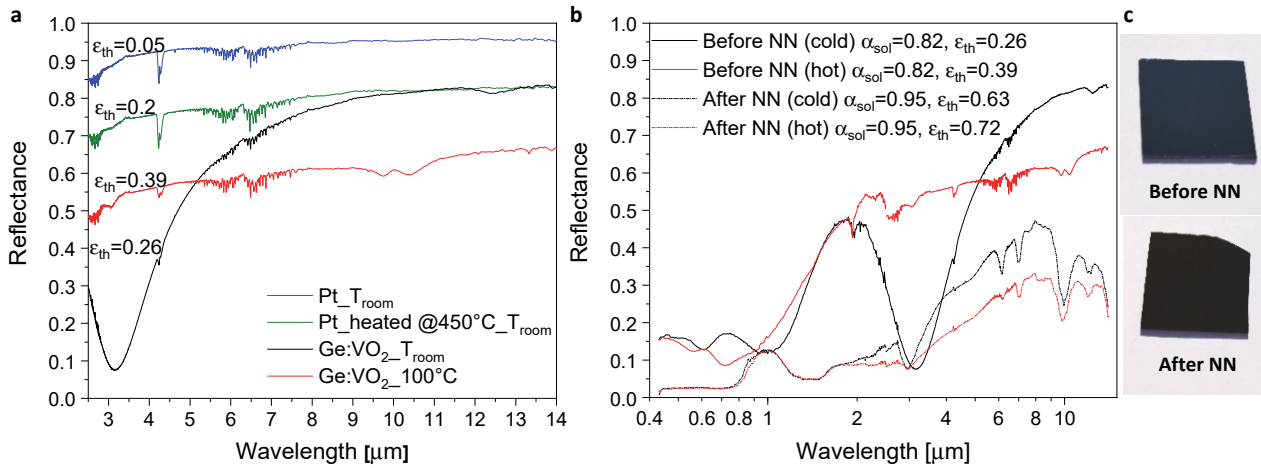
Figure 7.7. a) FTIR spectral curves of the as received and 450°C heated Pt substrates measured at room temperature and the thermochromic sample measured below and above the transition temperature. The emittance of the thermochromic sample in the low temperature phase is limited by the underlying Pt substrate, roughened during the 450°C deposition process. b) Spectral reflectance curves of the thermochromic samples before (solid lines) and after (dashed lines) the growth of nanoneedles (NN). The samples are measured below and above the thermochromic transition temperature and the corresponding solar absorbtance and thermal emittance values are calculated. c) Photograph showing the blue color of the sample before the growth of nanoneedles and a deep black after the growth of nanoneedles.

After the growth of black spinel nanoneedles, the solar absorptance of the samples is improved, by an important 13 percentage points, to nearly 0.95 (from 0.82) at both low and high temperatures. Up to 800 nm wavelength, the measured reflectance curves are completely flat, suggesting a perfect absorber in that spectral region. However, a reflection peak centered around 1 µm wavelength is responsible for the solar absorptance being limited to 95%. Concerning the thermal emittance, the temperature dependent modulation is maintained, confirming the feasibility of nanostructured thermochromic absorbers with very high solar absorptance and dynamic, temperature dependent thermal emittance. Nonetheless, the calculated thermal emittance values are rather high, increasing from 0.63 to above 0.72 with temperature. The selectivity of the nanostructured absorber must be improved and, likely, the length of the nanoneedles must be reduced.

Indeed, cross-section SEM images confirm that the nanoneedles are about 13-14 µm long and the diameter at the base is ≈450 – 500 nm. For a better selectivity, shorter nanoneedles are recommended. Furthermore, the nanoneedles appear to be fragile, getting considerably damaged during transport. Plane view SEM images of the sample before transport show very sharp needles, while the vast majority of the needles are broken after shipping (Figure 7.8).
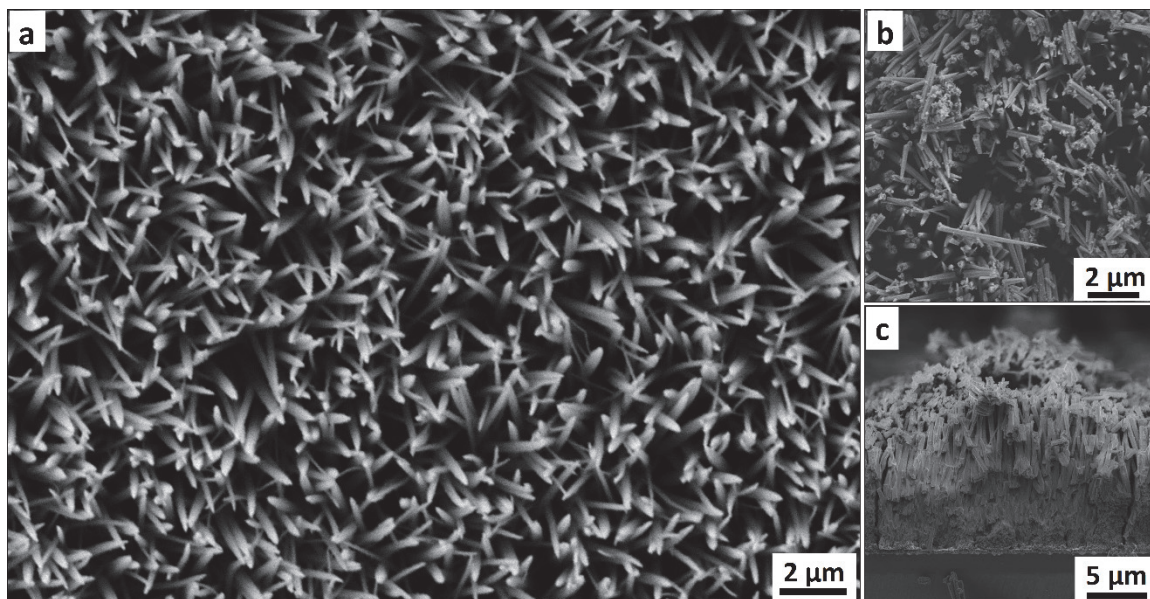
Figure 7.8. Top-view SEM imaging of the nanoneedles before transport (a) and after handling and transport (b-c). Cross-section SEM showing 13-14 µm long nanoneedles (d). SEM image credit: Ka Man Chung and Dr. Olivia Bouvard.

## 7.3 Plasmonic absorbers

Besides the good optical selectivity, the appeal of plasmonic absorbers resides in the ease of tuning their optical properties by changing the geometry of the plasmonic structures. Indeed, plasmonic absorbers based on various metals such (e.g. W, Ag, Au or Ti) have been reported, suggesting that the absorptance of nanostructured layers is mainly dependent on the geometry of the structures rather than the optical properties of the material itself.

Nanostructuring of large surfaces, with commonly used electron beam lithography, is time and cost intensive. Instead, an additive fabrication method combining UV nano-imprint lithography (UV-NIL) – for creating the nanopatterned mask, and magnetron sputtering – for the growth of metallic particles, has been proposed recently [Mitteramskogler, 2019]. It promises a faster and cheaper approach for large area fabrication (roll-to-roll or roll-to-plate) of samples with high-resolution nanofeatures.

The method consists of multiple steps that are graphically summarized in Figure 7.9. First, the lift-off layer is spin-coated, followed by the deposition of an imprint resist. The sample is then nanoimprinted with the negative of a PDMS (polydimethylsiloxane) stamp of selected geometry. The imprint resist is then plasma etched in order to expose the underlying lift-off layer. Next, a wet chemical development selectively etches the lift-off layer creating the necessary undercuts for mask lift-off. Then, the desired metal is sputtered onto the sample. Finally, the mask is lifted-off by wet chemical means. Only the metal nanoparticles, deposited on the surfaces uncovered by the mask, are left behind.
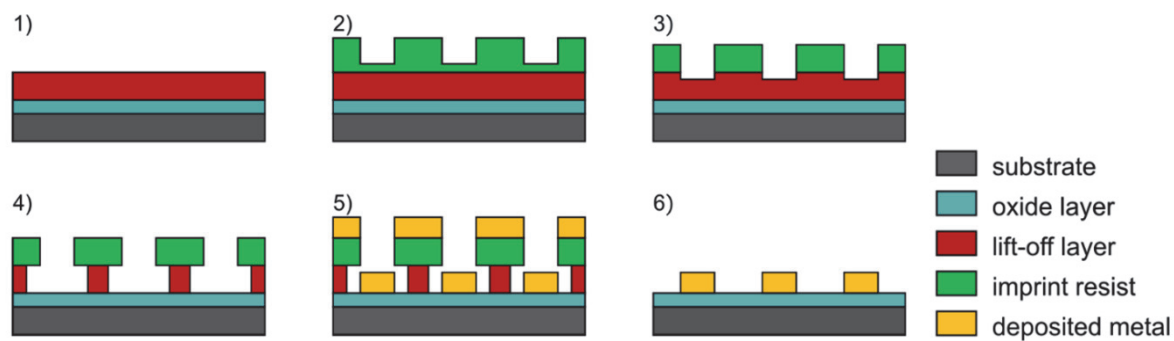
Figure 7.9. Schematic of the fabrication procedure: 1) spincoating of the lift-off layer; 2) UV nanoimprint lithography (to transfer the nanopattern from the stamp to the substrate); 3) reactive ion etching; 4) wet chemical development; 5) metal sputtering; 6) mask lift-off. Reproduced from [Mitteramskogler, 2019].

This fabrication method has been successfully demonstrated for elliptical shaped W nanoparticles, of ≈250 nm and ≈440 nm axes, deposited on Si wafer. The regularity of the well-defined, high resolution nanoparticles is remarkable (Figure 7.10). The resulting nanostructured surfaces were visually black.
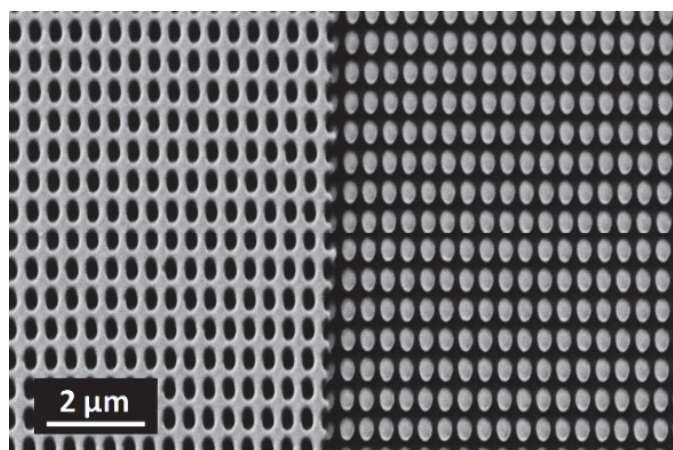


Figure 7.10. SEM image of the elliptical W nanostructures on Si wafer, after mask lift-off (right) and the W coated mask before lift-off (left). Reproduced from [Mitteramskogler, 2019].

Stemming from these very promising results, like in the case of spinel oxide nanoneedles, a collaboration was set up with the authors of the cited study, in particular with Tina Mitteramskogler, affiliated to the Austrian company Profactor. The aim was to pattern the surface of thermochromic multilayered absorbers with metallic nanoparticles as means to increase the solar absorptance, while maintaining the temperature dependent thermal modulation in the infrared spectral range.

The thermochromic multilayered sample selected for nanostructuring has the following composition:

- Si wafer substrate,

- ≈135 nm W layer, to render the substrate IR reflective and stable at high deposition temperatures,

- ≈35 nm $SiO_2$ interlayer, to help the adhesion between the thermochromic and W layer,

- ≈350 nm thick $VO_2$ film for an important modulation of the thermal emittance.

For the nanoimprint step, an available, large-area 8x8 cm$^2$ hole pattern master with 145 nm wide holes has been selected. This deposition mask shall generate the inverse structure of 145 nm wide pillars on the film surface.

In a first approach Ti is sputtered on the imprinted sample. However, the mask lift-off is unsuccessful as the Ti appears to "glue" the nanopatterned mask to the substrate, causing lift-off problems already at 8 nm film thickness. Therefore, a second metal deposition is carried out using W. This time, the wet chemical development is successful and the nanostructured absorber is characterized by SEM and spectral reflectance measurement.

The top-view SEM images show the regularly placed, circular W structures of ≈200 nm diameter (Figure 7.11). This is larger than the expected width of 145 nm for the metallic pillars. A similarly significant difference between the mask hole diameter and obtained nanoparticles has been observed in [Mitteramskogler, 2019]. The broadening of the holes of the mask has been attributed to a non-zero, lateral etch rate during the reactive ion etching (step 3). Some of metallic nanoparticles might be removed during the lift-off, leaving behind spots of exposed, thermochromic grains laying beneath. Cross sectional SEM images reveal all the multilayers and their corresponding thicknesses. The height of the W nanoparticles is ≈110 nm. In the backscattered electron image, the individual W nanoparticles are easily distinguishable. So is the W coating on the Si substrate, as both appear brighter than the rest of the multilayer, due to the high atomic numer of tungsten.
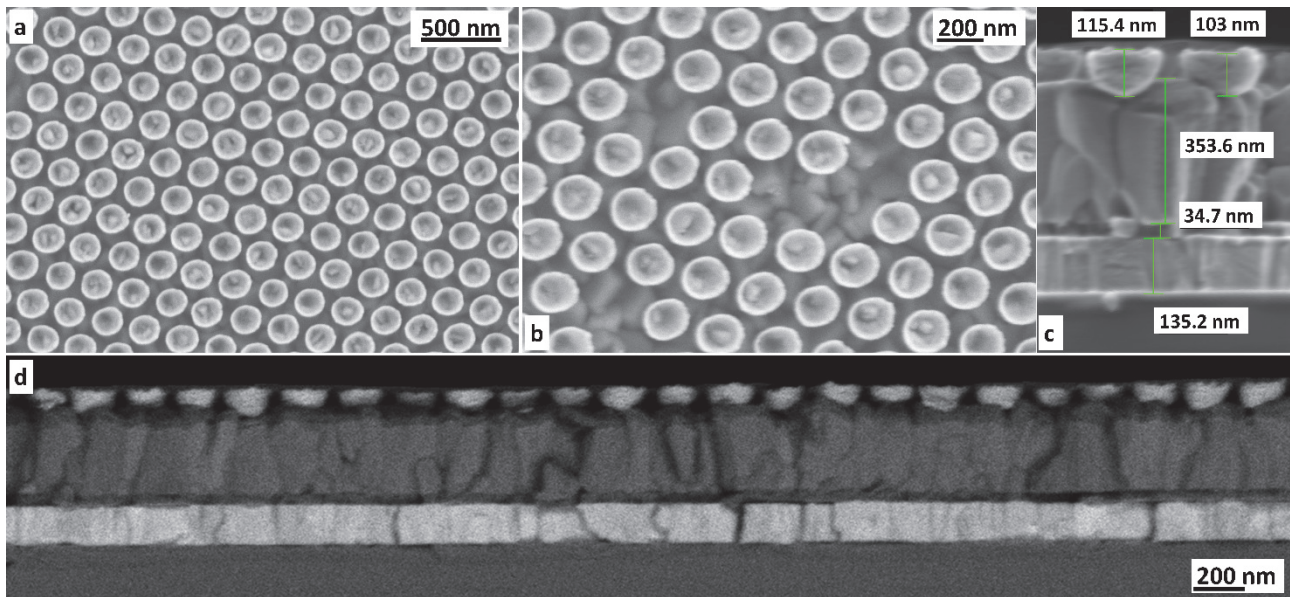


Figure 7.11. Top-view SEM image of the 200 nm wide W nanoparticles (a-b) and secondary (c) and backscattered electron (d) image of the multilayer cross section with the corresponding layer thicknesses. SEM image credit: Dr. Olivia Bouvard.

Next, the optical performance of the new, plasmonic absorber is compared with the performance of the thermochromic absorber before the nanostructuring. The corresponding spectral reflectance curves are compared both below and above the critical phase transition temperature (Figure 7.12).
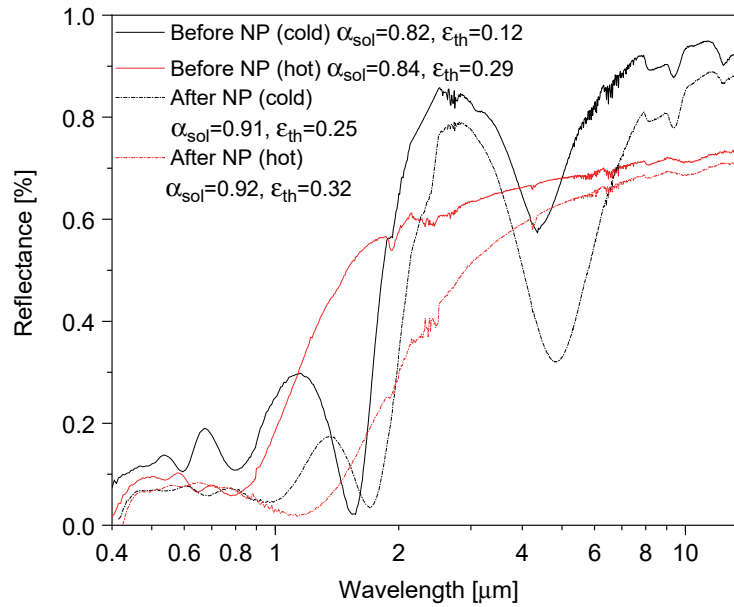
Figure 7.12. Spectral reflectance curve of the thermochromic absorber before and after nanopatterning, measured both at room temperature and at 100°C.

It is found that surface nanostructuring increases the solar absorptance of the samples by 8-9 percentage points, while a thermal emittance modulation of ≈7 percentage points is maintained (compared to the ≈17% modulation in the non-structured samples). The solar absorptance is significantly boosted and, unlike, in the case of spinel nanoneedle absorbers, the selectivity of the nanoimprinted samples is rather high. Nonetheless, optimization of the nanopattern geometry might limit the decrease in thermal emittance modulation.

In this chapter, exciting, novel thermochromic concepts for the enhancement of solar absorptance and thermal emittance modulation have been explored. The proposed approaches are in their explorative stages and improvements could be suggested for all three directions discussed. Nonetheless, proof of concept has been provided for Fabry-Pérot interferometer inspired thermochromic multilayers and for enhanced nanostrcutred solar absorbers – by nanoneedle growth and nanopatterning.

Additionally, the thermochromic $VO_2$ and $VO_2$:Ge films developed in this work have proven valuable for nano- and microelectronic device applications as well. In the framework of collaboration with the Nanelectronic Device Laboratory (Nanolab) of EPFL, led by Prof. Mihai Adrian Ionescu, thermochromic thin films have been successfuly employed for tunable steep-slope transistors, reconfigurable RF phase shifters, terahertz detection, tunable microwave filters, rectifiers and inductors. The fruitful collaboration led to numerous quality publications, listed in the "List of Publications" section. Published articles are attached to the Annex of this document.

# Chapter 8    Conclusions and outlook

This thesis has focused on the study of pure and doped VO$_2$ thermochromic thin films. The development of smart solar absorber coatings with a dynamic, temperature dependent optical response as a result of the metal-to-insulator phase transition of VO$_2$, constitutes the main objective of this research. However, the outcomes of this work have implications beyond the field of solar absorbers spanning from fundamental insights on doping of thermochromic thin films to prospective use in the nano-/micro-electronics, nanophotonic, thermochromic meta-materials and radiative cooling applications.

This chapter concludes the thesis with a summary of its main achievements and its implications on future research are highlighted.

## 8.1    Outcomes of the thesis

The study of pure VO$_2$ thin films sputtered onto various substrates reveals **the importance of substrate choice** even for film thicknesses of a couple hundred nanometers. GaN and Al$_2$O$_3$ substrates are particularly well-suited for the growth of high quality, switching films with large thermochromic modulation of above four orders of magnitude. Generally, for the same deposition method, the modulation magnitude is limited with decreasing film thickness. Here, **the minimum thickness** for sputtered films, exhibiting a thermochromic switch, is **identified at only 30 nm**. Even more remarkable is the more than three order magnitude transition reported for such a thin film.

Comparisons of conventional and high-power impulse magnetron sputtering reveal that **at higher deposition temperatures, HiPIMS leads to denser films with superior thermochromic modulation**, while at **lower deposition temperatures, magnetron sputtering is more favorable**. This is speculated to be the result of a high-energy ion induced amorphization in the HiPIMS process. For practical applications and industrialization, reducing the deposition temperature is critical. Switching thermochromic films are reported for **substrate temperatures as low as ≈310°C**. Experimental evidence of a small, but sudden **thermochromic modulation in La$_{0.7}$Sr$_{0.3}$MnO$_3$ perovskites above 150°C** is provided.

Local STM probing of pure and Ge doped VO$_2$ films allow for the determination of the band gap at the individual grain level. The gaps of the pure and doped grains do not differ appreciably, however, agglomerations can take elongated structures in the doped films.

An **increase of the thermochromic phase transition temperature up to ≈96°C is achieved by Ge doping of VO$_2$ films**. Despite the long-standing debate about the origin of the phase transition in VO$_2$, recent papers seem to converge on the importance of electron-electron interactions leading the MIT. However, compared to conventional semiconductor doping, relatively high concentrations of Ge are needed to change the transition temperature – ≈5.9 at.% Ge for $T_C$ ≈ 96°C. The mechanism governing the MIT might differ from the one controlling the transition temperature. Our experimental observations are in accordance with recent

theoretical calculations (DFT GGA+U), where an increase in the energy difference between the metallic and insulating phases, leading to an increase of $T_C$, is calculated for $VO_2:GeO_2$ alloys [Lu, 2019].

Besides raising the phase transition temperature, **Ge doping/alloying of VO₂** brings additional benefits for solar absorber applications as it **leads to the increase of thermal emittance modulation Δε**, especially due to an increase of the thermal emittance in the high-temperature state. The successful deposition of switching films from V-Ge alloy targets proves the feasibility of $VO_2:Ge$ films for industrial upscaling.

First thermochromic absorber coatings based on $VO_2/VO_2:Ge$ and nanocrystalline $CuCoMnO_x$ spinel absorber show a large thermal emittance modulation, Δε > 0.3, but also an increase in solar absorptance with temperature. Optical simulations suggest that adding a layer with relatively high n and k, such as $Ti_{1-x}Al_xN$, between the substrate and the thermochromic layer might reverse the switch in solar absorptance so that it decreases with increasing temperature. The concept is then adapted to industrial absorber designs and **improved absorbers based on Al//TiAlSiN//VO₂:Ge//SiO₂** multilayers are deposited. To our knowledge, **thermochromic absorbers with decreasing $α_{sol}$ and increasing $ε_{th}$ over the phase transition** are reported here for the first time.

The lifetime of the improved thermochromic absorbers has been evaluated and **the requirements of a minimum service life of 25 years have been met according to the ISO 22975-3:2014 standard**. Samples successfully passed both accelerated aging test in dry air at 300°C during 600 h and in 100% relative humidity at 40°C during 600 h. Samples with newly exposed interfaces between the thermochromic layer and air show a steady degradation of the switching properties, but as-deposited samples with unaltered $SiO_2$ top-layer are remarkably stable during aging. This underlines **the importance of complete coverage of the thermochromic layers by the antireflective and oxidation barrier top layers**.

Simulation of the corresponding thermochromic collector indicates **a nearly 20°C drop in stagnation temperature, to $T_{stagnation}$ ≈ 159°C**. Such an important limitation, is expected to significantly shorten the duration of stagnation conditions. Glycol degradation is also hindered, bringing about important reductions in maintenance costs. Moreover, at stagnation temperatures only few degrees lower, at ≈ 150°C and at 2 – 2.5 bar overpressure typically present in such systems, evaporation of the heat transfer fluid in the collector loops is entirely avoided.

Finally, several advanced thermochromic concepts are proposed. **Fabry-Pérot interferometer inspired multilayered coatings exhibit unusually high thermal modulation of 0.5 based on merely 30 nm thick, switching VO₂ films**. Surface nanostructuring is shown to enhance the solar absorptance of thermochromic absorbers. **Light-trapping Co₃O₄ spinel nanoneedles increase the solar absorptance** by 13 percentage points, to $α_{sol}$ = 0.95, while the emittance modulation of the thermochromic absorber is maintained. **Plasmonic absorbers** with regularly spaced, W nanoparticles deposited on the thermochromic layer, **exhibiting good selectivity and temperature dependent emittance, are fabricated by means of nanoimprint lithography and sputtering**.

## 8.2   Outlook

The successful integration of the developed thermochromic layer into an industrial absorber design, and the fabrication of laboratory sized absorbers with positive emittance and negative absorptance modulation reported here for the first time, bring to the forefront the remaining issues towards its industrialization. The high temperature deposition of around 450°C represents the main challenge for industrial upscaling. Lowering the substrate temperature by a suitable seed layer or by a plasma enhanced CVD process should be investigated.

HiPIMS is shown to lead to superior film quality, hence, it should be further studied as an alternative to conventional magnetron sputtering. The denser HiPIMS films, with larger electrical modulation, fewer defects and grain boundaries could be advantageous for applications where charge transport properties are critical.

The newly installed STM and STS, together with the already in place, vacuum connected X-ray and UV photoelectron spectrometer, constitute a powerful and rather unique in-situ characterization platform for the sputtered thermochromic layers. STM and STS open up the possibility to study pure and doped thermochromic films locally, at the nanoscale level. It might be possible to observe the opening and closing of the band gap, even for individual, nanometric grains. XPS and UPS can help understand the physics at the interlayers between thermochromic films and other oxide or metal layers that is of fundamental importance for microelectronic device applications.

The experimental validation of the giant emittance modulation of $\approx 0.8$ in the mid-infrared spectral range ($2.5 - 10$ μm) predicted by simulations in Fabry-Pérot inspired multilayers is still pending.

Lastly, the combination of MIT driven thermochromic behavior, with nanoscale structuring remains a rich field for exploration. Reflectance/transmittance of single or multilayers can be tailored to well-defined wavelengths by suitable nanopattern designs. The study of plasmonic resonances in thermochromic metasurfaces and nanophotonic devices is still in its early stages.

# List of publications

## Journal papers

**Krammer A.**, Magrez A., Vitale W.A., Mocny P., Jeanneret P., Guibert E., Whitlow H.J., Ionescu A.M., Schüler A. (2017). Elevated transition temperature in Ge doped VO2 thin films. Journal of Applied Physics, 122 (4), 045304. DOI: 10.1063/1.4995965

Müller A.A., Moldoveanu A., Asavei V., Khadar R.A., Sanabria-Codesal E., **Krammer A.**, Fernandez-Bolaños M., Cavalieri M., Zhang J., Casu E., Schüler A., Ionescu A.M. (2019). 3D Smith charts scattering parameters frequency-dependent orientation analysis and complex-scalar multi-parameter characterization applied to Peano reconfigurable vanadium dioxide inductors. Scientific Reports, 9 (1), 18346. DOI: 10.1038/s41598-019-54600-5

Ni W., **Krammer A.**, Hsu C.-S., Chen H.M., Schüler A., Hu X. (2019). $Ni_3N$ as an Active Hydrogen Oxidation Reaction Catalyst in Alkaline Medium. Angewandte Chemie - International Edition, 58 (22), pp. 7445-7449. DOI: 10.1002/anie.201902751

Casu E.A., Oliva N., Cavalieri M., Muller A.A., Fumarola A., Vitale W.A., **Krammer A.**, Schuler A., Fernandez-Bolanos M., Ionescu A.M. (2018). Tunable RF Phase Shifters Based on Vanadium Dioxide Metal Insulator Transition. IEEE Journal of the Electron Devices Society, 6, art. no. 8368187, pp. 965-971. DOI: 10.1109/JEDS.2018.2837869

Casu E.A., Muller A.A., Fernandez-Bolanos M., Fumarola A., **Krammer A.**, Schuler A., Ionescu A.M. (2018). Vanadium Oxide Bandstop Tunable Filter for Ka Frequency Bands Based on a Novel Reconfigurable Spiral Shape Defected Ground Plane CPW. IEEE Access, 6, pp. 12206-12212. DOI: 10.1109/ACCESS.2018.2795463

Oliva N., Casu E.A., Yan C., **Krammer A.**, Rosca T., Magrez A., Stolichnov I., Schueler A., Martin O.J.F., Ionescu A.M. (2017). Van der Waals $MoS_2$/$VO_2$ heterostructure junction with tunable rectifier behavior and efficient photoresponse. Scientific Reports, 7 (1), 14250. DOI: 10.1038/s41598-017-12950-y

Vitale W.A., Casu E.A., Biswas A., Rosca T., Alper C., **Krammer A.**, Luong G.V., Zhao Q.-T., Mantl S., Schüler A., Ionescu A.M. (2017). A Steep-Slope Transistor Combining Phase-Change and Band-to-Band-Tunneling to Achieve a sub-Unity Body Factor. Scientific Reports, 7 (1), 355. DOI: 10.1038/s41598-017-00359-6

# Conference papers

**Krammer A.**, Schüler A. (2019). Predicting the thermal performance of thermochromic flat plate solar collectors. Journal of Physics: Conference Series, 1343 (1), 012201. DOI: 10.1088/1742-6596/1343/1/012201

**Krammer A.**, Demière F.T., Schüler A. (2017). Infrared optical properties of doped and pure thermochromic coatings for solar thermal absorbers. ISES Solar World Congress 2017 - IEA SHC International Conference on Solar Heating and Cooling for Buildings and Industry 2017, Proceedings, pp. 1008-1014. DOI: 10.18086/swc.2017.17.04

**Krammer A.**, Bouvard O., Schüler A. (2017). Study of Si doped $VO_2$ thin films for solar thermal applications. Energy Procedia, 122, pp. 745-750. DOI: 10.1016/j.egypro.2017.07.390

**Krammer A.**, Gremaud A., Bouvard O., Sanjines R., Schüler A. (2016). In situ photoelectron spectroscopic characterization of reactively sputtered, doped vanadium oxide thin films. Surface and Interface Analysis, 48 (7), pp. 440-444. DOI: 10.1002/sia.5989


Daviran S., **Krammer A.**, Schüler A. (2019). In-situ and post annealing effect on the microstructure and the optical properties of black Cu-Co-Mn oxide spinel coating for Parabolic Trough Collector (PTC) applications. Journal of Physics: Conference Series, 1343 (1), 012200. DOI: 10.1088/1742-6596/1343/1/012200

Qaderi F., Muller A., **Krammer A.**, Veljovic M., Ollmann Z., Hayati M., Skrivervik A., Schueler A., Feurer T., Ionescu A. (2019). Millimeter-wave-triggering of insulator-to-metal transition in Vanadium dioxide. International Conference on Infrared, Millimeter, and Terahertz Waves, IRMMW-THz, 8874271. DOI: 10.1109/IRMMW-THz.2019.8874271

Müller A.A., Abdul Khadar R., Casu E.A., **Krammer A.**, Cavalleri M., Schuler A., Zhang J., Ionescu A.M. (2019). A Novel Reconfigurable CMOS Compatible Ka Band Bandstop Structure Using Split-Ring Resonators and Vanadium Dioxide (VO) Phase Change Switches. IEEE MTT-S International Microwave Symposium Digest, 8701121, pp. 865-868.

Oliva N., Casu E.A., Yan C., **Krammer A.**, Magrez A., Schueler A., Martin O.J.F., Ionescu A.M. (2018). $MoS_2/VO_2$ vdW heterojunction devices: Tunable rectifiers, photodiodes and field effect transistors. Technical Digest - International Electron Devices Meeting, IEDM, pp. 36.1.1-36.1.4. DOI: 10.1109/IEDM.2017.8268503

Casu E.A., Vitale W.A., Tamagnone M., Lopez M.M., Oliva N., **Krammer A.**, Schuler A., Fernandez-Bolanos M., Ionescu A.M. (2017). Shunt capacitive switches based on $VO_2$ metal insulator transition for RF phase shifter applications. European Solid-State Device Research Conference, 8066634, pp. 232-235. DOI: 10.1109/ESSDERC.2017.8066634

Casu E.A., Vitale W.A., Oliva N., Rosca T., Biswas A., Alper C., **Krammer A.**, Luong G.V., Zhao Q.T., Mantl S., Schuler A., Seabaugh A., Ionescu A.M. (2017). Hybrid phase-change - Tunnel FET (PC-TFET) switch with sub-threshold swing < 10mV/decade and sub-0.1 body factor: Digital and analog benchmarking. Technical Digest - International Electron Devices Meeting, IEDM, 7838452, pp. 19.3.1-19.3.4. DOI: 10.1109/IEDM.2016.7838452

Bouvard O., **Krammer A.**, Schüler A. (2016). In situ core-level and valence-band photoelectron spectroscopy of reactively sputtered tungsten oxide films. Surface and Interface Analysis, 48 (7), pp. 660-663. DOI: 10.1002/sia.5927

# Annexes

## Annex 1. XPS core level spectra of $La_{1-x}Sr_xMnO_3$ thin films.
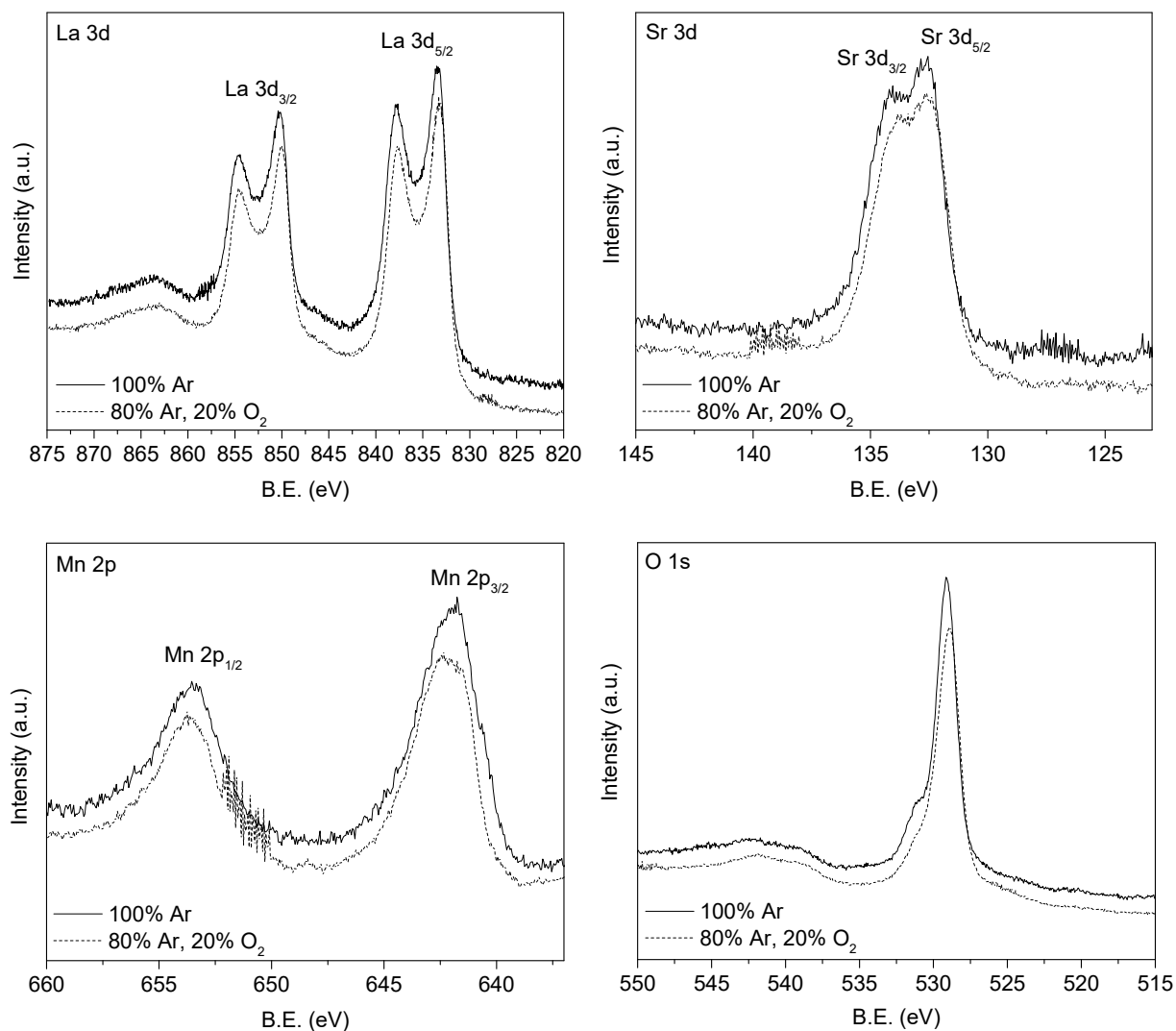


In-line XPS core level spectra of La 3d, Sr 3d, Mn 2p and O 1s (measured with Mg Kα X-ray source with hν = 1253.6 eV, at a pass energy of 29.925 eV).

# Annex 2. Solar collector parameters used for the SolCoSi simulation.

| Parameter | Collector X |
|---|---|
| **Gross dimensions** | |
| Length [m] | 2.043 |
| Width [m] | 1.15 |
| Thickness [m] | 0.083 |
| **Aperture Dimensions (cover)** | |
| Length [m] | 1.992 |
| Width [m] | 1.098 |
| **Cover** | |
| Number of covers | 1 |
| Material | Glass |
| Thermal Conductivity [W/mK] | 1.0 |
| Transmittance | 0.9 |
| Emittance | 0.88 |
| Refractive index | 1.526 |
| Thickness [mm] | 4.0 |
| Textured | Yes |
| **Internal arrangement** | |
| Number of tubes | 9 |
| Tube to tube spacing [mm] | 116.0 |
| Cover-plate air spacing [mm] | 9.7 |
| Plate-insulation air spacing [mm] | 22.0 |
| **Absorber plate** | |
| Material | Aluminium |
| Thermal conductivity [W/mK] | 200.0 |
| Absorptance | 0.95 |
| Emittance | 0.05 |
| Thickness [mm] | 0.4 |
| **Tube** | |
| Material | Copper |
| Thermal Conductivity [W/mK] | 398.0 |
| Outer Diameter [mm] | 12.7 |
| Inner Diameter [mm] | 11.4 |
| **Insulation** | |
| Back Insulation Material | Polyurethane |
| Thermal conductivity [W/mK] | 0.0269 |
| Emittance | 0.92 |
| Thickness [mm] | 40.0 |
| Lateral Insulation Material | Polyurethane |
| Thermal conductivity [W/mK] | 0.0225 |
| Thickness [mm] | 25.0 |
| Box Material | Aluminium |
| Thermal conductivity [W/mK] | 200.0 |
| Emittance | 0.02 |
| Thickness [mm] | 0.5 |
| **Test Conditions** | |
| Incident solar radiation (G) [W/m$^2$] | 832.0 |
| Diffuse radiation proportion (Gd/G) | 0.2 |
| Ambient temperature [°C] | 24.8 |
| Wind speed [m/s] | 2.5 |
| Collector slope [°] | 15.0 |
| Fluid | Water |
| Mass flow rate [kg/min] | 1.81 |

# Annex 3. Co-authored articles on VO₂-based nanoelectronic devices

**OPEN**

# 3D Smith charts scattering parameters frequency-dependent orientation analysis and complex-scalar multi-parameter characterization applied to Peano reconfigurable vanadium dioxide inductors

Andrei A. Muller[1]*, Alin Moldoveanu [2], Victor Asavei [2], Riyaz A. Khadar[3], Esther Sanabria-Codesal[4], Anna Krammer[5], Montserrat Fernandez-Bolaños[1], Matteo Cavalieri[1], Junrui Zhang[1], Emanuele Casu[1], Andreas Schuler[5] & Adrian M. Ionescu[1]

Recently, the field of Metal-Insulator-Transition (MIT) materials has emerged as an unconventional solution for novel energy efficient electronic functions, such as steep slope subthermionic switches, neuromorphic hardware, reconfigurable radiofrequency functions, new types of sensors, terahertz and optoelectronic devices. Employing radiofrequency (RF) electronic circuits with a MIT material like vanadium Dioxide, $VO_2$, requires appropriate characterization tools and fabrication processes. In this work, we develop and use 3D Smith charts for devices and circuits having complex frequency dependences, like the ones resulting using MIT materials. The novel foundation of a 3D Smith chart involves here the geometrical fundamental notions of oriented curvature and variable homothety in order to clarify first theoretical inconsistencies in Foster and Non Foster circuits, where the driving point impedances exhibit mixed clockwise and counter-clockwise frequency dependent (oriented) paths on the Smith chart as frequency increases. We show here the unique visualization capability of a 3D Smith chart, which allows to quantify orientation over variable frequency. The new 3D Smith chart is applied as a joint complex-scalar 3D multi-parameter modelling and characterization environment for reconfigurable RF design exploiting Metal-Insulator-Transition (MIT) materials. We report fabricated inductors with record quality factors using $VO_2$ phase transition to program multiple tuning states, operating in the range 4 GHz to 10 GHz.

The Smith chart, invented in 1939[1], is a graphical tool widely used in various fields of electrical engineering and applied physics when dealing with frequency dependent reflection coefficients or impedances. The Smith chart is extensively employed in the design/measurement stage of a large variety of circuits, from metasurfaces[2] to coils[3] (Supplementary Fig. 3 in[3]) or scanning microwave microscopy[4], while being mostly present in microwave-terahertz frequency region in the design and characterization of antennas[5], transmission lines[6,7],

[1]Nanoelectronic Devices Laboratory (NanoLab), École Polytechnique Fédérale de Lausanne (EPFL), 1015, Lausanne, Switzerland. [2]Department of Computer Science and Engineering, Faculty of Automatic Control and Computers, University Politehnica of Bucharest, 060042, Bucharest, Romania. [3]Powerlab, École Polytechnique Fédérale de Lausanne (EPFL), 1015, Lausanne, Switzerland. [4]Departamento de Matemática Aplicada, Universitat Politècnica de València, 46022, Valencia, Spain. [5]Solar Energy and Building Physics Laboratory (LESO-PB), École Polytechnique Fédérale de Lausanne (EPFL), 1015, Lausanne, Switzerland. *email: andrei.muller@epfl.ch
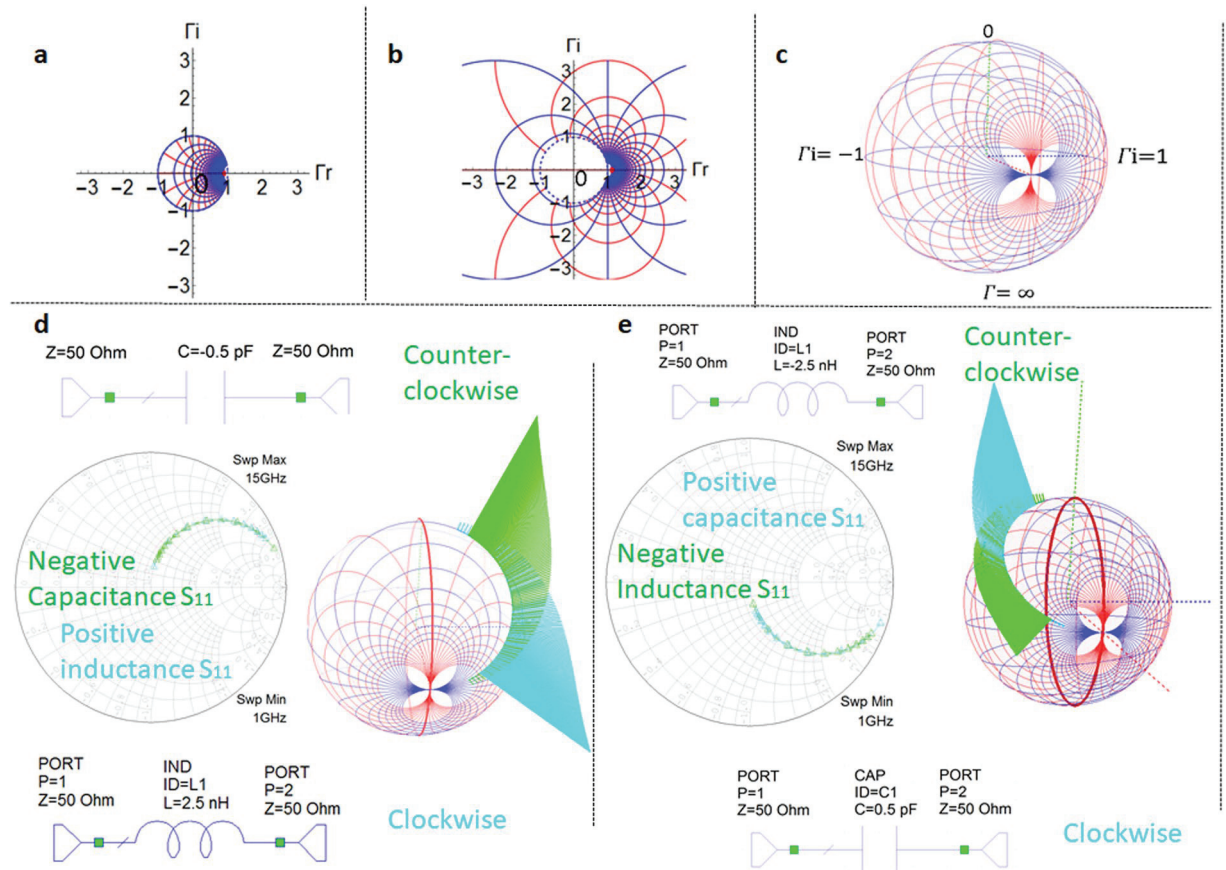
**Figure 1.** Smith chart limitations and clockwise and counter-clockwise frequency dependency of Foster and non-Foster elements on a newly introduced frequency dependent 3D Smith chart. (**a**) Smith chart. (**b**) Extended Smith chart (**c**), 3D Smith chart as in 2018 (without frequency dependency). (**d**) 3D Smith chart representation of the two port reflection coefficient and newly implemented frequency dependent 3D Smith chart representation for it. For a capacitor with purely negative capacitance and an inductor with positive inductance their reflection coefficient frequency representation overlaps on the Smith chart for a wide frequency range, their orientation changes cannot be distinguished. On the newly implemented frequency dependent 3D Smith chart (when compared to our previous works in[11,13,14]) one can clearly see their clockwise motion with increasing frequency for the inductor while the counter-clockwise motion for the capacitor with negative capacitance. (**e**) 3D Smith chart representation of the reflection coefficient and newly implemented frequency dependent 3D Smith chart for a negative valued inductor and capacitor with positive capacitance. Again, their trace is identical on a Smith chart, their intrinsic opposed frequency dependency cannot be seen. On the 3D Smith chart one can directly see the clockwise motion of the reflection coefficient of the capacitor and the counter-clockwise motion of the reflection coefficient of the negative valued inductor.

power amplifiers[8], filters[9] or acoustic resonators[10]. The 3D Smith chart proposed in[11] generalizes the Smith chart (which is limited within the unit circle to circuits with reflection coefficients ($\Gamma = \Gamma_r + j\Gamma_i$) magnitudes smaller than unity Fig. 1a) onto the Riemann sphere in order to make it usable for all circuits (Fig. 1b,c) further conveying the theoretical support and advance for an intuitive spherical drawing for which the first insights have been presented in[12]. The next developments of the 3D Smith chart[13,14] propose a Java tool with the 3D Smith chart which additionally displays the group delay and amplifier stability circles too.

An essential drawback of the Smith chart and previous 3D Smith chart representations[1–14] is the lack of visualization of the variable parameter (frequency), thus the orientation changes and dynamics of the scattering parameters (S) frequency dependency being impossible to be pictured. Although many circuits exhibit a clockwise orientation of their driving point impedances and reflection parameters curves as frequency increases[2–5,9], (– unspecified)[6,10], the absence of a clockwise motion (i.e. discontinuity points or counter-clockwise motion) was often reported leading to diverse interpretations. In active devices (transistors), as for example in[15,16] it is referred as "kink-phenomenon", in lossless (purely reactive) non-Foster circuits (such as negative capacitors and inductors)[17–20], as an intrinsic phenomenon. Unfortunately, this counter-clockwise dynamics phenomenon recurrent existence in lossy circuits with non-Foster elements[19,21–24], led to some misleading conclusions: in[21–24] the authors assume that the existence of this phenomenon proves the presence of a non-Foster element, while in[25] it is stated that passive linear devices cannot exhibit driving point immittances with counter-clockwise frequency dependency on the Smith chart.

Because of their lack in zooming capacity, 2D Smith chart representations may oversee also the changes of orientation occurring for the input impedances and reflection coefficients (while increasingly sweeping the frequency), in simple passive networks too. These reversals occur in networks with only Foster elements too as empirically observed in[26,27]. Otherwise orientation reversal phenomenon which occurs in lossy networks with Foster elements is often overlooked or seen as an interpolation error and its presence is often ignored. Since the paths of the reflection coefficients of distinct circuits may coincide within a specific frequency on the Smith chart (as for negative inductors and positive capacitors and viceversa[17,19,20,26]) a frequency dependency visualization is missing in order to get an insight beyond the reflection coefficients paths, regarding their dynamics within it.

From the (differential) geometrical point of view the input impedance and reflection coefficients are particular cases of parametric curves of the frequency variable for each single RF circuit. Their parametric curves equations describe more than a simple geometrical image (their path on the Smith chart), they also contain the information about their motion on it (as for example: orientation and speed).

For this purpose, we first introduce here the notion of oriented curvature $k$[28] (in our case, frequency dependent- $k(\omega)$ where $\omega$ represents the angular frequency and apply it to the reflection coefficients analysis. We prove the mixed clockwise-counter-clockwise orientation phenomenon in lossy circuits with Foster elements and propose a frequency orientation quantification (while increasing the sweeping range) with a new implementation within the 3D Smith chart tool by using the topology of the Riemann sphere[29,30]. Thus, while (increasingly) sweeping the frequency, a new vision to detect this orientation reversal for both Foster and Non-Foster[17–24,31–33] elements-based networks is first presented. This phenomenon was impossible to quantify for a 2D parametrical plot such as the Smith chart or basic 3D Smith chart (where only the Riemann sphere surface is used).

Further the 3D Smith chart is additionally exploited and developed here in order to display simultaneously parameters needed in reconfigurable frequency designs while dealing with inductors. Frequency dependent inductances based on the $Y_{11}$[34–36] admittance parameter (shunt models $Lshunt$), series models of inductances $Lseries$ based on the $Y_{21}$[37,38] parameter, quality factors[34–39] ($Q$), self-resonant frequencies, Smith chart information[39] ($\Gamma$) need ideally all to be simultaneously modeled and analyzed over a wide frequency range during the designs and characterizing stages of inductors. This leads[34–39] to a larger number of graphics or to different scaling in order to grasp all parameters of interest. Here all these factors are implemented and analyzed on a single combined mode of display using the 3D Smith chart topology and different perspectives.

The newly developed capabilities are particularly suited to explore reconfigurable microwave characterizations, here with reconfigurable CMOS-compatible inductors equivalent circuit modelling for microwaves frequencies using a phase change (PC) material like vanadium Dioxide ($VO_2$)[37,38,40–49] for tuning the values of inductance. Indeed, it is known that $VO_2$ behaves like an insulator under its phase transition temperature Tc $= 68\,°C$ (or higher when doped[42]) with monoclinic crystal structure[40] while deposited on $SiO_2/Si$ substrates. Because of its ease of integration, reversible insulator to metal transition (IMT), low transition temperature and fast switching time, the employment of $VO_2$ as a reconfigurable radio frequency (RF) material has been just recently investigated for a variety of RF-reconfigurable devices[37,38,40,44,45]. Still, much of existing studies are carried out in the frequency range of terahertz or far-infrared[41,43,46,48], leaving (RF) $VO_2$ a largely uncharted area for exploration in development. The conductivity levels of $VO_2$ in its insulating (off) state and in its conductive (on) state vary over a wide range depending on the substrate[37,38,40–49] causing limitations in the RF devices performances (being below 50,000 S/m for $SiO_2/Si$ depositions in the on state).

The on state (limited) conductivity levels of $VO_2$ restricted the maximum quality factors ($Q_{max\_on}$) of the reconfigurable inductors fabricated with this PC material to sub-unitary values[38], or to values below three in[37] for CMOS compatible processes on $SiO_2/Si$ substrates.

Here, after evaluating the $VO_2$ conductive/insulating properties, using the new implemented multi-parameter displays, we design and fabricate a new type of $SiO_2/Si$ CMOS compatible reconfigurable inductors with $VO_2$ switches based on Peano curves[50] and extract their equivalent circuit while analyzing their behavior in a complex-scalar 3D Smith chart-based environment. The aim was to improve the performances obtained in[37] on $SiO_2/Si$ substrates in terms of: $Q_{max\_on}$ tuning range and $Q_{max\_on}/Q_{max\_off}$ ratio (where $Q_{max\_off}$ denotes the maximum quality factor in the insulating phase of the $VO_2$).

The experimentally fabricated and measured reconfigurable inductors improve by 2.33 times the $Q_{max\_on}$ values previously reported in[37] for the $VO_2$ based inductors fabricated within the same CMOS technology on $SiO_2/Si$ substrates (and by orders of magnitude in respect to[38]), while also increasing the number of reconfiguring states too (from two in[37] to three here). Further due to their original geometry the inductors exhibit a tuning range of 77% (improving the 55% in[37] or 32% in[38]) and have a $Q_{max\_on}/Q_{max\_off}$ ratio of 0.87 unlike 0.27 in our previous work[37]. It is worth pointing out that the inductor while facing the limited conductivity levels of $VO_2$ on $SiO_2/Si$ substrates reveals a 2.33 better $Q_{max\_on}$ value in in respect to other $VO_2$ based reconfigurable inductors such as the $SiO_2/Sapphire$ inductors reported in[51] where the conductivity levels of $VO_2$ exceed 300.000 S/m.

## Oriented Curvature of Input Impedances, Reflection Coefficients, Slope of Reactance and 3d Smith Chart Implementation of Frequency Dependency Orientation

Based on $k(\omega)$[28] described in detail within the Supplementary Material, we show that the changes in sign of the reactance frequency derivative do not always imply changes in orientation neither for the input impedance nor for the reflection coefficient of 1- port networks (when losses occur). We provide the conditions and equations under which one may have the same orientation (more details in Supplementary Section 1) for both reflection coefficient and input impedances. The lossless (reactive) cases (purely Foster[17,18,27] and non-Foster[17–20]) become particular cases where the reflection coefficients are direct inversive (Mobius) and indirect inversive transformations[30] of the oriented imaginary axes of the impedance plane. The clockwise and counter-clockwise motions on circles are a consequence of the reactance slope and sign in the lossless cases.
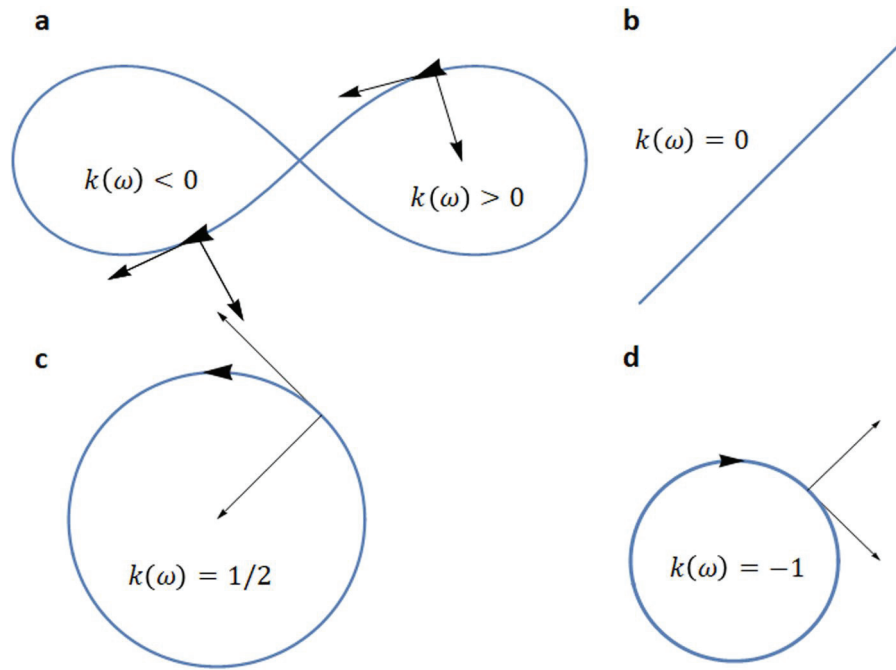
**Figure 2.** Oriented curvature k($\omega$) and its sign sgn(k($\omega$)) for various motions on various reflection coefficient or impedance curves $C(j\omega)$. (**a**) $k(\omega) > 0$ when $C(j\omega)$ is counter-clockwise oriented; $k(\omega) < 0$ where $C(j\omega)$ is clockwise oriented. (**b**) $k(\omega) = 0$ for any line shape of $C(j\omega)$. (**c**) When $C(j\omega)$ has a circle shape of radius 2 and a counter-clockwise motion $k(\omega) = 1/2$. (**d**) When $C(j\omega)$ has a circle shape of radius 1 and a clockwise motion $k(\omega) = -1$.

By introducing the geometrical notion of oriented curvature in this field we prove that the assumptions made by other authors[21–25] may not apply (see Supplementary Section 1). Further, as seen also for the input impedance of an antenna in[27], the negative frequency derivative of the reactance of a lossy 1-port network does not imply counter-clockwise motions in the case of lossy 1-port networks. The paths of both 1-port and 2-port networks (such as in Fig. 1) become simple consequences of the magnitude and sign changes of $k(\omega)$ $(sgn(k(\omega)))$:

For any parametric curve $C(j\omega)$(1) (a) (all reflection coefficients and input impedances are particular cases of frequency dependent parametric curves) its corresponding $k(\omega)$is given by (1) (b).

$$C(j\omega) = a(\omega) + jb(\omega)(a) \quad k(\omega) = \frac{-b'(\omega)a''(\omega) + a'(\omega)b''(\omega)}{(a'(\omega)^2 + b'(\omega)^2)^{3/2}} = \frac{\begin{vmatrix} a'(\omega) & b'(\omega) \\ a''(\omega) & b''(\omega) \end{vmatrix}}{(a'(\omega)^2 + b'(\omega)^2)^{3/2}}(b)$$
(1)

Figure 2 illustrates the concept of oriented curvature along several frequency dependent curves.

Consider now a 1-port network terminated on a resistive load $r$. The input impedance is given by (2), where $r_m(\omega)$ denotes its resistive part and $x_m(\omega)$ its reactive part, while its reflection coefficient is given by (3). Computing the oriented curvature values for both of them (Supplementary Section 1) we get $k_{zm}(\omega)$ (the oriented curvature of the input impedance) and $k_{\Gamma_{1zm}}(\omega)$ (the oriented curvature of the 1-port reflection coefficient) as (4) and (5).

$$z_m(j\omega) = r_m(\omega) + jx_m(\omega)$$
(2)

$$\Gamma_{1zm}(j\omega) = \frac{z_m(j\omega)/r - 1}{z_m(j\omega)/r + 1}$$
(3)

$$k_{zm}(\omega) = \frac{r'_m(\omega)^2 \left(\frac{x'_m(\omega)}{r'_m(\omega)}\right)'}{(r'_m(\omega)^2 + x'_m(\omega)^2)^{3/2}}$$
(4)

$$k_{\Gamma_{1zm}}(\omega) = \frac{r'_m(\omega)^2((r + r_m(\omega))^2 + x_m(\omega)^2)\left(\frac{x'_m(\omega)}{r'_m(\omega)}\right)' + 2x_m(\omega)^2(r'_m(\omega)^2 + x'_m(\omega)^2)\left(\frac{r + r_m(\omega)}{x_m(\omega)}\right)'}{2r(r'_m(\omega)^2 + x'_m(\omega)^2)^{3/2}}$$
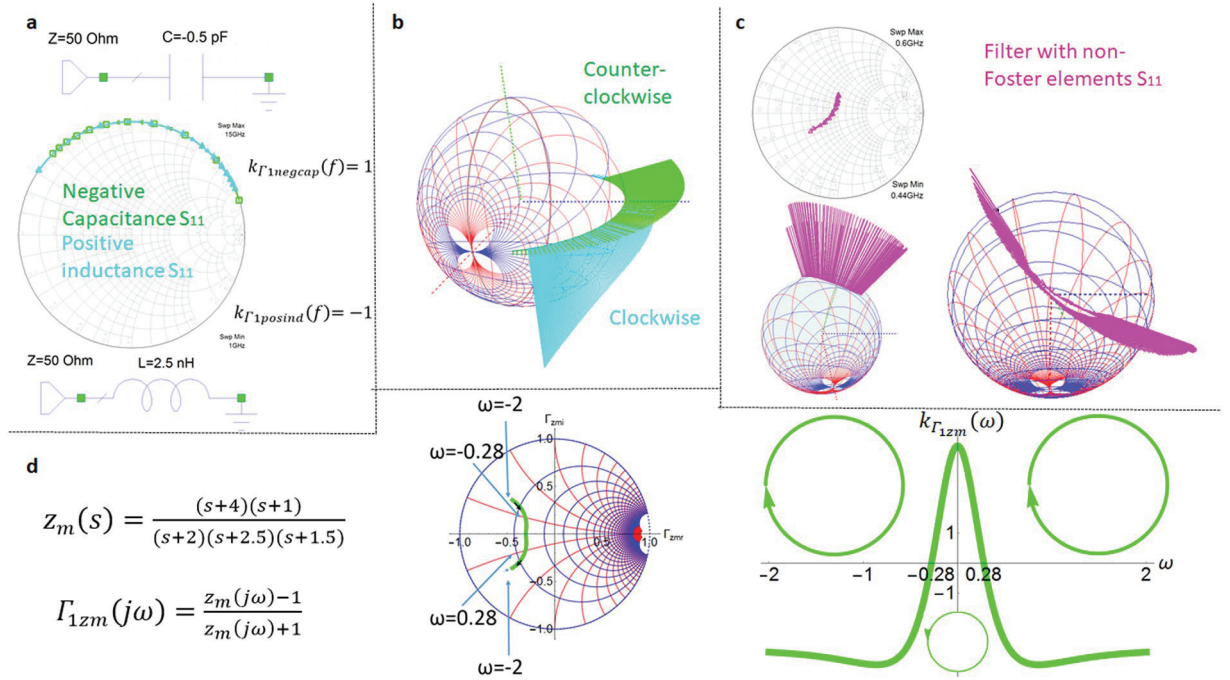(5)

**Figure 3.** Reflection coefficient orientation changes and the sign of the oriented curvature for different circuits. (**a**) Smith chart representation of the reflection coefficient for a 1-port negative capacitance (purely non-Foster circuit) and a positive inductance (purely Foster). For a capacitor with purely negative capacitance and an inductor with positive inductance their reflection coefficients $\Gamma_{1zm}(j\omega)$ overlap on the Smith chart on a wide frequency range. Their opposite orientation is given by the different sign of their oriented curvature $k_{\Gamma_{1zm}}(\omega)$. Their same path is given by the same absolute value of their oriented curvature. (**b**) On the newly implemented frequency dependent 3D Smith chart one can see the clockwise motion with increasing frequency for the inductor with positive inductance and the counter-clockwise motion for the negative valued capacitor, the motion is on the contour of the equatorial plane (lossless circuits). (**c**) Mixed motion for a fabricated circuit containing non-Foster (lossy elements). (**d**) Mixed clockwise and counter-clockwise motion of the reflection coefficient of a passive lossy network described by the positive real function $z_m(s)$ with the 1 port reflection coefficient (for $s = j\omega$) $\Gamma_{1zm}(j\omega)$. The reflection coefficient has a clockwise orientation from $-2 < \omega < -0.28$ and for $0.28 < \omega < 2$, while counter-clockwise orientation for $-0.28 < \omega < 0.28$. The sign changes of its 1-port reflection coefficient curvature $k_{\Gamma_{1zm}}(\omega)(5)$ generates the changes of orientation of its path on the Smith chart. It is interesting to notice that mixed motion can exist on limited bandwidth also for lossy circuits with only Foster elements and thus that the counter-clockwise motion is by no means a prove of an existence of a non-Foster element in the network. A more detailed description on oriented curvature and 1-port and two port networks is given in Supplementary Section 1.

Denoting with $x_{mF}(\omega)$ and $B_{mF}(\omega)$ the reactance and susceptance of purely Foster elements and with $x_{mNF}(\omega)$ and $B_{mNF}(\omega)$ the ones for Non Foster elements we obtain: for Foster networks $r_m(\omega) = 0$ while $\frac{dx_{mF}(\omega)}{d\omega} > 0$ and $\frac{dB_{mF}(\omega)}{d\omega} > 0$ and using (3)-(4) we get the input impedance and 1 –port reflection coefficient curvatures for them as: $k_{Fzm}(\omega) = 0$ and $k_{\Gamma_{1zm}}(\omega) = -1$ (Supplementary Section 1). For Non-Foster networks $r_m(\omega) = 0$ too, while $\frac{dx_{mNF}(\omega)}{d\omega} < 0$ and $\frac{dB_{mNF}(\omega)}{d\omega} < 0$ hold thus via (4) and (5) we get the input impedance and 1 –port reflection coefficient curvatures for them as $k_{NFzm}(\omega) = 0$ and $k_{\Gamma_{1zmNF}}(\omega) = 1$.

In the case of two port networks with equal port impedances similar computations can be done for purely Foster and non-Foster elements resulting in the corresponding reflection coefficients $\Gamma_{2zmF}$ and $\Gamma_{2zmNF}$ (6) with their corresponding oriented curvatures (computed in Supplementary Section 1) $k_{\Gamma_{2zmF}}(\omega) = -2$ and $k_{\Gamma_{2zmNF}}(\omega) = 2$.

$$\Gamma_{2zmF}(j\omega) = \frac{jx_{mF}(\omega)}{jx_{mF}(\omega) + 2}(a) \qquad \Gamma_{2NF}(j\omega) = \frac{-jx_F(\omega)}{-jx_F(\omega) + 2}(b) \qquad (6)$$

Their oriented curvature magnitudes explain the reflection coefficients paths on 0.5 radius circles in Fig. 1d,e on the Smith chart and 3D Smith chart (see Supplementary Section 1). Their oriented curvature opposite signs in (6) determines their reversed orientation.

The reflection coefficients of purely reactive 1-port elements are given in Fig. 3a–d (purely reactive Foster and non-Foster circuits in Fig. 3a, lossy circuits with non-Foster elements in Fig. 3c and lossy circuits with Foster
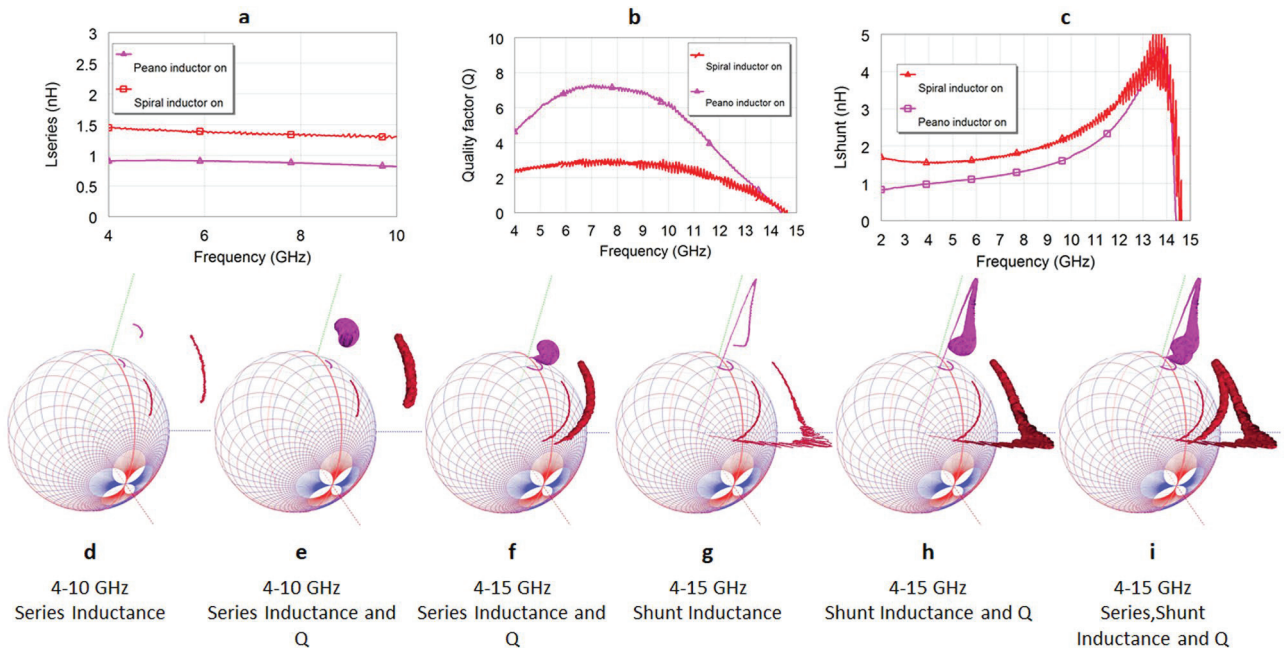
**Figure 4.** Series, shunt and quality factor frequency variations representations on a 2D plot and simultaneous 3D Smith chart visualization for the new fabricated Peano (pink) inductor in the conductive state of VO$_2$ versus previously reported best performing inductor (red) using VO$_2$ in same technology[37]. (**a**) 2D series inductance representation versus frequency: both Peano inductor and previously reported inductor[37] show stable series inductance in within the 4GHz-10GHz frequency range. (**b**) 2D frequency dependency of quality factors in the 4 GHz-15 GHz frequency range. (**c**) Shunt inductance frequency dependency shows linearity on a sharper frequency range (see Supplementary Section 3) for both inductors. (**d**) 3D Smith chart representation of series inductance over the S$_{11}$ parameters in the 4 GHz-10 GHz frequency range. (**e**) 3D Smith chart representation of series inductance and quality factors 4GHz-10GHz over the series inductances 3D curves. (**f**) 3D Smith chart representation of series inductance and quality factors 4GHz-15GHz. The Qs start descending to 0 close to 15 GHz (the cylinders radius becomes 0 when Q becomes negative) for both models while the S$_{11}$ parameters crossed into the West hemisphere of the Smith chart (capacitive region). (**g**) 3D Smith chart representation of shunt inductance 4GHz-15GHz. One may see that the shunt inductance becomes negative below 15 GHz (entering the 3D Smith chart). (**h**) 3D Smith chart representation of shunt inductance and quality factors 4GHz-15GHz. (**i**) Simultaneously 3D Smith chart representation of series, shunt inductance and quality factors (along both series and shunt inductance) in the 4GHz-15GHz range.

elements in Fig. 3d). The results in Fig. 3d show that reflection coefficients and input impedance orientation reversal can occur at lossy 1-port networks containing only Foster elements too.

The results plotted in Figs. 1,e and 3b,c show the new 3D Smith chart implementations capable of detecting orientation changes phenomenon.

The main new insight is given by the representation of the frequency parameter over the 3D Smith chart representation of the reflection coefficient $S_{11_{3d}}(j\omega)$ via a variable homothety with its center in the center of the 3D Smith chart: each frequency that corresponds to a point of the 3D Smith chart reflection point of the $S_{11_{3d}}(j\omega)$ curve will be displayed as a segment on the line that passes from the center of the 3D sphere and the point of the 3D Smith chart surface curve of $S_{11_{3d}}(j\omega)$. The length of the segment will be given by the normalized frequency and the direction will be outwards of the surface of the 3D sphere. Figure 1d displays in the 3D Smith chart surrounding space the counter-clockwise dynamics of the two port negative capacitor reflection coefficient while the clockwise dynamics of the two port reflection coefficient of the positive inductor. In Fig. 1e one may see the clockwise frequency increasing orientation of the reflection coefficient of the positive capacitor and the counter-clockwise orientation of the negative inductor. (Supplementary Section 2 describes the 3D implementation in detail).

The Smith chart plot can detect the magnitude of the curvature $|k_{\Gamma 2F}(\omega)|$ (which gives the path of the reflection coefficient-curve shape) but cannot perceive its sign which determines its direction; the new 3D Smith chart frequency orientation quantification and visualization implementation (the frequency sweeping is always increasing in our modelling) detects its sign (see additional video) and thus its orientation. In the cases presented in Fig. 1d,e, $|k_{\Gamma 2F}(\omega)|$ is constant but not zero thus the shape of the curves is a circle. The same happens in Fig. 3a,b. In more complex circuits one does not deal with reflection coefficients curves with constant curvatures anymore, $k_{\Gamma_{1zm}}(\omega)$, $k_{\Gamma 2F}(\omega)$ alternate in sign and magnitude values exhibiting orientation changes for both Foster and non-Foster circuits as seen in Fig. 3c,d. In Fig. 3d it can be seen that even a network characterized by a positive real function can generate mixed oriented curvature in its input impedance and reflection coefficient. These reversals of
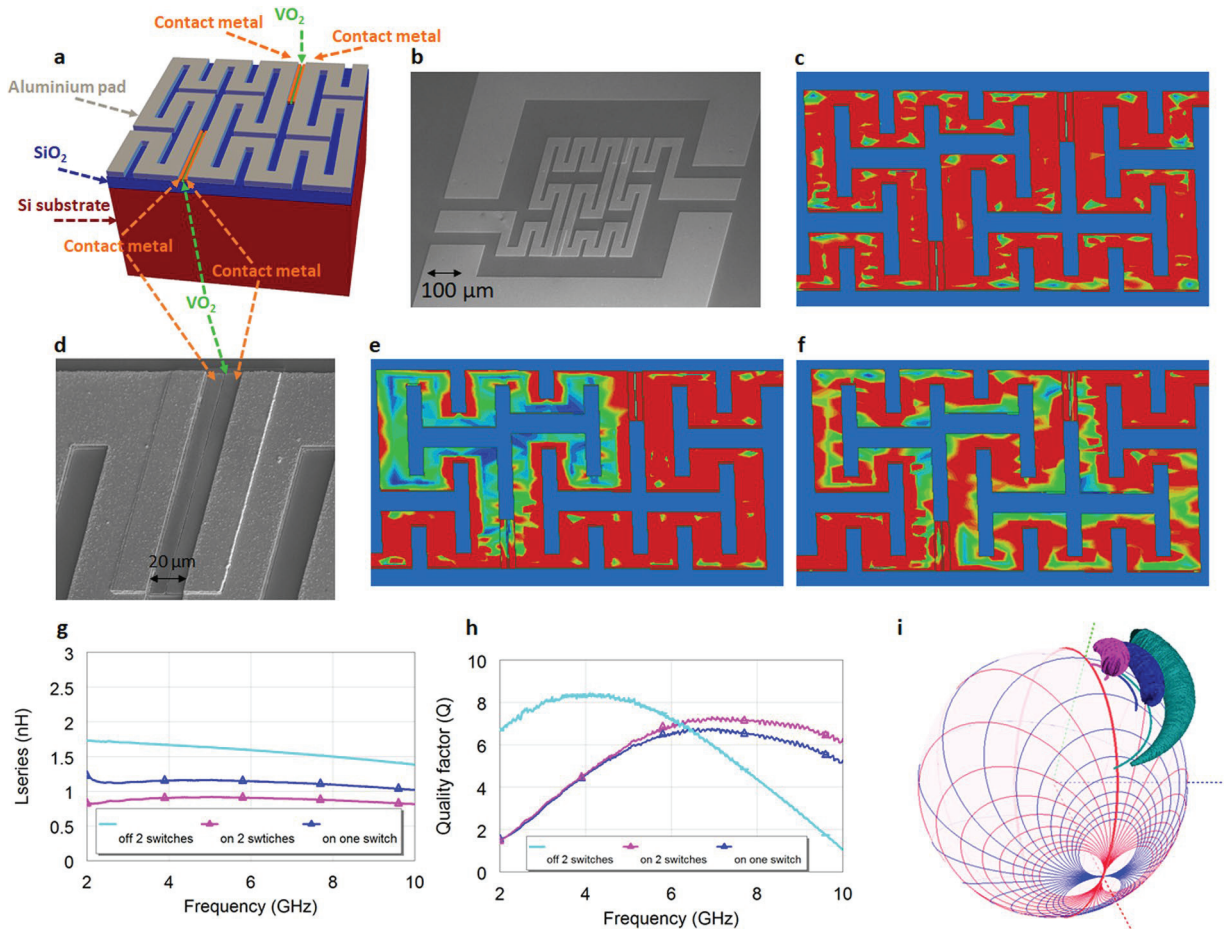
**Figure 5.** Fabricated VO$_2$ reconfigurable Peano inductor geometry and performances. (**a**) Cross sectional view (**b**), SEM photo of the inductors. (**c**) Current distribution (5 GHz) in the off state for an inductor with 2 switches. The current ignores the VO$_2$ switches and goes through all the windings in its path from port 1 (input) to port 2 (output). (**d**) VO$_2$ switch fabricated photo: a gap in the contact metal of 0.6 μm is left in order to contact the VO$_2$ layer. In the insulating phase of VO$_2$ the switch is in off state (acting like a lossy dielectric), in the conductive state of the VO$_2$ the 600 nm gap plays an important role to minimize the conductive losses since the VO$_2$ has a limited 48,000 S/m conductivity on the SiO$_2$/Si substrate. (**e**) Current distribution (5 GHz) in the hypothetical on state of one switch while the other is in the off state. The current ignores the off state VO$_2$ switch and follows a shorter path from input to output. (**f**) Current distribution (5 GHz) in the on state for an inductor with 2 switches. All current distributions are within a range from 0.5 A/m (dark blue) to 5.2 A/m (intense red) using the same scale. (**g**) Series inductance of the fabricated inductors with 2 switches, in on state and off state, series inductance of an inductor with one switch in on state. (**h**) Quality factor of the inductor with 2 switches in off state and on state, and of an inductor with one switch (on state). (**i**) Simultaneous 3D Smith chart representation for the 2 GHz-10 GHz frequency of the series inductance and quality factors for all 3 situations.

orientation may be easy overlooked on the Smith chart if the zooming scales are not properly chosen but using (4) and (5) this is clearly discovered in Fig. 3d within the sign changes of $k_{\Gamma_{1zmF}}(\omega)$.

## New 3D visualization insights of frequency dependent series and shunt inductances and quality factors.

The S parameters of the inductors are directly converted by the new implementations in the 3D Smith conceptual software tool into the series inductance model $Lseries(\omega)$[37,38] and shunt inductance model $Lshunt(\omega)$[34–36] using classical conversion techniques of two port parameters (see Supplementary Section 2). The series and shunt inductances values are then normalized to their maximum value over the frequency range of interest and we get the corresponding normalized values $Lseries_N(\omega)$ and $Lshunt_N(\omega)$. The reflection parameter $S_{11}(j\omega)$ of the inductor is then plotted first on the surface of the 3D Smith chart as $S_{11_{3d}}(j\omega)$ using the previously implemented features[11,13]. Then the 3D space surrounding the 3D Smith chart is used by means of a variable homothety with the homothetic center in the center of the sphere through the $S_{11_{3d}}(j\omega)$ parameter of the inductors. The $S_{11_{3d}}(j\omega)$ parameter is sent now here to another point in 3D at a distance corresponding to $Lseries_N$ or $Lshunt_N$:
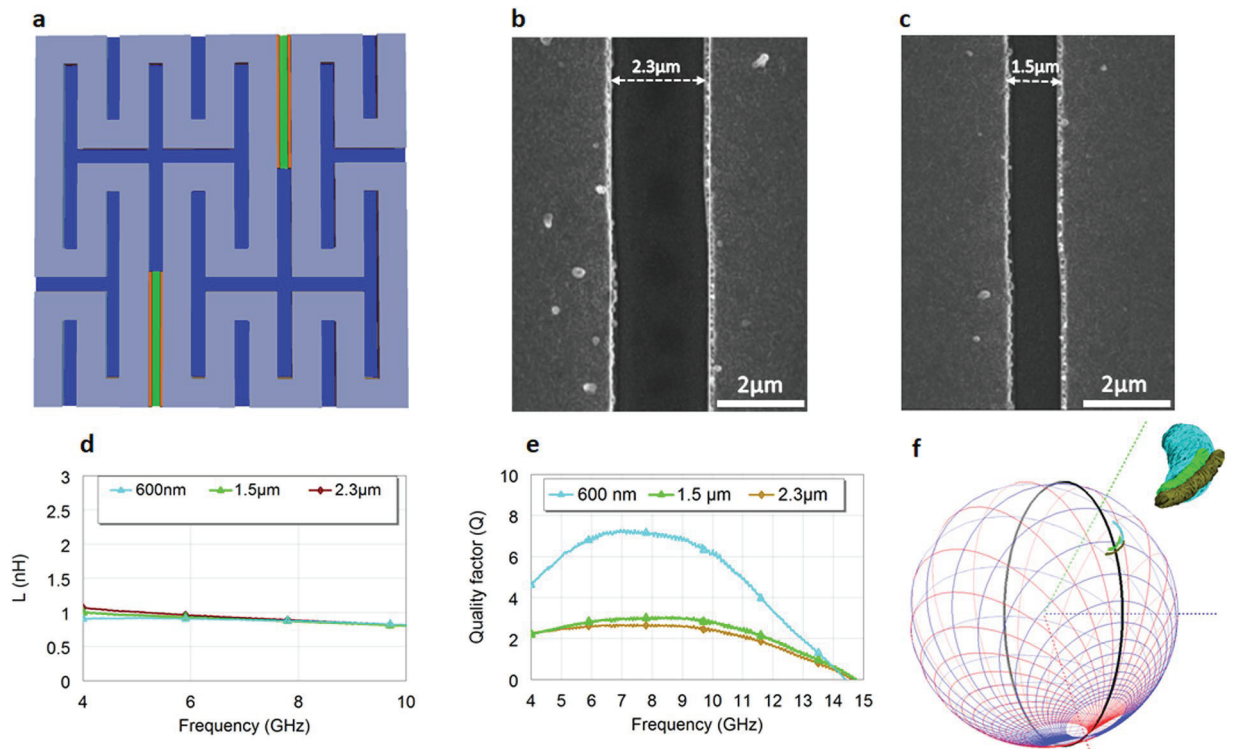
**Figure 6.** Fabricated VO$_2$ reconfigurable Peano inductors with additional various switches lengths and their influence in the on state. (**a**) Top view of the inductor-whose cross section is depicted in Fig. 5a. (**b**) SEM photo of a 2.3 μm long switch. (**c**) SEM photo of a 1.5 μm long switch. (**d**) Extracted (from the measured S parameters): Lseries of the inductor with 2 switches in on state for 600 nm long switches, 1.5 μm and 2.3 μm. (**e**), Q of the inductor with 2 switches in on state, for the 600 nm long switches, 1.5 μm and 2.3 μm. (**f**) Simultaneous 3D Smith chart representation for the 4 GHz-10 GHz frequency of the Lseries, Q and $S_{11}$ parameters for the three different inductors with 600 nm long switches, 1.5 μm and 2.3 μm long switches.

$$Lseries, \ shunt_{3d}(\omega) = (LseriesN, \ shunt_N(\omega) + 1) * S_{11_{3d}}(j\omega) \tag{7}$$

$Q(\omega)$ of the inductors is also computed by the new 3D Smith chart tool implementation using classical conversion formulas (from the S parameters) (see Supplementary Section 2) and normalized to its maximum value over the frequency range of interest obtaining $Q_N(\omega)$. Using the 3D representation of the *Lseries, shunt*$_{3d}(\omega)$ curves we then use the normal plane of the curves to associate to each (frequency) point of the curves the $Q(\omega)$ as a cylinder $Q_{3D}(\omega)$ of variable radius associated to its normalized value $Q_N(\omega)$. In Fig. 4 one may see the new representations done for the novel fabricated Peano inductor whose performances are compared with the spiral inductor in[37] (the description on the new inductor design will be presented in the following section).

The new implementation allows the concurrent view of complex valued-scalar parameters: $S(j\omega)$, $Lseries_{3d}(\omega)$, $Lshunt_{3d}(\omega)$, $Q_{3D}(\omega)$ and frequency (not plotted in Fig. 4 since the dynamics of $S_{11}(j\omega)$ is clockwise anyway in this case, unlike the cases presented in Fig. 3). The use of different perspectives and the topology of the 3D Smith chart permits one thus to simultaneously analyze complex parameters (Smith chart) and visualize series and shunt inductances and *Q*s all on the same interactive display. This plays an insightful role in investigation for directly understanding multiple phenomenon on a single view. The information contained in Fig. 4a–c can be visualized together using three scaling on a common 2D plot, however still without having any information on $S_{11}(j\omega)$ of the inductor. In Fig. 4d we may see just $S_{11_{3d}}(j\omega)$ and $Lseries_{3d}(\omega)$, the display contains already more information than in the 2D Fig. 4a, allowing us to understand that the series inductance model is linear for both analyzed inductors and that $S_{11_{3d}}(j\omega)$ is still in the East hemisphere (in the 4 GHz-10 GHz frequency range) (inductive). Additionally, the zeros of the $S_{11}(j\omega)$ are strongly related to the zeros of the $Y_{11}(j\omega)$ of an inductor and under certain circumstances (in some) identical (no resistive losses in their equivalent Pi model), thus a change of hemisphere of the $S_{11}(j\omega)$ is strongly related to the self-resonances of the inductors model implying in most cases that the $Q$ fails to be positive anymore (see Supplementary Section 3). In Fig. 4e we can see $S_{11_{3d}}(j\omega)$, $Lseries_{3d}(\omega)$ and $Q_{3D}(\omega)$ for the 4 GHz-10 GHz frequency range, again the information contained offers an insight on three parameters impossible to visualize together in 2D. In Fig. 4f we may see how by increasing the analysis range up to 15 GHz the $Q$s for both inductors become zero, while the $S_{11_{3d}}(j\omega)$ enters the capacitive hemisphere too. It is interesting to notice that the series inductance model stays linear. Using the 3D Smith chart tool (see Supplementary Video) one may see the exact frequencies at which $S_{11_{3d}}(j\omega)$ changes hemisphere and the frequency for which $Q$ becomes zero (the 3D gen-
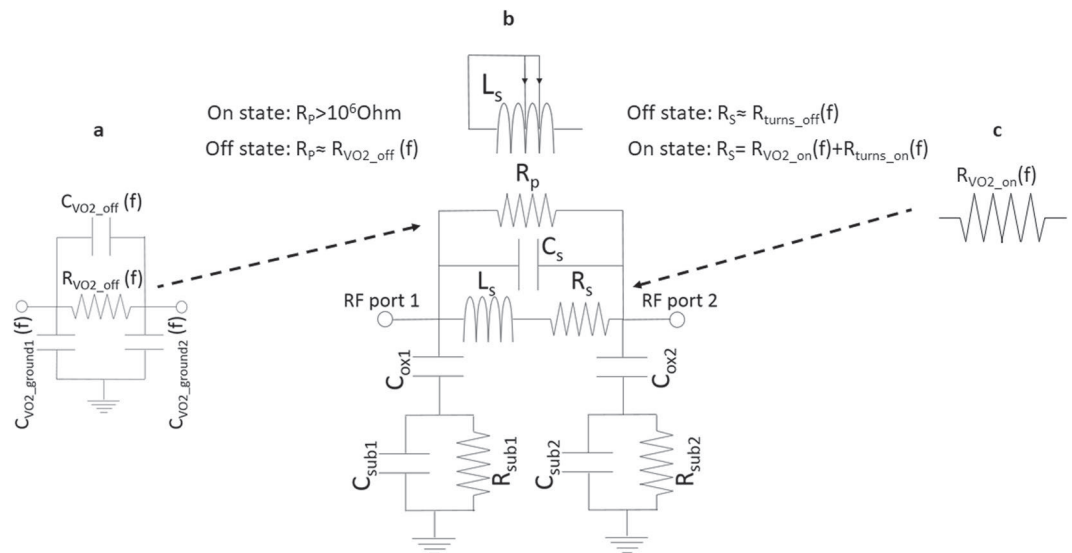
**Figure 7.** Proposed equivalent circuit of the Peano reconfigurable inductors and $VO_2$ switches in the off and on state for the 4 GHz-10 GHz frequency range. (**a**) Off state modelling of the $VO_2$ switch: $R_{VO2\_off}$ is modelling the undesired losses in between the adjacent turns where the $VO_2$ switches are present. Ideally $R_{VO2\_off} = \infty$, however the non-zero conductivity of $VO_2$ (whose measurement in DC is present in Fig. 9-Methods) will generate undesired conductive losses between turns. Similarly, the frequency dependent dielectric constant of the $VO_2$ can in theory generate undesired couplings between the adjacent turns where the $VO_2$ is present: $C_{VO2\_off}$, $C_{VO2\_ground1}$ and $C_{VO2\_ground2}$ are modelling the coupling losses between the $VO_2$ switches and coplanar waveguide ground planes. (**b**) Extracted equivalent circuit of the inductor: $L_s$ stands for the series inductance, $C_s$ stands for the inter-turns capacitance, $C_{ox1}$, $C_{ox2}$, $C_{sub1}$, $C_{sub2}$, $R_{sub1}$, $R_{sub2}$ describe the RF losses within the various substrates layers. $R_p$ is modelling the undesired conductive losses between the adjacent turns due to the $VO_2$ conductivity. In the off state we would like $R_p$ to be $\infty$, however the conductive losses in the $VO_2$ switches will make this term being un-unneglectable. $R_s$ is modelling the series resistance-dependent on the Al deposition and trace width, (counting the on/off resistances corresponding to the current paths through the turns $R_{turns\_on}$/$R_{turns\_off}$), but including too the $VO_2$ resistive losses $R_{VO2\_on}$ in the on state of the switches. (**c**) On state modelling of the $VO_2$ switch: $R_{VO2\_on}$ is modelling the undesired resistive losses due to the limited conductivity of the $VO_2$ in the on state. This resistance will contribute to a higher value of the $R_s$ in the on state since the current will pass through the switches.

eralized cylinders become curves-their radius becomes zero (at 14.44 GHz for both inductors). In Fig. 4g $S_{11_{3d}}(j\omega)$, $Lshunt_{3d}(\omega)$ models become negative starting 14.44 GHz for both inductors and thus they enter the interior of the 3D Smith chart from that frequency point. In Fig. 4h we may see $S_{11_{3d}}(j\omega)$, $Lshunt_{3d}(\omega)$ and $Q_{3D}(\omega)$, clearly $Q_{3D}(\omega)$ becomes zero once $Lshunt_{3d}(\omega)$ enters the 3D Smith chart. In Fig. 4i all these parameters are shown together.

**Peano reconfigurable inductors using $VO_2$ switches.** As a case study of the 3D Smith chart and its usefulness for radiofrequency characterization with $VO_2$, and with the aim to improve our reported results in[37] (in terms of $Q_{max\_on}$, $Q_{max\_on}/Q_{max\_off}$, tuning states and tuning range) we have first designed, fabricated and then extracted its equivalent circuit a reconfigurable inductor based on the Peano curve of order 2 by means of $VO_2$ switches (Figs. 5–8).

The design of the inductor was done using the similar procedures as in[37], targeting an extracted *Lseries* of around 1.5 nH in the off state of the both switches and of 0.9 nH in the on state of both while reaching around 1.3 nH if only one switch is used, while targeting to maximize the *Q* within 4–10 GHz frequency in the on state of the $VO_2$ where conductivity levels prove to be below 50,000 S/m (please see the Fig. 9 in the Methods).

Their Peano geometry is presented in Fig. 5. In Fig. 5a one may see the cross-sectional view of the technology used. The inductors were fabricated using standard microelectronic processes starting with a high-resistivity (10000 $\Omega$·cm) 525 $\mu$m thick silicon substrate. A 300 nm thick amorphous silicon layer was first deposited to improve radiofrequency performances[52,53]. The substrate was then passivated with 500 nm $SiO_2$ deposited by sputtering. 140 nm-thick $VO_2$ and films a Pulsed Laser Deposition (PLD). The film was then patterned using photolithography followed by dry etching and Cr (20 nm)/Al (400 nm) bi-layer was deposited to contact the patterned $VO_2$ film. This thin contact layer allowed here the realization of smaller than 0.6 $\mu$m gaps between the contact pads (unlike 2 $\mu$m in our previous work[37] or 1 $\mu$m in[54]). Additionally, a 2.4 $\mu$m-thick Al layer was deposited on top of these contact pads by conventional lift-off methods to provide low RF losses (to create the final CPW elements), the photo of the fabricated inductor being shown in Fig. 5b.

$VO_2$ limited on state conductivity levels on Si/$SiO_2$ substrates constitute a challenge for the reconfigurable $VO_2$ RF design[54], while to reduce its impact, 1 $\mu$m switches were employed in the fabricated designs[37,54].
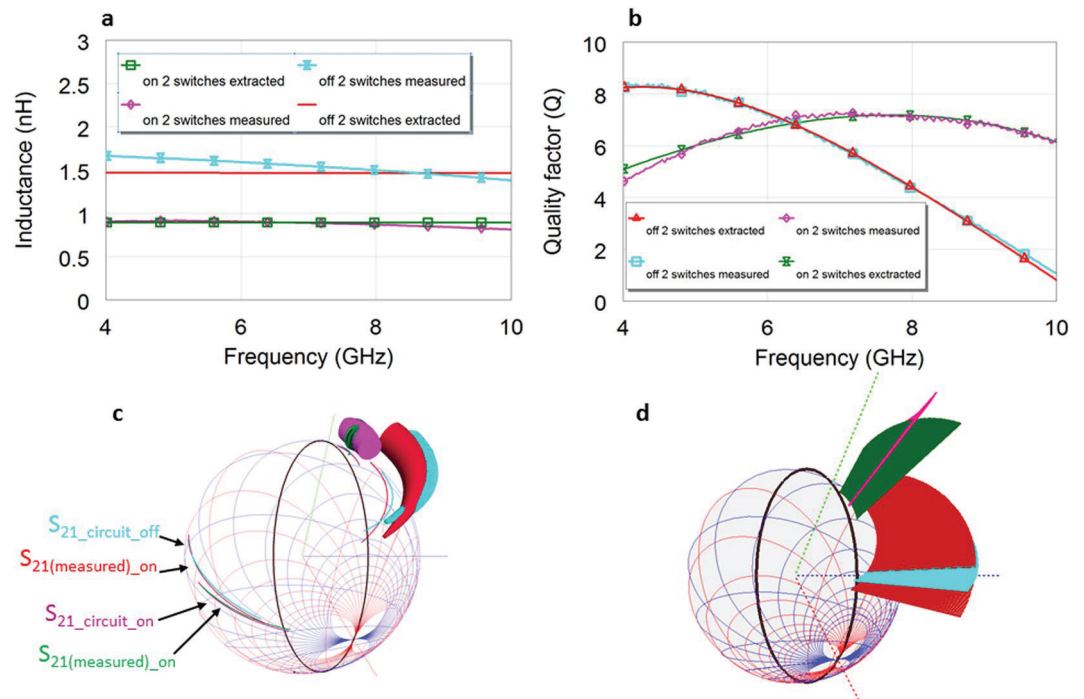
**Figure 8.** Fabricated VO$_2$ reconfigurable Peano inductor equivalent circuit modelling within 4 GHz-10 GHz for the inductor with 2 switches, in on state and off state compared to measured ones. (**a**) The resulted fitting of the equivalent circuit extracted Lseries_circuit and Lseries from the measured S parameters. The values are extracted optimizing simultaneously the Lseries_circuit, Q_circuit, module and phase of the $S_{ij\_circuit}(j\omega)$ (2 scalar parameters and 3 complex values due to reciprocity). Off state values: L$_S$ = 1.48 nH R$_S$ = 2.79 Ohms, R$_p$ = 1341 Ohms, C$_s$ = 0.17fF, C$_{ox1}$ = C$_{ox2}$ = 721 fF, C$_{sub2}$ = C$_{sub2}$ = 201 fF, R$_{sub1}$ = R$_{sub2}$ > 10$^8$ Ohm. On state values: L$_S$ = 0.90 nH, R$_S$ = 4.01 Ohms, R$_p$ = 10$^7$ Ohm, C$_s$ = 0.15fF, C$_{ox1}$ = C$_{ox2}$ = 724 fF, C$_{sub1}$ = C$_{sub2}$ = 201 fF, R$_{sub1}$ = R$_{sub2}$ > 10$^8$ Ohm. (**b**) Scalar Q and extracted Q_circuit resulted fitting (**c**), Simultaneous 3D Smith chart representation for Lseries_circuit, Q_circuit, $S_{ij\_circuit}(j\omega)$, and Lseries, Q, S parameters of the measured inductors. The fitting of the $S_{21}$ parameters is almost perfect, the fitting of the $S_{11}$ parameters (whose values are extremely small in magnitude) is not perfect-but it overlaps on a specific frequency range too. $S_{11}$ is more sensitive to the frequency dependency of the elements neglected in the simplified equivalent circuit in Fig. 7b. (**d**) Simultaneous 3D Smith chart representation for all the $S_{11}$ ($S_{ij\_circuit}(j\omega)$ and measured $S_{11}(j\omega)$) parameters and their frequency dependency. It is interesting to notice their change of hemisphere just below 10 GHz for the off state modeled and measured inductors (this happening before their Q becomes 0-the radius of the cylinders in c is not yet zero, or in b one may see still the positive values of Q). This means that the imaginary part of $S_{11}$ becomes "capacitive" before its Y$_{11}$ imaginary part becomes 0-which determines the sign changes in Q. Referring to[56,57] the classical quality factor[34–39] analysed and implemented here too is a measure of the inductor performances while short-cutting the second port. If the inductor is connected in shunt in the final circuit the change of hemisphere of $S_{11}$ below 10 GHz can be neglected, else depending on the configuration in which this is finally used- the change of hemisphere warns that under 50 Ohm load the inductor starts behaving capacitive before 10 GHz.

The small length of the VO$_2$ switches obtained here, below 0.6 μm, at the limit of photolithography, minimizes the losses while in the on state (measured as 48,000 S/m), while their increased width (120 μm) contributes too to this effort (a tilted photo of the switch in Fig. 5b, is in detail in (Supplementary Section 3). Switch photos and current distributions are further shown in Fig. 5c–f.

In order to validate this claim we additionally fabricated inductors with 1.5 μm and 2.3 switches lengths (Fig. 6a–c and visualized their underwhelming performances in Fig. 6c,d.

The inductor has been simulated in the Ansys HFSS commercial software tool while visualizing the extracted inductances and Q on the new 3D Smith chart tool. The position of the VO$_2$ switches was optimized in order to maximize Q$_{max\_on}$, Q$_{max\_on}$/Q$_{max\_off}$, tuning states and tuning range: the final current distribution at 5 GHz being shown as simulated in Fig. 5c (when both switches are off), Fig. 5e when one switch is off and one on and Fig. 5f with both switches on.

The measured inductances and Qs plotted in Fig. 4a,b are compared to our previous work[37] for the on state of the inductor with two switches show ("on" when measured at 100 °C): Peano inductors more than double the Qs while also dealing with a smaller inductance (0.9 nH unlike 1.35 nH in[37], while usually the Q$_{max}$ decrease a lot while using lower inductances[34]) for the 5GHz-10 GHz frequency range. Further the series inductance is stable with an average value of 0.95 nH within the 4GHz-10 GHz frequency range and thus over-performing our previous reported results[37]. In terms of shunt inductance (untreated in[37,38]) the inductor is stable within the 3 GHz-6 GHz frequency range with an average of 1nH as seen in Fig. 4c.

The overall performances of the inductor with two switches on, two switches off and of a fabricated inductor with one switch on are all plotted together in Fig. 5g (series inductances), Fig. 5h $Qs$ and Fig. 5i both $Qs$ and normalized 3D series inductances and $Qs$. The results show 77% tuning range and $Q_{max\_on}/Q_{max\_off}$ 0.88 and thus 3.26 times higher than $Q_{max\_on}/Q_{max\_off}$ reported in[37]. The $Q_{max\_on}$ exceeds 7 being comparable with the off state even though the inductance is tuned with 77% down to 0.95 nH.

On the other hand, the frequency dependency of the off state $Q_{off}(\omega)$ is comparable with the one reported in[37] (although dealing with a smaller inductance than in[37]). Overall exhibiting a better performance (in terms of $Q_{off}$ $(\omega)$) in the low GHz frequency range and a more stable frequency dependency linearity (in terms of series inductance) the values are facing the same trend as in[37]. The maximum value is limited as in[37] by the CMOS compatible CPW SiO$_2$/Si technology used with Al metallization, (Supplementary Section 3).

**Peano reconfigurable inductors modelling and characterization.** The simplified proposed equivalent circuit of the inductor based on the Fig. 5 inductor's layout, together with switches equivalent circuit models are presented in Fig. 7a–c. The simplified (frequency independent) Pi model proposed in Fig. 7 uses the classical elements present in inductor modelling[38,55] as described in Fig. 7. The only additional element added is $R_p$ - which is modelling the conductive losses in the adjacent turns due to the presence of the VO$_2$ and fabrication flow. In the off state the value of $Rp$ (instead of tending to $\infty$) will be affected by the conductive losses in the VO$_2$ (as described in Fig. 7).VO$_2$, whose DC conductivity is presented in Fig. 9 will have higher conductivity losses in RF ranges[44], losses which in the off state will contribute to conductive losses between the turns. In the on state on the other hand, the presence of the VO$_2$ (see Fig. 5f) on the main current path will influence the series resistive losses $R_s$ in increasing its value. $R_s$ will thus have an additional component in the on state (besides the turns resistance corresponding to the on state current path), component which will be generated by the VO$_2$ resistive losses in the on state.

The extraction of the inductor equivalent circuit parameters is done using an original approach, based on common optimization of 3 (complex) S parameters ($S_{21}(j\omega) = S_{12}(j\omega)$, due to reciprocity) and extracted $Lseries$ and $Q$. Thus we impose the measured $S_{ij}(j\omega) = S_{ij\_circuit}(j\omega)$-where the last denote the equivalent circuit S parameters (and i = 1, 2) and the $Lseries$ and $Q$ to be equal to the extracted $Lseries\_circuit$ and $Q\_circuit$ of the proposed equivalent circuit. It is worth mentioning that the extraction of the equivalent circuit is usually done using just fitting scalar parameters: series or shunt inductance and $Q$- as in[34](by us)[35], (Supplementary File), or only series inductance[38]. These approaches are however incomplete, since the $Q$ model classically used[34–38], is neglecting the right arm of the Pi model, being based on $Y_{11}$, thus having the second port grounded[56,57]. These $Q$ values (from both measured and equivalent circuit extracted models $Q\_circuit$) are accurate only if the inductor is used connected to a ground load[56,57]. The extracted inductance fitting on the other hand is modeling just an element of the equivalent circuit, model based on only one of the $Y_{11}$ or $Y_{21}$[34–38] parameters, thus the overall S parameters may not fit at all even though $Q$ and extracted inductance fitting is reached.

Visualizing the fitting of $S_{ij}(j\omega)$ and $S_{ij\_circuit}(j\omega)$ only on the (2D) Smith chart, as in Figs. 1d,e and 3a may lead to possibly inaccurate solutions, since the paths on the Smith chart may coincide for two circuits on a frequency range even though their nature can be different (which determines their frequency parametrization).

Here we take benefit of the new 3D Smith chart implementations and while using the AWR Microwave Office optimization tool, we simultaneously optimize in the extraction process all $S_{ij\_circuit}(j\omega)$, $Lseries\_circuit$ and $Q\_circuit$ while visualizing this complex-scalar process on the 3D Smith chart.

Figure 8a,b show the results on a classical 2D scalar plot, while Fig. 8c,d on the 3D Smith chart plot. The $S_{21\_circuit}(j\omega)$ parameter fitting is almost perfect (in both states) (all being in the West hemisphere), while the $S_{11\_circuit}(j\omega)$-starts diverging slightly from $S_{11}(j\omega)$ in phase at the higher frequencies for both on and off states.

Finally, it can be observed in Fig. 8c or 8d that both off state $S_{11}(j\omega)$ and $S_{11\_circuit}(j\omega)$ change the hemisphere before 10 GHz (i.e. imag $S_{11}(j\omega)$ and $S_{11\_circuit}(j\omega)$ becomes negative), while their $Q$ remains positive (the radius of the generalized cylinders being not yet a point), showing the good match (both change hemisphere) but also the limitations of the inductor when used in a different configuration[57] than grounded. An inductor $S_{11}(j\omega)$ parameter should stay in the inductive part of the Smith chart (East hemisphere-3D Smith chart) for the entire frequency range of interest in order to assure its validity of use under any resistive loads conditions.

## Conclusions

We have first reported new theoretical foundations for a frequency-dependent 3D Smith with 3D visualization methods for the orientation of parametric curves and used them to quantify and understand curvature reversal, while sweeping the frequency, for driving point impedances and reflection coefficients of circuits in the RF frequency bands. Further we have additionally extended the capabilities of the 3D Smith chart tool to simultaneously visualize a variety of frequency dependent scalar-complex valued parameters required in the inductor modelling and thus proposed a unique multi-parameter display. We demonstrated by fabrication and measurements, original Peano reconfigurable inductors by employing the phase change VO$_2$ materials in CPW/CMOS compatible technology on SiO$_2$. The reported inductors improve the previously reported state of art in the incipient field of VO$_2$ reconfigurable inductors design for the S, C and X bands of the radio frequency spectrum.

## Methods

**Fabrication.** The devices were fabricated using a high resistivity (10000 $\Omega$·cm) Si wafer (525 µm) as the starting substrate. A 300 nm-thick amorphous Si was deposited by low pressure chemical vapor deposition (LPCVD), to reduce the losses during measurement. A surface passivation using 500 nm sputtered SiO$_2$ was then carried out, followed by deposition of 140 nm -thick VO$_2$ using a Pulsed Laser Deposition (PLD) system. The film was deposited by pulsed lased deposition (PLD) using a Solmates SMP 800 system. The deposition was performed at 400 °C in oxygen ambient, with a chamber pressure of 0.01 mbar. The ablated V$_2$O$_5$ target was placed at 60 mm
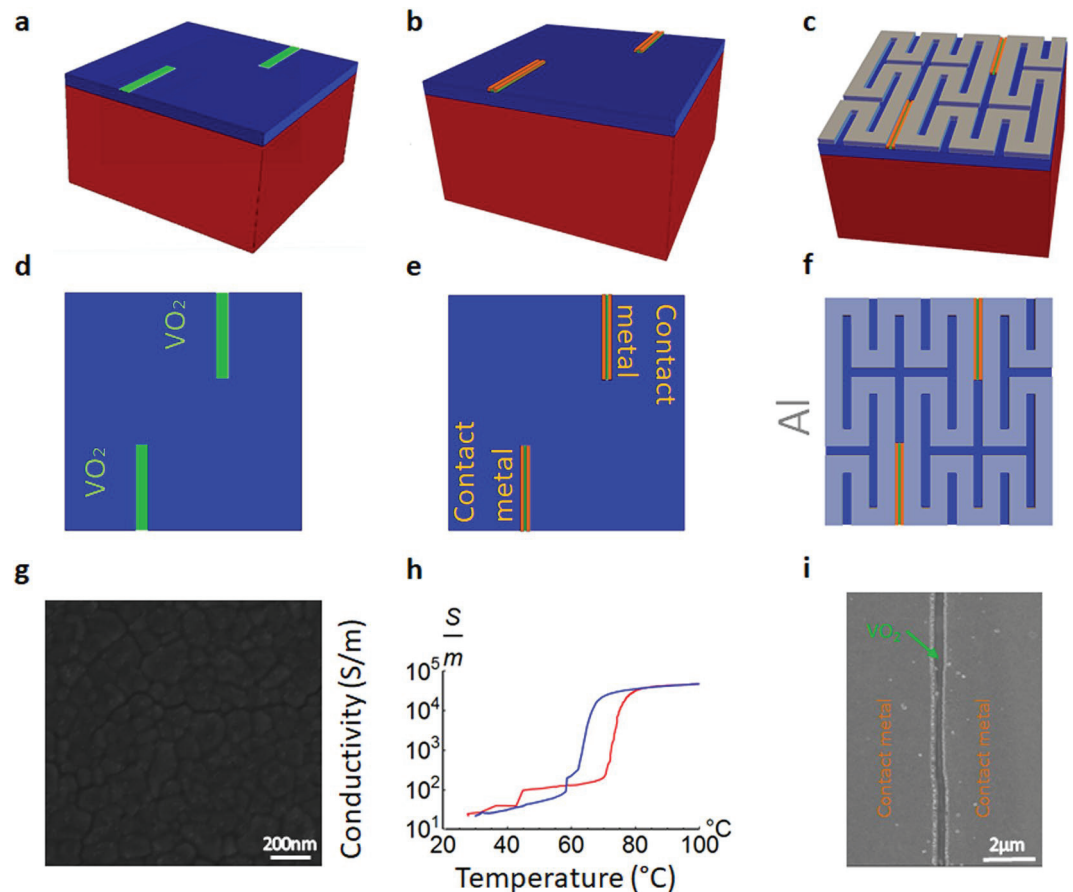
**Figure 9.** Methods|Fabrication flow and $VO_2$ characterization description. (**a**) $VO_2$ deposition via PLD, followed by a photolithography step and dry etching of the $VO_2$. (**b**) Cr-20 nm/Al 400 nm contact metal deposition by evaporation after a subsequent photolithography and patterning on the $VO_2$ (**c**), Al evaporation and lift off for top metallization. (**d**) Top view of (**a**). (**e**) Top view of (**b**). (**f**) Top view of (**c**). (**g**) Grain size of the PLD $VO_2$ deposition. (**h**) Conductivity levels in heating (red) and in cooling (blue). (**i**) Switch SEM photo: The gap in the contact metal is below 600 nm over the entire width of the switches. This gap where only $VO_2$ is active represents the switch length.

distance from the wafer. Further the deposition, an annealing of 10 min at 475 °C was performed without breaking the vacuum in the chamber.

The electrical properties of the films were studied from room temperature up to 100 °C by determining their temperature dependent electrical resistivity converted than in conductivity. This was done by standard four-point probe measurements using a semiconductor parameter analyzer (HP 4156 C) and a control on the sample temperature up to 100 °C.

The fabrication process for the Peano inductors on the above substrate then commenced with a photolithography step to pattern the $VO_2$ followed dry etching to remove the $VO_2$ from the unwanted areas. A Cr-20 nm/Al-400 nm bi-layer metal stack was then deposited by evaporation after a subsequent photolithography step on the patterned $VO_2$. This thin metallization made it possible to realize sub-micron gaps (600 nm) which is critical for extracting a good Q in the conductive state of $VO_2$ for the inductors. This was followed by deposition of a 2.4 μm-thick Al layer on these contact pads by conventional lithography followed by metal lift-off procedure to form the CPW elements with low RF losses.

**Devices simulation and characterization.** The numerical simulations of the inductor and filters were done in HFSS ANSYS commercial software relying on the finite element method (FEM) to solve Maxwell equations. Considering the full wave electromagnetic simulation technique, we used the modal solution type for the inductors and the terminal solution type for the filter simulations. The conductivity of the Al was decreased to $3.1*10^7$ S/m and the $VO_2$ switches were modeled for the inductors as simple dielectrics with 20 S/m losses and a loss tangent of 0 in the off state. In the on state, the $VO_2$ switches were simulated as lossy metals of a conductivity of 48,000 S/m. Subsequently full inductors and filters models were built in the software according to the actual physical structure fabricated. The Peano shapes were implemented using the Equation Curve facility of the tool, their equations being written parametrically and where needed rotations and reflections were used for the very final shapes.

The devices were measured with the Anrtisu Vector Star VNA in a Cascade Summit prober with controllable chuck temperature who was set to 20 °C in the "off state" and 100 °C in the on state. For the 2D graphical interpretation the measured S parameters were converted using the Anritsu Star VNA installed Microwave Office too into the desired parameters analysed. In order to obtain the extracted equivalent circuit parameters circuit we used the Genetic Algorithm of the Anritsu-AWR MW Office installed tool and optimization of 3 complex parameters and $Sij(j\omega) = Sij\_circuit(j\omega)$ and two scalars: $Lseries = Lseries\_circuit$ and $Q = Q\_circuit$ – in the 4 GHz–10 GHz range using 15,000 iterations.

**3D smith chart implementation.** The 3D Smith Chart application is developed using the Java programming language and the following libraries and development environment are used:

- 3D rendering: OpenGL through the Java Binding for the Open GL API (JOGL2) library;
- Mathematical operations and complex data representation: The Apache Commons Mathematics Library;
- Development environment: The NetBeans IDE with Beans Binding Library for the implementation of the application GUI and JOGL2 usage.

Further implementation details about the new mode of visualization, new simulation parameters used in the paper and their 3D representation on the Riemann sphere can be found in Supplementary Section 2.

**Mathematical modelling of curvature.** The calculations for the oriented curvature was performed using Mathematica software tool by writing the frequency parametric equations of the curves analyzed.

## References

1. Smith, P. H. Transmission-line calculator. *Electronics* **12**, 29–31 (1939).
2. Zhu, B. O., Zhao, J. & Feng, Y. Active impedance metasurface with full 360° reflection phase tuning. *Sci. Rep.* **3**, 3059 (2013).
3. Thang, B., Sodickson, D. K. & Cloos, M. A. A high-impedance detector-array glove for magnetic resonance imaging of the hand. *Nat. Biomed. Eng.* **2**, 570–577 (2018).
4. Tuca, S.-S. *et al.* Calibrated complex impedance of CHO cells and E. coli bacteria at GHz frequencies using scanning microwave microscopy. *Nanotechnology* **27**, 135702 (2016).
5. Qu, L. *et al.* Mode-Controlled Wideband Slot-Fed Ground Radiation Antenna Utilizing Metal Loads for Mobile Applications. *IEEE Trans. Antennas Propag.* **65**(2), 867–872 (2017).
6. Chu, H. C. & Ma, T. Beamwidth switchable planar microstrip series-fed slot array using reconfigurable synthesized transmission lines. *IEEE Trans. Antennas Propag.* **65**(7), 3766–3771 (2017).
7. Liu, C. *et al.* Long-distance propagation of short-wavelength spin waves. *Nat. Commun.* **9**, 738 (2018).
8. Liu, S. & Liu, A. A novel design methodology for high-efficiency current-mode and voltage-Mode Class-E Power Amplifiers in Wireless Power Transfer systems. *IEEE Trans. Power Electron.* **32**(6), 4514–4521 (2017).
9. Ma, J., Steer, M. B. & Jiang, X. An acoustic filter based on layered structure. *Appl. Phys. Lett.* **106**, 111903 (2015).
10. Dubois, M.-A. & Murait, P. Properties of aluminum nitride thin films for piezoelectric transducers and microwave filter applications. *Appl. Phys. Lett.* **74**(20), 3032–3034 (1999).
11. Muller, A. A., Soto, P., Dascalu, D., Neculoiu, D. & Boria, V. E. A 3d Smith chart based on the Riemann sphere for active and passive microwave circuits. *IEEE Microw. and Wireless Compon. Lett.* **21**(6), 286–288 (2011).
12. Zelley, C. A spherical representation of the Smith chart. *IEEE Microw. Mag.* **8**(3), 60–66 (2007).
13. Muller, A. A., Sanabria-Codesal, E., Moldoveanu, A., Asavei, V. & Lucyszyn, S. Extended capabilities with group delay and resonator quality factor. *IEEE Trans. Microw. Theory Techn.* **65**(1), 10–17 (2017).
14. Muller, A. A., Moldoveanu A., Asavei V. & Fleischer C. 3D Smith chart tool, www.3dsmithchart.com (2019).
15. Shan, A. A. *et al.* Physics-based multi-bias RF large-signal GaN HEMT modeling and parameter extraction flow. *IEEE J. Electron Devices Soc.* **5**(5), 310–318 (2017).
16. Lu, S.-S., Meng, C. & Chen, T.-W. The origin of the kink phenomenon of transistor scattering parameter $S_{22}$. *IEEE Trans. Microw. Theory Techn.* **49**(2), 333–340 (2001).
17. Mirzaei, H. & Eleftheriades, G. V. Realizing non-Foster reactive elements using negative-group-delay networks. *IEEE Trans. Microw. Theory Techn.* **61**(12), 4322–4332 (2013).
18. Muller, A. A. & Lucyszyn, S. Properties of purely reactive Foster and Non-Foster passive networks. *IET Electron. Lett.* **51**(23), 1882–1884 (2015).
19. Jacob, M. M. Non-Foster circuits for high performance antennas: advantages and practical limitations. In *PhD thesis* San Diego UCSD, https://escholarship.org/uc/item/2pq549c3 (2016).
20. Sievenpiper, D., Jacob, M., Long, J. Materials and components with a negative frequency derivative of reactance. In UCSD presentation, https://e3s-center.berkeley.edu/wp-content/uploads/2017/07/PEB2012_7_DSievenpiper_Webfinal.pdf (2017).
21. Tade, O. O., Gardner. P., Hall, S. S. Negative impedance converters for broadband antenna matching. In 2012 *42nd European Microwave Conference* (2012), https://ieeexplore.ieee.org/document/6459295 (2012).
22. Tade, O. O., Gardner. P., Hall, S. S. Broadband matching of small antennas using negative impedance converters. In 2012 *IEEE International Symposium on Antenna and Propagation and USNC-URSI National Radio Science meeting*, https://ieeexplore.ieee.org/document/6348833 (2012).
23. Tade, O. O., Gardner, P. & Hall, S. S. Antenna bandwidth broadening with a negative impedance converter. *Int. J. Microwave T.* **5**(3), 249–260 (2013).
24. Hrabar, S., Krois, I. & Kiricenko, A. Towards active dispersion less ENZ metamaterial for cloaking applications. *Metamaterials* **4**(2-3), 89–97 (2010).
25. Goldstone, L. A Low VSWR matching technique. (Correspondence and author's reply). *IRE Trans. Microw. Theory Techn.* **5l**(2), 163 (1957).
26. Munk, B.A. *Metamaterials: Critique and Alternatives*. John Wiley& Sons Inc., New Jersey, USA (2009).
27. Best, S. R. The Foster reactance theorem and quality Factor for antennas. *IEEE Antennas Wireless Propag. Lett.* **3**, 306–309 (2004).
28. Berger, M. *A Panoramic View Of Riemannian Geometry*. Springer, Berlin (2003).
29. Bochert, M. Infinite Regions of Various Geometries. *Bull. Amer. Math. Soc.* **20**(4), 185–200 (1914).
30. Brannan, D. A., Esplen, M. F., Gray, J. J. *Geometry*. Cambridge University Press, New York (2007).

31. Shi, T., Tang, M.-C., Wu, Z., Xu, H., Ziolkowski, R.W., Improved signal-to Noise Ratio (SNR), Bandwitdh-enhanced electrically small antenna augmented with Internal non-Foster elements. *IEEE Trans. Antennas Propag*. In press, https://ieeexplore.ieee.org/stamp/stamp.jsp?tp=&arnumber=8624545&tag=1 (2019).
32. Kemp, A. M. *et al*. A high Q piezoelectric resonator as a portable VLF transmitter. *Nat. Commun*. **10**, 1715 (2019).
33. Fleury, R., Sounas, D. & Alu, A. An invisible acoustic sensor based on parity-time symmetry. *Nat. Commun*. **6**, 5905 (2015).
34. Leroy, C. *et al*. High quality factor copper inductors integrated in deep dry-etched quartz substrates. *Microsyst. Technol*. **13**(11–12), 1483–1487 (2007).
35. Kang, J. *et al*. On-chip intercalated-graphene inductors for next-generation radio frequency electronics. *Nature Electronics* **1**, 46–51 (2018).
36. Wainstein, N. & Kvatinsky, S. Time-tunable inductors using mermistors. *IEEE Trans. Circuits Syst. I, Reg. papers* **65**(5), 1505–1515 (2018).
37. Casu, E. A. *et al*. A reconfigurable inductor based on Vanadium Dioxide insulator to metal transition. *IEEE Microw. Compon. Lett*. **29**(9), 795–797 (2018).
38. Wang, S., Wang, W., Shin, E., Quach & Subramanyam, G. Tunable inductors using vanadium dioxide as the control material. *Microw. Opt. Techn. Lett*. **59**(5), 1057–1061 (2017).
39. Jung, Y. H. *et al*. High-performance green flexible electronics based on biodegradable cellulose nanofibril paper. *Nat. Commun*. **6**, 7170 (2015).
40. Zhang, G., Ma, H., Lan, C., Gao, G. & Zhou, J. Microwave Tunable Metamaterial Based on Semiconductor-to-Metal Phase Transition. *Sci. Rep*. **7**, 577 (2017).
41. Prayakrao, S. *et al*. Tunable VO$_2$/Au hyperbolic metamaterial. *Appl. Phys. Lett*. **109**, 061105 (2016).
42. Krammer, A. *et al*. Elevated transition temperature in Ge doped VO2 thin films. *J. Appl. Phys*. **122**, 045304 (2017).
43. Stinson, H. T. *et al*. Imaging the nanoscale phase separation in vanadium dioxide thin films at terahertz frequencies. *Nat. Commun*. **9**, 3604 (2018).
44. Emond, N., Henadaoui, A., Delpart, S., Chaker, M. & Wu, K. Theoretical and Experimental Investigation of Thermo-Tunable Metal–Insulator–Vanadium Dioxide Coplanar Waveguide Structure. *IEEE Trans. Microw. Theory Techn*. **65**(5), 1443–1455 (2017).
45. Casu, E. A. *et al*. Vanadium Oxide bandstop tunable filter for Ka frequency bands based on a novel reconfigurable spiral shape defected ground plane CPW. *IEEE Access* **6**, 12206–12212 (2018).
46. Zheng, X., Xiao & Ling, Z. X. A Tunable Hybrid Metamaterial Reflective Polarization Converter Based on Vanadium Oxide Film. *Plasmonics* **13**(1), 287–291 (2018).
47. Kovacs, G. J. *et al*. Effect of the substrate on the insulator–metal transition of vanadium dioxide films. *J. Appl. Phys*. **109**(6), 063708 (2011).
48. Vitale, W. A. *et al*. Modulated scattering technique in the terahertz domain enabled by current actuated vanadium dioxide switches. *Sci. Rep*. **7**, 41546 (2017).
49. Vitale, W. A. *et al*. A Steep-Slope Transistor Combining Phase-Change and Band-to-Band-Tunneling to Achieve a sub-Unity Body Facto. *Sci. Rep*. **7**, 355 (2017).
50. Fan. J. A. *et al*. Fractal design concepts for stretchable electronics. *Nat. Commun*. **5**, no. 3266, (2014).
51. Li, L., Wang, W., Shin, E. & Subramananyam, G. Tunable inductors using integrated Vanadium Dioxide phase change thin films. *Advances in Condensed Matter Physics* **18**, 1–7 (2018).
52. Fernandez-Bolanos, M., Perruisseau-C., Dainesi, P. & Ionescu, A. M. RF Mems capacitive switch on semi-suspended CPW using low loss high resistivity silicon substrate. *Microelectron. Eng*. **85**(6), 1039–1042 (2008).
53. Gamble, H. S. *et al*. Low-Loss CPW lines on surface stabilized high-resistivity silicon. *IEEE Microw. Guided Wave Lett*. **9**(10), 395–397 (1999).
54. Muller, A. A. *et al*. A novel reconfigurable CMOS compatible Ka band bandstop structure using split-ring resonators and Vanadium Dioxide (VO$_2$) phase change switches. In 2019 IEEE MTT-S International Microwave Symposium digest, 865–867.
55. Yue, C. P. & Wong, S. S. Physical modeling of spiral inductors on silicon. *IEEE Trans. Electron Dev*. **47**(3), 560–568 (2000).
56. Horng, T. S., Peng, K. C. & Jau, J. K Tsai, S-parameter formulation of quality factor for a spiral inductor in generalized two-port configuration. In 2003 IEEE MTT-S International Microwave Symposium digest, 255–258.
57. Horng, T. S., Peng, K. C., Jau, J. K. & Tsai, Y. S. S-parameter formulation of quality factor for a spiral inductor in generalized two-port configuration. *IEEE Trans. Microw. Theory Techn*. **51**(11), 2197–2202 (2003).

## Acknowledgements

## Author contributions

A.A.M. proposed the new quantification model of the orientation of frequency over the 3D Smith chart, use of oriented curvature in the mathematical modelling, 3D series and shunt inductor Q inductor modelling, designed, fabricated and measured the devices with VO$_2$. A.M. supervised and guided the overall 3D Smith chart tool new capabilities implementations for this article. V.A. contributed to the development of the new 3D Smith chart concepts, their actual Java implementation and revised and arranged the paper. E.S.-C. refined and contributed extensively to the oriented curvature mathematical computations (equations). R.A.K. contributed with the fabrication and process flow in different stages, especially in obtaining the sub-micronic gaps in the Al via photolithography. A.K. contributed with the conductivity measurements of the VO$_2$. M.F.-B. contributed with constructive critical view in the preliminary design stages. M.C. made the PLD deposition of VO$_2$. J.Z. and E.C. contributed with the calibration of the measurement tool. A.S. supervised the work of A.K., A.M.I. lead the work of A.A.M. and guided the implementation stages for each part of the work.

## Competing interests

The authors declare no competing interests.

## Additional information

**Supplementary information** is available for this paper at https://doi.org/10.1038/s41598-019-54600-5.

**Correspondence** and requests for materials should be addressed to A.A.M.

**Reprints and permissions information** is available at www.nature.com/reprints.

**Publisher's note** Springer Nature remains neutral with regard to jurisdictional claims in published maps and institutional affiliations.

# Tunable RF Phase Shifters Based on Vanadium Dioxide Metal Insulator Transition

**EMANUELE ANDREA CASU**[ID] 1, **NICOLÒ OLIVA**[ID] 1, **MATTEO CAVALIERI**1, **ANDREI A. MÜLLER**[ID] 1,
**ALESSANDRO FUMAROLA**2, **WOLFGANG A. VITALE**1, **ANNA KRAMMER**3, **ANDREAS SCHÜLER**3,
**MONTSERRAT FERNÁNDEZ-BOLAÑOS**1, **AND ADRIAN M. IONESCU**1

1 Nanoelectronic Devices Laboratory, École Polytechnique Fédérale de Lausanne, 1015 Lausanne, Switzerland
2 Nano-Systems from Ions, Spins and Electrons, Max Plank Institute of Microstructure Physics, 06120 Halle, Germany
3 Solar Energy and Building Physics Laboratory, École Polytechnique Fédérale de Lausanne, 1015 Lausanne, Switzerland

CORRESPONDING AUTHOR: E. A. CASU (e-mail: emanuele.casu@epfl.ch)

This work was supported in part by the HORIZON2020 Phase-Change Switch Project under Grant. 737109, in part by the ERC Advanced
Grant "Millitech" of the European Commission and the Swiss Federal Office of Energy under Grant 8100072.

**ABSTRACT** This paper presents the design, fabrication, and electrical characterization of a reconfigurable RF capacitive shunt switch that exploits the electro-thermally triggered vanadium dioxide ($VO_2$) insulator to metal phase transition. The RF switch is further exploited to build wide-band RF true-time delay tunable phase shifters. By triggering the $VO_2$ switch insulator to metal transition (IMT), the total capacitance can be reconfigured from the series of two metal–insulator–metal (MIM) capacitors to a single MIM capacitor. The effect of bias voltage on losses and phase shift is investigated, explained, and compared to the state of the art in the field. We report thermal actuation of the devices by heating the devices above $VO_2$ IMT temperature. By cascading multiple stages a maximum of 40° per dB loss close to 7 GHz were obtained.

**INDEX TERMS** Vanadium dioxide, phase transition, RF switch, true-time delay, phase shifter, tunable capacitor.

## I. INTRODUCTION

Phase shifters are key components for beam-steering implementations, smart adaptive antennas and scanning applications for wideband communications and remote sensing systems. Phase shifter based on ferroelectric technology have been shown to offer interesting RF performances in terms of tunability, losses and power consumption [1], [2]. In parallel RF distributed MEMS transmission lines (DMTL) have been proven to be a very interesting solution to achieve a high phase shift over a wider frequency band if compared to traditional solid-state implementations (PIN diodes, GaAs FET), with a DC power consumption limited to tenths of milliwatts [3].

Strongly correlated functional oxides exhibiting metal to insulator transition have recently emerged in research as promising materials for a large number of applications, including steep-slope transistors [4], RF switches [5], [6], reconfigurable filters [7], [8] and antennas [9]. Vanadium

dioxide ($VO_2$) has proven to be one of the most interesting among such materials thanks to its large contrast in conductivity between its two states and the possibility of inducing the phase transition by electrical excitation [10].

Compared to MEMS switches, $VO_2$ switches offer clear advantages such as an easier integration in microelectronic technological processes, smaller footprint and a three order of magnitude faster switching time [11]. A switched line phase shifter with thermally actuated $VO_2$ switches has been previously demonstrated in microstrip technology [12].

In our previous work [13] we presented for the first time a shunt capacitive switch reconfigurable by means of electrically triggered $VO_2$ phase transition to build true-time delay phase shifters by periodically loading a coplanar waveguide (CPW) with capacitive switches (Fig. 1). We validated the concept by fabricating, designing and characterizing an 819 μm long unit. In this work, we show improved results for thermally actuated cells by demonstrating up to 40° phase
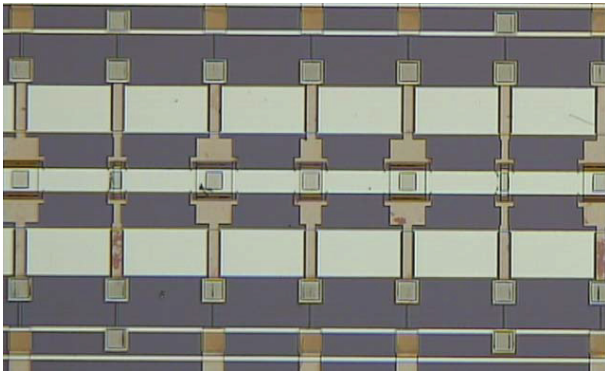
**FIGURE 1.** Optical image of the CPW phase shifter showing the cascaded VO$_2$-based capacitive shunt switches designed to achieve 3-bits phase states.

shift per dB loss at 7 GHz in a 6-cell phase shifter. We furthermore present two possible scheme to bias cascaded cells to obtain a multi-state tunable phase shift.

## II. RECONFIGURABLE CAPACITIVE SHUNT SWITCH

The reconfigurable capacitive shunt switch consists of two fixed MIM capacitors in series, $C_S$ and $C_G$, where the first can be short-circuited by actuating a VO$_2$ two-terminal switch (Fig. 2). Below the phase-transition temperature and when no bias is applied, the VO$_2$ is in its insulating state so that the switch exhibits a high resistance level and can be considered as an open circuit. The two capacitors are then electrically in series, offering an equivalent capacitance $C_{TOT} = C_G \cdot C_S/(C_G + C_S)$. Whenever a bias larger than the switch actuation voltage is applied, the VO$_2$ film phase changes to its conductive state and the switch exhibits a low resistance value. In this configuration, the $C_S$ capacitor is short-circuited by the switch and the equivalent capacitance between the signal and the ground line will be simply $C_G$. In this way the VO$_2$ switch allows reconfiguring the loading capacitance between $C_G$ and $C_{TOT}$.

The VO$_2$ switch can be electrically actuated by means of a bias line decoupled from the RF signal using a resistor fabricated with a 25 nm-thick Chromium (Cr) film. The switch resistance is in the high state until a critical DC power is achieved, which triggers a steep insulator to metal transition (Fig. 3). In order not to affect the RF performance, the switch dimensions are chosen to obtain a high value of resistance in the off-state ($> 1$ k$\Omega$) and low value in the on-state ($\sim 1$ $\Omega$), while keeping a reasonably low actuation voltage. Thus, given a 200 nm VO$_2$ thickness, the switch was designed with a width of 30 $\mu$m and a length of 1 $\mu$m.

## III. FABRICATION

The phase shifter was fabricated using standard microelectronics processes starting with a high-resistivity 525 $\mu$m thick silicon substrate passivated with 500 nm LPCVD-deposited SiO$_2$ (Fig. 4). The VO$_2$ film was prepared by reactive magnetron sputtering deposition starting from a Vanadium target, as described in [4]. After the deposition,

a resistivity ratio between insulating and conducting phase higher than 3 decades was measured with Van der Pauw measurements performed at different temperatures (Fig. 5). The film was then patterned by using photolithography and wet etching. The bias resistors were realized by lift-off of a 25 nm thick Cr film. A 200 nm thick Al film was subsequently deposited and patterned with lift-off to act as bottom metal. A 200 nm thick SiO$_2$ film was sputtered as insulating layer and as a dielectric for MIM capacitors. Vias were opened by photolithography and dry etching. A final 800 nm thick Al top metal layer was deposited to create the CPW and the contacts on the bottom metal bias lines.

## IV. UNIT CELL PERFORMANCE

The CPW was designed with a signal line width ($w$) of 100 $\mu$m and a ground plane spacing ($g$) of 150 $\mu$m to obtain an unloaded characteristic impedance of 65 $\Omega$. The design of the unit cell for the phase shifter was done following the method described in [14] in order to maximize the phase shift for the minimum insertion loss (*IL*). Starting from the chosen values of characteristic impedances in the ON and OFF state, respectively $Z_{ON} = 42$ $\Omega$ and $Z_{OFF} = 58$ $\Omega$, and having chosen the Bragg frequency to be three times the frequency of design for the phase shifter, for a design frequency of 10 GHz the required unit cell length (*CL*) was calculated to be 819 $\mu$m. The computed capacitances were $C_{ON} = 143$ fF and $C_{OFF} = 26$ fF resulting in a capacitance ratio of 5.5. Thus the MIM capacitances for the reconfigurable capacitive shunt switch are calculated as $C_S = 31.7$ fF and $C_G = 143$ fF. A schematic of the mask of the single cell is shown in Fig. 6.

The device was characterized by using an Anritsu VectorStar MS4647B Vector Network Analyser to measure *S*-parameters, a HP 4155B Semiconductor Parameter Analyser to provide the bias to operate the VO$_2$ switches and a Cascade Summit prober with a thermo-chuck to control the substrate temperature.

Fig. 7 shows a comparison between Ansys HFSS simulations of *S*-parameters and measurements with no bias applied at 20°C (OFF state) and 100°C (ON state), well above the phase transition temperature where the VO$_2$ film becomes fully conductive (see Fig. 5). When the switches are turned off (20 °C and no bias) the insertion loss is 0.43 dB at 10 GHz, while in the ON state the insertion losses are increased both in simulation and measurements. The discrepancy between measured and simulated values can be attributed to resistive losses along the line and in the VO$_2$ switch for the ON state, besides extra reflection due to parasitic capacitances caused by biasing lines not included in the simulations.

The devices were measured for different bias values above the actuation voltage of the VO$_2$ switches (Fig. 8). While the insertion loss seems to increase by increasing the bias, the loss at the design frequency is improved when the switch is at its lowest possible resistance value, obtained measuring at 100 °C. This behavior can be explained looking at
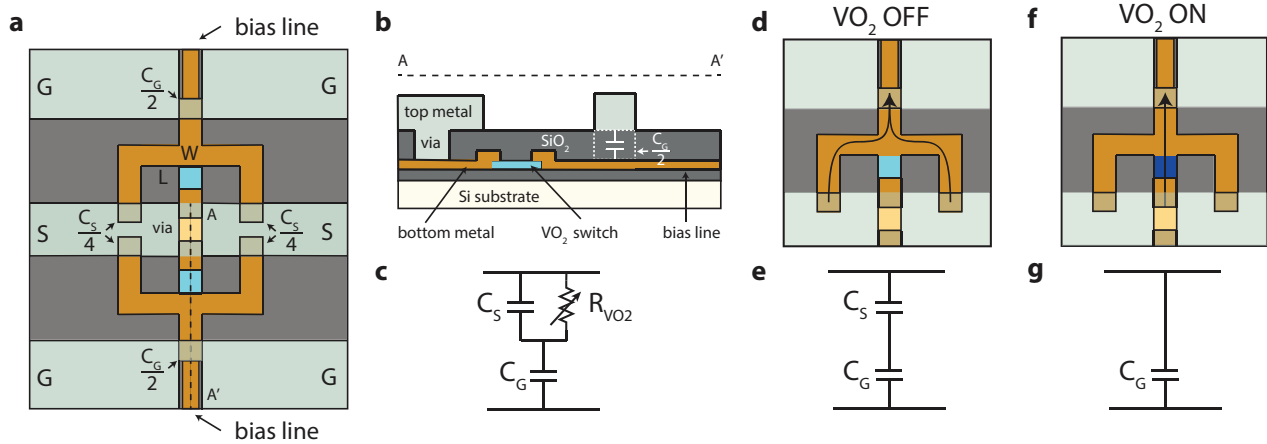
**FIGURE 2.** a) Schematic of the reconfigurable capacitive shunt switch. A via connects the signal top metal line with a metal line underneath in contact with a VO$_2$ switch. Four MIM capacitors (C$_S$/4), two per side, lay between the signal line and the underneath metal, whilst other two MIM capacitors (C$_G$/2), one per side, lay between the ground planes and the underneath metal. b) Cross-section beween signal and ground plane highlighting the via between the two metals, the VO$_2$ switch and the capacitance C$_G$/2. c) Equivalent circuit of the capacitive divider, with the VO$_2$ switch modeled as a variable resistor $R_{VO2}$. d) Preferential path seen by the signal when the VO$_2$ is in insulating phase, with an equivalent capacitance given by the series of C$_S$ and C$_G$. e) Equivalent circuit for the insulating phase, where the switch can be modeled as an open switch ($R_{VO2} > 1\,k\Omega$). f) When the VO$_2$ film is in its conducting phase the capacitors C$_S$/4 are short-circuited by the switch ($R_{VO2} \sim 1\Omega$) and g) the equivalent capacitance seen between signal and ground equals C$_G$.
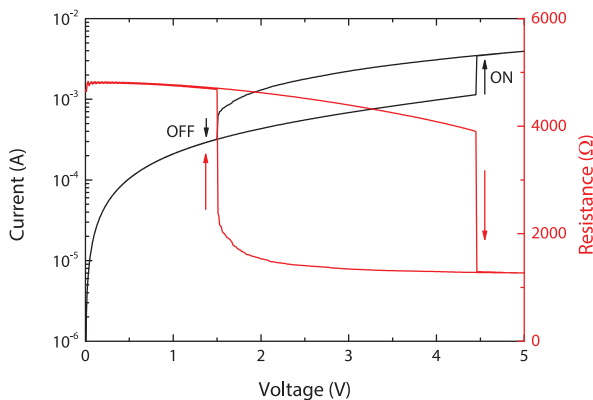


**FIGURE 3.** Current versus voltage electrical characteristic and extracted resistance of the VO$_2$ switch with an integrated serpentine resistor of 1.2 k$\Omega$ in series. The arrows indicates the insulator-metal transition and metal insulator transition.



**FIGURE 4.** Fabrication process of the capacitive shunt switch with VO$_2$ switches and integrated bias resistors.
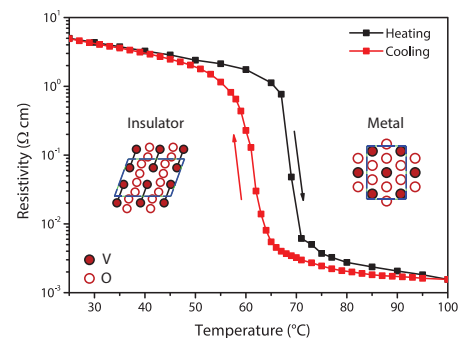


**FIGURE 5.** Dependence of resistivity on temperature for the deposited VO$_2$ film.

the losses not due to reflection. While in the OFF state the insertion losses and no-reflection losses are almost coincident, indicating a good match, in the ON state the behavior depends on the bias. At 20 V the *IL* and total losses are similar, while at 30 V and 40 V a considerable part of the *IL* is due to the mismatch. At 100 °C the *IL* are lower than at the considered bias points and the no-reflection losses are minimized, showing better accordance with the FEM simulations.

The measured phase shift with respect to the OFF state increases with the applied bias but tends to saturate around 5 GHz for 40 V bias, while at 100 °C it is linear over the considered frequency band (Fig. 9). The phase shift per dB loss shows as well that the best trade-off is obtained for higher bias and indicates that best performances are obtained at 100 °C, where a maximum of 16° per dB loss is obtained slightly below the design frequency.
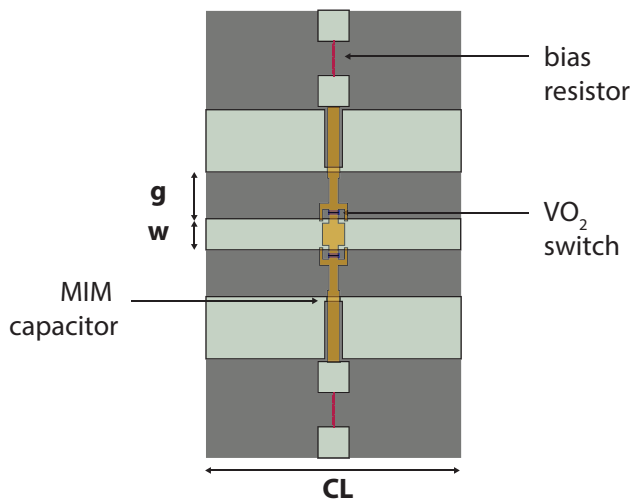
**FIGURE 6. Schematic of the unit cell with indicated dimensions** $w = 100$ μm, $g = 150$ μm and $CL = 819$ μm.
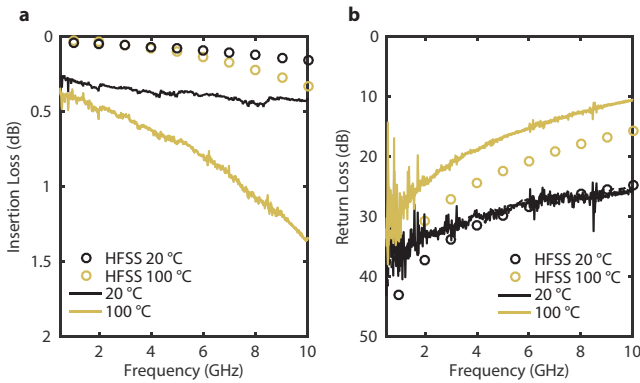


**FIGURE 7. (a) Insertion Loss and (b) Return Loss of the measured unit cell at 20 °C and 100 °C. Circles correspond to ANSYS HFSS simulations. The simulations have been performed using the VO₂ resistivity measured at 20 °C for the OFF state and 100 °C for the ON state.**
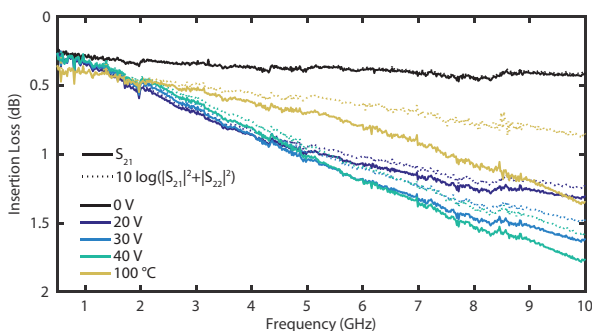


**FIGURE 8. Insertion loss (continuous lines) and no-reflection losses (dotted lines) versus frequency, measured at 20 °C substrate temperature for 0 V, 20 V, 30 V and 40 V bias voltage and at 100 °C with no applied bias.**

The limited performance of the device when electrically actuated suggests that for the applied bias voltages, the conduction channel in the VO₂ switch does not extend to the entire film width [15] and the resulting resistance is still
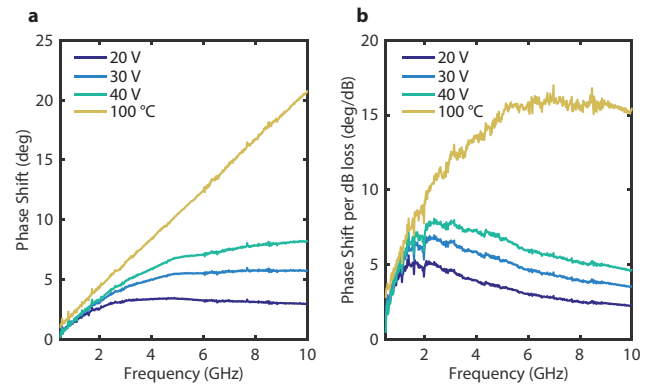


**FIGURE 9. (a) Phase shift and (b) phase shift per dB loss extracted from** *S*-parameter measurements at 20 °C for 0 V, 20 V, 30 V and 40 V bias voltage at and at 100 °C with no applied bias.
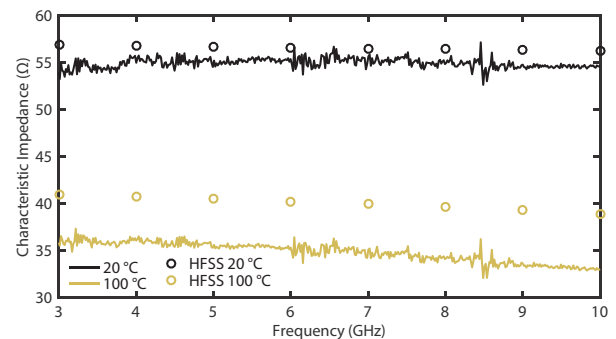


**FIGURE 10. Equivalent characteristic impedance of the unit cell, extracted from measurements at room temperature and at 100 °C (solid lines), and from ANSYS HFSS simulations (circles ).**

not low enough to grant a full capacitance reconfiguration and to prevent significant RF losses. We can assume that by applying a larger bias voltage, thus by injecting a larger current, the performance will converge to the one measured at 100 °C.

The equivalent characteristic impedance of the loaded line was calculated using the method proposed in [16] and it is shown in Fig. 10. In the OFF state the extracted characteristic impedance is about 55 Ω at 10 GHz, not far from the simulated value of 56 Ω. In the ON state at 100 °C the extracted characteristic impedance is lower than the simulated one, in accordance with the larger measured phase shift and larger insertion loss due to reflection.

## V. PHASE SHIFTER

In order to improve the performance, new devices were fabricated starting from a 300 nm thick VO₂ film deposited by Pulsed Laser Deposition (Solmates SMP 800) in oxygen atmosphere of a V₂O₅ target. The bottom metal was realized with Ti/Al respectively 20 nm and 800 nm thick, while the top-metal was made of a 2 μm thick Al film. The thicker VO₂ and metal layers provide lower resistive loss compared to the previously used process. The design of the cell was slightly varied and a tapered ground plane was
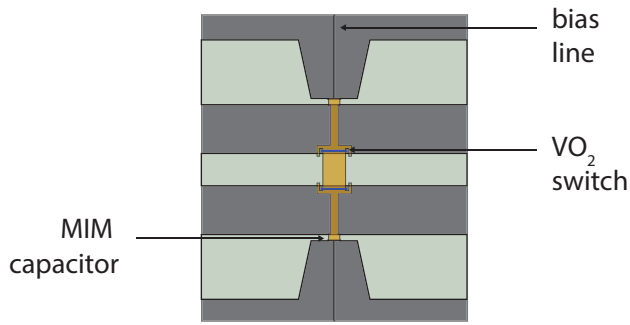
**FIGURE 11.** Schematic of the improved phase-shifter unit cell with tapered ground plane in proximity of the biasing line.
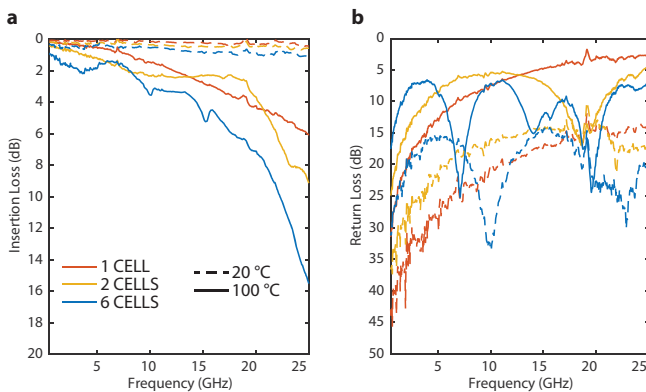


**FIGURE 12.** Measured (a) insertion loss and (b) return loss for 1,2 and 6-stage phase shifter with all stages in off-state (measured at 20 °C, dashed line) and all stages in on-state (measured at 100 °C, solid line).
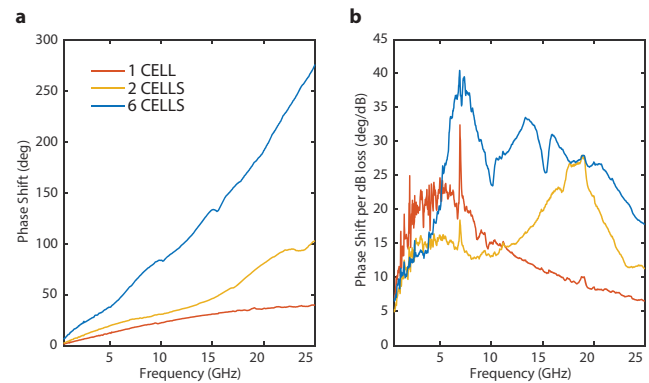


**FIGURE 13.** (a) Phase shift and (b) phase shift per dB loss for 1,2 and 6-stage shifter between the two extreme states: all stages in off-state at 20 °C and all in on-state at 100 °C.
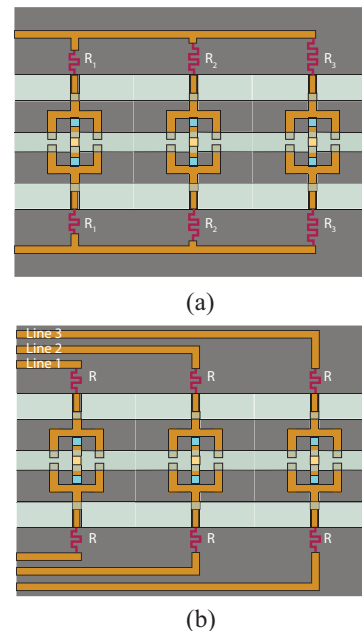


**FIGURE 14.** a) Biasing schemes with single bias line but different resistor values for each stage to modify the threshold voltages of the VO₂ switches and (b) scheme with separate biasing "bit" line for each stage.

designed to minimize the parasitic capacitance between the biasing line and the ground plane itself. The cell length and capacitors dimension were kept the same. The VO₂ switch width was increased to 70 µm, while the length was kept 1 µm. A schematic of the mask of the new single cell is shown in Fig. 11.

In Fig. 12 we report the S-parameter in OFF and ON states (measured with no applied bias at temperatures of 20°C and 100°C, respectively) of three different phase shifters composed by one, two and six cells. Fig. 13 shows that by cascading multiple stages a larger phase shift can be obtained and an improved phase shift per dB loss of 40° is achieved since reflection losses do not sum up from stage to stage.

## VI. MULTISTAGE ACTUATION

To obtain the desired phase shift we can cascade multiple unit cell in a CPW. We propose two different biasing schemes to control each cell (Fig. 14). In the first scheme, the actuation voltage of the VO₂ switch of each stage is set to a specific value by engineering the corresponding biasing resistor value. The actuation is then performed using the RF signal line as bias line and a common DC ground line for all the stages. When a certain DC bias is applied to the signal line the obtained phase shift will be deriving from the stages with actuation threshold below the applied bias. Increasing

the bias, other stages will be actuated and the phase shift will increase. In the second scheme, separate bias "bit" lines are created for each stage or set of stages and the RF signal line is used as a DC ground: when a bit line is set to a voltage higher than the switch threshold voltage, bit to "1", the corresponding stage will turn ON and provide a phase shift.

Using this latter "multi-bit" scheme we can make predictions on a phase shifter desing by matematically cascading the S-parameter of the unit cell shown in Fig. 12. Considering a phase shifter made out of three of this cell, each one controllable with a separate bit line, we show in Fig. 15 the calculated losses for the phase shifter in four configuration, all stages OFF (000), first stage ON (100), first two stages ON (110), all stages ON (111). Fig. 16 report the obtained phase shift with respect to the all OFF (000) state.
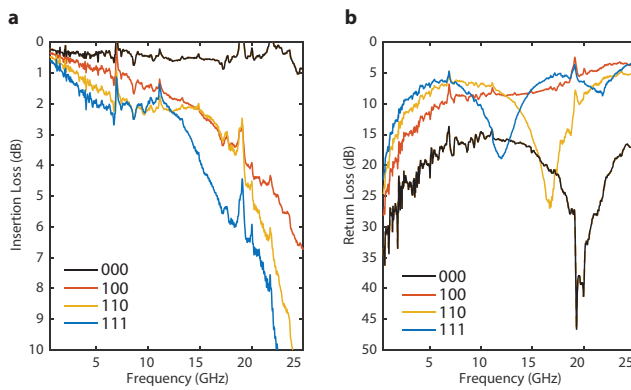
**FIGURE 15.** Predicted (a) insertion loss and (b) return loss for a 3-stage phase shifter biased with three bit lines in four different configuration, where bit "0" stands for OFF state of the cell and bit "1" stands for ON state.
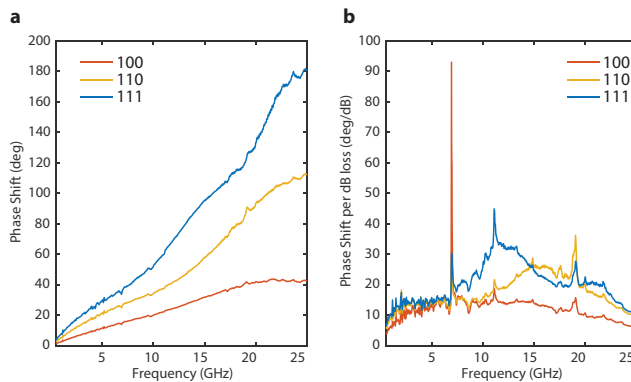


**FIGURE 16.** Predicted (a) Phase shift and (b) phase shift per dB loss of a 3-stage phase shifter biased with three bit lines for the indicated bits states compared to the all OFF state (000).

As expected, when turning ON more stages the phase shift increases and the phase shift per dB loss is maximized.

## VII. CONCLUSION

We reported a VO$_2$-based capacitive shunt switch as fundamental building block that can be cascaded to obtain TTD phase shifters. The working principles as well as the fabrication method have been presented and validated by simulating, designing, fabricating and characterizing a unit cell. The extracted considerable insertion losses are largely due to the impedance mismatch and could be easily reduced by improving the MIM capacitors design. The measurements at different bias voltage and at high temperature have revealed the need of a better optimization of the VO$_2$ switch in order to have lower resistance values in the electrically actuated ON state so to match the good performance obtained at high temperatures.

A 6-stage phase shifter was fabricated and measured. A 40° phase shift per dB loss was achieved around 7 GHz, showing that the VO$_2$-based reconfigurable capacitive switches can offer a unique opportunity to build ultrafast

and reliable phase shifters. Moreover, we presented two possible biasing strategies for multistage actuations to achieve a tunable phase shift by controlling it with either several bits line or with a single analog one. VO$_2$ based phase shifters are realized with an easier and cheaper fabrication process with respect the RF MEMS counterpart and have 100 to 1000 time faster switching time, which makes them interesting for fast airborne applications. Actuation voltages can be potentially lower than RF MEMS ones while the insertion loss is expected to decrease by further improving the VO$_2$ material properties and design implementation.

## REFERENCES

[1] J. Park, J. W. Lu, D. S. Boesch, S. Stemmer, and R. A. York, "Distributed phase shifter with pyrochlore bismuth zinc niobate thin films," *IEEE Microw. Compon. Lett.*, vol. 16, no. 5, pp. 264–266, May 2006.

[2] D. Kuylenstierna, A. Vorobiev, P. Linnér, and S. Gevorgian, "Composite right/left handed transmission line phase shifter using ferroelectric varactors," *IEEE Microw. Wireless Compon. Lett.*, vol. 16, no. 4, pp. 167–169, Apr. 2006.

[3] A. Chakraborty and B. Gupta, "Paradigm phase shift: RF MEMS phase shifters: An overview," *IEEE Microw. Mag.*, vol. 18, no. 1, pp. 22–41, Jan./Feb. 2017.

[4] W. A. Vitale *et al.*, "A steep-slope transistor combining phase-change and band-to-band-tunneling to achieve a sub-unity body factor," *Sci. Rep.*, vol. 7, no. 1, p. 355, 2017.

[5] S. D. Ha, Y. Zhou, C. J. Fisher, S. Ramanathan, and J. P. Treadway, "Electrical switching dynamics and broadband microwave characteristics of VO$_2$ radio frequency devices," *J. Appl. Phys.*, vol. 113, no. 18, May 2013, Art. no. 184501.

[6] W. A. Vitale *et al.*, "Steep slope VO2 switches for wide-band (DC-40 GHz) reconfigurable electronics," in *Device Res. Conf. Dig. (DRC)*, Santa Barbara, CA, USA, 2014, pp. 29–30.

[7] D. Bouyge and A. Crunteanu, "Applications of vanadium dioxide (VO2)-loaded electrically small resonators in the design of tunable filters," in *Proc. Eur. Microw. Conf.*, Sep. 2010, pp. 822–825.

[8] W. A. Vitale *et al.*, "Electrothermal actuation of vanadium dioxide for tunable capacitors and microwave filters with integrated microheaters," *Sensors Actuators A Phys.*, vol. 241, pp. 245–253, Apr. 2016.

[9] T. S. Teeslink, D. Torres, J. L. Ebel, N. Sepulveda, and D. E. Anagnostou, "Reconfigurable bowtie antenna using metal-insulator transition in vanadium dioxide," *IEEE Antennas Wireless Propag. Lett.*, vol. 14, pp. 1381–1384, 2015.

[10] Z. Yang, C. Ko, and S. Ramanathan, "Oxide electronics utilizing ultrafast metal-insulator transitions," *Annu. Rev. Mater. Res.*, vol. 41, no. 1, pp. 337–367, Aug. 2011.

[11] J. Leroy *et al.*, "High-speed metal-insulator transition in vanadium dioxide films induced by an electrical pulsed voltage over nano-gap electrodes," *Appl. Phys. Lett.*, vol. 100, no. 21, May 2012, Art. no. 213507.

[12] C. Hillman *et al.*, "An ultra-low loss millimeter-wave solid state switch technology based on the metal—Insulator—Transition of vanadium dioxide," in *Proc. IEEE MTT-S Int. Microw. Symp. (IMS)*, Tampa, FL, USA, 2014, pp. 1–4.

[13] E. A. Casu *et al.*, "Shunt capacitive switches based on VO2 metal insulator transition for RF phase shifter applications," in *Proc. 47th Eur. Solid-State Device Res. Conf. (ESSDERC)*, Leuven, Belgium, 2017, pp. 232–235.

[14] G. M. Rebeiz, *RF MEMS*. Hoboken, NJ, USA: Wiley, 2003.

[15] J. Yoon, G. Lee, C. Park, B. S. Mun, and H. Ju, "Investigation of length-dependent characteristics of the voltage-induced metal insulator transition in VO$_2$ film devices," *Appl. Phys. Lett.*, vol. 105, no. 8, Aug. 2014, Art. no. 83503.

[16] J. Perruisseau-Carrier, R. Fritschi, P. Crespo-Valero, and A. K. Skrivervik, "Modeling of periodic distributed MEMS—Application to the design of variable true-time delay lines," *IEEE Trans. Microw. Theory Tech.*, vol. 54, no. 1, pp. 383–392, Jan. 2006.

# Vanadium Oxide Bandstop Tunable Filter for Ka Frequency Bands Based on a Novel Reconfigurable Spiral Shape Defected Ground Plane CPW

**EMANUELE ANDREA CASU[1], ANDREI A. MÜLLER[1], MONTSERRAT FERNÁNDEZ-BOLAÑOS[1], ALESSANDRO FUMAROLA[2], ANNA KRAMMER[3], ANDREAS SCHÜLER[3], AND ADRIAN M. IONESCU[1]**

[1]Nanoelectronic Devices Laboratory, École Polytechnique Fédérale de Lausanne, CH-1015 Lausanne, Switzerland
[2]Max Planck Institute of Microstructure Physics, 06120 Halle, Germany
[3]Solar Energy and Building Physics Laboratory, École Polytechnique Fédérale de Lausanne, CH-1015 Lausanne, Switzerland

Corresponding author: Andrei A. Müller (andrei.muller@epfl.ch)

**ABSTRACT** This paper proposes and validates a new principle in coplanar waveguide (CPW) bandstop filter tuning by shortcutting defected ground plane (DGS) inductor shaped spirals to modify the resonant frequency. The tunable filter is fabricated on a high-resistivity silicon substrate based on a CMOS compatible technology using a 1 $\mu$m $\times$ 10 $\mu$m long and 300 nm thick vanadium oxide ($VO_2$) switch by exploiting its insulator to metal transition. The filter is designed to work in $K_a$ band with tunable central frequencies ranging from 28.2 GHz to 35 GHz. The measured results show a tuning range of more than 19 %, a low insertion loss in the neighboring frequency bands (below 2 dB at 20 GHz and 40 GHz in on/off-states) while a maximum rejection level close to 18 dB in off-state, limited by the no RF-ideal CMOS compatible substrate. The filter has a footprint of only 0.084 $\cdot \lambda_0 \times$ 0.037 $\cdot \lambda_0$ (where $\lambda_0$ represents the free space wavelength at the highest resonance frequency) thus making it the most compact configuration using CPW DGS structures for the $K_a$ frequency band. In addition, a more compact filter concept based on the Peano space filling curve is introduced to increase the tuning range while minimizing the DGS area.

**INDEX TERMS** Microwave filters, millimeter wave technology, thin films, vanadium oxide.

## I. INTRODUCTION

The recent fast development of the future space communication in the $K_a$ frequency band [1] motivates the research of new tunable components for this frequency range applications, among which tunable bandstop filters [2] play a major role.

Because of its ease of integration, reversible insulator to metal transition (IMT), low transition temperature and fast switching time, the employment of Vanadium Dioxide ($VO_2$) as a reconfigurable RF material has been recently investigated for a variety of microwave devices [2]–[4] and employed in bandstop filter design in [2] up to 22.5 GHz by means of a defected ground plane design (DGS) [2], [5]. DGS were introduced in 2000 [5] and have since then [6] been

extensively used both in microstrip and coplanar waveguide technology (CPW) for microwave filter design at a variety of frequencies [5]–[14].

In CPW technology by embedding a DGS, depending on the shape and substrate properties several tunable bandstop filters [2], [6], [9], [13] and bandstop structures [7], [8] were reported. However only very few $K_a$ frequency band bandstop filters were proposed [2], [11]–[13] and among them even fewer [2], [13] were reconfigurable or fabricated [13]. A summary of the $K_a$ band DGS CPW bandstop filters performances is shown in Table 1, while Table 2 depicts other fabricated $K_a$ CPW bandstop filters performances. Table 1 and Table 2 show the features of these filters in terms of tuning range, tunability (defined as in [2] as $|f_{max} - f_{min}|/f_{max}$ where

**TABLE 1.** Ka Bandstop filter performances in CPW technology using DGS.

| | Frequency (GHz) | Measured | Tunability % | $Q_{max}$ | *IL* 20 GHz/40 GHz (dB) | Size: $(b×a)/\lambda_0^2$ | Max *IL*(dB) Ka band |
|---|---|---|---|---|---|---|---|
| [2] (Fig. 8) | 26.6-30.6 | No | 13 % | $Q_{max} <27$ | 3/1 on-state 2.5/2.8 off-state | 0.14×0.04 | 18.8/16 |
| [11] | ~32 | Yes | No | $Q_{max} =27$ | 1/1 | 0.05×0.02 | ~8 |
| [12] | ~28 | No | No | $Q_{max}>30$ | 1/not reported | 0.13×0.092 | ~26 |
| This work | 28.27-35.00 | Yes | 19.2 % | $Q_{on}=14$ $Q_{off}=35$ | 1.9/1 on-state 1.2/2.4 off-state | 0.076×0.033 | 12.8/18.3 |

**TABLE 2.** Other recent Microwave CPW fabricated bandstop filter performances.

| | Frequency (GHz) | Measured | Tunability % | Size: $(b×a)/\lambda_0^2$ | Max *IL* (dB) (different states) |
|---|---|---|---|---|---|
| [13] | 35-38 | Yes | 9 % | 0.18×0.123 | 20.2/18 |
| [9] | 1.69-2.16 | Yes | 22 % | 0.13×0.05 | 30/16 |

$f_{max}$ stands for the highest frequency and $f_{min}$ for the minimum frequency), maximum insertion loss (*IL*), quality factor $Q$ defined as $f_0/B_{3dB}$ ($f_0$ where $B_{3dB}$ denotes the bandwidth at 3 dB) and size (defined as in Fig.1 as the area of the defected part $b \times a$ of the transmission line divided by the squared free space wavelength $\lambda_0^2$ at the highest resonance frequency tuned).
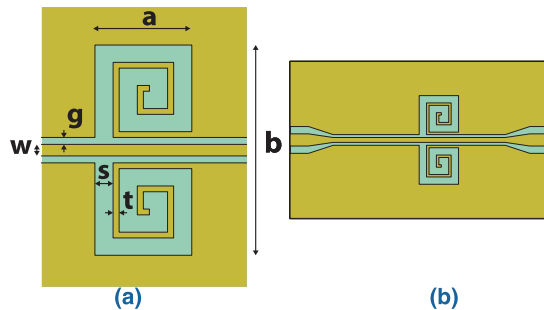


**FIGURE 1.** (a) Layout of the proposed DGS shape and its area defined as $a \times b$ (area of a rectangle covering the defected shape) with $w = 40$ μm and $g = 24$ μm, $s = 60$ μm, $t = 20$ μm and $a = 320$ μm, (b) including the matching network to a CPW line with $w = 100$ μm central width line and $g = 60$ μm employed for the measurement of the device.

The forms of the reported DGS used in tunable bandstop filters or resonators structures include mainly squares and rectangles [2], [6], square patches [7], [8], a succession of square patches [9] or a succession of squares [10].

From the tuning mechanism viewpoint the fabricated reported bandstop filters employing DGS (considering the entire microwave frequency spectrum) use varactors [7], [9] or PIN diodes [8] for tuning ranges not exceeding 10 GHz and VO₂ [2] for the 19.8-22.5 GHz frequency ranges.

In this paper we introduce to the best of our knowledge a new tuning mechanism for the CPW DGS bandstop filter design by shortcutting the turns of spiral inductors [11], [14] by using a 300 nm × 1 μm × 10 μm VO₂ tuning switch, where

the resonant frequency is controlled by the DGS inductor self resonance. In [15] tunable inductors with VO₂ have been proposed with a different switching mechanism and not as DGS.

In terms of normalized size ($b \times a/\lambda_0^2$) the proposed filters occupy around half of the area of the other $K_a$ band tunable reported CPW DGS filters [2] (Table 1) or other bandstop filters employing a DGS form (Table 2) [9], [13].

The fabricated filter has a high tuning range of 19 % while exhibiting lower losses in the K band and at 40 GHz than the CPW DGS measured filters present in literature for the same frequency band [11]. The fabrication is done in CMOS compatible technology and the tuning is achieved by heating the VO₂ film above the IMT temperature (68 °C) causing its conductivity to increase of about three orders of magnitude. The off-state is defined for the VO₂ film in its insulating phase (at 20 °C) with low conductivity while for the on-state the film is in its metallic phase (above the temperature) and thus presents higher conductivity. The maximum *IL* in the on-state is directly influenced by the properties of the used VO₂ film, since the switches are used as series elements (differently from [2] where capacitive switches were proposed).

The paper presents first the design mechanism employing tunable inductors DGS, then it introduces the fabrication process and presents the measurement of the fabricated devices. In the discussion section it introduces a new conceptual layout based on a space filling curve.

## II. DESIGN OF FIXED BANDSTOP FILTERS USING SPIRAL DEFECTED GROUND PLANE

### A. SIMULATION OF THE FILTER WITHOUT TUNING MECHANISM IN ON-STATE

The design of the spiral DGS follows the principles presented in [11] and [14] for non-reconfigurable bandstop filters. The substrate used is as in [11] a silicon wafer

(with relative dielectric permittivity $\varepsilon_r = 11.7$ and thickness of $h = 525$ μm) passivated with 500 nm $SiO_2$. The CPW line parameters are presented in Fig. 2. where $w$ denotes the width of the central line while $g$ the distance between the central line and the ground planes ($w = 40$ μm and $g = 24$ μm) . The metallization is a 2000 nm thick aluminum film.

The values for the spiral DGS are chosen in order to get a resonant frequency around 28 GHz while obtaining attenuation levels higher than the ones reported in [11] for the same substrate (and frequency band) and keeping the $IL$ below 2 dB in the K band and at 40 GHz.

The attenuation values obtained could be improved by increasing the metal thickness, by using a more conductive metal or by using the improved substrates as presented in [16], but the aim of this work is to focus on the new compact tuning principle while aiming enhanced results compared to [2] and [11] where the same substrate is used.

The physical filter layout values presented in Fig. 1(a) and the final filter layout presented in Fig. 1(b) are obtained using the Ansys HFSS terminal solutions solver. The optimized matching network added in Fig. 1(b) is needed to test the filter employing the measuring equipment used.
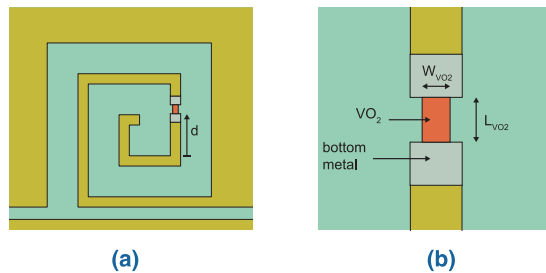


**FIGURE 2.** (a) $VO_2$ (orange) interrupting the spiral inductor DGS in the off-state and continuing it in the on-state. (b) Closer view of the $VO_2$ switch with its geometrical parameters.

The tuning mechanism proposed in this paper consists in cutting a gap in the spiral inductor DGS and adding in it a thin $VO_2$ layer. The position of the gap changes the resonant frequency of the filter in the ''off-state'', while its length has an important impact on the filter performances in the on-state. Fig. 2(a) and (b) depict the gap positioning $d$ and the $VO_2$ integration and geometrical parameters. The results in terms of magnitude of the scattering transmission parameter $S_{21}$ are presented in Fig. 3 considering first the ideal presented in Fig. 1. The obtained values show a 19.8 dB insertion loss at $f_0 = 28.1$ GHz and a quality factor $Q = 28$, similar to the values obtained in [17].

## B. SIMULATION OF THE FILTER WITH TUNING MECHANISM IN THE ON-STATE

Fig. 4 shows the performances in the ''on-state'' of the filter with integrated $VO_2$ in the gap (Fig. 2.) by considering first different gap lengths. As the length increases from 1 μm to 11 μm the maximum $IL$ decreases from around 17.67 dB to 9.4 dB, while the $Q$ of the filters decreases too. Fig. 5
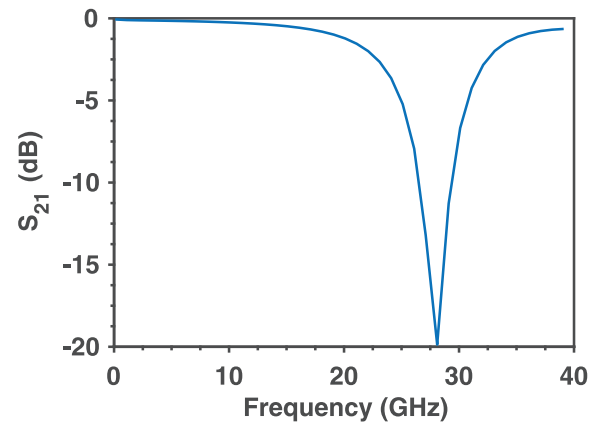


**FIGURE 3.** Simulated transmission parameter $S_{21}$ magnitude for the structure in Fig. 1(b).
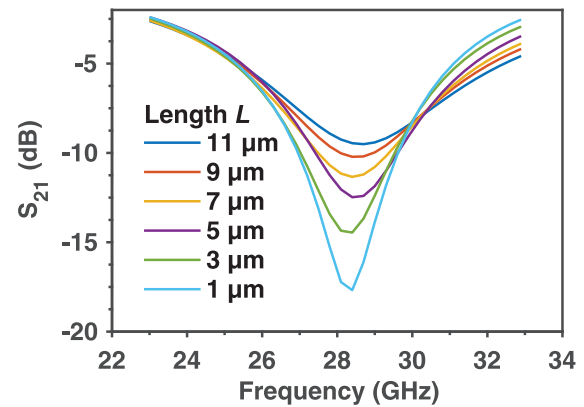


**FIGURE 4.** Simulated magnitude of the transmission parameter $S_{21}$ for different length of the $VO_2$ filled gap considering a 30000 S/m conductivity of the chosen thin film, a width of 20 μm and a thickness of 300 nm.



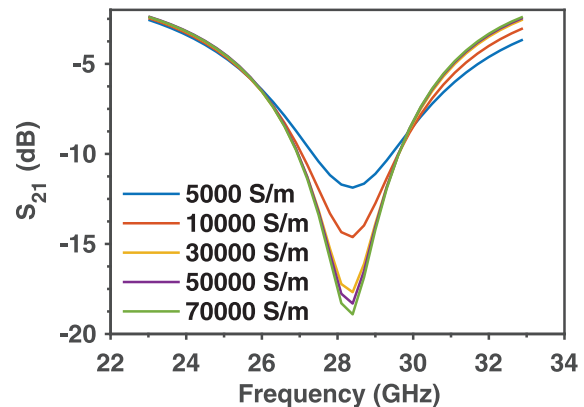**FIGURE 5.** Simulated magnitude of the transmission parameter $S_{21}$ for varying conductivity of the $VO_2$ thin film for a width of 20 μm, a length of 1 μm and a thickness of 300 nm.

shows the influence of the $VO_2$ film conductivity in its metallic phase. It can be seen that the use of a low conductive $VO_2$ film affects the maximum $IL$ for fixed geometrical values of the film.
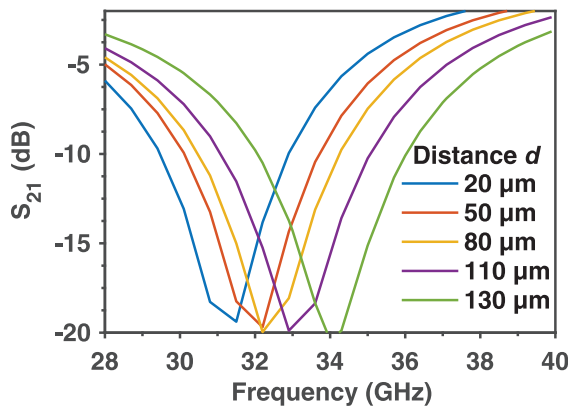
**FIGURE 6.** Simulated magnitude of the transmission parameter $S_{21}$ for different position $d$ of the VO$_2$ switch along the spiral (as indicated in Fig. 3) in the off-state.

## C. SIMULATION OF THE FILTER WITH TUNING MECHANISM IN THE OFF-STATE

The DGS can be seen like a dual of a spiral inductor which has two spirals short-cutted when the VO$_2$ is in the non-conductive state (off). The position of the switch along the spiral determines the value of the inductance in the off-state and thus sets the resonant frequency. Fig. 6 shows the effect of changing the value of $d$ (position of the cut along the spiral): the resonance frequency increases as $d$ is increased and the cut is done further away from the reference in Fig. 2 (a). One can see a shift from 28 GHz in the on-state to around 34 GHz in the off-state as $d$ reaches 130 μm. It is worth mentioning that a further displacement of the cut position along the spiral would further increase the tuning range. The results presented in Fig. 6. are based on a VO$_2$ switch of length of $L_{VO2} = 1$ μm considering a constant relative dielectric permittivity of $\varepsilon_r = 30$ for the thin film.

The final parameters of the fabricated filter are $a = 320$ μm, $d = 130$ μm with a VO$_2$ switch of length $L_{VO2} = 1$ μm and width $W_{VO2} = 10$ μm.
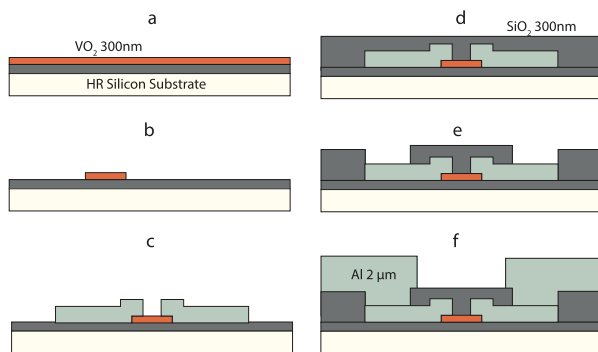


**FIGURE 7.** Fabrication process of the vanadium oxide tunable band-stop filters. (a) VO$_2$ sputtering. (b) VO$_2$ patterning. (c) Ti 20 nm/Al 800 nm Lift-Off. (d) SiO$_2$ sputtering. (e) VIAS opening. (f) Al sputtering and etching.

## III. FABRICATION

The filters were fabricated using standard microelectronics processes starting with a high-resistivity (10000 Ω · cm) 525 μm thick silicon substrate (Fig. 7). A 300 nm thick
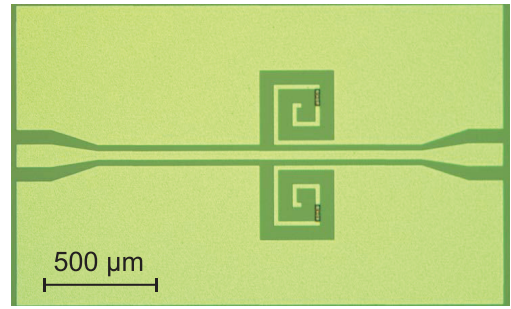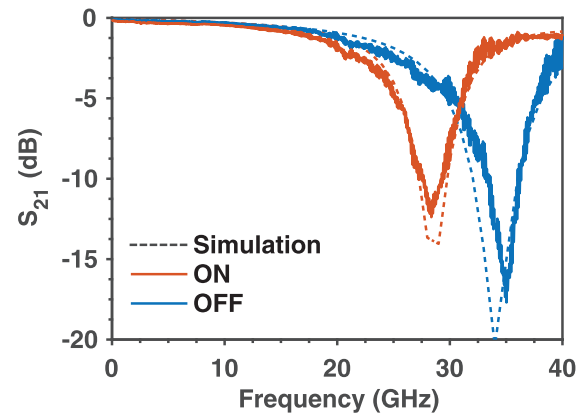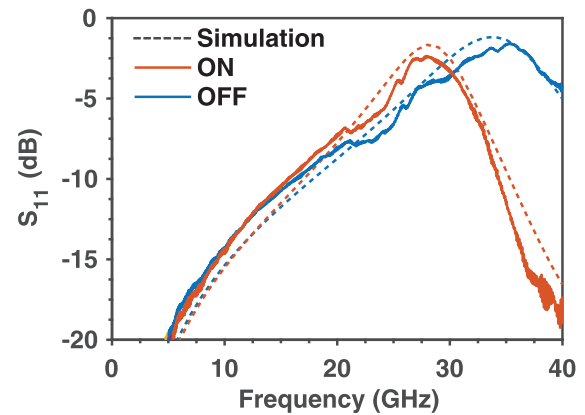


**FIGURE 8.** Optical image of the fabricated tunable band-stop filter.



(a)



(b)

**FIGURE 9.** Measured magnitudes of the $S_{21}$ (a) and $S_{11}$ (b) parameters at 20 °C (OFF) and at 100 °C (ON) (solid lines) versus simulated with Ansys HFSS for the corresponding conductivity values of the VO$_2$ film (dotted lines) (The simulations are done for a VO$_2$ film width of 10 μm, a length of 1 μm and a thickness of 300 nm as fabricated while using a conductivity of 30000 S/m in the On-state).

amorphous silicon layer was deposited to improve radiofrequency performances [16]. The substrate was then passivated with 500 nm SiO$_2$ deposited by sputtering. The VO$_2$ film was prepared by reactive magnetron sputtering deposition starting from a Vanadium target [18]. The film was then patterned using photolithography and wet etching. To contact the VO$_2$ 20 nm of Titanium and 800 nm of Aluminum film were subsequently deposited with e-beam evaporation and patterned with lift-off. A 300 nm thick SiO$_2$ film was then

sputtered. Vias were opened by photolithography and dry etching of SiO$_2$ to contact the bottom metal and a final 2 μm thick Aluminum top metal layer was deposited to create the CPW. Fig. 8 shows an optical image of fabricated filter.
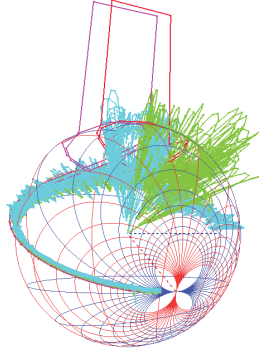


**FIGURE 10.** Measured group delay in the range 0-40 GHz represented over the $S_{21}$ parameters with the 3D Smith chart [19], [20]. The group delay peaks do not exceed in absolute value 0.27 ns (off measured - green, on measured - cyan, off simulated - red, on simulated - violet).

## IV. MEASUREMENTS AND DISCUSSION

Fig. 9 presents the measured magnitude of the $S_{21}$ parameters at 20 °C for the off-state and 100 °C for the on-state (well above the insulator to metal transition temperature of the VO$_2$ film) and shows good agreement with the simulations. The group delay, shown in Fig. 10 by using [19] and [20], has a flat value in both states presenting measured peak variations below 0.27 ns, slightly larger than the simulated value of 0.25 ns, but similar to the reported values in [17]. It is worth mentioning the almost indistinguishable difference between the simulated complex $S_{21}$ parameters and measured ones in both states (plotted on the surface of the 3D Smith chart)
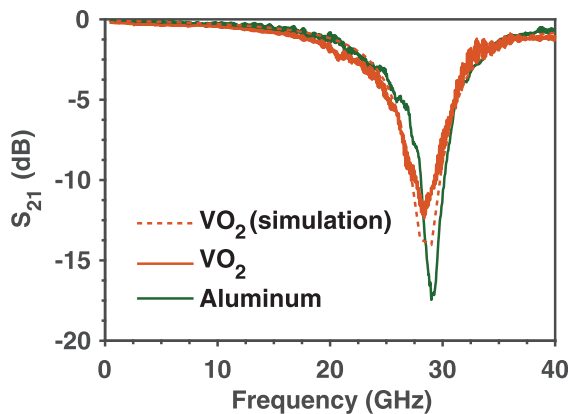


**FIGURE 11.** Measured magnitude of the $S_{21}$ parameter for a structure with VO$_2$ switch at 100 °C (ON) (red solid lines), for a structure with Aluminum instead of VO$_2$ (green) and for the simulated Ansys HFSS for the 30000 S/m conductivity values of the VO$_2$ film in the on-state (dashed red line).

In order to better understand the *IL* performances in the on-state we fabricated a test device where the VO$_2$ film is replaced with a metallic strip and we obtained the results in Fig. 11, showing the limitation caused by the thin film
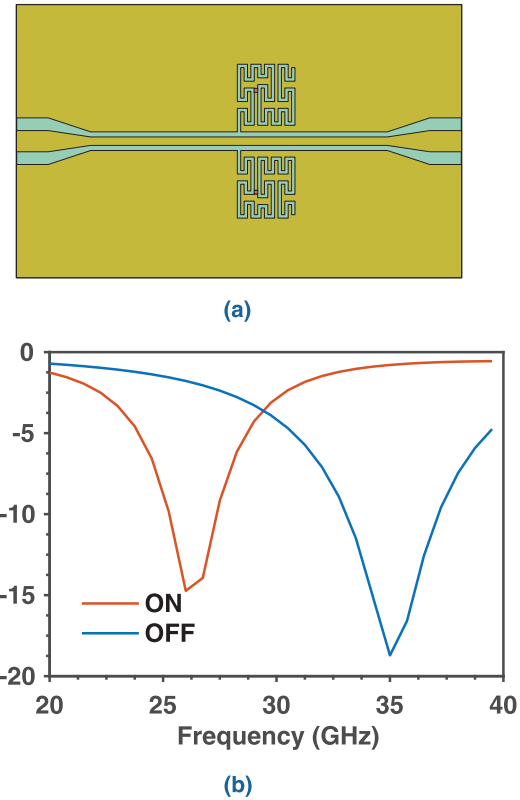


**(a)**



**(b)**

**FIGURE 12.** (a) Conceptual Peano curve shaped DGS band stop filter (switch position is with red color) filter and (b) corresponding $S_{21}$ parameters magnitudes simulated with Ansys HFSS. Normalized filter size = $b \times a/\lambda_0^2 = 0.08 \times 0.03$.

non ideal behavior (we used in the simulations a value of 30000 S/m for the expected conductivity). To avoid an excessive quality factor drop below unity as in [15] where the VO$_2$ was used (in a completely different approach) in spiral inductor design, a very short VO$_2$ gap (1 μm) was used.

In the off-state the frequency shift could be attributed to the modelling used for the VO$_2$ permittivity, which changes as the frequency increases [3] and whose exact value is difficult to predict.

Using the same tuning concept, inspired from the Peano space filling curve [21], which was used very recently in other microwave applications [22], we introduce to the best of our knowledge for the first time a Peano DGS for the bandstop filter tuning. The position of the VO$_2$ switch in this layout allows changing the resonance frequency in various ways (an example being presented in Fig. 12), offering thus a flexible tuning capability. Again the maximum *IL* are limited by the substrate losses, switching losses but the proposed design allows minimizing the area while increasing the tuning range.

## V. CONCLUSION

We have reported the first VO$_2$ based K$_a$ band CPW DGS experimental bandstop tunable filter. The filter occupies the smallest area in respect to all other CPW DGS tunable filters

known to the authors in terms of area divided by the square of free space wavelength (defined at the highest tuned resonance frequency) while exhibiting a tunability of 19 %. The use of $VO_2$ as a contact series switch shows the high dependence of the maximum *IL* obtained at the tuned resonance frequency on the conductivity and length/width of the $VO_2$ thin film. Even if the on-state performances of the filters are limited by the $VO_2$ conductivity and by the non-ideal silicon substrate, the tuning defected shape principles introduced may be of further interest for the microwaves community. Last, based on the same tuning principle we introduce a new type of conceptual Peano filter prototype for minimizing the DGS area while adding a potential degree of flexibility in the tuning capabilities.

## REFERENCES

[1] NASA Glenn Research Center. *Press release, Ka Band Represents the Future of Satellite Communications*. Accessed: Aug. 2017. [Online]. Available: https://www.nasa.gov/mission_pages/station/research/news/ka_band

[2] W. A. Vitale *et al.*, "Electrothermal actuation of vanadium dioxide for tunable capacitors and microwave filters with integrated microheaters," *Sensors Actuat. A, Phys.*, vol. 241, pp. 245–253, Apr. 2016.

[3] N. Edmond, A. Hendaoui, S. Delprat, M. Chaker, and K. Wu, "Theoretical and experimental investigation of thermo-tunable metal-insulator-vanadium dioxide coplanar waveguide structure," *IEEE Trans. Microw. Theory Techn.*, vol. 65, no. 5, pp. 1443–1455, May 2017.

[4] E. A. Casu *et al.*, "Shunt capacitive switches based on $VO_2$ metal insulator transition for RF phase shifter applications," in *Proc. ESSDERC*, Leuven, Belgium, Sep. 2017, pp. 232–235.

[5] C. S. Kim, J. S. Park, D. Ahn, and J. B. Lim, "A novel 1-D periodic defected ground structure for planar circuits," *IEEE Microw. Wireless Lett.*, vol. 10, no. 4, pp. 131–133, Apr. 2000.

[6] M. K. Khandelwal, B. K. Kanaujia, and S. Kumar, "Defected ground structure: Fundamentals, analysis, and applications in modern wireless trends," *Hindawi Int. J. Antennas Propag.*, vol. 2017, Feb. 2017, Art. no. 2018527.

[7] A. M. E. Safwat, F. Podevin, P. Ferrari, and A. Vilcot, "Tunable bandstop defected ground structure resonator using reconfigurable dumbbell-shaped coplanar waveguide," *IEEE Trans. Microw. Theory Techn.*, vol. 54, no. 9, pp. 3559–3564, Sep. 2006.

[8] H. B. El-Shaarawy, F. Cocceti, R. Plana, M. El-Said, and E. A. Hashish, "Novel reconfigurable defected ground structure resonator on coplanar waveguide," *IEEE Trans. Microw. Theory Techn.*, vol. 58, no. 11, pp. 3622–3628, Nov. 2010.

[9] J. Wang, H. Ning, and L. Mao, "A compact reconfigurable bandstop resonator using defected ground structure on coplanar waveguide," *IEEE Antennas Wireless Propag. Lett.*, vol. 11, pp. 457–459, Apr. 2012.

[10] A. Chernov, Y. Prokopenko, and G. A. E. Vandenbosch, "Continuously tunable band-stop filter based on coplanar waveguide with defected ground structure," in *Proc. Int. Conf. Electron. Nanotechnol. (ELNANO)*, Apr. 2017, pp. 187–189.

[11] D. Schlieter and R. M. Henderson, "Silicon integrated defected ground structures," in *Proc. IEEE Topic. Meeting Silicon Monolithic Integr. Circuits RF Syst. (SiRF)*, New Orleans, LA, USA, Jan. 2010, pp. 92–95.

[12] Y.-L. Lai and P.-Y. Cheng, "CPW filters with defected ground structures for RF and microwave applications," in *Proc. Joint Conf. Inf. Sci.*, Kaohsiung, Taiwan, Oct. 2006, pp. 8–11.

[13] B. Pradhan and B. Gupta, "Ka-band tunable filter using metamaterials and RF MEMS varactors," *J. Mciroelectromech. Syst.*, vol. 24, no. 5, pp. 1453–1461, Oct. 2015.

[14] J.-S. Lim, C.-S. Kim, Y.-T. Lee, D. Ahn, and S. Nam, "A spiral-shaped defected ground structure for coplanar waveguide," *IEEE Microw. Wireless Compon. Lett.*, vol. 12, no. 9, pp. 330–332, Sep. 2002.

[15] S. Wang, W. Wang, E. Shin, T. Quach, and G. Subramanyam, "Tunable inductors using vanadium dioxide as the control material," *Microw. Opt. Techn. Lett.*, vol. 59, no. 5, pp. 1057–1061, May 2017.

[16] M. Fernández-Bolaños, J. Perruisseau-Carrier, P. Dainesi, and A. M. Ionescu, "RF MEMS capacitive switch on semi-suspended CPW using low-loss high-resistivity silicon substrate," *Microelectron. Eng.*, vol. 85, no. 6, pp. 1039–1042, Jun. 2008.

[17] X. Zuo and J. Yu, "A stepped-impedance bandstop filter with extended upper passbands and improved pass-band reflections," *AIP Adv.*, vol. 6, no. 9, pp. 1–6, Nov. 2016.

[18] W. A. Vitale *et al.*, "A steep-slope transistor combining phase-change and band-to-band-tunneling to achieve a sub-unity body factor," *Sci. Rep.*, vol. 7, no. 1, p. 355, 2017.

[19] A. A. Muller, P. Soto, D. Dascalu, D. Neculoiu, and V. E. Boria, "A 3-D smith chart based on the Riemann sphere for active and passive microwave circuits," *IEEE Microw. Compon. Lett.*, vol. 21, no. 6, pp. 286–288, Jun. 2011.

[20] A. A. Muller, E. Sanabria-Codesal, A. Moldoveanu, V. Asavei, and S. Lucyszyn, "Extended capabilities of the 3-D smith chart with group delay and resonator quality factor," *IEEE Trans. Microw. Theory Techn.*, vol. 65, no. 1, pp. 10–17, Jan. 2017.

[21] B. B. Mandelbrot, *The Fractal Geometry of Nature*. San Francisco, CA, USA: W. H. Freeman, 1982.

[22] A. Chakraborty and B. Gupta, "Development of compact 180° phase shifters based on MEMS technology," *Sens. Actuators A, Phys.*, vol. 247, pp. 187–198, Aug. 2016.

**EMANUELE ANDREA CASU** received the M.Sc. degree in micro and nano technologies for integrated systems jointly from Lausanne EPFL, Grenoble INP, and Politecnico di Torino in 2012. He is currently pursuing the Ph.D. degree with EPFL. His master's thesis was on oxides growth and characterization on graphene with the IBM Thomas J. Watson Research Center. In 2010, he had an undergraduate internship in a startup company, EULEGO srl, Turin, where he was focused on C programming for safety-critical embedded system. Since 2013, he has been with the Laboratory of Micro/Nanoelectronic Devices, EPFL, where he has been involved in MEMS resonators for communication and sensing applications, steep-slope switches based on insulator to metal transition, TMDC/$VO_2$ junctions, and reconfigurable RF functions based on $VO_2$.

**ANDREI A. MÜLLER** received the Ph.D. degree in telecommunications engineering from the University Politehnica of Bucharest in 2011. In 2012, he held a post-doctoral position with the Labsticc-CNRS Brest, France, with a focus on filter design. He received a four-year Marie Curie Integration Grant Fellowship, from the European Union, UPV Valencia, Spain, from 2013 to 2017. Since 2017, he has been with the Nanolab/EPFL, with a focus on microwave circuit design of smart materials. He received the Gheorghe Cartianu Award from the Romanian Academy for the 2011 *IEEE MWCL* article, A 3D Smith chart based on the Riemann Sphere for active and Passive Microwave Circuits, and launched in 2017 the first 3-D Smith chart tool. He has been an Associate Editor for the IEEE Access Journal since 2016.

**MONTSERRAT FERNÁNDEZ-BOLAÑOS** received the Ph.D. degree in microsystems and microelectronics from the École polytechnique fédérale de Lausanne (EPFL), Switzerland, in 2010. Since 2010, she has been a Scientific Collaborator, with the IBM Research Zurich, where she has been involved in NEM relay logic circuit for ultralow-power applications and also with the Swiss Federal Department of Defense, as a Research Project Manager in radars. She is currently a Senior Scientist and the Deputy of the Laboratory of Micro/Nanoelectronic Devices, EPFL. Her research interests include advanced materials and technologies for reconfigurable electronic devices including RF MEMS and metal-insulator transition vanadium dioxide. She has authored over 80 articles in international journals and conference proceeding. She is a member of the TPC Committee of IEDM and ESSDERC conferences since 2016.

**ALESSANDRO FUMAROLA** received the M.S. degree in nanotechnology jointly from the Polytechnic of Turin, INP Grenoble, and EPFL Lausanne. He is currently pursuing the Ph.D. degree with the Max Planck Institute for Microstructure Physics, Halle. He was with IBM Research-Almaden. His research interests include non-Von Neumann computing, phase-change materials, and magnetic microsystems.

**ANDREAS SCHÜLER** received the master's degree in physics from the University of Freiburg im Breisgau and the University of Michigan, Ann Arbor, and the Ph.D. degree from the University of Basel, with a focus on the electronic and optical properites of novel nanocomposite materials for solar selective absorber coatings. He started up a research group devoted to nanotechnology for solar energy conversion at the École polytechnique fédérale de Lausanne (EPFL). He is currently a Lecturer with EPFL and a Supervisor for Ph.D. and master's students. He was the Principal Organizer of the E-MRS Symposium on Carbon-Based Nanostructured Composite Films at the E-MRS Spring Meeting 2008, in Strasbourg, France, and received the Solar Energy Journal Best Technical Paper Award in 2007 and 2013.

**ANNA KRAMMER** received the M.Sc. degree in functional advanced materials and engineering jointly from INP Grenoble and TU Darmstadt. In 2015, she completed the master's thesis with the Solar Energy and Building Physics Laboratory, EPFL Lausanne, where she is currently pursuing the Ph.D. degree. Her Ph.D. topic was on thermochromic $VO_2$ based switchable absorber coatings for solar thermal applications.

**ADRIAN M. IONESCU** received the Ph.D. degree from the National Polytechnic Institute of Grenoble in France. He is currently a Full Professor with the Swiss Federal Institute of Technology, Lausanne (EPFL) in Switzerland. He has held staff and/or visiting positions with LETI-CEA, Grenoble, LPCS-ENSERG, and Stanford University from 1998 to 1999. He is the Director of the Laboratory of Micro/Nanoelectronic Devices (Nanolab), EPFL. He has authored over 250 articles in international journals and conference proceedings. His research interests include micro-and nanoelectronic devices aimed at integrated circuit design, particularly process development, modeling, and electrical characterization.

● ● ●

# SCIENTIFIC REPORTS

**OPEN**

# Van der Waals MoS$_2$/VO$_2$ heterostructure junction with tunable rectifier behavior and efficient photoresponse

Nicoló Oliva[1], Emanuele Andrea Casu[1], Chen Yan [2], Anna Krammer[3], Teodor Rosca[1], Arnaud Magrez[4], Igor Stolichnov[1], Andreas Schueler[3], Olivier J. F. Martin [2] & Adrian Mihai Ionescu[1]

Junctions between n-type semiconductors of different electron affinity show rectification if the junction is abrupt enough. With the advent of 2D materials, we are able to realize thin van der Waals (vdW) heterostructures based on a large diversity of materials. In parallel, strongly correlated functional oxides have emerged, having the ability to show reversible insulator-to-metal (IMT) phase transition by collapsing their electronic bandgap under a certain external stimulus. Here, we report for the first time the electronic and optoelectronic characterization of ultra-thin n-n heterojunctions fabricated using deterministic assembly of multilayer molybdenum disulphide (MoS$_2$) on a phase transition material, vanadium dioxide (VO$_2$). The vdW MoS$_2$/VO$_2$ heterojunction combines the excellent blocking capability of an n-n junction with a high conductivity in on-state, and it can be turned into a Schottky rectifier at high applied voltage or at temperatures higher than 68 °C, exploiting the metal state of VO$_2$. We report tunable diode-like current rectification with a good diode ideality factor of 1.75 and excellent conductance swing of 120 mV/dec. Finally, we demonstrate unique tunable photosensitivity and excellent junction photoresponse in the 500/650 nm wavelength range.

VO$_2$ is a strongly correlated functional oxide exhibiting an IMT at 340 K[1–4]. In the so-called insulating state at room temperature, VO$_2$ is a semiconductor with a 0.6 eV band gap and monoclinic crystal structure, while above the transition temperature it exhibits a rutile structure and a metallic behavior with a resistivity drop up to 5 orders of magnitude in the bulk material[1,2]. The IMT can be induced by thermal, electrical, magnetic or optical excitations[3] and is typically hysteretic. The electrically induced phase transition results in an extremely steep drop of the resistivity that has been exploited to realize VO$_2$ two-terminal switches[3,4]. Coupled VO$_2$ oscillators have been recently demonstrated together with their potential for neuromorphic pattern recognition applications[5]. The IMT of VO$_2$ resistors connected in series to the source or gate of field-effect devices has been exploited to demonstrate switching slopes well below the 60 mV/dec Boltzman limit constraining the MOSFET subthreshold slope[6,7]. VO$_2$ resistance-to-capacitance reversible reconfigurability is also appealing for RF applications[4]. However, the small band gap of VO$_2$ in its insulating state determines a small resistivity and high leakage currents in VO$_2$ switches. Moreover, the electrical induced phase transition requires typically several hundreds of μW to few mW of power[3,4]. VO$_2$ three terminal gated devices have been proposed and investigated with the purpose of decreasing the voltage and current required to trigger the IMT, but the large electron density necessary for the phase transition at room temperature is difficult to achieve by exploiting the gate control only[8,9]. Large insulating state leakage and reduced gate control on the carrier density are currently two fundamental challenges on the road for VO$_2$ based devices and circuits.

Here, we demonstrate for the first time a two terminal device based on a vdW heterostructure junction formed by VO$_2$ and multilayer MoS$_2$ flakes. Bulk-like MoS$_2$ is an indirect band-gap semiconductor with a 1.3 eV band

[1]Nanoelectronic Devices Laboratory (NanoLab), École Polytechnique Fédérale de Lausanne (EPFL), 1015, Lausanne, Switzerland. [2]Nanophotonics and Metrology Laboratory (NAM), École Polytechnique Fédérale de Lausanne (EPFL), 1015, Lausanne, Switzerland. [3]Solar Energy and Building Physics Laboratory (LESO-PB), École Polytechnique Fédérale de Lausanne (EPFL), 1015, Lausanne, Switzerland. [4]Istitut de Physique (IPHYS), École Polytechnique Fédérale de Lausanne (EPFL), 1015, Lausanne, Switzerland. Correspondence and requests for materials should be addressed to N.O. (email: nicolo.oliva@epfl.ch)
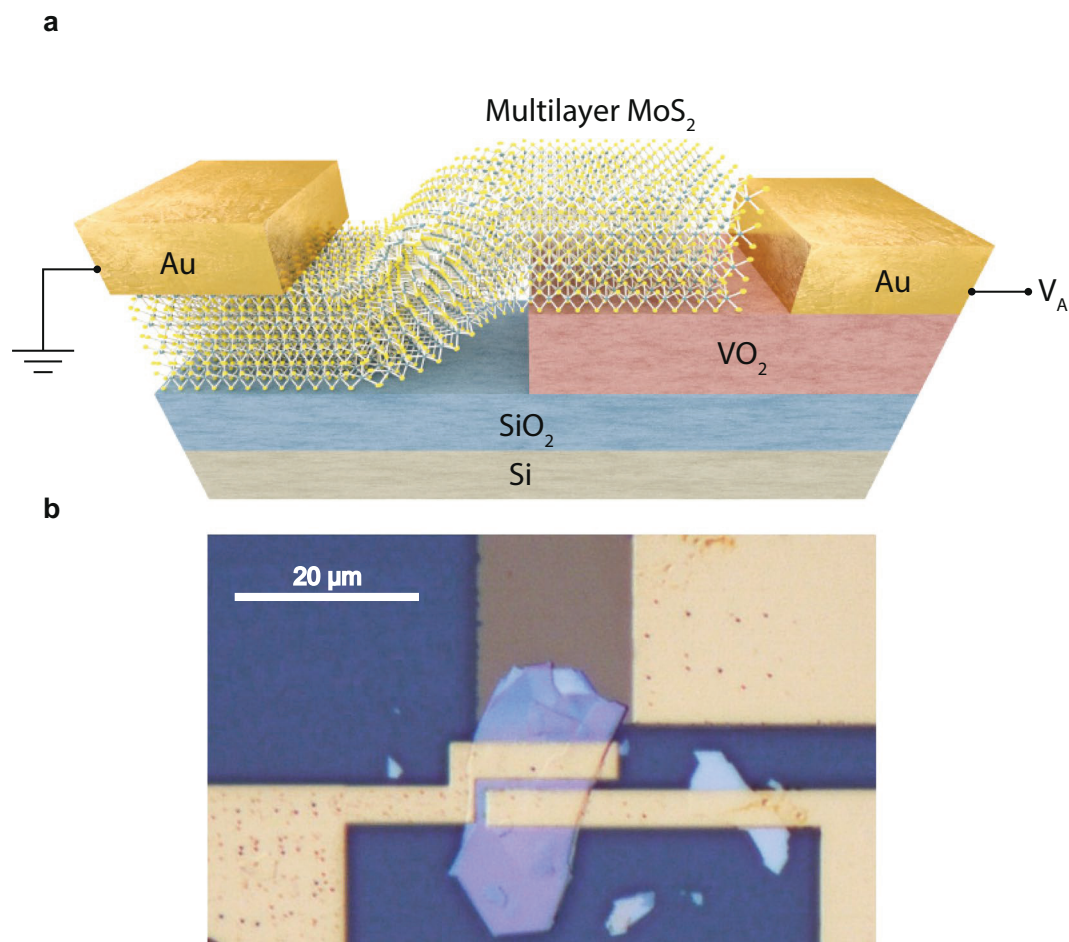
**Figure 1.** VdW MoS$_2$/VO$_2$ heterojunction schematic. (**a**) Three-dimensional schematic view of the MoS$_2$/VO$_2$ heterojunction with the bias configuration used in the experiments. The MoS$_2$ contact is grounded while the bias is applied and swept on the metal contact on VO$_2$. (**b**), Optical image of the fabricated heterojunction composed of a multilayer MoS$_2$ flake and VO$_2$ pre-patterned structure. Gold contacts to the two sides of the junction have been deposited to characterize the device. Two distinct set of contacts were deposited on the MoS$_2$ flakes to verify their electrical behavior.

gap[10,11], which forms a type II n-n heterojunction when in contact with VO$_2$. The proposed device shows an excellent tunable rectification behavior and can be turned into a Schottky rectifier at high applied voltage or increased temperature by triggering the VO$_2$ IMT. With respect to pure VO$_2$ switches, this heterostructure delivers a lower leakage current in the diode subthreshold region and it could lead to the realization of more energy efficient VO$_2$ devices. Compared to monolayer MoS$_2$, multilayer flakes reduce the risk of damages due to the large power flowing in the devices when electrically actuated and provide lower contact resistance[12]. The fabricated devices proved to be photosensitive in the visible spectral range as a result of light absorption in the MoS$_2$ side of the junction. We report here a complete photoresponse characterization including the impact of the thermally induced IMT of VO$_2$. The extracted responsivities exceed the results reported for other photodiodes based on multilayer MoS$_2$ flakes[11,13,14].

## Results
### Electrical characterization of the heterojunction.
The schematic of the conceptual vdW MoS$_2$/VO$_2$ heterojunction together with the basic biasing scheme used for the experiments are depicted in Fig. 1a: the MoS$_2$ contact is grounded and the voltage is applied and swept on the metal contact on VO$_2$. An optical microscopy image of a fabricated MoS$_2$/VO$_2$ heterojunction with the electrical contacts to the two sides of the junction is reported in Fig. 1b. Two separate set of gold contacts were deposited on the MoS$_2$ flake to verify their ohmic behavior (see Supplementary Information Fig. S1a). The thickness of the exfoliated flakes has been estimated by atomic force microscopy, and the devices described in the following have been realized with flakes thicknesses ranging from 80 to 100 nm. The VO$_2$ and the SiO$_2$ films are respectively 75 nm and 2 μm thick. Details on device fabrication are reported in the methods section. The X-ray diffraction study and resistivity curve of as deposited VO$_2$ film, which demonstrates the absence of other vanadium oxide phases potentially detrimental for the device operation, are shown in Supplementary Information Figs S2a and S2b.
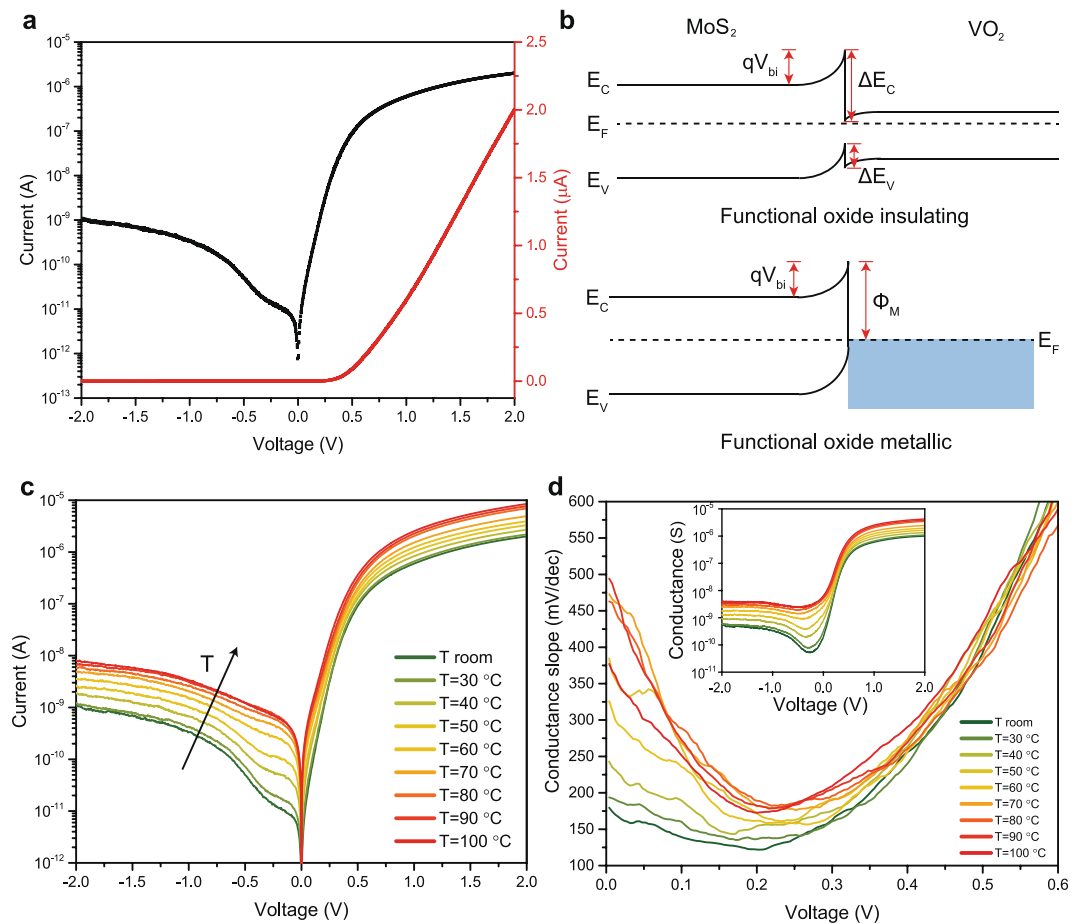
**Figure 2.** Electrical characteristic of the $MoS_2/VO_2$ heterojunction. (**a**) Electrical I–V double-sweep characteristic of device D1 at room temperature in semi-logarithmic (black) and linear (red) scales. The device presents a rectification behavior with no significant hysteresis. (**b**) Qualitative band diagram of the $MoS_2/VO_2$ heterojunction for the insulating and metallic phase of the functional oxide. The VdW gap at the junction is not represented and the polycrystalline nature of $VO_2$ is not considered. (**c**) Evolution of the electrical characteristic of D1 with increasing temperature. Both forward and reverse current are boosted by the temperature increase, with a more pronounced enhancement in the window around the IMT temperature (60–80 °C). (**d**) Extracted conductance slope from the exponential regime of the forward current. The conductance slope increases across the $VO_2$ IMT. Inset: conductance of device D1.

The current voltage characteristic of a first device (D1) at room temperature is shown in Fig. 2a. The $MoS_2/VO_2$ heterojunction exhibits a clear rectifying behavior with a rectification ratio $I_F/I_R$ larger than $10^3$ and an extracted $I_F/I_S$ exceeding $10^5$, where $I_F$, $I_R$ and $I_S$ are respectively forward, reverse and saturation current. Under positive bias, the current shows an exponential increase that becomes linear under larger voltages because of the series resistance. The behavior of the junction can be explained in terms of the qualitative band diagram in Fig. 2b (see Supplementary Information Fig. S3 for more information). Both $MoS_2$ and the insulating phase of $VO_2$ are intrinsically n-type materials[15,16]. Since $MoS_2$ workfunction is smaller than $VO_2$ one, at the formation of the heterostructure electrons are transferred from the first to the second, resulting in the depicted band alignment, Fig. 2b. The large conduction band discontinuity ($\Delta E_C$), estimated by the affinity rule to be roughly 1 eV, is the main responsible for the asymmetric conduction of the junction. Applying a positive bias to $VO_2$, electron injection from $MoS_2$ conduction band to $VO_2$ conduction band is favored, resulting in an exponential increase of the current. Conversely, under reverse bias electrons are injected from $VO_2$ to $MoS_2$, but they face the large $\Delta E_C$ barrier. Overall, the realized junction behaves as an n-n heterostructure with type II band alignment and is able to provide a good rectification. The device I–V characteristic in the exponential region can be approximated with the Shockley diode equation providing an extracted ideality factor of 1.75, while the non-saturating reverse current is better described by the Fang and Howard model[17] specifically developed for n-n junctions and capable of analytically capturing the increase of diode current with the absolute value of the reverse bias (see Supplementary Information Fig. S4b,c).

The characterization of the heterojunction device in a wide range of increasing temperature is of particular interest because $VO_2$ transition from the semiconductor to the metallic phase around 68 °C is expected to increase the conductance of the junction by collapsing the $VO_2$ bandgap. The I–V curves measured with the temperature
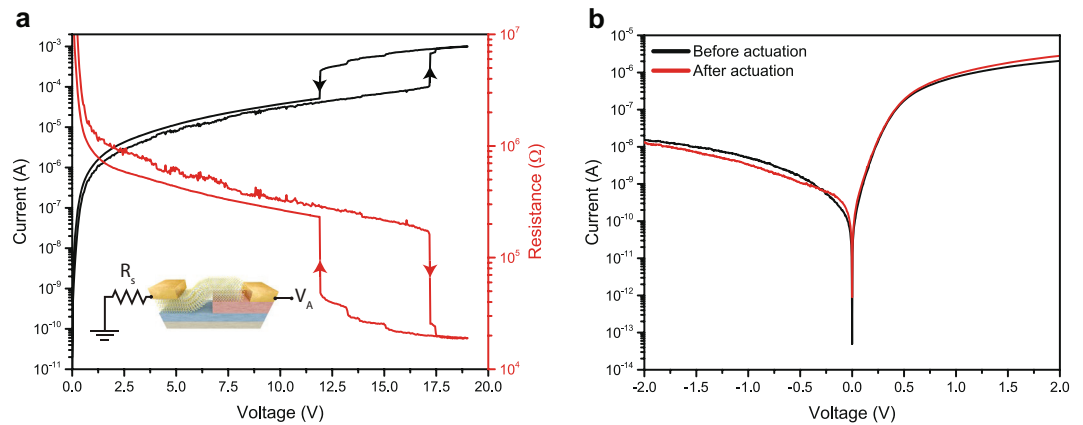
**Figure 3.** Electrically induced IMT of the VO$_2$ side of the heterojunction. (**a**) Electrical characteristic of device D2 under large applied bias, sufficient to trigger the IMT of VO$_2$ close to 17.5 V. Inset: biasing scheme used for the experiment. A discrete resistor R$_S$ of 1 kΩ is connected in series to the device to limit the current in the low resistance state. (**b**) I–V curve of D2 measured before and after having electrically induced the IMT of VO$_2$. The comparison between the two curves shows that the phase change of VO$_2$ and the actuation power has no permanent effect on the electrical behavior of the heterojunction.

as a parameter are shown in Fig. 2c. Both forward and reverse current increase with temperature and a significant current enhancement is observed close to the IMT temperature. Above it, the temperature dependence of the characteristic is less pronounced and the device behaves as a Schottky rectifier. The band diagram of the junction with metallic VO$_2$ is drawn in Fig. 2b. The Schottky barrier ($\Phi_M$) is estimated to be 0.3 eV larger than $\Delta E_C$, and the built-in voltage should increase slightly since VO$_2$ work function is reported to increase across the IMT[2]. The reverse current increase with raising temperature can be explained with the growth of electron density in VO$_2$ conduction band, changing from $10^{18}$ cm$^{-3}$ in the insulating phase to $10^{23}$ cm$^{-3}$ in the metallic one[18]. The boost of forward current can be attributed to the stronger thermionic injection in VO$_2$ conduction band from MoS$_2$ conduction band, but it is mitigated by the slight increase of the built-in voltage. The rectification ratio with metallic VO$_2$ is slightly degraded with respect to the semiconductor junction but it remains larger than $10^3$. In order to characterize the junction conduction we extracted the conductance slope[19] $S_G = (\partial log G/\partial V)^{-1}$ for the forward current at different temperatures (Fig. 2d). At room temperature, the device exhibits an excellent minimum $S_G$ value of 120 mV/dec, which suggests that the heterojunction is abrupt and has a reduced density of interface defects. This observation is further supported by the absence of any hysteresis of the I–V characteristics (see Fig. 2a) in double-sweep measurements and by a low extracted quality factor of 1.75 in forward bias. The conductance slope increases across the MIT and tend to decrease after the phase transition.

**Demonstration of electrically induced reversible IMT.** The capability of electrically inducing the IMT of the VO$_2$ layer in the heterostructure in a room temperature experiment is shown in Fig. 3. This measurement has been performed on another device (D2) with the same structure of D1. The biasing configuration used for the measurements is the same shown in Fig. 1b, with the addition of a series resistance R$_S$ of 1 kΩ to limit the maximum current. The I–V curve of the heterojunction (Fig. 3a) exhibits two steep jumps in correspondence of the IMT and MIT of VO$_2$, separated by a hysteresis window. The voltage required to trigger the IMT is significantly larger with respect to the values that can be achieved in pure VO$_2$ switches[4] (see Supplementary Information Fig. S5). The high actuation voltage is due to the resistance of the heterojunction and to the relatively large distance between the MoS$_2$ edge and VO$_2$ metallic contact (more than 1 μm for D2). Remarkably, the proposed device delivers a lower leakage current in the diode subthreshold region with respect to pure VO$_2$ switches. This feature combined with the possibility of modulating dynamically the IMT threshold by gating the MoS$_2$ side of the junction could pave the way to more energy efficient VO$_2$ switches. For the device of Fig. 3, the power thresholds required to electrically induce the IMT and MIT transitions from an n-n heterojunction to a Schottky diode and vice versa are respectively 1.83 mW and 2.89 mW. We verified that the actuation power density required to trigger the IMT did not alter the electrical behavior of the heterojunction by measuring the electrical characteristic of D2 before and after the electrical induced IMT. Figure 3b shows a direct comparison of the two I–V curves: no major variations are observed, demonstrating a full reversibility of the VO$_2$ phase change and the stability of the heterojunction conduction.

**Photoresponse characterization.** The photoresponse of device D1, whose dark I–V curve is reported in Fig. 2a, was characterized by illuminating the device with a focused light beam with controllable wavelength and power. The incident power density has been maintained well below the values required[3] to optically trigger or affect VO$_2$ IMT throughout all the measurements performed. The photosensitive area of the device corresponds to the overlap between the MoS$_2$ flake and VO$_2$ (see Fig. 1a), and it is estimated to be 104 μm$^2$. Contributions to the photoresponse at zero applied bias from the MoS$_2$ region far from the heterojunction have been found to be negligible coherently with the ohmic nature of the realized contacts (see Supplementary Information Fig. S1a,b). Moreover, the MoS$_2$ region far from the junction shows a small contrast between the dark and illuminated
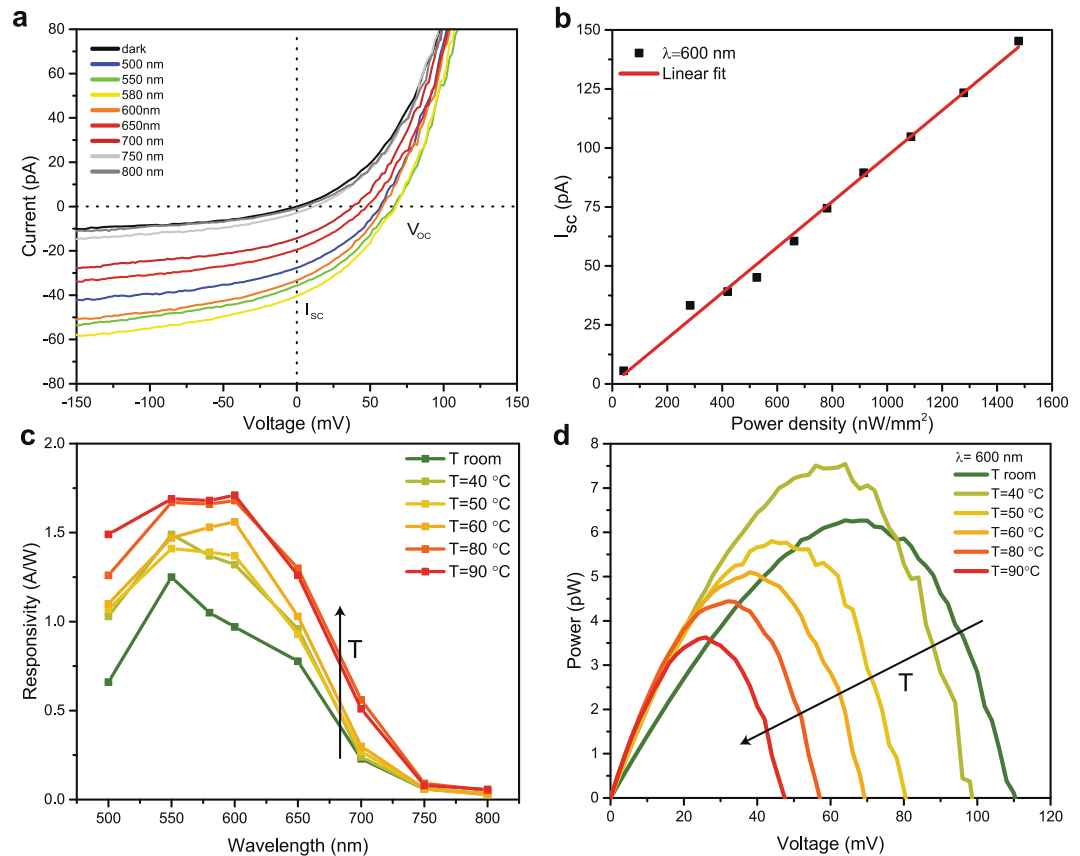
**Figure 4.** Photoresponse of MoS$_2$/VO$_2$ heterojunction. (**a**) I–V characteristic of D1 in linear scale under different illumination wavelengths, from 500 nm to 800 nm. The measurements have been performed under an incident power density close to 330 nW/mm$^2$ for all the wavelengths and at room temperature. (**b**) Short circuit current of the heterostructure as a function of the incident power density, showing a linear dependency. (**c**) Spectral evolution of the photoresponsivity measured at different temperatures. At room temperature, a responsivity larger than the one of conventional silicon p-n photodiode is measured in the spectral range 500/650 nm. The responsivity in the visible spectrum is boosted by the increase of temperature and it saturates for temperatures above the IMT of VO$_2$. (**d**) Electrical power generated by the photodiode under 600 nm illumination with an incident power density of 1.48 μW/mm$^2$. The electrical power that the heterojunction can effectively harvest decreases with the increase of the temperature.

IV curves measured across the set of contacts deposited on MoS$_2$ (see Supplementary Information Fig. S1c). Figure 4a shows the impact of different illumination wavelengths with similar incident power density on the I–V curve of D1, resulting in a non-zero short circuit current I$_{SC}$ and open circuit voltage V$_{OC}$. A schematic representation of the origin of the photovoltaic effect in the heterojunction is reported in Supplementary Information Fig. S6. The measured I$_{SC}$ shows a linear dependency with respect to the incident power density, as shown in Fig. 4b for illumination at 600 nm wavelength. We characterized the time domain photoresponse of the device by measuring the evolution of I$_{SC}$ in response to ON/OFF and OFF/ON transitions of the light source. The device shows a symmetrical rise and decay time and the extracted response time at room temperature is 3.5 ms (see Supplementary Information Fig. S7). This value is considerably smaller than the ones reported in literature for several other implementations of MoS$_2$ based photodetectors[20,21] but still significantly larger than the response time in conventional Si photodiodes[21].

We characterized the impact of temperature on the wavelength resolved photoresponsivity $R$ at zero applied bias, defined as the ratio between the photogenerated current and the incident power on the device (Fig. 4c). The cut-off wavelength is located between 750 and 800 nm and it does not change with temperature, suggesting that light absorption happens mostly in the MoS$_2$ side of the heterojunction[14]. At room temperature, a maximum photoresponsivity of 1.25 A/W was measured at 550 nm, and values exceeding silicon photodiode performance have been obtained in the 500/650 nm range[13]. Responsivity values larger than one have already been reported in p-n junctions based on doped multilayer MoS$_2$ flakes, and can be attributed to the efficient photocarrier separation operated by the built in voltage of the junction[21,22]. The photoresponsivity in the visible range is clearly boosted by the temperature rise and tends to saturate above the VO$_2$ IMT temperature. This enhancement can be explained by different mechanisms. First, the increase of VO$_2$ work function with temperature[2,15] determines a larger built-in voltage and therefore a stronger electric field at the junction that provides a more efficient separation of photogenerated carriers. Secondly, the MoS$_2$ depleted thickness could increase because of VO$_2$ work

function and carrier density boost[18], resulting in an increase of the photosensitive volume. Moreover, another contribution could come from the variation of the optical properties of $VO_2$ producing potential optical interference effects responsible for an enhanced light absorption. Indeed, recent studies reported that the photoluminescence monolayer $MoS_2$ flakes on $VO_2$ substrates increases upon heating $VO_2$ above the IMT temperature, most likely because of constructive optical interference[23,24].

We extracted the generated electrical power $P_{el}$ as a function of the applied voltage at different temperatures under 600 nm illumination with an incident power density of $1.48\,\mu W/mm^2$ (Fig. 4d). The increase of temperature produces a boost of $I_{SC}$ and a larger reverse current (Fig. 2c). This is related to a more favorable leakage path for photogenerated carriers, which causes a drop of $V_{OC}$. Since $V_{OC}$ decreases at a faster rate than $I_{SC}$ grows (see Supplementary Information Fig. S8), the harvesting of the optical power becomes less efficient at high temperatures[14]. Therefore, the IMT of $VO_2$ is beneficial for the heterostructure photosensitivity but appears detrimental for its photovoltaic performance.

## Discussion

In conclusion, we investigated a novel two-terminal device based on a VdW n-n heterojunction between $VO_2$ and multilayer $MoS_2$ flakes. The demonstrated devices show a rectifying electrical behavior, with rectification ratio larger than $10^3$, ideality factor of 1.75 and excellent forward conductance slope. The proposed heterojunction can be turned into a Schottky rectifier by electrically or thermally inducing the $VO_2$ IMT. The electrically induced IMT is proved to be fully reversible and the $MoS_2/VO_2$ heterostructure grants a lower subthreshold leakage current with respect to pure $VO_2$ switches. The envisioned possibility of modulating the IMT threshold voltage by gating the junction to electrostatically control the band alignment of the heterojunction could open a new category of $VO_2$ based solid state devices with promising applications for steep slope electronic switches. Finally, we characterized the optical sensitivity of the heterojunction and obtained external photoresponsivities exceeding the results reported for several other implementations of photodiodes based on multilayer $MoS_2$ flakes[11,13,14]. The fast transient response measured suggests that the device photoresponse is not dominated by trap-assisted optical absorption. The responsivity value is increasing with temperature and saturates above the $VO_2$ IMT. The use of monolayer $MoS_2$ for the realization of the heterostructure could result in a considerable enhancement of the photoresponsivity because of the direct band gap and the larger built-in voltage[23–25]. Large-area $MoS_2$ synthesis techniques could allow a large scale, cheap fabrication of $MoS_2/VO_2$ heterojunction devices[26,27]. Moreover, recent reports of low-thermal budget deposition of $VO_2$ thin films by pulsed laser deposition (PLD) are promising for the realization of CMOS compatible heterostructures[28].

## Methods

**$VO_2$ deposition.**     The 75 nm thick $VO_2$ film was deposited on $SiO_2$ substrate by reactive DC magnetron sputtering in high-vacuum conditions. The chamber was pumped to a base pressure lower than $5 \cdot 10^{-8}$ mbar. The power on the V metal target (2 inch diameter, 99.95% purity) was set to 150 W. Ar process gas (purity 99.999%) was introduced in the chamber and the flow was regulated by a mass flow controller. During deposition, the oxygen pressure was kept constant by a Proportional Integral Derivative (PID) feedback control. This regulated the oxygen flow based on the pressure readings of a Zirox XS22 lambda-probe oxygen sensor. The process pressure was $7.45 \pm 0.01 \cdot 10^{-3}$ mbar and the oxygen partial pressure $4.86 \pm 0.03 \cdot 10^{-4}$ mbar. The temperature was measured by a stationary thermocouple above the rotating substrate holder and was kept constant at 600 °C. During deposition the substrate was rotating at 15 rpm. An *in situ* annealing was adopted during the slow cooling of the sample (30 °C/min).

**$MoS_2$ synthesis.**     $MoS_2$ powder was synthesized by heating a mixture containing stoichiometric amounts of molybdenum (99.9% pure, Alfa Aesar) and sulfur (99.999% pure, Alfa Aesar) at 1000 °C for 7 days in an evacuated and sealed quartz ampule. The mixture was slowly heated from room temperature to 1000 °C for 12 h in order to avoid any explosion due to the strong exothermic reaction and the high volatility of sulfur. From this powder, $MoS_2$ crystals were grown using chemical vapor transport (CVT) with iodine as transport agent at ca. 5 mg/cm³. All quartz tubes used for vapor transport typically have an inner diameter of 16 mm and a length of 20 cm. The total powder charge is 5 g. A very slight excess of sulfur is always included (typically 0.5 wt % of the charge) to ensure the stoichiometry in the resulting crystals. The excess of sulfur is not incorporated into the dichalcogenide crystals but condenses as elemental sulfur onto the wall of the quartz tube at the end of the CVT process. The source and growth zones were kept at 1060 and 1010 °C, respectively, for 7 days in evacuated and sealed quartz ampules. After this time the furnace is turned off, a small fraction of the charge is transported toward the colder end of the tube, forming crystals with diameters of about 2−8 mm and thick tens of microns. The resulting crystals were washed with acetone and dried in vacuum. X-ray diffraction study has shown that $MoS_2$ obtained in this way belongs to the 2 H polymorphism. A full characterization of the synthetized bulk samples is presented elsewhere[29].

**Device fabrication.**     Electron beam lithography (EBL) on negative AZ nLof 2020:PGMEA 1:1 resist and wet etching in diluted commercial Cr etch solution were used to pattern the $VO_2$ film sputtered on a 2 μm thick $SiO_2$ layer. $MoS_2$ multilayer flakes have been exfoliated on a PDMS stamp by using the scotch-tape micromechanical cleavage method and then deterministically transferred[30] on the edge between $VO_2$ pre-patterned structures and the $SiO_2$ layer. The two-terminal devices were completed with a further EBL step and metal evaporation to deposit by lift-off 100 nm thick gold contacts on $VO_2$ and $MoS_2$. Gold was selected for the electrical connections in order to provide ohmic contacts to both $VO_2$ and $MoS_2$ (see Supplementary Information Fig. S1). The thickness of the transferred flakes was measured by atomic force microscopy, and the devices discussed in the text were realized with flakes thickness ranging from 80 to 100 nm.

**Electrical and optical characterization.**    All the measurements were carried on in ambient atmosphere and at temperatures ranging from ambient value to 100 °C. DC electrical measurements were performed using a HP4156A Semiconductor Parameter Analyzer and a Cascade Summit probe station. The light source used for optical characterization is a SuperK EXTREME supercontinuum white light lasers with a series SuperK SELECT multi-line tunable filter to select the wavelength within a minimum bandwidth of $+/-5\,nm$. The optical power was measured with an 818-SL/DB Silicon Photodetector. The light beam was focused on the sample through optical microscopy lenses, resulting in a spot size of $0.25\,mm^2$.

## References

1. Aetukuri, N. B. *et al*. Control of the metal–insulator transition in vanadium dioxide by modifying orbital occupancy. *Nat. Phys.* **9**, 661–666 (2013).
2. Ko, C., Yang, Z. & Ramanathan, S. Work function of vanadium dioxide thin films across the metal-insulator transition and the role of surface nonstoichiometry. *ACS Appl. Mater. Interfaces* **3**, 3396–401 (2011).
3. Seo, G., Kim, B. J., Wook, Lee, Y. & Kim, H. T. Photo-assisted bistable switching using Mott transition in two-terminal VO₂ device. *Appl. Phys. Lett.* **100**, 2–5 (2012).
4. Vitale, W. A., Moldovan, C. F., Paone, A., Schuler, A. & Ionescu, A. M. CMOS-compatible abrupt switches based on VO₂ metal-insulator transition. *2015 Jt. Int. EUROSOI Work. Int. Conf. Ultim. Integr. Silicon* 53–56. doi:https://doi.org/10.1109/ULIS.2015.7063771 (2015).
5. Datta, S., Shukla, N., Cotter, M., Parihar, A. & Raychowdhury, A. Neuro Inspired Computing with Coupled Relaxation Oscillators. *Proc. 51st Annu. Des. Autom. Conf. Des. Autom. Conf. - DAC 14* 1–6 (2014).
6. Shukla, N. *et al*. A steep-slope transistor based on abrupt electronic phase transition. *Nat. Commun.* **6**, 7812 (2015).
7. Casu, E. A. *et al*. Hybrid Phase-Change – Tunnel FET (PC-TFET) Switch with Subthreshold Swing <10mV/decade and sub-0.1 body factor: digital and analog benchmarking. In 2016 *IEEE International Electron Devices Meeting* (2016).
8. Yang, Z., Zhou, Y. & Ramanathan, S. Studies on room-temperature electric-field effect in ionic-liquid gated VO₂ three-terminal devices. *J. Appl. Phys.* **111**, (2012).
9. Ruzmetov, D., Gopalakrishnan, G., Ko, C., Narayanamurti, V. & Ramanathan, S. Three-terminal field effect devices utilizing thin film vanadium oxide as the channel layer. *J. Appl. Phys.* **107**, (2010).
10. Zhang, Y., Ye, J., Matsuhashi, Y. & Iwasa, Y. Ambipolar MoS₂ thin flake transistors. *Nano Lett.* **12**, 1136–1140 (2012).
11. Wi, S. *et al*. Enhancement of Photovoltaic Response in Multilayer MoS₂ Induced by Plasma Doping. *ACS Nano* **8**(5), 5270–5281 (2014).
12. A. Allain, J. Kang, K. Banerjee, and A. Kis, Electrical contacts to two-dimensional semiconductors., *Nat. Mater.*, vol. 14, no. 12, pp. 1195–205, (2015).
13. Ahn, J. *et al*. Transition metal dichalcogenide heterojunction PN diode toward ultimate photovoltaic benefits. *2D Mater.* **3**, 45011 (2016).
14. Svatek, S. A. *et al*. Gate Tunable Photovoltaic Effect in MoS₂ vertical P-N Homostructures. *J. Mater. Chem. C* **5**, 854–861 (2017).
15. Zhou, Y. & Ramanathan, S. GaN/VO₂ heteroepitaxial p-n junctions: Band offset and minority carrier dynamics. *J. Appl. Phys.* **113**, (2013).
16. Radisavljevic, B., Radenovic, A., Brivio, J., Giacometti, V. & Kis, A. Single-layer MoS₂ transistors. *Nat. Nanotechnol.* **6**, 147–50 (2011).
17. Fang, F. F. & Howard, W. E. Effect of crystal orientation on Ge-GaAs heterojunctions. *J. Appl. Phys.* **35**, 612–617 (1964).
18. Stefanovich, G., Pergament, A. & Stefanovich, D. Electrical switching and Mott transition in VO₂. *J. Phys. Condens. Matter* **12**, 8837–8845 (2000).
19. Agarwal, S. & Yablonovitch, E. Band-Edge Steepness Obtained From Esaki/Backward Diode Current–Voltage Characteristics. *IEEE Trans. Electron Devices* **61**, 1488–1493 (2014).
20. Buscema, M. *et al*. Photocurrent generation with two-dimensional van der Waals semiconductors. *Chem Soc Rev* **44**, 3691–3718 (2015).
21. M. S. Choi *et al*. Lateral MoS₂ p-n junction formed by chemical doping for use in high-performance optoelectronics, *ACS Nano*, vol. 8, no. 9, pp. 9332–9340, 2014.
22. Zhong, X. *et al*. Multi-layered MoS₂ phototransistors as high performance photovoltaic cells and self-powered photodetectors. *RSC Adv.* **5**, 45239–45248 (2015).
23. Hou, J. *et al*. Modulating Photoluminescence of Monolayer Molybdenum Disulfide by Metal-Insulator Phase Transition in Active Substrates. *Small* 3976–3984 (2016).
24. Lin, Y.-C. *et al*. Photoluminescence of monolayer transition metal dichalcogenides integrated with VO₂. *J. Phys. Condens. Matter* **28**, 504001 (2016).
25. Lopez-Sanchez, O., Lembke, D., Kayci, M., Radenovic, A. & Kis, A. Ultrasensitive photodetectors based on monolayer MoS₂. *Nat. Nanotechnol.* **8**, 497–501 (2013).
26. Coleman, J. N. *et al*. Two-dimensional nanosheets produced by liquid exfoliation of layered materials. *Science* **331**, 568–571 (2011).
27. Liu, K. K. *et al*. Growth of large-area and highly crystalline MoS₂ thin layers on insulating substrates. *Nano Lett.* **12**, 1538–1544 (2012).
28. Marvel, R. E., Harl, R. R., Craciun, V., Rogers, B. R. & Haglund, R. F. Influence of deposition process and substrate on the phase transition of vanadium dioxide thin films. *Acta Mater.* **91**, 217–226 (2015).
29. A. Pisoni, *et al*., The role of transport agents in MoS₂ single crystals, J. Phys. Chem. C, vol. 119, no. 8, pp. 3918–3922 (2015).
30. A. Castellanos-Gomez *et al*. and G. a Steele, Deterministic transfer of two-dimensional materials by all-dry viscoelastic stamping, *2D Mater.*, vol. 1, no. 1, p. 11002, (2014).

## Acknowledgements

## Author Contributions

N.O. and A.M.I. developed the device principle. N.O. and E.A.C. worked on device fabrication. A.K. and A.S. deposited and characterized the VO₂ thin films. A.M. synthetized the MoS₂ bulk sample. I.S. performed AFM and XRD measurements. N.O. performed electrical and optical measurements and the data analysis. N.O., C.Y., O.M. and T.R. built the optical setup. N.O., E.A.C., T.R. and A.M.I. wrote the manuscript.

## Additional Information

**Supplementary information** accompanies this paper at https://doi.org/10.1038/s41598-017-12950-y.

**Competing Interests:** The authors declare that they have no competing interests.

**Publisher's note:** Springer Nature remains neutral with regard to jurisdictional claims in published maps and institutional affiliations.

# SCIENTIFIC REPORTS

# A Steep-Slope Transistor Combining Phase-Change and Band-to-Band-Tunneling to Achieve a sub-Unity Body Factor

Wolfgang A. Vitale[1], Emanuele A. Casu[1], Arnab Biswas[1], Teodor Rosca[1], Cem Alper[1], Anna Krammer[2], Gia V. Luong[3], Qing-T. Zhao[3], Siegfried Mantl[3], Andreas Schüler[2] & A. M. Ionescu[1]

Steep-slope transistors allow to scale down the supply voltage and the energy per computed bit of information as compared to conventional field-effect transistors (FETs), due to their sub-60 mV/ decade subthreshold swing at room temperature. Currently pursued approaches to achieve such a subthermionic subthreshold swing consist in alternative carrier injection mechanisms, like quantum mechanical band-to-band tunneling (BTBT) in Tunnel FETs or abrupt phase-change in metal-insulator transition (MIT) devices. The strengths of the BTBT and MIT have been combined in a hybrid device architecture called phase-change tunnel FET (PC-TFET), in which the abrupt MIT in vanadium dioxide ($VO_2$) lowers the subthreshold swing of strained-silicon nanowire TFETs. In this work, we demonstrate that the principle underlying the low swing in the PC-TFET relates to a sub-unity body factor achieved by an internal differential gate voltage amplification. We study the effect of temperature on the switching ratio and the swing of the PC-TFET, reporting values as low as 4.0 mV/decade at 25 °C, 7.8 mV/ decade at 45 °C. We discuss how the unique characteristics of the PC-TFET open new perspectives, beyond FETs and other steep-slope transistors, for low power electronics, analog circuits and neuromorphic computing.

Complementary metal-oxide semiconductor (CMOS) technology has been the core of micro/nanoelectronics industry for decades. In the Dennardian scaling era of MOS transistors, extraordinary improvements in terms of switching speed, device density, functionality and cost have been achieved by the additive application of several technology boosters such as substrate engineering, strain, multi-gate, high-k/metal gate stacks and high-mobility channel materials. However, the concept of a metal-oxide-semiconductor field-effect transistor (MOSFET) remained unchanged. Recently, aggressive scaling of the gate length dimensions down to few tens of nanometers is facing major challenges in terms of process variability, high leakage power, unscalable voltage supply and degraded current switching ratios[1].

The quest for a new beyond CMOS switch, addressing essentially leakage power and voltage scaling, encompasses new device concepts and materials, capable to complement MOSFETs and to be integrated on advanced CMOS platforms[2, 3]. A fundamental target is the reduction of the subthreshold swing $SS$ ($=dV_g/dlogI_d$), which in a conventional MOSFET is limited to 60 mV/decade at room temperature ($T = 300$ K) due to the thermionic carrier injection mechanism[4]. A steep-slope switch, with $SS < 60$ mV/decade, would allow to scale down the supply voltage and to enable future low-power computing[5]. Different steep-slope device principles have been proposed for this purpose, exploiting negative capacitance[6], movable electro-mechanical gates[7], impact ionization[8] and tunnel field-effect transistors (TFETs) based on quantum mechanical band-to-band tunnelling[9] (BTBT). TFET is currently considered the most promising steep-slope solid-state switch among alternative technologies, with experimentally demonstrated $SS$ values of the order of 30 mV/decade at room temperature[10] mainly limited into a range of low currents. However, the tunnelling conduction mechanism limits the device performance in terms of 'on' current, $I_{ON}$, and the frequency of operation.

[1]Nanoelectronic Devices Laboratory (NanoLab), École Polytechnique Fédérale de Lausanne (EPFL), 1015, Lausanne, Switzerland. [2]Solar Energy and Building Physics Laboratory (LESO-PB), École Polytechnique Fédérale de Lausanne (EPFL), 1015, Lausanne, Switzerland. [3]Peter Grünberg Institut 9 (PGI-9), Forschungszentrum Jülich, 52425, Jülich, Germany. Correspondence and requests for materials should be addressed to W.A.V. (email: wolfgang.vitale@epfl.ch)
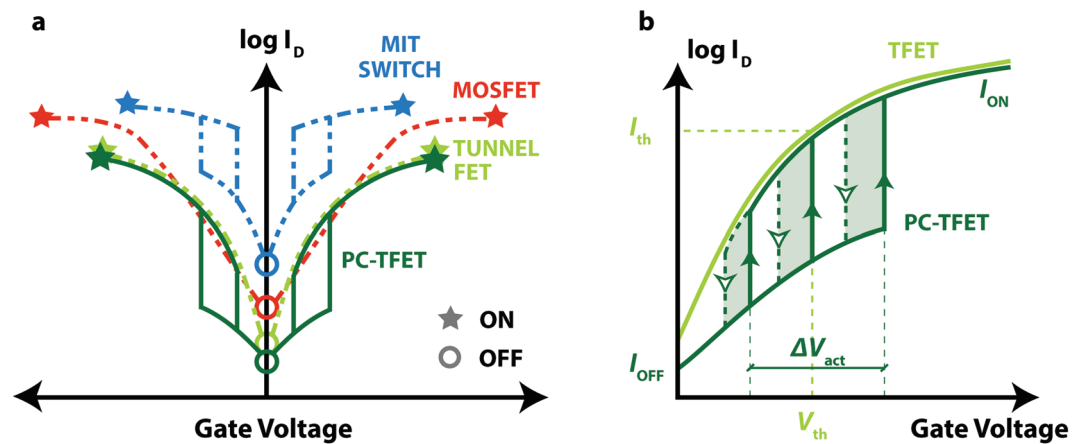
**Figure 1.** Comparison of three steep-slope switches: TFET, MIT and proposed PC-TFET. (**a**) Transfer characteristics for the PC-TFET and other steep-slope switches (TFET, MIT switch) achieving lower subthreshold swing than the MOSFET. (**b**) PC-TFET characteristics for different values of the MIT switch threshold voltage $V_{act}$, compared to the transfer characteristics of the TFET component with threshold voltage $V_{th}$. The hysteresis areas for three different values of $V_{act}$ are highlighted by the shaded regions.

Recently, phase change materials such as correlated functional oxides have been proposed as a promising solution for beyond CMOS electronics. External excitations applied to phase change materials can induce a phase transition accompanied by a drastic change in their conduction properties[11–19]. One of the most studied phase change materials is vanadium dioxide ($VO_2$), which exhibits a metal-insulator transition (MIT) corresponding to a structural phase transition at a critical temperature $T_{MIT}$ (340 K in bulk $VO_2$[20–22]). When $VO_2$ temperature is increased above $T_{MIT}$, the material transitions from a monoclinic phase to a tetragonal rutile structure, concomitant with the closing of an energy gap $E_g \approx 0.6$ eV in the 3d conduction band and a steep decrease in resistivity, up to 5 orders of magnitude in bulk $VO_2$. When the $VO_2$ temperature is decreased, the transition back to the monoclinic phase is observed for values below $T_{MIT}$, giving rise to a hysteresis with width depending on the quality of the material. $VO_2$ holds great potential for beyond CMOS electronics because the MIT can be induced by electrical excitations, enabling applications based on volatile resistive switching. The $VO_2$-based MIT switch in 2-terminal configuration shows interesting properties such as abrupt increase in current with applied voltage[23–31], fast switching time[32–34], high reliability[35, 36], negative differential resistance[37–40], memristive switching[41, 42] and low temperature dependence of transition dynamics[43, 44]. However, the main drawback of the 2-terminal MIT switch is the relatively high leakage current $I_{OFF}$ due to the small bandgap of $VO_2$ in the insulating state. While this problem can be mitigated by $VO_2$ doping[45], the most effective solution would be the development of 3-terminal switches in which a $VO_2$ channel undertakes a gate-driven phase change. The development of such a device was attempted first with standard MOSFET structures using $VO_2$ as the semiconducting material[46], but the observed conductance modulation by gate voltage was limited to a small percentage[47–50]. This encouraged the investigation of the use of electrolyte gating to obtain very high electric fields at the interface between $VO_2$ and an ionic liquid[51, 52], inducing a higher channel conductance modulation due to the creation of oxygen vacancies[53–55] or protonation[56] but with a much slower switching time[57, 58].

In order to overcome these issues, the phase-change tunnel FET (PC-TFET) has been proposed[59] as a hybrid design integration of a tunnel FET and a 2-terminal MIT switch, combining the strengths of the two devices and resulting in the first solid-state $VO_2$-based 3-terminal switch with simultaneous very low $I_{OFF}$ current, high $I_{ON}/I_{OFF}$ ratio and ultra-steep subthreshold swing (Fig. 1a), performance that cannot be individually achieved by a TFET or a MIT switch. The transfer characteristics of the PC-TFET are qualitatively compared to the ones of the TFET used as a component part in Fig. 1b. The main working principle of the PC-TFET is to feedback (by an appropriate gate or source connection) the ultra-abrupt switching in the MIT material into a TFET characteristic, used to block the current in the OFF state. The phase change in the MIT switch corresponds to the actuation voltage $V_{act}$ (tunable by the design of the MIT component) allowing to switch from a high resistance state to a low resistance state, in which the current follows the transfer characteristics of the TFET. For ideal performance, the $V_{act}$ of a 2-terminal MIT switch should be aligned with the TFET threshold voltage $V_{th}$ (defined by the constant current method). Figure 1a and b also depict the resulting hysteretic behaviour of the PC-TFET, inherited from its MIT component. In this work, we discuss in detail the PC-TFET principle, its integration and the method of extraction of the body factor. Moreover, we further characterize the PC-TFET to discuss its temperature dependence and possible applications for analog circuits and neuromorphic computing.

## Results

**Hybrid PC-TFET: principle.** The principle of the PC-TFET steep slope hybrid device is to simultaneously use two physical mechanisms to lower the subthreshold swing factors *m* and *n*, respectively the body factor
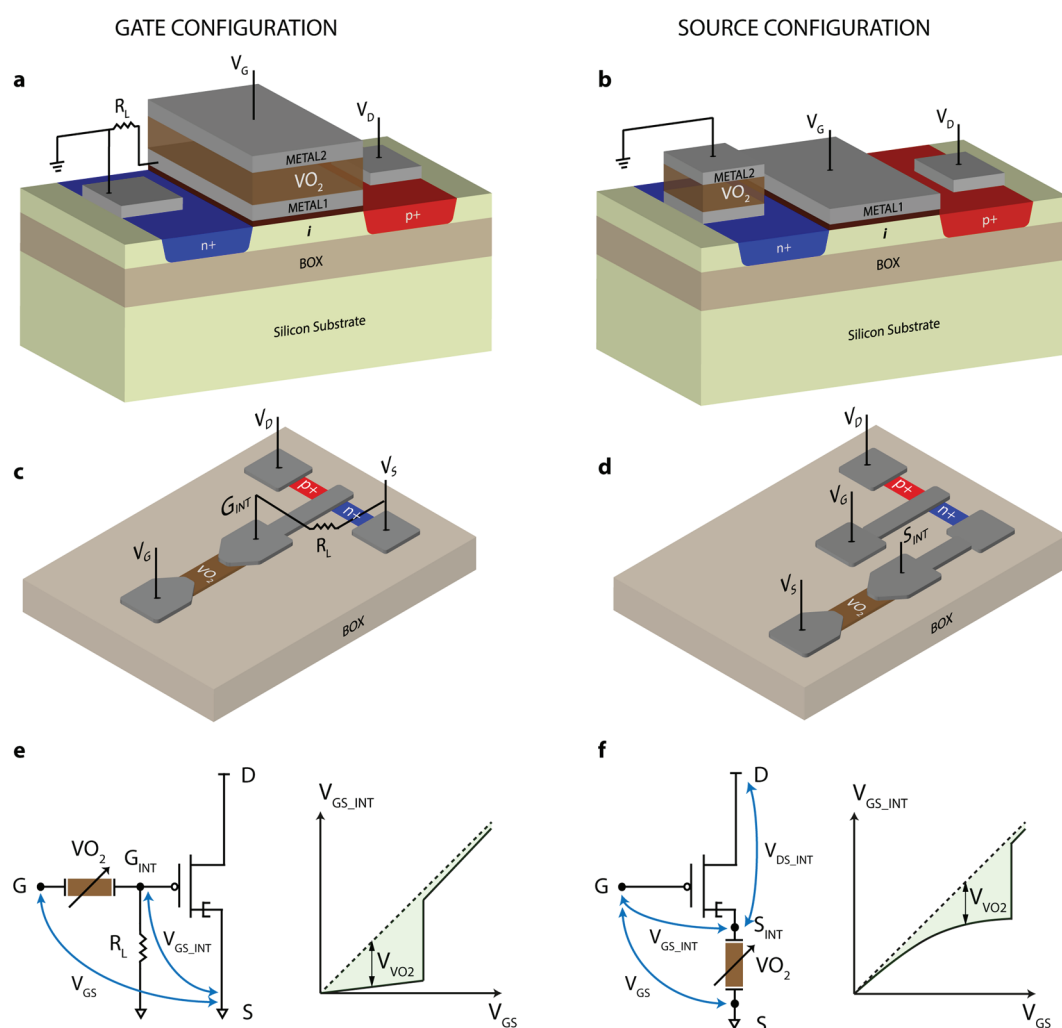
**Figure 2.** Phase change TFET integration in gate and source configuration. (**a,b**) 3D schematic diagrams of the PC-TFET integrating vertical VO$_2$ switches. (**c,d**) 3D schematic diagrams of the PC-TFET integrating planar VO$_2$ switches. (**e,f**) Equivalent circuits showing the internal TFET gate voltage $V_{GS\_INT}$ amplified by the MIT switch phase change, induced by the external gate voltage $V_{GS}$.

(mirroring the differential amplification of surface potential) and the carrier injection mechanism in the conduction channel (by band-to-band-tunnelling in a gated p-i-n junction):

$$SS = \frac{dV_{GS}}{d(\log_{10}I_{DS})} = \overbrace{\frac{dV_{GS}}{dV_{GS\_INT}}\frac{dV_{GS\_INT}}{d\Psi_S}}^{m}\overbrace{\frac{d\Psi_S}{d(\log_{10}I_{DS})}}^{n}$$

(1)

while the use of band-to-band tunnelling is intrinsically offering a straightforward solution to a potentially lower than 60 mV/decade $n$-factor, for lowering $m$, in contrast with any other previous reports, we do not use any negative capacitance principle but a simple circuit technique exploiting the abrupt switching in a 2-terminal MIT device connected in a voltage divider placed in the gate or in the source of a TFET. It is worth noting that reducing the body factor, $m$, of a TFET below 1, corresponds to a less explored approach (previously proposed by Ionescu[60]) to boost the abruptness of subthreshold characteristics of a TFET.

In the following, we study two PC-TFET designs, in which the MIT switch is connected to the gate (Fig. 2a,c,e, "gate configuration") or to the source (Fig. 2b,d,f, "source configuration") terminal of the TFET. In both cases the state of the MIT switch is controlled by the gate voltage $V_{GS}$ and the phase change induces an internal differential amplification of the voltage drop $V_{GS\_INT}$ between the gate and source terminals of the TFET ($dV_{GS\_INT}/V_{GS} \gg 1$) resulting in a steep increase in current $I_{DS}$.

Figure 2a shows the hybrid design integration of a 3-terminal TFET and a 2-terminal VO$_2$ switch to obtain the PC-TFET gate configuration. A VO$_2$ thin film is deposited and patterned on top of the gate terminal of the TFET, and a second metal layer is used to contact it and define the gate electrode of the PC-TFET. The same design can be adapted to the source configuration, shown in Fig. 2b, where the VO$_2$ switch is built on top of the source terminal of the TFET. An alternative design exploiting planar VO$_2$ switches is reported in Fig. 2c for the gate configuration and Fig. 2d for the source configuration.

Figure 2e presents the equivalent circuit and voltage distribution for the PC-TFET in gate configuration. A load resistance $R_L$ is used to allow a current flow high enough to reach the power threshold of the $VO_2$ switch[43]. The value of $R_L$ is selected in order to have $R_{VO2\_OFF} >> R_L >> R_{VO2\_ON}$, where $R_{VO2\_OFF}$ is the resistance of the MIT switch in the insulating state and $R_{VO2\_ON}$ is the resistance in the metallic state. As $V_{GS}$ is ramped up in this configuration, the $VO_2$ material is initially in the highly resistive state, hence most of the voltage drops on the MIT switch ($V_{VO2} \approx V_{GS}$) and $V_{GS\_INT}$ stays low. Once the voltage is high enough to induce the metallic state in $VO_2$, $V_{VO2}$ drops to a very low value and $V_{GS\_INT}$ experiences a steep transition to a value approaching $V_{GS}$.

Figure 2f presents the equivalent circuit and voltage distribution for the PC-TFET in source configuration. In this case the MIT switch is connected to the internal source terminal of the TFET and both the internal voltage drops $V_{GS\_INT}$ and $V_{DS\_INT}$ are changing while sweeping $V_{GS}$ depending on $V_{VO2}$, such that $V_{GS} - V_{GS\_INT} = V_{DS} - V_{DS\_INT} = V_{VO2}$. For low values of $V_{GS}$, the $VO_2$ material is in its insulating state but the TFET channel resistance is much higher, effectively blocking the leakage through the MIT switch and keeping a low $I_{OFF}$ current. Hence $V_{GS\_INT}$ follows $V_{GS}$. Increasing $V_{GS}$, the tunnelling current increases steadily until the TFET resistance becomes comparable with $R_{VO2\_OFF}$. At this point the rise in $V_{GS\_INT}$ decreases and the MIT switch approaches its power threshold. Once $VO_2$ switches to its metallic state, $V_{GS\_INT}$ jumps abruptly to values near $V_{GS}$. It is clear that the source configuration is very suitable for the lowest power consumption and aggressive scaling as it does not require any additional load resistor (which is the TFET itself) and there is no power dissipation in such a load. However, as it will be shown later, the gate configuration is particularly interesting for its steeper characteristics.

The source configuration is similar to a previously reported solution based on III–V FinFET transistors and $VO_2$ switches[61]. However, that work exploited classical FinFETs with thermionic subthreshold swing and with very high leakage current to induce the phase change in $VO_2$, and as a consequence the $I_{ON}/I_{OFF}$ ratio was limited to $4 \times 10^2$ and the region of abrupt switching was observed over less than a decade of current, whereas the PC-TFET achieves simultaneously low $I_{OFF}$ and high $I_{ON}/I_{OFF}$ ratio.

## PC-TFET in gate configuration.

The experimental demonstration of the PC-TFET has been achieved by fabricating and characterizing TFETs and $VO_2$ switches connected as explained in the previous section (Fig. 2e,f). During the experimental tests, the gate voltage is doubly swept and the voltage of the internal node is recorded with a high impedance voltmeter in the whole range of device operation. This allows us to carefully derive the internal amplification and the effect of the MIT transition point on the TFET characteristics by extracting its intrinsic gate and drain voltages.

The TFETs used in this work are based on a strained silicon gate-all-around (GAA) nanowire (NW) technology[62, 63] with a NW cross section of $40 \times 5\,nm^2$ and a gate length of 350 nm. In order to enable a low power design of the PC-TFET, it is necessary to minimize the power threshold of the MIT switch. Based on an electrothermal model considering Joule heating as the triggering mechanism for the abrupt MIT transition[26, 64], a convenient device geometry is achieved by reducing the $VO_2$ volume between the two electrodes of the MIT switch[65]. In this work such a low power actuation of a MIT switch is achieved by fabricating nanogap planar switches on a $Si/SiO_2$ substrate, limiting the $VO_2$ volume between the electrodes to values as low as $200 \times 100 \times 100\,nm^3$ (see Supplementary Fig. 1 for details on the process flow and Supplementary Fig. 2 for images of a final device).

Figure 3a shows the $I_{DS}$-$V_{GS}$ characteristics of a TFET for different values of $V_{DS}$, ranging from $-0.25$ V to $-1$ V. The TFET biased at $V_{DS} = -0.75$ V exhibits very low $I_{OFF} = 69.1$ pA, very good $I_{ON}/I_{OFF} = 1.0 \times 10^7$ ratio, low gate leakage $I_G < 8$ nA up to $V_{GS} = -2$ V (see Supplementary Fig. 3), and a good average subthreshold slope over 4 decades of current: $SS_{TFET} = \partial V_{GS}/\partial \log_{10}(I_{DS}) = 112$ mV/decade. Figure 3b shows the I–V characteristics of a $VO_2$ switch at different temperatures, ranging from 25 °C to 55 °C. A 1 kΩ resistor is connected in series to the MIT switch in order to limit the current in the metallic state and prevent excessive overheating of the device. The switch design has been optimized for its use in the PC-TFET, presenting a low actuation voltage $V_{act} = -0.93$ V at room temperature, steep slope of the transition ($SS_{VO2} = 18.7$ mV/decade) and capability to drive high $I_{ON}$ current. The transition presents limited hysteresis width ($<0.2$ V at room temperature) when the voltage is removed and the switch reverts to the OFF state. Increasing temperature, the actuation voltage decreases while the $I_{ON}$ and the slope remain stable ($SS_{VO2} = 17.7$ mV/decade at 35 °C, 23 mV/decade at 45 °C) until reaching values near $T_{MIT}$, where the sharp transition is lost. This behaviour can be explained by an electrothermal actuation model based on Joule heating[66].

Figure 3c shows the $I_{DS}$-$V_{GS}$ characteristics of the PC-TFET in gate configuration at different temperatures, biased at $V_{DS} = -0.75$ V and using a load resistance $R_L = 1$ kΩ. Different values of $R_L$ allow to shift the $V_{GS\_act}$ level necessary to induce the phase transition (as described by additional measurements reported in Supplementary Fig. 4). Once $VO_2$ undergoes the phase transition to the low resistivity state, we observe a sharp rise in $I_{DS}$ current up to values approaching the ones of the TFET at the same biasing conditions. The PC-TFET at room temperature has lower $I_{OFF} = 29.5$ pA (12.3 pA/μm normalized by the TFET width) than the TFET, comparable $I_{ON}/I_{OFF}$ ratio ($5.5 \times 10^6$) and a subthreshold slope vastly superior to the ones of state-of-the-art TFET devices reported to date: $SS_{PC\_TFET} = 4.0$ mV/decade at 25 °C, 7.8 mV/decade at 45 °C. This is due to the internal amplification of $V_{GS\_INT}$, reported in Fig. 3d, in which we observe a very steep transition from low voltage levels to values near the TFET threshold voltage (e.g. from $-0.14$ V to $-0.49$ V at room temperature within a $V_{GS} = 10$ mV step). The output characteristics of a PC-TFET in gate configuration are reported in Supplementary Fig. 5. Due to the relatively significant power consumption in the resistive divider at the gate terminal, practically dictated by the $VO_2$ actuation (see Fig. 3b), the PC-TFET in gate configuration is not providing substantial advantages for low power electronics. However, the very abrupt transition in the PC-TFET in gate configuration can be exploited for analog circuit applications such as a voltage-controlled buffered oscillator (see Supplementary Fig. 6).

## PC-TFET in source configuration.

Figure 4a shows the $I_{DS}$-$V_{GS}$ characteristics of the TFET component used to implement the PC-TFET in source configuration for different values of $V_{DS}$, ranging from $-0.25$ V to
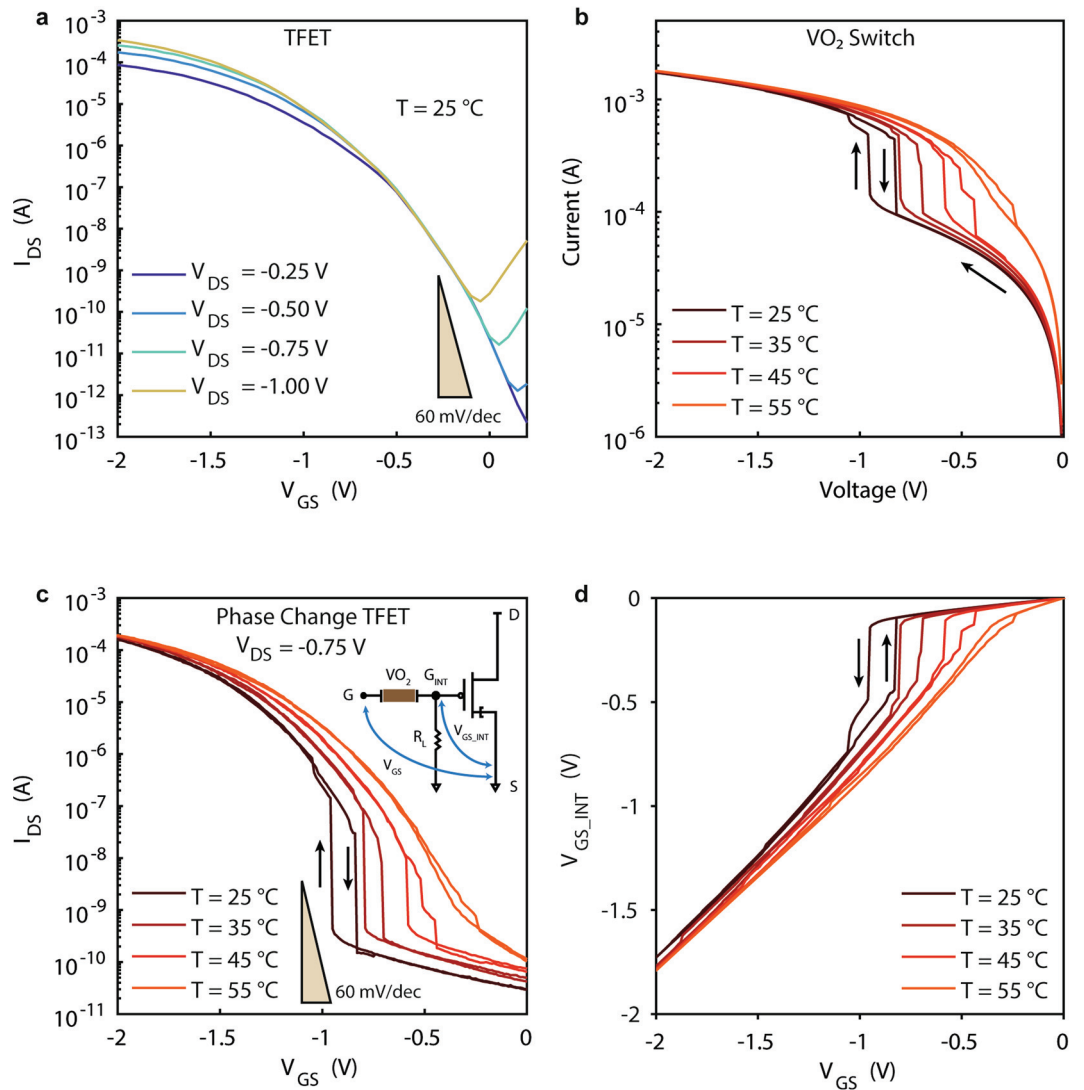
**Figure 3.** Experimental demonstration of Phase Change TFET in gate configuration. (**a**) $I_{DS}$-$V_{GS}$ transfer characteristic of the TFET for different applied $V_{DS}$. (**b**) I-V characteristic of the VO$_2$ switch measured at different temperatures with a series resistance of 1 kΩ. (**c**) $I_{DS}$-$V_{GS}$ obtained combining (a) and (b) in gate configuration with a load resistance of $R_L = 1$ kΩ between the gate terminal and ground and an applied $V_{DS} = -0.75$ V. (**d**) Internal gate voltage $V_{GS\_INT}$ biasing the TFET in function of the external applied $V_{GS}$.

−1.5 V. The TFET measured at $T = 55$ °C and biased at $V_{DS} = -0.75$ V presents an average subthreshold swing $SS_{TFET} \approx 180$ mV/dec and a current ratio of $6.3 \times 10^5$ in a 2 V gate voltage window. Figure 4b shows the I-V characteristics of the VO$_2$ switch used in this case, with a series resistance of 3 kΩ. The actuation voltage decreases with temperature from −2.61 V at 25 °C to −1.19 V at 55 °C, while the steep slope is preserved up to values approaching $T_{MIT}$ ($SS_{VO2} = 11.9$ mV/decade at $T = 25$ °C, 22.3 mV/decade at $T = 55$ °C).

Figure 4c depicts the $I_{DS}$-$V_{GS}$ characteristics of the PC-TFET in source configuration. The $V_{DS}$ has been increased to −2 V and the measurement is reported at 55 °C in order to reach the current levels necessary to induce the transition at $V_{GS} < 4$ V. The PC-TFET in source configuration combines the strengths of the two component devices, presenting a high $I_{ON}/I_{OFF}$ ratio, a low $I_{OFF}$ current and a low $I_G$ gate leakage comparable to the TFET, while the subthreshold slope is similar to the one of the VO$_2$ switch ($SS_{PC\_TFET} = 20.6$ mV/dec). The sub-thermionic (<60 mV/dec) value for the slope at the phase change transition is due to a similar internal gate voltage amplification mechanism exploited for the gate configuration, with the difference that both the intrinsic gate and drain voltages are simultaneously switching abruptly: $V_{GS\_INT} = V_{GS} - R_{VO2} \cdot I_D$ and $V_{DS\_INT} = V_{DS} - R_{VO2} \cdot I_D$ (see Fig. 4d). However, as shown in Fig. 4d, in this case the amplification occurs for values of $V_{GS\_INT}$ above the TFET threshold (from −2.54 V to −3.31 V within a $V_{GS} = 10$ mV step), resulting in a less abrupt increase in $I_{DS}$. Moreover, our experiments show that the $V_{DS\_INT}$ change while sweeping $V_{GS}$ is quantitatively less important than the effect of $dV_{GS\_INT}/dV_G$ amplification (see Supplementary Fig. 7).

The output characteristics of a hybrid PC-TFET in source configuration are reported in Fig. 5a, pointing out a very particular behaviour that could be further exploited in energy efficient logic or neuromorphic circuits.
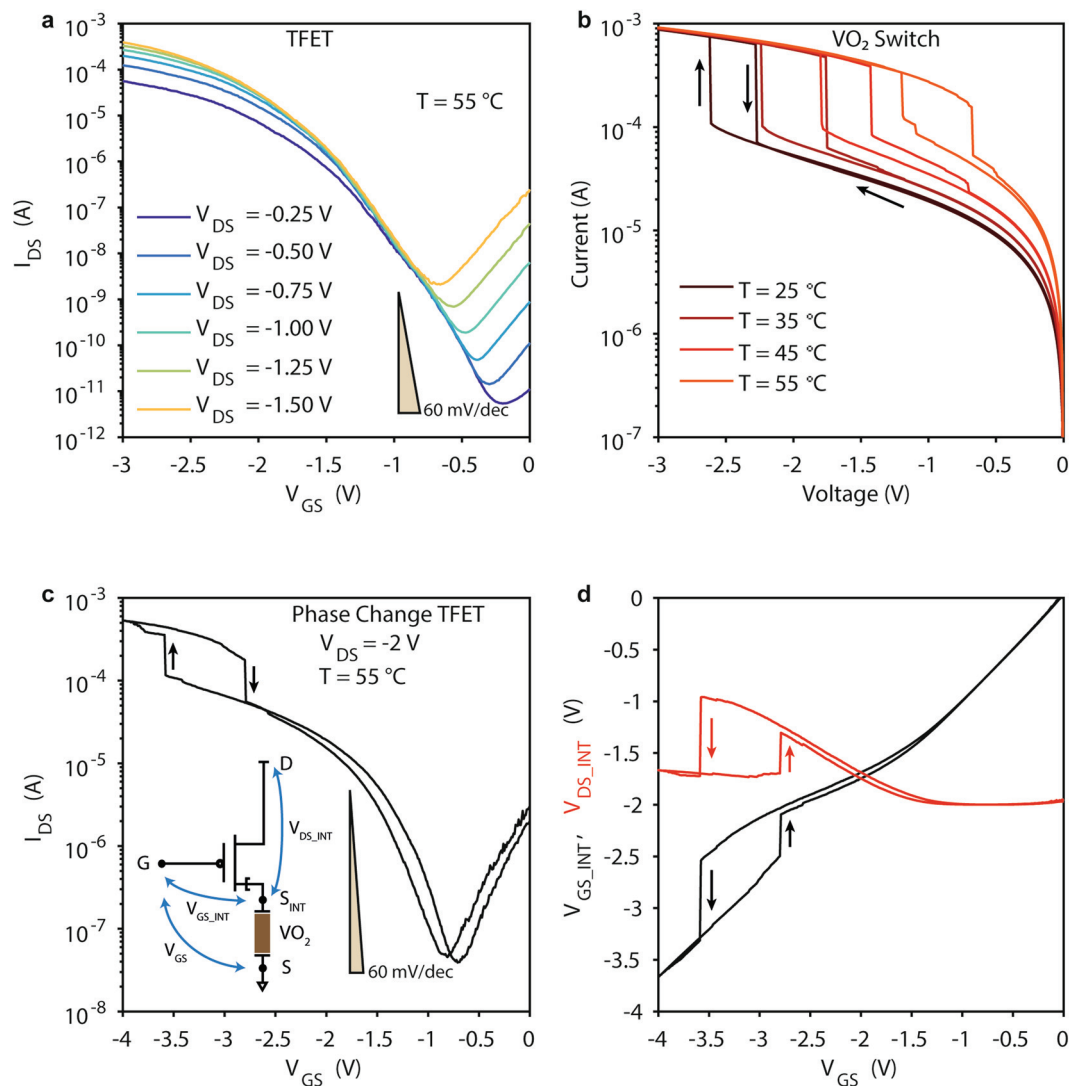
**Figure 4.** Experimental demonstration of Phase Change TFET in source configuration. (**a**) $I_{DS}$-$V_{GS}$ transfer characteristic of the TFET component for different applied $V_{DS}$ measured at $T = 55$ °C. (**b**) I-V characteristic of the VO$_2$ switch measured at different temperatures with a series resistance of $3 \, \text{k}\Omega$. (**c**) $I_{DS}$-$V_{GS}$ of PC-TFET obtained introducing the VO$_2$ switch in the TFET source terminal; measurements performed at $T = 55$ °C with an applied external $V_{DS} = -2$ V. (**d**) Intrinsic TFET gate voltage $V_{GS\_INT}$ and drain voltage $V_{DS\_INT}$ versus applied $V_{GS}$.

The VO$_2$ phase change induces a very abrupt switching in the PC-TFET output characteristics, corresponding, in absolute values, to a *higher* $V_{GS\_INT}$ and a *higher* $V_{DS\_INT}$, as pointed out by Fig. 5b. The output characteristics of PC-TFET inherit from the MIT transition points a hysteretic behaviour, which has a direct consequence on the effective drive current (because of the different trajectory on the output characteristics in logical switching) if such device is used for building CMOS inverters. Moreover, the low leakage current in the PC-TFET, negligible with respect to the drain current over the whole domain of operation (see Supplementary Fig. 8), makes it promising for energy efficient implementations of neuromorphic circuits based on relaxation oscillators[67, 68].

**Body factor reduction in PC-TFET.** The deep subthermionic switching in the PC-TFET can be explained by its sub-unity body factor due to the internal gate voltage amplification. The relation between the subthreshold slope and the body factor has been captured in equation (1), with the transistor body factor $m = \mathrm{d}V_{GS}/\mathrm{d}\Psi_S$ expressed as the inverse of the differential amplification of the surface potential with respect to the extrinsic gate voltage. In a conventional MOSFETs the body factor is dependent on a capacitance ratio between the gate oxide capacitance, $C_{ox}$, and the depletion capacitance, $C_d$, $m = 1 + C_d/C_{ox}$, resulting in a lower bound, $m \geq 1$. Here, we show that this limit is overcome in the PC-TFET because the body factor $m$ can be expressed in function of $V_{GS\_INT}$ and becomes:
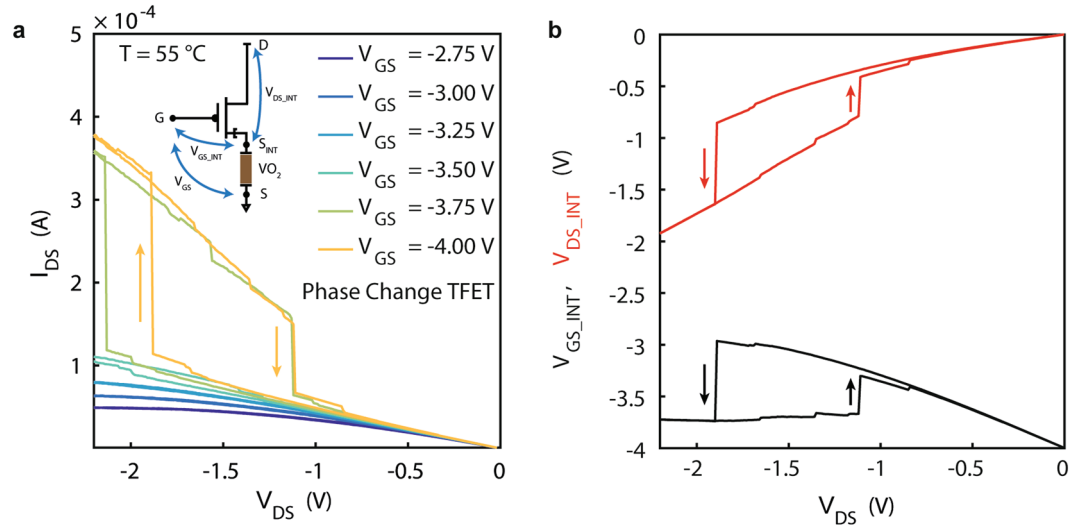
**Figure 5.** Output characteristics and drain voltage switching of Phase Change TFET in source configuration. (**a**) Output characteristics of PC-TFET in source configuration for different applied $V_{GS}$ (ranging from $-2.75\,V$ to $-4\,V$) measured at $T = 55\,°C$. (**b**) Intrinsic TFET gate voltage $V_{GS\_INT}$ and drain voltage $V_{DS\_INT}$ versus applied $V_{DS}$.

$$m = \left[\frac{d\varPsi_S}{dV_{GS\_INT}}\frac{dV_{GS\_INT}}{dV_{GS}}\right]^{-1} = \left(1 + \frac{C_d}{C_{ox}}\right)\frac{dV_{GS}}{dV_{GS\_INT}} \tag{2}$$

hence, when maximizing the internal gain of the PC-TFET, $G = dV_{GS\_INT}/dV_{GS} >> 1$, and given that in fully depleted body devices $(1 + C_d/C_{ox})\sim 1$, it follows that $m << 1$, showing that the body factor is a booster of the TFET subthreshold swing. We extract the body factor from our experimental results, starting from calculating the surface potential as a function of $V_{GS}$ as shown in Fig. 6a, for the gate configuration, and Fig. 6b, for the source configuration. On the same figures we include the measured internal gain, $G$, whose experimental values are used to extract $m$, using equation (2). The values of $\varPsi_S(V_{GS})$ are obtained by means of technology computer-aided design (TCAD) simulations of NW-TFETs identical to the fabricated structures, biased with the experimental values of $V_{GS\_INT}$ and $V_{DS}$ for the gate configuration (Fig. 3d), $V_{GS\_INT}$ and $V_{DS\_INT}$ for the source configuration (Fig. 4d). We observe a steep change in $\varPsi_S$ (resulting in a very low $m$) in correspondence of the $V_{GS}$ values for which a high internal gain amplification is recorded, highlighting the key role of the internal gain in the steep switching characteristics of the PC-TFET.

Figure 6c,d show $m$ in function of the measured $I_{DS}$, respectively for the gate and source configurations. In both cases the experimentally extracted body factor shows a less than 0.1 value in the transition region. The PC-TFET in gate configuration presents a value of $m$ of $\sim 0.05$ $(<<1)$ for more than two decades of current, from 0.43 nA to 142.3 nA in the OFF to ON transition and from 27.5 nA to 0.15 nA in the OFF to ON transition. The PC-TFET in source configuration shows similar values of $m$ (0.025 in the OFF to ON transition, 0.5 in the ON to OFF). It is worth noting that the low-$m$ region is extended for more decades of current in the gate configuration due to the better alignment of the internal gain peaks and the TFET threshold region.

## Discussion

We reported the PC-TFET as a novel hybrid steep-slope electronic switch, combining two steep switching mechanisms in a single device, and its detailed characterization in a broad range of temperatures up to values approaching the transition temperature of $VO_2$. The unique combination of BTBT in TFET and MIT in $VO_2$ leads to excellent figures of merit for digital electronics such as an $I_{on}/I_{off}$ ratio better than $5.5 \times 10^6$ and a subthreshold swing lower than 10 mV/dec over 3 decades of currents. We observe low dependence on temperature of the swing of the PC-TFET in gate configuration, ranging from 4.0 mV/dec at room temperature to 7.8 mV/dec at 45 °C. Moreover, we have demonstrated that the underlying mechanism for the abrupt switching behaviour is the internal gate voltage amplification, leading to a sub-unity equivalent body factor. Such lower-than-1 body factor to achieve subthermionic switching is a much more general design criterion than the previous principle of negative capacitance, serving as a performance booster for both TFETs and MOSFETs. The PC-TFET represents an important step forward for beyond CMOS electronics, exploiting for the first time the full potential of the $VO_2$ MIT in in an electrically gated 3-terminal architecture and opening new perspectives for low power electronics and neuromorphic computing.

## Methods

**Fabrication of experimental devices.** $VO_2$ nanogap switches were fabricated on a silicon substrate with a 200 nm thick $SiO_2$ layer on top. The $VO_2$ layer was deposited by reactive magnetron sputtering at 600 °C of a pure
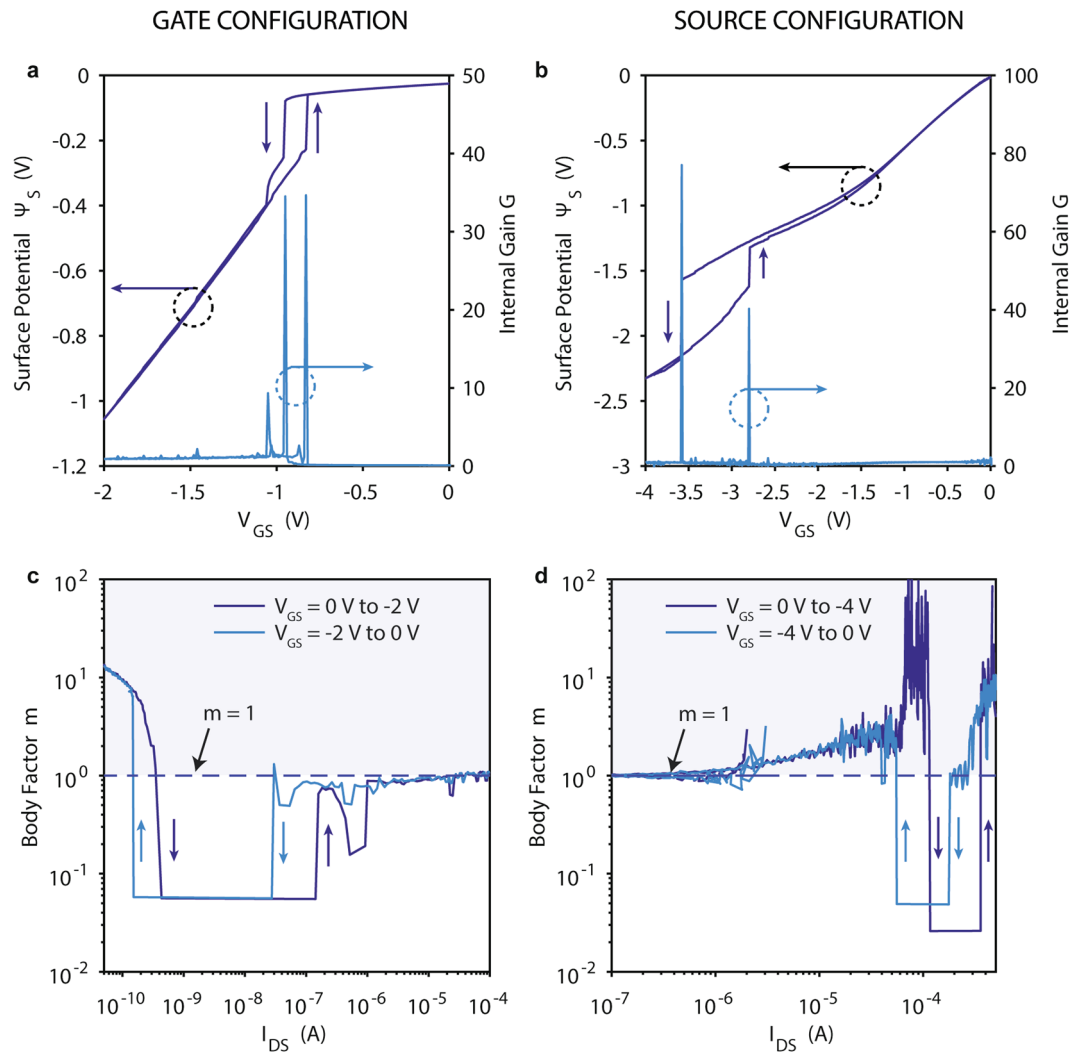
GATE CONFIGURATION

SOURCE CONFIGURATION



**Figure 6.** Surface potential and body factor in Phase Change TFET. (**a,b**) Dependence on $V_{GS}$ of the surface potential, $\Psi_S$, and internal gain, $G = dV_{GS\_INT}/dV_{GS}$, for gate and source configurations. The reference level for the surface potential is taken at the source terminal. (**c,d**) Body factor as a function of $I_{DS}$ for gate and source configurations; the dashed lines represent the $m \geq 1$ limit overcome thanks to the internal $V_{GS\_INT}$ amplification.

vanadium target, with detailed experimental conditions reported elsewhere[69]. Electrical contacts were defined by electron beam lithography on PMMA/MMA and lift-off of a 100 nm thick platinum film deposited by sputtering. The $VO_2$ areas around the switch are then removed by electron beam lithography on ZEP and ion beam etching. Strained silicon GAA TFETs have been fabricated on a silicon on insulator substrate using a process based on doping segregation from $NiSi_2$[70].

**TCAD simulations for surface potential extraction.** TCAD simulations were performed using Sentaurus TCAD Suite 2014.09. We simulated a strained silicon double gate TFET with channel thickness $T_{CH} = 5$ nm, oxide thickness $T_{OX} = 3$ nm with $HfO_2$ ($\varepsilon_r = 22$) gate metal workfunction of $\phi_m = 4.1$ eV corresponding to TiN. The source doping is $N_S = 1 \times 10^{20}$ cm$^{-3}$ and the drain doping is $N_D = 1 \times 10^{19}$ cm$^{-3}$ with abrupt junctions. Since the semiconductor layer is extremely thin, we have enlarged the bandgap by 70 meV, corresponding to the quantized state of the [100] ellipsoids. However, this increase is cancelled out by the strain on the nanowires, which results in an overall bandgap reduction of $\Delta E_g = -25$ meV. All the simulated surface potential values reported in this work are taken from 0.1 Å below the semiconductor-oxide interface. The surface potential plots in function of $V_{GS}$ (Fig. 5a,b) are taken at the tunneling junction, while the full potential profile across the channel is reported in Supplementary Fig. 9.

## References

1. Iwai, H. Technology roadmap for 22nm and beyond. In *2009 2nd Int. Work. Electron Devices Semicond. Technol.* 1–4, doi:10.1109/EDST.2009.5166100 (IEEE, 2009).
2. Bernstein, K., Cavin, R. K., Porod, W., Seabaugh, A. & Welser, J. Device and Architecture Outlook for Beyond CMOS Switches. *Proc. IEEE* **98**, 2169–2184 (2010).
3. Seabaugh, A. C. & Zhang, Q. Low-voltage tunnel transistors for beyond CMOS logic. *Proc. IEEE* **98**, 2095–2110 (2010).

4. Lundstrom, M. S. The MOSFET Revisited: Device Physics and Modeling at the Nanoscale. In *2006 IEEE international SOI Conferencee Proceedings* 1–3, doi:10.1109/SOI.2006.284404 (IEEE, 2006).
5. Ionescu, A. M. & Riel, H. Tunnel field-effect transistors as energy-efficient electronic switches. *Nature* **479**, 329–337 (2011).
6. Salahuddin, S. & Datta, S. Use of negative capacitance to provide voltage amplification for low power nanoscale devices. *Nano Lett.* **8**, 405–410 (2008).
7. Abele, N. *et al.* Suspended-gate MOSFET: bringing new MEMS functionality into solid-state MOS transistor. In *IEEE Int. Electron Devices Meet. 2005. IEDM Tech. Dig.* 479–481, doi:10.1109/IEDM.2005.1609384 (IEEE, 2005).
8. Gopalakrishnan, K., Griffin, P. B. & Plummer, J. D. I-MOS: a novel semiconductor device with a subthreshold slope lower than kT/q. In *Dig. Int. Electron Devices Meet*. 289–292, doi:10.1109/IEDM.2002.1175835 (IEEE, 2002).
9. Boucart, K. & Ionescu, A. M. Double-gate tunnel FET with high-k gate dielectric. *IEEE Trans. Electron Devices* **54**, 1725–1733 (2007).
10. Sarkar, D. *et al.* A subthermionic tunnel field-effect transistor with an atomically thin channel. *Nature* **526**, 91–95 (2015).
11. Newns, D. M. *et al.* Mott transition field effect transistor. *Appl. Phys. Lett.* **73**, 780 (1998).
12. Inoue, I. H. Electrostatic carrier doping to perovskite transition-metal oxides. *Semicond. Sci. Technol.* **20**, S112–S120 (2005).
13. Inoue, I. H. & Rozenberg, M. J. Taming the mott transition for a novel mott transistor. *Adv. Funct. Mater.* **18**, 2289–2292 (2008).
14. Ha, S. D. & Ramanathan, S. Adaptive oxide electronics: A review. *J. Appl. Phys.* **110**, 071101 (2011).
15. Yang, Z., Ko, C. & Ramanathan, S. Oxide Electronics Utilizing Ultrafast Metal-Insulator Transitions. *Annu. Rev. Mater. Res.* **41**, 337–367 (2011).
16. Basov, D. N., Averitt, R. D., Van Der Marel, D., Dressel, M. & Haule, K. Electrodynamics of correlated electron materials. *Rev. Mod. Phys.* **83**, 471–541 (2011).
17. Zhou, Y. & Ramanathan, S. Correlated Electron Materials and Field Effect Transistors for Logic: A Review. *Crit. Rev. Solid State Mater. Sci* **38**, 286–317 (2013).
18. Mannhart, J. & Haensch, W. Device physics: Put the pedal to the metal. *Nature* **487**, 436–437 (2012).
19. Shi, J., Zhou, Y. & Ramanathan, S. Colossal resistance switching and band gap modulation in a perovskite nickelate by electron doping. *Nat. Commun.* **5**, 4860 (2014).
20. Morin, F. J. Oxides which show a metal-to-insulator transition at the neel temperature. *Phys. Rev. Lett.* **3**, 34–36 (1959).
21. Mott, N. F. Metal-insulator transition. *Rev. Mod. Phys.* **40**, 677–683 (1968).
22. Goodenough, J. B. The two components of the crystallographic transition in $VO_2$. *J. Solid State Chem.* **3**, 490–500 (1971).
23. Lee, S. B., Kim, K., Oh, J. S., Kahng, B. & Lee, J. S. Origin of variation in switching voltages in threshold-switching phenomena of $VO_2$ thin films. *Appl. Phys. Lett.* **102**, 63501 (2013).
24. Simon Mun, B. *et al.* Role of joule heating effect and bulk-surface phases in voltage-driven metal-insulator transition in $VO_2$ crystal. *Appl. Phys. Lett.* **103** (2013).
25. Yoon, J., Lee, G., Park, C., Mun, B. S. & Ju, H. Investigation of length-dependent characteristics of the voltage-induced metal insulator transition in $VO_2$ film devices. *Appl. Phys. Lett.* **105**, 83503 (2014).
26. Jordan, T. S. *et al.* Model and Characterization of $VO_2$ Thin-Film Switching Devices. *IEEE Trans. Electron Devices* **61**, 813–819 (2014).
27. Rathi, S. *et al.* Postfabrication annealing effects on insulator-metal transitions in $VO_2$ thin-film devices. *ACS Appl. Mater. Interfaces* **6**, 19718–19725 (2014).
28. Rathi, S. *et al.* Unravelling the switching mechanisms in electric field induced insulator–metal transitions in $VO_2$ nanobeams. *J. Phys. D. Appl. Phys.* **47**, 295101 (2014).
29. Joushaghani, A. *et al.* Voltage-controlled switching and thermal effects in $VO_2$ nano-gap junctions. *Appl. Phys. Lett.* **104**, 221904 (2014).
30. Singh, S. *et al.* Proliferation of metallic domains caused by inhomogeneous heating near the electrically driven transition in $VO_2$ nanobeams. *Phys. Rev. B* **92**, 155121 (2015).
31. Li, D. *et al.* Joule Heating-Induced Metal–Insulator Transition in Epitaxial $VO_2/TiO_2$ Devices. *ACS Appl. Mater. Interfaces* acsami.6b03501, doi:10.1021/acsami.6b03501 (2016).
32. Chae, B. G., Kim, H. T., Youn, D. H. & Kang, K. Y. Abrupt metal-insulator transition observed in $VO_2$ thin films induced by a switching voltage pulse. *Phys. B Condens. Matter* **369**, 76–80 (2005).
33. Leroy, J. *et al.* High-speed metal-insulator transition in vanadium dioxide films induced by an electrical pulsed voltage over nano-gap electrodes. *Appl. Phys. Lett.* **100**, 213507 (2012).
34. Zhou, Y. *et al.* Voltage-Triggered Ultrafast Phase Transition in Vanadium Dioxide Switches. *IEEE Electron Device Lett* **34**, 220–222 (2013).
35. Vitale, W. A. *et al.* Steep slope $VO_2$ switches for wide-band (DC-40 GHz) reconfigurable electronics. In *72nd Device Research Conference* 29–30, doi:10.1109/DRC.2014.6872284 (IEEE, 2014).
36. Radu, I. P. *et al.* Switching mechanism in two-terminal vanadium dioxide devices. *Nanotechnology* **26**, 165202 (2015).
37. Sakai, J. High-efficiency voltage oscillation in $VO_2$ planer-type junctions with infinite negative differential resistance. *J. Appl. Phys.* **103**, 103708 (2008).
38. Lee, Y. W. *et al.* Metal-insulator transition-induced electrical oscillation in vanadium dioxide thin film. *Appl. Phys. Lett.* **92** (2008).
39. Shukla, N. *et al.* Synchronized charge oscillations in correlated electron systems. *Sci. Rep* **4**, 4964 (2014).
40. Beaumont, A., Leroy, J., Orlianges, J.-C. & Crunteanu, A. Current-induced electrical self-oscillations across out-of-plane threshold switches based on $VO_2$ layers integrated in crossbars geometry. *J. Appl. Phys.* **115**, 154502 (2014).
41. Bae, S. H. *et al.* The memristive properties of a single $VO_2$ nanowire with switching controlled by self-heating. *Adv. Mater.* **25**, 5098–5103 (2013).
42. Seo, G., Kim, B. J., Kim, H. T. & Lee, Y. W. Thermally- or optically-biased memristive switching in two-terminal $VO_2$ devices. *Curr. Appl. Phys.* **14**, 1251–1256 (2014).
43. Vitale, W. A. *et al.* Steep-Slope Metal–Insulator-Transition $VO_2$ Switches With Temperature-Stable High $I_{ON}$. *IEEE Electron Device Lett* **36**, 972–974 (2015).
44. Vitale, W. A. *et al.* Field-enhanced design of steep-slope $VO_2$ switches for low actuation voltage. In *2016 46th European Solid-State Device Research Conference* (*ESSDERC*), 352–355, doi:10.1109/ESSDERC.2016.7599659 (IEEE, 2016).
45. Krammer, A., Gremaud, A., Bouvard, O., Sanjines, R. & Schüler, A. *In situ* photoelectron spectroscopic characterization of reactively sputtered, doped vanadium oxide thin films. *Surf. Interface Anal.* 1–5, doi:10.1002/sia.5989 (2016).
46. Kim, H.-T. *et al.* Mechanism and observation of Mott transition in $VO_2$-based two- and three-terminal devices. *New J. Phys.* **6**, 52–52 (2004).
47. Ruzmetov, D., Gopalakrishnan, G., Ko, C., Narayanamurti, V. & Ramanathan, S. Three-terminal field effect devices utilizing thin film vanadium oxide as the channel layer. *J. Appl. Phys.* **107**, 114516 (2010).
48. Sengupta, S. *et al.* Field-effect modulation of conductance in $VO_2$ nanobeam transistors with HfO2 as the gate dielectric. *Appl. Phys. Lett.* **99**, 62114 (2011).
49. Martens, K. *et al.* Field Effect and Strongly Localized Carriers in the Metal-Insulator Transition Material $VO_2$. *Phys. Rev. Lett.* **115**, 196401 (2015).
50. Wei, T., Kanki, T., Fujiwara, K., Chikanari, M. & Tanaka, H. Electric field-induced transport modulation in $VO_2$ FETs with high-k oxide/organic parylene-C hybrid gate dielectric. *Appl. Phys. Lett.* **108**, 53503 (2016).

51. Nakano, M. *et al.* Collective bulk carrier delocalization driven by electrostatic surface charge accumulation. *Nature* **487**, 459–62 (2012).
52. Liu, K. *et al.* Dense electron system from gate-controlled surface metal-insulator transition. *Nano Lett.* **12**, 6272–7 (2012).
53. Jeong, J. *et al.* Suppression of Metal-Insulator Transition in VO₂ by Electric Field-Induced Oxygen Vacancy Formation. *Science* **339**, 1402–1405 (2013).
54. Karel, J. *et al.* Distinct Electronic Structure of the Electrolyte Gate Induced Conducting Phase in Vanadium Dioxide Revealed by High Energy Photoelectron Spectroscopy. *ACS Nano* **8**, 5748–5789 (2014).
55. Jeong, J. *et al.* Giant reversible, facet-dependent, structural changes in a correlated-electron insulator induced by ionic liquid gating. *Proc. Natl. Acad. Sci* **112**, 1013–1018 (2015).
56. Shibuya, K. & Sawa, A. Modulation of Metal-Insulator Transition in VO₂ by Electrolyte Gating-Induced Protonation. *Adv. Electron. Mater* **2**, 1500131 (2016).
57. Zhou, Y. & Ramanathan, S. Relaxation dynamics of ionic liquid-VO₂ interfaces and influence in electric double-layer transistors. *J. Appl. Phys.* **111**, 84508 (2012).
58. Peng, X. *et al.* Efficient and Hysteresis-Free Field Effect Modulation of Ambipolarly Doped Vanadium Dioxide Nanowires. *Phys. Rev. Appl* **5**, 54008 (2016).
59. Casu, E. A. *et al.* Hybrid Phase-Change – Tunnel FET (PC-TFET) Switch with Subthreshold Swing <10 mV/decade and sub-0.1 body factor: digital and analog benchmarking. In 2*016 IEEE International Electron Devices Meeting* (2016).
60. Ionescu, A. M. Ferroelectric tunnel FET switch and memory. US patent (2010).
61. Shukla, N. *et al.* A steep-slope transistor based on abrupt electronic phase transition. *Nat. Commun.* **6**, 7812 (2015).
62. Zhao, Q. T. *et al.* Strained Si and SiGe nanowire tunnel FETs for logic and analog applications. *IEEE J. Electron Devices Soc* **3**, 103–114 (2015).
63. Knoll, L. *et al.* Strained Si and SiGe tunnel-FETs and complementary tunnel-FET inverters with minimum gate lengths of 50 nm. *Solid. State. Electron.* **97**, 76–81 (2014).
64. Zimmers, A. *et al.* Role of Thermal Heating on the Voltage Induced Insulator-Metal Transition in VO₂. *Phys. Rev. Lett.* **110**, 56601 (2013).
65. Joushaghani, A. *et al.* Characteristics of the Current-Controlled Phase Transition of VO₂ Microwires for Hybrid Optoelectronic Devices. *Photonics* **2**, 916–932 (2015).
66. Vitale, W. A., Moldovan, C. F., Paone, A., Schüler, A. & Ionescu, A. M. Investigation of the Metal-Insulator Transition in VO₂ for Electronic Switches with Sub-1 mV/Decade Steep Subthreshold Slope. In *Silicon Nanoelectronics Workshop*, doi:10.1109/SNW.2016.7578041 (2016).
67. Shukla, N. *et al.* Pairwise coupled hybrid vanadium dioxide-MOSFET (HVFET) oscillators for non-boolean associative computing. In *2014 IEEE International Electron Devices Meeting* 28.7.1-28.7.4, doi:10.1109/IEDM.2014.7047129 (IEEE, 2014).
68. Jerry, M. *et al.* Phase transition oxide neuron for spiking neural networks. In *74th Annual Device Research Conference* 1-2, doi:10.1109/DRC.2016.7548503 (IEEE, 2016).
69. Vitale, W. A., Moldovan, C. F., Paone, A., Schüler, A. & Ionescu, A. M. Fabrication of CMOS-compatible abrupt electronic switches based on vanadium dioxide. *Microelectron. Eng.* **145**, 117–119 (2015).
70. Luong, G. V., Trellenkamp, S., Zhao, Q. T., Mantl, S. & Bourdelle, K. K. Strained Si nanowire GAA n-TFETs for low supply voltages. *EUROSOI-ULIS 2015 - 2015 Jt. Int. EUROSOI Work. Int. Conf. Ultim. Integr. Silicon* 65–68, doi:10.1109/ULIS.2015.7063774 (2015).

## Acknowledgements

## Author Contributions

W.A.V., E.A.C. and A.B. performed the experiments. W.A.V., E.A.C. and C.A. analyzed the data. T.R. designed and simulated the circuit applications. A.K. and A.S. deposited the VO₂ films. E.A.C. fabricated the VO₂ switches. G.V.L., Q.-T.Z. and S.M. designed and fabricated the TFETs. W.A.V. and A.M.I. wrote the manuscript. All authors discussed the results and commented on the manuscript. A.M.I. directed the overall research project.

## Additional Information

**Supplementary information** accompanies this paper at doi:10.1038/s41598-017-00359-6

**Competing Interests:** The authors declare that they have no competing interests.

**Publisher's note:** Springer Nature remains neutral with regard to jurisdictional claims in published maps and institutional affiliations.

# References

Aetukuri N. B., Gray A. X., Drouard M., Cossale M., Gao L., Reid A. H., Kukreja R., Ohldag H., Jenkins C. A., Arenholz E., Roche K. P., Dürr H. A., Samant M. G., Parkin S. S. P. (2013). Control of the metal-insulator transition in vanadium dioxide by modifying orbital occupancy. Nature Physics, 9(10), 661–666. https://doi.org/10.1038/nphys2733

Ammar M. R., Napierala C., Laffez P. (2009). Infrared thermochromic behaviour of a composite $Sm_{0.65}Ca_{0.35}MnO_3$-poly(styrene-co-acrylonitrile) film. Smart Materials and Structures, 18(5). DOI: 10.1088/0964-1726/18/5/055002

Appavoo K., Wang B., Brady N. F., Seo M., Nag J., Prasankumar R. P., Hilton D. J., Pantelides S. T., Haglund R. F. (2014). Ultra-fast phase transition via catastrophic phonon collapse driven by plasmonic hot-electron injection. Nano Letters, 14(3), 1127–1133. https://doi.org/10.1021/nl4044828

Bai L., Li Q., Corr S. A., Meng Y., Park C., Sinogeikin S. V, Ko C., Wu J., Shen, G. (2015). Pressure-induced phase transitions and metallization in $VO_2$. Physical Review B, 91, 104110. https://doi.org/10.1103/PhysRevB.91.104110

Baldi A., Borsa D.M., Schreuders H., Rector J.H., Atmakidis T., Bakker M., Zondag H.A., van Helden W.G.J., Dam B., Griessen R. (2008). Mg–Ti–H thin films as switchable solar absorbers. International Journal of Hydrogen Energy, 33 (12), 3188-3192. https://doi.org/10.1016/j.ijhydene.2008.01.026

Barradas N. P., Jeynes C., Webb R. P. (1997). Simulated annealing analysis of Rutherford backscattering data. Applied Physics Letters, 71(2), 291. https://doi.org/10.1063/1.119524

Bayón R., San Vicente G., Maffiotte C., Morales A. (2008a). Preparation of selective absorbers based on CuMn spinels by dip-coating method. Renewable Energy 33 (2), 348–353. DOI: https://doi.org/10.1016/j.renene.2007.05.017

Bayón R., San Vicente G., Maffiotte C., Morales A. (2008b). Characterization of copper–manganese-oxide thin films deposited by dip-coating. Solar Energy Materials and Solar Cells 92 (10), 1211–1216. DOI: https://doi.org/10.1016/j.solmat.2008.04.011

Belkind A., Freilich A., Scholl R. (1998). Electrical dynamics of pulsed plasmas. 41st Annual Technical Conference Proceedings, Society of Vacuum Coaters, p. 321.

Benkahoul M., Chaker M., Margot J., Haddad E., Kruzelecky R., Wong B., Jamroz W., Poinas P. (2011). Thermochromic $VO_2$ film deposited on Al with tunable thermal emissivity for space applications. Solar Energy Materials and Solar Cells, 95(12), 3504–3508. https://doi.org/10.1016/j.solmat.2011.08.014

Bertacco R., Contour J. P., Barthélemy A., Olivier J. (2002). Evidence for strontium segregation in $La_{0.7}Sr_{0.3}MnO_3$ thin films grown by pulsed laser deposition: Consequences for tunnelling junctions. Surface Science, 511(1–3), 366–372. https://doi.org/10.1016/S0039-6028(02)01546-7

Bhosle V., Narayan J. (2007). Epitaxial growth and magnetic properties of $La_{0.7}Sr_{0.3}MnO_3$ films on (0001) sapphire. Applied Physics Letters, 90(10). https://doi.org/10.1063/1.2472537

Biermann S., Poteryaev A., Lichtenstein A. I., Georges A. (2005). Dynamical Singlets and Correlation-Assisted Peierls Transition in $VO_2$. Physical Review Letters, 94(2), 026404. https://doi.org/10.1103/PhysRevLett.94.026404

Biesinger M. C., Lau L. W. M., Gerson A. R., Smart R. St. C. (2010). Resolving surface chemical states in XPS analysis of first row transition metals, oxides and hydroxides: Sc, Ti, V, Cu and Zn. Applied Surface Science 257 (3), 887–898. DOI: https://doi.org/10.1016/j.apsusc.2010.07.086

Biesinger M. C., Payne B. P., Grosvenor A. P., Lau L. W. M., Gerson A. R., Smart R. St. C. (2011). Resolving surface chemical states in XPS analysis of first row transition metals, oxides and hydroxides: Cr, Mn, Fe, Co and Ni. Applied Surface Science 257 (7), 2717–2730. DOI: https://doi.org/10.1016/j.apsusc.2010.10.051

Binnig G., Rohrer H., Gerber C., Weibel E. (1983). 7 × 7 Reconstruction on Si(111) Resolved in Real Space. Physical Review Letters 50(2), 120–123. https://doi.org/10.1103/PhysRevLett.50.120

Boileau A., Capon F., Barrat S., Laffez P., Pierson J. F. (2012). Thermochromic effect at room temperature of $Sm_{0.5}Ca_{0.5}MnO_3$ thin films. Journal of Applied Physics, 111, 113517. https://doi.org/10.1063/1.4722264

Brahlek M., Zhang L., Lapano J., Zhang H. T., Engel-Herbert R., Shukla N., Datta S., Paik H., Schlom D. G. (2017). Opportunities in vanadium-based strongly correlated electron systems. MRS Communications, 7(1), 27–52. https://doi.org/10.1557/mrc.2017.2

Brassard D., Fourmaux S., Jean-Jacques M., Kieffer J. C., El Khakani M. A. (2005). Grain Size Effect on the Semiconductor-Metal Phase Transition Characteristics of Magnetron-Sputtered $VO_2$ Thin Films. Applied Physics Letters 87(5), 1–4. DOI: 10.1063/1.2001139

Broemme A. D. D. (1990). Physico-chemical investigations on Co-Mn-oxide spinels. Technische Universiteit Eindhoven. DOI: 10.6100/IR332566

Brückner W., Moldenhauer W., Wich H., Wolf E., Oppermann H., Gerlach U., Reichelt, W. (1975). The range of homogeneity of $VO_2$ and the influence of the composition on the physical properties. II. The change of the physical properties in the range of homogeneity. Physica Status Solidi (a), 29(1), 63–70. doi:10.1002/pssa.2210290107

Budai J. D., Hong J., Manley M. E., Specht E. D., Li C. W., Tischler J. Z., Abernathy D. L., Said A. H., Leu B. M., Boatner L. A., McQueeney R. J., Delaire O. (2014). Metallization of vanadium dioxide driven by large phonon entropy. Nature, 515(7528), 535–539. https://doi.org/10.1038/nature13865

Cadafalch J. (2009). A detailed numerical model for flat-plate solar thermal devices. Solar Energy 83 (12), 2157–2164. DOI: https://doi.org/10.1016/j.solener.2009.08.013

Case F. C. (1984). Modifications in the phase transition properties of predeposited $VO_2$ films. Journal of Vacuum Science & Technology A: Vacuum, Surfaces, and Films, 2(4), 1509–1512. https://doi.org/10.1116/1.572462

Cavalleri A., Dekorsy T., Chong H. H. W., Kieffer J. C., Schoenlein R. W. (2004). Evidence for a structurally-driven insulator-to-metal transition in $VO_2$: A view from the ultrafast timescale. Physical Review B - Condensed Matter and Materials Physics, 70(16), 1–4. https://doi.org/10.1103/PhysRevB.70.161102

Cavalleri A., Tóth Cs., Siders C. W., Squier J. A., Ráksi F., Forget P., Kieffer J. C. (2001). Femtosecond structural dynamics in $VO_2$ during an ultrafast solid-solid phase transition. Physical Review Letters, 87(23), 237401-1-4. https://doi.org/10.1103/PhysRevLett.87.237401

Chang T., Cao X., Li N., Long S., Zhu Y., Huang J., Luo H., Jin P. (2019). Mitigating Deterioration of Vanadium Dioxide Thermochromic Films by Interfacial Encapsulation. Matter, 1(3), 734–744. https://doi.org/10.1016/j.matt.2019.04.004

Chang Y. J., Yang J. S., Kim Y. S., Kim D. H., Noh T. W., Kim D.-W., Oh E. , Kahng B., Chung J.-S. (2007). Surface versus bulk characterizations of electronic inhomogeneity in a $VO_2$ thin film. Physical Review B 76, 075118. DOI: 10.1103/PhysRevB.76.075118

Chen B., Yang D., Charpentier P. A., Zeman M. (2009). $Al^{3+}$-doped vanadium dioxide thin films deposited by PLD. Solar Energy Materials and Solar Cells 93(9), 1550–1554. DOI: 10.1016/j.solmat.2009.04.005

Chen S., Liu J., Wang L., Luo H., Gao Y. (2014). Unraveling Mechanism on Reducing Thermal Hysteresis Width of $VO_2$ by Ti Doping: A Joint Experimental and Theoretical Study. The Journal of Physical Chemistry C, 118(33), 18938–18944. https://doi.org/10.1021/jp5056842

Cheng K., Yang F., Wang G., Yin J., Cao D. (2013). Facile synthesis of porous (Co, Mn)$_3$O$_4$ nanowires free-standing on a Ni foam and their catalytic performance for $H_2O_2$ electroreduction. Journal of Materials Chemistry A 1, 1669-1676. DOI: https://doi.org/10.1039/c2ta00219a

Cheng S. L., Du C. H., Chuang T. H., Lin J. G. (2019). Atomic replacement effects on the band structure of doped perovskite thin films. Scientific Reports, 9(1). https://doi.org/10.1038/s41598-019-44104-7

Demeter M., Neumann M., Reichelt W. (2000). Mixed-valence vanadium oxides studied by XPS. Surface Science 454-456, 41-44. DOI: 10.1016/S0039-6028(00)00111-4

Demichelis F., Kaniadakis G., Tagliaferro A., Tresso E. (1987). New approach to optical analysis of absorbing thin solid films. Applied Optics 26(9), 1737-1740. https://doi.org/10.1364/AO.26.001737

Dorywalski K., Maciejewski I., Krzyżyński T. (2015) Spectroscopic ellipsometry technique as a materials characterization tool for mechatronic systems—The case of composition and doping concentration monitoring in SBN crystals. Mechatronics 37, 33–41. https://doi.org/10.1016/j.mechatronics.2015.11.005

Du J., Gao Y., Luo H., Kang L., Zhang Z., Chen Z., Cao C. (2011). Significant changes in phase-transition hysteresis for Ti-doped $VO_2$ films prepared by polymer-assisted deposition. Solar Energy Materials and Solar Cells 95(2), 469–475. DOI: 10.1016/j.solmat.2010.08.035

Duffie J.A., Beckman W.A. (1998). Solar Engineering of Thermal Processes, Wiley.

Émond N., Hendaoui A., Chaker M. (2015). Low resistivity $W_xV_{1-x}O_2$-based multilayer structure with high temperature coefficient of resistance for microbolometer applications. Applied Physics Letters, 107(14), 143507. DOI: 10.1063/1.4932954

Eyert V. (2002). The metal-insulator transitions of $VO_2$: A band theoretical approach. Annalen Der Physik (Leipzig), 11(9), 650–702. https://doi.org/10.1002/1521-3889(200210)11:9<650::AID-ANDP650>3.0.CO;2-K

Eyert V. (2011). $VO_2$: A novel view from band theory. Physical Review Letters, 107(1). https://doi.org/10.1103/PhysRevLett.107.016401

Fan L. L., Chen S., Wu Y. F., Chen F. H., Chu W. S., Chen X., Zou C.W, Wu Z. Y. (2013). Growth and phase transition characteristics of pure M-phase $VO_2$ epitaxial film prepared by oxide molecular beam epitaxy. Applied Physics Letters, 103(13). https://doi.org/10.1063/1.4823511

Farchado M., Rodríguez J. M., San Vicente G., Germán N., Morales A. (2018). Optical parameters of a novel competitive selective absorber for low temperature solar thermal applications. Solar Energy Materials and Solar Cells 178, 234–239. DOI: https://doi.org/10.1016/j.solmat.2018.01.031

Feng C., McEnaney K., Chen G., Ren Z. (2014). A Review of Cermet-Based Spectrally Selective Solar Absorbers. Energy & Environmental Science 7(5), 1615. http://dx.doi.org/10.1039/c3ee43825b

FOEN (2019). Federal Office for the Environment, Swiss climate policy. Accessed from: https://www.bafu.admin.ch/bafu/en/home/topics/climate/info-specialists/climate-policy.html

Fortier J. P., Baloukas B., Zabeida O., Klemberg-Sapieha J. E., Martinu L. (2014). Thermochromic $VO_2$ thin films deposited by HiPIMS. Solar Energy Materials and Solar Cells 125, 291–296. https://doi.org/10.1016/j.solmat.2014.03.007

Futaki H., Kobayashi K., Aoki M., Shimoda T., Yamada E., Narita K. (1968). Thermistor composition containing vanadium dioxide. U.S. patent 3,402,131.

García-Valladares O., Velázquez N. (2009). Numerical simulation of parabolic trough solar collector: Improvement using counter flow concentric circular heat exchangers. International Journal of Heat and Mass Transfer 52 (3-4), 597–609. DOI: https://doi.org/10.1016/j.ijheatmasstransfer.2008.08.004

Geng Q.-F., Zhao X., Gao X.-H., Liu G. (2011). Sol-Gel Combustion-Derived $CoCuMnO_x$ Spinels as Pigment for Spectrally Selective Paints. Journal of the American Ceramic Society 94 (3), 827–832. DOI: https://doi.org/10.1111/j.1551-2916.2010.04182.x

Gentle A., Smith G. B. (2008). Dual metal–insulator and insulator–insulator switching in nanoscale and Al doped $VO_2$. Journal of Physics D: Applied Physics 41, 015402. DOI: 10.1088/0022-3727/41/1/015402

Goodenough J.B. (1971). The two components of the crystallographic transition in $VO_2$. Journal of Solid State Chemistry 3(4), 490–500. https://doi.org/10.1016/0022-4596(71)90091-0

Gopalakrishnan G., Ruzmetov D., Ramanathan S. (2009). On the triggering mechanism for the metal-insulator transition in thin film $VO_2$ devices: Electric field versus thermal effects. Journal of Materials Science, 44(19), 5345–5353. https://doi.org/10.1007/s10853-009-3442-7

Granqvist C. G. (1990). Window coatings for the future. Thin Solid Films, 193–194, 730–741. https://doi.org/10.1016/0040-6090(90)90225-3

Grant (2019). Solar range. Solar thermal water heating systems. https://www.grantuk.com/media/2994/grant-solar-range-brochure-september-2018.pdf. (Accessed December 2019).

Guinneton F., Sauques L., Valmalette J.-C., Cros F., Gavarri J.-R. (2004). Optimized infrared switching properties in thermochromic vanadium dioxide thin films: role of deposition process and microstructure. Thin Solid Films 446 (2), 287-295. DOI: https://doi.org/10.1016/j.tsf.2003.09.062

Guzman G., Beteille F., Morineau R., Livage J. (1996). Electrical switching in $VO_2$ sol-gel films. Journal of Materials Chemistry, 6(3), 505–506. https://doi.org/10.1039/JM9960600505

Haddad E., Kruzelecky R.V., Wong B.C., Jamroz W., Soltani M., Chaker M., Benkahoul M., Poinas P. (2009). Tuneable emittance thin film coatings for thermal control.

He M., Chen R. (2015). Structural and optical properties of $CuMnCoO_x$ spinel thin films prepared by a citric acid-based sol–gel dip coating route for solar absorber applications. Journal of Sol-Gel Science and Technology 74 (2), 528–536. DOI: https://doi.org/10.1007/s10971-015-3630-7

Hendaoui A., Émond N., Chaker M., Haddad É. (2013). Highly tunable-emittance radiator based on semiconductor-metal transition of $VO_2$ thin films. Applied Physics Letters, 102(6). https://doi.org/10.1063/1.4792277

Hirotsu Y., Tsunashima Y., Nagakura S., Kuwamoto H., Sato H. (1982). High-resolution electron microscopy of microsyntactic intergrowth in $V_nO_{2n-1}$. Journal of Solid State Chemistry, 43(1), 33–44. DOI: 10.1016/0022-4596(82)90212-2

Hood P. J., Denatale J. F. (1991). Millimeter-wave dielectric properties of epitaxial vanadium dioxide thin films. Journal of Applied Physics 70, 376–381. DOI: 10.1063/1.350285

Huang Z., Zhou W., Ouyang C., Wu J., Zhang F., Huang J., Gao Y., Chu J. (2015). High performance of Mn-Co-Ni-O spinel nanofilms sputtered from acetate precursors. Scientific Reports 5, 10899. DOI: https://doi.org/10.1038/srep10899

Huffman T. J., Hendriks C., Walter E. J., Yoon J., Ju H., Smith R., Carr G. L., Krakauer H., Qazilbash M. M. (2016). The insulating phases of vanadium dioxide are Mott-Hubbard insulators. Physical Review B 95, 075125. https://doi.org/10.1103/PhysRevB.95.075125

Hüfner S. (2003). Photoelectron Spectroscopy. Principles and Applications. Third Edition, Springer.

Huot G., Roecker C., Schüler A. (2008). Evaluation of the Potential of Optical Switching Materials for Overheating Protection of Thermal Solar Collectors. Swiss Federal Office of Energy Report 2008.

Hussain Z., Salim M. A., Khan M. A., Khawaja E. E. (1989). X-ray photoelectron and auger spectroscopy study of copper-sodium-germanate glasses. Journal of Non-Crystalline Solids 110 (1), 44-52. DOI: https://doi.org/10.1016/0022-3093(89)90180-4

Hutchins M.G. (2003). Spectrally selective materials for efficient visible, solar and thermal radiation control in Solar Thermal Technologies for Buildings: The State of the Art, Editor M. Santamouris.

H&M Analytical (2015). http://handmanalytical.com/pdfs/grazing_incidence.pdf (Accessed September 2015).

Ibrahim K., Taha H., Rahman M.M., Kabir H., Jiang Z-T. (2018). Solar selective performance of metal nitride/oxynitride based magnetron sputtered thin film coatings: a comprehensive review, Journal of Optics 20(3), 033001. https://doi.org/10.1088/2040-8986/aaa2c5

IEA SHC Task 49 (2015). International Energy Agency Solar Heating and Cooling Programme Task 49, Deliverable A1.2 - Overheating prevention and stagnation handling in solar process heat applications

IEA SHC Task 54 (2018). International Energy Agency Solar Heating and Cooling Programme Task 54, Price Reduction of Solar Thermal Systems - Reduction of Maintenance Costs by Preventing Overheating. Info Sheet B03

IEA-SHC (2016). International Energy Agency Solar Heating and Cooling Programme Task 49, Deliverable A1.3 - Process Heat Collectors - State of the Art and Available Medium Temperature Collectors

IEA-SHC (2019). International Energy Agency Solar Heating and Cooling Programme, Solar Heat Worldwide. Global Market Development and Trends in 2018. Detailed Market Figures 2017. 2019 Edition

Inaba K. (2014). General features of GaN-related materials. Technical Article. Rigaku Journal 30(1).

ITIA. (2019). International Tungsten Industry Association (ITIA). Tungsten properties. http://www.itia.info/tungsten-properties.html. (Accessed on 09/12/2019).

Jack S., Parzefall J., Luttmann T., Janßen P., Giovannetti F. (2014). Flat Plate Aluminum Heat Pipe Collector with Inherently Limited Stagnation Temperature. Energy Procedia 48, 105 – 113. https://doi.org/10.1016/j.egypro.2014.02.013

Jaffari G. H., Mahmood W. (2017). Investigation of phase evolution and control over phase transformation temperature and thermal hysteresis using stoichiometry and co-doping in $VO_2$ thin films. AIP Advances, 7(11). https://doi.org/10.1063/1.5003964

Jalili H., Han J. W., Kuru Y., Cai Z., Yildiz B. (2011). New insights into the strain coupling to surface chemistry, electronic structure, and reactivity of $La_{0.7}Sr_{0.3}MnO_3$. Journal of Physical Chemistry Letters, 2(7), 801–807. https://doi.org/10.1021/jz200160b

Jeong J., Aetukuri N., Graf T., Schladt T. D., Samant M. G., Parkin S. S. P. (2013). Suppression of metal-insulator transition in $VO_2$ by electric field-induced oxygen vacancy formation. Science, 339(6126), 1402–1405. https://doi.org/10.1126/science.1230512

Jiang M., Cao X., Bao S., Zhou H., Jin P. (2014). Regulation of the phase transition temperature of $VO_2$ thin films deposited by reactive magnetron sputtering without doping. Thin Solid Films, 562, 314–318. https://doi.org/10.1016/j.tsf.2014.04.090

Jin P., Yoshimura K., Tanemura S. (1997). Dependence of microstructure and thermochromism on substrate temperature for sputter-deposited $VO_2$ epitaxial films. Journal of Vacuum Science & Technology A: Vacuum, Surfaces, and Films 15(3), 1113. DOI: 10.1116/1.580439

Jin S., Tiefel T. H., McCormack M., Fastnacht R. A., Ramesh R., Chen L. H. (1994). Thousandfold change in resistivity in magnetoresistive La-Ca-Mn-O films. Science, 264(5157), 413–415. https://doi.org/10.1126/science.264.5157.413

Joly M., Antonetti Y., Python M., Gonzalez M., Gascou T., Scartezzini J.-L., Schüler A. (2013). Novel black selective coating for tubular solar absorbers based on a sol–gel method. Solar Energy 94, 233–239. DOI: 10.1016/j.solener.2013.05.009

Joly M., Bouvard O., Gascou T., Antonetti Y., Python M., González Lazo M. A., Loesch P., Hessler-Wyser A., Schüler A. (2015). Optical and structural analysis of sol–gel derived Cu–Co–Mn–Si oxides for black selective solar nanocomposite multi-layered coatings. Solar Energy Materials and Solar Cells 143, 573–580. DOI: 10.1016/j.solmat.2015.06.058

Kalogirou S.A. (2004). Solar thermal collectors and applications. Progress in Energy and Combustion Science 30, 231-295.

Kaluža L., Orel B., Dražič G., Kohl M. (2001). Sol–gel derived $CuCoMnO_x$ spinel coatings for solar absorbers: Structural and optical properties. Solar Energy Materials and Solar Cells 70 (2), 187–201. DOI: https://doi.org/10.1016/S0927-0248(01)00024-1

Katzke H., Tolédano P., Depmeier W. (2003). Theory of morphotropic transformations in vanadium oxides. Physical Review B - Condensed Matter and Materials Physics, 68(2). https://doi.org/10.1103/PhysRevB.68.024109

Kemmler A., Spillmann T., Koziel S. (2018). Der Energieverbrauch der Privaten Haushalte 2000 – 2017. SFOE Report 2018.

Kim D. H., Kwok H. S. (1994). Pulsed laser deposition of VO2 thin films. Applied Physics Letters, 65(25), 3188–3190. https://doi.org/10.1063/1.112476

Kim H., Charipar N., Osofsky M., Qadri S. B., Piqué A. (2014). Optimization of the semiconductor-metal transition in $VO_2$ epitaxial thin films as a function of oxygen growth pressure. Applied Physics Letters, 104(8). https://doi.org/10.1063/1.4866806

Kim S., Kim K., Kang C. J., Min B. I. (2013). Correlation-assisted phonon softening and the orbital-selective Peierls transition in $VO_2$. Physical Review B - Condensed Matter and Materials Physics, 87(19). https://doi.org/10.1103/PhysRevB.87.195106

Kimizuka N., Ishii M., Kawada I., Saeki M., Nakahira M. (1974). Behavior of vanadium dioxide single crystals synthesized under the various oxygen partial pressures at 1500 K. Journal of Solid State Chemistry, 9(1), 69–77. https://doi.org/10.1016/0022-4596(74)90056-5

Knibbs R. H. (1969). The measurement of thermal expansion coefficient of tungsten at elevated temperatures. Journal of Physics E: Scientific Instruments, 2(6), 515–517. https://doi.org/10.1088/0022-3735/2/6/311

Kouznetsov V., Macák K., Schneider J.M., Helmersson U., Petrov I. (1999). A novel pulsed magnetron sputter technique utilizing very high target power densities. Surface and Coatings Technology 122(2-3), 290-293. https://doi.org/10.1016/S0257-8972(99)00292-3

Krammer A., Magrez A., Vitale W. A., Mocny P., Jeanneret P., Guibert E., Whitlow H. J., Ionescu A. M., Schüler A. (2017a). Elevated transition temperature in Ge doped $VO_2$ thin films. Journal of Applied Phyics 122, 045304. https://doi.org/10.1063/1.4995965

Krammer A., Demière F.T., Schüler A. (2017b). Infrared optical properties of doped and pure thermochromic coatings for solar thermal absorbers. Proceedings of SWC2017, 1-7. https://doi.org/10.18086/swc.2017.17.04

Krammer A., Bouvard O., Schüler A. (2017c). Study of Si doped $VO_2$ thin films for solar thermal applications. Energy Procedia 122, 745-750. https://doi.org/10.1016/j.egypro.2017.07.390

Krammer A., Gremaud A., Bouvard O., Sanjines R., Schüler A. (2016). In situ photoelectron spectroscopic characterization of reactively sputtered, doped vanadium oxide thin films. Surface and Interface Analysis 48(7), 440-444. https://doi.org/10.1002/sia.5989

Kucharczyk D., Niklewski T. (1979). Accurate X-ray determination of the lattice parameters and the thermal expansion coefficients of $VO_2$ near the transition temperature. Journal of Applied Crystallography, 12(4), 370–373. https://doi.org/10.1107/s0021889879012711

Kuhn J., Bobrowski N., Lübcke P., Vogel L., Platt U. (2014). A Fabry–Perot interferometer-based camera for two-dimensional mapping of $SO_2$ distributions. Atmospheric Measurement Techniques, 7(11), 3705–3715. https://doi.org/10.5194/amt-7-3705-2014

Kukuruznyak D. A., Moyer J. G., Prowse M. S., Nguyen N., Rehr J. J., Ohuchi F. S. (2006). Relationship between electronic and crystal structure in Cu–Ni–Co–Mn–O spinels: Part B: Binding energy anomaly in $Cu^{1+}$ photoemission spectrum. Journal of Electron Spectroscopy and Related Phenomena 150 (2-3), 282–287. DOI: https://doi.org/10.1016/j.elspec.2005.06.013

Ladd L. A., Paul W. (1969). Optical and Transport Properties of High Quality Crystals of $V_2O_4$ Near the Metallic Transition temperature. Solid State Communications, 7(4), 425–428. DOI: https://doi.org/10.1016/0038-1098(69)90888-6

Laffez P., Zaghrioui M., Reversat L., Ruello P. (2006). Electron doped $(Sm_{1-x},Ca_x)MnO_3$ perovskite manganite as potential infrared thermochromic switch. Applied Physics Letters, 89, 81909. https://doi.org/10.1063/1.2236290

Lahav A., Grim K. A., Blech I. A. (1990). Measurement of thermal expansion coefficients of W, WSi, WN, and WSiN thin film metallizations. Journal of Applied Physics, 67(2), 734–738. https://doi.org/10.1063/1.345779

Langell M. A., Anderson M. D., Carson G. A., Peng L., Smith S. (1999). Valence-band electronic structure of $Co_3O_4$ epitaxy on CoO(100), Physical Review B 59, 4791. DOI: https://doi.org/10.1103/PhysRevB.59.4791

Le T. L., Guillemet-Fritsch S., Dufour P., Tenailleau C. (2016). Microstructural and optical properties of spinel oxide $M_xCo_2 – xMnO_4$ (M = Ni, Zn or Cu; 0<x<1) thin films prepared by inorganic polycondensation and dip-coating methods. Thin Solid Films 612, 14–21. DOI: https://doi.org/10.1016/j.tsf.2016.05.030

Lee D., Chung B., Shi Y., Kim G. Y., Campbell N., Xue F., … Eom C. B. (2018). Isostructural metal-insulator transition in $VO_2$. Science, 362(6418), 1037–1040. https://doi.org/10.1126/science.aam9189

Lee H. S., Park H. H. (2015a). Band structure analysis of $La_{0.7}Sr_{0.3}MnO_3$ perovskite manganite using a synchrotron. Advances in Condensed Matter Physics. https://doi.org/10.1155/2015/746475

Lee S., Meyer T. L., Sohn C., Lee D., Nichols J., Lee D., Seo S. S. A., Freeland J. W., Noh T. W., Lee H. N. (2015b). Electronic structure and insulating gap in epitaxial $VO_2$ polymorphs. APL Materials 3, 126109. https://doi.org/10.1063/1.4939004

Lee S., Hippalgaonkar K., Yang F., Hong J., Ko C., Suh J., … Wu J. (2017). Anomalously low electronic thermal conductivity in metallic vanadium dioxide. Science, 355(6323), 371–374. https://doi.org/10.1126/science.aag0410

Leroux Ch., Nihoul G., Van Tendeloo G. (1998). From $VO_2(B)$ to $VO_2(R)$: Theoretical structures of $VO_2$ polymorphs and in situ electron microscopy. Physical Review B, 57(9), 5111 - 5121. DOI: 10.1103/PhysRevB.57.5111

Leroy J., Crunteanu A., Bessaudou A., Cosset F., Champeaux C., Orlianges J. C. (2012). High-speed metal-insulator transition in vanadium dioxide films induced by an electrical pulsed voltage over nano-gap electrodes. Applied Physics Letters, 100(21). https://doi.org/10.1063/1.4721520

Li G.-H., Dai L.-Z., Lu D.-S., Peng S.-Y. (1990). Characterization of copper cobalt mixed oxide. Journal of Solid State Chemistry 89 (1), 167–173. DOI: https://doi.org/10.1016/0022-4596(90)90308-K

Li J., Xiong S., Li X., Qian Y. (2013). A facile route to synthesize multiporous $MnCo_2O_4$ and $CoMn_2O_4$ spinel quasi-hollow spheres with improved lithium storage properties. Nanoscale 5, 2045-2054. DOI: https://doi.org/10.1039/c2nr33576j

Liu K., Lee S., Yang S., Delaire O., Wu, J. (2018). Recent progresses on physics and applications of vanadium dioxide. Materials Today. 21(8), Pages 875 - 896. https://doi.org/10.1016/j.mattod.2018.03.029

Liu S. M., Zhu X. B., Yang J., Song W. H., Dai J. M., Sun Y. P. (2006). The effect of grain boundary on the properties of $La_{0.7}Sr_{0.3}MnO_3$ thin films prepared by chemical solution deposition. Ceramics International, 32(2), 157–162. https://doi.org/10.1016/j.ceramint.2005.01.012

Lopez R., Haynes T. E., Boatner L. A., Feldman L. C., Haglund, R. F. (2002). Size effects in the structural phase transition of VO2 nanoparticles. Physical Review B 65(22), 224113. DOI: 10.1103/PhysRevB.65.224113

Loquai S., Baloukas B., Klemberg-Sapieha J. E., Martinu L. (2017). HiPIMS-deposited thermochromic $VO_2$ films with high environmental stability. Solar Energy Materials and Solar Cells, 160, 217–224. https://doi.org/10.1016/j.solmat.2016.10.038

Loquai S., Baloukas B., Zabeida O., Klemberg-Sapieha J. E., Martinu L. (2016). HiPIMS-deposited thermochromic $VO_2$ films on polymeric substrates. Solar Energy Materials and Solar Cells, 155, 60–69. https://doi.org/10.1016/j.solmat.2016.04.048

Lu H., Guo Y., Robertson J. (2019). Electronic structure of metallic and insulating phases of vanadium dioxide and its oxide alloys. Physical Review Materials, 3(9). https://doi.org/10.1103/PhysRevMaterials.3.094603

MacChesney J.B., Guggenheim H.J. (1969). Growth and electrical properties of vanadium dioxide single crystals containing selected impurity ions. Journal of Physics and Chemistry of Solids 30(2), 225-234. https://doi.org/10.1016/0022-3697(69)90303-5

Mack I. (2008). Development of innovative coatings for sun protection glasses based on the theory of the optimal spectral transmittance. PhD Thesis, University of Basel.

Macleod H.A. (2010). Thin-Film Optical Filters (Chapter 2), 4th Edition, CRC Press.

Mahendiran R., Tiwary S. K., Raychaudhuri A. K., Ramakrishnan T. V, Mahesh R., Rangavittal N., Rao C. N. R. (1996). Structure, electron-transport properties, and giant magnetoresistance of hole-doped $LaMnO_3$ systems. Physical Review B, 53(6), 3348. https://doi.org/10.1103/PhysRevB.53.3348

Mercs D., Didelot A., Capon F., Pierson J.-F., Hafner B., Pazidis A., Föste S., Reineke-Koch R. (2016). Innovative Smart Selective Coating to Avoid Overheating in Highly Efficient Thermal Solar Collectors. Energy Procedia 91, 84–93. https://doi.org/10.1016/j.egypro.2016.06.177.

Mitteramskogler T., Haslinger M. J., Wennberg A., Fernandez-Martínez I., Muehlberger M., Krause M., Guillén E. (2019). Preparation and Characterization of Solar Thermal Absorbers by Nanoimprint Lithography and Sputtering. MRS Advances, 4(35), 1905–1911. https://doi.org/10.1557/adv.2019.285

Miyazaki K., Shibuya K., Suzuki M., Wado H., Sawa A. (2014). Correlation between thermal hysteresis width and broadening of metal–insulator transition in Cr- and Nb-doped $VO_2$ films. Japanese Journal of Applied Physics 53, 71102. https://doi.org/10.7567/JJAP.53.071102

Molle A., Bhuiyan Md. N. K., Tallarida G., Fanciulli M. (2006). In situ chemical and structural investigations of the oxidation of Ge(001) substrates by atomic oxygen. Applied Physics Letters 89, 083504. https://doi.org/10.1063/1.2337543

Morin F. J. (1959). Oxides which show a metal-to-insulator transition at the neel temperature. Physical Review Letters, 3(1), 34–36. https://doi.org/10.1103/PhysRevLett.3.34

Morrison V. R., Chatelain R. P., Tiwari K. L., Hendaoui A., Bruhács A., Chaker M., Siwick B. J. (2014). A photoinduced metal-like phase of monoclinic $VO_2$ revealed by ultrafast electron diffraction. Science, 346(6208), 445–448. https://doi.org/10.1126/science.1253779

Nag J. (2011). The solid-solid phase transition in vanadium dioxide thin films: synthesis, physics and application. PhD Thesis, Vanderbilt University.

Nakano M., Shibuya K., Okuyama D., Hatano T., Ono S., Kawasaki M., Iwasa Y., Tokura, Y. (2012). Collective bulk carrier delocalization driven by electrostatic surface charge accumulation. Nature, 487(7408), 459–462. https://doi.org/10.1038/nature11296

Oku M., Hirokawa K. (1976). X-ray photoelectron spectroscopy of $Co_3O_4$, $Fe_3O_4$, $Mn_3O_4$, and related compounds. Journal of Electron Spectroscopy and Related Phenomena 8 (5), 475–481. DOI: https://doi.org/10.1016/0368-2048(76)80034-5

Oku M., Hirokawa K., Ikeda S. (1975). X-ray photoelectron spectroscopy of manganese—oxygen systems. Journal of Electron Spectroscopy and Related Phenomena 7 (5), 465–473. DOI: https://doi.org/10.1016/0368-2048(75)85010-9

Otto M. R., René de Cotret L. P., Valverde-Chavez D. A., Tiwari K. L., Émond N., Chaker M., Cooke D. G., Siwick B. J. (2019). How optical excitation controls the structure and properties of vanadium dioxide. Proceedings of the National Academy of Sciences of the United States of America, 116(2), 450–455. https://doi.org/10.1073/pnas.1808414115

Paone A., Geiger M., Sanjines R., Schüler A. (2014). Thermal solar collector with $VO_2$ absorber coating and $V_{1-x}W_xO_2$ thermochromic glazing - Temperature matching and triggering. Solar Energy, 110, 151–159. https://doi.org/10.1016/j.solener.2014.08.033

Paone A., Joly M., Sanjines R., Romanyuk A., Scartezzini J.-L., Schüler A. (2009). Thermochromic films of $VO_2$:W for smart solar energy applications. Proceedings of SPIE - The International Society for Optical Engineering 7410. https://doi.org/10.1117/12.826143.

Paone A., Sanjines R., Jeanneret P., Whitlow H.J., Guibert E., Guibert G., Bussy F., Scartezzini J.-L., Schüler A. (2015a). Influence of doping in thermochromic $V_{1-x}W_xO_2$ and $V_{1-x}Al_xO_2$ thin films: Twice improved doping efficiency in $V_{1-x}W_xO_2$. Journal of Alloys and Compounds 621, 206–211. DOI: 10.1016/j.jallcom.2014.08.264

Paone A., Sanjines R., Jeanneret P., Schüler A. (2015b). Temperature-dependent multiangle FTIR NIR-MIR ellipsometry of thermochromic $VO_2$ and $V_{1-x}W_xO_2$ films. Solar Energy 118, 107-116. https://doi.org/10.1016/j.solener.2015.05.020

Pérez-Espinosa R., García-Valladares O. (2018). Solar Collector Simulator (SolCoSi): A new validated model for predicting the thermal performance of flat plate solar collectors. Journal of Renewable and Sustainable Energy 10, 013705. DOI: https://doi.org/10.1063/1.5004428

Perucchi A., Baldassarre L., Postorino P., Lupi S. (2009). Optical properties across the insulator to metal transitions in vanadium oxide compounds. Journal of Physics Condensed Matter, 21(32). https://doi.org/10.1088/0953-8984/21/32/323202

Phillips T. E., Murphy R. A., Poehler T. O. (1987). Electrical studies of reactively sputtered Fe-doped $VO_2$ thin films. Materials Research Bulletin 22(8), 1113–1123. DOI: 10.1016/0025-5408(87)90241-8

Pouget J. P., Launois H. (1976). Metal-insulator phase transition in $VO_2$. Journal de Physique Colloques, 37 (C4) pp.C4-49-C4-57. https://doi.org/10.1051/jphyscol:1976408.

Prabhakaran K., Nishioka T., Sumitomo K., Kobayashi Y., Ogino T. (1993). In situ oxidation of a thin layer of Ge on Si(001): Observation of GeO to $SiO_2$ transition. Applied Physics Letters 62, 864. https://doi.org/10.1063/1.108548

Qazilbash M. M., Brehm M., Chae B.-G., Ho P.-C., Andreev G. O., Kim B.-J., Yun S. J., Balatsky A. V., Maple M. B., Keilmann F., Kim H.-T., Basov D. N. (2007). Mott transition in $VO_2$ revealed by infrared spectroscopy and nano-imaging. Science, 318(5857), 1750–1753. https://doi.org/10.1126/science.1150124

Qazilbash M. M., Burch K. S., Whisler D., Shrekenhamer D., Chae B. G., Kim H. T., Basov D. N. (2006). Correlated metallic state of vanadium dioxide. Physical Review B - Condensed Matter and Materials Physics, 74(20). https://doi.org/10.1103/PhysRevB.74.205118

Rakotoniaina J.C., Mokrani-Tamellin R., Gavarri J.R., Vacquier G., Casalot A., Calvarin G. (1993). The Thermochromic Vanadium Dioxide: I. Role of Stresses and Substitution on Switching Properties. Journal of Solid State Chemistry 103(1), 81-94. https://doi.org/10.1006/jssc.1993.1081

Rao C.N., Raveau B. (1998). Colossal Magnetoresistance, Charge Ordering and Related Properties of Manganese Oxides, pp. 1-42. World Scientific. https://doi.org/10.1142/9789812816795_0001

Rebouta L., Capela P., Andritschky M., Matilainen A., Santilli P., Pischow K., Alves E. (2012). Characterization of TiAlSiN/TiAlSiON/$SiO_2$ optical stack designed by modelling calculations for solar selective applications. Solar Energy Materials and Solar Cells 105, 202–207. https://doi.org/10.1016/J.SOLMAT.2012.06.011

Rice T. M., Launois H., Pouget J. P. (1994). Comment on "$VO_2$: Peierls or Mott-Hubbard? A View from Band Theory". Physical Review Letters, 73(22), 3042–3042. https://doi.org/10.1103/PhysRevLett.73.3042

Rubin E. B., Shin S., Chen Y., Chen R. (2019). High-temperature stable refractory nanoneedles with over 99% solar absorptance. APL Materials, 7(3). https://doi.org/10.1063/1.5084086

Ruzmetov D., Zawilski K.T., Narayanamurti V., Ramanathan S. (2007). Structure-Functional Property Relationships in Rf-Sputtered Vanadium Dioxide Thin Films. Journal of Applied Physics 102(11), 113715. DOI: 10.1063/1.2817818

Savosolar Oyj (2019). https://savosolar.com/ (Accessed December 2019).

Sawatzky G.A., Post D. (1979). X-ray photoelectron and Auger spectroscopy study of some vanadium oxides. Physical Review B, 20(4), 1546. DOI: 10.1103/PhysRevB.20.1546

Schiebler B., Jack S., Dieckmann H., Giovannetti F. (2018). Experimental and theoretical investigations on temperature limitation in solar thermal collectors with heat pipes: Effect of superheating on the maximum temperature. Solar Energy 171, 271 – 278. https://doi.org/10.1016/j.solener.2018.06.036

Schüler A., Oelhafen P. (2001a). In situ core-level and valence-band photoelectron spectroscopy of reactively sputtered titanium aluminum nitride films. Physical Review B 63, 115413. DOI: 10.1103/PhysRevB.63.115413

Schüler A., Thommen V., Reimann P., Oelhafen P., Francz G., Zehnder T., Düggelin M., Mathys D., Guggenheim R. (2001b). Structural and optical properties of titanium aluminum nitride films ($Ti_{1-x}Al_xN$). Journal of Vacuum Science & Technology A 19(3), 922. DOI: https://doi.org/10.1116/1.1359532

Schwingenschlögl U., Eyert V. (2004). The vanadium Magnéli phases $V_nO_{2n-1}$. Annalen Der Physik, 13(9), 475–510. https://doi.org/10.1002/andp.200410099

Sciencewise.info (2019) http://sciencewise.info/resource/Bragg%27s_law/hyperphysics.phy-astr.gsu.edu (Accessed December 2019).

Scofield J. H. (1976). Hartree-Slater subshell photoionization cross-sections at 1254 and 1487 eV. Journal of Electron Spectroscopy and Related Phenomena, 8(2), 129–137. https://doi.org/10.1016/0368-2048(76)80015-1

SFOE (2019). Swiss Federal Office of Energy, Energy in buildings. Accessed from: https://www.bfe.admin.ch/bfe/en/home/supply/energy-efficiency/energy-in-buildings.html

Shannon R.D. (1976). Revised Effective Ionic Radii and Systematic Studies of Interatomic Distances in Halides and Chalcogenides. Acta Crystallographica A32, 751-767. https://doi.org/10.1107/S0567739476001551

Shen X., Xu G., Shao C., Cheng C. (2009). Temperature dependence of infrared emissivity of doped manganese oxides in different wavebands (3-5 and 8-14 µm). Journal of Alloys and Compounds, 479(1–2), 420–422. https://doi.org/10.1016/j.jallcom.2008.12.090

Shimakawa Y., Yoshitake T., Kubo Y., Machida T., Shinagawa K., Okamoto A., Nakamura Y., Ochi A., Tachikawa S., Ohnishi A. (2002). A variable-emittance radiator based on a metal-insulator transition of (La,Sr)$MnO_3$ thin films. Applied Physics Letters 80, 4864. https://doi.org/10.1063/1.1489079

Shin S., Suga S., Taniguchi M., Fujisawa M., Kanzaki H., Fujimori A., Daimon H., Ueda Y., Kosuge K., Kachi S. (1990). Vacuum-ultraviolet reflectance and photoemission study of the metal-insulator phase transitions in $VO_2$, $V_6O_{13}$, and $V_2O_3$. Physical Review B 41, p. 4993–5009. DOI: 10.1103/physrevb.41.4993

Siegel R., Howell J. (2002). Thermal Radiation Heat Transfer. 4th edition, Taylor & Francis.

Soltani M., Chaker M., Jiang X. X., Nikanpour D., Margot, J. (2006). Thermochromic $La_{1-x}Sr_xMnO_3$ (x=0.1, 0.175, and 0.3) smart coatings grown by reactive pulsed laser deposition. Journal of Vacuum Science & Technology A: Vacuum, Surfaces, and Films, 24(4), 1518–1523. https://doi.org/10.1116/1.2204923

Sommers C., Doniach S. (1978). First principles calculation of the intra-atomic correlation energy in $VO_2$. Solid State Communications, 28(1), 133–135. https://doi.org/10.1016/0038-1098(78)90343-5

Stefanovich G., Pergament A., Stefanovich D. (2000). Electrical switching and Mott transition in $VO_2$. Journal of Physics Condensed Matter, 12(41), 8837–8845. https://doi.org/10.1088/0953-8984/12/41/310

Suman S., Khan M.K., Pathak M. (2015). Performance enhancement of solar collectors—A review. Renewable and Sustainable Energy Reviews 49, 192-210.

Sun K., Riedel C. A., Urbani A., Simeoni M., Mengali S., Zalkovskij M., Bilenberg B., de Groot C. H., Muskens O. L. (2018). $VO_2$ Thermochromic Metamaterial-Based Smart Optical Solar Reflector. https://doi.org/10.1021/acsphotonics.8b00119

SunWindEnergy (2017). https://www.sunwindenergy.com/content/pushing-stagnation-temperature (Accessed December 2019).

Tachikawa S., Shimazaki K., Ohnishi A., Hirosawa H., Shimakawa Y., Ochi A., Okamoto A., Nakamura Y. (2003). Smart radiation device based on a perovskite manganese oxide. Proceedings of the 9$^{th}$ International Symposium on Materials in a Space Environment.

Tang C., Georgopoulos P., Fine M. E., Cohen J. B., Nygren M., Knapp G. S., Aldred A. (1985). Local atomic and electronic arrangements in $W_xV_{1-x}O_2$. Physical Review B, 31(2), 1000–1011. https://doi.org/10.1103/PhysRevB.31.1000

Tang G., Yu Y., Cao Y., Chen W. (2008). The thermochromic properties of $La_{1-x}Sr_xMnO_3$ compounds. Solar Energy Materials and Solar Cells, 92(10), 1298–1301. https://doi.org/10.1016/j.solmat.2008.05.001

Tavares A.C., da Silva Pereira M. I., Mendonça M. H., Nunes M. R., Costa F. M., Sá C.M. (1998). XPS and voltammetric studies on $Ni_{1-x}Cu_xCo_2O_4$ spinel oxide electrodes. Journal of Electroanalytical Chemistry 449 (1-2), 91–100. https://doi.org/10.1016/S0022-0728(98)00045-X

Teodorescu G. (2007). Radiative emissivity of metals and oxidized metals at high temperature. PhD Thesis, Auburn University.

Theiss W. (2012). SCOUT Technical manual. Hard- and Software for Optical Spectroscopy. www.mtheis.com

TIGI (2018). http://tigisolar.com (Accessed December 2019).

Tran F., Blaha P. (2017). Importance of the Kinetic Energy Density for Band Gap Calculations in Solids with Density Functional Theory. The Journal of Physical Chemistry A 121 (17), 3318-3325. https://doi.org/10.1021/acs.jpca.7b02882

Trixler F. (2013). Quantum Tunnelling to the Origin and Evolution of Life. Current Organic Chemistry 17(16), 1758–1770. https://doi.org/10.2174/13852728113179990083

Valente-Feliciano A.-M. (2013). HIPIMS: A new generation of thin film deposition techniques for SRF applications*. Proceedings of SRF, 754-760.

Verleur H. W., Barker A. S., Berglund C. N. (1968). Optical Properties of $VO_2$ between 0.25 and 5 eV. Physical Review 172, 788–798. DOI: https://doi.org/10.1103/PhysRev.172.788

Viessmann (2019). Technology Brochure. Solar thermal systems. Vitosol. Accessed from: viessmann.com/com/en/product_range.html

Vince J., Šurca Vuk A., Opara Krašovec U., Orel B., Köhl M., Heck M. (2003). Solar absorber coatings based on CoCuMnOx spinels prepared via the sol–gel process: structural and optical properties. Solar Energy Materials and Solar Cells 79 (3), 313–330. https://doi.org/10.1016/S0927-0248(02)00457-9

Vitale W. A., Casu E. A., Biswas A., Rosca T., Alper C., Krammer A., Luong G. V., Zhao Q.-T., Mantl S., Schüler A., Ionescu A. M. (2017). A Steep-Slope Transistor Combining Phase-Change and Band-to-Band-Tunneling to Achieve a sub-Unity Body Factor. Scientific Reports, 7(355). https://doi.org/10.1038/s41598-017-00359-6

Vitale W. A., Petit L., Moldovan C. F., Fernández-Bolaños M., Paone A., Schüler A., Ionescu A. M. (2016). Electrothermal actuation of vanadium dioxide for tunable capacitors and microwave filters with integrated microheaters. Sensors and Actuators, A: Physical, 241, 245–253. https://doi.org/10.1016/j.sna.2016.01.027

Vlček J., Kolenatý D., Houška J., Kozák T., Čerstvý R. (2017). Controlled reactive HiPIMS - Effective technique for low-temperature (300°C) synthesis of VO₂ films with semiconductor-to-metal transition. Journal of Physics D: Applied Physics 50(38). https://doi.org/10.1088/1361-6463/aa8356

VTT (2017). VTT Technology 287, Solar heating and cooling in Northern and Central Europe. Pilot plants in Finland and Germany.

Wagner C.D., Naumkin A.V., Kraut-Vass A., Allison J.W., Powell C.J. (2012). NIST Standard Reference Database 20, Version 4.1 (web version) (http://srdata.nist.gov/xps/). DOI: http://dx.doi.org/10.18434/T4T88K

Wang H., Yi X., Chen S., Fu X. (2005). Fabrication of vanadium oxide micro-optical switches. Sensors and Actuators, A: Physical 122, 108–112. https://doi.org/10.1016/j.sna.2005.03.063

Wang Y., Lany S., Ghanbaja J., Fagot-Revurat Y., Chen Y. P., Soldera F., Horwat D., Mücklich F., Pierson J. F. (2016). Electronic structures of $Cu_2O$, $Cu_4O_3$, and $CuO$: A joint experimental and theoretical study. Physical Review B 94, 245418. DOI: 10.1103/PhysRevB.94.245418

Weber C., O'Regan D. D., Hine N. D. M., Payne M. C., Kotliar G., Littlewood P. B. (2012). Vanadium dioxide: A Peierls-Mott insulator stable against disorder. Physical Review Letters 108, 256402. DOI: 10.1103/PhysRevLett.108.256402

Wei W., Chen W., Ivey D. G. (2008). Rock Salt-Spinel Structural Transformation in Anodically Electrodeposited Mn-Co-O Nanocrystals. Chemistry of Materials 20 (5), 1941-1947. DOI: https://doi.org/10.1021/cm703464p

Wentzcovitch R. M., Schulz W. W., Allen P. B. (1994). $VO_2$: Peierls or Mott-Hubbard? A view from band theory. Physical Review Letters, 72(21), 3389–3392. https://doi.org/10.1103/PhysRevLett.72.3389

Wu C., Qiu J., Wang J., Xu M., Wang L. (2010). Thermochromic property of $La_{0.8}Sr_{0.2}MnO_3$ thin-film material sputtered on quartz glass. Journal of Alloys and Compounds, 506(2), 22-24. https://doi.org/10.1016/j.jallcom.2010.07.112

Wu Y., Fan L., Huang W., Chen S., Chen S., Chen F., Zou C., Wu Z. (2014). Depressed transition temperature of $W_xV_{1-x}O_2$: Mechanistic insights from the X-ray absorption fine structure (XAFS) spectroscopy. Physical Chemistry Chemical Physics, 16(33), 17705–17714. https://doi.org/10.1039/c4cp01661k

Wu Y., Fan L., Liu Q., Chen S., Huang W., Chen F., Liao G., Zou C., Wu Z. (2015). Decoupling the Lattice Distortion and Charge Doping Effects on the Phase Transition Behavior of $VO_2$ by Titanium ($Ti^{4+}$) Doping. Scientific Reports 5(1), 9328. DOI: 10.1038/srep09328

Yang B. L., Chan S. F., Chang W. S., Chen Y. Z. (1991). Surface enrichment in mixed oxides of Cu, Co, and Mn, and its effect on CO oxidation. Journal of Catalysis 130 (1), 52–61. DOI: 10.1016/0021-9517(91)90091-H

Yin W., Wolf S., Ko C., Ramanathan S., Reinke P. (2011). Nanoscale probing of electronic band gap and topography of $VO_2$ thin film surfaces by scanning tunneling microscopy. Journal of Applied Physics 109, 024311. DOI: 10.1063/1.3528167

Yunphuttha C., Porntheeraphat S., Wongchaisuwat A., Tangbunsuk S., Marr D. W. M., Viravathana P. (2016). Characterization of $La_{1-x}Sr_xMnO_3$ perovskite catalysts for hydrogen peroxide reduction. Physical Chemistry Chemical Physics, 18(25), 16786–16793. https://doi.org/10.1039/c6cp02338j

Zatsepin A.F., Zatsepin D.A., Zhidkov I.S., Kurmaev E.Z., Fitting H.-J., Schmidt B., Mikhailovich A.P., Lawniczak-Jablonska K. (2015). Formation of Ge0 and $GeO_x$ nanoclusters in $Ge^+$-implanted $SiO_2$/Si thin-film heterostructures under rapid thermal annealing. Applied Surface Science 349, 780 – 784. https://doi.org/10.1016/j.apsusc.2015.05.090

Zhang H. T., Zhang L., Mukherjee D., Zheng Y. X., Haislmaier R. C., Alem N., Engel-Herbert R. (2015). Wafer-scale growth of $VO_2$ thin films using a combinatorial approach. Nature Communications, 6, 8475. DOI : 10.1038/ncomms9475

Zhang H., Chang H. L. M., Guo J., Zhang T. J. (1994). Microstructure of epitaxial $VO_2$ thin films deposited on (1120) sapphire by MOCVD. Journal of Material Research 9(9), 2264-2271. https://doi.org/10.1557/JMR.1994.2264

Zhang H., Wu Z., Yan D., Xu X., Jiang Y. (2014). Tunable hysteresis in metal-insulator transition of nanostructured vanadium oxide thin films deposited by reactive direct current magnetron sputtering. Thin Solid Films, 552, 218–224. https://doi.org/10.1016/j.tsf.2013.12.007

Zhang S., Kim I. S., Lauhon L. J. (2011). Stoichiometry engineering of monoclinic to rutile phase transition in suspended single crystalline vanadium dioxide nanobeams. Nano Letters, 11(4), 1443–1447. https://doi.org/10.1021/nl103925m

Zhao L., Miao L., Liu C., Li C., Asaka T., Kang Y., Iwamoto Y., Tanemura S., Gu H., Su H. (2014). Solution-Processed $VO_2$-$SiO_2$ Composite Films with Simultaneously Enhanced Luminous Transmittance, Solar Modulation Ability and Anti-Oxidation property. Scientific Reports, 4(7000). https://doi.org/10.1038/srep07000

Zhou Y., Ramanathan S. (2012). Heteroepitaxial $VO_2$ thin films on GaN: Structure and metal-insulator transition characteristics. Journal of Applied Physics, 112(7), 074114. https://doi.org/10.1063/1.4758185

Zhu J., Gao Q. (2009). Mesoporous $MCo_2O_4$ (M = Cu, Mn and Ni) spinels: Structural replication, characterization and catalytic application in CO oxidation. Microporous and Mesoporous Materials 124(1-3), 144–152. DOI:10.1016/j.micromeso.2009.05.003

Zimmermann R., Claessen R., Reinert F., Steiner P., Hüfner S. (1998). Strong hybridization in vanadium oxides: evidence from photoemission and absorption spectroscopy. Journal of Physics: Condensed Matter 10 (25), 5697–5716. DOI: 10.1088/0953-8984/10/25/018

Zylbersztejn A., Mott, N. F. (1975). Metal-insulator transition in vanadium dioxide. Physical Review B, 11(11), 4383–4395. https://doi.org/10.1103/PhysRevB.11.4383

# Acknowledgements

# Curriculum Vitae

# Anna Krammer

## Personal Info

📍 Chemin de Mornex 7
1003 Lausanne

📞 +41 77 945 19 30

@ anna.krammer@epfl.ch

📅 1990-10-05

## Software

MS Office, Inventor, OriginPro, TfCalc, Adobe Illustrator.

## Skills

ultra-high vacuum deposition,
PVD (magnetron sputtering, HiPIMS)
scanning tunneling & electron microscopy
X-ray diffraction
X-ray and UV photoelectron spectroscopy
Fourier transform infrared spectrometry
UV-VIS spectrometry, ellipsometry
academic writing, teaching

## Languages

English — Bilingual Proficiency

French — Intermediate Level B2

Hungarian — Native Proficiency

Romanian — Bilingual Proficiency

## Interests

---

Researcher in the domain of solar energy with background in chemical engineering and materials science. Main focus on thermochromic thin films for novel switchable solar absorber coatings. Experience with vacuum processes, magnetron sputtering and a wide range of material characterisation techniques. Involved with teaching (Building Physics Course) and supervision of master students in materials science practical projects.

## Education

**2015 - 2020**
**EPFL**

### PhD student at École polytechnique fédérale de Lausanne, Switzerland

Solar Energy and Building Physics Laboratory (LESO-PB)
Study of thermochromic vanadium dioxide based switchable selective absorber coatings for overheating protection of solar thermal collectors.

**2014 - 2015**
TECHNISCHE UNIVERSITÄT DARMSTADT

### Master of Engineering, Technical University of Darmstad, Germany

Master in Functionalized Advanced Materials and Engineering
Cumulative GPA: 1.3
Focus on: Mechanical Properties of Ceramic Materials, Materials Chemistry, Ceramic Materials, Electrochemistry in Energy Applications

**2013 - 2014**
Grenoble INP phelma

### Master of Engineering, Institut National Polytechnique de Grenoble, France

Master in Functionalized Advanced Materials and Engineering
Cumulative GPA: 15.3/20
Focus on: Solid State Chemistry; Thin Films, surfaces and interfaces; Functional Materials Physics; Functional Polymers; Semiconductor Physics.

**2009 - 2013**

### Bachelor of Engineering, Babes-Bolyai University, Romania

Major in Chemical Engineering, Minor in Science and Engineering of Oxidic Materials and Nanomaterials
Cumulative GPA: 9.42/10
Study Abroad – Erasmus exchange student Budapest University of Technology and Economics Budapest, Hungary spring semester 2012

## Experience

**2015 - present**

### École polytechnique fédérale de Lausanne

Graduate Teaching Assistant
Building Physics Course (thermodynamics, acoustics, photometry etc)

**May - September 2014**

### École polytechnique fédérale de Lausanne

Research Intern at the Solar Energy and Building Physics Laboratory
Development of thermochromic coatings for solar thermal collectors

**July - August 2012**

### National Institute for Research and Development in Electrical Engineering, ICPE-CA

Research Intern
Synthesis of ceramic microspheres for thermo insulating coatings